

# Optimized Core Design of a Supercritical Carbon Dioxide-Cooled Fast Reactor

By

Christopher S. Handwerk

B.S. Systems Engineering  
United States Naval Academy, 1996

S.M. Nuclear Engineering  
S.M. Technology and Policy  
Massachusetts Institute of Technology, 1998

SUBMITTED TO THE DEPARTMENT OF NUCLEAR SCIENCE AND ENGINEERING IN  
PARTIAL FULFILLMENT OF THE REQUIREMENTS FOR THE DEGREE OF

DOCTOR OF PHILOSOPHY IN NUCLEAR SCIENCE AND ENGINEERING  
AT THE  
MASSACHUSETTS INSTITUTE OF TECHNOLOGY

JUNE 2007

The author hereby grants MIT permission to reproduce and to distribute  
publicly paper and electronic copies of this report document in whole or in part

Copyright © Massachusetts Institute of Technology (MIT)

All rights reserved



Signature of Author: \_\_\_\_\_

Department of Nuclear Science and Engineering

April 19, 2007

Certified by: \_\_\_\_\_

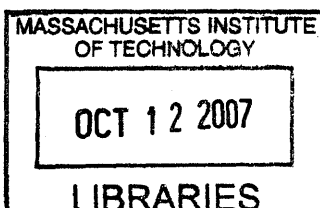
Prof. Michael J. Driscoll – Thesis Co-supervisor  
Professor Emeritus of Nuclear Science and Engineering

Certified by: \_\_\_\_\_

Dr. Pavel Hejzlar – Thesis Co-supervisor  
Principal Research Scientist

Accepted by: \_\_\_\_\_

Dr. Jeffrey A. Coderre  
Chairman, Department Committee on Graduate Students



ARCHIVES



# Optimized Core Design of a Supercritical Carbon Dioxide-Cooled Fast Reactor

By  
Christopher S. Handwerk

Submitted to the Department of Nuclear Science and Engineering on April 19, 2007 in partial fulfillment of the requirements for the degree of Doctor of Philosophy in  
Nuclear Science and Engineering

## Abstract

Spurred by the renewed interest in nuclear power, Gas-cooled Fast Reactors (GFRs) have received increasing attention in the past decade. Motivated by the goals of the Generation-IV International Forum (GIF), a GFR cooled by supercritical carbon dioxide (S-CO<sub>2</sub>), fueled with Light Water Reactor spent fuel transuranics, and directly coupled with a Brayton cycle is under investigation as part of a larger research effort at MIT. While the original GFR chosen by the GIF is a 600MW<sub>th</sub> version using Helium as a coolant, the work presented here is for a 2400 MW<sub>th</sub> core using S-CO<sub>2</sub> as a coolant, which has comparable thermal efficiency (~45%) at much lower temperatures (650°C v. 850°C)

A reactor core for use in this direct cycle S-CO<sub>2</sub> GFR has been designed which satisfies established neutronic and thermal-hydraulic steady state design criteria, while concurrently supporting the Gen-IV criteria of sustainability, safety, proliferation, and economics. Use of innovative Tube-in-Duct (TID) fuel has been central to accomplishing this objective, as it provides a higher fuel volume fraction and lower fuel temperatures and pressure drop when compared to traditional pin-type fuel. Further, this large fuel volume fraction allows for a large enough heavy metal loading for a sustainable core lifetime without the need for external blankets, enhancing the proliferation resistance of such an approach.

Use of Beryllium Oxide (BeO) as a diluent is explored as a means for both power shaping and coolant void reactivity (CVR) reduction in fast reactors. Results show that relatively flat power profiles can be maintained throughout a batch-loaded “battery” core life using a combination of enrichment and diluent zoning, due to the slight moderating effect of the BeO. Combining BeO diluent with the innovative strategy of using a thick volume of S-CO<sub>2</sub> coolant as the radial reflector yields negative CVR values throughout core life, a rare, if not unique accomplishment for fast reactors. The ability to maintain negative CVR comes from a combination of the effects of spectral softening due to the BeO diluent and the enhanced leakage upon voiding of the S-CO<sub>2</sub> radial reflector.

In support of assessing the neutronic self-controllability of this core, a simple first-order steady state design metric is developed, modified from other established methodology to suit the uniqueness of this core concept. The results of this analysis show that the core will passively shut itself down without violation of established core thermal limits in the event of several limiting Anticipated Transients Without SCRAM (ATWS) scenarios, except for a Loss of Coolant Without SCRAM at End of Core life. Since most of the requisites for passive core shutdown have been demonstrated within the parameter uncertainties of current estimates, the candidate core design is deemed sufficiently safe. Further, design solutions for fixing this deficiency are proposed.

Alternative cores using traditional pin-type fuel and innovative Internally-Cooled Annular Fuel (ICAF) have also been evaluated. While the performance of the TID core is superior, the results of the pin-type core show promise, pending design modification and relaxation of the imposed core pressure drop constraint, which would come at the expense of cycle efficiency and increased decay heat removal power requirements. Nevertheless, no improvement would be able to achieve a sustainable core (i.e. conversion ratio=1) using oxide fuel without the use of external blankets for pin fuel, even without the use of diluent in the fuel.

A comprehensive comparison of the thermal hydraulic and neutronic performance of TID fuel with that of the traditional pin-type fuel, as well as with the ICAF is also made, showing the fundamental reasons for their difference in performance.

**Thesis Co-supervisor:** Prof. Michael J. Driscoll  
**Title:** Professor Emeritus of Nuclear Science and Engineering

**Thesis Co-supervisor:** Dr. Pavel Hejzlar  
**Title:** Principal Research Scientist



## **Acknowledgements**

I am greatly appreciative of the Nuclear Energy Research Initiative (NERI) grant from the U. S. Department of Energy, “Optimized, Competitive Supercritical-CO<sub>2</sub> Cycle GRF for Gen-IV Service” (Project Number 04-044), which made this work possible.

First, I would like to thank my thesis advisor, Prof. Mike Driscoll, for his patience, wisdom, and careful and thoughtful attention to this research. His wide-ranging knowledge and youthful enthusiasm have made work on this project that much more enjoyable. I feel fortunate for my long standing relationship with him, as he not only shepherded me through the PhD process, but also served as an advisor during my master’s research several years ago.

Equally important in this whole process was my thesis reader, Dr. Pavel Hejzlar. Not only did his technical competence and acumen in reactor design and engineering prove invaluable, but his infectious enthusiasm and availability to provide support whenever needed (sometimes on short notice) was greatly appreciated. His love for his work serves as an excellent example for all professionally minded people.

Dr. Mike Pope was a collaborator on much of the work in this thesis, especially in the beginning of this project. Mike’s technical insights and immeasurable patience provided a large part of the foundation upon which this work was built. His help and friendship were highly valued and were a large part of what made this experience not only possible, but also enjoyable.

Nate Carstens provided integral technical support, as he built and helped troubleshoot the numerous problems that occurred with the main computing facility used to perform the majority of the calculations in this work, the 30 machine parallel computing “Echelon” Beowulf cluster. Not only did I learn a lot about computers from Nate, I made a new friend.

Several NSE departmental staff members were extremely helpful throughout this process. Rachel Morton provided excellent technical support with computing issues, as well as thought-provoking conversation. Richard St. Clair was helpful in providing valuable administrative support.

Other collaborators who were helpful include Prof. Eugene Shwageraus, of Ben Gurion University of the Negev in Israel, Dr. Zhiwen Xu, and Dr. Pete Yarsky. Prof. Shwageraus was extremely helpful in providing data on his concurrent work on the Lead Fast Reactor (LFR).

Finally and most importantly, I could not have done any of this without my family. I am thankful for being born to parents who always loved and encouraged me, no matter how silly my ideas seemed to them. I am lucky to have such a great life partner in my wife, Ashley, whose love and support allowed me to progress through this journey. Finally, I am fortunate to have such great kids, Samantha and Keller, who always remind me of what is most important in life.

## Table of Contents

<b>ABSTRACT .....</b>	<b>3</b>
<b>ACKNOWLEDGEMENTS.....</b>	<b>5</b>
<b>TABLE OF CONTENTS.....</b>	<b>6</b>
<b>TABLE OF FIGURES .....</b>	<b>10</b>
<b>TABLE OF TABLES.....</b>	<b>13</b>
<b>NOMENCLATURE.....</b>	<b>15</b>
<b>1 INTRODUCTION .....</b>	<b>17</b>
<b>FOREWORD.....</b>	<b>17</b>
<b>1.1 MOTIVATION .....</b>	<b>18</b>
<i>1.1.1 The History of the GFR .....</i>	<i>19</i>
<i>1.1.2 Selection of S-CO<sub>2</sub> as a coolant.....</i>	<i>21</i>
<b>1.2 OBJECTIVES OF THIS WORK .....</b>	<b>22</b>
<b>1.3 MAIN CHALLENGES AND CONTRIBUTIONS OF THIS WORK.....</b>	<b>25</b>
<i>1.3.1 Power Shaping in a Fast Reactor.....</i>	<i>25</i>
<i>1.3.2 Evolution Toward a Passively Safe GFR: Negative Coolant Void Reactivity.....</i>	<i>25</i>
<i>1.3.3 Quantitative Comparison of TID and pin-type fuel.....</i>	<i>26</i>
<b>1.4 ORGANIZATION OF THIS REPORT.....</b>	<b>27</b>
<b>2 GENERAL PLANT INFORMATION .....</b>	<b>29</b>
<b>2.1 INTRODUCTION .....</b>	<b>29</b>
<b>2.2 PLANT LAYOUT .....</b>	<b>30</b>
<b>2.3 S-CO<sub>2</sub> BRAYTON RECOMPRESSION CYCLE.....</b>	<b>32</b>
<b>2.4 THE TUBE-IN-DUCT (TID) FUEL ASSEMBLY.....</b>	<b>33</b>
<b>2.5 FUEL CYCLE CONCEPT.....</b>	<b>37</b>
<b>2.6 SUMMARY.....</b>	<b>40</b>
<b>3 THE DILUENT APPROACH.....</b>	<b>41</b>
<b>3.1 INTRODUCTION .....</b>	<b>41</b>
<b>3.2 TRADITIONAL MEANS OF SHAPING POWER.....</b>	<b>41</b>
<b>3.3 USE OF DILUENT TO SHAPE POWER .....</b>	<b>45</b>
<i>3.3.1 Root Cause of How Diluent Shapes Power .....</i>	<i>45</i>
<i>3.3.2 Use of Diluent to Shape Radial Power .....</i>	<i>52</i>
<i>3.3.3 Use of Diluent for Axial Power Shaping .....</i>	<i>54</i>
<b>3.4 USE OF DILUENT FOR COOLANT VOID REACTIVITY (CVR) REDUCTION.....</b>	<b>60</b>
<b>3.5 DILUENT MATERIAL SELECTION.....</b>	<b>63</b>
<i>3.5.1 Unique Issues Associated with the Use of BeO as a Diluent.....</i>	<i>66</i>
<b>3.6 OPTIMUM DILUENT CONCENTRATION .....</b>	<b>68</b>
<i>3.6.1 BeO Volume Fraction and Coolant Void Reactivity at Beginning of Life .....</i>	<i>69</i>
<i>3.6.2 BeO Concentration and Reactivity Limited Burnup .....</i>	<i>74</i>
<i>3.6.3 BeO Concentration and Coolant Void Reactivity at End of Life (EOL) .....</i>	<i>76</i>
<i>3.6.4 Summary of Diluent Concentration and Coolant Void Reactivity Study.....</i>	<i>81</i>
<b>3.7 SUMMARY AND CONCLUSIONS .....</b>	<b>82</b>
<b>4 TUBE-IN DUCT (TID) FUEL ASSEMBLY CORE DESIGN .....</b>	<b>84</b>
<b>4.1 INTRODUCTION .....</b>	<b>84</b>
<b>4.2 S-CO<sub>2</sub> RADIAL REFLECTOR .....</b>	<b>85</b>
<b>4.3 SELECTION OF AN AXIAL REFLECTOR.....</b>	<b>89</b>
<i>4.3.1 Chemical Compatibility.....</i>	<i>91</i>
<i>4.3.2 Material Properties .....</i>	<i>93</i>
<i>4.3.3 Beginning of Life (BOL) Coolant Void Reactivity (CVR).....</i>	<i>95</i>

4.3.4	<i>Semi-infinite Assembly Comparative Analysis</i> .....	95
4.3.5	<i>Selection of an Axial Reflector Material</i> .....	97
4.4	ASSESSMENT OF CORE PERFORMANCE: 1 <sup>ST</sup> CYCLE .....	98
4.4.1	<i>Intra-Assembly Peaking Factor</i> .....	100
4.4.2	<i>Achievable Burnup</i> .....	101
4.4.3	<i>Radial Power Peaking</i> .....	101
4.4.4	<i>Passive Reactivity Control</i> .....	102
4.4.5	<i>Thermal Hydraulic Results</i> .....	103
4.4.6	<i>Active Reactivity Control</i> .....	108
4.5	ASSESSMENT OF CORE PERFORMANCE: 2 <sup>ND</sup> AND 3 <sup>RD</sup> CYCLES .....	110
4.5.1	<i>Achievable Burnup</i> .....	112
4.5.2	<i>Radial Power Peaking</i> .....	116
4.5.3	<i>Passive Reactivity Control</i> .....	119
4.6	REACTOR PRESSURE VESSEL FLUENCE.....	119
4.6.1	<i>Determination of an Effective Fluence Limit</i> .....	120
4.6.2	<i>RPV Fluence Results</i> .....	122
4.7	CHEMICAL COMPATIBILITY .....	125
4.8	NEUTRON AND GAMMA HEATING.....	128
4.9	SUMMARY AND CONCLUSIONS .....	129
<b>5</b>	<b>COMPARISON OF DIFFERENT FUEL TYPES AND DILUENT STRATEGIES.....</b>	<b>130</b>
5.1	INTRODUCTION .....	130
5.2	NEUTRONIC STUDY.....	132
5.2.1	<i>Minimization of Coolant Void Reactivity (CVR)</i> .....	134
5.2.2	<i>Maximization of Reactivity Limited Burnup and Minimization of Critical Enrichment</i> .....	140
5.2.3	<i>Optimization among all of the variables</i> .....	143
5.2.4	<i>Neutronic Study Conclusions</i> .....	145
5.3	THERMAL-HYDRAULIC STUDY .....	146
5.3.1	<i>Pin-Type Fuel Thermal Hydraulic Results</i> .....	150
5.3.2	<i>TID Thermal Hydraulic Results</i> .....	153
5.3.3	<i>ICAF Thermal Hydraulic Results</i> .....	155
5.3.4	<i>Comparative Thermal Hydraulic Results</i> .....	156
5.4	CONCLUSIONS.....	159
<b>6</b>	<b>PIN TYPE CORE DESIGN.....</b>	<b>160</b>
6.1	INTRODUCTION .....	160
6.2	INTEGRATED NEUTRONIC-THERMAL HYDRAULIC CORE DESIGN PROCESS .....	160
6.3	THERMAL-HYDRAULIC ANALYSIS AND RESULTS .....	163
6.4	NEUTRONIC ANALYSIS AND RESULTS.....	166
6.4.1	<i>Achievable Burnup</i> .....	167
6.4.2	<i>Radial Power Peaking</i> .....	168
6.4.3	<i>Passive Reactivity Control</i> .....	169
6.4.4	<i>Active Reactivity Control</i> .....	171
6.4.5	<i>Increase in the Active Height of the Core</i> .....	172
6.5	SUMMARY AND CONCLUSIONS .....	175
<b>7</b>	<b>INTERNALLY COOLED ANNULAR FUEL (ICAF) CORE DESIGN.....</b>	<b>177</b>
7.1	INTRODUCTION .....	177
7.2	THERMAL HYDRAULIC ANALYSIS AND RESULTS.....	178
7.3	NEUTRONIC ANALYSIS AND RESULTS.....	180
7.3.1	<i>Achievable Burnup</i> .....	181
7.3.2	<i>Radial Power Peaking</i> .....	182
7.3.3	<i>Passive Reactivity Control</i> .....	183
7.3.4	<i>Active Reactivity Control</i> .....	184
7.4	SUMMARY AND CONCLUSIONS .....	184

<b>8</b>	<b>WASTE MANAGEMENT</b>	<b>185</b>
8.1	INTRODUCTION	185
8.2	TC-99 AND I-129 PRODUCTION IN THE TID CORE	189
8.3	MA/TRU MANAGEMENT OF TID CORE	192
8.4	PROLIFERATION RESISTANCE OF TID FUEL	195
8.5	COMPARATIVE ANALYSIS OF MA/TRU MANAGEMENT OF GFR CORES OF DIFFERENT FUEL TYPES ...	197
8.6	INVESTIGATION INTO SUITABLE INERT MATRIX FUELS FOR ACTINIDE BURNING	199
8.6.1	<i>Neutronic Considerations of Using Inert Matrix Fuels</i>	200
8.6.2	<i>Selection of an Appropriate Inert Matrix Fuel</i>	201
8.6.3	<i>Chemical Compatibility of Inert Matrix Fuel Material and S-CO<sub>2</sub></i>	205
8.6.4	<i>Quantitative Assessment of Fertile Matrix and Inert Matrix Fuels</i>	207
8.6.4.1	Reactivity Swing and Reactivity Limited Lifetime	208
8.6.4.2	Coolant Void Reactivity (CVR) and Effective Delayed Neutron Fraction ( $\beta_{eff}$ )	210
8.6.4.3	Doppler Coefficient of Reactivity	211
8.6.4.4	Actinide (MA/TRU) Burning Capability	212
8.6.4.5	Summary	214
8.7	SUMMARY AND CONCLUSIONS	216
<b>9</b>	<b>PRELIMINARY NEUTRONIC SAFETY ASSESSMENT</b>	<b>218</b>
9.1	INTRODUCTION	218
9.2	QUASI-STATIC METHOD	220
9.2.1	<i>Loss of Heat Sink Without SCRAM (LOHSWS)</i>	224
9.2.2	<i>Transient Overpower Without SCRAM (TOPWS)</i>	225
9.2.3	<i>Loss of Flow Without SCRAM (LOFWS)</i>	226
9.2.4	<i>Combined Loss of Flow and Heat Sink without SCRAM (CLOFHSWS)</i>	228
9.2.5	<i>Loss of Coolant Without SCRAM (LOCAWS)</i>	229
9.2.6	<i>Comparison of ATWS Scenarios</i>	231
9.2.7	<i>Results</i>	237
9.2.7.1	Calculation of Doppler Coefficient of Reactivity	239
9.2.7.2	Results Using the Original QSM	241
9.2.7.3	Results Using the Revised QSM (DCGQSM)	243
9.3	WATER INGRESS	249
9.4	CONCLUSIONS	251
<b>10</b>	<b>ECONOMIC ANALYSIS</b>	<b>253</b>
10.1	INTRODUCTION	253
10.2	NUCLEAR COST MODEL	254
10.2.1	<i>Capital Cost</i>	254
10.2.2	<i>Front End Fuel Cycle Cost</i>	257
10.2.3	<i>Back End Fuel Cycle Costs</i>	263
10.2.4	<i>Operations and Maintenance (O&amp;M) Costs and Decontamination and Disposal (D&amp;D) Costs</i>	264
10.3	ECONOMIC FACTORS FOR IMPLEMENTING PIN TYPE OR ICAF CORES	266
10.4	SUMMARY	269
<b>11</b>	<b>SUMMARY, CONCLUSIONS, AND RECOMMENDED FUTURE WORK</b>	<b>272</b>
11.1	INTRODUCTION	272
11.2	THE USE OF DILUENT IN A GFR	274
11.3	TID CORE DESIGN	280
11.4	COMPARISON OF DIFFERENT FUEL TYPES AND DILUENT STRATEGIES	287
11.5	COMPARISON AMONG TID, PIN TYPE, AND ICAF CORE DESIGNS	289
11.6	WASTE MANAGEMENT	292
11.7	PRELIMINARY NEUTRONIC SAFETY ASSESSMENT	294
11.8	ECONOMIC ANALYSIS	294
11.9	CONCLUSIONS	296

11.10	RECOMMENDED FUTURE WORK .....	297
<b>A</b>	<b>COMPUTATIONAL TOOLS .....</b>	<b>300</b>
A.1	INTRODUCTION .....	300
A.2	NEUTRONIC ANALYSIS TOOLS .....	300
A.2.1	<i>MCODE</i> .....	300
A.2.2	<i>MCNP</i> .....	301
A.2.3	<i>ORIGEN</i> .....	302
A.2.4	<i>NJOY</i> .....	302
A.3	THERMAL HYDRAULIC ANALYSIS TOOLS .....	303
A.3.1	<i>FLOWSPLIT</i> .....	303
A.3.2	<i>ANNULCO2</i> .....	303
A.4	CHEMICAL COMPATIBILITY CODE .....	304
A.4.1	<i>HSC Chemistry® 5.1</i> .....	304
<b>B</b>	<b>MATLAB INTERFACES .....</b>	<b>305</b>
B.1	INTRODUCTION .....	305
B.2	FLOWSPLIT-MATLAB INTERFACE .....	306
B.3	THERMAL-HYDRAULIC CALCULATIONS ALGORITHMS .....	309
B.3.1	<i>FLOWSPLIT-MATLAB Interface MATLAB Files</i> .....	314
B.4	ANNULCO2-MATLAB INTERFACE .....	329
B.4.1	<i>ANNULCO2-MATLAB Interface MATLAB Files</i> .....	331
<b>C</b>	<b>EXAMPLE INPUT DECKS .....</b>	<b>336</b>
	<b>REFERENCES .....</b>	<b>358</b>

## Table of Figures

Figure 2.1: Conceptual Drawing of the 1200 MW <sub>e</sub> 2-Loop Plant Layout.....	30
Figure 2.2: Simplified Plant Layout – Cartoon Depiction.....	31
Figure 2.3: S-CO <sub>2</sub> Brayton Recompression Cycle [from Dostal et al., 2004] .....	32
Figure 2.4: Horizontal Cross Section of a Tube-in-Duct (TID) Fuel Assembly .....	34
Figure 2.5: 3-Dimensional Rendering of a Hex-nut Fuel Pellet.....	34
Figure 2.6: Vertical Cross Section of a Tube-in-Duct (TID) Fuel Assembly.....	35
Figure 2.7: Fuel Cycle Flowchart.....	38
Figure 3.1: Radial Power Profile as a Function of Burnup for a 2-zone Enrichment Zoned Core .....	42
Figure 3.2: Radial Power Shape as a Function of Burnup for a 2-zone Enrichment Zoned Core after Exchanging Inner and Outer Fuel at 20 MWD/kg.....	43
Figure 3.3: Core Eigenvalue as a function of Burnup: Shuffling v. not shuffling at 20 MWD/kg for a 2-zone Enrichment Zoned Core.....	43
Figure 3.4: Effect of Diluent Concentration on the Neutron Energy Spectrum .....	45
Figure 3.5: Comparison of Axial Power Shapes for 2 cases in a Semi-Infinite Assembly .....	47
Figure 3.6: Comparison of Axial Power Shapes for 3 cases in a Semi-Infinite Assembly .....	47
Figure 3.7: Comparison of Axial Power Shapes for Candidate Diluents in a Semi-Infinite Assembly .....	48
Figure 3.8: Comparison of Microscopic Fission Cross Sections.....	49
Figure 3.9: Comparison of Neutron Energy Spectra: No diluent and Reduced volume Fraction Cases .....	50
Figure 3.10: Comparison of Neutron Energy Spectra: No Diluent and SiC Cases .....	50
Figure 3.11: Comparison of Neutron Energy Spectra: No Diluent and BeO Cases .....	51
Figure 3.12: Comparison of Neutron Energy Spectra: No Diluent and TiC Cases .....	51
Figure 3.13: Illustrative Example of Using Diluent to Shape Radial Power For a Core with Uniform .....	52
Figure 3.14: Eigenvalue-burnup Comparison between the Two Enrichment Zone Core with no Diluent and the Uniform Enrichment Three Diluent Zone Core.....	53
Figure 3.15: Coolant Subchannel Unit Cell .....	55
Figure 3.16: Comparison of Axial Power Profiles Used for FLOWSPLIT Analysis of Axial Cladding Temperature Flattening.....	57
Figure 3.17: Comparison of Wall Temperature Profiles in the Peak Channel Assuming a 1.1 Radial Peaking Factor (using FLOWSPLIT).....	58
Figure 3.18: Axial Power Shapes Resulting from Axial Diluent Zoning.....	59
Figure 3.19: Comparison of Wall Temperature Profiles Resulting from Attempts at Axial Power Shaping in the Peak Channel (assuming a 1.1 Radial Peaking Factor).....	59
Figure 3.20: Illustration of the Effect of Spectral Softening on Coolant Void Reactivity .....	62
Figure 3.21: Microscopic Cross Section for the Be-9( $\gamma,n$ )Be-8 Reaction .....	67
Figure 3.22: Void ( $\Delta k$ and $\$$ ) and $\beta_{\text{eff}}$ as a function of BeO volume fraction at BOL.....	69
Figure 3.23: Fission Fraction of 4 Largest Isotopic Contributors at BOL.....	70
Figure 3.24: Microscopic Fission Cross Section of Pu-239 and U-238 (top to bottom) .....	71
Figure 3.25: Behavior of $\beta_{\text{eff}}$ and $\bar{\beta}$ as a function of BeO volume fraction at BOL .....	72
Figure 3.26: Void ( $\Delta k$ and $\$$ ) and $\bar{\beta}$ as a function of BeO volume fraction.....	73
Figure 3.27: Reactivity Limited Burnup as a function of BeO Concentration .....	74
Figure 3.28: Reactivity Limited Lifetime as a function of BeO Concentration .....	75
Figure 3.29: Reactivity Limited Burnup as a function of BeO Concentration .....	75
Figure 3.30: Reactivity Swing as a function of BeO Concentration .....	76
Figure 3.31: Void ( $\Delta k$ and $\$$ ) and $\beta_{\text{eff}}$ as a function of BeO volume fraction at EOL.....	77
Figure 3.32 : Fission Fraction of 5 Largest Isotopic Contributors at EOL.....	77
Figure 3.33: Comparison of the Microscopic Capture to Fission Cross Section Ratio of Pu-239 and Pu-241 ....	78
Figure 3.34: Behavior of $\beta_{\text{eff}}$ , $\bar{\beta}$ , and $I$ as a function of BeO volume fraction at EOL.....	80
Figure 3.35: Void ( $\Delta k$ and $\$$ ) and $\bar{\beta}$ as a function of BeO volume fraction at EOL .....	80
Figure 3.36: Ratio of EOL/BOL Void Reactivities.....	81
Figure 3.37: Illustration of Fundamental Trade-offs in Neutronic Performance from the Use of Diluent.....	83
Figure 4.1: 1/6 <sup>th</sup> Core Map of the S-CO <sub>2</sub> Reflected Strategy .....	86

Figure 4.2: Axial Cross Section of the S-CO <sub>2</sub> Reflected Strategy .....	86
Figure 4.3: Microscopic Scattering Cross Section of Titanium .....	90
Figure 4.4: Reactivity Limited Burnup and Reactivity Swing of Axial Reflector Candidate Materials .....	96
Figure 4.5: Intra-Assembly Power Distribution .....	100
Figure 4.6: Excess Reactivity as a Function of Burnup for the 1 <sup>st</sup> Cycle of the TID Core.....	101
Figure 4.7: Unrodded Radial Power Shape as a Function of Burnup for the TID Core for the 1 <sup>st</sup> Cycle.....	102
Figure 4.8: Clad Thickness-Clad Outer Diameter Correlation (from [Garkisch and Petrovic, 2004]).....	106
Figure 4.9: Gap Thickness-Clad Outer Diameter Correlation (from [Garkisch and Petrovic, 2004]).....	106
Figure 4.10: Acceptable T/H Envelope for the TID Fuel Assembly Core .....	107
Figure 4.11: Illustration of Fuel Cycle Mass Flow.....	111
Figure 4.12: Excess Reactivity as a Function of Burnup for All Three Cycles of the TID Core .....	113
Figure 4.13: Comparison of Am-242m Burnup-dependent Composition Among All Three Cycles .....	114
Figure 4.14: Comparison of Excess Reactivity for the First Cycle with and without Am-242m.....	114
Figure 4.15: Unrodded Radial Power Shape as a Function of Burnup for the TID Core for the 2 <sup>nd</sup> Cycle.....	116
Figure 4.16: Unrodded Radial Power Shape as a Function of Burnup for the TID Core for the 3 <sup>rd</sup> Cycle .....	117
Figure 4.17: Unrodded Radial Power Shape as a Function of Burnup for the TID Core:.....	117
Figure 4.18: Unrodded Radial Power Shape as a Function of Burnup for the TID Core:.....	118
Figure 4.19: Generic Example of the Effect of Irradiation on the Integrity of a RPV [taken from USNRC, 2001] .....	120
Figure 4.20: Core Layout Used for RPV Fluence Calculations [case (1)] .....	123
Figure 4.21: Equilibrium Composition for the UO <sub>2</sub> -CO <sub>2</sub> Reaction as a Function of Temperature .....	126
Figure 4.22: Equilibrium Compositions for the UO <sub>2</sub> -BeO-CO <sub>2</sub> System as a Function of Temperature .....	127
Figure 5.1: Unit Cell Representation of the Three Different Fuel Types Studied.....	131
Figure 5.2: Comparison of Neutron Spectra of Heterogeneous Cases .....	134
Figure 5.3: Comparison of Neutron Spectra of Homogeneous Cases .....	135
Figure 5.4: Comparison of BOL Coolant Void Reactivity (CVR) Behavior among Diluent Approaches for Varying BeO Volume Fraction in the Assembly .....	136
Figure 5.5: Comparison of BOL Coolant Void Reactivity (CVR) Behavior among Diluent Approaches for Varying Fuel Volume Fraction in the Assembly .....	136
Figure 5.6: Relationship between BOL CVR and Pu-239 Fission Fraction for the Homogeneous Diluent Cases .....	137
Figure 5.7: Relationship between N <sub>49</sub> /N <sub>28</sub> and TRU Enrichment.....	139
Figure 5.8: Fuel Cycle Cost as a Function of Burnup for Different Unit Fuel Costs .....	141
Figure 5.9: Reactivity Limited Burnup as a Function of Critical Enrichment .....	142
Figure 5.10: Reactivity Limited Burnup as a Function of BeO Volume Fraction.....	143
Figure 5.11: BOL Coolant Void Reactivity (CVR) as a Function of BeO Volume Fraction.....	144
Figure 5.12: Critical Enrichment as a Function of BeO Volume Fraction .....	144
Figure 5.13: Acceptable T/H Envelope for Pin-type Fuel with No BeO.....	151
Figure 5.14: Acceptable T/H Envelope for Pin-type Fuel with BeO.....	151
Figure 5.15: Acceptable T/H Envelope for Pin-type Fuel with a BeO Slug .....	152
Figure 5.16: Acceptable T/H Envelope for TID Fuel with No BeO.....	153
Figure 5.17: Acceptable T/H Envelope for TID Fuel with BeO .....	153
Figure 5.18: Acceptable T/H Envelope for TID Fuel with BeO with Revised Scale.....	154
Figure 5.19: Acceptable T/H Envelope for ICAF with No BeO .....	155
Figure 5.20: Acceptable T/H Envelope for ICAF with BeO .....	155
Figure 6.1: Flowchart of the Integrated Neutronic/Thermal Hydraulic Core Design Process.....	161
Figure 6.2: Acceptable T/H Envelope for the Pin Core .....	165
Figure 6.3: Pin-Type Core Layout and Key Parameters .....	166
Figure 6.4: Comparison of Reactivity Limited Burnups of the TID and Pin-type Cores .....	167
Figure 6.5: Unrodded Radial Power Shape as a Function of Burnup for the Pin Type Core .....	168
Figure 6.6: Comparison of BOL Pin-type Core and TID Core Neutron Energy Spectra.....	170
Figure 6.7: Comparison of Reactivity Limited Burnups Among TID and Pin Core Options .....	174
Figure 6.8: Unrodded Radial Power Shape as a Function of Burnup for the Taller Pin Type Core.....	174
Figure 7.1: Unit Cell Representation of Internally Cooled Annular Fuel (ICAF).....	177
Figure 7.2: Acceptable T/H Envelope for the ICAF Core.....	178
Figure 7.3: Pin-Type Core Layout and Key Parameters .....	180

Figure 7.4: Comparison of Reactivity Limited Burnups of the TID and Pin-Type, and ICAF Cores.....	181
Figure 7.5: Unrodded Radial Power Shape as a Function of Burnup for the ICAF Type Core .....	182
Figure 8.1: Isotopic Contribution of Spent LWR Fuel to Radiotoxicity [ORNL, 1995].....	186
Figure 8.2: Expected Radiation Exposure from Yucca Mountain by Constituent .....	187
Figure 8.3: The Impact of Removing Actinides from Nuclear Waste on Radiotoxicity [Hejzlar, 2005].....	188
Figure 8.4: Comparison of Neutron Energy Spectra for GFR Fuel with and without diluent with a LFR.....	191
Figure 8.5: Microscopic Cross Section for Absorption (Capture) for Tc-99 and I-129 .....	191
Figure 8.6: Comparison of Neutron Spectra of the TID, Pin and ICAF GFR Cores.....	199
Figure 8.7: Thermal Conductivity of MgO shown in Comparison with that of UO <sub>2</sub> (reprinted from [Medvedev, 2004]).....	204
Figure 8.8: Equilibrium Compositions of the S-CO <sub>2</sub> -MgO Reaction.....	205
Figure 8.9: Equilibrium Compositions of the S-CO <sub>2</sub> -MgO Reaction, expanded scale.....	206
Figure 8.10: Semi-Infinite Assembly Eigenvalue Comparison among the Fertile and IMF Assemblies.....	209
Figure 8.11: Comparison of Neutron Energy Spectra for the Fertile and IMF Assemblies .....	213
Figure 9.1: Illustration of How the Results of the Quasi-Static Method Should be Viewed.....	221
Figure 9.2: Simplified Plant Layout – Line Diagram.....	223
Figure 9.3: Simplified Plant Layout – Cartoon Depiction.....	223
Figure 9.4: Core Reactivity as a Function of Fuel Temperature .....	241
Figure 9.5: Acceptable T/H Envelope for TID Fuel with BeO and $\overline{\Delta T_f}$ limit.....	247
Figure 9.6: Effect of Water Ingress on Criticality at BOL and MOL for the TID GFR Core .....	250
Figure 10.1: Levelized Fuel Cycle Cost as a Function of Burnup for the GFR v. an LWR.....	258
Figure 10.2: Levelized Fuel Cycle Cost as a Function of Specific Power for the GFR v. an LWR.....	259
Figure 10.3: LWR and GFR Front End of the Fuel Cycle Flowcharts.....	260
Figure 10.4: Cost of Electricity Comparison between the Candidate GFR and an advanced LWR.....	269
Figure 11.1: Effect of Diluent Concentration on the Neutron Energy Spectrum .....	275
Figure 11.2: Unrodded Radial Power Shape as a Function of Burnup for the TID Core for the 1 <sup>st</sup> Cycle.....	276
Figure 11.3: Illustration of the Effect of Spectral Softening on Coolant Void Reactivity .....	277
Figure 11.4: Illustration of Fundamental Trade-offs in Neutronic Performance from the Use of Diluent.....	280
Figure 11.5: 1/6 <sup>th</sup> Core Map of the S-CO <sub>2</sub> Reflected Strategy .....	283
Figure 11.6: Axial Cross Section of the S-CO <sub>2</sub> Reflected Strategy.....	283
Figure 11.7: Acceptable T/H Envelope for TID Fuel with BeO .....	288
Figure 11.8: Comparison of Reactivity Limited Burnups of the TID and Pin-Type, and ICAF Cores.....	291
Figure B.1: Roadmap for FLOWSPLIT-MATLAB Interface.....	308
Figure B.2: Pictorial Representation of a Hexagonal Infinite Lattice .....	309
Figure B.3: Roadmap for FLOWSPLIT-ANNULCO <sub>2</sub> Interface .....	330



## Table of Tables

Table 1.1: Characteristics of Early GCFRs (taken from [Driscoll et al, 2003]) .....	20
Table 1.2: Objectives of this Work as They Relate to Generation-IV Criteria.....	24
Table 2.1: Key Plant Parameters .....	29
Table 2.2: Current Status of Ex-core GFR Plant Features .....	39
Table 3.1: Suggested Criteria for Evaluation in Diluent Selection .....	64
Table 3.2: Comparison of BOL and EOL CVR among Candidate Diluents .....	64
Table 3.3: Effects of Diluent on Coolant Void Reactivity at BOL and EOL .....	79
Table 4.1: Key Parameters of the TID Fuel Assembly Core Design.....	84
Table 4.2: Calculation of Bare Core (radially and axially) Leakage .....	87
Table 4.3: Calculation of Radially Bare, Axially Reflected Core Leakage.....	87
Table 4.4: Chemical Compatibility of Axial Reflector Candidate Materials .....	92
Table 4.5: Select Material Properties of Axial Reflector Candidate Materials .....	93
Table 4.6: Prediction of Heat Capacities of Axial Reflector Candidate Materials .....	94
Table 4.7: Whole Core BOL $k_{eff}$ and CVR for Axial Reflector Candidate Materials .....	95
Table 4.8: Semi-Infinite CVR over Core Life for Axial Reflector Candidate Materials.....	96
Table 4.9: Summary of Results from the Axial Reflector Candidate Study.....	98
Table 4.10: Neutronic and Thermal Hydraulic Goals for the 1 <sup>st</sup> Cycle of the TID Core Design .....	99
Table 4.11: Coolant Void Reactivity Values for the TID Core.....	103
Table 4.12: $k_{eff}$ Values for Stuck Rod Scenarios at the Most Reactive Time in Life for the TID Core.....	109
Table 4.13: Control Rod Worth at the Most Reactive Time in Life for the TID Core .....	110
Table 4.14: Comparison of U/Pu/MA/TRU Vectors for All Cycles .....	112
Table 4.15: Neutronic Performance Parameter Comparison Among All Three Cycles of the TID Core .....	113
Table 4.16: Unrodded Coolant Void Reactivity Values for the TID Core for All Three Cycles .....	119
Table 4.17: RPV Fluence Calculation Results .....	124
Table 4.18: Chemical Compatibility Results for Core Materials .....	125
Table 4.19: Photon and Gamma Heating for the Semi-Infinite Assembly and Whole Core Models.....	128
Table 5.1: Fuel Types and Diluent Strategies Chosen for Comparison.....	131
Table 5.2: Neutronically Assessed Cases of Fuel Types and Diluent Strategies.....	132
Table 5.3: Constraints and Parameters Used for the Thermal Hydraulic Study.....	150
Table 5.4: Key for Graphical Representation of Thermal Hydraulic Limits.....	150
Table 5.5: Qualitative Ranking, Best to Worst, of Fuel Types.....	156
Table 5.6: Quantitative Comparison Among Fuel Types where $vf_A$ is Maximized .....	157
Table 5.7: Thermal Hydraulic Results for other TID cases.....	158
Table 6.1: Comparison of Thermal Hydraulic Parameters for TID and Pin Core Designs where Performance is Optimized .....	166
Table 6.2: Coolant Void Reactivity at BOL and EOL for the Pin Core Design.....	169
Table 6.3: $k_{eff}$ Values for Stuck Rod Scenarios at the Most Reactive Time in Life for the Pin-Type Core .....	171
Table 6.4: Control Rod Worth at the Most Reactive Time in Life for the Pin-Type Core.....	171
Table 6.5: Void Reactivity Comparison between the Pin-Type Core and the 1m Taller Pin-Type Core.....	173
Table 6.6: Comparison of Key Neutronic Performance Criteria Among the TID and Pin-Type Cores.....	175
Table 7.1: Comparison of Thermal-Hydraulic Parameters for TID and Pin Core Designs where Performance is Optimized .....	179
Table 7.2: Coolant Void Reactivity at BOL and EOL for the Pin Core Design.....	183
Table 8.1: Comparison of Operating Characteristics of an LWR, GFR, and LFR.....	188
Table 8.2: Comparison of Long Lived Net Fission Product Production Among a PWR, GFR, and LFR .....	189
Table 8.3: Comparison of Spectrum-Averaged Cross Sections ( $\sigma_a$ ) and Fission Yields .....	190
Table 8.4: Detailed Mass Flow of Key MA/TRU Isotopes for All 3 cycles of the Candidate GFR Lifetime....	193
Table 8.5: Comparison of Net Pu and MA Production Among a PWR, GFR, and LFR .....	194
Table 8.6: Detailed Mass Flow of Key MA/TRU Isotopes for All 3 cycles of the LFR Lifetime (Reprinted from [Todreas and Hejzlar, 2007]) .....	195
Table 8.7: Comparison of Pu Component of TRU Vectors for LWR and GFR Spent Fuel.....	197
Table 8.8: Comparison of Net Pu and MA Production and Initial Core Loading .....	198
Table 8.9: Gibbs Free Energy of the MgO-SCO <sub>2</sub> system.....	207

Table 8.10: Comparison of Characteristics of the Semi-Infinite Fertile and IMF Assemblies .....	209
Table 8.11: Comparison of Unrodded CVR and $\beta_{\text{eff}}$ for the IMF and Fertile Assemblies .....	210
Table 8.12: Comparison of Unrodded Doppler Reactivity Coefficient for the IMF and Fertile Assemblies.....	211
Table 8.13: Comparison of Actinide Destruction Capability for the IMF and Fertile Assemblies .....	212
Table 8.14: Summary of Performance Comparison between the Fertile and IMF Assemblies.....	214
Table 9.1: Limiting Transients and Installed Defenses .....	219
Table 9.2: Loss of Flow Scenarios (Without SCRAM) and Accompanying Effect on Heat Sink .....	227
Table 9.3: Assumptions Made for Key Parameters in the ATWS scenarios from the Initial Steady State Condition to the Final Steady State Condition.....	231
Table 9.4: Summary of Reactivity Insertion Mechanisms for Transients in the Direct Cycle GFR Quasi-Static Method (DCGQSM) .....	231
Table 9.5: Summary of Asymptotic Outlet Temperatures for Bounding ATWS Scenarios.....	232
Table 9.6: Summary of Limiting Reactivity Relationships that Provide the Passive Safety Envelope for the DCGQSM .....	237
Table 9.7: Summary of Reactivity Parameters for the GFR TID Core .....	239
Table 9.8: Limiting ATWS Scenarios and Applicable Limits for the Original QSM .....	242
Table 9.9: Summary of Passive Safety Evaluation Using the Original QSM .....	242
Table 9.10: Evaluation of Whether LOCAWS or CLOFHSWS is More Limiting Throughout Core Life.....	243
Table 9.11: Summary of Passive Safety Evaluation Using DCGQSM .....	243
Table 9.12: Passive Safety Evaluation against the CLOFHSWS/LOCAWS Scenario .....	244
Table 9.13: Values Necessary to Satisfy Passive Safety at EOL for the LOCAWS Scenario .....	245
Table 9.14: Comparison of geometries which maximize $\nu_{\text{A}}$ with and without the $\overline{\Delta T}_f$ limit .....	248
Table 10.1: Capital Cost Estimates [from NEA, 2002].....	254
Table 10.2: Levelized Capital Cost Estimates of the candidate GFR v. an advanced LWR .....	255
Table 10.3: Levelized Fuel Cycle Cost Estimates of the candidate GFR v. an advanced LWR .....	258
Table 10.4: Supporting Assumptions and Results of Fuel Cycle Costs of the Candidate GFR v. an LWR.....	262
Table 10.5: Spent Fuel Volume and Annual Levelized Storage Costs of the Candidate GFR v. an LWR .....	264
Table 10.6: Levelized O&M and D&D Cost Estimates of the candidate GFR v. an advanced LWR.....	265
Table 10.7: Comparison of Spent Fuel Volume and Annual Levelized Storage Costs .....	267
Table 10.8: Comparison of Front End Fuel Cycle Cost Factors.....	268
Table 11.1: Key GFR Plant Parameters .....	272
Table 11.2: Key Parameters of the TID Fuel Assembly Core Design.....	281
Table 11.3: Neutronic and Thermal Hydraulic Goals for the 1 <sup>st</sup> Cycle of the TID Core Design .....	284
Table 11.4: Neutronic Performance Parameter Comparison Among All Three Cycles of the TID Core .....	285
Table 11.5: Comparison of Key Parameters Among the TID and Pin-Type Cores .....	290
Table 11.6: Comparison of the Cost of Electricity among an LWR and.....	295
Table B.1: Description of MATLAB Scripts for the FLOWSPLIT-MATLAB Interface.....	306

## Nomenclature

ABR	<u>A</u> ctinide <u>B</u> urner <u>R</u> eactor
AFCI	<u>A</u> dvanced <u>F</u> uel <u>C</u> ycle <u>I</u> nitiative
ANL	<u>A</u> rgonne <u>N</u> ational <u>L</u> aboratory
ATWS	<u>A</u> nticipated <u>T</u> ransient <u>W</u> ithout <u>S</u> CRAM
$\beta_{\text{eff}}$	Effective delayed neutron fraction
BeO	<u>B</u> eryllium <u>O</u> xide
BOC	<u>B</u> eginning <u>O</u> f <u>C</u> ycle
BOL	<u>B</u> eginning <u>O</u> f <u>L</u> ife
CLOFHSWS	<u>C</u> ombined <u>L</u> oss <u>O</u> f <u>F</u> low and <u>H</u> eat <u>S</u> ink <u>W</u> ithout <u>S</u> CRAM
COE	<u>C</u> ost <u>O</u> f <u>E</u> lectricity
CR	<u>C</u> onversion <u>R</u> atio
CVR	<u>C</u> oolant <u>V</u> oid <u>R</u> eactivity
D&D	<u>D</u> econtamination & <u>D</u> isposal
DCGQSM	<u>D</u> irect <u>C</u> ycle <u>G</u> FR <u>Q</u> uasi <u>S</u> tatic <u>M</u> ethod
DHR	<u>D</u> ecay <u>H</u> eat <u>R</u> emoval
ECS	<u>E</u> mergency <u>C</u> ooling <u>S</u> ystem
EFPD	<u>E</u> ffective <u>F</u> ull <u>P</u> ower <u>D</u> ays
EFPY	<u>E</u> ffective <u>F</u> ull <u>P</u> ower <u>Y</u> ears
EOC	<u>E</u> nd <u>O</u> f <u>C</u> ycle
EOL	<u>E</u> nd <u>O</u> f <u>L</u> ife
GFR	<u>G</u> as-cooled <u>F</u> ast <u>R</u> eactor (also GCFR)
GIF	<u>G</u> eneration-IV International <u>F</u> orum
GNEP	<u>G</u> lobal <u>N</u> uclear <u>E</u> nergy <u>P</u> artnership
H/D	<u>H</u> eight to <u>D</u> iameter Ratio, used to characterize wire wrap
ICAF	<u>I</u> nternally <u>C</u> ooled <u>A</u> nnular <u>F</u> uel
IFR	<u>I</u> ntegral <u>F</u> ast <u>R</u> eactor
IMF	<u>I</u> nter <u>M</u> atrix <u>F</u> uel
$k_{\text{eff}}$	Effective multiplication factor, also known as the core eigenvalue
LFR	<u>L</u> ead <u>F</u> ast <u>R</u> eactor
LMR	<u>L</u> iquid <u>M</u> etal <u>R</u> eactor
LOCA	<u>L</u> oss <u>O</u> f <u>C</u> oolant <u>A</u> ccident
LOCAWS	<u>L</u> oss <u>O</u> f <u>C</u> oolant <u>A</u> ccident <u>W</u> ithout <u>S</u> CRAM
LOFWS	<u>L</u> oss <u>O</u> f <u>F</u> low <u>W</u> ithout <u>S</u> CRAM
LOHSWS	<u>L</u> oss <u>O</u> f <u>H</u> eat <u>S</u> ink <u>W</u> ithout <u>S</u> CRAM
LWR	<u>L</u> ight <u>W</u> ater <u>R</u> eactor
MA	<u>M</u> inor <u>A</u> ctinides
MCNP	<u>M</u> onte <u>C</u> arlo <u>N</u> -Particle code
MCODE	<u>M</u> CNP <u>O</u> RIGEN <u>D</u> epletion code
MOL	<u>M</u> iddle <u>O</u> f <u>L</u> ife, typically at the burnup where cycle excess reactivity is greatest
O&M	<u>O</u> perations & <u>M</u> aintenance
ODS	<u>O</u> xide <u>D</u> ispersion <u>S</u> trengthened stainless steel
ORIGEN	<u>O</u> ak <u>R</u> idge <u>I</u> sotope <u>G</u> ENERation and depletion code
PCIV	<u>P</u> restressed <u>C</u> ast <u>I</u> ron <u>V</u> essel
pcm	per cent mille ( $10^{-5}$ )

PCR <sub>V</sub>	<u>P</u> restressed <u>C</u> oncrete <u>R</u> eactor <u>V</u> essel
PCS	<u>P</u> ower <u>C</u> onversion <u>S</u> ystem
P/D	<u>P</u> itch to <u>D</u> iameter Ratio
PRA	<u>P</u> robabilistic <u>R</u> isk <u>A</u> ssessment
QSM	<u>Q</u> uasi <u>S</u> tatic <u>M</u> ethod
S-CO <sub>2</sub>	Supercritical Carbon Dioxide
SCRAM	<u>S</u> afety <u>C</u> ontrol <u>R</u> od <u>A</u> xe <u>M</u> an (rapid control rod insertion)
SCS	<u>S</u> hutdown <u>C</u> ooling <u>S</u> ystem
SCWR	<u>S</u> upercritical <u>W</u> ater <u>R</u> eactor
SiC	<u>S</u> ilicon <u>C</u> arbide
T/H	<u>T</u> hermal- <u>H</u> ydraulic
TiC	<u>T</u> itanium <u>C</u> arbide
TID	<u>T</u> ube- <u>I</u> n- <u>D</u> uct
TOPWS	<u>T</u> ransient <u>O</u> ver <u>P</u> ower <u>W</u> ithout <u>S</u> CRAM
TRU	<u>T</u> Rans <u>U</u> ranics
$v_c$	Coolant volume fraction
$v_f$	Fuel volume fraction
w/o	Weight percent

# 1 Introduction

## ***Foreword***

The objective of the present work was to design a reactor core for use in a direct cycle supercritical carbon dioxide (S-CO<sub>2</sub>) Gas-cooled Fast Reactor (GFR) and assess its performance, relative to both currently established guidelines as well as other competing Generation-IV reactor options. This work is part of a larger research effort, the Nuclear Energy Research Initiative (NERI) funded “Optimized, Competitive Supercritical-CO<sub>2</sub> Cycle GFR for Gen-IV Service” (Project 04-44), which seeks to develop an integrated overall plant design for such a GFR, based on the compact and highly efficient, direct S-CO<sub>2</sub> Brayton cycle. This project has three major tasks:

### **Task 1. Core Design and Performance Assessment**

- Optimize features of vented fuel concept using tube-in-duct assemblies
- Develop pin type core design as a benchmark for comparisons and as a fallback option
- Confirm the burning capability of Transuranics (TRU) and Minor Actinides (MA)

### **Task 2. PRA Guided Design of Safety Systems**

- Develop decay heat removal design for accident, normal shutdown, and refueling.
- Develop improved emergency power systems, such as microturbines or fuel cells.
- Develop both active and passive means of shutdown assurance to preclude an Anticipated Transient Without SCRAM (ATWS).

### **Task 3. Overall Plant Design and Economic Assessment.**

- Design power cycles for core exit temperatures ranging from 550 to 700°C.
- Demonstrate integration with high-temperature electrolysis of steam for H<sub>2</sub> production.
- Estimate busbar costs of electricity relative to other reactor options.

While the focus of the work presented here is Task 1, elements of the third bullets of Tasks 2 and 3 are also included in this work.

## **1.1 Motivation**

Spurred by the renewed interest in nuclear power, Gas-cooled Fast Reactors (GFRs) have received increasing attention in the past decade. While extensive work had been done on this and other fast breeder reactor concepts in the 1960s and 1970s, concerns over the associated proliferation aspects of such a strategy and waning interest in the expansion of nuclear energy due to economic unattractiveness and declining public acceptance led to the cessation of funding on these projects in the early 1980s. With the advent of more proliferation resistant fuel reprocessing technologies, an industrial experience base in reprocessing (in France and Japan), the improved economic performance of existing nuclear reactors, the growing burden of current LWR waste, and the specter of climate change looming, carbon-free nuclear technologies utilizing a closed fuel cycle have become appreciably more attractive. All of these factors led to the end of a nearly two decade long hiatus from GFR research and development (R&D).

Specifically, the United States has participated in the Generation-IV International Forum (GIF), a group of 10 member countries which seeks to shape and collaborate on the R&D needs of the next generation of nuclear reactors, learning from the lessons of the previous 50 years of reactor experience. The GIF selected six promising reactor types that it believed would satisfy the attributes of a next generation reactor, which the GIF defined under the rubrics of enhanced safety, sustainability/waste minimization, improved economics, and proliferation resistance [GIF, 2002]. The GFR was one of the six reactor types selected, based on its top-ranking in sustainability, and good rating in safety, economics, and in proliferation resistance and physical protection [Weaver et al, 2004]. Domestically, the United States has implemented several expansive R&D programs, e.g. the Advanced Fuel Cycle Initiative (AFCI) and the Global Nuclear Energy Partnership (GNEP), which support the mission of developing technologies for the next generation of nuclear power. Clearly, there is widespread support and sound, justifiable reasoning for the current GFR development efforts.

### 1.1.1 The History of the GFR

Work on Gas Cooled Fast Reactors (GCFRs)\* began as early as 1964, with General Atomic Company issuing the first report on a helium-cooled version [Gratton, 2003]. Gaseous coolant was considered as an alternative to liquid metal for development of a fast breeder reactor program during the 1960s and 1970s in order to meet the predicted rapid expansion of nuclear power. Specifically, gas offers the advantages of neutronic inertness, physical transparency, avoidance of coolant activation (for He), increased breeding gain, and existence as a single phase in the reactor coolant system [Gratton, 1981]. However, due to the lower heat transfer capability of gas as compared to liquid metal, two technical solutions were required to approach the thermal performance of liquid metal: (1) cladding roughening and (2) much higher gas pressures. While roughening the cladding did help to lower the film temperature drop, and hence peak cladding temperatures, it had the negative consequence of increasing core pressure drop, which increased circulator power requirements and inhibited natural circulation flow during decay heat removal [Gratton, 1981]. Increasing the pressure of the primary coolant system required much more robust barriers and consequently increased plant capital costs and potentially worsened the safety problems associated with a loss of coolant accident (LOCA) [Gratton, 2003]. The successful implementation of the Prestressed Concrete Reactor Vessel (PCRVR) by the French and British in the 1960s established the feasibility of the cost-effective, robust pressure boundary necessary to make a gas-cooled fast reactor concept work, igniting a two-decade-long process of design conceptualization and development [Gratton, 1981].

Gas cooled fast reactor work can be categorized into the two timeframes which define its major periods of research and development: (1) 1964-1982 and (2) 1998-present. GCFR work in the first time period was dominated by three major design efforts: (1) the General Atomic Company GCFR (2) the European Gas Breeder Reactor Association (GBRA) Gas

---

\* Early work on this concept referred to these reactors as Gas Cooled Fast Reactors (GCFRs). The recently renewed interest in this concept has changed the nomenclature to GFRs. Hence, reference to design work prior to the early 1980's will use the abbreviation "GCFR" while reference to modern designs, i.e. late 1990's and later, will use GFR.

Breeder Reactor-4 (GBR-4) and (3) the UK's GCFR-AGR. Table 1.1 (taken from [Driscoll et al, 2003]) compares some of the key characteristics of these early designs.

**Table 1.1: Characteristics of Early GCFRs (taken from [Driscoll et al, 2003])**

	GA GCFR	GBR 4	GCFR-AGR
Timeframe	1961-1981	1969-1980	1965-1982
Designer	General Atomic Company (USA)	Gas Breeder Reactor Association (Europe)	CEGB (UK)
Power (MW <sub>e</sub> )	300	1200	635
Power Conversion Cycle	Indirect Rankine	Indirect Rankine	Indirect Rankine
Coolant	He	He	CO <sub>2</sub>
Primary System Pressure (MPa)	9	9	4.1
Core Coolant Outlet Temperature (°C)	575	565	525
Core Flow	Down, later up	Upflow	Upflow
Fuel	MOX	MOX	MOX
Cladding	Steel	Steel	Steel
Average Power Density (kW/l)	235	188	170
Specific Power, kW/kg <sub>HM</sub>	95	81	58
Pressure Vessel	PCRv	PCRv	PCRv
Shutdown Heat Removal	3 Auxiliary Loops	3 Auxiliary Loops	4 Auxiliary Loops
References	[Shenoy et al, 2003] [USDOE, 1980]	[Gratton, 1981] [GBRA, 1974] [Kemmish, 1982]	[Kemmish, 1982] [Kemmish et al, 1982]

Two of the three major concepts and the efforts of more than 16 organizations from 10 countries during the early R&D period used helium as the coolant. Aside from some of the benefits that helium enjoys over CO<sub>2</sub> (which will be discussed later), this was primarily as a result of these organizations' concurrent involvement in the development of the High Temperature Reactor (HTR). The HTR is a thermal spectrum version of the GCFR and many of these organizations saw the GCFR as a natural follow-on [Gratton, 1981]. Similarly, most of the recently renewed interest in GFRs has been focused on using helium as a coolant for the same reason, as extensive R&D has been undertaken in the past decade on helium-cooled, thermal spectrum HTRs [Gratton, 2003]. However, it should be noted that



the majority of the commercial gas-reactor operating experience base has come from reactors cooled by CO<sub>2</sub> in England. It is for this reason that the GCFR-AGR efforts by the British used CO<sub>2</sub> coolant. In fact, the primary driver for this program was to capitalize on the existing construction and operating experience by retrofitting the design of the AGRs to accommodate a fast reactor core [Gratton, 1981 and Gratton, 2003].

The more modern era of GFR development began in 1998 when a consortium of British and Japanese companies began to explore a CO<sub>2</sub>-cooled fast reactor called the Enhanced Gas-Cooled Reactor (EGCR) [Gratton, 2003]. Again, CO<sub>2</sub> was chosen in an effort to build on the industrial experience of the British over the previous several decades. Shortly following that, the United States and nine other nations entered into the GIF, ushering in a new world-wide era of interest in GFRs and other advanced reactor technologies.

It should be noted that the GFR chosen by the GIF is being explored with two different coolants, based on an examination of 3 different Power Conversion Systems (PCSs): (1) Helium cooled, direct power conversion cycle at 5-7 MPa and 850°C core outlet temperature (2) Helium cooled (5-7 MPa), indirect power conversion cycle using S-CO<sub>2</sub> at 20 MPa and 550°C and (3) S-CO<sub>2</sub> cooled, direct power conversion cycle at 20 MPa and 550°C outlet temperature [Weaver et al, 2004]. The work presented here is a slight variation on the third option, where the outlet temperature has been increased to 650°C to enhance PCS efficiency. The reference case chosen by the GIF is the first option. As well, the original GFR chosen by the GIF is a 600MW<sub>th</sub> version, whereas the later GIF effort and the work presented here is for a 2400 MW<sub>th</sub> core. The decision to develop a much larger scale reactor in this work was based on both the modularity of the Brayton S-CO<sub>2</sub> PCS and the effect of economies of scale.

#### 1.1.2 Selection of S-CO<sub>2</sub> as a coolant

While more traditional GFR strategies employ helium as the coolant, the work presented here uses S-CO<sub>2</sub> for several reasons. The thermophysical properties of S-CO<sub>2</sub> as a coolant and power cycle working fluid allow for comparable performance to helium at lower temperatures at the reactor outlet/turbine inlet, i.e. 650°C v. 850°C. This alleviates problems associated with core materials performance at elevated temperature and allows for the use of

existing materials; for example, British AGRs are CO<sub>2</sub> cooled with a core exit temperature of 650°C. As well, the thermophysical properties of S-CO<sub>2</sub> make it more attractive from a decay heat removal perspective, as a much lower containment pressure is acceptable for the promotion of natural circulation than with helium. [Okano et al., 2002] Further, much recent development has been done on the S-CO<sub>2</sub> Brayton Cycle, which shows great promise as a Power Conversion System with predicted thermal efficiencies between 45-50% [Hejzlar et al., 2005] [Dostal et al., 2006]. This provides economic benefits not only from the high thermal efficiency, but also from being able to use a direct cycle. The downside to using S-CO<sub>2</sub> is that it must be kept at a high pressure in order to ensure efficient power cycle operation, i.e. 20 MPa v. 8 MPa for Helium, which requires a more robust pressure boundary. However, as shown in [Hejzlar et al., 2006], high pressure and medium temperature (20 MPa and ~650°C) are less challenging than the medium pressure and high temperature (8 MPa and ~850°C) conditions that exist for helium, due to the much lower allowable stresses at higher temperatures. Should the robust pressure boundary provided to the S-CO<sub>2</sub> cycle in the form of a PCRV or PCIV fail, the higher molecular weight of CO<sub>2</sub> (and higher density) gives it a lower sonic velocity, limiting its flow during a depressurization accident, and hence leading to a longer time to complete depressurization when compared to helium [Gratton, 2003].

## **1.2 Objectives of this Work**

In accordance with the goals of the GIF for next generation reactors, the core design presented here optimizes performance with respect to sustainability, safety, proliferation, and economics.

### ***Sustainability***

With respect to sustainability, the goal was to design a fast spectrum reactor that used legacy LWR spent fuel in a fuel cycle with a conversion ratio of as close to 1 as possible. Coupled with this is the idea of transmuting the fission products (Tc-99 and I-129) and minor actinides (MA's - neptunium, americium, and curium) that contribute the greatest burden to the (Yucca Mountain) waste repository, while minimizing the overall waste production.

## ***Safety***

Introducing the aforementioned MA's into the fuel cycle can create problems with respect to safety by reducing the delayed neutron fraction, which increases the effect of any reactivity insertion. Further, introduction of MA's reduces the Doppler coefficient of reactivity, reducing the beneficial effect of negative reactivity feedback upon a power excursion. As well, due to the use of Pu and MA in the fuel, fast reactors are subject to a large increase in reactivity due to coolant voiding. In an effort to ensure that this reactor design meets the stringent standard of inherent or passive safety expected of modern designs, a primary goal of the present work was to design a reactor with negative coolant void reactivity throughout core life as a first step toward achieving overall passive safety. A secondary goal stemming from this was to design a neutronicly passively safe GFR, such that upon an Anticipated Transient Without SCRAM (ATWS), the reactor will shut itself down. This standard may seem overly stringent, until it is remembered that this feat was demonstrated by the Integral Fast Reactor in the 1980s [Planchon et al, 1987].

## ***Proliferation***

While proliferation is a significant issue, it can only largely be addressed in terms of the detailed ex-reactor activities of the fuel cycle. It is addressed in this work by burning Plutonium and TRU from legacy LWR waste. First, this keeps the weapons-attractive isotopes of Plutonium intermingled with other TRU, making the Plutonium harder to extract in the event of diversion. Second, it leaves no opportunity in the fuel cycle where the Plutonium is physically separate from the other TRU. Finally, burning the legacy TRU from LWRs prevents the buildup of Plutonium stockpiles and puts the Plutonium in a safe, inaccessible place for long periods of time, i.e. in the GFR. Inherent in this approach to proliferation resistance is the avoidance of radial or axial U-238 blankets, so as not to produce clean weapons grade Plutonium in a convenient form for recovery. This requires a complete departure from traditional GFR core design philosophy. The innovative Tube-in-Duct (TID) fuel assembly, whose large fuel volume fraction provides for a larger heavy metal loading than traditional pin-type fuel, enables the achievement of long cycle lengths and a sustainable fuel cycle without the use of external blankets.

## ***Economics***

Finally, designing a reactor with reasonable capital, O&M, and fuel cycle costs when compared to LWRs, as well as other Gen-IV designs, is a goal that has been established to satisfy the economics component of the Gen-IV charter. This has been the primary motivation for adopting a direct (closed) Brayton cycle PCS.

In order to support the overarching principles set forth by the GIF, other subsidiary general design criteria must be satisfied, i.e. neutronics, thermal hydraulics, materials, etc. This work focuses primarily on the steady-state neutronic and thermal hydraulic aspects of such a design, which will be explored in detail in the coming chapters. For the purposes of the objectives associated with this work, it was sought to achieve a design which not only satisfies neutronic and thermal hydraulic criteria, but optimizes the performance of the core. Table 1.2 outlines the objectives of this work and how they correspond to the Gen-IV criteria, where applicable.

**Table 1.2: Objectives of this Work as They Relate to Generation-IV Criteria**

<b>Objective</b>	<b>Gen-IV Criteria Satisfied</b>
1. Design a fast reactor to burn legacy spent LWR fuel	Waste/Sustainability
2. Design a reactor with a conversion ratio ~1	Waste/Sustainability/Proliferation
3. Minimize impact of GFR on waste repository with respect to waste volume and radiotoxicity	Waste/Sustainability
4. Maintain negative coolant void reactivity throughout core life	Safety
5. Design a passively safe GFR	Safety
6. Minimize weapons-attractive Pu production and make its extraction from the fuel difficult	Proliferation
7. Design a reactor with reasonable capital, O&M, and fuel cycle costs	Economics
8. Design a reactor which satisfies appropriate neutronic and thermal-hydraulic criteria while optimizing core performance	Supports all Gen-IV criteria

## **1.3 Main Challenges and Contributions of this Work**

### **1.3.1 Power Shaping in a Fast Reactor**

Among the numerous challenges associated with designing a fast reactor is devising a core with acceptable power peaking. Power peaking is more limiting in a GFR than in LWRs or liquid metal cooled reactors because of the small heat transfer coefficients achievable with gas coolants; hence, low power peaking is very desirable. While power shaping for thermal reactors can be achieved through conventional methods, i.e. burnable poisons, enrichment zoning, and fuel shuffling, achieving an acceptable power shape throughout core life presents a greater challenge in a fast reactor. With a harder neutron energy spectrum, fast reactors can not use burnable poisons effectively for power shaping, as neutron energies are typically above the range where neutrons are parasitically absorbed at rates comparable to heavy metals. While enrichment zoning is a viable beginning of life (BOL) option, the power shape varies significantly over core life with such a strategy, exceeding desired limits. Frequent fuel shuffling is another solution; however, this penalizes operations and economics.

This work explores and successfully implements a moderating diluent in the fuel in an effort to not only shape power at the beginning of core life, but also to help maintain a relatively flat power shape throughout core life. The diluent is the fast reactor analog to burnable poisons in an LWR, with the added benefit of not being subject to significant depletion during burn-up. Hence, the diluent maintains its potency throughout core life without any concerns over a residual reactivity penalty. This is a significant contribution as it allows optimal use of core resources.

### **1.3.2 Evolution Toward a Passively Safe GFR: Negative Coolant Void Reactivity**

The larger scope of the entire MIT GFR effort is to design a passively safe GFR. This means passive safety not only thermal-hydraulically, i.e. post-LOCA decay heat removal (DHR), but also neutronicallly, i.e. inherent safe-shutdown of the core. While other work has shown that the former is not feasible [Pope et al, 2006], the present work is concerned with the latter. While neutronic safety has many components, the aspect that

presents arguably the greatest challenge and the largest contribution to severe accident scenarios in a fast reactor is the coolant void reactivity (CVR). Previous solutions have reduced the severity of this problem, but have not eliminated the need for active and fast reactivity insertion mechanisms to compensate for this effect. Keeping CVR negative without otherwise seriously compromising core performance is one of the means used toward achieving the goal of passive neutronic safety.

This work successfully maintains  $CVR \leq 0$  through the symbiotic combination of diluent use in the fuel and the innovative use of an S-CO<sub>2</sub> reflector. By keeping CVR negative throughout core life, the severity of one of the most serious accidents for this type of reactor, the Loss of Coolant Accident (LOCA), is greatly reduced. This is a significant contribution as there are very few, if any, practically realizable fast reactors that have been conceptualized with a negative CVR throughout life.

While CVR is only one aspect of neutronic safety, a method for rapidly assessing design choices and their impact on passive safety has also been developed in this work, based heavily on a method previously developed by Argonne National Laboratory (ANL) for the Integral Fast Reactor (IFR). This tool is also a contribution as it allows feedback throughout the design process without undertaking lengthy and expensive safety analyses.

### 1.3.3 Quantitative Comparison of TID and pin-type fuel

Used in much recent research here at MIT, the Tube-in-Duct (TID) fuel assembly promises lower cladding temperatures and pressure drop while providing a larger fuel volume fraction than conventional pin-type fuel [Pope et al, 2005]. While TID fuel has been explored and compared piecemeal in many other works, this work comprehensively compares the thermal hydraulic and neutronic performance of this fuel type with that of the traditional pin-type fuel, as well as with the innovative Internally-Cooled Annular Fuel (ICAF) [Hejzlar et. al, 2001 and Hejzlar et. al, 2004]. ICAF is an annular pellet which has both traditional external, as well as innovative internal, cladding and cooling developed at MIT as means for extracting more power from existing LWRs.

## **1.4 Organization of this Report**

Chapter 2 provides an overview of the plant of which this reactor core is a part, as well as research being performed in the other areas of GFR development. This is both to give the present work context and to serve as a reference for related efforts.

Chapter 3 introduces the use of diluent in fast reactor fuel as a means for helping to shape power distributions and reduce coolant void reactivity. An investigation into the optimum diluent material and concentration will also be presented.

Chapter 4 presents the primary core design developed, using Tube-in-Duct (TID) fuel. Assessments of axial and radial reflector materials, core neutronic and thermal hydraulic performance, reactor pressure vessel fluence, and the chemical compatibility of core materials with the S-CO<sub>2</sub> coolant will be made.

Chapter 5 compares several different fuel types and strategies for using diluent, using both neutronic and thermal hydraulic criteria as a basis for evaluation. This is in an effort to show which fuel type among three candidate options provides the best performance and to determine the best way in which to use the diluent in the fuel.

Chapter 6 presents a core design using pin-type fuel, as an alternative to the TID fuel design presented in Chapter 4. This is both as a means of whole core comparison with the TID core and as a fallback measure in the event that TID fuel is ultimately found unsuitable for use in a GFR.

Chapter 7 is similar to Chapter 6 in approach, as it presents a core design as an alternative to the two previously presented designs, this time using Internally Cooled Annular Fuel (ICAF). ICAF is explored as it provides for much lower fuel and cladding temperatures and consequently provides for larger safety margins.

Chapter 8 analyzes the mass flows of key isotopes of interest in an effort to evaluate the sustainability, waste production, and proliferation resistance of this reactor concept, all in accordance with Gen-IV design criteria. As well, an investigation into a suitable inert matrix fuel (IMF) for the S-CO<sub>2</sub> cooled GFR is made, should it be desired that this reactor be used

as a dedicated burner instead of its current mode of breeder-burner. Finally, a quantitative evaluation of the performance of this IMF against that of the TID (U,TRU)O<sub>2</sub> fuel used as the primary design option is made.

A preliminary safety evaluation is performed in Chapter 9. A revised method for using a simple first-order metric to assess the passive safety of a direct-cycle S-CO<sub>2</sub> GFR during the design process is developed and applied to the core designs presented heretofore. Design solutions for implementing the lessons learned from this analysis are also presented.

Chapter 10 presents an economic analysis of the core designs presented in this work, in an effort to measure their suitability in meeting the Gen-IV criteria of economic competitiveness.

Finally, in Chapter 11, this body of work is summarized, with relevant conclusions highlighted and the areas needed for future work discussed.

Appendices are included which describe the computational tools used in this work (Appendices A and B), as well as provide an example of the pertinent input decks (Appendix C).



## 2 General Plant Information

### 2.1 Introduction

While the research presented in this work deals mainly with the design and optimization of the nuclear reactor core, it is important to understand the larger framework into which it fits. In this chapter, important background information from other sources, many of which are collaborative, will be provided so that the core design discussed in the remainder of this work can be put into the proper context. Table 2.1 provides a list of the key parameters for the entire plant.

**Table 2.1: Key Plant Parameters**

<b>Parameter</b>	<b>Value</b>
Core Thermal Output	2400 MW <sub>th</sub>
Power Conversion System (PCS)	Brayton Recompression Cycle [Dostal et al., 2004]
Number of PCS loops	2
Plant Electrical Output	1200 MW <sub>e</sub>
PCS Thermal/Net Efficiency	51/47
Primary to Secondary Plant Coupling	Direct
Primary Coolant/PCS Working Fluid	S-CO <sub>2</sub>
Core Inlet Temperature	485.5°C
Core Outlet Temperature	650°C
Peak Coolant Pressure	20 MPa
Plant Lifetime	60 years
Number of refueling cycles	3
Number of refueling batches	1
Decay Heat Removal (DHR) Capability	(3-4)x(50-100)% Shutdown Cooling Systems (SCSs) – exact configuration TBD [Pope et al., 2006]
DHR System Working Fluid	CO <sub>2</sub> (reactor side) H <sub>2</sub> O (ultimate heat sink side)

## 2.2 Plant Layout

Motivated by the extensive work done at MIT, other leading international universities, and national laboratories on the development of a S-CO<sub>2</sub> Brayton Cycle Power Conversion System, the core design presented in this work is only one part of the larger effort to design a Generation-IV nuclear power plant. Other work on this plant concept is ongoing and has been divided into the following areas: (1) plant layout [Gibbs et al., 2007] (2) S-CO<sub>2</sub> Brayton Cycle optimization, control, and turbomachinery design [Dostal et al., 2004; Dostal et al., 2006; and Carstens et al., 2006] (3) thermal hydraulic design, dealing mainly with the removal of decay heat in a post-accident scenario [Pope et al., 2006] and (4) Probabilistic Risk Assessment (PRA) aided design [Delaney et al., 2005]. While all of these areas are of importance in order to establish the feasibility of such a concept, only the plant layout will be discussed here. It should also be noted that studies using this type of plant for hydrogen production have also been undertaken [Memmott et al., 2006].

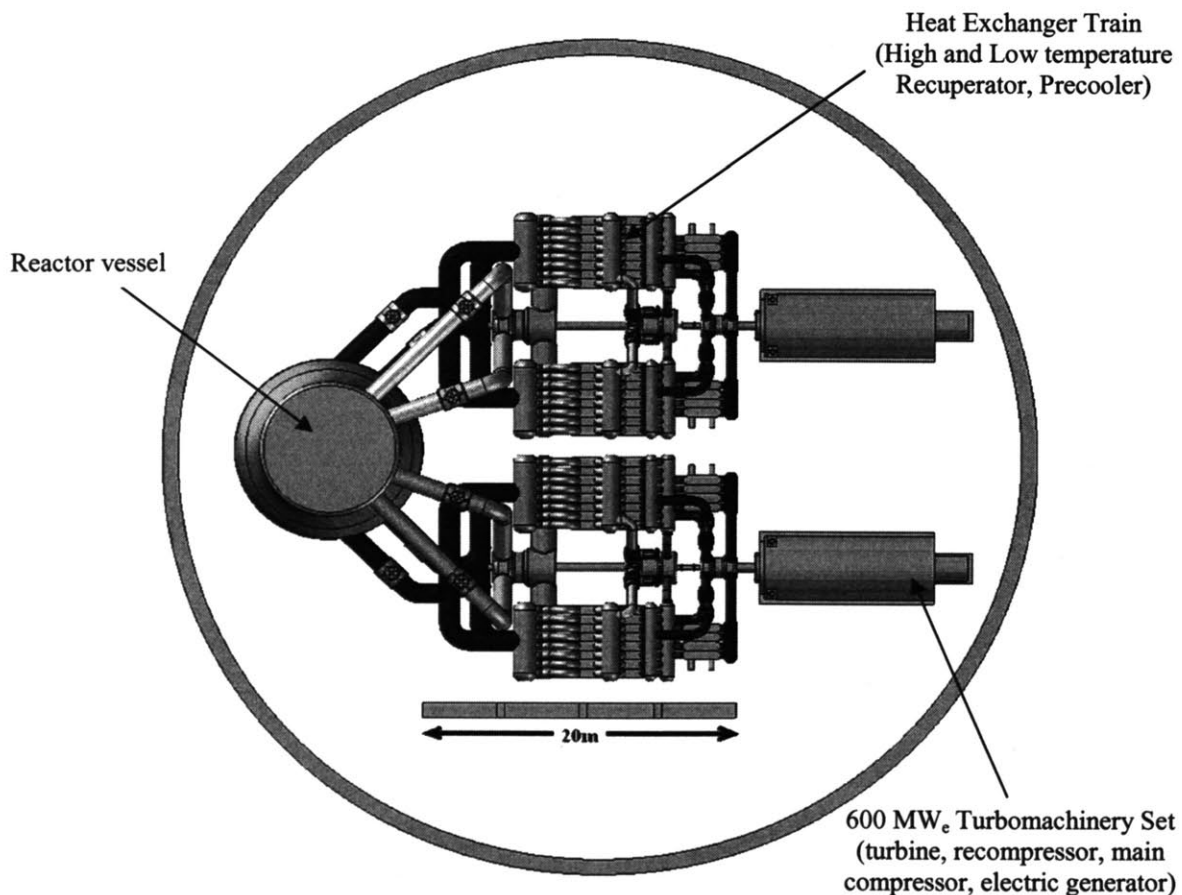
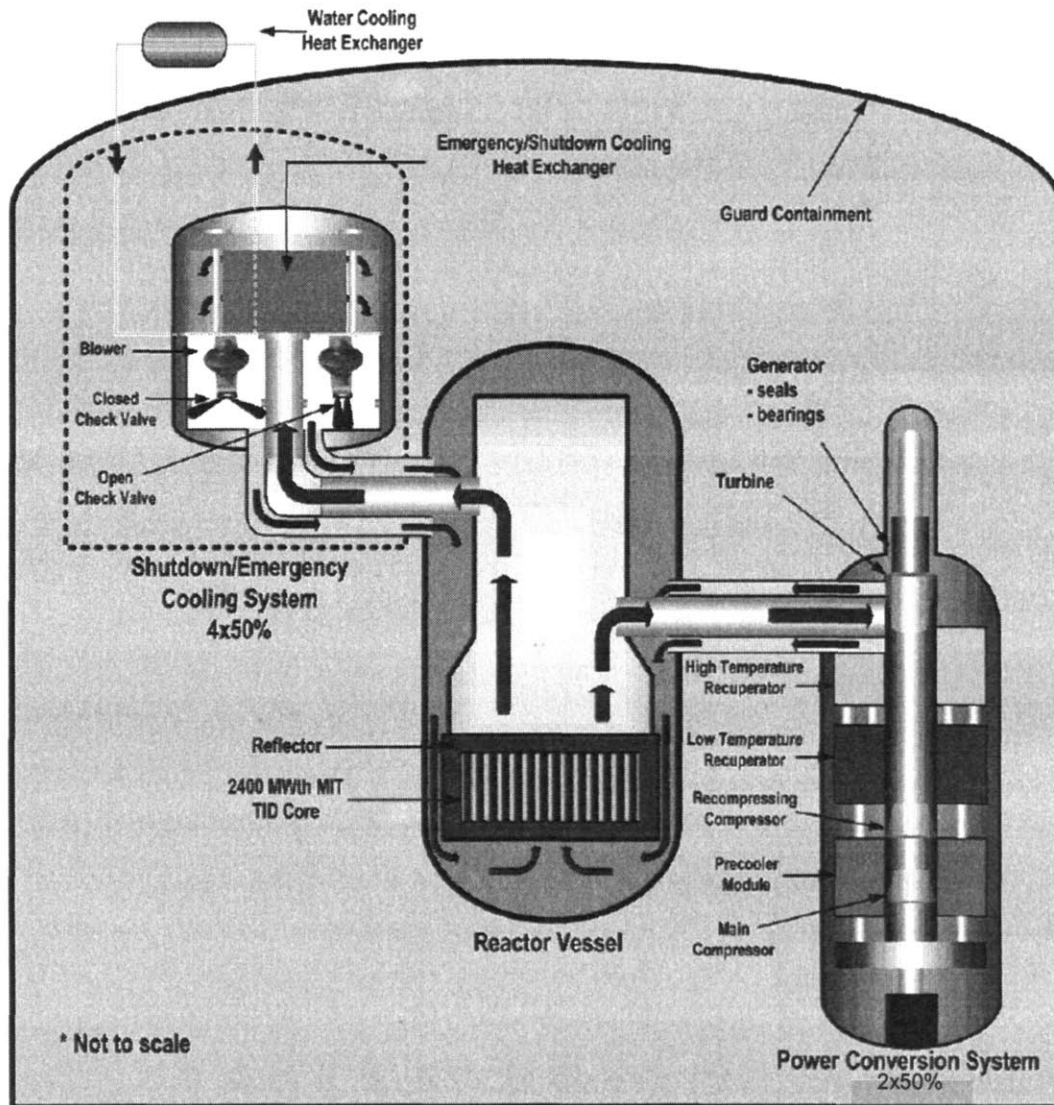


Figure 2.1: Conceptual Drawing of the 1200 MWe 2-Loop Plant Layout



**Figure 2.2: Simplified Plant Layout – Cartoon Depiction**

Figure 2.1 [Gibbs et. al, 2007] and Figure 2.2 show artists' renderings of the layout of the plant. Of note in Figure 2.1 are the two parallel  $600 \text{ MW}_e$  turbomachinery sets (turbine, recompressor, main compressor, and electric generator) each served by four heat exchanger trains (high and low temperature recuperators, and precooler) in two pairs on both upper and lower floors, straddling the shaft. Note that Figure 2.1 is a top-view drawing and only the two upper floor trains per shaft can be seen. Several constraints contributed to the determination of the chosen layout. First, turbine capacity is limited at about  $600 \text{ MW}_e$ , based on keeping turbine blade stress to within acceptable limits and shaft rpm to 1800, a

standard electric generator value. Second, the ductwork and valving was limited to about 1 meter in order to match current practice [Legault et al., 2006]. Third, in order to respect pipe size constraints and keep pressure drop within tolerable limits, heat exchanger train capacity is limited to  $\sim 320 \text{ MW}_{\text{th}}$  (corresponding to  $\sim 150 \text{ MW}_{\text{e}}$ ); hence, the need for 8 total heat exchanger trains, with 4 trains servicing each  $600 \text{ MW}_{\text{e}}$  turbomachinery set. Finally, in order to achieve this compact plant layout, Heatric<sup>TM</sup> Printed Circuit Heat Exchangers (PCHE) were chosen, which offer a compact design, low pressure drop, high effectiveness and the ability to operate with a very large pressure difference between the hot and cold sides of the heat exchanger [Gezelius et. al, 2004]. This type of heat exchanger has been designed to withstand pressures up to 60 MPa or temperatures up to  $900^{\circ}\text{C}$ , which make it well suited for use in this reactor plant [Heatric<sup>TM</sup>, 2007]. The entire layout shown in Figure 2.1 can fit inside a 54 meter diameter containment, able to sustain a high enough post-LOCA pressure such that natural circulation decay heat removal is possible [Gibbs et al., 2007].

### 2.3 S-CO<sub>2</sub> Brayton Recompression Cycle

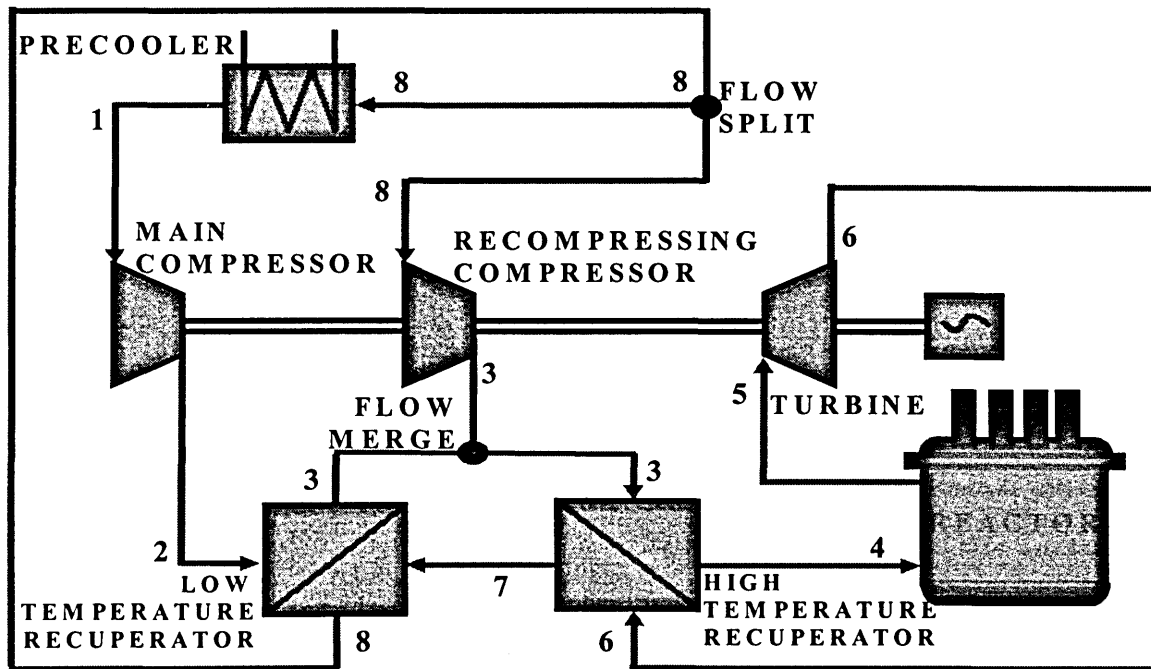


Figure 2.3: S-CO<sub>2</sub> Brayton Recompression Cycle [from Dostal et al., 2004]

Much recent work has gone into the development of a S-CO<sub>2</sub> Brayton Recompression Cycle for use as a Power Conversion System (PCS) both in the US and abroad [Dostal et al., 2004][Dostal et al., 2006][CANES, 2007]. Figure 2.3 shows the layout of the version of the PCS that has been chosen for this reactor plant. The key feature of this cycle which differentiates it from the traditional Brayton cycle and improves its efficiency is the operation of the main compressor near the critical point of CO<sub>2</sub>, where density is very high, and the introduction of another compressor, i.e. a recompressing compressor, before the pre-cooler. This recompressing compressor is fed by diverted flow from the entrance to the pre-cooler. Flow is then fed to a high and low temperature recuperator, another differentiating feature from the traditional Brayton cycle where there is typically only one recuperator [Dostal et al., 2004]. This arrangement avoids the pinch point in the recuperator which would otherwise occur if a simple Brayton cycle layout were used.

#### **2.4 The Tube-in-Duct (TID) fuel assembly**

Central to the design of this reactor core is the use of innovative Tube-in Duct (TID) fuel assemblies. [Pope et al., 2005] A TID fuel assembly is made up of a hexagonal outer can that has tubular coolant channels placed in a triangular lattice within the outer can, with “hex-nut” fuel pellets that fit around each of the coolant channels. Essentially, it is an “inside-out” version of a conventional fast reactor triangular lattice pin-type assembly, where the fuel and the coolant switch places. Figure 2.4 through Figure 2.6 displays drawings of the TID fuel assembly to help the reader visualize this concept.

The TID fuel assembly allows a higher fuel volume fraction,  $v_f$ , than a comparable pin-type core with the same Pitch to Diameter (P/D) ratio. This is favorable for numerous neutronic reasons. First, for a fixed unit cell size, a higher  $v_f$  means a lower coolant volume fraction,  $v_c$ . As a result, the moderation by the coolant plays a much smaller role and its loss results in a smaller increase in neutron energy upon voiding. Hence, as will be shown later, the addition of positive coolant void reactivity is smaller. With respect to radial power shaping, the high fuel volume fraction provided by the TID assembly permits the use of a diluent in the fuel while still allowing enough of a heavy metal loading to enable not only

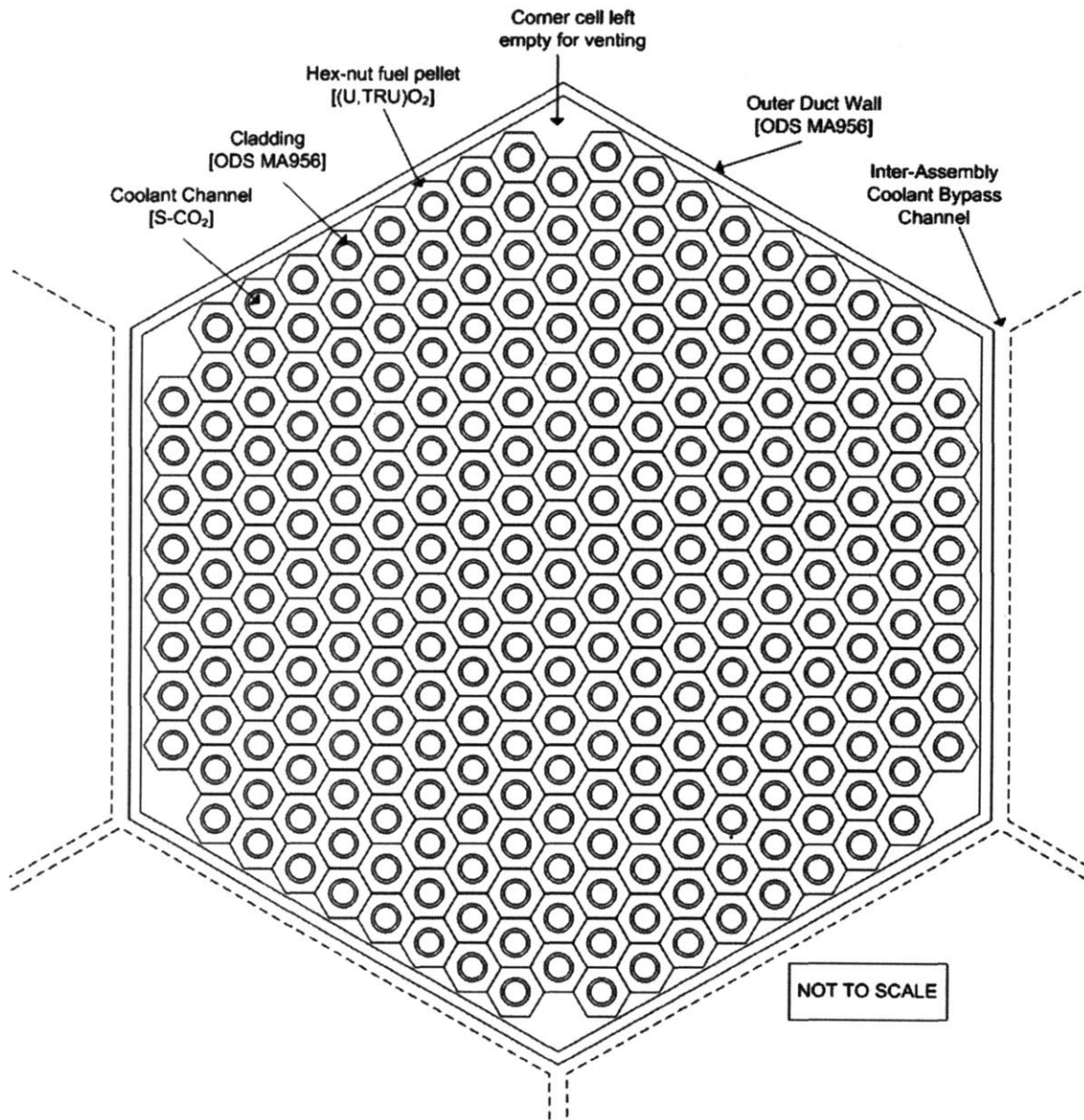


**Figure 2.4: Horizontal Cross Section of a Tube-in-Duct (TID) Fuel Assembly**

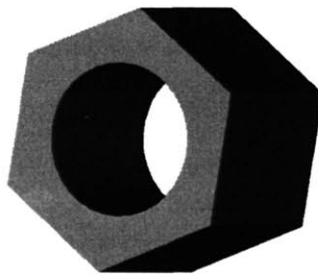


**Figure 2.5: 3-Dimensional Rendering of a Hex-nut Fuel Pellet**

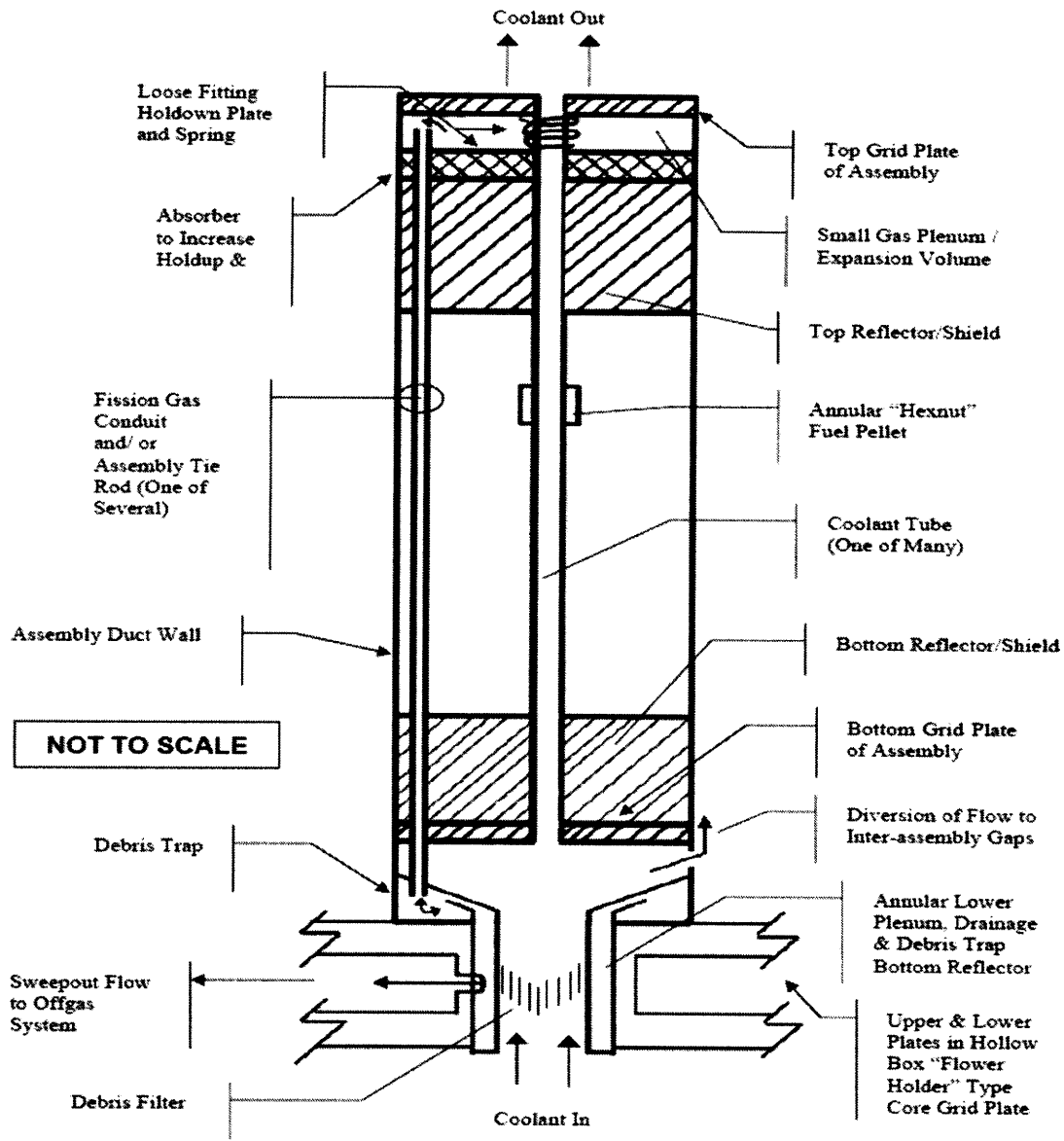


Figure 2.6: Vertical Cross Section of a Tube-in-Duct (TID) Fuel Assembly

criticality, but also sufficient conversion ratio during burnup to achieve a sustainable core without the need for external blankets. This provides a proliferation benefit as it causes the weapons-attractive isotopes (e.g. Pu-239) to be intimately mixed with other radioactive transuranics and fission products, making extraction more difficult.

The TID fuel also enjoys thermal-hydraulic advantages when compared to its pin-type contemporaries. For a given fuel volume fraction, TID fuel assemblies provide not only lower fuel temperatures [Hankel, 1960], but also significantly lower pressure drops. Further,

TID fuel assemblies eliminate the need for wire-wrap or grid spacers, adding an additional benefit from a pressure drop perspective. Reducing the P/D ratio in pin type cores in order to increase the fuel volume fraction and enjoy neutronic benefits similar to a TID fuel assembly would result in less favorable thermal hydraulic performance, specifically with respect to pressure drop and fuel and cladding temperatures (this will be shown in Chapter 5).

A unique feature of the TID fuel assembly is that the fission gas created in the fuel is directly vented to the coolant via the off-gas system illustrated in Figure 2.6. As the fission gas is created and diffuses through the upper reflector, upper shield, and an absorber (to increase the holdup of fission products), it is then temporarily held in a small gas plenum/expansion volume before it moves down the fission gas conduit. This conduit is long enough such that the short-lived radioactive fission products will have a chance to decay, reducing the radioactivity that is added to the gas collection system. Then, the fission gas goes through a debris trap, in order to catch any entrained non-gaseous material. Finally, the fission gas is swept out to the off-gas system, where there is chemical treatment and filtering prior to return to the main S-CO<sub>2</sub> coolant system. This off-gas system is currently only a conceptual design and requires further work in order to verify its feasibility.

While it may seem unusual to intentionally defeat the first line of defense against fission product release, the vented feature of the TID fuel assembly is necessary, due to the high operating pressure of this plant (~20 MPa) and the high cladding temperatures (~800°C). Without venting these assemblies, the large differential pressure that would exist across the cladding wall would result in stress-induced creep. This would almost certainly violate the integrity of the fuel assembly and cause larger scale fission product release and fuel reconfiguration. Hence, by designing for a small, controlled release of fission products, the larger, more catastrophic alternative is avoided. Precedent for such an approach exists, as similar venting systems were used in the General Atomics pin-type GCFR design of the 1970's [Capana et al., 1974], evaluated for use in Liquid Metal Fast Breeder Reactors (LMFBRs) [O'Neill et al, 1965] and implemented successfully in the Peach Bottom High Temperature Gas Reactor (HTGR) [de Hoffman and Rickard, 1965]. The Dounreay Fast Reactor in Great Britain also employed vented fuel [UKAEA, 2004].



While the TID fuel assembly shows much promise for application in this and other reactor designs, its primary drawback is that it has never been fully designed, built, or tested. Therefore, while much of the design in this work will use this promising concept, alternatives using the traditional and well-tested pin-type fuel will also be explored in Chapters 5 and 6.

## **2.5 Fuel Cycle Concept**

Motivated by the Generation-IV International Forum's goal of sustainability, one of the main reasons for choosing a fast-spectrum reactor is to help destroy some of the legacy waste burden from LWRs [GIF, 2002]. Further, it is desirable to provide a fuel cycle which can minimize the waste it creates and provide a means for self-sustainability, to minimize the impact on existing Uranium resources. These philosophical thrusts are at the core of the fuel cycle envisioned for this reactor, depicted in Figure 2.7.

In the first cycle, fuel would be taken from spent LWR fuel that has been discharged at a burnup of about 30 MWd/kg and has been kept in storage for about 30 years. This concept is based on using spent fuel from the 1970s, when burnups were at about that level. First, the spent LWR fuel would be sent to a reprocessing plant and have the fission products removed. Then, the Transuranics (TRU) from this spent fuel would be used in the first cycle fuel for the GFR. The first cycle fuel would have TRU enrichment and diluent addition to an appropriate weight percent ( $\text{w}/\text{o}$ ) and volume fraction, respectively, with the balance of the fuel made up by natural uranium. For this work, natural uranium is chosen to make up the balance of the fuel form in all cycles due to its abundance and ease of processing and fabrication. It should be noted, however, that depleted uranium, either diffusion plant tails or from LWR or GFR spent fuel (discussed later), could also be used to make up this balance, as shown in Figure 2.7. Once the fuel from the first cycle is discharged, it will be stored for a cooling time of 7 years to allow shorter lived fission products and (some) TRU to decay and permit easier handling and reprocessing of the spent fuel. Then the fuel will be reprocessed for use in the second cycle, enriched to the appropriate TRU  $\text{w}/\text{o}$ , and combined with the applicable diluent volume fraction, again with the remainder of the fuel being made up by Natural Uranium. The fission products are diverted for storage and disposal. The process is repeated for the third and final fuel cycle.

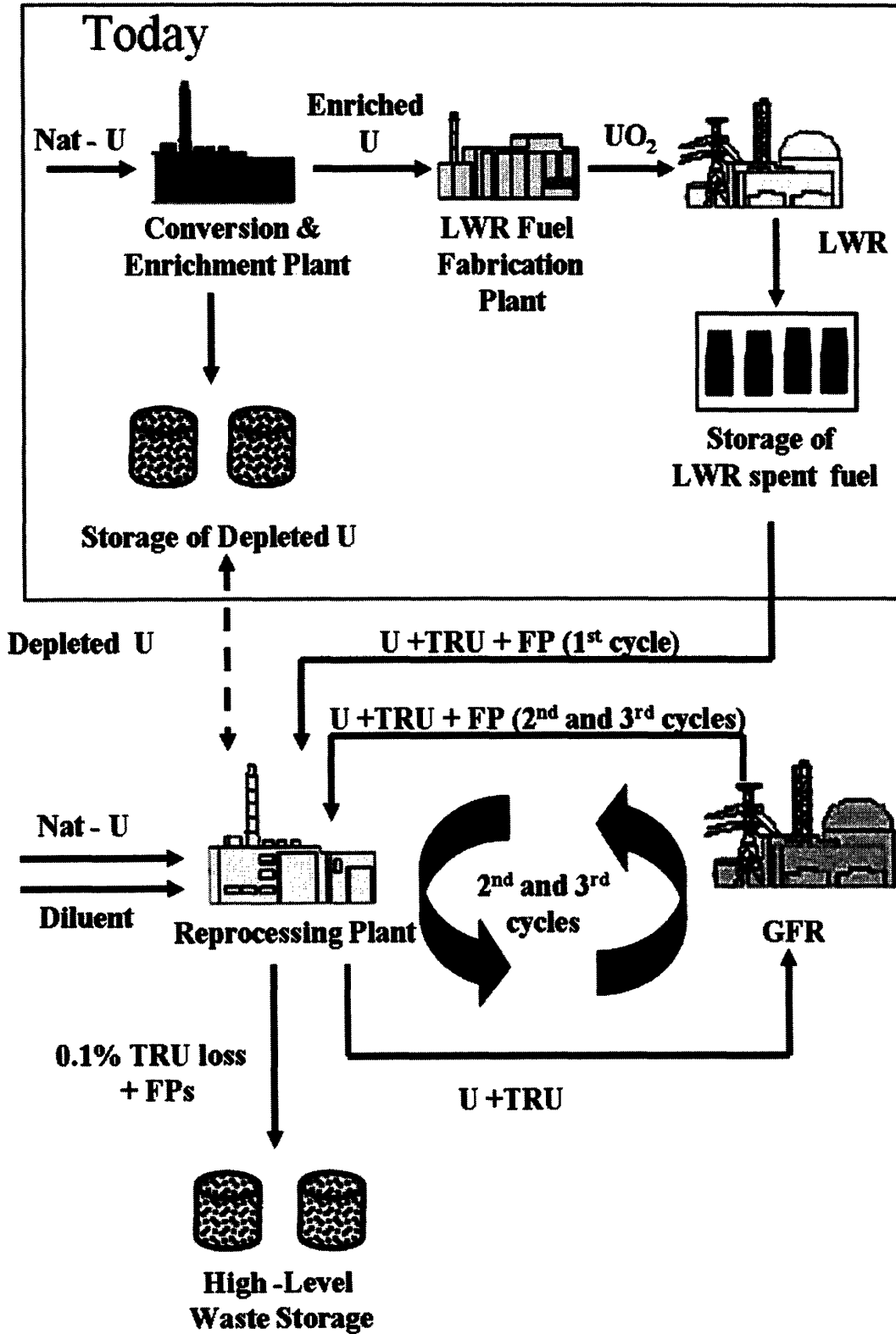


Figure 2.7: Fuel Cycle Flowchart

In order to implement such a strategy in a cost-effective manner, either a “reactor park” or a central reprocessing facility strategy, with fabrication on-site, is envisioned. While the details of national and international arrangements remain to be worked out, the fuel cycle concept presented here provides a sound basis for meeting Gen-IV, AFCI, and GNEP goals. In particular, note that a batch-loaded “battery” core is planned, with 15-20 years between refuelings, which minimizes access to ex-core fissile material. The details of the mass flows and material compositions used in this strategy will be discussed in a later chapter.

**Table 2.2: Current Status of Ex-core GFR Plant Features**

<b>Subsystem</b>	<b>Features</b>	<b>Comments</b>
<b>Safety Systems</b>		
Shutdown Cooling System (SCS)/ Decay Heat Removal (DHR) System	<ul style="list-style-type: none"> <li>• Combined shutdown &amp; emergency, (3-4)x(50-100)% capable, forced convection</li> <li>• Natural convection supplemented</li> <li>• Water boiler heat sink</li> </ul>	<ul style="list-style-type: none"> <li>• Based on MIT/CEA/ANL INERI project design.</li> <li>• For <math>P \geq 0.7</math> MPa natural convection alone may suffice</li> </ul>
Emergency Power	Fuel cells to supplement diesels	Fuel cells projected to be more reliable than diesels alone in the long run
<b>Plant</b>		
Power Conversion System (PCS)	<ul style="list-style-type: none"> <li>• S-CO<sub>2</sub> Brayton direct</li> <li>• 2 x 600 MW<sub>e</sub> loops</li> <li>• Temperature: 650°C core exit/turbine inlet</li> <li>• Pressure: 20 MPa</li> </ul>	AGRs in UK use CO <sub>2</sub> coolant at 4 MPa and have T~650°C
Reactor Vessel	PCIV	Vessel houses loop isolation and check valves plus shutdown cooling heat exchangers
Containment	<ul style="list-style-type: none"> <li>• PWR type</li> <li>• Steel liner reinforced</li> <li>• 0.7 MPa capability</li> <li>• 70,000 m<sup>3</sup> free volume</li> <li>• Filtered/vented</li> </ul>	<ul style="list-style-type: none"> <li>• CO<sub>2</sub> can be added to adjust pressure</li> <li>• Internally insulated</li> </ul>
H <sub>2</sub> production by steam electrolysis	<ul style="list-style-type: none"> <li>• Separate water boiler loops (4) @ 10% of reactor power</li> <li>• Recuperation of H<sub>2</sub> &amp; O<sub>2</sub> heat allows cell operation at 850°C</li> </ul>	Water boiler loops can also serve for self-powered decay heat removal

## **2.6 Summary**

Information regarding the whole plant has been presented here, in order to serve as a reference for the larger scope of which the present work is a part. General plant layout and parameter information has been provided, along with a discussion about the use of the innovative Tube-in-Duct (TID) fuel assembly and the fuel cycle envisioned for this reactor plant. Table 2.2 summarizes the relevant features.

## **3 The Diluent Approach**

### **3.1 Introduction**

Among the numerous challenges associated with designing a fast reactor is devising a core with acceptable power peaking and coolant void reactivity (CVR). Power peaking is more limiting in a GFR than in LWRs or liquid metal cooled reactors because of the smaller heat transfer coefficients achievable with gas coolants; hence, low power peaking is very desirable. The hard energy spectrum of a GFR presents unique design challenges as it renders the traditional LWR means for power shaping, burnable poisons, impotent. While enrichment zoning is a viable beginning of life (BOL) option and has been used in prior fast reactor design philosophy, the power shape varies significantly over core life with such a strategy, exceeding desired limits. Frequent fuel shuffling is another solution; however, this penalizes operations and economics.

Positive CVR is a perennial concern in fast reactors, which imposes a significant design challenge. Previous solutions to this problem have reduced the severity of this problem, but have not eliminated the need for active reactivity insertion mechanisms to compensate for this effect. The larger scope of this work is to design a passively safe GFR. Keeping CVR negative without otherwise seriously compromising core performance will be explored as one means towards achieving this larger goal.

### **3.2 Traditional Means of Shaping Power**

With burnable poison use eliminated as means for power shaping due to its impracticality for fast reactor applications, only enrichment zoning and frequent fuel shuffling remain as options from among the traditional means for effectively shaping power.

In order to test the ability of enrichment zoning to help shape power, a simple two zone enrichment strategy was tested on an early iteration of the current core design. Figure 3.1 shows that a fairly flat radial power shape with a peak of 1.13 can be achieved at beginning of life (BOL). While this is extremely promising, it does not prove useful, as the difference in enrichments between the two radial zones causes uneven burnup and breeding between the zones and gives an unacceptably high radial power peak: as great as 1.47 at Middle of Life (MOL).

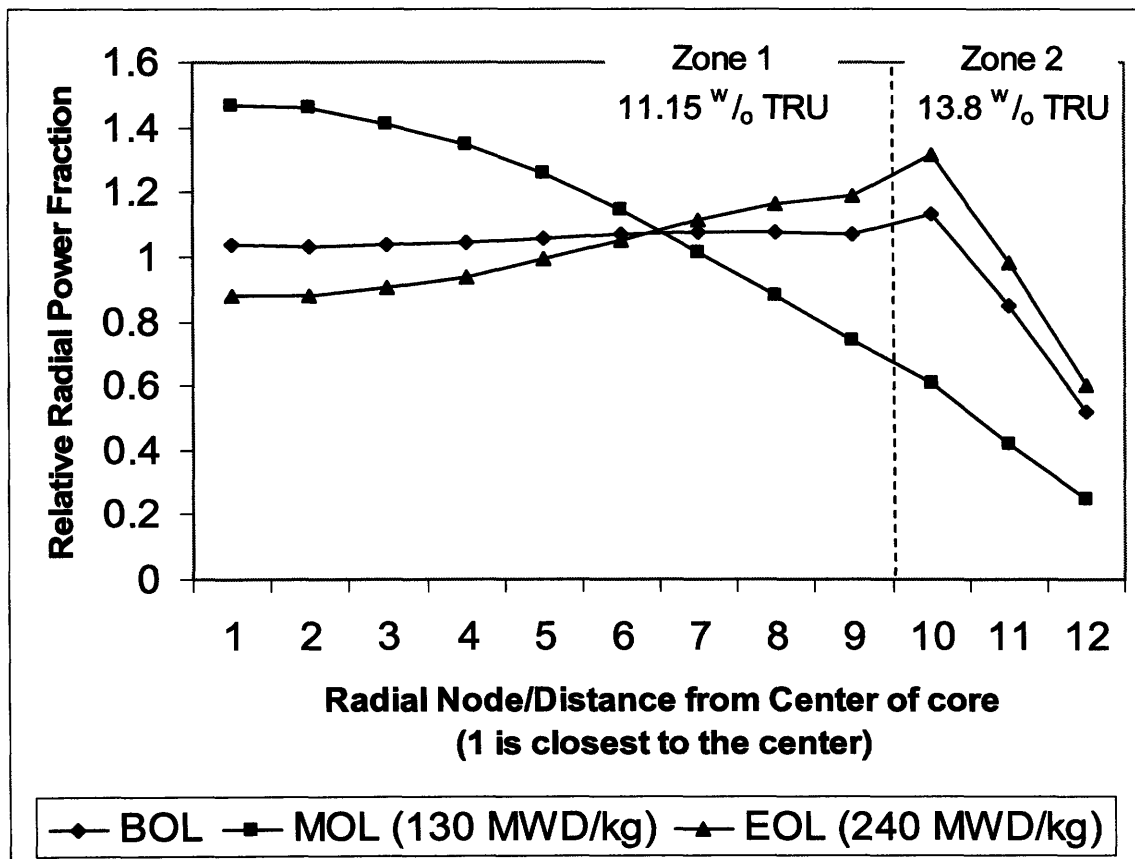


Figure 3.1: Radial Power Profile as a Function of Burnup for a 2-zone Enrichment Zoned Core

Next, the remaining traditional method of radial power shaping, frequent fuel shuffling, was evaluated. In an effort to stay within the radial power peaking limits, a shuffling scheme for the 2 zone core was implemented once the fuel had been in the core for 20 MWD/kg or 2.7 years. This burnup was chosen for 2 reasons: (1) at 20 MWD/kg, the radial power peak was already 1.34, above the target of 1.3 and (2) at a 90% capacity factor, this represents a 3 year cycle, probably as long as operators will be comfortable with running

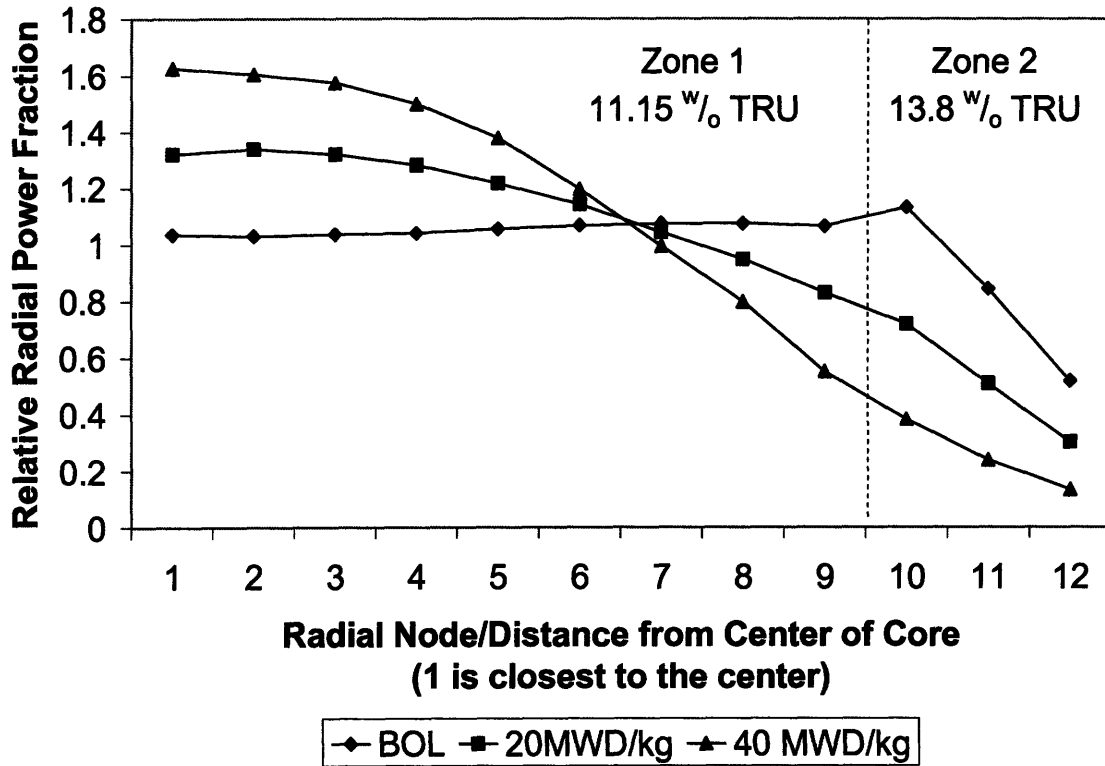


Figure 3.2: Radial Power Shape as a Function of Burnup for a 2-zone Enrichment Zoned Core after Exchanging Inner and Outer Fuel at 20 MWd/kg

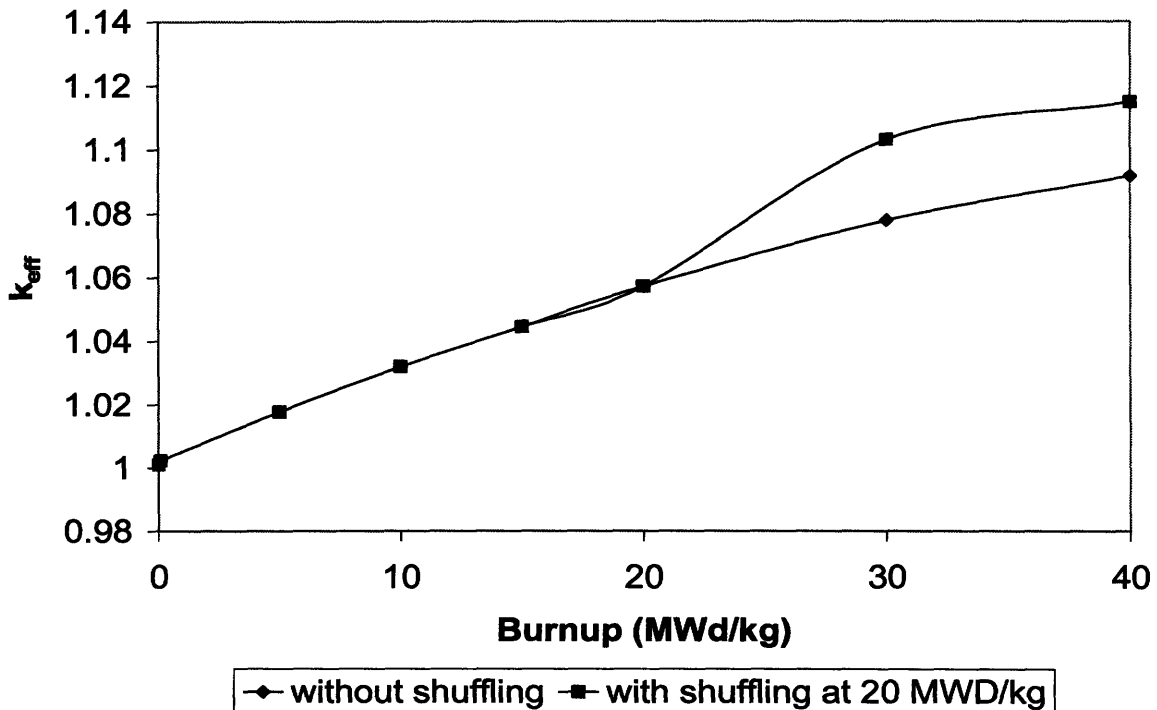


Figure 3.3: Core Eigenvalue as a function of Burnup: Shuffling v. not shuffling at 20 MWd/kg for a 2-zone Enrichment Zoned Core

a reactor between shutdowns (at least until experience is gained with longer intra-shutdown periods). The shuffling scheme used was to swap the inner and outer zone of fuel. Since the number of assemblies in the inner zone (217) was greater than those in the outer zone (180), some of the fuel (37 of the assemblies in the 7<sup>th</sup> ring of the core for an 11 ring core) was not shuffled.

Examining first the behavior of the radial power shape with respect to burnup, it can be seen in Figure 3.2 that swapping the fuel at 20 MWD/kg worsens the radial power peak at 40 MWD/kg to 1.62. This is significantly above the target of 1.3 and suggests that the higher enrichment fuel originally in the outer region is not depleted enough at 20 MWD/kg to have the effect of flattening the radial power profile when shuffled to the inner region. This is further supported by looking at the core eigenvalue as a function of burnup in Figure 3.3, which shows a sharp increase in  $k_{\text{eff}}$  when the fuel is shuffled.

Another important insight gained from Figure 3.3 is the large reactivity swing inherent in this type of core, as the largest eigenvalue in this figure for the unshuffled case is  $\sim 1.09$  and rising. Assuming a value of  $\beta_{\text{eff}}$  of 0.004 (which is conservatively high, by most fast reactor standards), the reactivity swing will be about \$28 ( $=0.11257/0.004$ ) for the unshuffled case, as the peak eigenvalue reaches 1.11257 (not shown). This reactivity swing will require a large amount of active reactivity control, which translates into a large number of control assemblies in order to keep the most reactive assembly below \$0.50. This limit of \$0.50 for a single control assembly is based on keeping accident scenario control of the core manageable and for providing margin for protection against super-prompt-criticality in the event of inadvertent control rod malfunction, e.g. unexpected continuous withdrawal or ejection. The large reactivity swing is disadvantageous not only because it places a large amount of reactivity in the core that must be mitigated in the event of a severe accident, but also because it requires a large number of control assemblies, which results in either displacement of fuel or an increase in core size, both of which are undesirable.

Given the failure of traditional methods to provide adequate radial power control, a new strategy will need to be implemented in order to get an acceptable radial power peak over core lifetime. Further, it would be desirable to reduce the apparently large reactivity



swing inherent in this type of core. One solution might be to increase the number of enrichment zones used to flatten the radial power shape. This would not be desirable, as this would both complicate the fuel loading pattern and would not eliminate the spatial power swings over burnup seen with the two zone case that led to unacceptably high power peaking. Hence, a more elegant solution is needed.

### 3.3 Use of Diluent to Shape Power

#### 3.3.1 Root Cause of How Diluent Shapes Power

The approach used in this work to shape radial power is to blend a material, i.e. a “diluent,” into the fuel. The diluent has the effect of both reducing the fuel concentration and softening the neutron energy spectrum. By varying the concentration of the diluent, it is possible to vary these two effects and hence, effectively shape power.

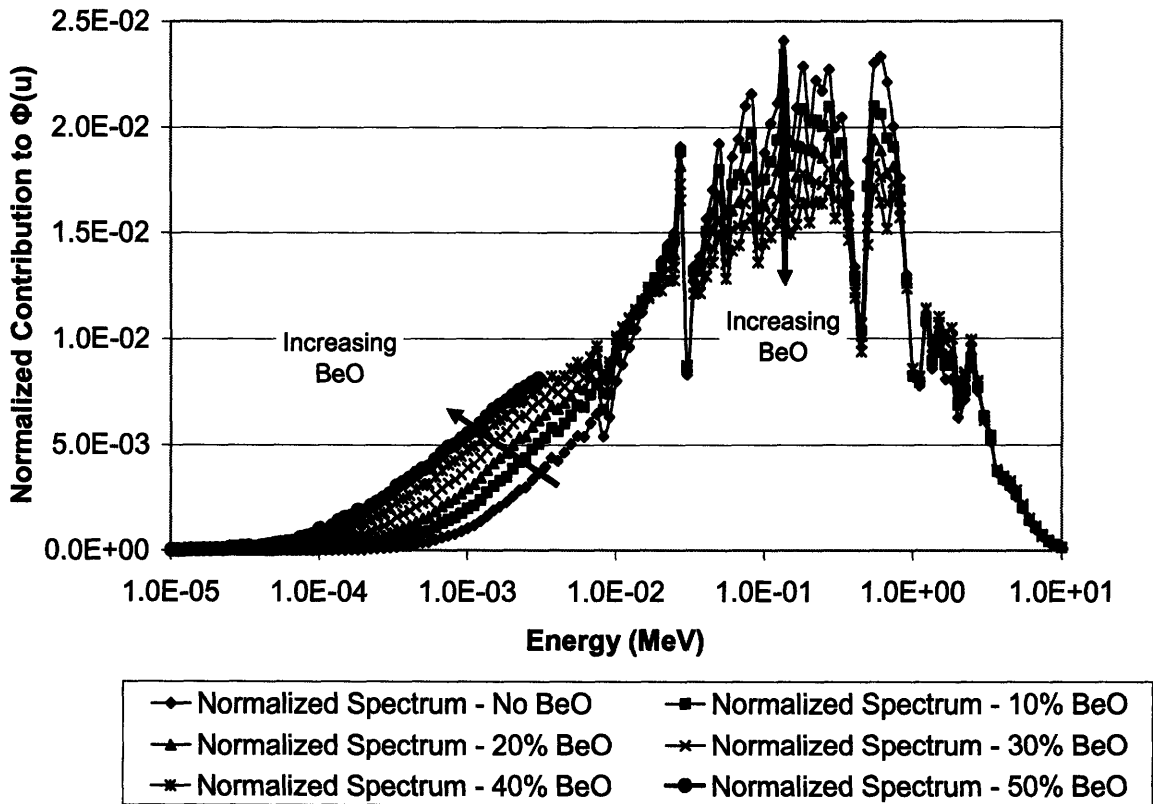


Figure 3.4: Effect of Diluent Concentration on the Neutron Energy Spectrum

The softening effect of the diluent on the neutron spectrum is clearly illustrated in Figure 3.4\*, where the neutron energy spectra of a semi-infinite assembly (normal leakage axially, mirror boundary conditions radially) of varying diluent concentrations (with enrichment adjusted to get the same eigenvalue) are compared.† Addition of diluent to the fuel provides local moderation which is sufficient enough to lower enough of the neutron population's energy below the fast fission threshold of many of the transuranic nuclides without lowering it so much as to completely prohibit fast fission. In this way, power can be effectively shaped in a fast reactor. As well, integrating diluent into the fuel also has the effect of displacing fuel, which will also have the effect of locally suppressing power and achieving the goal of power shaping. The question now arises of which effect, spectral softening or reduced fuel volume fraction, is dominant.

In order to determine which effect dominates, a 10 axial node semi-infinite assembly model, i.e. perfectly reflected radially with an albedo of 1 and reflected axially with the same axial reflector and shield thicknesses used in the whole core model, was developed for MCNP to compare 5 different cases. These cases are all at the same TRU enrichment: (1) a base case with no diluent, (2) a case with no diluent but containing the same volume fraction of fuel as the cases with diluent (i.e. using voids as diluent), (3) a case with SiC diluent, (4) a case with BeO diluent, and (5) a case with TiC diluent. Cases (2) – (5) have the fuel volume fraction reduced to 76.7% in nodes 1-3 and 8-10 and 60% in nodes 4-7, with the balance of material being made up by the diluent of interest for cases (3) – (5).

Figure 3.5 through Figure 3.7 shows the resulting axial power profiles for cases (1)-(5). Comparing the power shape for the “NO DILUENT” case, i.e. base case, and the reduced volume fraction case in Figure 3.5 shows that the void-displaced fuel has little effect on power shaping. Figure 3.6 compares these two cases to the case with a SiC diluent. From this figure we can conclude that the power shaping effect of diluents must come from

---

\* Note that in this and all other neutron spectra throughout this work, the abscissa represents the fractional contribution of a given lethargy bin, normalized to the total integrated value. The energy bins are of equal width in terms of lethargy, i.e.  $\Delta u$ .

† Note that in this example, the diluent of choice is Beryllium Oxide (BeO), while several other illustrative examples in this chapter use SiC or TiC as a diluent. The relative merits of each as a diluent will be discussed later, with BeO used as the preferred diluent throughout the remainder of this work.

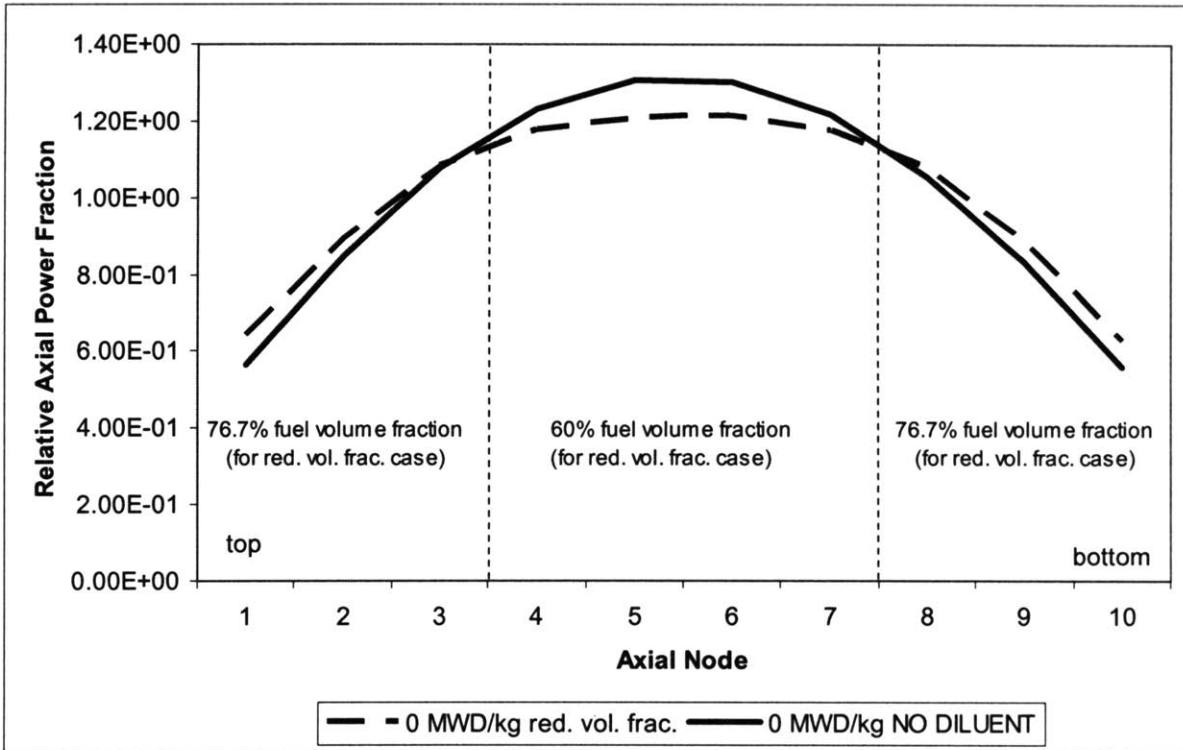


Figure 3.5: Comparison of Axial Power Shapes for 2 cases in a Semi-Infinite Assembly (Reference v. "void" dilution)

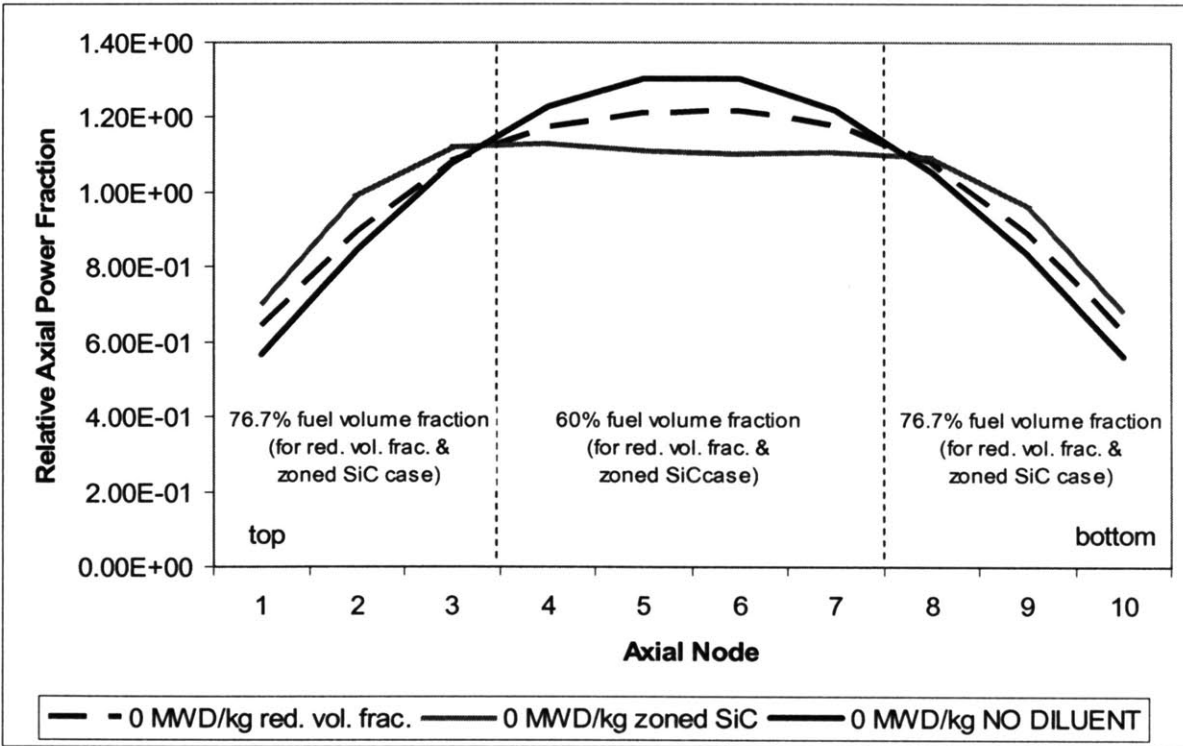
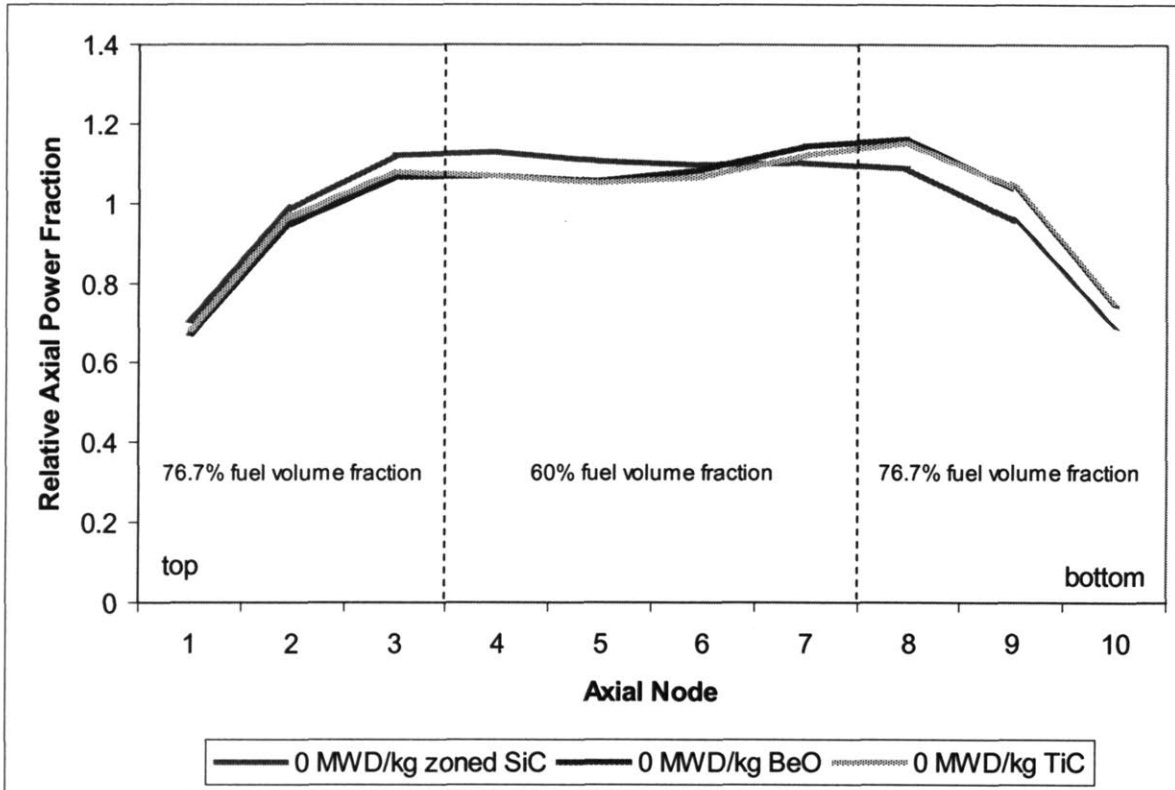


Figure 3.6: Comparison of Axial Power Shapes for 3 cases in a Semi-Infinite Assembly (Zoned SiC v. Reference and "void" dilution)



**Figure 3.7: Comparison of Axial Power Shapes for Candidate Diluents in a Semi-Infinite Assembly (Zoned SiC v. Zoned BeO v. Zoned TiC)**

something other than reduced fuel volume fraction, as the SiC diluent case shows a much more pronounced effect on the axial power shape. Figure 3.7 demonstrates a similar power shaping effect from the other candidate diluents, TiC and BeO. Note that the larger bulge in the axial power shape for the BeO and TiC cases is due to the statistical uncertainty associated with a low precision Monte Carlo simulation. Higher resolution runs yielded symmetric power shapes, as expected.

Since the reduced fuel volume is not the primary reason that these diluents are so effective at shaping power, the effect of spectral softening was examined next. Figure 3.8 shows the fission cross sections for the four isotopes that contribute the greatest to the fission reaction rate in this core at beginning of life (in order of contribution): Pu-239, U-238, Pu-240 and U-235. Note that the fission cross sections for Pu-239 and U-235 generally increase as energy decreases but are relatively constant over the energy range of interest in this core ( $10^{-5}$  MeV to 10 MeV). However, the fission cross sections of U-238 and Pu-240 have sharp increases between 0.1 and 2 MeV. Since the mean energy of the undiluted case ( $\sim 0.47$  MeV)

is right on this precipitous incline, any shift downward in neutron energy would lower the effective fission cross section for these isotopes, and consequently lower the power produced. As well, the lower amount of fuel present would also contribute to a lower fission rate per unit volume.

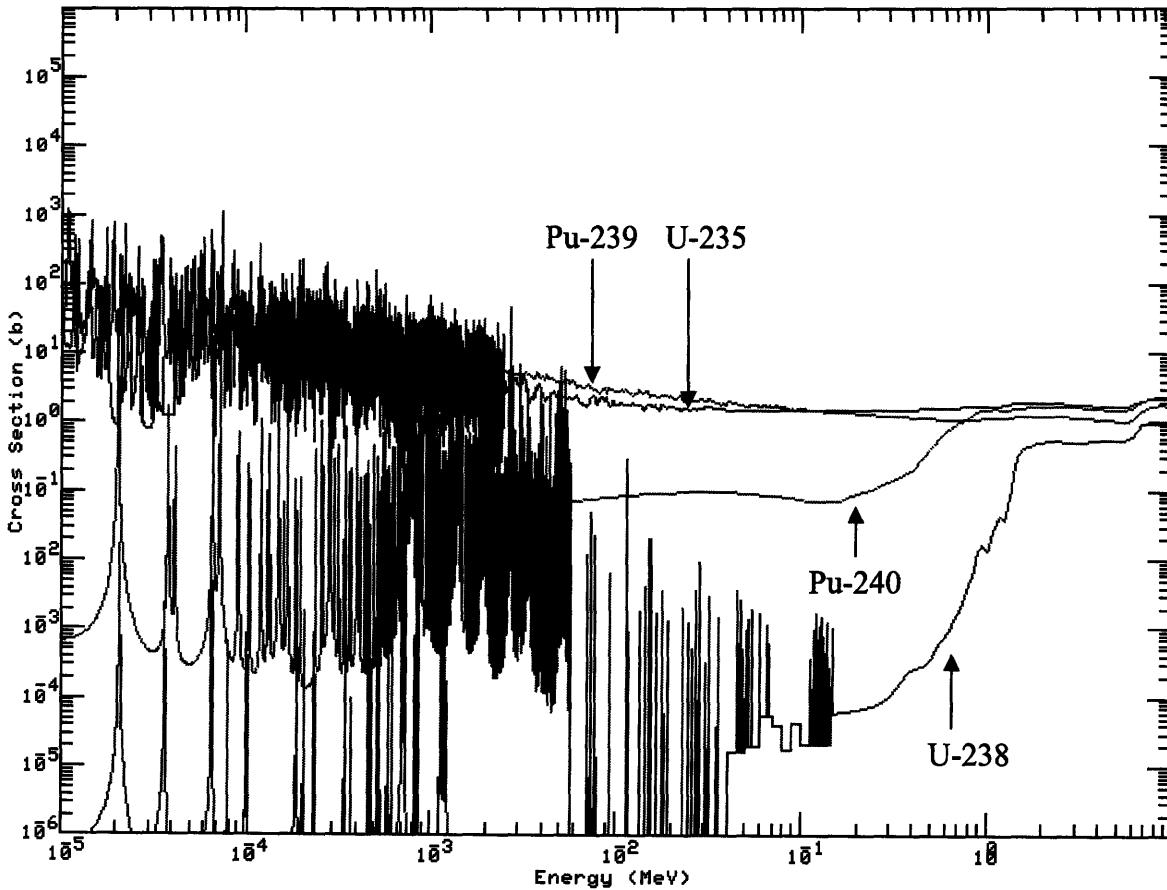


**Figure 3.8: Comparison of Microscopic Fission Cross Sections**

Comparing the neutron energy spectra (of one of the middle nodes of the semi-infinite assembly at 40% diluent) of the 4 reduced fuel volume fraction cases, 3 of which contain diluent, with the undiluted base case in Figure 3.9-Figure 3.12, a spectral softening effect is shown with each of the diluents (BeO, TiC, SiC), but is absent for the reduced fuel volume fraction case with no diluent. Combining these results with the axial power shapes (shown in Figure 3.5-Figure 3.7) and the fission cross sections of the key isotopes (shown in Figure 3.8), this spectral softening effect can be seen as the dominant mechanism for the power shaping effect that we have seen. The reduced fuel volume fraction also contributes,

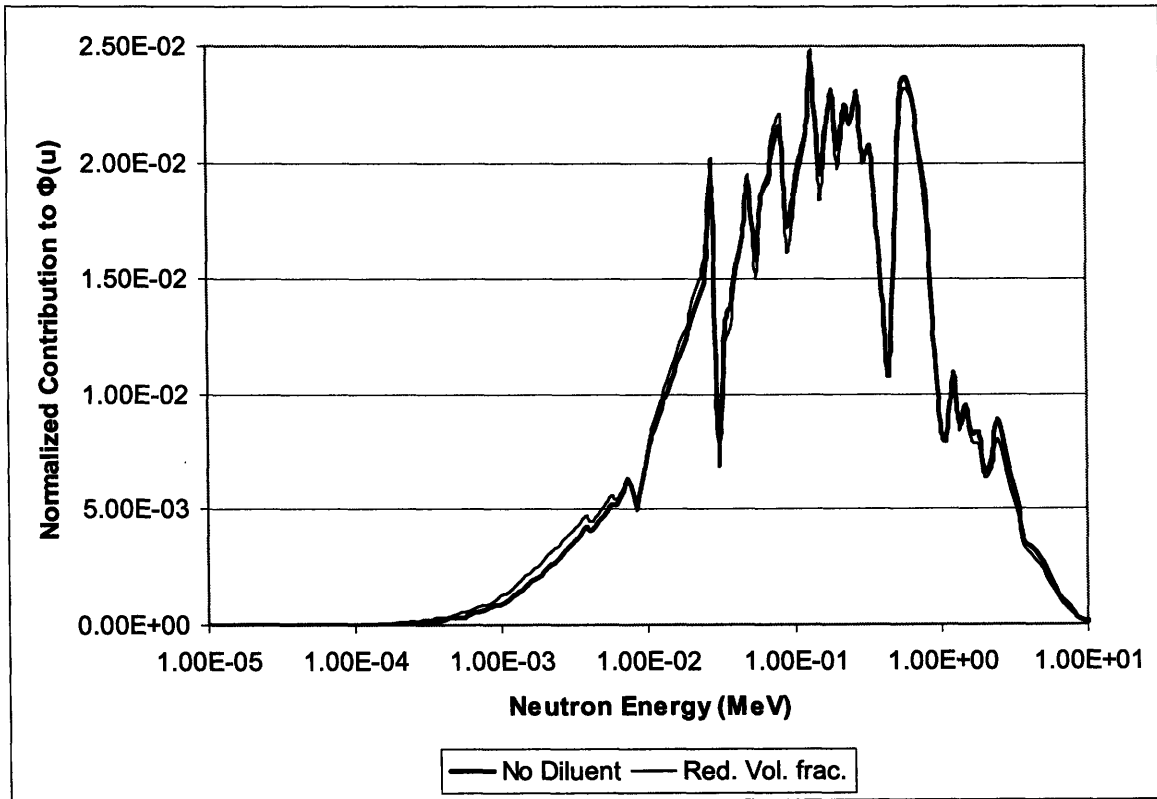


Figure 3.9: Comparison of Neutron Energy Spectra: No diluent and Reduced volume Fraction Cases

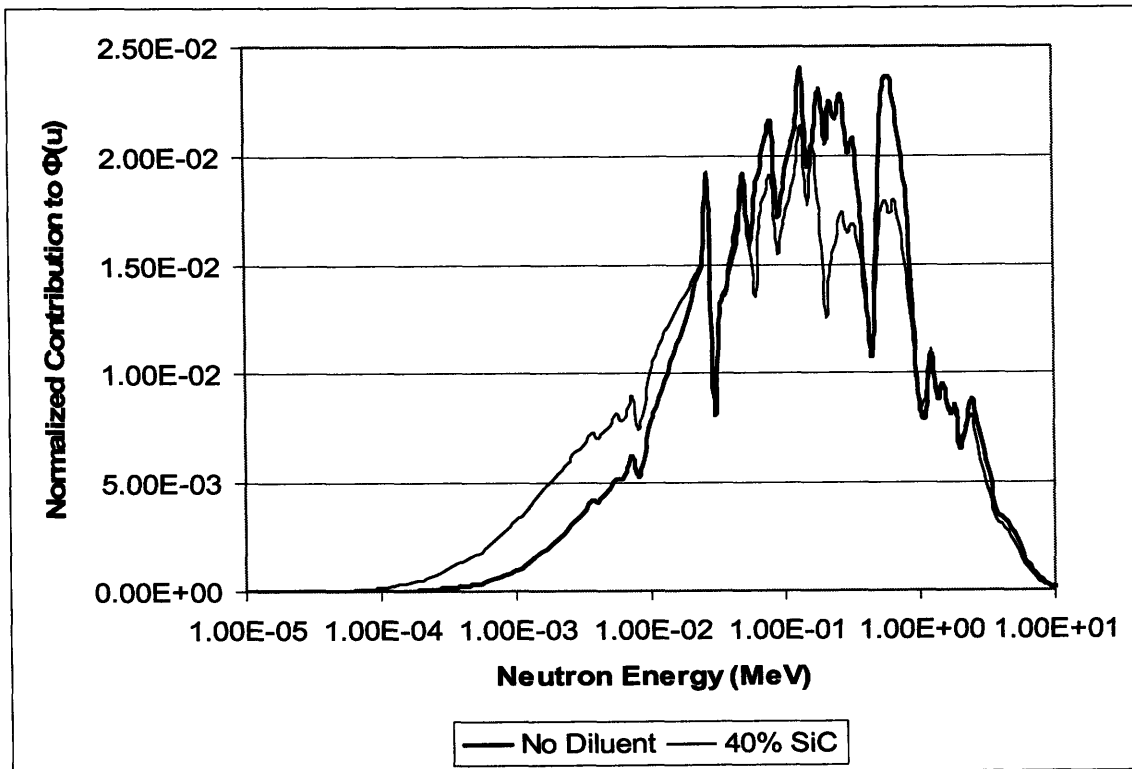


Figure 3.10: Comparison of Neutron Energy Spectra: No Diluent and SiC Cases

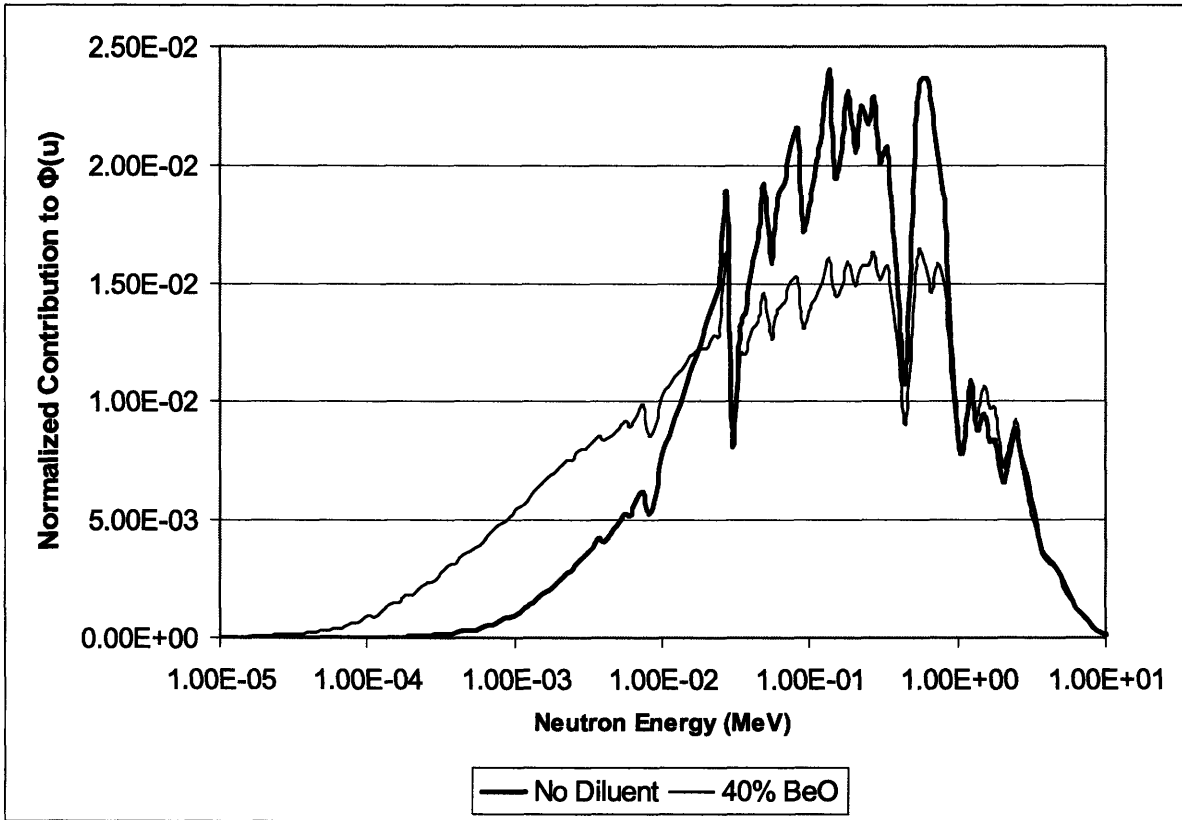


Figure 3.11: Comparison of Neutron Energy Spectra: No Diluent and BeO Cases

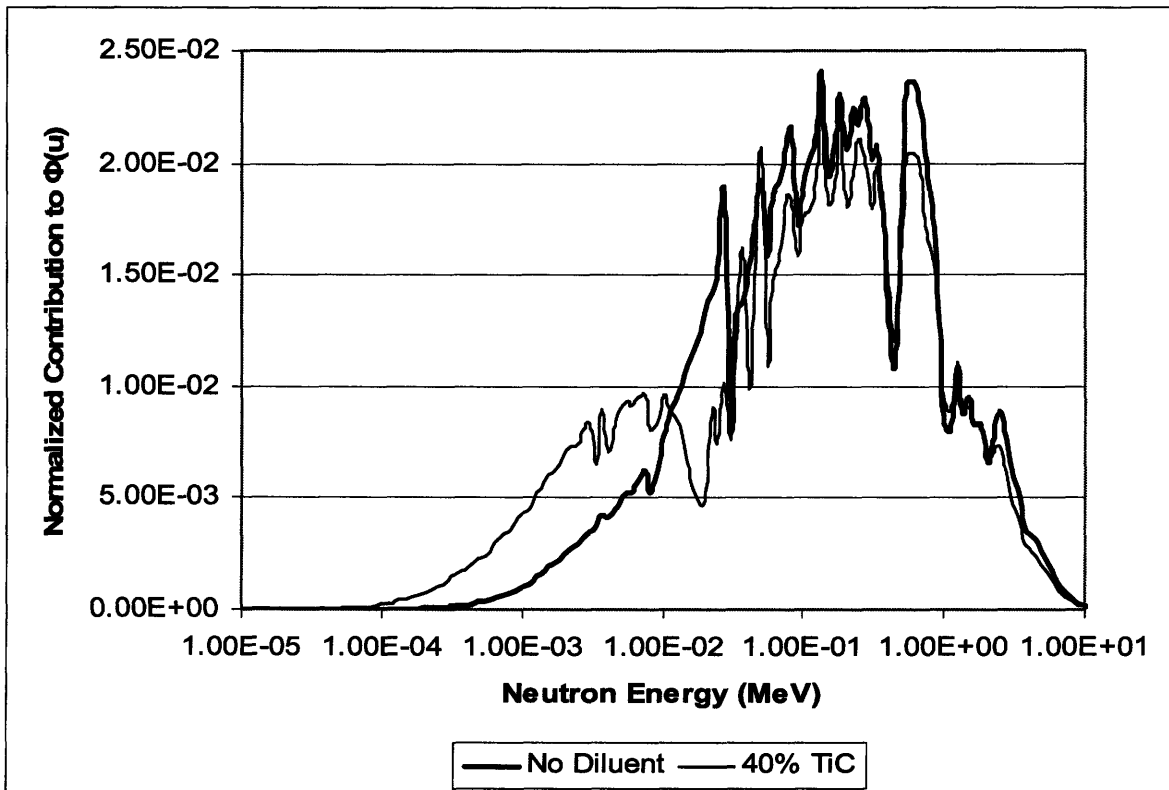


Figure 3.12: Comparison of Neutron Energy Spectra: No Diluent and TiC Cases

as there is less fuel there to fission (and hence, create power); however, it does not act preferentially with respect to geometric location, as the diluent has been shown to.

### 3.3.2 Use of Diluent to Shape Radial Power

An illustrative example of how diluent zoning can be used to shape radial power is shown in Figure 3.13, where a uniform TRU enrichment of 14.2 % is used and a Silicon Carbide (SiC) diluent is added in 3 zones, each of differing concentration. Comparing this figure with the results shown in Figure 3.1 and Figure 3.2 shows that not only can a fairly flat radial power profile be achieved at BOL using only diluent zoning, i.e. peak <1.2, but that the radial power profile can be kept relatively flat over a long period of burnup, with the maximum peak occurring at EOL and staying below 1.3. The ability to maintain a relatively constant radial power profile over core life results from the moderating properties of the diluent. Since the diluent does not get used up like a more traditional burnable poison, it maintains its potency throughout core life.

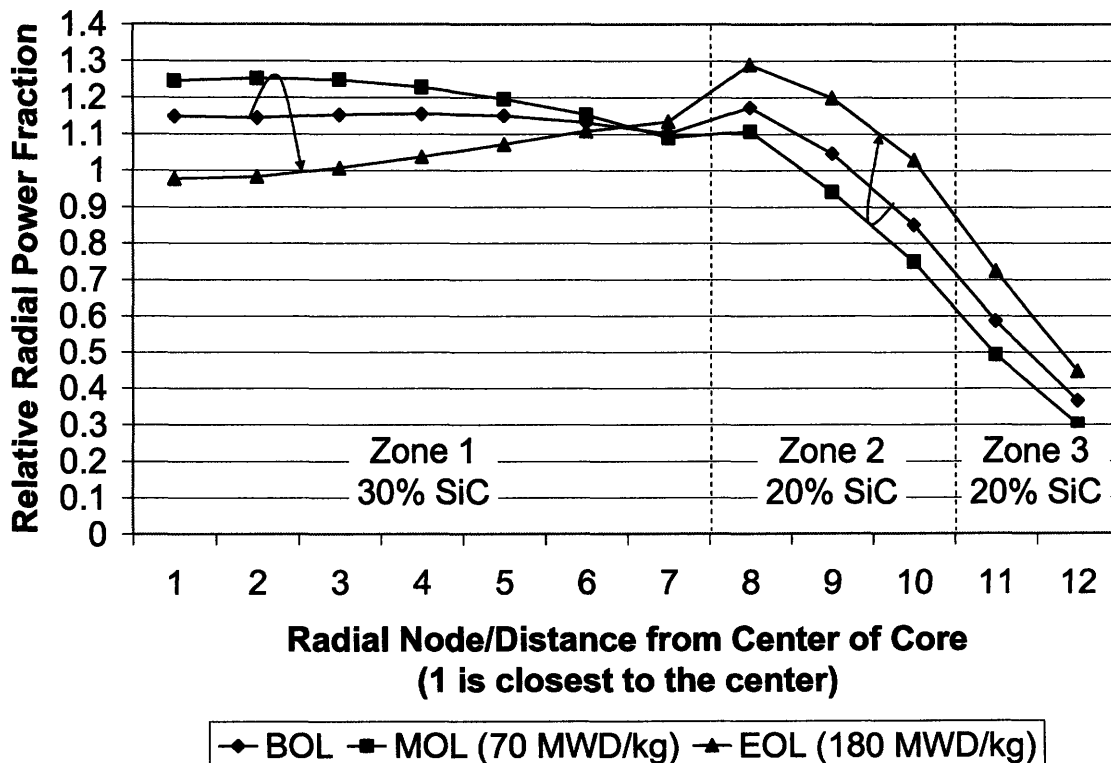


Figure 3.13: Illustrative Example of Using Diluent to Shape Radial Power For a Core with Uniform 14.2 % TRU Enrichment and Three Zones of Diluent



There are several other important results of diluent use that can be gleaned from a comparison of the information in Figure 3.1, Figure 3.3, and Figure 3.13. First, it should be noted that the addition of the diluent to the fuel causes the BOL critical enrichment to increase from a core average value of 12.35 % (in Figure 3.1) to 14.2 % (in Figure 3.13). This is due to the moderating property of the diluent which softens the neutron energy spectrum enough to inhibit fast fission without completely prohibiting it. This effect is most pronounced in the two isotopes which account for the majority of the fissions in the core, Pu-239 (65-70%) and U-238 (15-20%). Specifically, it lowers the fission cross section of U-238 while that for Pu-239 stays roughly constant (shown in Figure 3.8). Concomitantly, the moderating effect increases the capture cross section in these two isotopes, as well as the other Actinides present. Hence, a higher enrichment of fuel is necessary to make up for this lower capability to fission and higher propensity to capture in order to achieve the same core eigenvalue. Second, comparing the EOL burnup values displayed in Figure 3.1 and Figure 3.13 suggests that addition of a diluent reduces the reactivity limited lifetime of the core.

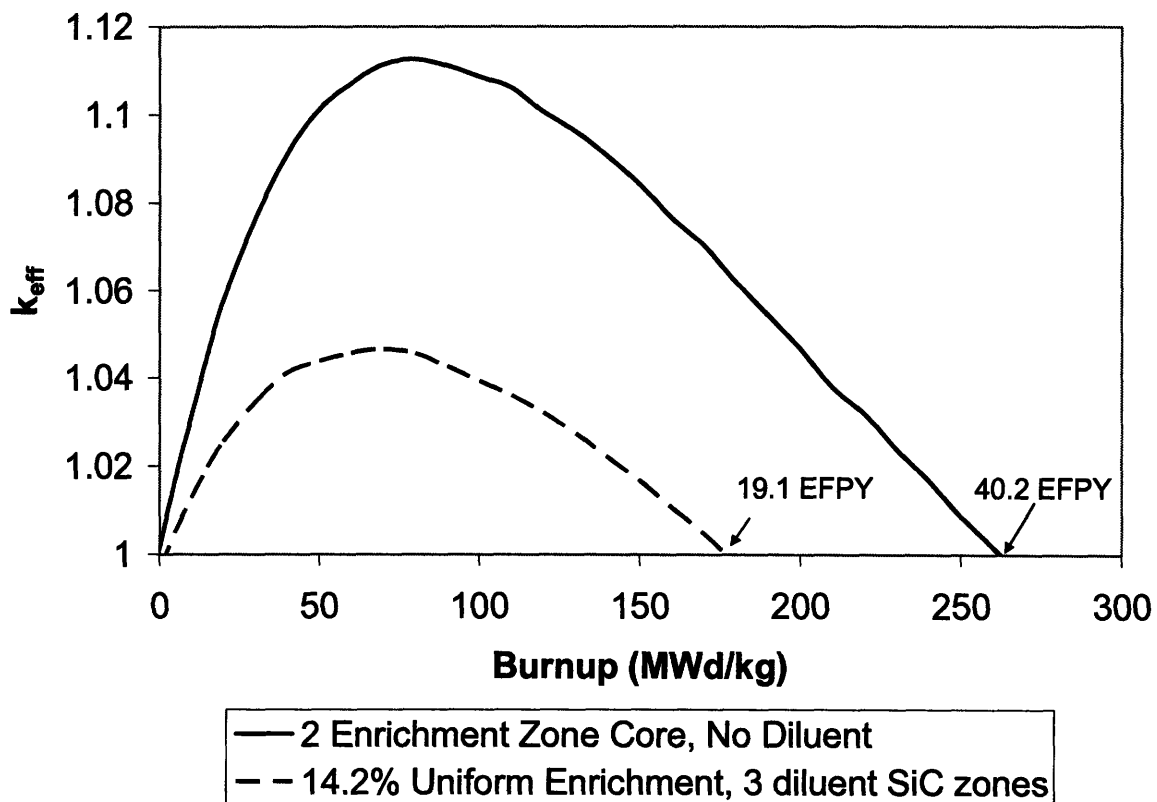


Figure 3.14: Eigenvalue-burnup Comparison between the Two Enrichment Zone Core with no Diluent and the Uniform Enrichment Three Diluent Zone Core

Looking at the excess reactivity curve of the cores represented in Figure 3.1 and Figure 3.13 in Figure 3.14 shows that not only does the diluent have the effect of reducing the reactivity limited burnup of the core, but it also significantly reduces the reactivity swing. This is both advantageous and disadvantageous, as the reduced reactivity swing bodes well for reducing active reactivity control requirements and protection against severe accidents, while the shortened reactivity limited burnup has negative economic consequences. The smaller reactivity swing and the shortened reactivity limited burnup are a direct consequence of the spectral softening effect of the diluent, which reduces the reproduction factor,  $\eta$ , for the key primary fissile isotopes of interest in this core, Pu-239 and Pu-241. A lower reproduction factor means a lower number of excess neutrons ( $\eta-1$ ) available for converting the fertile isotopes, i.e. U-238, Pu-240, to fissile isotopes, hence limiting the amount of excess reactivity and achievable burnup.

### 3.3.3 Use of Diluent for Axial Power Shaping

Axial power shaping is employed for both thermal hydraulic and neutronic reasons. Neutronically, it is desirable because the flatter the axial power shape, the more uniform the burning of the fuel. Thermal hydraulically, it is desirable to produce a relatively flat cladding temperature profile, as the cladding is the part of the core which typically operates with the smallest margin to material failure. Hence, the absence of peaks in the axial cladding temperature profile is desirable, as it is the peak value that limits the fuel thermal performance. However, an axially flat power shape will not produce an axially flat cladding temperature profile. Consequently, the thermal hydraulic and neutronic goals of axial power shaping each require a different axial power shape. It is typically the thermal hydraulic constraints that dominate as they are more performance limiting.

In order to determine the ideal axial power shape to produce a flat axial cladding temperature profile a coolant subchannel unit cell, with mass entering and leaving vertically and heat entering horizontally is shown in Figure 3.15. Axially,

$$\dot{Q} = \dot{m} C_p \Delta T_b \quad \{3.1\}$$

where:

$\dot{Q}$  = thermal power  
 $\dot{m}$  = mass flow rate  
 $C_p$  = Specific Heat Capacity at constant pressure  
 $\Delta T_b$  = Change in coolant bulk temperature

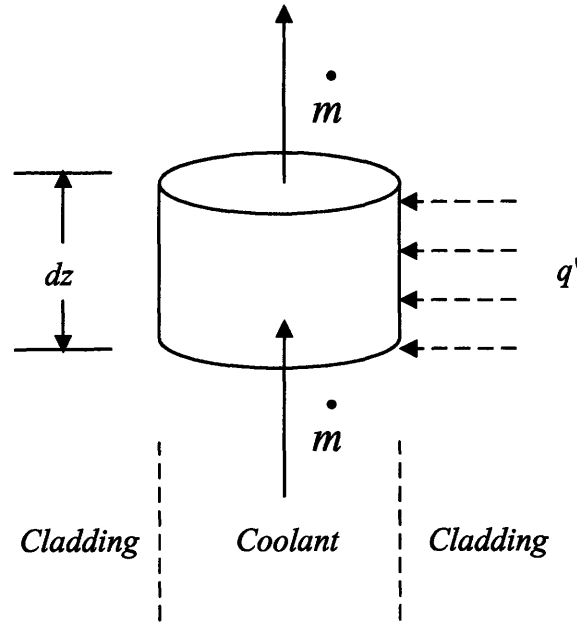


**Figure 3.15: Coolant Subchannel Unit Cell**

Applying this relation to the unit cell:

$$q'(z)dz = \dot{m} C_p dT_b(z)$$

where:

$q'(z)$  = Linear heat generation rate as a function of axial position,  $z$

$dz$  = incremental height of unit cell

$T_b(z)$  = Coolant bulk temperature as a function of axial position,  $z$

Rearranging:

$$\frac{dT_b(z)}{dz} = \frac{q'(z)}{\dot{m} C_p} \quad \{3.2\}$$

Now looking at the relationship for heat transfer between the cladding and the coolant in the radial direction:

$$q''(z) = \bar{h}[T_{co}(z) - T_b(z)] = \frac{q'(z)}{P_h}$$

where:

$q''(z)$  = Heat flux as a function of axial position,  $z$

$\bar{h}$  = spatially averaged heat transfer coefficient

$T_{co}(z)$  = Cladding outer temperature (i.e. at the cladding-coolant interface) as a function of axial position,  $z$

Taking the derivative with respect to  $z$  and rearranging:

$$\frac{dT_{co}(z)}{dz} = \frac{1}{hP_h} \frac{dq'(z)}{dz} + \frac{dT_b(z)}{dz} \quad \{3.3\}$$

Setting Eq. {3.3} equal to zero (in order to get a flat axial cladding temperature profile) and rearranging:

$$\frac{dT_b(z)}{dz} = -\frac{1}{hP_h} \frac{dq'(z)}{dz} \quad \{3.4\}$$

Substituting {3.4} into {3.2} and rearranging:

$$q'(z) + \left( \frac{\dot{m}C_p}{hP_h} \right) \frac{dq'(z)}{dz} = 0 \quad \{3.5\}$$

which is a homogeneous first order differential equation, whose solution gives the axial power shape that will give a flat axial cladding temperature profile:

$$q'(z) = Ce^{-z/A} \quad \{3.6\}$$

where:

$q'(z)$  = axial distribution of linear heat generation rate

$z$  = axial height

$$A = \frac{\dot{m}C_p}{hP_h}$$

$C$  = a constant whose value depends on channel geometry

Hence, the most desirable axial power shape is exponential with a peak at the channel inlet, i.e. inlet-peaked.

Using FLOWSPLIT, an in-house code developed at MIT [Hejzlar, 1994], the effects of axial power shaping were examined by calculating the axial cladding temperatures resulting from hypothetical axial power shapes. Figure 3.16 shows the four axial power shapes that are evaluated: inlet peaked, uniform, chopped cosine with a peak of 1.3, and two-tier with a higher value for the bottom half of the core than the for the upper half of the core. The chopped cosine power shape with a peak of 1.3 is explored, as calculations show that this is the axial power shape that exists in the core without any effort made at axial power shaping. This case can be seen in the “no diluent” case in Figure 3.5 and would apply to an axially uniform application of diluent, as there would be no geometric preference given to spectral softening. As well, the last power shape mentioned is explored in an effort to flatten the axial cladding temperature profile, but providing more power in the bottom of the core, and thus mimicking the optimum, inlet-peaked power profile. The axial cladding

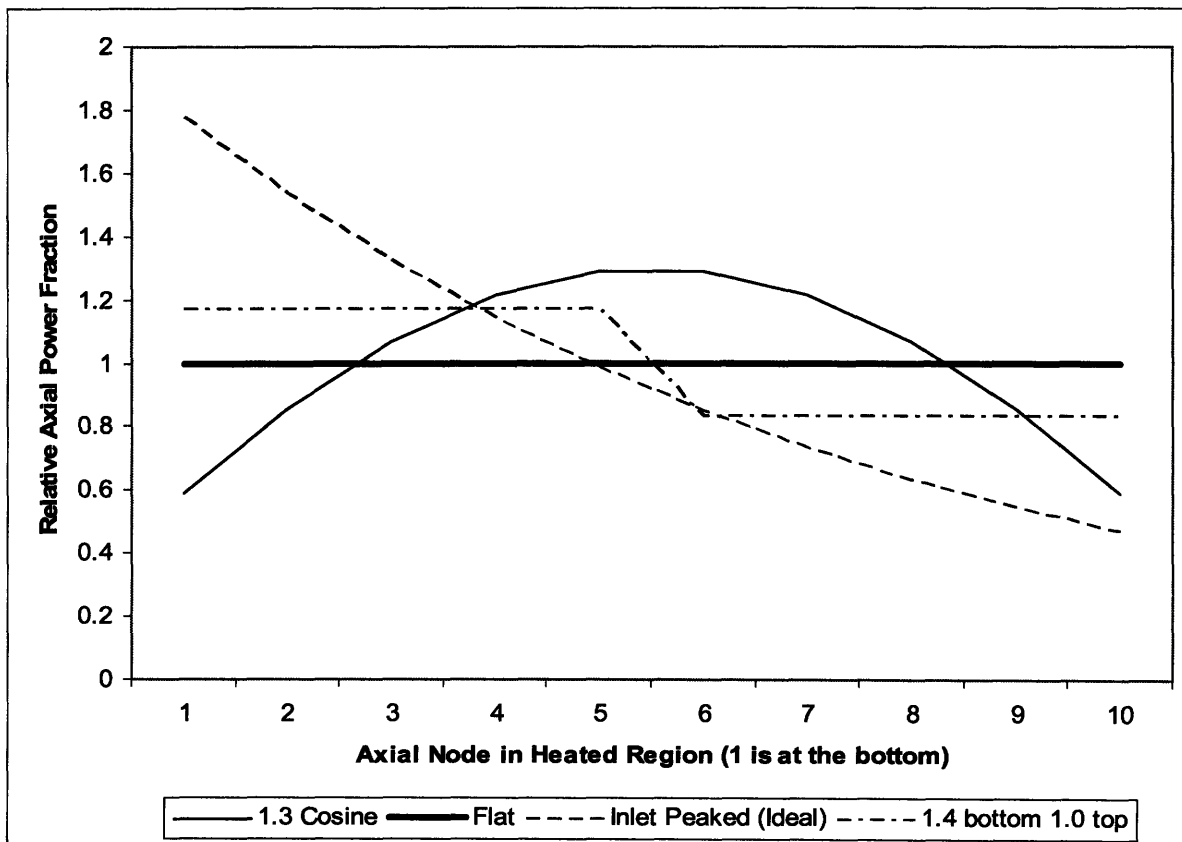
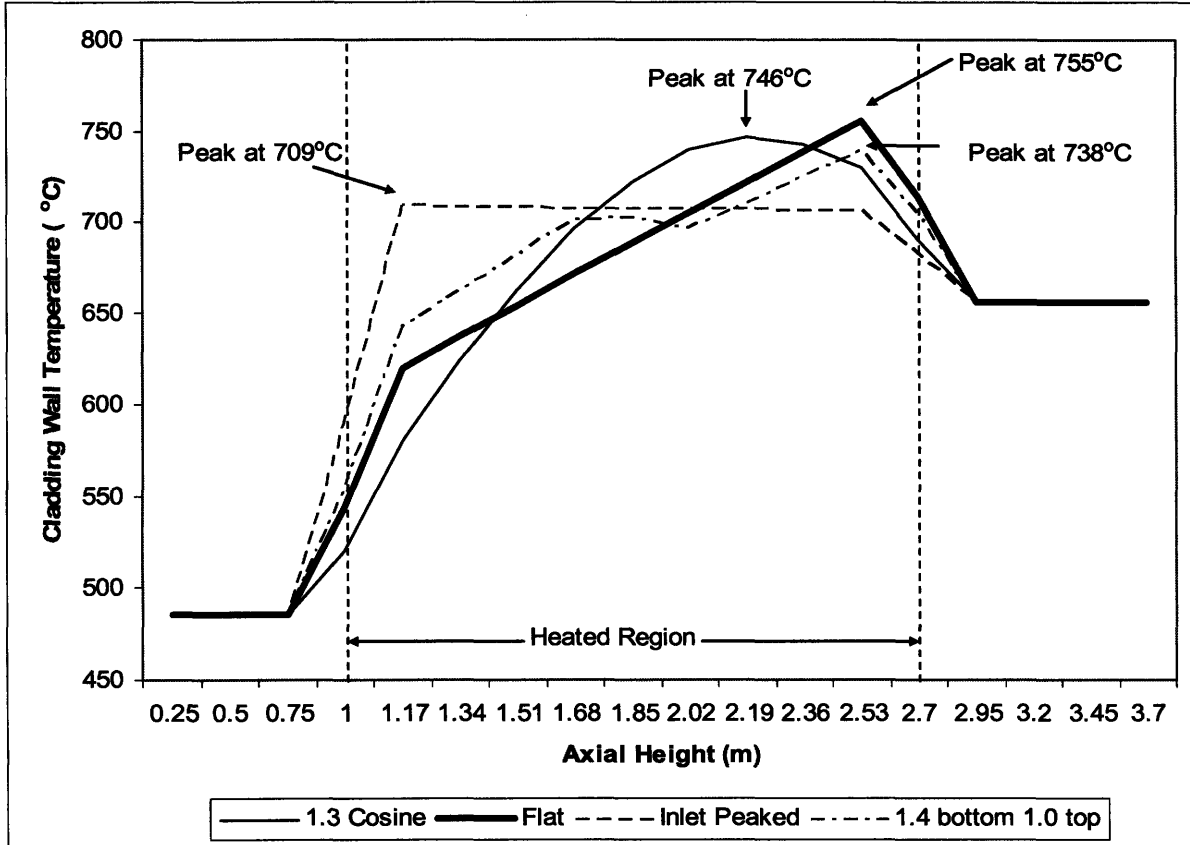


Figure 3.16: Comparison of Axial Power Profiles Used for FLOWSPLIT Analysis of Axial Cladding Temperature Flattening



**Figure 3.17: Comparison of Wall Temperature Profiles in the Peak Channel Assuming a 1.1 Radial Peaking Factor (using FLOWSPLIT)**

temperature profiles that result from the axial power shapes in Figure 3.16 are shown in Figure 3.17. A radial peaking factor of 1.1 is used for illustrative purposes and a change in this value should not appreciably affect the relative magnitude of these results with respect to each other.

Of interest is that the power shape which provides the theoretically lowest possible peak cladding temperature (an inlet peaked power distribution) yields a peak cladding temperature only 37 degrees lower than the default, unshaped axial power profile, a cosine shape with a peak to average ratio of 1.3. Hence, the best improvement that can be made by axial power shaping is to reduce the peak cladding temperature by only 37°C.

It is important to remember that the modest benefit of axial power shaping assumes that a truly inlet peaked power profile is achievable. In an effort to achieve the optimum inlet peaked axial power shape, different axial diluent zoning schemes were explored, subject to the following constraints: (1) no more than 3 axial zones of diluent were used and (2) the

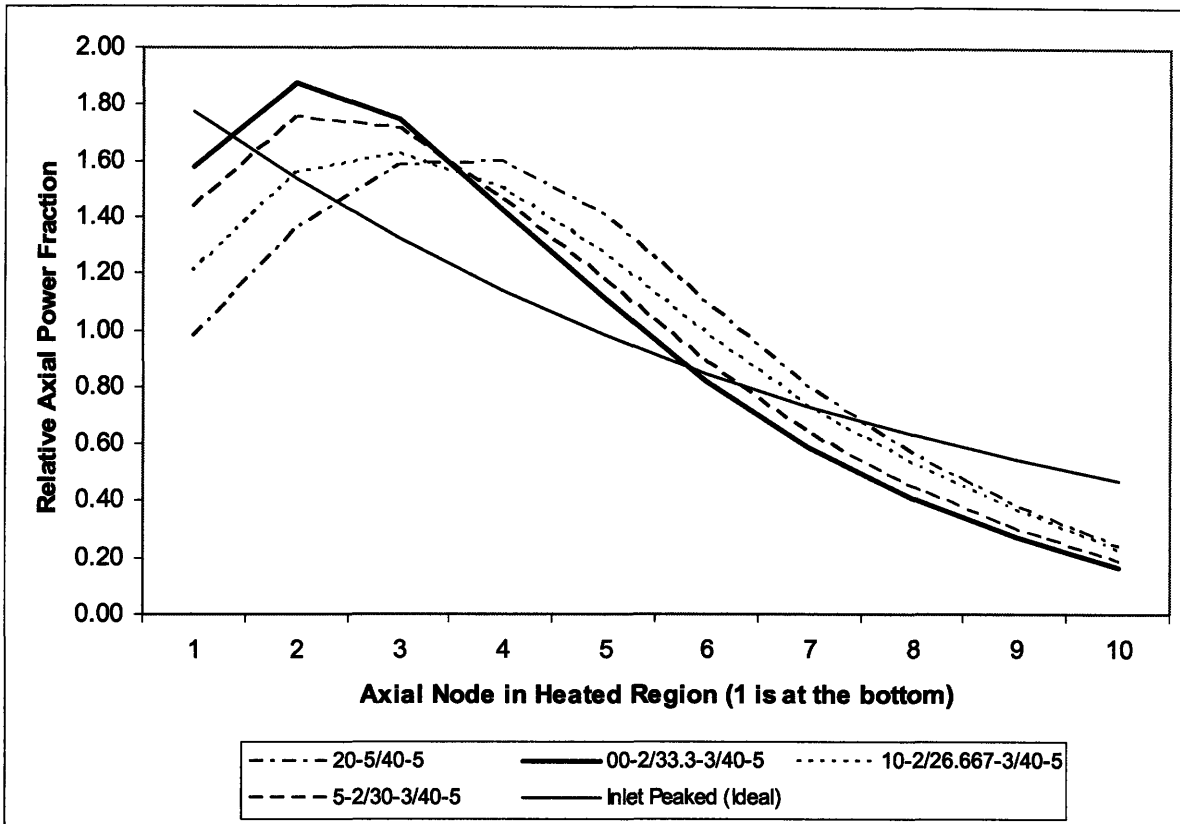


Figure 3.18: Axial Power Shapes Resulting from Axial Diluent Zoning

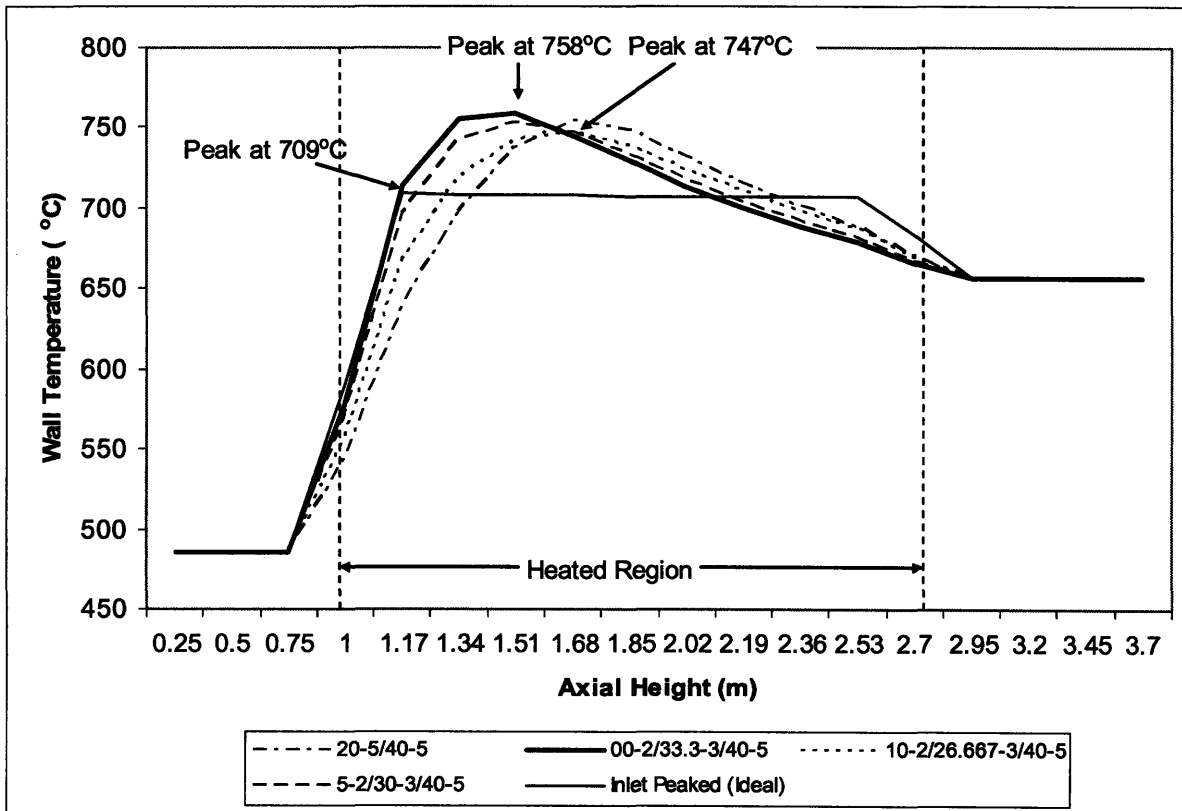


Figure 3.19: Comparison of Wall Temperature Profiles Resulting from Attempts at Axial Power Shaping in the Peak Channel (assuming a 1.1 Radial Peaking Factor)

volume averaged diluent concentration should be consistent, 30% in this case. Figure 3.18 shows the axial power shapes achieved as a result of the axial diluent zoning, with a brief description of the distribution of diluent in the legend of the figure, e.g. 20-5/40-5 means 20% diluent in the first 5 axial nodes and 40% diluent in the next 5 axial nodes. As well, the ideal inlet peaked power shape is shown, for comparison. While the optimum inlet-peaked power shape can be closely mimicked through the use of axial diluent zoning, it cannot be exactly duplicated, due to axial leakage. Exact duplication of the inlet power shape would require an infinite reflector, which would be prohibitively expensive and may affect macro core neutronic performance in undesirable ways.

Figure 3.19 shows the axial cladding temperature profiles that result from the axial power shapes shown in Figure 3.18, along with that resulting from the “ideal” axial power shape. While diluent was successful in helping to shape the axial power, the axial power profiles produced were unable to yield a peak cladding temperature comparable to that of the ideal case. In fact, comparing the lowest peak cladding temperature resulting from axial power shaping in Figure 3.19 (747°C) with that of the default, “do-nothing” approach in Figure 3.17 (746°C) shows that it is more desirable to **not** shape axial power. This is due to the fact that shaping to mimic the ideal axial power shape creates a large peak in power, but not in the optimal axial location to obtain a flat axial cladding temperature profile. Hence, in this core design, there will be no attempt at axial power shaping. Efforts and analysis will only be directed toward shaping the radial power profile using diluent. Should shaping of the axial cladding temperature profile prove necessary, other means such as the use of small fins, cladding surface roughening, or dimpling are available. It should be noted that these solutions come at the price of increased pressure drop, which increases circulator work (i.e. “pumping power”) requirements during both normal operation and decay heat removal.

### **3.4 Use of Diluent for Coolant Void Reactivity (CVR) Reduction**

The spectral softening effect resulting from the use of diluent is also beneficial from a coolant void reactivity (CVR) standpoint. CVR is due to 3 sources: (1) spectral hardening, (2) coolant absorption, and (3) neutron leakage. Since there is no significant effect associated with addition of diluent with respect to the last two sources, the major effect that



the diluent has is to counteract the first source by softening of the spectrum. Ignoring the effects of leakage, this can be seen by:

$$k_{\infty} = \nu \frac{\Sigma_f^f}{\Sigma_a^t} \quad \{3.7\}$$

where:

$k_{\infty}$  = infinite medium multiplication factor

$\nu$  = average number of neutrons per fission

$\Sigma_f^f$  = macroscopic fission cross section of the fuel

$\Sigma_a^t$  = macroscopic absorption cross section of all of the core materials

Since  $\Sigma_a^t \approx \Sigma_a^f$  for the semi-infinite assembly case, assuming that the contribution to absorption by the coolant and cladding material are negligible, and:

$$\Sigma_f^f = N^f * \sigma_f^f$$

$$\Sigma_a^f = N^f * \sigma_a^f$$

where:

$N^f$  = Number density of the fuel

$\sigma_f^f$  = microscopic fission cross section of the fuel

$\sigma_a^f$  = microscopic absorption cross section of the fuel =  $\sigma_f^f + \sigma_{\gamma}^f$

where:

$\sigma_{\gamma}^f$  = microscopic capture cross section of the fuel

Equation {3.7} becomes:

$$k_{\infty} \alpha \frac{\sigma_f^f}{\sigma_f^f + \sigma_{\gamma}^f} = \frac{1}{\frac{\sigma_f^f + \sigma_{\gamma}^f}{\sigma_f^f}} = \frac{1}{1 + \frac{\sigma_{\gamma}^f}{\sigma_f^f}} \quad \{3.8\}$$

Thus:

$$\Delta\rho = \rho_f - \rho_i = \frac{k_{\infty,v} - 1}{k_{\infty,v}} - \frac{k_{\infty,i} - 1}{k_{\infty,i}} = \frac{1}{k_{\infty,i}} - \frac{1}{k_{\infty,v}} \quad \{3.9\}$$

where:

$\rho$  = reactivity

the subscript “v” denotes the voided case  
the subscript “i” denotes the initial unvoided case

Substituting Eq. {3.8} into {3.9}:

$$\Delta\rho_{VOID} \propto \frac{1}{1 + \frac{\sigma_{\gamma,i}^f}{\sigma_{f,i}^f}} - \frac{1}{1 + \frac{\sigma_{\gamma,v}^f}{\sigma_{f,v}^f}} = \frac{\sigma_{\gamma,i}^f}{\sigma_{f,i}^f} - \frac{\sigma_{\gamma,v}^f}{\sigma_{f,v}^f} \quad \{3.10\}$$

Hence, the reactivity inserted by voiding of the coolant is proportional to the ratio of the capture to fission microscopic cross sections of the unvoided case less that of the voided case. Reactivity in this core is driven primarily by Pu-239, which accounts for ~65-70% of fissions throughout core life. Looking at this ratio for Pu-239 as a function of energy in Figure 3.20 shows that for the undiluted case, as the spectrum hardens due to voiding, the voided ratio is smaller than the initial, unvoided ratio and positive reactivity is inserted. However, when diluent is added to the fuel, the initial neutron energy in the unvoided core is

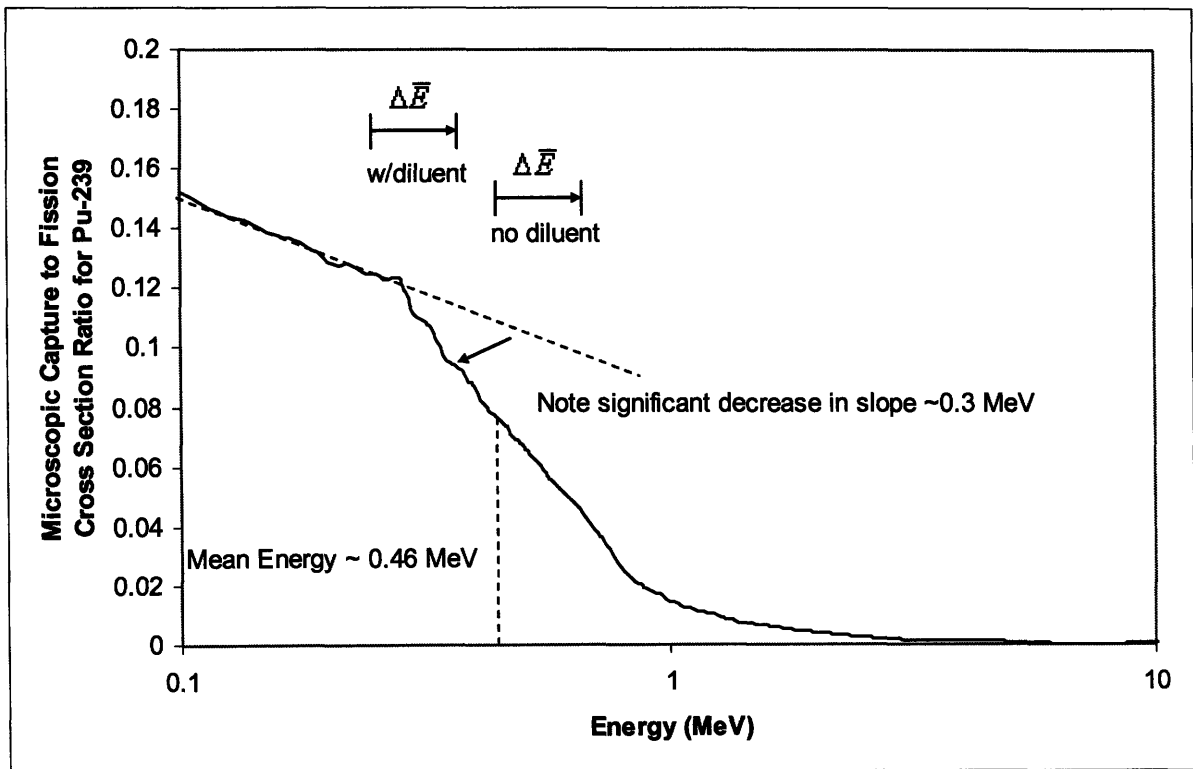


Figure 3.20: Illustration of the Effect of Spectral Softening on Coolant Void Reactivity

lower than that of the undiluted case, shifting the neutron energy increase that occurs upon voiding to begin at lower energies. Since the mean neutron energy in the system is at approximately 0.46 MeV and is near a discontinuity in the slope of the capture to fission cross section ratio (at about 0.3 MeV), lowering the energy through the use of diluent reduces the difference between the ratio for the voided and unvoided cases. It is in this way that softening the neutron energy spectrum through the use of diluent reduces CVR.

It should be noted that a concurrent effect of the use of diluent is to also enhance the Doppler fuel reactivity coefficient, as the softening of the neutron spectrum pushes more neutrons into the resonance region. It has been calculated that the use of diluent enhances Doppler feedback by a factor of 3-4 more than other contemporary fast reactor designs. As well, use of diluent enhances the worth of traditional reactivity control absorbers, e.g. B<sub>4</sub>C control rods, in a fast reactor environment. More discussion of these effects and their implications will be explored later.

### **3.5 Diluent Material Selection**

Three diluents have been used in the illustrative examples in this chapter thus far: SiC, BeO, and TiC. The next logical question is: which is the best among them? In order to decide, the criteria in Table 3.1 are suggested for evaluation. Note that the criteria presented in Table 3.1 are very similar to those that will be presented for selection of an Inert Matrix Fuel. As well, it should be noted that some of the desired trends for the neutronic performance criterion represent competing effects with diluent use, as discussed throughout this chapter.

All three of the candidate diluent materials were also assessed for their suitability as axial reflector materials using many of the criteria in Table 3.1, the results of which are discussed in another chapter of this work. As well, an extensive study of each material would be necessary to truly assess its suitability as a fuel diluent in a fast reactor, including in-pile irradiation testing. Absent that, some aspects of the key neutronic and thermo-physical behavior of the candidate diluents are explored here.

**Table 3.1: Suggested Criteria for Evaluation in Diluent Selection**

Parameter	Desired Trend
1. Neutronic performance	<ul style="list-style-type: none"> <li>▪ Ability to effectively shape power</li> <li>▪ Reduction in CVR</li> <li>▪ Low Reactivity Swing</li> <li>▪ Minimal Effect on Reactivity Limited Burnup</li> <li>▪ Minimal Effect on Critical Enrichment</li> <li>▪ Reasonable augmentation of Doppler Feedback</li> </ul>
2. Chemical compatibility with the coolant	Compatible
3. Chemical compatibility with the fuel	Compatible
4. Chemical compatibility with the clad	Compatible
5. Performance under irradiation	Resistant to irradiation damage
6. Thermal conductivity	Large
7. Heat capacity	Large
8. Melting or phase transformation temperature	High
9. Crystal structure in the operating temperature range	Stable
10. Thermal Expansion	Low
11. Mechanical Properties	Favorable
12. Economics	Reasonably priced and available
13. Consideration of the end state, i.e. to be reprocessed or sent to a geologic repository	N/A
14. Handling and fabrication	Easy
15. Reprocessing	Easy
16. Industrial Experience	Available

**Table 3.2: Comparison of BOL and EOL CVR among Candidate Diluents**

	BOL CVR	STDEV ( $\sigma$ )	EOL CVR	STDEV ( $\sigma$ )	EOL /BOL CVR Ratio	BOL $k_{eff}$
No diluent	0.00801	0.000672	0.00984	0.000502	1.23	1.13009
Red. Vol. Fraction	0.1107	0.000595	0.01267	0.000502	1.14	1.08084
SiC	0.00626	0.000488	0.00754	0.00051	1.20	1.00153
BeO	0.00292	0.000554	0.00434	0.000554	1.49	0.97497

Previously, Figure 3.10-Figure 3.12 showed that each candidate diluent appreciably softened the neutron energy spectrum and Figure 3.7 showed that each is effective in shaping power. Given that each diluent is roughly equivalent in these areas of neutronic

performance, a comparison among these options with respect to Coolant Void Reactivity (CVR) was made. Using the same semi-infinite assembly models used in Section 3.3.1, the CVR at BOL and EOL were calculated, as shown in Table 3.2.

The fact that each of these calculations was performed with the same TRU enrichment at BOL and the same volume fraction of diluent (except the “No diluent” case, which is presented as a basis for comparison) is important when comparing CVR’s. This ensures that the same amount of heavy metal, specifically Pu-239, is resident in each of these semi-infinite assemblies, and allows comparison of each of these cases to show only the diluent’s spectral softening effect on CVR. Comparing the SiC and BeO diluent with the reduced volume fraction case shows that BeO provides the greatest spectral softening and hence, the greatest CVR reduction. This spectral softening is also evident in the fact that BeO has the lowest BOL  $k_{\text{eff}}$  and the highest EOL/BOL Void Ratio, a consequence of more neutrons in the epithermal region throughout core life, which results in more Pu-241 at EOL. With all other neutronic factors being relatively equal and CVR being a large neutronic concern, BeO has been chosen as the diluent of choice for this work. An obvious drawback of such a choice is that given the larger spectral softening of BeO and consequent lower BOL  $k_{\text{eff}}$ , a higher TRU enrichment will be necessary to sustain criticality at BOL. However, other fundamental neutronics trade-offs, i.e. lower reactivity swing, discussed both in previous and future sections of this work will justify such a choice.

While the relative neutronic benefits of the candidate diluents have been compared, the diluents provide similar benefits in other areas of performance. Fortuitously, work is concurrently being performed to assess the thermo physical benefits and suitability of SiC and BeO as diluents in LWR fuel [Khan et. al, 2005][Sarma et. al, 2005]. This work shows a substantial improvement in thermal conductivity for fuel using these diluents, specifically a 50% increase in thermal conductivity for a 10% diluent content [Sarma et. al, 2005]. This adds a thermal hydraulic benefit to the use of diluent in addition to the neutronic ones already enumerated.

### 3.5.1 Unique Issues Associated with the Use of BeO as a Diluent

While BeO shows much promise as a candidate diluent, there are some potential drawbacks to its use in a fast reactor environment. Experiments have shown that BeO shows anisotropic growth with accumulation of fast neutron fluence, which can result in microcracking and ultimately pulverization. Fortunately, these effects can be mitigated by irradiation at higher temperatures (650°C-1100°C) and by manufacturing with finer grain sizes [Hickman et. al, 1964, Keilholtz et. al, 1964]. While these results give an initial indication of performance under irradiation, it is important to note that all of these observations were made with the diluent in monolithic form and say nothing about its performance in an integrated fuel form. As well, BeO has previously been used in a fast reactor, specifically the Southwest Experimental Fast Oxide Reactor (SEFOR). [McVean et al, 1966].

It should also be noted that beryllium is toxic, and prolonged exposure can have long lasting health effects [*Nuclear News*, 2006]. While BeO has been used in numerous other nuclear reactor and weapons applications and there are other harmful substances used in the manufacturing and processing of fuel, this presents an added complication.

Be-9 is unique neutronically in that it more likely to undergo the following reactions than most other elements:  $(n,2n)$ ,  $(n,\alpha)$ , and  $(\gamma,n)$ . Of interest is that it has been hypothesized that the production effect of the  $(n,2n)$  reaction can be cancelled by the consumption effect of the  $(n,\alpha)$  process. This extra alpha (helium) production could affect irradiation growth in the fuel, depending upon two factors: (1) the amount of extra alpha created from this process and (2) the propensity of the fuel matrix to retain this excess alpha. It should be noted that there are two effects which will likely mitigate this extra He buildup: (1) venting of the fuel assemblies and (2) Be undergoes an  $(\alpha,n)$  reaction, e.g. as in a Pu-Be neutron source. The extent of this effect should be examined further in future work, preferably in in-pile irradiation experiments. The remaining Be-9 $(\gamma,n)$ Be-8 reaction is a threshold reaction ( $E=1.67$  MeV), making Be-9 act as a source of neutrons in the presence of photons of sufficient energy [USAEC, 1958]. Shown in Figure 3.21, the microscopic cross section for this  $(\gamma,n)$  reaction is so small that it should not appreciably affect reactor operations at power.

While there are certainly some unique issues associated with the use of BeO as a diluent, other candidate diluents present uniquely limiting characteristics as well. For instance, SiC is insoluble in nitric acid, making the prospect of reprocessing fuel with a SiC diluent discouraging, given current fuel reprocessing technologies. Consequently, a much more in-depth study of each of the candidate diluents, based on the list of factors presented in Section 3.5, needs to be undertaken (including irradiation testing in an integrated fuel form) prior to ultimate selection.

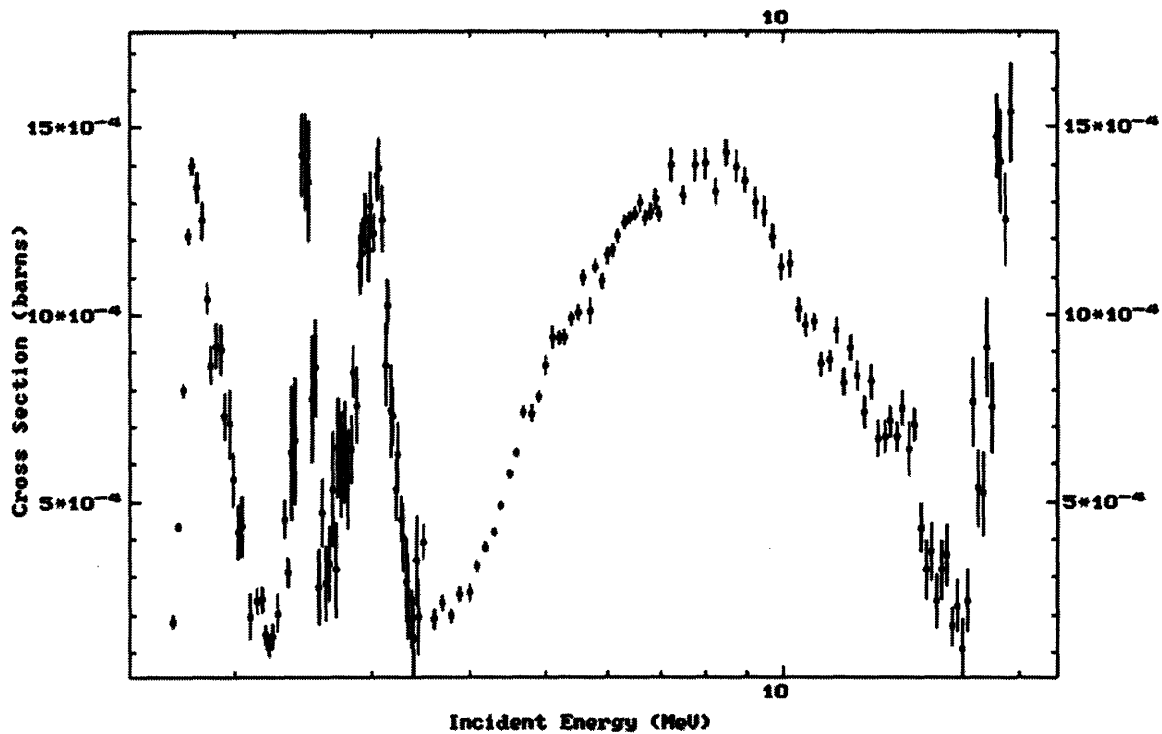


Figure 3.21: Microscopic Cross Section for the  $\text{Be-9}(\gamma, n)\text{Be-8}$  Reaction

While the results in this work from this point forward will use BeO as a diluent, the usefulness of SiC as a diluent has also been demonstrated. Should an insurmountable difficulty be encountered with the implementation of BeO, it should be remembered that SiC has been shown to give similar benefits as a diluent, at the expense of a smaller effect on CVR. Finally, the effect of a moderating diluent on the neutronic performance in a fast reactor has been generally demonstrated. Hence, there may be another suitable material which provides comparable neutronic performance to BeO or SiC with fewer disadvantages in the other categories evaluated for diluent selection.

### **3.6 Optimum Diluent Concentration**

Incorporating diluent into a core design can lower CVR to below \$1 at BOL, which prevents the core from achieving super-prompt criticality upon voiding, i.e. a Loss of Coolant Accident (LOCA). While this improvement in safety is laudable, it does not satisfy the overall goal of this work of designing a passively safe S-CO<sub>2</sub> GFR. Specifically, a negative CVR throughout core life is desired. Since motivation for further reduction of void reactivity has been given, an investigation into how void reactivity is affected by BeO diluent concentration was initiated. Accounting for the trade-offs between diluent and core performance parameters seen thus far, answers to the following questions were sought:

1. What is the relationship between volume fraction of BeO and void reactivity at beginning of core life (BOL)?
2. What is the relationship between BeO concentration and reactivity limited burnup?
3. What is the relationship between BeO concentration and the increase in void reactivity from BOL to end of core life (EOL)?

This study used a semi-infinite assembly (normal leakage axially, reflected boundary conditions radially, and no control rods anywhere), where the BeO concentration was varied in an effort to determine the relationship between BeO volume fraction and the parameters of interest. Correspondingly, the (U,TRU)O<sub>2</sub> concentration was varied to get a beginning of life  $k_{\text{eff}}$  close to 1.



### 3.6.1 BeO Volume Fraction and Coolant Void Reactivity at Beginning of Life

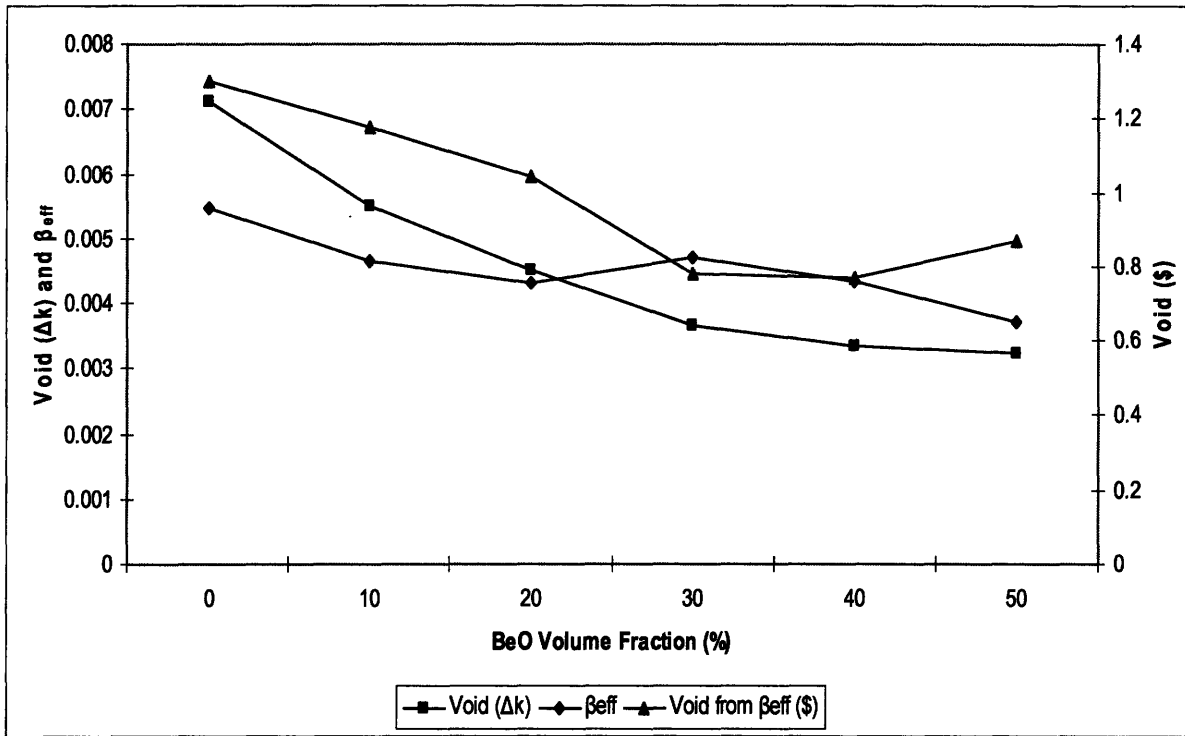


Figure 3.22: Void ( $\Delta k$  and  $\$$ ) and  $\beta_{eff}$  as a function of BeO volume fraction at BOL

Figure 3.22 provides a graphical representation of how the parameters associated with void reactivity vary with diluent concentration. Looking first at the  $\Delta k$  void values, a diminishing returns or saturation effect is seen as BeO volume fraction increases. This can be explained by understanding that as BeO volume fraction increases, the neutron spectrum softens, as shown in Figure 3.4. Since Pu-239 is the largest contributor to fission (~60-80% of all fissions, depending upon diluent concentration and time in life) and the predominant contributor to void reactivity at beginning of life, we will examine the behavior of Pu-239 in order to understand the void reactivity results from varying BeO concentration. Further, Eq. {3.10} showed:

$$\Delta\rho_{VOID} \propto \frac{\sigma_{\gamma,i}^f}{\sigma_{f,i}^f} - \frac{\sigma_{\gamma,v}^f}{\sigma_{f,v}^f}$$

Looking at the ratio of the capture to fission microscopic cross section for Pu-239 in Figure 3.20 shows that as the average neutron energy softens (as is the case with increasing BeO concentration), the value of this ratio for the unvoided case moves to lower energies.

As this ratio moves to lower energies, the increase in energy due to voiding will produce smaller additions of reactivity, owing to the discontinuity in slope shown Figure 3.20 at around 0.3 MeV. However, a concurrent effect of increasing BeO concentration is to increase the fission fraction, hence importance, of Pu-239, as shown in Figure 3.23. This increase in fission fraction stems from the spectral softening of the diluent, which significantly reduces the microscopic fission cross section ( $\sigma_f$ ) for U-238 while the spectrum averaged  $\sigma_f$  for Pu-239 increases ( $10^{-5}$  MeV to 10 MeV), as shown in Figure 3.24. Hence, while increasing BeO concentration may soften the energy spectrum and reduce the magnitude of positive void reactivity, it also has the effect of increasing the fission fraction of Pu-239 in the core, which increases the contribution of Pu-239 to positive void reactivity. From Figure 3.22, this trade-off is apparent as the reduction in void reactivity from spectral softening decreases with increasing diluent concentration.

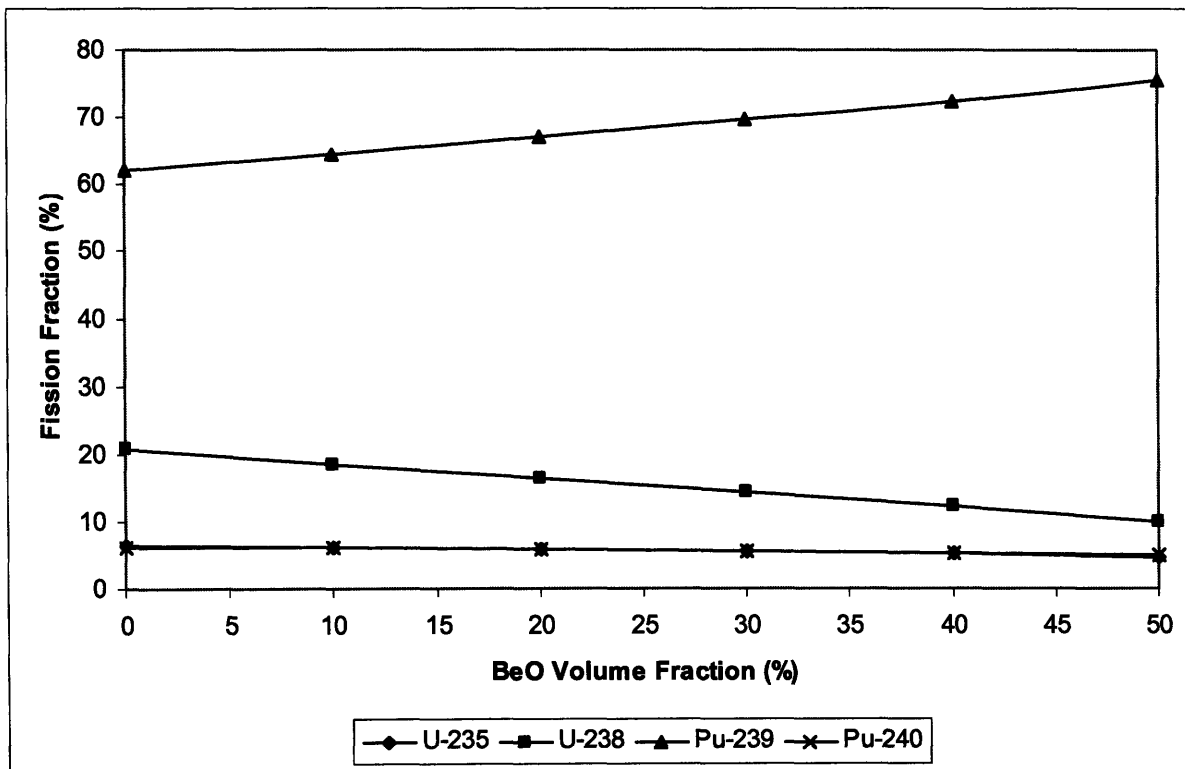


Figure 3.23: Fission Fraction of 4 Largest Isotopic Contributors at BOL

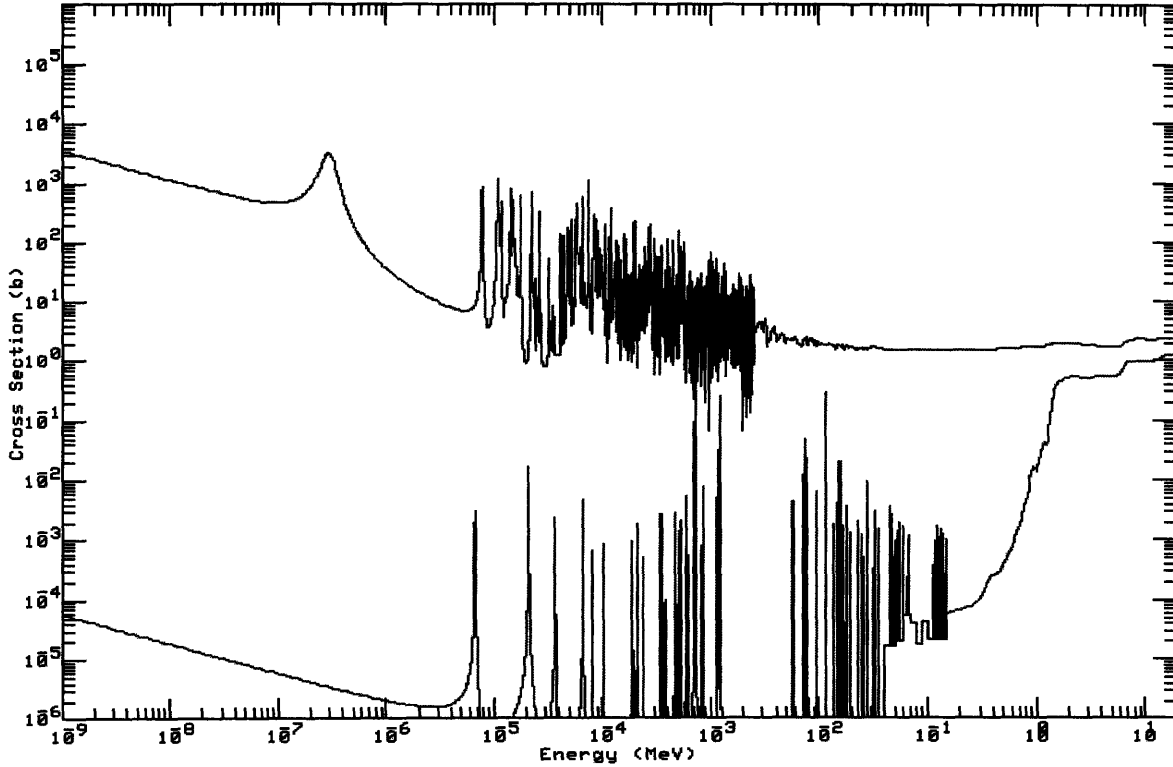


Figure 3.24: Microscopic Fission Cross Section of Pu-239 and U-238 (top to bottom)

A curious artifact of this investigation is the wavy behavior of  $\beta_{\text{eff}}$  seen in Figure 3.22. Using data obtained from MCODE, the respective values of  $\bar{\beta}$  for the various diluent volume fractions were calculated in an effort to understand this wavy behavior. These results, shown in Figure 3.25, demonstrate that the waviness of  $\beta_{\text{eff}}$  is likely due to the statistical uncertainty associated with the process used to generate the values of  $\beta_{\text{eff}}$  in MCNP.  $\beta_{\text{eff}}$  and  $\bar{\beta}$  are related by:

$$\beta_{\text{eff}} = I\bar{\beta} \quad \{3.11\}$$

where

$\beta_{\text{eff}}$  = effective delayed neutron fraction - fraction of all thermal neutrons born delayed

$I$  = importance factor, which is a correction factor that accounts for the lower leakage and fast fission contribution of delayed neutrons (due to their being born at lower energies than fission neutrons).

$\bar{\beta}$  = average delayed neutron fraction – calculated from the fission-fraction-weighted average delayed neutron yield of the isotopes in the fuel

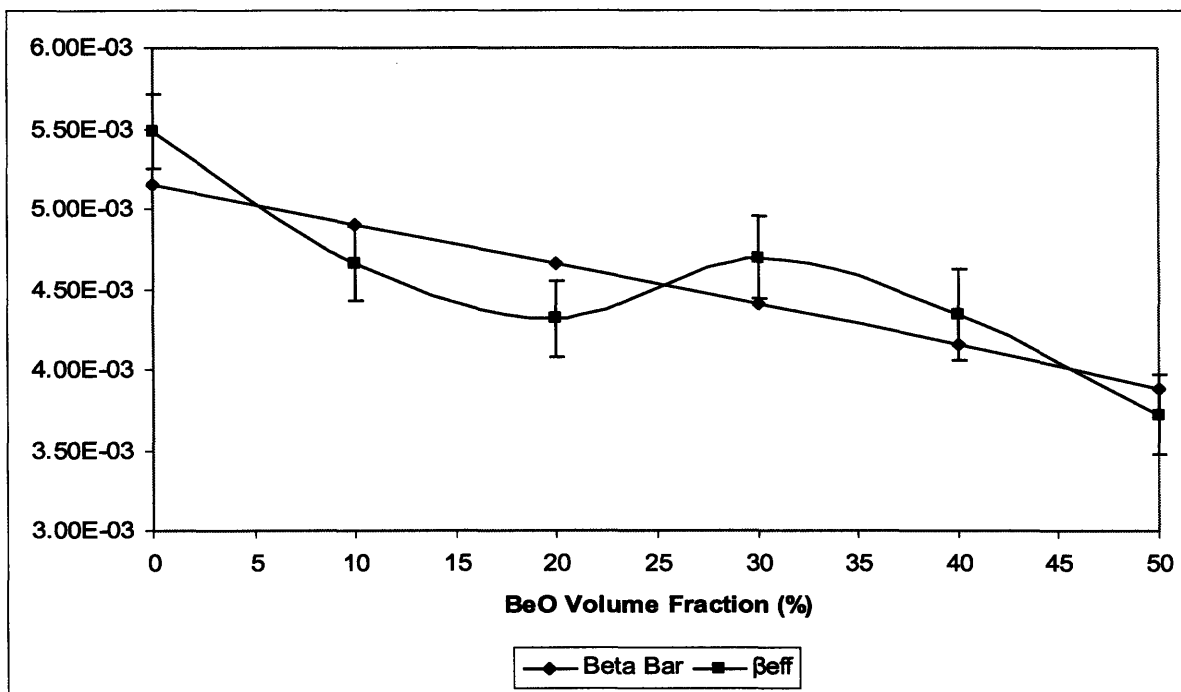


Figure 3.25: Behavior of  $\beta_{\text{eff}}$  and  $\bar{\beta}$  as a function of BeO volume fraction at BOL

The reduction in  $\bar{\beta}$  with respect to increasing BeO volume fraction can be explained by the fact that as BeO concentration increases, the fission fraction of Pu-239 increases and the fission fraction of U-238 decreases, as shown in Figure 3.23. Since Pu-239 has a much lower delayed neutron fraction than its chief isotopic competitor at BOL, U-238, as the contributions of Pu-239 increase and U-238 decrease, the value of  $\bar{\beta}$  decreases. This effect is despite the fact that Pu-239 concentration decreases as BeO volume fraction increases. This can all be explained by the spectral softening effect of BeO which increases the fission contribution of Pu-239 relative to U-238. As the spectrum softens, the spectrum averaged - microscopic fission cross section ( $\sigma_f$ ) of Pu-239 stays relatively constant (within the region of interest) while that for U-238 decreases (shown in Figure 3.24).

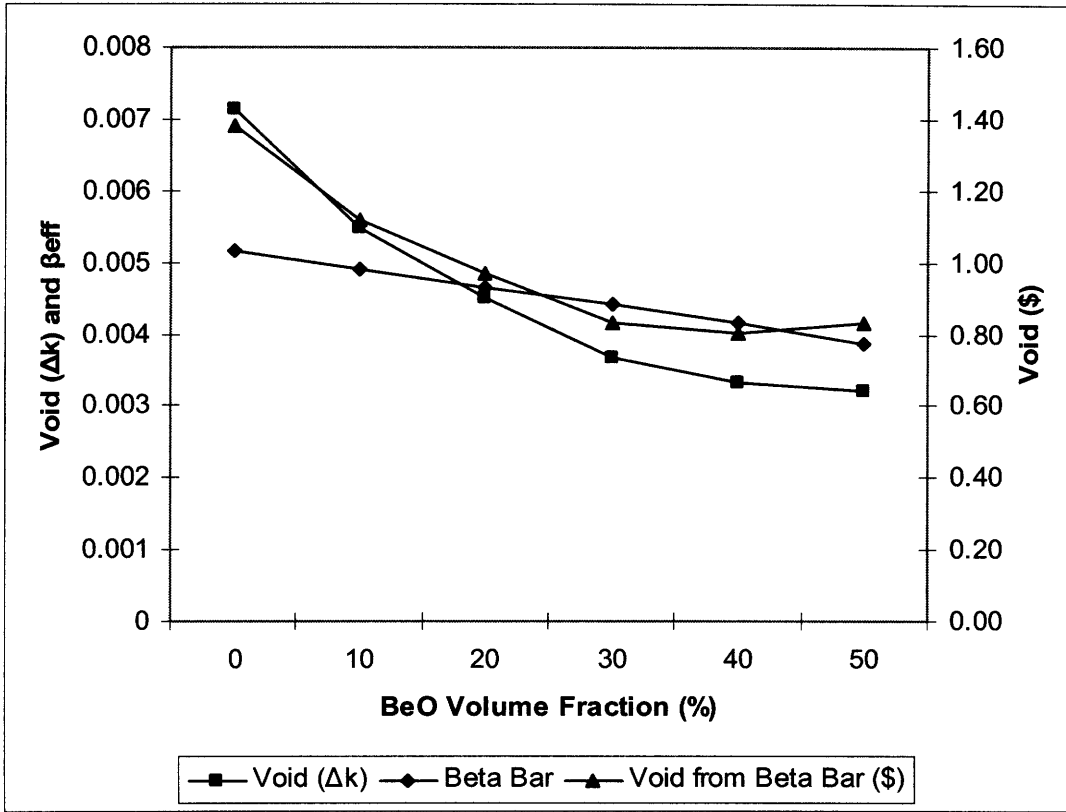


Figure 3.26: Void ( $\Delta k$  and  $\$$ ) and  $\bar{\beta}$  as a function of BeO volume fraction

Comparing  $\beta_{\text{eff}}$  and  $\bar{\beta}$  in Figure 3.25 shows that  $\beta_{\text{eff}}$  varies around  $\bar{\beta}$ . Further, since the neutron energy spectra shown in Figure 3.4 have a mean value around that of the delayed neutron energy spectrum (and hence closely mimic that of the delayed neutron energy spectrum), an importance factor,  $I$ , of 1 is expected. Noting the  $1-\sigma$  uncertainty displayed in Figure 3.25, it can be concluded that this waviness is due to the uncertainty associated with calculating  $\beta_{\text{eff}}$  from eigenvalues using a low-fidelity Monte Carlo process.

Results using  $\bar{\beta}$  instead of  $\beta_{\text{eff}}$  in order to estimate the magnitude of void reactivity in  $\$$  are plotted in Figure 3.26. It should be noted that while the actual values vary from those plotted in Figure 3.25, the overall trend is the same: as BeO concentration increases, a diminishing returns effect is seen with respect to void reactivity, to the point where it saturates around 30-40% BeO.

### 3.6.2 BeO Concentration and Reactivity Limited Burnup

While a general relationship between BeO concentration and beginning of life coolant void reactivity has been established, the relationship between BeO volume fraction and other core design parameters must be examined in order to better optimize the core design. For example, a large BeO concentration may be beneficial from a void reactivity standpoint, but its effect on spectral softening may reduce the reactivity limited burnup to a point where such a core is not economically viable.

Figure 3.27-Figure 3.30 shows how the reactivity limited burnup, reactivity limited lifetime, and reactivity swing change with respect to BeO concentration. As expected, as BeO concentration increases, reactivity limited burnup and lifetime decrease as does reactivity swing. As shown in Figure 3.27 and Figure 3.28, reactivity limited burnup and reactivity limited lifetime vary with BeO concentration in the same manner. Figure 3.29 and Figure 3.30 show that the relationships between reactivity limited burnup and reactivity swing with BeO concentration are nearly linear (reactivity limited lifetime varies linearly with BeO concentration as well, but is not shown for the sake of brevity). Note that data points for a BeO concentration of 50% are not included in Figure 3.29 and Figure 3.30, as the reactivity limited lifetime for this diluent concentration is  $<0$ , as shown in Figure 3.27.

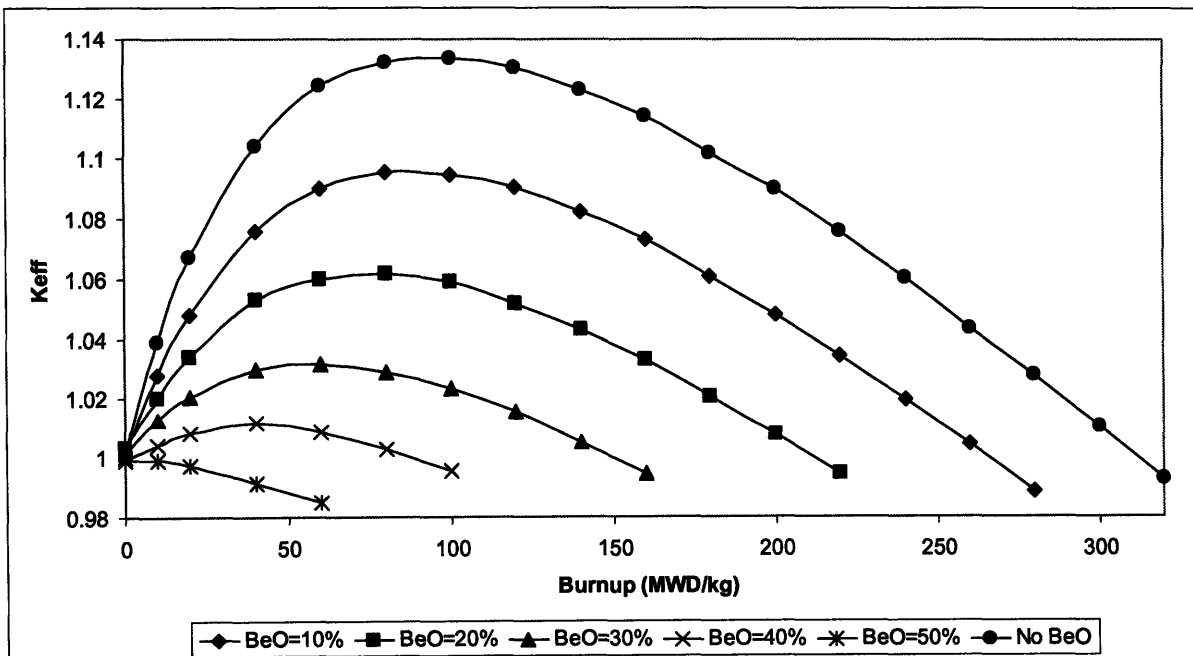


Figure 3.27: Reactivity Limited Burnup as a function of BeO Concentration

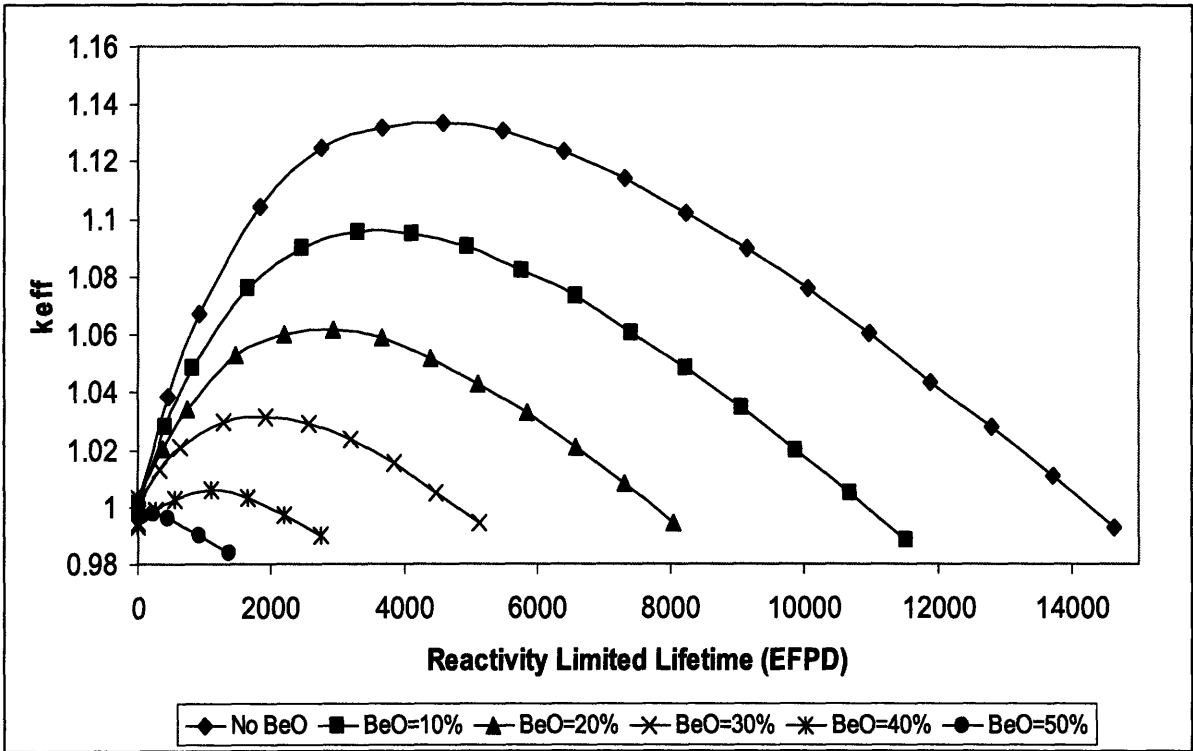


Figure 3.28: Reactivity Limited Lifetime as a function of BeO Concentration

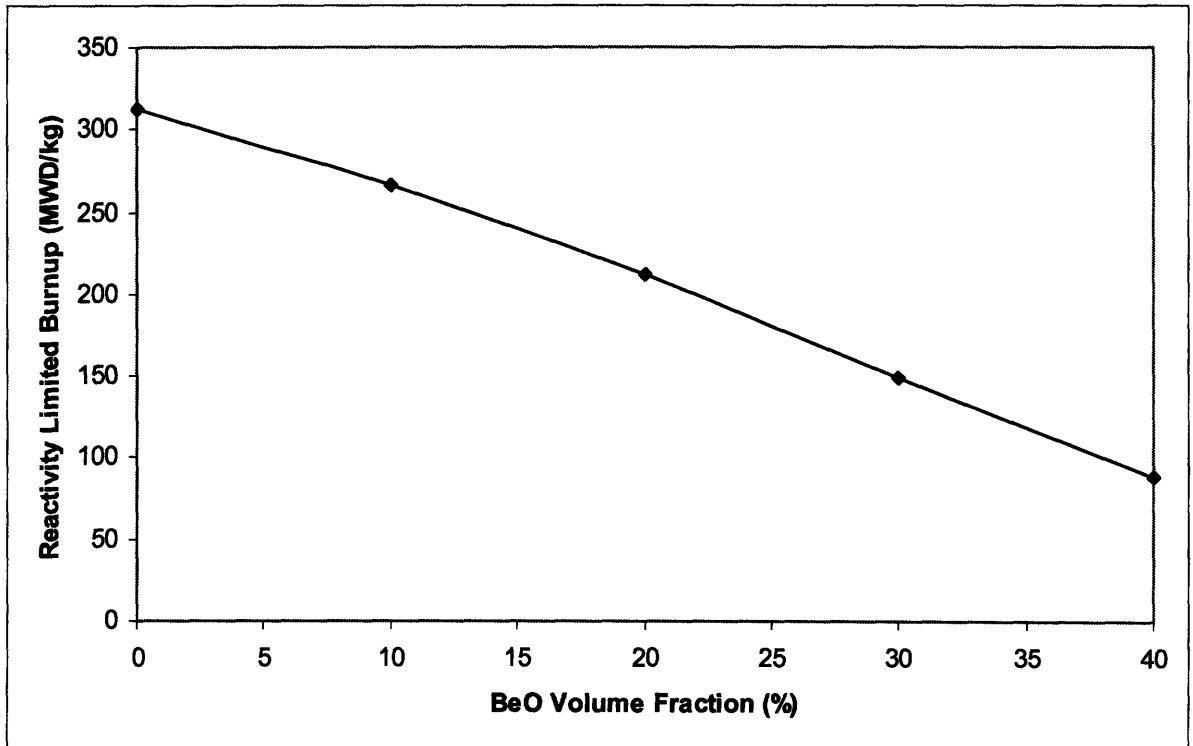
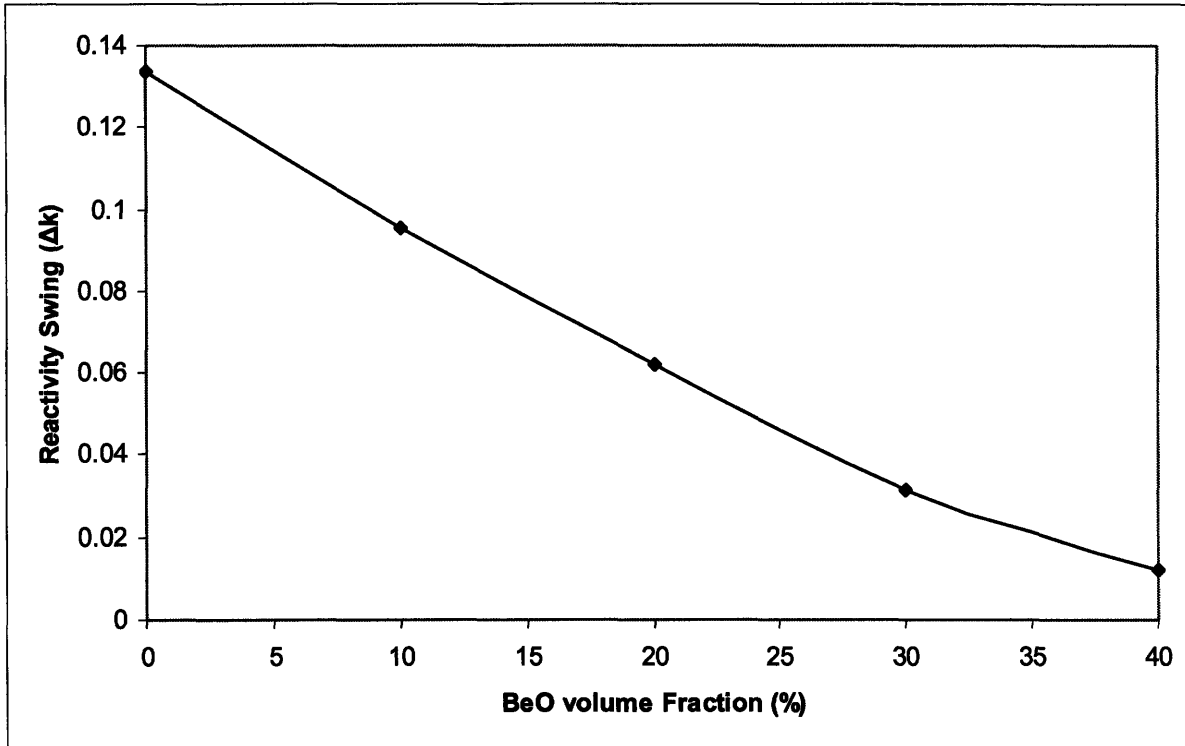


Figure 3.29: Reactivity Limited Burnup as a function of BeO Concentration



**Figure 3.30: Reactivity Swing as a function of BeO Concentration**

### 3.6.3 BeO Concentration and Coolant Void Reactivity at End of Life (EOL)

Figure 3.31 provides a graphical representation of how the parameters associated with coolant void reactivity (CVR) vary with diluent concentration at EOL. While a diminishing returns or saturation effect is seen as BeO volume fraction increases for CVR at BOL (shown in Figure 3.26), Figure 3.31 shows a roughly linear relationship between void reactivity and BeO concentration at EOL. This can be explained by Figure 3.32, which shows the fission fraction of the 5 largest isotopic contributors at EOL. Comparing the EOL fission fractions with those at BOL (shown in Figure 3.23) shows that Pu-239 is the largest contributor to fission in both cases. At BOL, it varies nearly linearly with BeO concentration (and hence, TRU enrichment) between ~60-75%, while at EOL it is independent of BeO concentration and stays roughly constant at ~70%. Further, the contributions (i.e. fission fraction) of the other 4 major isotopes at EOL are roughly independent of BeO concentration.



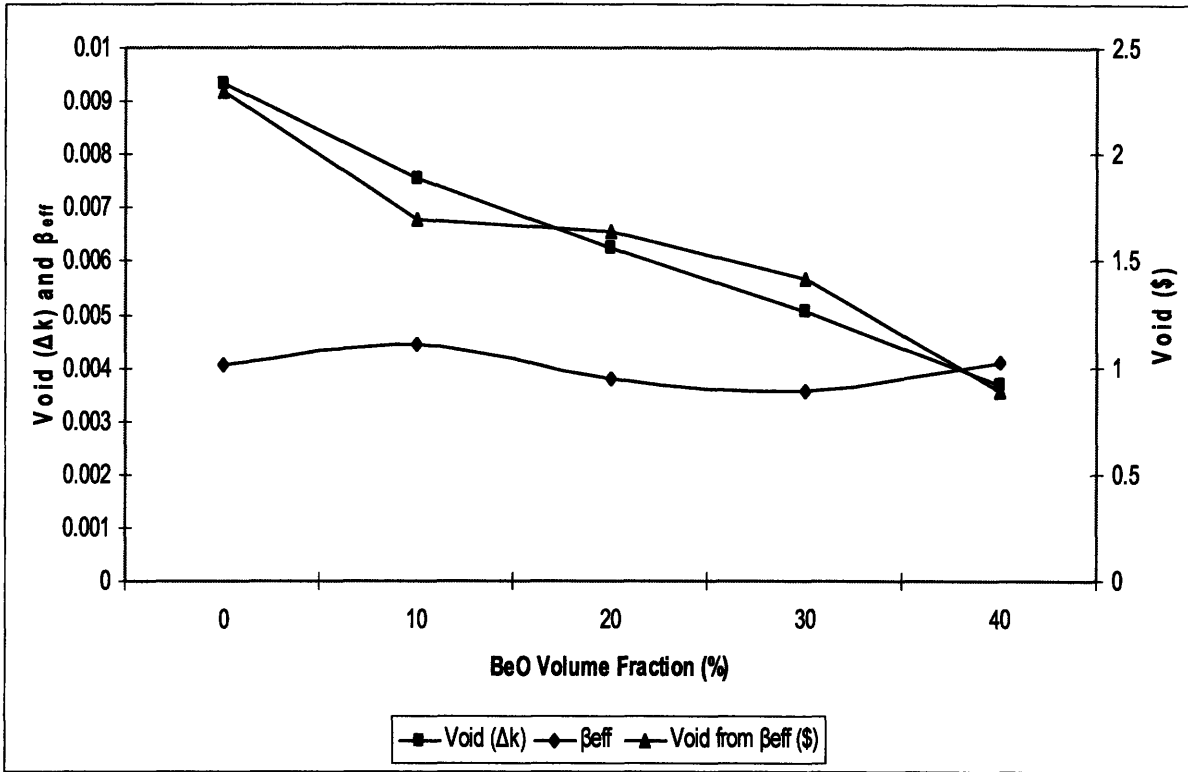


Figure 3.31: Void ( $\Delta k$  and \$) and  $\beta_{eff}$  as a function of BeO volume fraction at EOL

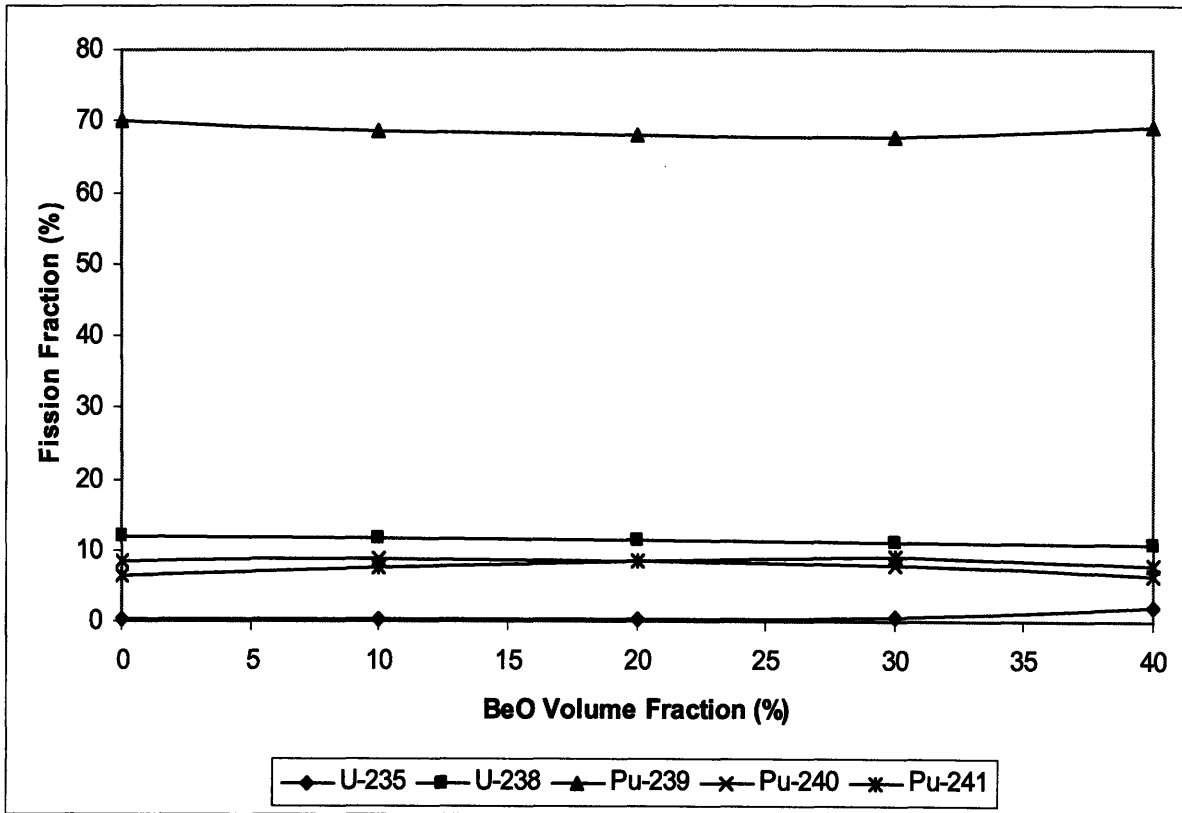


Figure 3.32 : Fission Fraction of 5 Largest Isotopic Contributors at EOL

Given these 2 key observations and the explanation of the behavior of void reactivity with BeO concentration at BOL, the linear behavior of void reactivity at EOL can be explained by the spectral softening effect of BeO. As shown in Eq. {1.5} previously, as BeO concentration increases and the neutron spectrum softens, the effect of positive void reactivity in Pu-239 decreases. Since the fission fraction, hence importance, of Pu-239 stays roughly constant with BeO concentration, there is no competing effect of change in Pu-239 fission fraction contributing to positive void reactivity, as there is at BOL. This is due to the enhanced breeding of Pu-241 through spectral softening to keep the Pu-239 fission fraction constant with respect to BeO concentration at EOL. Unlike the effect of reducing CVR with spectral softening seen with Pu-239 due to the discontinuity in slope of the microscopic capture to fission cross section ratio, Pu-241 does not have a similar discontinuity of slope, as shown in Figure 3.33. Consequently, there is no spectral softening effect with respect to CVR for Pu-241 and this isotope serves only to compete with Pu-239 and keep its fission fraction relatively constant with respect to diluent concentration.

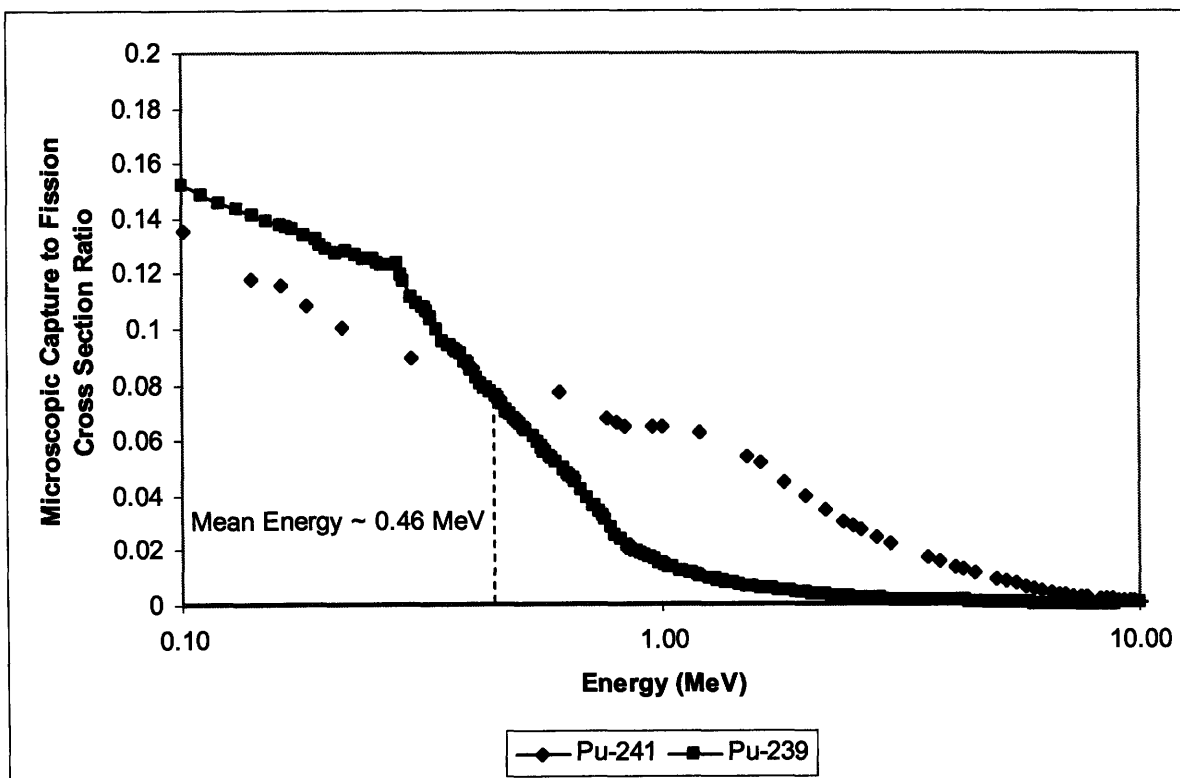


Figure 3.33: Comparison of the Microscopic Capture to Fission Cross Section Ratio of Pu-239 and Pu-241

The different effects on CVR from the use of diluent at BOL and EOL are compared in Table 3.3.

**Table 3.3: Effects of Diluent on Coolant Void Reactivity at BOL and EOL**

Time in Core Life	Factor	Effect on Spectral Softening
BOL	$\Delta\rho = \left(\frac{\sigma_\gamma}{\sigma_f}\right)_{UNVOIDED} - \left(\frac{\sigma_\gamma}{\sigma_f}\right)_{VOIDED}$	Reduce (+) CVR
	↑ fission fraction of Pu-239	Increase (+) CVR
EOL	$\Delta\rho = \left(\frac{\sigma_\gamma}{\sigma_f}\right)_{UNVOIDED} - \left(\frac{\sigma_\gamma}{\sigma_f}\right)_{VOIDED}$	Reduce (+) CVR
	Breeding of Pu-241 keeps fission fraction of Pu-239 ↔	N/A

Again, a more detailed understanding of the waviness of  $\beta_{\text{eff}}$  seen in Figure 3.31 is desired, as was explored for the BOL case. Comparing  $\beta_{\text{eff}}$ ,  $\bar{\beta}$ , and the importance factor (I) in Figure 3.34 shows that  $\beta_{\text{eff}}$  varies in the same manner as  $\bar{\beta}$  with respect to BeO volume fraction. This can be explained by the subtle variations in fission fraction seen by the 5 key isotopes at EOL, shown in Figure 3.32. Since these 5 isotopes all have maxima and minima at different BeO concentrations and do not follow the same predictable pattern (as the 4 key isotopes do at BOL), erratic behavior of  $\beta_{\text{eff}}$  and  $\bar{\beta}$  is expected. As well, the importance factor is relatively constant throughout BeO volume fraction variations, suggesting that the wavy behavior is due to this unique isotopic variation coupled with the low-fidelity Monte Carlo uncertainty discussed for the BOL case.

Results using  $\bar{\beta}$  instead of  $\beta_{\text{eff}}$  in order to estimate the magnitude of void reactivity in \$ are plotted in Figure 3.35. It should be noted that the same linear behavior seen for void reactivity in Figure 3.31 is seen in Figure 3.35. Further, the scale of Figure 3.35 shows that the wavy behavior of  $\bar{\beta}$  is somewhat exaggerated in Figure 3.34, where a much finer resolution is used for the ordinate.

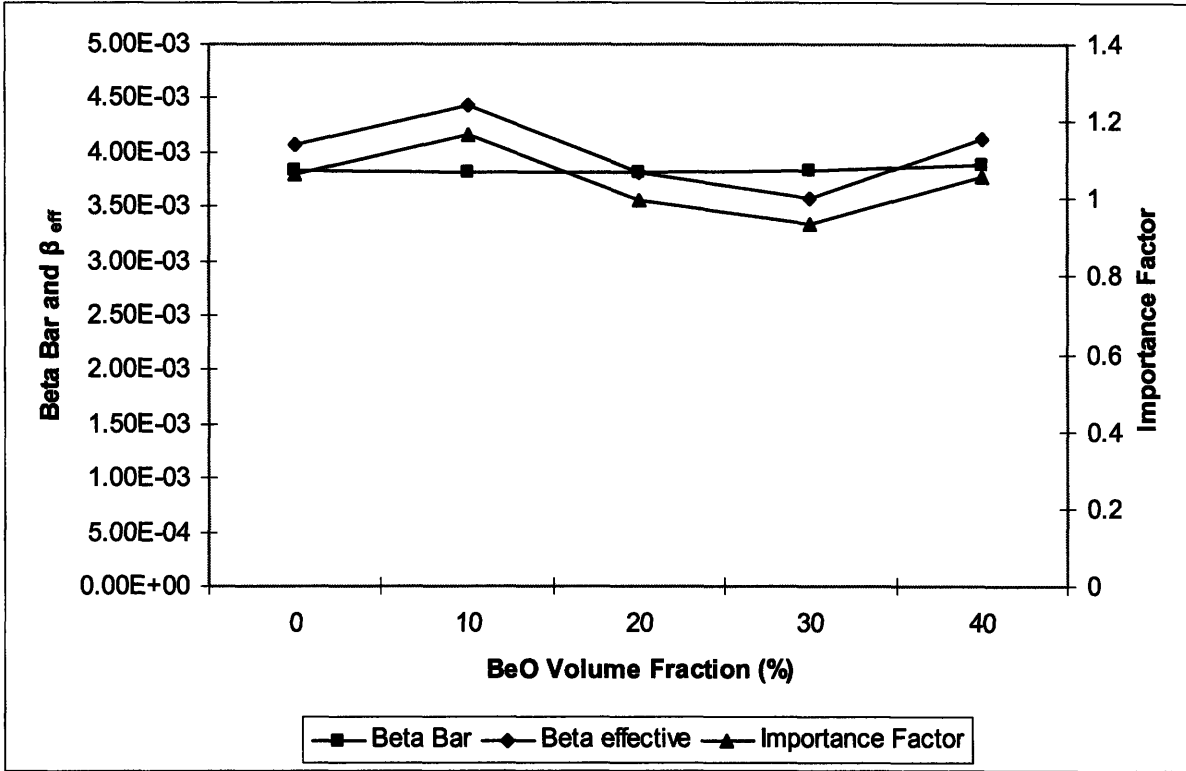


Figure 3.34: Behavior of  $\beta_{eff}$ ,  $\bar{\beta}$ , and I as a function of BeO volume fraction at EOL

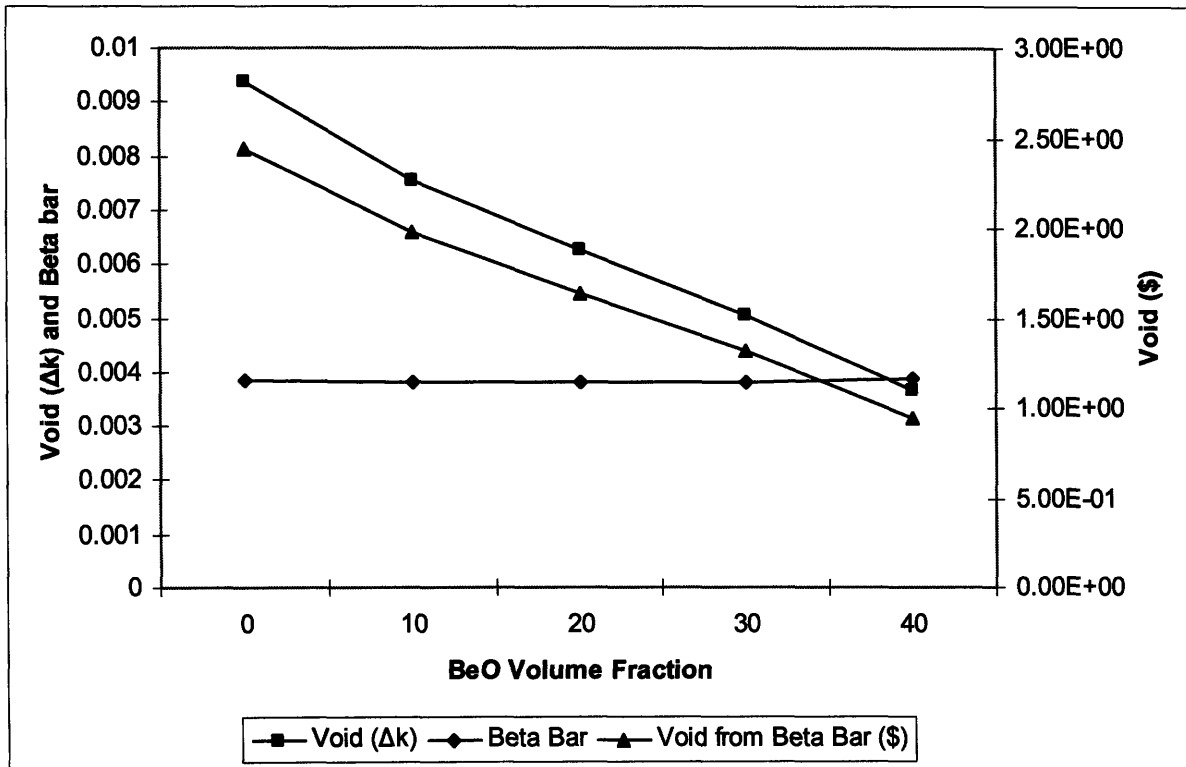


Figure 3.35: Void ( $\Delta k$  and \$) and  $\bar{\beta}$  as a function of BeO volume fraction at EOL

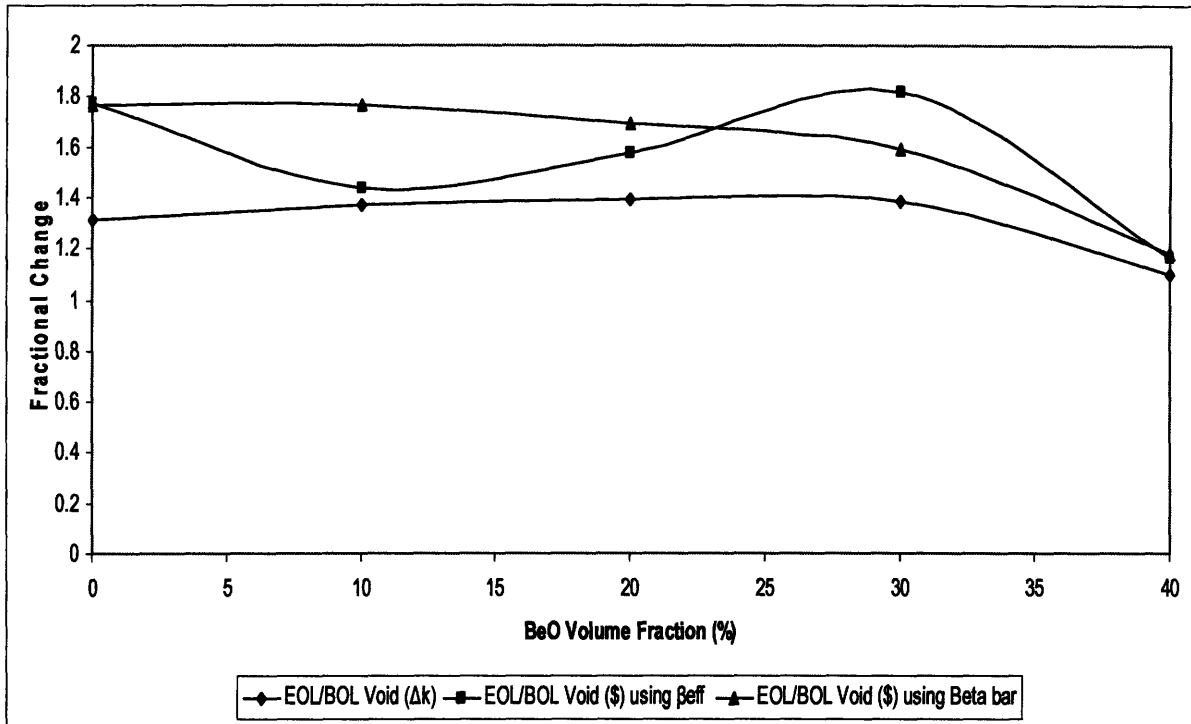


Figure 3.36: Ratio of EOL/BOL Void Reactivities

One further analysis that is a useful product of this study is how the void reactivity increases from BOL to EOL with respect to BeO concentration. Shown in Figure 3.36, the increase in void reactivity from BOL to EOL generally decreases as BeO concentration increases. This is due to the larger reduction in void reactivity for increased diluent concentration at EOL, as compared to that for BOL. The wavy behavior of EOL/BOL void in \$ when using  $\beta_{eff}$  shown in Figure 3.36 can be explained by the effect of isotopic importance variation with respect to diluent concentration seen at EOL and the propagation of the Monte Carlo uncertainty shown in Figure 3.25 and Figure 3.34.

#### 3.6.4 Summary of Diluent Concentration and Coolant Void Reactivity Study

The key findings of the optimum diluent concentration study follow:

1. There is a saturation effect with respect to BOL void reactivity as BeO is added. This is due to the spectral softening effect, which creates a tradeoff between lowering the positive coolant void reactivity from Pu-239 and increasing the fission fraction of Pu-239, which contributes to an overall greater positive void reactivity.

2. Reactivity limited burnup and reactivity swing decrease nearly linearly with increasing BeO volume fraction.
3. EOL void reactivity decreases roughly linearly with increasing BeO concentration. This is due to the spectral softening effect of BeO, which increases with increasing diluent concentration. The competing effect of increased Pu-239 fission fraction is not seen as with the BOL case, as the spectral softening breeds enough Pu-241 to keep the Pu-239 fission fraction constant with respect to BeO concentration.
4. The increase in EOL void reactivity with respect to BOL void reactivity decreases with increasing BeO concentration.

The results of this study are useful in showing the trends and trade-offs associated with the use of diluent in fast reactor fuel. Application of these results to the core design will be discussed later in this work.

### **3.7 Summary and Conclusions**

In this chapter, we have explored the use of diluent as a means for shaping power, as traditional means were not able to provide satisfactory results for a fast reactor. Using diluent also had the concomitant effect of reducing coolant void reactivity (CVR). Both of these effects of diluent use are primarily due to spectral softening. With respect to power shaping, spectral softening lowers the neutron energy enough to inhibit, but not completely preclude, fast fission in the transuranic isotopes which make up the fuel for this reactor. A secondary and much more minor effect of diluent use is to displace fuel, which contributes insignificantly to power shaping. With respect to CVR reduction, spectral softening reduces the increase in the ratio of the microscopic fission to capture cross section in Pu-239 when the core voids, lessening the amount of positive reactivity inserted.

By varying the volumetric content of the diluent with position, the ability to shape power is achieved. While it is possible to shape both the radial and axial power profile using diluent, results show that no benefit with respect to peak cladding temperature can be obtained from implementing an axial diluent zoning strategy. This stems mainly from the fact that the ideal power profile (an inlet peaked, exponentially decreasing shape) for axial

cladding temperature flattening is impossible to obtain in practice, owing to axial leakage. Consequently, the default axial power shape (a chopped cosine with a peak of 1.3) yields peak axial cladding temperatures comparable to or better than those obtained as a result of attempts at axial power shaping using diluent.

Several candidate diluents were used in the examples provided in this chapter to show the potency of the use of diluent. Of the options, BeO has been selected as the diluent of choice for this work, owing largely to its greater effect on CVR reduction. It should be remembered, however, that the efficacy of a moderating diluent in a fast reactor has been generally demonstrated, should BeO prove unsuitable for use in the future.

Throughout the many cases presented using diluent in this chapter, several fundamental trade-offs have become apparent as a result of using a moderating diluent in fast reactor fuel. These trade-offs are shown in Figure 3.37 and highlight that the use of diluent adds another key dimension to core design in fast reactors.

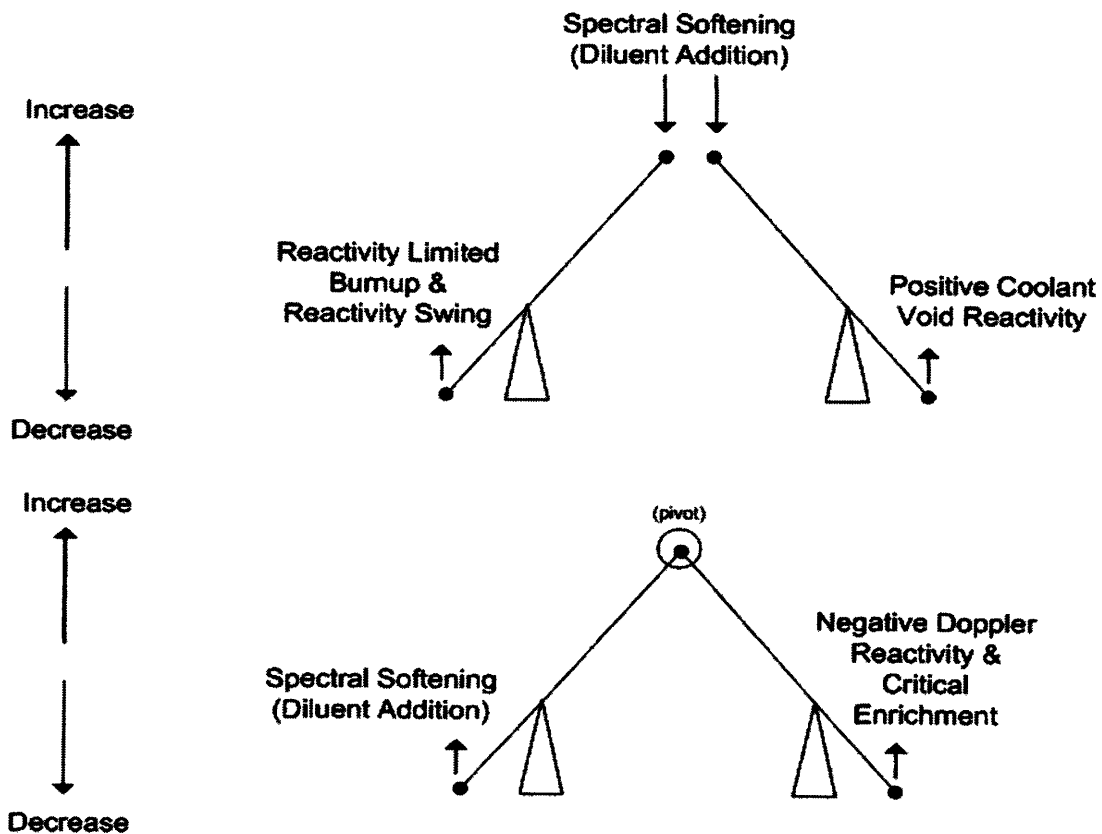


Figure 3.37: Illustration of Fundamental Trade-offs in Neutronic Performance from the Use of Diluent

## 4 TUBE-IN DUCT (TID) FUEL ASSEMBLY CORE DESIGN

### 4.1 Introduction

Table 4.1: Key Parameters of the TID Fuel Assembly Core Design

Parameter	Value
<b>Whole Core Parameters</b>	
Thermal Power	2400 MW <sub>th</sub>
Specific Power	20.7 kW/kg <sub>HM</sub>
Power Density	85.4 kW/l
Number of fuel batches	1
Reactivity Limited Burnup	1 <sup>st</sup> cycle: 140 MWd/kg, 18.48 EFPY 2 <sup>nd</sup> cycle: 133 MWd/kg, 17.66 EFPY 3 <sup>rd</sup> cycle: 130 MWd/kg, 17.16 EFPY
System Pressure	20 MPa
Core Inlet Temperature	485.5°C
Core Outlet Temperature	650°C
Active Core Height	1.54 m
Effective Core Diameter	4.81 m
H/D (active core)	0.32
Reflector	S-CO <sub>2</sub> (radial), Ti (axial)
Shielding (radial and axial)	99 w/o B <sub>4</sub> C
<b>Fuel Assembly Parameters</b>	
Fuel Assembly Description	Tube-in-Duct (TID)
Fuel Enrichment	16.6% TRU (1 <sup>st</sup> cycle)
Assembly inner can flat-to-flat distance	22.32 cm (cold), 22.49 cm (hot)
Assembly outer can thickness	0.2 cm (cold), 0.2015 cm (hot)
Inter-Assembly gap size	0.28 cm (cold), 0.111 (hot)
Cladding thickness	0.07 cm
Coolant hole diameter	0.7 cm
Fuel, volume %	(U-TRU)O <sub>2</sub> , 59
Cladding, volume %	ODS MA956, 14
Coolant, volume %	S-CO <sub>2</sub> , 27

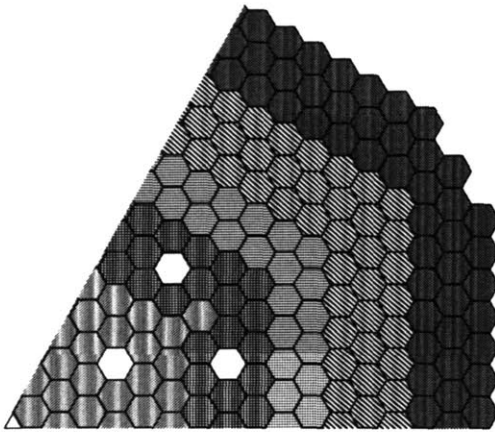


Using the design philosophies, processes, and ideas introduced in the preceding chapters, a core has been designed using the Tube-in-Duct (TID) fuel form. Table 4.1 lists the key parameters of this core design, while the rest of this chapter defines acceptable neutronic and thermal hydraulic constraints and evaluates the core design against these limits.

## **4.2 S-CO<sub>2</sub> Radial Reflector**

While coolant void reactivities (CVRs) of  $\leq 1$  were demonstrated in the previous chapter, these values of void reactivity are still too high to meet a passive safety standard. This passive safety standard is based on inherent core shutdown during an anticipated transient (e. g. Loss of Flow Accident, Loss of Heat Sink) with a concurrent failure of the reactor protective complex, i.e. Anticipated Transient Without SCRAM (ATWS), adopted from the work done for the Integral Fast Reactor (IFR) in [Wade and Chang, 1988]. The IFR can accommodate positive CVR in combination with other negative reactivity feedbacks. Because the loss of pressure and introduction of reactivity from a loss of coolant in a GFR is much faster than in the IFR, the CVR requirement in the GFR is more stringent. Ideally, CVR  $\leq 0$  throughout core life are desirable. In this work, this standard of passive safety has been expanded to include the Loss of Coolant Accident (LOCA). In a GFR, a LOCA presents one of the most limiting accident scenarios, as significant positive reactivity is typically inserted upon core voiding. Hence, if a reactor can be designed where negative reactivity is inserted upon coolant voiding, the reactor is much more inherently safe. As well, this standard supports the goal of enhanced safety of the Generation IV International Forum.

Consequently, strategies for reducing the void reactivity beyond the use of diluent were explored. One such approach is the use of the S-CO<sub>2</sub> coolant as a radial reflector. This would ensure that upon a LOCA and concurrent coolant voiding, the reflector would void or “disappear,” enhancing leakage and reducing coolant void reactivity. Radial (i.e. 1/6<sup>th</sup> core representation) and axial cross sections of this strategy are shown in Figure 4.1 and Figure 4.2. Note that the radial S-CO<sub>2</sub> reflector exists axially only along the fueled region of the core.









-  Control Assembly
-  Inner fuel zone
-  Middle fuel zone
-  Outer fuel zone
-  S-CO<sub>2</sub> Reflector
-  B<sub>4</sub>C Shield

Figure 4.1: 1/6<sup>th</sup> Core Map of the S-CO<sub>2</sub> Reflected Strategy

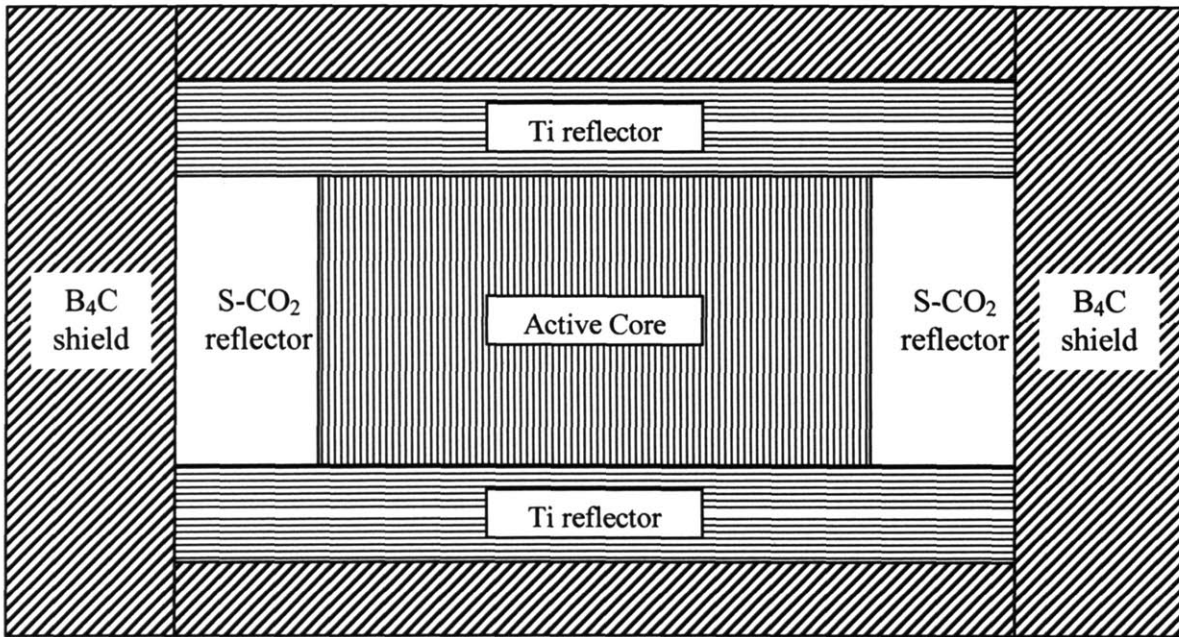


Figure 4.2: Axial Cross Section of the S-CO<sub>2</sub> Reflected Strategy

Implementing a more transparent medium such as S-CO<sub>2</sub> as the reflector certainly raises some concerns about the technical feasibility of such an option. First, with a lower

albedo reflector, the enrichment necessary to sustain criticality would need to be higher, increasing fuel costs. However, given the large size of the candidate core, the low height to diameter ratio (0.32), and the low coolant volume fraction, the radial leakage is relatively low. In fact, the leakage of an earlier iteration of the core design presented in this chapter was calculated. While the leakage values calculated were for a different core, the design was

**Table 4.2: Calculation of Bare Core (radially and axially) Leakage**

	E<0.1 MeV	1.0>E>0.1 MeV	E>1.0 MeV	TOTAL
<b>Radial Boundary (bare)</b>				
Outward Current	2.31%	3.72%	1.61%	7.64%
Inward Current	0	0	0	0
NET (Outward)	2.31%	3.72%	1.61%	7.64%
<b>Upper Axial Boundary/Lower Axial Boundary (bare)</b>				
Outward Current	1.47%	1.79%	0.829	4.09%
Inward Current	0	0	0	0
NET (Outward)	1.47%	1.79%	0.829	4.09%

**Table 4.3: Calculation of Radially Bare, Axially Reflected Core Leakage**

	E<0.1 MeV	1.0>E>0.1 MeV	E>1.0 MeV	TOTAL
<b>Radial Boundary (bare)</b>				
Outward Current	1.74%	2.86%	0.98%	5.58%
Inward Current	~0	~0	~0	~0
NET (Outward)	1.74%	2.86%	0.98%	5.58%
<b>Upper Axial Boundary (reflected)</b>				
Outward Current	4.38%	3.80%	1.37%	9.56%
Inward Current	3.87%	2.71%	0.44%	7.02%
NET (Outward)	0.51%	1.09%	0.93%	2.54%
<b>Lower Axial Boundary (reflected)</b>				
Outward Current	5.14%	4.24%	1.53%	10.9%
Inward Current	4.87%	3.17%	0.49%	8.52%
NET (Outward)	0.27%	1.07%	1.04%	2.38%

similar enough in enrichment zoning, diluent loading, assembly size, overall core dimensions, and axial reflector and shield material and geometry that the results presented here can be thought of as fairly representative of the current design. Using MCNP, incoming and outgoing neutron currents were computed for the core using two different scenarios: (1)

no axial or radial reflector or shield, i.e. completely bare and (2) no radial reflector or shield, but the same axial reflector strategy used in the TID candidate core (40 cm of Ti and 60 cm of 99 % B<sub>4</sub>C). The results presented in Table 4.2 and Table 4.3 show that the core has very low radial and axial leakage. Specifically, the radial leakage for the axially reflected, radially bare case is only ~6%. Note that leakage in this core is much less than in older breeder designs using radial and axial U-238 blankets where ~1/3 of the neutrons leak out of the enriched fuel zones.

To lend further support to the idea that a S-CO<sub>2</sub> radial reflector would not prohibitively increase critical enrichment, the reactivity penalty associated with using this kind of radial reflector vs. using a solid radial reflector, e.g. a TiC/Ti combination, was calculated (again for an earlier and similar iteration of the current core design). This calculation was performed by taking the same exact core and computing the eigenvalue for both a TiC/Ti reflector (radial row closest to the core was TiC, other 2 radial reflector rows were Ti) and a S-CO<sub>2</sub> reflector (3 radial rows), with 2 rows of B<sub>4</sub>C shielding outboard of the reflector. The difference in reactivity between these two cores was only ~\$5.23 further supporting the idea that the low leakage core would not need a significant increase in enrichment with a S-CO<sub>2</sub> radial reflector in order to sustain criticality. A similar calculation was performed where again the same exact core was compared with different reflector materials, this time with S-CO<sub>2</sub> and He, both at 20 MPa and with no radial shielding. Two interesting results were found from these calculations. First, using He instead of S-CO<sub>2</sub> yielded a reactivity penalty of about \$1.34, showing that S-CO<sub>2</sub> scatters slightly better than Helium at the same pressure. Second, the small reactivity penalty associated with the relatively transparent Helium acting as a radial reflector further demonstrates the low leakage nature of this core.

The low leakage behavior of this core is due not only to the large size of the core, but also due to the extremely large fuel volume fraction inherent in the use of Tube-in-Duct (TID) fuel assemblies. Further, adjustment of the BeO concentration in the core in order to flatten the radial power (specifically, reduction of BeO in the periphery) has reduced the need for an increase in enrichment due to increased radial reflector transparency. Consequently,

the BOL enrichment of the S-CO<sub>2</sub> reflected core is nearly the same as that of its predecessor in the design process, a candidate core with a TiC/Ti radial reflector.

The other potentially significant problem with using S-CO<sub>2</sub> as a radial reflector is the increased fluence on the reactor pressure vessel (RPV). With a more transparent radial reflector, more high energy neutrons will impinge upon the RPV, increasing the damage and limiting the service life of this component. The offsetting effect to the increased transparency of the reflector is that the core has relatively low leakage; therefore, while fast neutrons may have greater ease in getting to the RPV, there are less of them to get there in the first place. A more detailed investigation into the effect of RPV fluence and different shielding strategies (including optimization of composition) will be discussed later in this chapter.

Two important technical details arise in a discussion of a S-CO<sub>2</sub> radial reflector. First, the prospect of core flow bypass exists with the use of such a radial reflector strategy. However, selective orificing between the lower Ti axial reflector and the active core region, proper sizing of the inter-assembly flow channels, and ensuring adequate radial hydraulic communication at several axial levels of the active core region could alleviate this potential problem. Second, the “empty” S-CO<sub>2</sub> space in the radial region of the active core presents a challenge with respect to the structural design and integrity of the core. A possible solution is to use empty ducts adjacent to the active core region. The reflection that the ODS outer cans would provide has been calculated to be minimal, adding only about \$0.50 of reactivity while still allowing a negative CVR throughout core life. These design details are beyond the scope of this work and certainly require further design effort.

### **4.3 Selection of an Axial Reflector**

A study was undertaken in order to determine the best axial reflector for the candidate TID core. Given that a S-CO<sub>2</sub> radial reflector is a key component of the design solution to reduce coolant void reactivity throughout core life, all core dimensions and materials were kept the same in this study as for the reference TID core, with the exception of the material used for the axial reflector. Eight candidate materials were chosen for this study for various reasons: Ti, BeO, TiO<sub>2</sub>, PbO, Zr<sub>3</sub>Si<sub>2</sub>, SiO<sub>2</sub>, SiC, and CaO. Ti was chosen as a basis for

subsequent comparisons as it is used in the reference core design as the axial reflector material. This selection was based on the small “hump” seen in the microscopic scattering cross section at energies around the mean neutron energy in this core (shown in Figure 4.3); hence, when the core voids and the mean neutron energy shifts slightly upward, the microscopic scattering cross section of Ti goes down, reflection is reduced, leakage is enhanced, and the coolant void reactivity (CVR) is reduced. BeO was selected as a candidate due to its use as a reflector in other fast reactors, namely SEFOR. TiO<sub>2</sub> was considered due to its neutronic resemblance to Ti and enhanced chemical stability, as TiO<sub>2</sub> is a product of the chemical reaction between Ti and S-CO<sub>2</sub>. PbO was examined based on previous work which used a PbO glass as a core catcher, in order to help with any hypothesized accident. Zr<sub>3</sub>Si<sub>2</sub> was evaluated as it is the reflector material of choice for the French (CEA) GFR program. SiO<sub>2</sub> and SiC were explored due to the favorable neutronic properties of Si with respect to coolant voiding and CVR (i.e. higher microscopic cross section for absorption at higher energies). SiO<sub>2</sub> is especially attractive due to its excellent chemical stability and the relative abundance of a cheap supply (i.e. SiO<sub>2</sub> is sand). Finally, CaO was considered for the same reasons that SiO<sub>2</sub> was (i.e. favorable neutronic performance of Ca, and CaO is limestone).

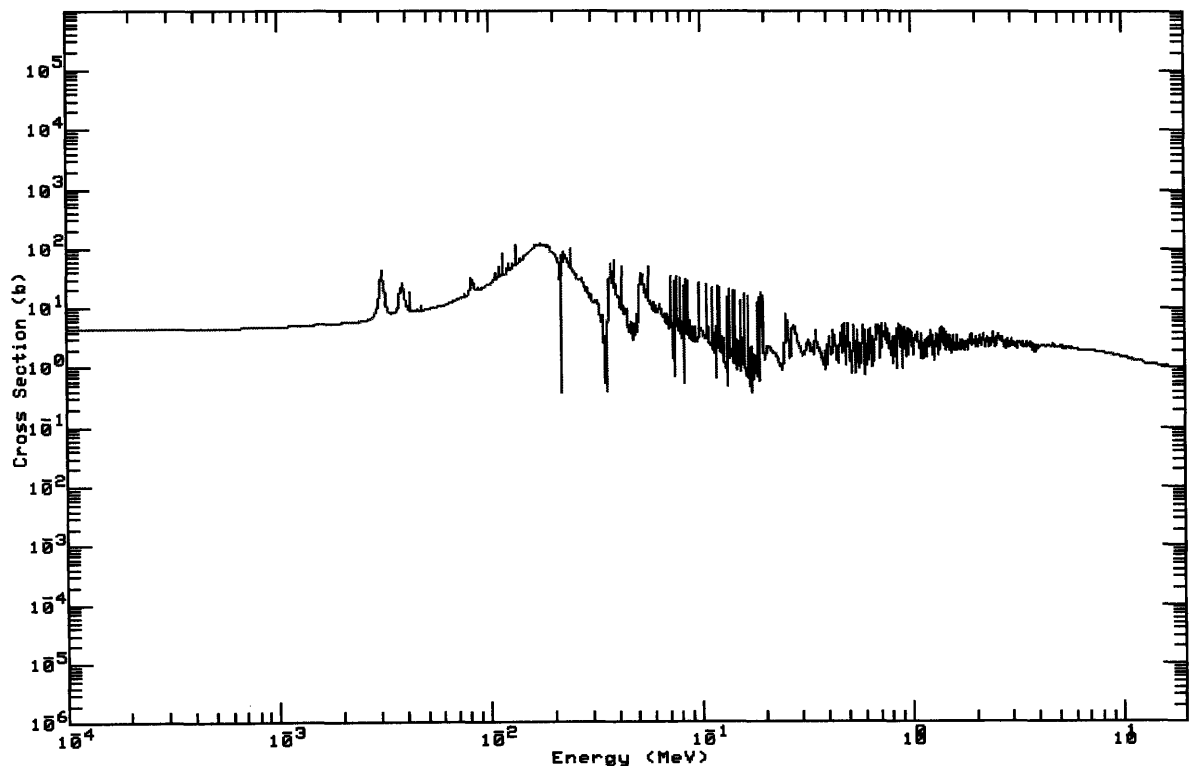


Figure 4.3: Microscopic Scattering Cross Section of Titanium

The eight candidate materials were judged based on performance in the following areas:

- Chemical compatibility
- Material Properties
- Beginning of Life (BOL) coolant void reactivity (CVR), as assessed via a whole core model
- Comparatively, using a semi-infinite fuel assembly:
  - Reactivity limited burnup
  - Reactivity swing
  - BOL CVR
  - End of Life (EOL) CVR

#### 4.3.1 Chemical Compatibility

Since the TID fuel assemblies are vented to the coolant in order to keep the differential pressure across the cladding and duct wall reasonable, the chemical compatibility of the S-CO<sub>2</sub> coolant with the materials inside the assembly is important. Since the fuel assembly includes the fuel as well as the axial shield and reflector, the chemical compatibility of these species with the coolant must be examined in order to determine the suitability of axial reflector candidates. Chemical compatibility was assessed quantitatively using the computer code HSC Chemistry® 5.1 [Roine, 2002]. There are several parts of HSC that were used to predict the chemical stability of a given material. First, the “Equilibrium Composition” module was used, where one can input the amount of two reagents and HSC will predict the type and amount of products formed, based on an extensive chemical database. Next, once it was determined which species were most likely to be formed, the “Reaction Equations” module was used to determine the Gibbs Free Energy of this chemical process. The Gibbs Free Energy ( $\Delta G$ ) will tell if a given chemical reaction is thermodynamically favorable. If  $\Delta G$  is large and negative, the reaction will tend to form a large quantity of products; if it is large and positive, only small quantities of product will ever be formed. It should be noted that the Gibbs Free Energy only gives an indication of whether a reaction will happen or not, and says nothing about the rate at which that reaction will occur. As well, the calculations described above are made assuming that all of the reagents are homogeneously mixed and have a chance to react. Hence, geometry is disregarded and the results are extremely conservative. Still, the above mentioned tools give a good first order metric for assessing chemical compatibility.

Table 4.4 lists the chemical reactions between the candidate axial reflector materials and S-CO<sub>2</sub> at several different temperatures, which span a range of both normal operation and predicted accident conditions. Note that Zr<sub>3</sub>Si<sub>2</sub> is not present, as it is a new material and does not exist in the chemical database of HSC 5.1. Of the 7 candidate materials evaluated, 5 have positive Gibbs Free Energies (ΔG) for the temperature range of interest, indicating that they are not very chemically reactive with S-CO<sub>2</sub>. While Ti and SiC both have negative ΔG values, suggesting chemical reactivity, a search of the literature on these two materials suggests that their initial reaction with S-CO<sub>2</sub> forms a thin, passive oxidation layer which inhibits further reaction. [Opila and Nguyen, 1998 and O’Driscoll, 1958] Hence, despite the negative ΔG values, Ti and SiC are relatively chemically stable in S-CO<sub>2</sub>. While the chemical compatibility of Zr<sub>3</sub>Si<sub>2</sub> remains to be determined, the chemical stability criterion does not eliminate any of the other candidate materials.

**Table 4.4: Chemical Compatibility of Axial Reflector Candidate Materials**

<b>Reaction</b>	<b>Temp(°C)</b>	<b>ΔG (kcal)</b>
$6\text{Ti} + 6\text{CO}_2(\text{g}) \rightarrow \text{TiO}_2 + \text{TiO}_2(\text{A}) + 3\text{C} + 2\text{C}(\text{D}) + \text{CO}(\text{g}) + \text{Ti}_4\text{O}_7$	500	-552
	1000	-447
	1500	-342
$\text{TiO}_2 + 2\text{CO}_2(\text{g}) \rightarrow \text{TiO}_2(\text{A}) + 2\text{CO}(\text{g}) + \text{O}_2(\text{g})$	500	104
	1000	84
	1500	63
$3\text{BeO} + 3\text{CO}_2(\text{g}) \rightarrow \text{BeCO}_3 + \text{BeO}(\text{A}) + \text{BeO}(\text{B}) + 2\text{CO}(\text{g}) + \text{O}_2(\text{g})$	500	126
	1000	124
	1500	121
$6\text{PbO} + 3\text{CO}_2(\text{g}) \rightarrow \text{PbCO}_3 + \text{PbO}(\text{R}) + \text{PbO}^*\text{PbCO}_3 + \text{PbO}(\text{g}) + \text{Pb}(\text{g}) + \text{CO}(\text{g}) + \text{O}_2(\text{g})$	500	161
	1000	141
	1500	125
$10\text{SiO}_2 + 2\text{CO}_2(\text{g}) \rightarrow \text{SiO}_2(\text{Q}) + \text{SiO}_2(\text{H}) + \text{SiO}_2(\text{B}) + \text{SiO}_2(\text{CR}) + \text{SiO}_2(\text{T}) + \text{SiO}_2(\text{G}) + \text{SiO}_2(\text{V}) + \text{SiO}_2(\text{CRS}) + \text{SiO}_2(\text{C}) + \text{SiO}_2(\text{S}) + 2\text{CO}(\text{g}) + \text{O}_2(\text{g})$	500	122
	1000	103
	1500	85
$6\text{SiC} + 7\text{CO}_2(\text{g}) \rightarrow 2\text{CO}(\text{g}) + 6\text{C} + \text{SiO}_2 + \text{SiO}_2(\text{Q}) + \text{SiO}_2(\text{B}) + \text{SiO}_2(\text{CR}) + \text{SiO}_2(\text{T}) + \text{SiO}_2(\text{V}) + 5\text{C}(\text{D})$	500	-427
	1000	-326
	1500	-228
$4\text{CaO} + 4\text{CO}_2(\text{g}) \rightarrow \text{CaCO}_3 + \text{CaCO}_3(\text{A}) + 2\text{Ca} + 2\text{O}_2(\text{g}) + 2\text{CO}(\text{g})$	500	341
	1000	330
	1500	314



### 4.3.2 Material Properties

In order to assess the candidate materials' suitability in a fast reactor environment, two key material properties, melting point and volumetric heat capacity, were examined. Melting point was looked at to determine if the material could maintain physical integrity at the high temperatures at which this reactor operates. Volumetric heat capacity was explored to see how such a material might be helpful in acting as a heat sink during an accident scenario.

**Table 4.5: Select Material Properties of Axial Reflector Candidate Materials**

<b>Axial Reflector Material</b>	<b>Melting Point (°C)</b>	<b>Temp (°C)</b>	<b>Heat Capacity (J/cm<sup>3</sup> K)</b>
Ti	1668	500	2.84
		1000	2.78
TiO <sub>2</sub>	1843	500	3.84
		1000	4.05
BeO	2578	500	5.54
		1000	6.06
PbO	887	500	2.33
		1000	Liquid
Zr <sub>3</sub> Si <sub>2</sub>	2000	UNKNOWN	
SiO <sub>2</sub>	1723	500	3.14
		1000	3.11
SiC	2830	500	3.52
		1000	3.96
CaO	2899	500	3.02
		1000	3.09

Table 4.5 shows the melting point and volumetric heat capacity for the eight candidate materials of interest. Immediately, PbO is eliminated from contention due to its low melting point. Since the upper axial reflector will be exposed to temperatures ~650°C, only a small temperature increase (< 250°C) would cause the upper axial reflector to melt. Hence, this material would not hold up well in an accident scenario. From a volumetric heat capacity standpoint, BeO stands out, as its heat capacity is nearly twice that of all other candidate materials, which have values that hover in the same general range. In order to

validate this difference and predict a value for  $Zr_3Si_2$  (for which data could not be obtained), the Law of Dulong and Petit was used, which predicts the heat capacity of a solid compound by [de Podesta 1996]:

$$C_v = 3pR \quad \{4.1\}$$

where:

$C_v$  = molar heat capacity at constant volume,  $J/(K \cdot mol)$

$p$  = atoms per molecule of compound

$R$  = universal gas constant,  $8.31 J/(K \cdot mol)$

**Table 4.6: Prediction of Heat Capacities of Axial Reflector Candidate Materials**

Candidate Material	Molecular Weight (g/mol)	Density (g/cc)	Molecular Density (mol/cc)	Heat Capacity predicted by the law of Dulong and Petit (J/K mol)	Heat Capacity predicted by the law of Dulong and Petit (J/cm <sup>3</sup> K)	Measured Heat Capacity (J/cm <sup>3</sup> K)
Ti	47.99	4.506	0.0939	24.93	2.34	2.78 – 2.84
TiO <sub>2</sub>	79.899	4.23	0.0529	74.79	3.96	3.84 – 4.05
BeO	25.012	3.01	0.1203	49.86	6.00	5.54 – 6.06
Zr <sub>3</sub> Si <sub>2</sub>	329.843	5.88	0.0178	124.65	2.22	??
SiO <sub>2</sub>	60.084	2.6	0.0433	74.79	3.24	3.11 – 3.14
SiC	40.097	3.16	0.0788	49.86	3.93	3.52 – 3.96
CaO	56.079	3.34	0.0596	49.86	2.97	3.02 – 3.09

Table 4.6 shows the results of using the Law of Dulong and Petit to predict heat capacities. The last two columns of the table show good agreement between the heat capacity predicted by the Law and the measured heat capacity. Further, these results verify the almost factor of 2 difference between BeO and the remaining candidates. Finally, given the excellent predictive capability shown in this table by the Law of Dulong and Petit, a reasonable value for  $Zr_3Si_2$  can be obtained. Note that for this analysis,  $C_v$  is assumed to be equal to  $C_p$  and is used to predict the heat capacities.

Using this materials property data, PbO can be eliminated as a candidate axial reflector. As well, 6 of the other candidates are shown to have comparable performance, with BeO giving the most favorable results as an outlier with a heat capacity nearly twice as large as the others.

### 4.3.3 Beginning of Life (BOL) Coolant Void Reactivity (CVR)

One of the most limiting design constraints in a fast reactor, coolant void reactivity (CVR) was assessed at the beginning of life for each candidate material. This assessment was performed as means for potential elimination of a candidate material if it showed significantly worse performance than the others. It should be noted that the same core (e.g. enrichment and diluent zoning in the core, geometric dimensions, etc.) was used for each trial and that only the material which was in the axial reflector was varied. This was in order to give a fair basis for comparison among the options.

**Table 4.7: Whole Core BOL  $k_{\text{eff}}$  and CVR for Axial Reflector Candidate Materials**

Axial Reflector Material	BOL $k_{\text{eff}}$	BOL CVR ( $\phi$ )
Ti	1.02059 (+/-0.00015)	-29 $\phi$ (+/-5 $\phi$ )
TiO <sub>2</sub>	1.02287 (+/-0.00013)	-23 $\phi$ (+/-5 $\phi$ )
BeO	1.02390 (+/-0.00015)	-21 $\phi$ (+/-5 $\phi$ )
PbO	1.02449 (+/-0.00012)	-17 $\phi$ (+/-4 $\phi$ )
Zr <sub>3</sub> Si <sub>2</sub>	1.02226 (+/-0.00013)	-32 $\phi$ (+/-5 $\phi$ )
SiO <sub>2</sub>	1.02167 (+/-0.00013)	-20 $\phi$ (+/-5 $\phi$ )
SiC	1.02246 (+/-0.00009)	-32 $\phi$ (+/-4 $\phi$ )
CaO	1.02038 (+/-0.00013)	-38 $\phi$ (+/-5 $\phi$ )

Table 4.7 shows the results of this assessment from both a BOL CVR and  $k_{\text{eff}}$  standpoint. The BOL  $k_{\text{eff}}$  values are included to show how well, on a comparative basis, each of these materials acts as an axial reflector. As was the case with the material properties, many of the materials exhibit comparable behavior. With respect to BOL CVR, the candidate materials can be arranged into 3 groups: (1) comparable performance with the Ti base case (Zr<sub>3</sub>Si<sub>2</sub>, SiC), (2) worse performance than the Ti base case (TiO<sub>2</sub>, BeO, SiO<sub>2</sub>) and (3) better performance than the Ti base case (CaO). Note that PbO is also assessed, to gain further support for its elimination as a candidate axial reflector due to poor performance (BOL CVR in this case). The better performance of CaO and comparable performance of Zr<sub>3</sub>Si<sub>2</sub> and SiC is due to the larger absorption cross sections of Ca and Si at higher energies.

### 4.3.4 Semi-infinite Assembly Comparative Analysis

Given that a whole core analysis is computationally intensive and time consuming and that the aim of this study was to find the best axial reflector on a comparative basis, a

semi-infinite assembly (mirror boundary conditions radially, normal boundary conditions axially) was analyzed using four key metrics to assess the relative merit of the seven remaining axial reflector candidate materials: reactivity limited burnup, reactivity swing, BOL CVR, and EOL CVR. The results of the first two metrics are shown in Figure 4.4, where there is little difference among the candidates. This correlates well with the  $k_{eff}$  results shown in Table 4.7, showing that the reflecting ability of all of these materials is roughly the same, as evidenced by their similar BOL  $k_{eff}$  values. Hence these two criteria will not be a deciding factor in the selection of an axial reflector material.

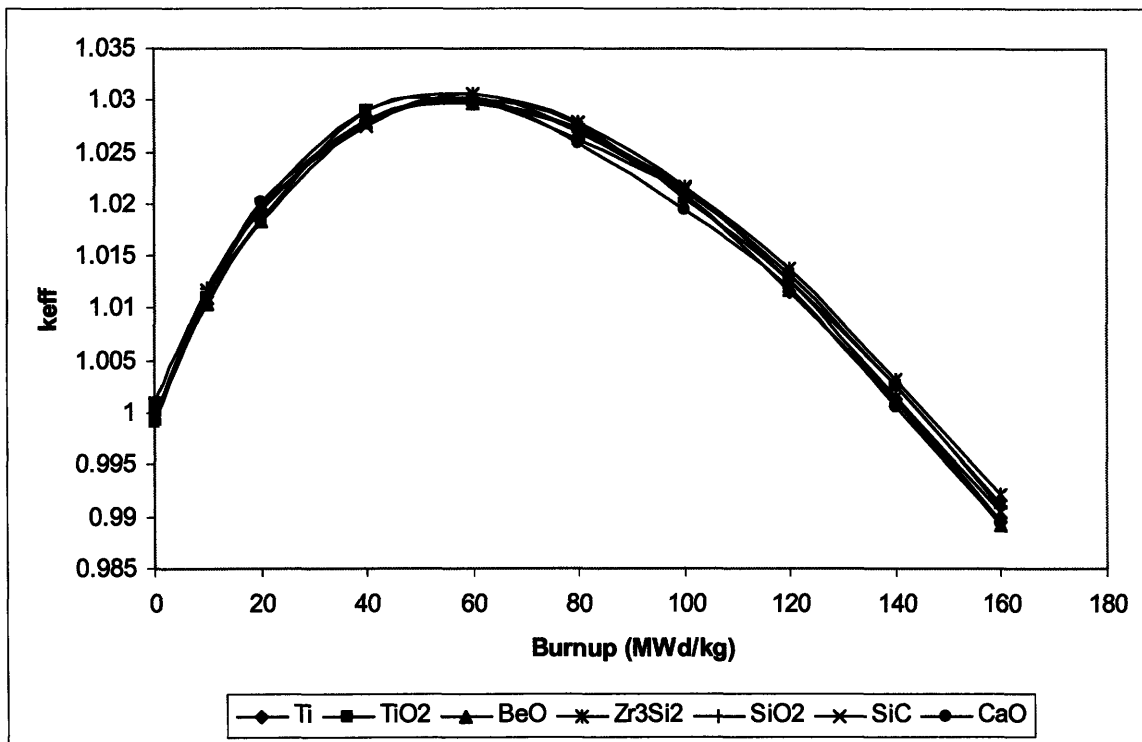


Figure 4.4: Reactivity Limited Burnup and Reactivity Swing of Axial Reflector Candidate Materials

Table 4.8: Semi-Infinite CVR over Core Life for Axial Reflector Candidate Materials

Axial Reflector Material	BOL CVR	EOL CVR
Ti	0.003179 (+/- 0.00028)	0.003605 (+/- 0.00028)
TiO <sub>2</sub>	0.003452 (+/- 0.00027)	0.003814 (+/- 0.00024)
BeO	0.002989 (+/- 0.00028)	0.003854 (+/- 0.00023)
Zr <sub>3</sub> Si <sub>2</sub>	0.0034 (+/- 0.00028)	0.003946 (+/- 0.00026)
SiO <sub>2</sub>	0.002651 (+/- 0.00025)	0.003915 (+/- 0.00024)
SiC	0.00276 (+/- 0.00026)	0.003746 (+/- 0.00025)
CaO	0.002704 (+/- 0.00026)	0.003989 (+/- 0.00024)

Next, the BOL and EOL CVR of the semi-infinite assembly were examined in order to study the trend of CVR over core life, shown in Table 4.8. It should be noted that all of these values for CVR are positive, as the leakage component of CVR is extremely low in the semi-infinite assembly, due to the radial mirror boundary conditions. Note that while 4 of the materials exhibit better BOL CVR than the current axial reflector of choice, Ti, none of them display an EOL CVR that is less than Ti, even when accounting for uncertainty. Hence, Ti is most likely to yield the lowest CVR throughout core life, given that all of the candidate materials displayed comparable predictors of Pu-239 behavior (reactivity swing and reactivity limited burnup in Figure 4.4). This is significant as Pu-239 has been shown to be the primary driver behind CVR.

#### 4.3.5 Selection of an Axial Reflector Material

Table 4.9 summarizes the results of the analyses that were performed in the previous 4 sections. While some materials show performance almost as good as Ti in some of the areas, none of the candidates exhibit performance better than Ti in all of the categories. While  $Zr_3Si_2$  shows some promise neutronically as an axial reflector from the results of this study, it is a new material about which little information is publicly available. As well, it does not have the benefit of years of development and study that the other materials have. Hence, the chemical compatibility with S-CO<sub>2</sub> and the material properties of the compound are either unknown or questionable. Further, the predicted heat capacity is comparable to Ti, but among the lowest of all of the candidate options, making it unattractive from a thermal hydraulic standpoint. As well, the cost of such a compound is in question. While BeO and CaO appear to be the closest competitors to Ti, neither can match the performance with respect to CVR throughout core life. Given all of this information, Ti has been chosen as the axial reflector material for the candidate core.

**Table 4.9: Summary of Results from the Axial Reflector Candidate Study**

	Chemical Compatibility w/ S-CO <sub>2</sub>	Material Properties	BOL Whole Core CVR	Semi-Infinite Assembly			
				Reactivity-Limited Burnup	Reactivity Swing	BOL CVR	EOL CVR
Ti	Compatible	=	=	=	=	=	=
TiO <sub>2</sub>	Compatible	=	-	=	=	-	-
BeO	Compatible	+ (High heat capacity)	-	=	=	+	-
PbO	Compatible	- (low melting point) ELIMINATED	X	X	X	X	X
Zr <sub>3</sub> Si <sub>2</sub>	Compatible	=	=	=	=	-	-
SiO <sub>2</sub>	Compatible	=	-	=	=	+	-
SiC	Compatible	=	=	=	=	+	-
CaO	Compatible	=	+	=	=	+	-

Legend: “=” - Comparable with Ti

“+” - Better than Ti

“-“ - Worse than Ti

#### **4.4 Assessment of Core Performance: 1<sup>st</sup> Cycle**

Using the criteria set forth in Table 4.10, the performance of the candidate core during the first operating cycle is assessed. Since current experience with LWRs shows that plant lifetimes of 60 years are achievable (based on material limits and degradation), the same design lifetime will be assumed for this reactor design. Based on the achievable reactivity limited lifetime demonstrated for the 1<sup>st</sup> cycle, this translates into a total of only 3 operating cycles for the reactor. An evaluation of the performance of the 1<sup>st</sup> cycle is separated from that of the 2<sup>nd</sup> and 3<sup>rd</sup> cycles as the first cycle uses TRU from LWR spent fuel, which has a different Pu and Minor Actinide vector than the fuel used in the 2<sup>nd</sup> and 3<sup>rd</sup> cycles, i.e. that which is reprocessed from the 1<sup>st</sup> and 2<sup>nd</sup> cycles. The results from the 2<sup>nd</sup> and 3<sup>rd</sup> cycles will be presented in a subsequent section.

As well, it should be remembered that the performance of the core presented in this section represents the limit of maximum achievable burnup, while still maintaining a negative CVR throughout cycle life and acceptable control rod worth. Reducing the BOL enrichment would certainly reduce the BOL eigenvalue, the cycle reactivity limited burnup,

the reactivity swing and CVR throughout core life. This limiting case is presented here to demonstrate the capabilities of such a core design.

**Table 4.10: Neutronic and Thermal Hydraulic Goals for the 1<sup>st</sup> Cycle of the TID Core Design**

Factor	Philosophy	Acceptable Value	Target Value	Current Value (TID, 1 <sup>st</sup> cycle)
<b>Achievable Burnup</b>	Achieve burnups such that the GFR (1) is cost competitive and (2) has fluence (both core and reactor pressure vessel) that is not excessive when compared to other options	100 MWD/kg (ave.)	150 MWD/kg (ave.)	140 MWD/kg (ave.)
<b>Radial Power Peaking</b>	Keep the radial power shape flat enough such that sufficient margin to thermal hydraulic limits is provided	1.3	1.2	1.34 @ 140 MWD/kg (unrodded)
<b>Passive Reactivity Control</b>	Keep coolant void reactivity low enough <u>over core life</u> such that it can be sufficiently offset by the accompanying effect of other passive reactivity mechanisms (i.e. Doppler, flowering, etc). Keep the method for doing this simple.	≤ \$1	≤ \$0	≤ \$0
<b>Peak Cladding Temperature (steady state)</b>	Keep the axial and radial power shapes such that sufficient margin to cladding failure is provided	800 °C	750 °C	810 °C
<b>Peak Fuel Temperature (steady state)</b>	Keep the axial and radial power shapes such that sufficient margin to fuel melting is provided	1800 °C	1700 °C	1770 °C
<b>Core Pressure Drop</b>	Keep the core pressure drop low enough such that (1) the S-CO <sub>2</sub> power conversion system operates at a good efficiency, and (2) natural and forced circulation are not significantly inhibited during decay heat removal	500 kPa	300 kPa	420 kPa
<b>Active Reactivity Control (Reactivity Swing/Control Rod Worth)</b>	Keep the reactivity swing low enough such that control rod worth does not become excessive (i.e. significantly beyond current experience, within rod ejection and stuck rod limits)	Within stuck rod, ejected rod, and current experience envelope	Within stuck rod, ejected rod, and current experience envelope	Within stuck rod, ejected rod, and current experience envelope

#### 4.4.1 Intra-Assembly Peaking Factor

In order to ensure that thermal hydraulic limits are observed for a given core design, the most limiting spatial location is examined. This location is typically determined through the combination of three power peaking factors: (1) an axial power peaking factor, (2) an inter-assembly radial power peaking factor, and (3) an intra-assembly radial power

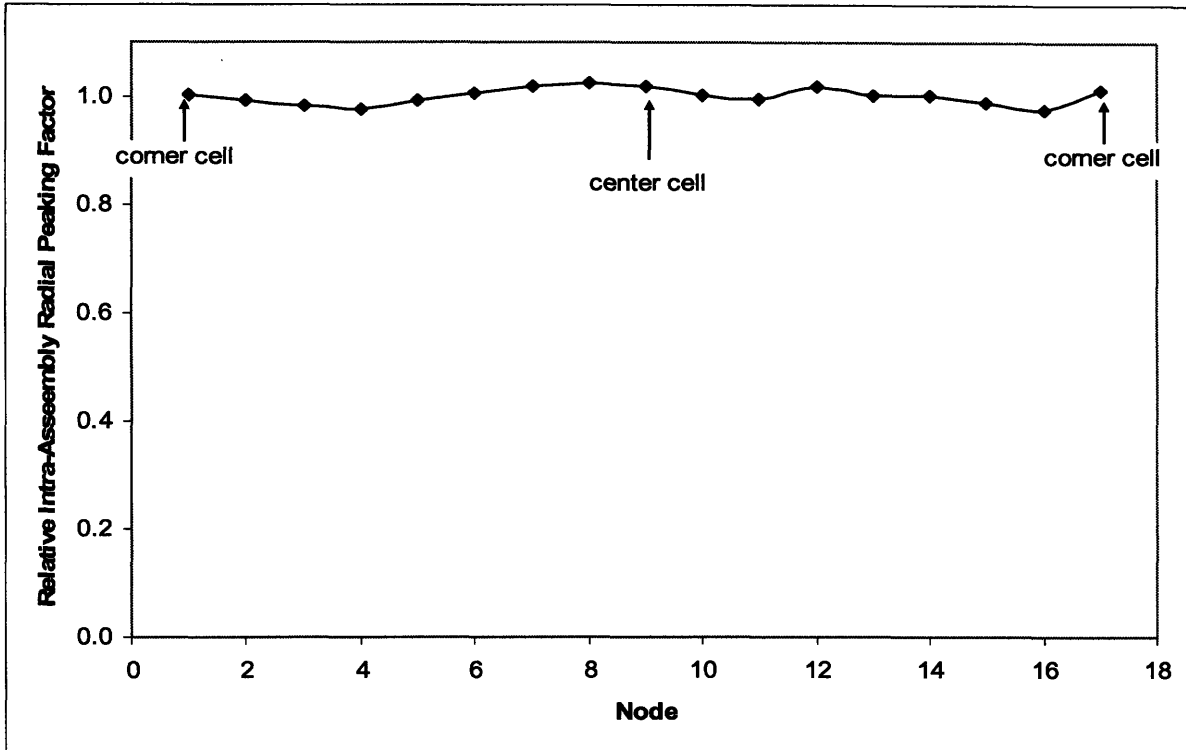


Figure 4.5: Intra-Assembly Power Distribution

peaking factor. While the first two factors are specifically addressed in Table 4.10, the third is not as it is nearly 1, and consequently, not a design concern. Figure 4.5 shows a representative intra-assembly power distribution, which is relatively flat and varies only between 0.975 and 1.02. Note that the slightly erratic behavior of the distribution is due to the uncertainty inherent in the Monte Carlo process used to generate these results. The flatness of this power profile is due to three factors: (1) the longer mean free path of a neutron in a fast reactor environment, (2) the homogeneous distribution of fuel and diluent throughout the assembly and (3) the large volume fraction of fuel inherent in using TID fuel. Hence, the intra-assembly peaking factor is not a constraint that needs consideration.



#### 4.4.2 Achievable Burnup

Figure 4.6 shows the behavior of  $k_{eff}$  with burnup and establishes the 1<sup>st</sup> cycle single batch core lifetime at ~140 MWD/kg or 18.48 Effective Full Power Years (EFPY). This core

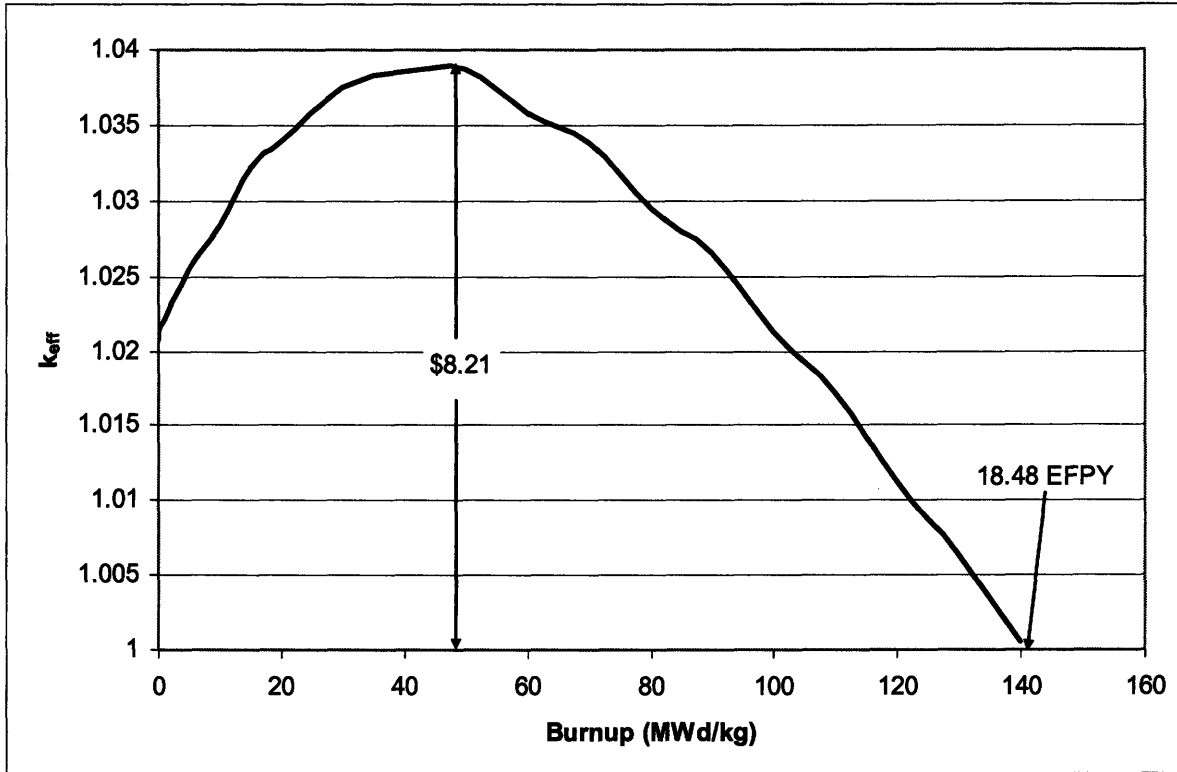


Figure 4.6: Excess Reactivity as a Function of Burnup for the 1<sup>st</sup> Cycle of the TID Core

lifetime value is long enough to be estimated as providing reasonably favorable economic conditions while short enough that it obeys realistic burnup constraints. The relatively low reactivity swing (~\$8.21) also demonstrated in this figure bodes well for meeting the criteria in Table 4.10 related to active reactivity control and control rod worth.

#### 4.4.3 Radial Power Peaking

Looking next at the behavior of the radial power shape over core life, Figure 4.7 shows how the radial power peak shifts over core life. Of note is that the unrodded radial power peaking factor varies between 1.11-1.21 for the first 120MWd/kg of burnup and then achieves its maximum value of 1.34 at EOL (140 MWD/kg). While the EOL value is in

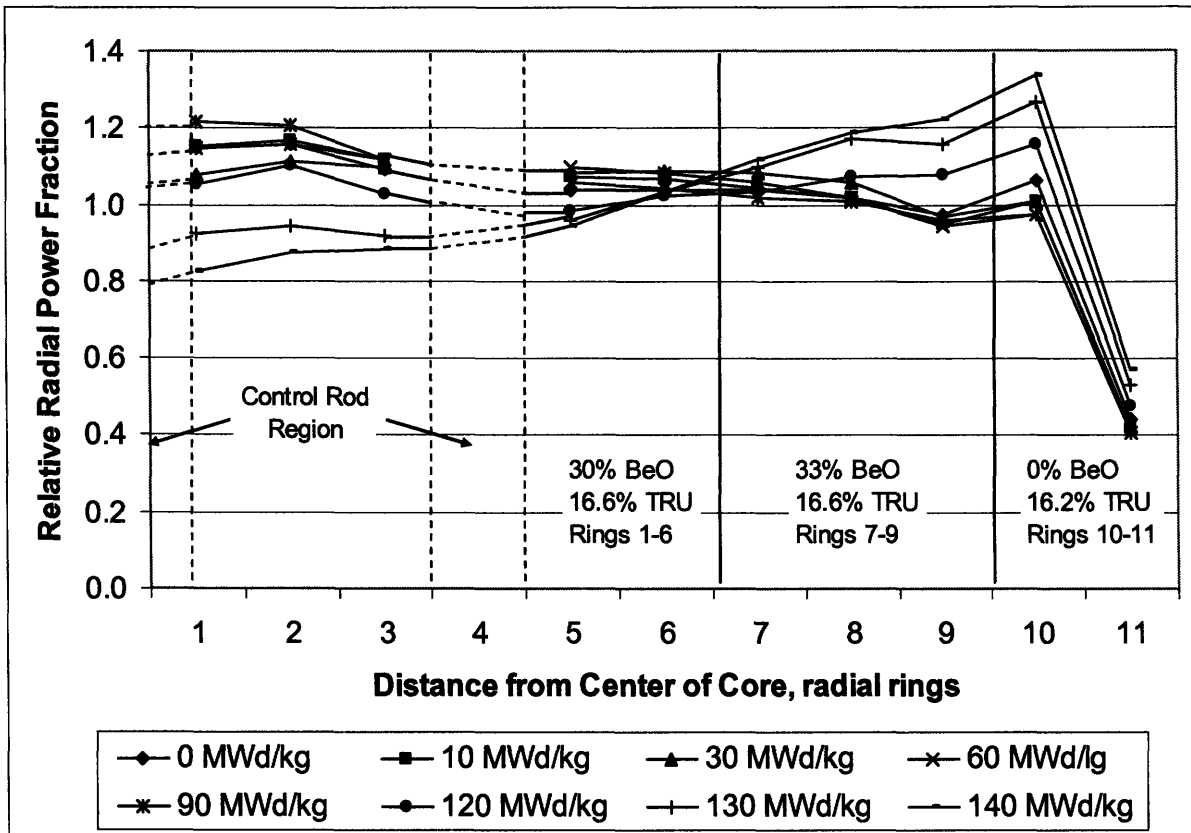


Figure 4.7: Unrodded Radial Power Shape as a Function of Burnup for the TID Core for the 1<sup>st</sup> Cycle

excess of the limit set in this analysis, the value of 1.34 is obtained without the benefit of control rods, while the 1.2 limit allows for the use of control rods in order to ensure that thermal-hydraulic limits are respected. Not only is the relatively flat radial power profile at BOL notable, but the fact that the radial power profile stays relatively flat for the first 120 MWd/kg is also noteworthy. Even flatter radial power shapes are possible using either (1) control assemblies for power shaping or (2) more experimentation with combinations of enrichment and diluent zoning, given the demonstrated potency of diluents.

#### 4.4.4 Passive Reactivity Control

In an effort to meet a stringent passive safety standard, it is desirable to keep the magnitude of any given reactivity insertion mechanism to  $\leq \$0$ . The most threatening of all of the reactivity insertion mechanisms in an accident scenario, coolant void reactivity (CVR) was assessed for the candidate core at different times in core life: BOL, MOL (at the most reactive time in core life, 30 MWD/kg), and EOL. Table 4.11 shows the results of MCNP

runs used to evaluate the void reactivity of the candidate core, assuming an instant depressurization from 20 MPa to 0.5 MPa (5 bars – the final pressure after depressurization into the containment). Of interest is that CVR values are negative for all times in core life, even when the uncertainty inherent in Monte Carlo calculations is accounted for. Note also that the unrodded and rodded, i.e. rods inserted to the critical position, scenarios are presented. Even with the implausible scenario of an unrodded core, the CVR is negative.

**Table 4.11: Coolant Void Reactivity Values for the TID Core**

Time in Life	keff, nominal	keff, voided	CVR $\Delta\rho$	STDEV ( $\sigma$ )	Effective Delayed Neutron Fraction ( $\beta_{eff}$ )	STDEV ( $\sigma$ )	CVR $\phi$	STDEV ( $\sigma$ ) $\phi$
<b>UNRODDED</b>								
BOL	1.02136	1.01948	-1.81E-03	2.19E-04	0.0046	1.7E-04	<b>-39</b>	<b>5</b>
MOL	1.03826	1.03804	-2.04E-04	2.00E-04	0.0045	1.9E-04	<b>-5</b>	<b>5</b>
EOL	1.00053	0.99895	-1.58E-03	1.98E-04	0.0044	1.9E-04	<b>-35</b>	<b>5</b>
<b>RODDED</b>								
BOL	1.00082	0.99597	-4.87E-03	2.12E-04	0.0045	2.1E-04	<b>-108</b>	<b>7</b>
MOL	1.00105	0.99563	-5.44E-03	2.13E-04	0.0046	2.1E-04	<b>-119</b>	<b>7</b>
EOL	1.00053	0.99895	-1.58E-03	1.98E-04	0.0044	1.9E-04	<b>-35</b>	<b>5</b>

Taking credit for the effect of control rods significantly decreases the value of CVR, as shown in Table 4.11. The much lower CVR values for the rodded case are due to the large increase in effective leakage introduced by the presence of the control rods. These low CVR values (as compared to other fast reactor designs) are due to a combination of the spectral softening effect of the diluent and the enhanced leakage of the radial reflector upon voiding. Further, the negative CVR throughout core life, coupled with a strongly negative Doppler reactivity coefficient (shown later), virtually ensures adequate passive safety performance (i.e. ability to inherently shut down without actuation of active reactivity control devices in the event of an accident). An initial assessment of passive safety will be undertaken in a later chapter.

#### 4.4.5 Thermal Hydraulic Results

Using FLOWSPLIT, an in-house FORTRAN thermal-hydraulics code developed at MIT, an assessment of steady state thermal hydraulic parameters of TID fueled cores with

different geometries was made [Hejzlar, 1994]. FLOWSPLIT required modifications from its original form in [Hejzlar, 1994] to account for the unique geometry of TID fuel and the effect of the BeO diluent on the fuel thermal conductivity [Pope et al., 2006]. As well, in order to look at a wide range of fuel geometries, a FLOWSPLIT-MATLAB interface was developed. This interface automated the generation of the applicable input deck for a given geometry, executed the appropriate program, processed the output data into a usable form, and then repeated the process until all desired geometries were evaluated. This interface, along with the algorithms developed to assess the thermal hydraulic performance of different core geometries, is explained in detail in Appendix B.

All thermal hydraulic results were calculated assuming (1) a chopped cosine shape for the axial power profile with a peak of 1.3 and (2) a 1.2 radial peaking factor to represent the hot pin. The axial power profile was chosen based on the findings regarding axial power shaping in the chapter called “The Diluent Effect.” Specifically, these results showed that axial power shaping could not produce an axial cladding temperature profile with a peak temperature less than that of the default power shape, a chopped cosine with a 1.3 peak. As for the radial peaking factor, 1.2 is a good estimate, as this has been demonstrated for most of core life. Any further enhancement of this figure will only provide added thermal hydraulic margin; in this way, 1.2 represents a conservative, bounding parameter. Further, it was assumed, based on previous analyses at MIT, that the use of BeO at concentrations  $\geq 10\%$  would enhance the fuel thermal conductivity by a factor of 1.5 [Pope et al., 2006].

Four thermal hydraulic constraints were used in assessing the available options:

1. Cladding Temperature:  $< 800^{\circ}\text{C}$
2. Fuel Temperature:  $< 1800^{\circ}\text{C}$
3. Pressure Drop:  $< 500\text{ kPa}$
4. Fuel volume fraction in the assembly ( $v_{fA}$ ):  $> 0$

The rationale for the temperatures and pressure in constraints 1-3 are contained in [Pope et al., 2006] and are repeated here for completeness:

*“The midwall peak clad temperature limit set by designers of the GA GCFR in the 1970’s was  $750^{\circ}\text{C}$ . [General Atomic Company, 1980] The ODS MA956 specified as the cladding material in this work has superior creep resistance to the stainless steel 316 specified for GCFR service. Since these fuel assemblies would be vented as were the GA GCFR assemblies, there will be no pressure differences across cladding which were also not*

*present in the GCFR design. Due to these factors, the clad surface temperature limit was set to 800°C.*

*In fuel assemblies where the fuel volume is not vented to an offgas system, fuel temperature limits are typically based on 1) no fuel melting and 2) limiting fission gas release to prevent excessive pressure in fuel pins. In a vented assembly, however, the fission gas release does not cause increased pressure across cladding. This allows for higher fuel temperatures than in invented [SIC] assemblies. For example, the steady state peak fuel temperature limit set for the GA GCFR design was 2650°C, the lower bound of the UO<sub>2</sub> fuel melting temperature. The peak fuel temperature limit of 1800°C set for our present design is based on 1) no melting of (U,TRU)O<sub>2</sub> fuel, 2) no melting of BeO diluent, and 3) chemical stability of the BeO/(U,TRU)O<sub>2</sub> mixture. The melting point of the (U,TRU)O<sub>2</sub> is assumed to be equal to the value for (U<sub>0.8</sub>Pu<sub>0.2</sub>)O<sub>2</sub> of 2750°C [Waltar, et. al., 1981] and BeO melts at around 2570°C. BeO is chemically stable with UO<sub>2</sub> and PuO<sub>2</sub> up to 2135°C. [Sarma et. al., 2005] Although in general it is desirable to have lower temperatures in fuel in order to reduce the stored energy at the outset of a transient, an exact steady state fuel temperature limit based on this constraint can only be determined through detailed transient calculations and is difficult to specify a priori.*

*The pressure drop across the core is an important design parameter. At full power operation, the core pressure drop directly impacts the compressor work (back work) and thus has direct bearing on the thermodynamic efficiency of the power cycle. The core's resistance to coolant flow also impacts blower power requirements during refueling and accident conditions. Also of great significance is the fact that a core with a high pressure drop will tend to perform poorly in natural circulation cooling at pressure or in a post-LOCA depressurized state. For this work, a full power core pressure drop limit of 500 kPa is set."*

The 4<sup>th</sup> constraint,  $vf_A$  is an issue with TID fuel, where certain geometries are not possible for the given clad and gap thickness correlation. As well, any clad and gap thickness would physically preclude a limited range of fuel geometries. It should be noted that the thickness of the clad and gap were not held constant, but rather were varied for each case using the clad thickness and fuel-clad gap correlations developed in [Garkisch and Petrovic, 2004] and shown in Figure 4.8 and Figure 4.9. Using these four criteria, a range of geometries, i.e. coolant channel diameter and P/D for TID fuel, was assessed against the criteria.

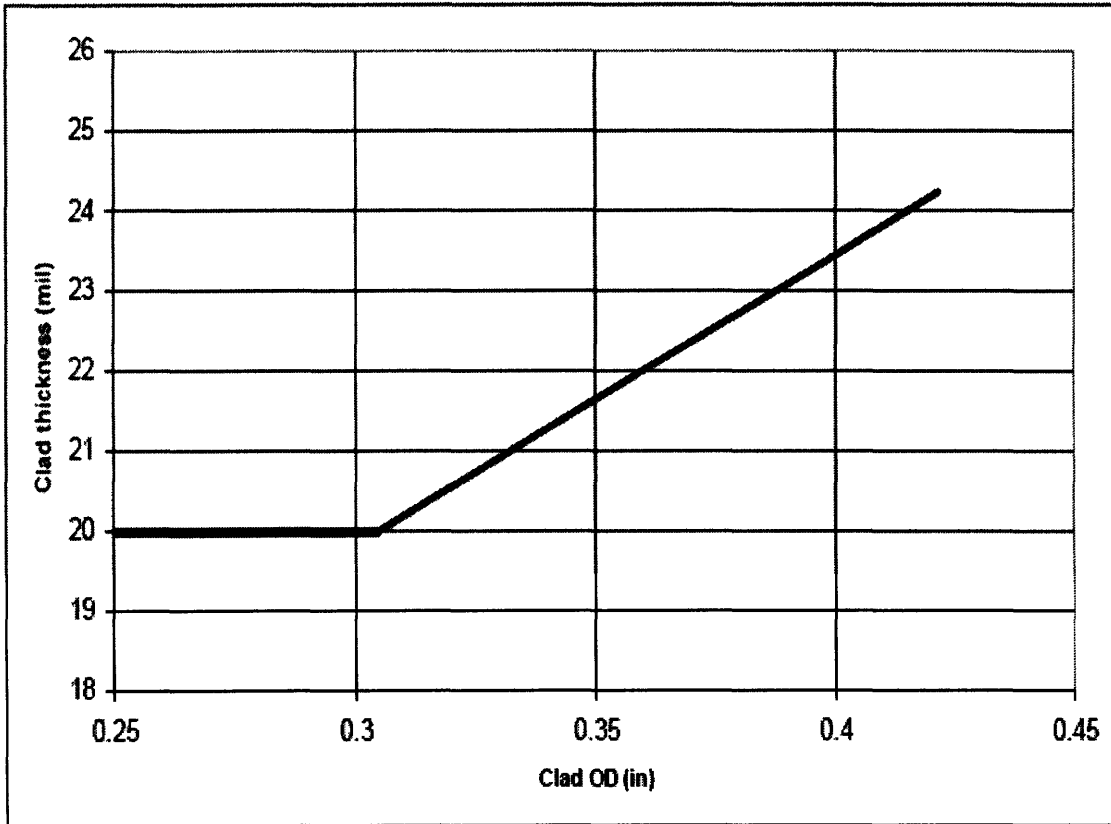


Figure 4.8: Clad Thickness-Clad Outer Diameter Correlation (from [Garkisch and Petrovic, 2004])

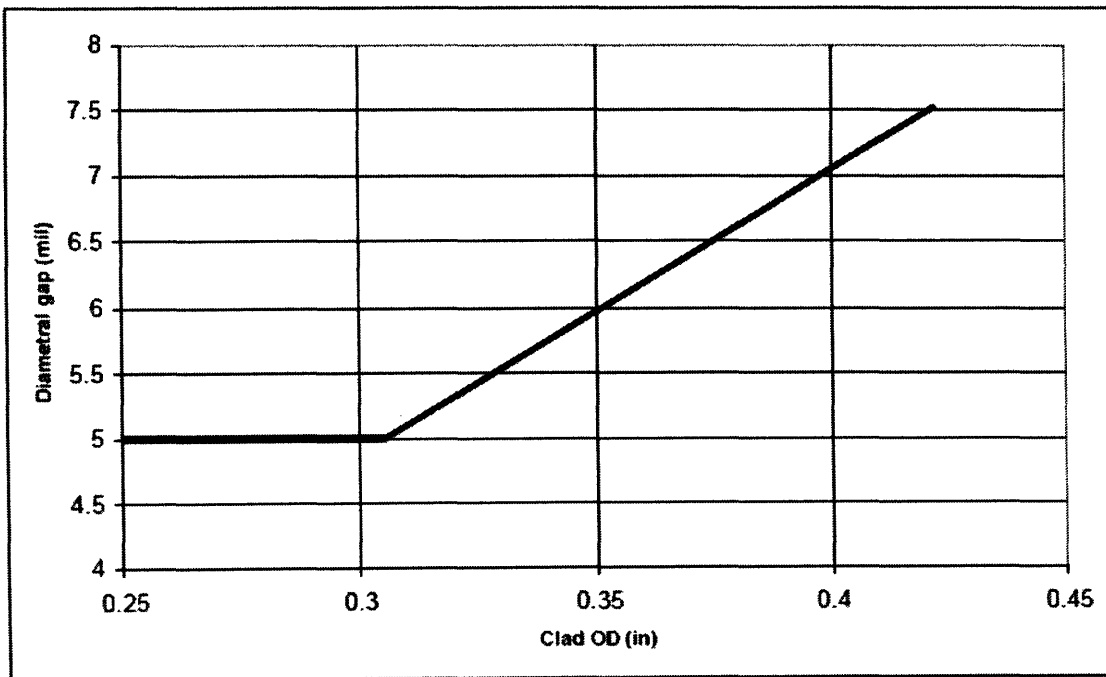
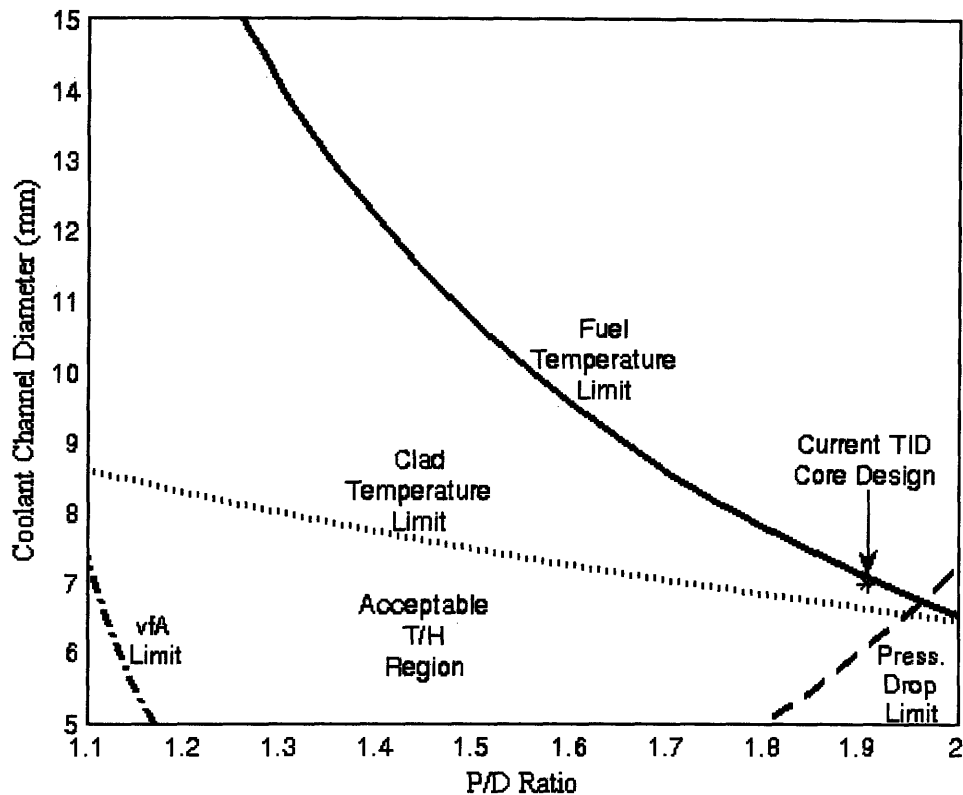


Figure 4.9: Gap Thickness-Clad Outer Diameter Correlation (from [Garkisch and Petrovic, 2004])



**Figure 4.10: Acceptable T/H Envelope for the TID Fuel Assembly Core**

Figure 4.10 shows the results of the thermal hydraulic calculations using the FLOWSPLIT-MATLAB interface, with the appropriate thermal hydraulic limits labeled and bounding a region of geometries in which all thermal hydraulic limits are satisfied, i.e. the “Acceptable T/H Region.” In order to determine which set of geometric parameters within this acceptable region optimizes performance, the region where the fuel volume fraction is maximized is chosen. This is because the greater the fuel volume fraction, the greater the heavy metal loading and hence, the longer the achievable burnup. However, increasing the heavy metal loading while maintaining the same thermal power will reduce the specific power of the core. Enhancing burnup capability will favorably affect the overall economic picture, while reducing specific power will unfavorably affect the fuel cycle cost component. On balance, the net economic effect should be positive and consequently maximizing reactivity limited burnup through maximizing the fuel volume fraction is the strategy chosen here. Other benefits of maximizing the  $vf_A$  include a greater volume for diluent and a minimization of the coolant volume fraction, both of which have been shown to help to minimize the effect of CVR. As well, more volume for diluent allows greater flexibility with

respect to varying diluent loading for radial power shaping. Not shown in Figure 4.10, the region of greatest  $vf_A$  is in the right-most corner of the acceptable T/H envelope. Note that the geometric parameters of the current TID core design are shown on this figure, just slightly outside of the acceptable T/H region but within the region of maximum fuel volume fraction. Specifically, this point respects all of the prescribed thermal hydraulic limits (Peak Fuel Temperature = 1770°C, Pressure Drop = 420 kPa,  $vf_A > 0$ ) except the cladding temperature limit. The calculated peak cladding temperature for this case is 810°C, whereas the limit has been established as 800°C.

While the actual value for the peak cladding temperature in this core exceeds the limit, several factors need to be remembered. First, the limit of 800°C is somewhat arbitrarily set, based on a 50°C increase for a new cladding material from the 750°C limit set by General Atomic for a different cladding material in use more than 25 years ago. In fact, the manufacturer of the cladding in use in this project advertises “excellent strength and fabricability with outstanding resistance to prolonged exposure up to 1300°C.” [Special Metals, 2004] While this 500°C of extra temperature margin is not fully captured, it certainly can be used to justify accepting a peak cladding temperature of 810°C. Second, the temperature calculations are based on a 1.2 radial peaking factor. While the current core design shows a maximum radial peaking factor of 1.34 with values less than 1.2 throughout much of core life (in Figure 4.7), experience with diluent zoning has shown that sustainable radial peaking factors of lower values, i.e. 1.15 and less, may be achievable throughout core life with further experimentation into diluent and enrichment zoning and control rod programming. For these reasons, the current core design’s peak cladding temperature can be accepted as within safe limits.

#### 4.4.6 Active Reactivity Control

Several MCNP runs were performed to determine if the core would be protected against the “stuck rod” criterion. This is where the control rods must have enough reactivity to make the reactor sub-critical with the most reactive rod stuck at the critical position at the most reactive time in core life. Therefore, calculations of  $k_{eff}$  with all control rods inserted fully except one (stuck at the position which originally provided criticality) were performed



at the most reactive time in core life, i.e. MOL, to determine if this core met this criterion. Since the core model used in MCNP is a 1/6<sup>th</sup> core model, inserting 1 rod in the 1/6<sup>th</sup> model was the equivalent of inserting 6 rods in the whole core model (similarly, inserting 1/6<sup>th</sup> of a control rod at the center of the model is analogous to inserting 1 rod in the whole core model). Figure 4.1 shows a schematic of the 1/6<sup>th</sup> core model and the accompanying control rod positions.

Table 4.12 shows the results of these MCNP runs. Clearly there is enough shutdown margin provided by the control rods to satisfy the one stuck rod criterion, no matter which rod gets stuck. Furthermore, the results in Table 4.12 show that the core is protected even if 6 rods get stuck at the most reactive time in core life. It is important to note that depletion in the Boron-10 control assemblies is not simulated with burnup, so the values listed in Table 4.12 are overly optimistic. However, there is enough negative reactivity associated with these control assemblies that these numbers can represent a good first order estimate of meeting the one stuck rod criterion.

**Table 4.12:  $k_{\text{eff}}$  Values for Stuck Rod Scenarios at the Most Reactive Time in Life for the TID Core**

	$k_{\text{eff}}$	STDEV ( $\sigma$ )
All rods at critical position	1.00105	0.00016
All rods in, center rod stuck at critical position	0.99372	0.0004
All rods in, all rods in 4th ring stuck at critical position	0.99793	0.0004
All rods in, all rods in 8th ring, position 2, stuck at critical position	0.99842	0.00038
All rods in, all rods in 8th ring, position 3, stuck at critical position	0.99799	0.00037

Several MCNP runs were performed in an effort to quantify the worth of each of the control rods within the core. Because of the 1/6<sup>th</sup> model symmetry, the worth of each of the corresponding 6 rods in the whole core, modeled as 1 rod in the 1/6<sup>th</sup> model, was assumed equal. Table 4.13 shows the results of these runs. Of interest is that the worth of all of the control rods (measured individually) is < \$0.65, with the average control rod worth measured from the all-rods-in and all-rods-out core eigenvalues ~\$0.48. As well, with the exception of the center rod, all of the values are fairly close, owing to the flat radial power distribution in the core. The relatively low control rod worth and even worth values throughout the core bode well for future safety analyses.

**Table 4.13: Control Rod Worth at the Most Reactive Time in Life for the TID Core**

	Worth ( $\Delta\rho$ )	Worth (\$)	STDEV ( $\sigma$ ) (\$)
Center Rod	2.81E-03	0.62	0.12
All Rods in 4th Ring (6)	1.06E-02	2.33	0.17
1 rod in 4th ring, assuming equal worth	1.76E-03	0.39	0.03
All Rods in 8th Ring, position 2 (6)	9.62E-03	2.12	0.16
1 rod in 8th ring, position 2, assuming equal worth	1.60E-03	0.35	0.03
All Rods in 8th Ring, position 3 (6)	9.18E-03	2.02	0.16
1 rod in 8th ring, position 3, assuming equal worth	1.53E-03	0.34	0.03
Total Worth all rods	4.11E-02	9.07	0.43
Average Control Rod Worth	2.16E-03	0.48	0.02

#### **4.5 Assessment of Core Performance: 2<sup>nd</sup> and 3<sup>rd</sup> Cycles**

In an effort to better understand how the core behaves and to understand what design challenges may be encountered through the use of the fuel cycle described in Section 2.6, a second and third cycle were simulated and analyzed. As described earlier, the TRU for the first cycle will come from spent LWR fuel, with the TRU for subsequent cycles coming from that which is recycled from the previous cycle. The general mass flow scheme is germane to all three cycles and an illustration is provided in Figure 4.11. Table 4.14 shows the mass vectors for all 3 cycles. Note that for cycles 2 and 3, there are 2 uranium vectors listed, “actual” and “used.” The “actual” uranium vector is the composition resulting from the previous cycle’s operation. The “used” vector represents the uranium vector used in all of the calculations, which is natural uranium in this case. Since natural uranium, i.e. “used,” has a larger amount of U-235 (more reactivity) and a slightly smaller amount of U-238 (less breeding potential, and hence, shorter reactivity limited burnup) than the depleted uranium at the end of the cycle, i.e. “actual,” it presents a more neutronic challenging and limiting case. Consequently, natural uranium was used as the uranium input for the beginning of each cycle in order to demonstrate the technical feasibility of the approach, with the assumption that the depleted (i.e. recycled) uranium case would be less limiting.

The same neutronic performance metrics used in Section 4.4 for the 1<sup>st</sup> cycle are used for the 2<sup>nd</sup> and 3<sup>rd</sup> cycle: (1) achievable burnup, (2) radial power peaking, and (3) passive

reactivity control. Steady state thermal hydraulic results are not revisited, as they are based largely on core geometry and macro-parameters, e.g. inlet temperature and coolant flow rate, which do not change from cycle to cycle. Further, the acceptable thermal hydraulic envelope presented in Section 4.4.5 is based on a maximum radial peaking factor of 1.2. Hence, as long as this constraint is met, the three chosen steady state thermal hydraulic criteria should

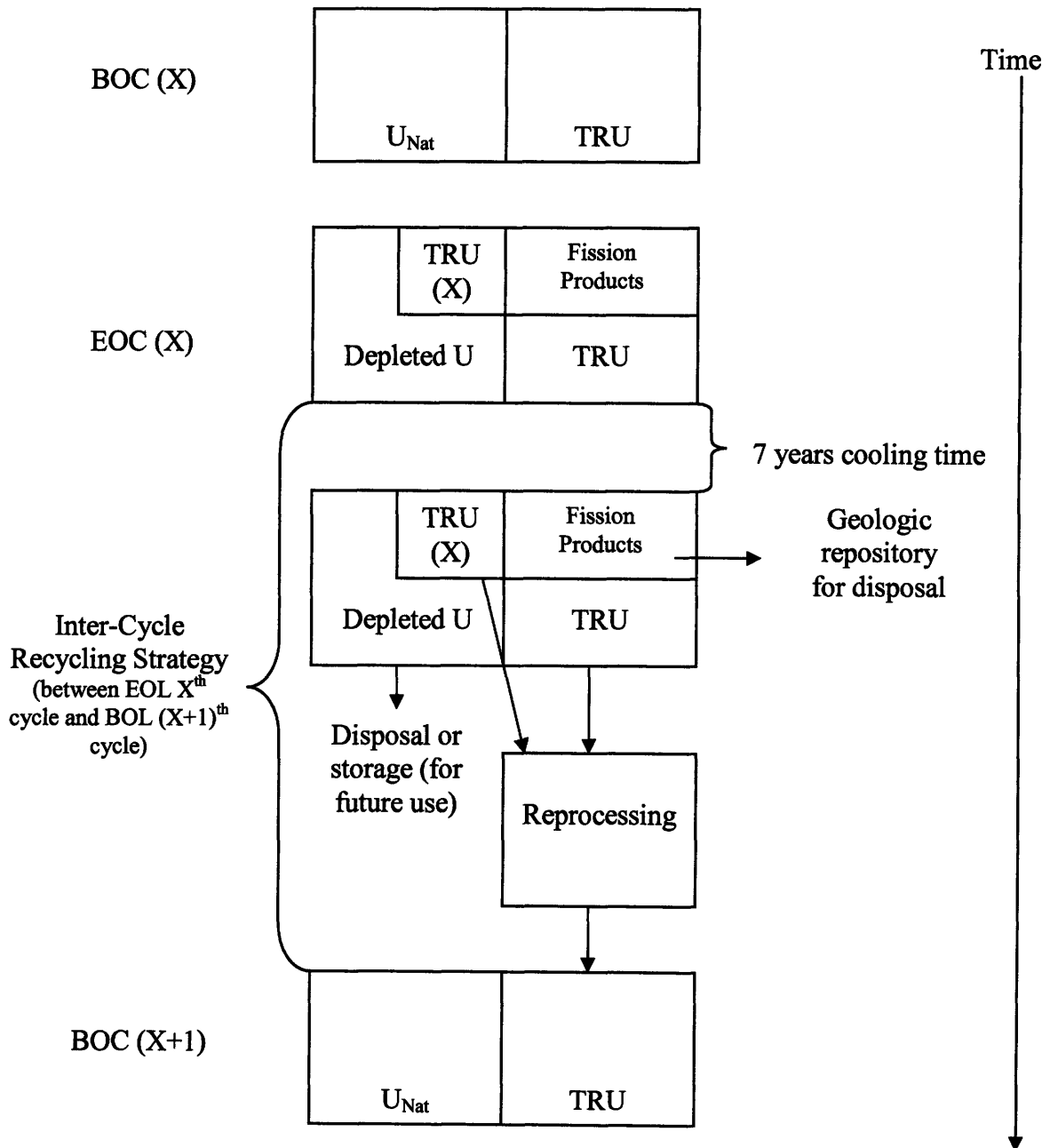


Figure 4.11: Illustration of Fuel Cycle Mass Flow

**Table 4.14: Comparison of U/Pu/MA/TRU Vectors for All Cycles**

	BOC1	BOC2	BOC2	BOC3	BOC3
		(actual)	(used)	(actual)	(used)
<b>U Vector (%)</b>					
U234	0.00000	0.00098	0.00000	0.00093	0.00000
U236	0.00000	0.00137	0.00000	0.00134	0.00000
U235	0.00711	0.00235	0.00711	0.00249	0.00711
U238	0.99413	0.99529	0.99413	0.99524	0.99413
<b>Pu Vector (%)</b>					
PU238	0.010	0.028		0.0245	
PU239	0.630	0.577		0.5710	
PU240	0.290	0.321		0.3355	
PU241	0.010	0.025		0.0276	
PU242	0.060	0.048		0.0414	
<b>MA Vector (%)</b>					
NP237	0.297	0.187		0.126	
AM241	0.647	0.575		0.583	
AM242m	0.000	0.033		0.032	
AM243	0.051	0.139		0.158	
CM243	0.000	0.001		0.001	
CM244	0.004	0.051		0.072	
CM245	0.000	0.012		0.022	
CM246	0.000	0.002		0.007	

<b>TRU Vector</b>			
	BOC1	BOC2	BOC3
Pu w/o	0.9	0.9286	0.9354
MA w/o	0.1	0.0714	0.0646

still be met. As well, an assessment of active reactivity control was not made for the 2<sup>nd</sup> and 3<sup>rd</sup> cycles, as the reactivity swing of these two cycles will be shown to be less than or equal to that of the first cycle. Since the control rod strategy has proven adequate for the first cycle, it should be equally as adequate for the 2<sup>nd</sup> and 3<sup>rd</sup> cycles.

#### 4.5.1 Achievable Burnup

Figure 4.12 shows the excess reactivity curves for all three cycles and Table 4.15 lists a comparison of some of the key neutronic performance parameters, both showing some interesting results. First, the reactivity limited burnup, effective full power lifetime and reactivity swing (in  $\Delta\rho$ ) is larger for the first cycle than for the second or third cycles. This is due to the buildup of Am-242m to near equilibrium levels in the first cycle, and relatively constant levels during the second and third cycles, as shown in Figure 4.13. While present in

only very small quantities (<50kg maximum in a core actinide inventory of nearly 116,000 kg), Am-242m has a significant effect on core reactivity. This is due to its very large fission cross section, which is at least an order of magnitude greater than the largest contributor to fission in this core, Pu-239, for much of the energy spectrum. This effect is quantified in

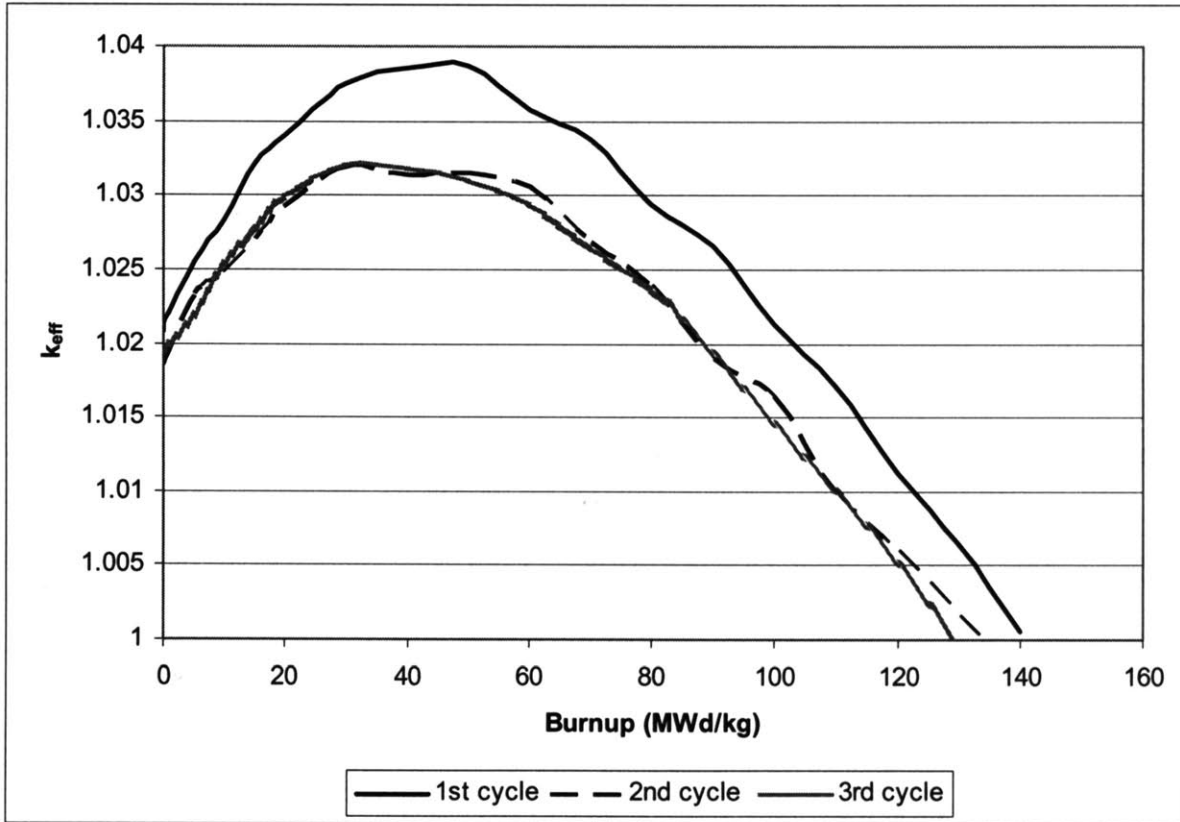


Figure 4.12: Excess Reactivity as a Function of Burnup for All Three Cycles of the TID Core

Table 4.15: Neutronic Performance Parameter Comparison Among All Three Cycles of the TID Core

	1 <sup>st</sup> Cycle	2 <sup>nd</sup> Cycle	3 <sup>rd</sup> Cycle
TRU Enrichment Zoning (w/o)	16.6/16.6/16.2	15.9/15.9/15.9	15.8/15.8/15.8
Diluent Zoning (%)	30/33/00	30/33/00	30/33/00
Reactivity Limited Burnup	140	133	130
Effective Full Power Lifetime (EFPY)	18.48	17.66	17.16
Reactivity Swing ( $\Delta\rho$ )	0.03726	0.03091	0.03106
$\beta_{eff}$ unrodded at time of peak excess reactivity	0.0045	0.0038	0.0040
Reactivity Swing	\$8.21	\$8.19	\$7.81

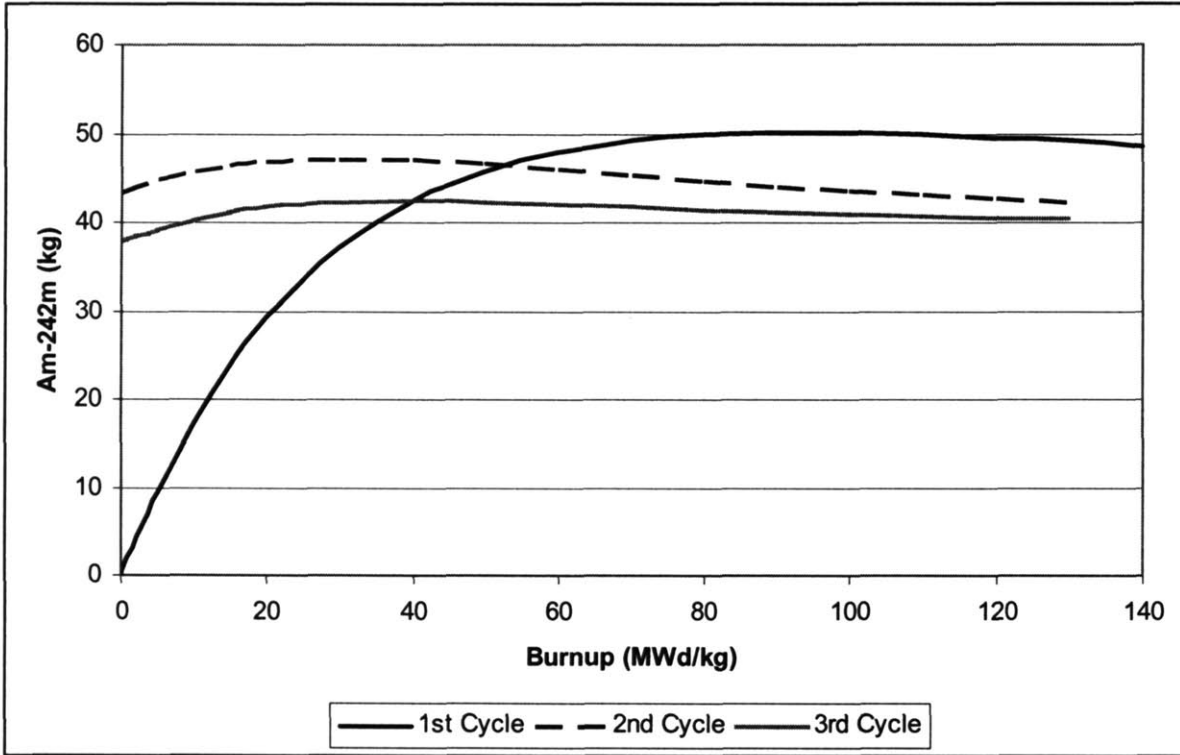


Figure 4.13: Comparison of Am-242m Burnup-dependent Composition Among All Three Cycles

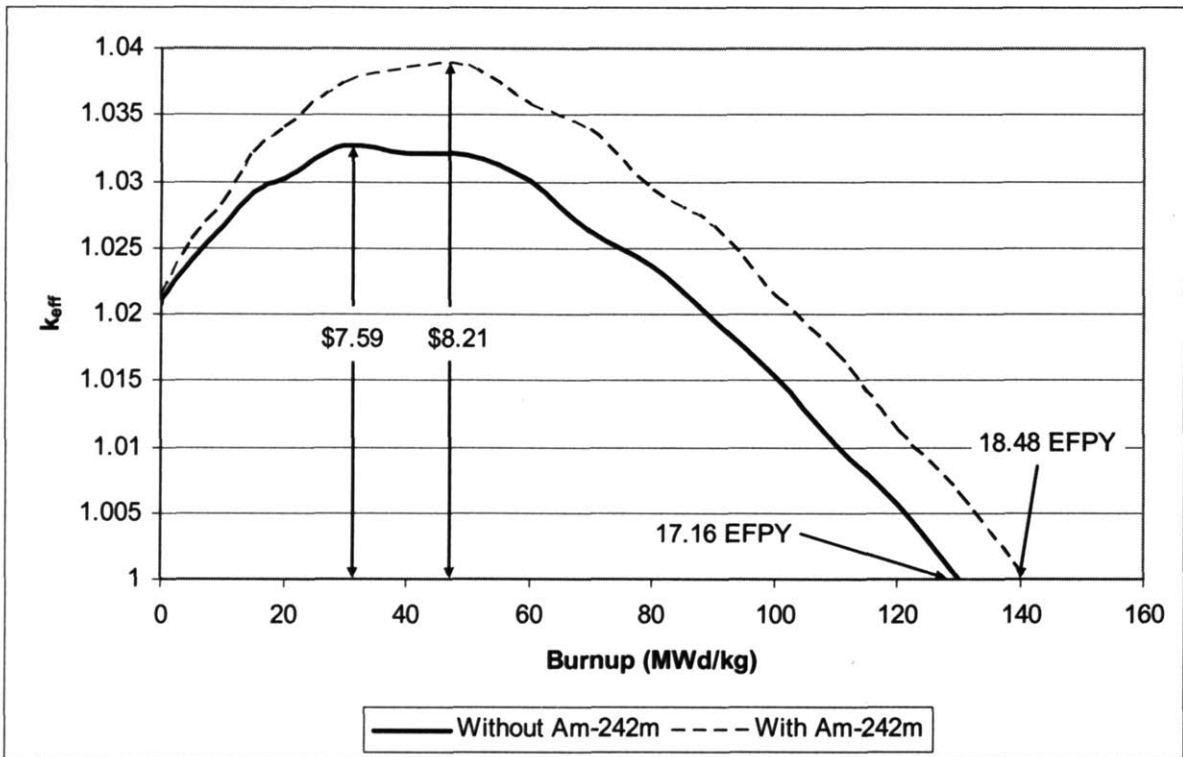


Figure 4.14: Comparison of Excess Reactivity for the First Cycle with and without Am-242m

Figure 4.14, where the reactivity limited burnup for the first cycle of the TID core is shown for the case where Am-242m is allowed to build-up to equilibrium, i.e. “With Am-242m,” and the case where Am-242m is not accounted for, i.e. “Without Am-242m.” This figure shows that only 50 kg of Am-242m can account for a difference in reactivity limited lifetime of ~1.3 EFPY and a reactivity swing of ~\$0.60, the worth of the most reactive control rod. As well, the lower BOC enrichment needed for the second and third cycles for roughly the same BOC core eigenvalue as the first cycle shows the potency of Am-242m. Note that the small difference in BOC core eigenvalue in Figure 4.12 between the first and subsequent cycles is due to inability to exactly match these values and not a consequence of the lower enrichment. Calculations show that raising second and third cycle enrichment by 0.1 % TRU causes the second and third BOC core eigenvalues to exceed that of the first.

This effect is unique to fast spectrum reactor operation, as Am-242m is produced from neutron capture in Am-241. While Am-241 is present in appreciable quantities in thermal reactors, the absorption cross section of Am-242m in the thermal region is appreciably larger than that of Am-241 [Ronen et al, 2006]. Hence, any Am-242m produced is immediately transmuted. However, the situation is reversed in a fast spectrum, so Am-242m can be produced in appreciable quantities in fast reactors. Further, once Am-241 captures a neutron, it can either produce Am-242g (a ground state of Am-242 with a half-life of 16 hrs) or Am-242m (a meta-stable state of Am-242 with a half-life of 141 years). A harder spectrum favors the production of the longer-lived Am-242m, while a softer spectrum favors the production of the shorter-lived Am-242g [Ronen et al, 2006]. While Am-242m and Am-242g have similar neutronic behavior at low energies, i.e. fission and absorption cross section values and behavior, the very short half-life of Am-242g prevents it from building up to appreciable quantities.

Another difference between the first cycle and the second and third cycles shown in Table 4.15 is the difference in reactivity swing. While the first cycle experiences a much larger reactivity swing than the second (and third) cycle in terms of  $\Delta\rho$ , the lower  $\beta_{\text{eff}}$  for the second cycle makes the reactivity swing in terms of \$ nearly equivalent for the first and second cycles. This lower value of  $\beta_{\text{eff}}$  is likely due to the larger percentage of Plutonium making up the TRU vector, as shown in Table 4.14. Similarly, the 3<sup>rd</sup> cycle has a

comparable Pu contribution to the TRU vector and results in a  $\beta_{\text{eff}}$  comparable to the 2<sup>nd</sup> cycle, when uncertainty is accounted for (shown in Table 4.16). This lower  $\beta_{\text{eff}}$  for the 3<sup>rd</sup> cycle also gives a reactivity swing in terms of \$ close to that of the 1<sup>st</sup> cycle.

#### 4.5.2 Radial Power Peaking

Figure 4.15 and Figure 4.16 show the unrodded radial power profile as a function of burnup for the 2<sup>nd</sup> and 3<sup>rd</sup> cycles respectively. While the unrodded radial power shapes do not meet the maximum radial power peak constraint of 1.2, the necessary and inevitable implementation of a control rod strategy (in order to keep the core from being supercritical) would like keep radial power peaking within limits. As well, comparing Figure 4.7 with Figure 4.15 and Figure 4.16 shows a distinct pattern which the radial power shape assumes over burnup with the use of the chosen diluent strategy. Initially, a relatively flat radial power profile (peak ~1.1-1.15) is achievable, with a slight peak near the center. This peak grows near the center to a value between 1.2-1.3 at the time of peak excess reactivity. Then, the power profile begins to flatten again, and the peak begins to shift to the periphery when

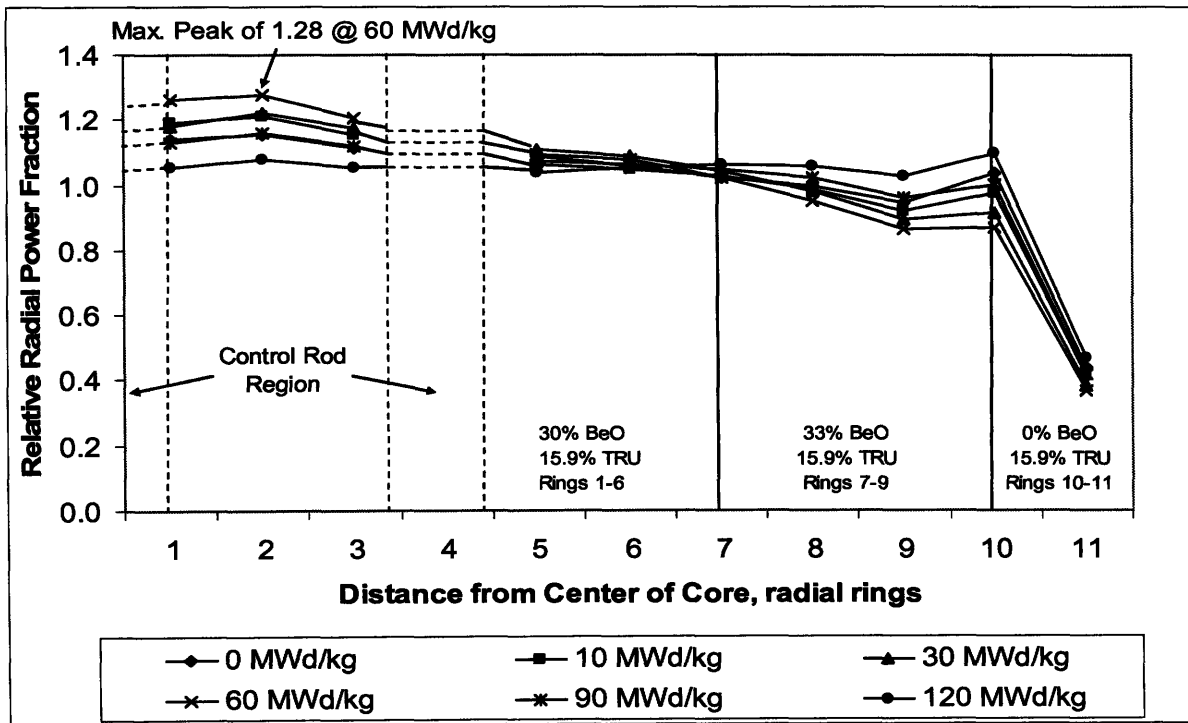


Figure 4.15: Unrodded Radial Power Shape as a Function of Burnup for the TID Core for the 2<sup>nd</sup> Cycle



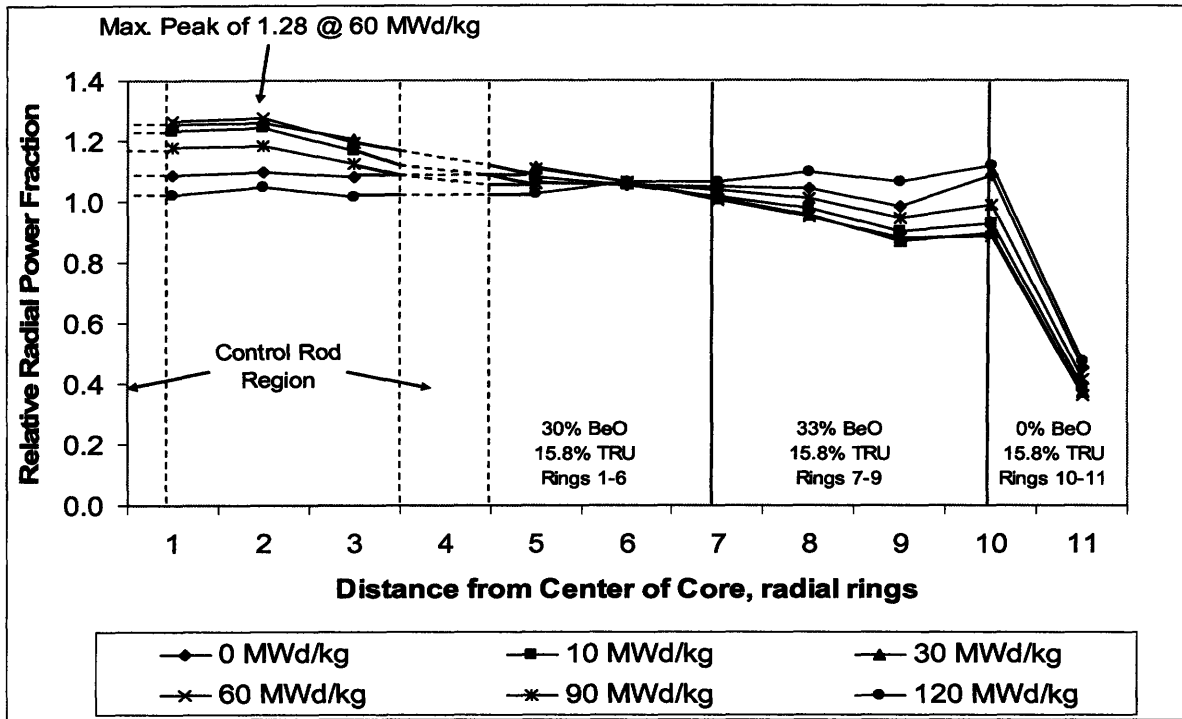


Figure 4.16: Unrodded Radial Power Shape as a Function of Burnup for the TID Core for the 3<sup>rd</sup> Cycle

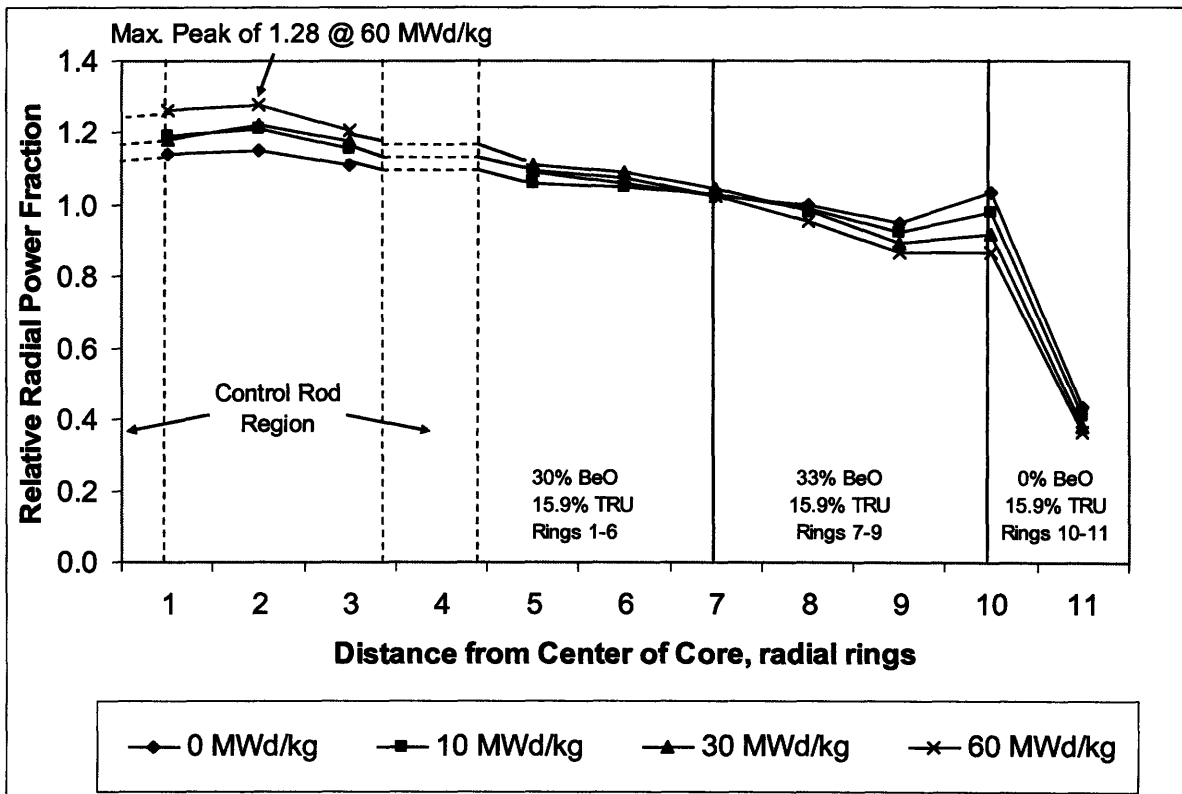
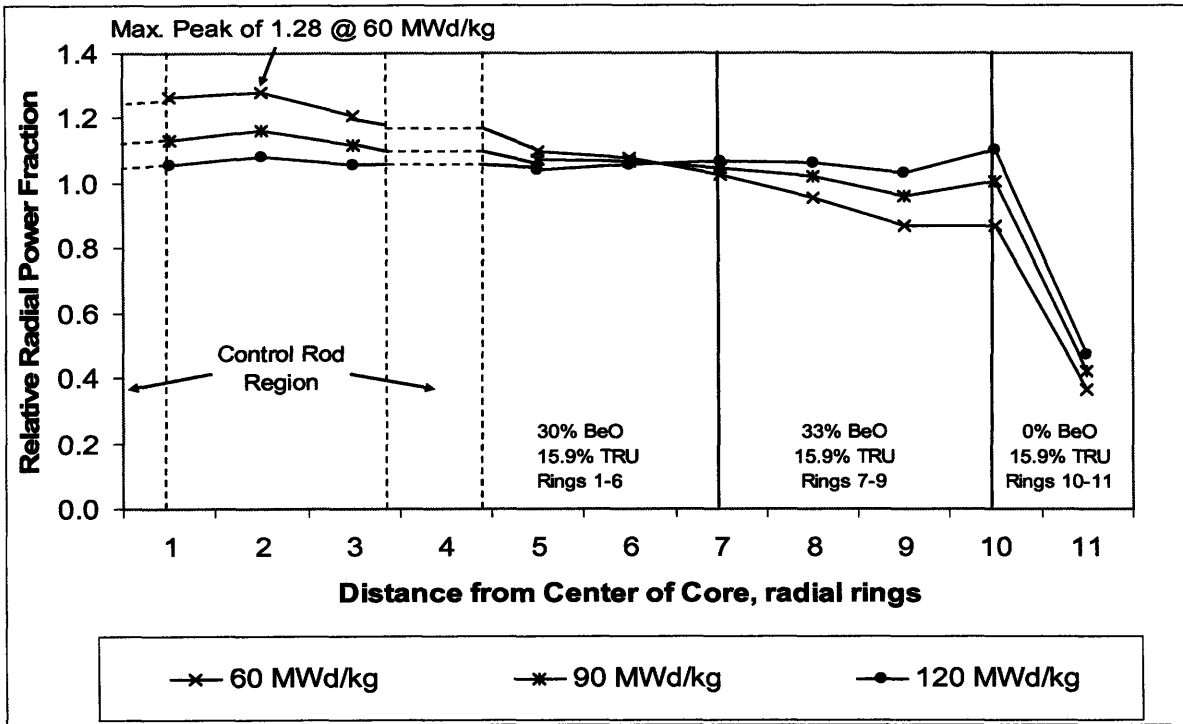


Figure 4.17: Unrodded Radial Power Shape as a Function of Burnup for the TID Core:  
2<sup>nd</sup> Cycle 0-60 MWd/kg



**Figure 4.18: Unrodded Radial Power Shape as a Function of Burnup for the TID Core:  
2<sup>nd</sup> Cycle 60-120 MWd/kg**

the cycle ends. While this effect may be difficult to discern in Figure 4.15 and Figure 4.16 for the 2<sup>nd</sup> and 3<sup>rd</sup> cycles, Figure 4.17 and Figure 4.18 break Figure 4.15 up into two parts, so that this effect is easier to visualize for the 2<sup>nd</sup> cycle, as an illustrative example.

A closer examination of Figure 4.15 and Figure 4.16 shows that there is some margin between the radial power peak at EOL and the limit of 1.2. A modification of the diluent strategy such that there was a lower peak in the middle of the core at BOL, i.e. a higher peak in the periphery, could keep the unrodded radial power profile below the limit of 1.2 in order to take advantage of both the pattern that the radial power profile shows throughout life and the extra margin at EOL. Hence, the peak would build-up in the center during the first part of the cycle, but stay below the limit of 1.2 at the time of peak excess reactivity, and then shift to the periphery later in life, all the while staying below the limit of 1.2. It should be remembered that the introduction of the control rods could require a change in this approach; however, the ability of diluent in shaping power has been shown to be effective and versatile enough to accommodate whatever radial power shape throughout core life that is desired. Another important conclusion that can be drawn from this section is that the diluent is

effective in shaping power, even though the Pu/MA vectors are different among the three cycles. This gives credence to this strategy as a robust one for power shaping in fast reactors.

#### 4.5.3 Passive Reactivity Control

Table 4.16 compares the values for CVR for all three cycles. It is important to note that the values presented in this table are for an unrodded core. As shown earlier, the more realistic rodded core scenario gives CVR values that are significantly more negative at BOL and MOL (the core operates with all rods removed at EOL in order to sustain criticality). Consequently, if the CVR is negative throughout core life in an unrodded scenario, it will be more negative throughout life once control rods are introduced. Despite the fact that the relative isotopic compositions change from cycle to cycle, the TID core is able to achieve negative values of CVR over its entire operating lifetime.

**Table 4.16: Unrodded Coolant Void Reactivity Values for the TID Core for All Three Cycles**

Time in Life	$k_{eff, nominal}$	$k_{eff, voided}$	CVR $\Delta\rho$	STDEV ( $\sigma$ )	Effective Delayed Neutron Fraction ( $\beta_{eff}$ )	STDEV ( $\sigma$ )	CVR $\phi$	$\sigma$ $\phi$
<b>UNRODDED – 1<sup>st</sup> cycle</b>								
BOL	1.02136	1.01948	-0.00181	2.19E-04	0.0046	1.7E-04	-39	5
MOL	1.03826	1.03804	-0.000204	2.00E-04	0.0045	1.9E-04	-5	5
EOL	1.00053	0.99895	-0.00158	1.98E-04	0.0044	1.9E-04	-35	5
<b>UNRODDED – 2<sup>nd</sup> cycle</b>								
BOL	1.01871	1.01666	-0.00198	1.98E-04	0.0046	1.89E-04	-42	5
MOL	1.03120	1.03088	-0.000301	1.84E-04	0.0038	1.72E-04	-8	5
EOL	1.00072	0.99940	-0.00132	1.84E-04	0.0041	1.84E-04	-32	5
<b>UNRODDED – 3<sup>rd</sup> cycle</b>								
BOL	1.01884	1.01726	-0.00152	2.05E-04	0.0043	1.81E-04	-35	5
MOL	1.03124	1.03073	-0.00048	2.13E-04	0.0040	1.99E-04	-12	5
EOL	0.99961	0.99811	-0.00150	1.84E-04	0.0042	1.99E-04	-36	5

#### 4.6 Reactor Pressure Vessel Fluence

Given that a S-CO<sub>2</sub> radial reflector has been decided upon in order to keep void reactivity negative throughout core life, concerns about reactor pressure vessel fluence are raised. This is because there will be less material to shield the vessel than if there were a

solid radial reflector. Mitigating this effect will be the low leakage inherent in a large sized core. Hence, not only should the amount of reactor pressure vessel fluence be quantified, but also an appropriate limit should be defined.

#### 4.6.1 Determination of an Effective Fluence Limit

Current guidance on the allowable fluence limit for the Reactor Pressure Vessels (RPVs) in Light Water Reactors (LWRs) can be found in USNRC Regulatory Guide (USNRCRG) 1.99, rev. 2 [USNRC, 1988]. While this guidance is specific to LWRs and has been developed from empirical evidence based on LWR experience, it provides insight into the mechanisms of degradation due to neutron fluence.

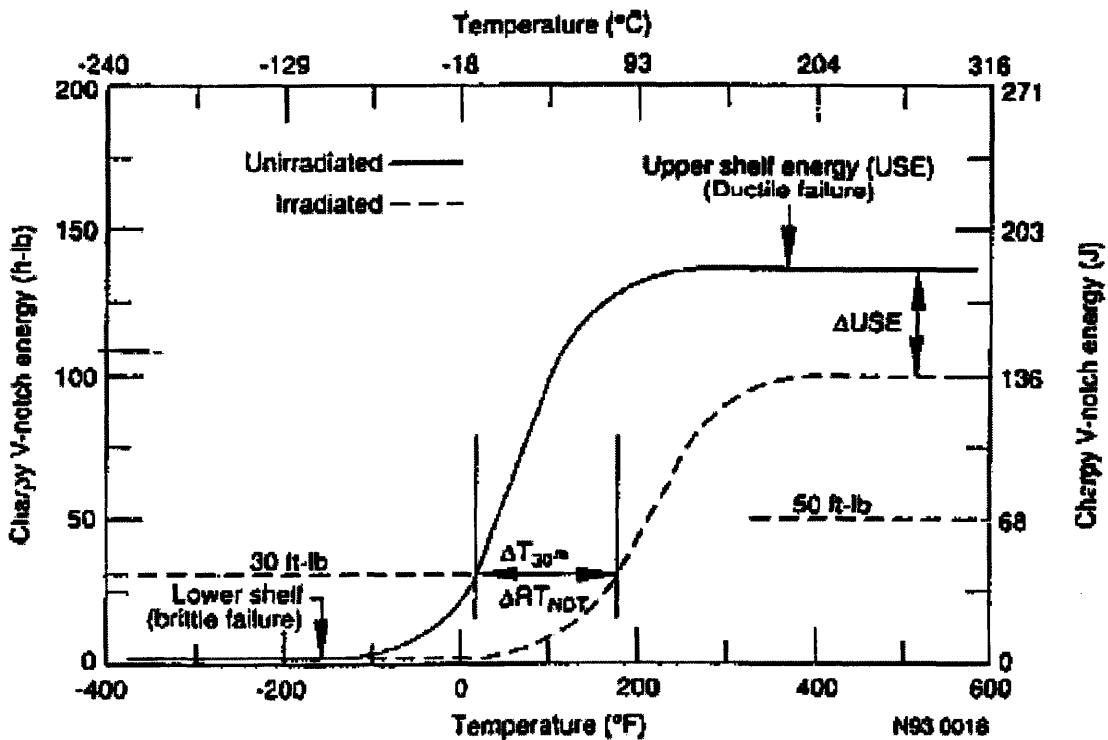


Figure 4.19: Generic Example of the Effect of Irradiation on the Integrity of a RPV [taken from USNRC, 2001]

At the most basic level, damage to the RPV occurs as a result of incident high energy neutrons interacting with the atoms in the lattice of the RPV material. These interactions can result in lattice vacancies, interstitials, dislocations, and impurities. This has two important effects with respect to the integrity of the RPV. First, this hardens the material, shifting the Nil Ductility Temperature (NDT) to a higher value. This is problematic, as the temperature at which the transition from ductile to brittle fracture increases, potentially limiting the ability

to safely cool down following power operation. Second, it lowers the amount of energy that the RPV can absorb prior to ductile failure (i.e. lowers the Charpy Upper Shelf Energy). Figure 4.19 shows these two effects in the form of two Charpy V-notch energy curves.

The shift in NDT is a function of RPV material composition (specifically Cu and Ni for the case of LWR RPVs made of SA508), irradiation temperature, and fast fluence. For LWR RPVs, current Cu and Ni contents range from 0.0 to 0.4 and 0.0 to 1.2 wt%, respectively [USNRC, 2001]. Other candidate RPV materials for GFRs may possess different amounts of these constituents, either enhancing or decreasing the susceptibility of the RPV to neutron embrittlement. As well, other constituents present in other RPV materials may introduce their own unique challenges with respect to irradiation. Hence, until a suitable new RPV material is decided upon and extensive materials evaluation and testing is performed, the data for LWR RPVs will have to suffice as a first order metric.

Chromium Martensitic Steels have shown much promise as candidate materials for use in GFR RPVs. Current testing and evaluation show that 2 ¼ Cr 1 Mo low alloy ferritic steel is an excellent candidate due to its cost, fabricability, and resistance to degradation under irradiation [Venkatesh, 2004]. 9Cr 1MoVNb steel was also considered, but has been found inferior with respect to availability, weldability, and fabricability [Venkatesh, 2004].

As irradiation temperature increases, the effect of neutron embrittlement decreases. USNRCRG 1.99 uses a temperature range of 525-590°F (274-310°C), above which the embrittlement can be assumed to be reduced, and below which it can be assumed increased [USNRC, 1988]. Assuming that the GFR RPV is made of a material similar to that of current LWRs, the higher operating temperatures of GFRs will provide an abating mechanism for RPV neutron embrittlement. However, it should be noted that other materials constraints associated with the use of these materials may require some cooling of the RPV, which may negate the abating effect of increased temperature.

Finally, fast fluence in [USNRC, 1988] as well as numerous other references on the topic is defined as the fluence of neutrons with energies  $\geq 1$  MeV. While this energy threshold has been chosen as the licensing basis and has generally been accepted as the standard when evaluating RPV damage in LWRs, [ASTM, 2005] suggests that significant

displacements, and hence damage, in iron can occur at energies as low as 0.01 MeV or 10 keV. Given the harder neutron spectra of GFRs, proper evaluation of RPV damage may need to include the effects of fluence for neutron energies 0.01 MeV-1 MeV.

As a reference, acceptable fast fluence limits for existing RPVs were sought. For modern day BWRs, fast fluences of  $2.2E17$  and  $5.5E18$   $n/cm^2$  have been calculated as acceptable for GE's BWR/6 and ABWR [General Electric, 2007]. Fast fluence limits as high as  $5E19$   $n/cm^2$  have been suggested for the RPV proposed for the Supercritical Water Reactor (SCWR) made of SA508 [Buongiorno et. al, 2001]. As well, a fluence limit of  $5E19$   $n/cm^2$  was found acceptable for  $2\frac{1}{4}$  1Mo low alloy ferritic steel, a promising candidate for GFR RPVs [Venkatesh, 2004]. [USNRC, 2004] gives EOL fluences for the AP1000 of  $9.762E19$   $n/cm^2$  for the vessel forging, and  $2.847E19$   $n/cm^2$  for the lower girth weld. These fluences have been accepted by the NRC as licensable.

Based on all of this, a conservative limit of  $2.5E19$   $n/cm^2$  ( $E>1$  MeV) has been chosen for reactor pressure vessel fluence calculations. The core is short enough ( $\sim 1.54m$ ) that a forging could be made large enough to cover this region axially without a weld. Since welds are the most susceptible parts of the RPV with respect to irradiation damage and [USNRC, 2004] gives a design whose weld fluence exceeds this value, this limit is overly conservative.

It should be noted that due to design constraints discussed in [Pope et al., 2006], a RPV will not be used to contain the core, but rather a Prestressed Cast Iron Vessel (PCIV). However, these calculations were performed for a RPV as a basis for comparison with current experience. The larger size of the PCIV compared to the RPV used in these studies adds another measure of conservatism. Furthermore, the PCIV has a steel liner which will require some level of protection.

#### 4.6.2 RPV Fluence Results

In an effort to quantify the effect of fluence on the RPV, a calculational model using MCNP was developed. Several cases were run in order to determine the effect of different shielding strategies on a RPV. It should be noted that the RPV used in these calculations was

sized without regard to manufacturing feasibility or thermal hydraulic requirements (e.g. allowing for a proper size downcomer). While many calculations were performed to this end, only 3 cases will be presented here: (1) shielding with 2 rows of  $B_4C$  (2) shielding with 3 rows of  $B_4C$ , and (3) shielding with 2 rows of  $B_4C$  and 1 row of  $ZrH_2$ . It should be noted that in all of these studies, all boron is enriched to 99<sup>w</sup>% and the 3 corner assemblies of the outer row of shielding were removed in order to make the core slightly more circular in order to more efficiently use the space inside of a circular RPV (shown in Figure 4.20). As well, the core used in these studies is a 12-ring core, whereas the candidate core presented throughout this chapter is an 11-ring core, composed of slightly different enrichments, diluent loadings, and assembly sizes. The 12-ring core was an earlier iteration of the final 11-ring design. However, the overall dimensions of the 11-ring and 12-ring cores were preserved, i.e. core diameter, such that the effect of the fluence on the RPV should be within the error bands presented. Further, the 11-ring core is composed of slightly larger assemblies, so the shielding assemblies in that core version are thicker than those presented here, adding a measure of conservatism to these results.

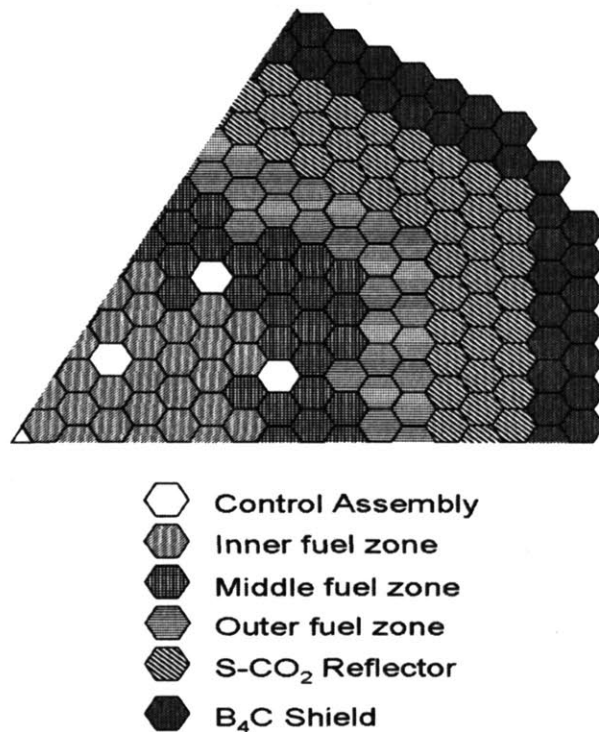


**Figure 4.20: Core Layout Used for RPV Fluence Calculations [case (1)]**

Table 4.17 shows the results of the shielding calculations. For each scenario, a range of values is given which represents the range of fluences seen by the 10 (equally sized) axial segments that the RPV was broken up into. As well, this range captures the large uncertainty inherent in any Monte Carlo shielding calculation and gives a rough first order estimate of the RPV fluence.

With only 2 rows of shielding, the fluence limit of  $2.5 \times 10^{19}$  n/cm<sup>2</sup> is exceeded before 1 core lifetime expires (15.76 EFPY for the 12-ring core design used). Adding a row of B<sub>4</sub>C shielding (case (2)) reduces fluence by a factor of 10, allowing fluence to stay within the limit for not only 1 core lifetime, but for 4 core lifetimes, approximately the same as the design lifetime of this reactor (~60 years). Another strategy that was explored was replacing a row of B<sub>4</sub>C with ZrH<sub>2</sub> in order to reduce the neutron energy incident upon the RPV, and hence the fluence > 1.0 MeV. From Table 4.17, one can see by comparing cases (2) and (3) that the gain in moderation roughly offsets the loss of absorption when a row of B<sub>4</sub>C is replaced with a row of ZrH<sub>2</sub>. As well, this effect was seen to be roughly independent of the position of the row of ZrH<sub>2</sub> (i.e. inner, middle, or outer – not shown here). In conclusion, 3 rows of B<sub>4</sub>C shielding should be sufficient to mitigate the damage to the RPV (or in this case, PCIV) from fast neutron bombardment for a design lifetime of 60 years. Furthermore, it is not ruled out that other shield material mixes could be developed which are superior.

**Table 4.17: RPV Fluence Calculation Results**

Reflector Strategy	E<0.1 MeV 1 Core Lifetime (n/cm <sup>2</sup> )	E<1.0 MeV 1 Core Lifetime (n/cm <sup>2</sup> )	E>1.0 MeV 1 Core Lifetime (n/cm <sup>2</sup> )	E>1.0 MeV 4 Core Lifetimes (n/cm <sup>2</sup> )	PROPOSED LIMIT
(1) 2 rows of B <sub>4</sub> C shielding	1.16x10 <sup>20</sup> - 2.65x10 <sup>20</sup>	6.44x10 <sup>19</sup> - 1.93x10 <sup>20</sup>	7.26x10 <sup>18</sup> - 4.10x10 <sup>19</sup>	2.90x10 <sup>19</sup> - 1.64x10 <sup>20</sup>	2.5x10 <sup>19</sup>
(2) 3 rows of B <sub>4</sub> C shielding	4.22x10 <sup>19</sup> - 9.50x10 <sup>19</sup>	6.89x10 <sup>19</sup> - 1.61x10 <sup>20</sup>	9.61x10 <sup>17</sup> - 4.85x10 <sup>18</sup>	3.84x10 <sup>18</sup> - 1.94x10 <sup>19</sup>	2.5x10 <sup>19</sup>
(3) 2 rows of B <sub>4</sub> C shielding with a row of ZrH <sub>2</sub>	4.89x10 <sup>19</sup> - 1.36x10 <sup>20</sup>	2.65x10 <sup>19</sup> - 9.49x10 <sup>19</sup>	8.33x10 <sup>17</sup> - 6.47x10 <sup>18</sup>	3.33x10 <sup>18</sup> - 2.59x10 <sup>19</sup>	2.5x10 <sup>19</sup>



## 4.7 Chemical Compatibility

Given the high operating pressure of the primary system, venting of assemblies is necessary in order to prevent large pressure gradients across the assembly wall that will likely lead to mechanical failure. This raises questions of the chemical compatibility of the material inside of the assemblies with the S-CO<sub>2</sub> coolant, which acts as yet another design constraint when selecting materials for this core.

While a detailed corrosion model and experiments would be necessary to determine the exact extent of the chemical compatibility of a candidate material with the S-CO<sub>2</sub> coolant at the elevated temperatures and pressures found in this core, a framework for a good first order metric of this factor has been established using a chemistry code called HSC 5.1 [Roine, 2002]. This framework is outlined in Section 4.3.1.

**Table 4.18: Chemical Compatibility Results for Core Materials**

Reaction	Temp(°C)	ΔG (kcal)
$9\text{UO}_2 + 6\text{CO}_2(\text{g}) \rightarrow \text{U}_4\text{O}_9 + \text{U}_3\text{O}_8 + \text{UO}_3 + 6\text{CO}(\text{g}) + 0.5\text{O}_2 + \text{UO}_3(\text{g})$	1000	215
	1500	101
	2000	85
$3\text{BeO} + 3\text{CO}_2(\text{g}) \rightarrow \text{BeCO}_3 + \text{BeO}(\text{A}) + \text{BeO}(\text{B}) + 2\text{CO}(\text{g}) + \text{O}_2(\text{g})$	1000	124
	1500	121
	2000	117
$6\text{CO}_2(\text{g}) + 6\text{Ti} \rightarrow \text{TiO}_2 + \text{TiO}_2(\text{A}) + 3\text{C} + 2\text{C}(\text{D}) + \text{CO}(\text{g}) + \text{Ti}_4\text{O}_7$	500	-552
	1000	-447
	1500	-342
$9.5\text{CO}_2(\text{g}) + 3\text{B}_4\text{C} \rightarrow 2\text{B}_2\text{O}_3 + 6.5\text{C} + 5\text{C}(\text{D}) + 2\text{B}_2\text{O}_3(\text{G}) + 2\text{B}_2\text{O}_3(\text{A}) + \text{CO}(\text{g})$	500	-631
	1000	-489
	1500	-377

Table 4.18 shows the results of this process for several key core materials. Specifically, the reaction governing the chemical interaction, accounting for all non-negligible products, is shown, along with its Gibbs Free Energy (ΔG) for several temperatures which span a temperature range of interest for that material. While Table 4.18 shows that the reaction of UO<sub>2</sub> with CO<sub>2</sub> yields a positive ΔG indicating that this reaction is

thermodynamically unfavorable, Figure 4.21\* shows that appreciable amounts of  $U_4O_9$  can be formed in the temperature range in which the fuel will operate. This is a concern as  $U_4O_9$  has a lower conductivity and melting point ( $1127^\circ\text{C}$  for  $U_4O_9$  v.  $2877^\circ\text{C}$  for  $UO_2$ ) than  $UO_2$ , increasing the possibility of local fuel melt [Roine, 2002 and IAEA, 1993]. While the fuel in the peak power location will operate at temperatures near  $1800^\circ\text{C}$  where the formation of  $U_4O_9$  is not a concern, fuel in lower power locations, especially near the fuel-coolant channel interface, will operate in the temperature region where  $U_4O_9$  formation is most aggressive.

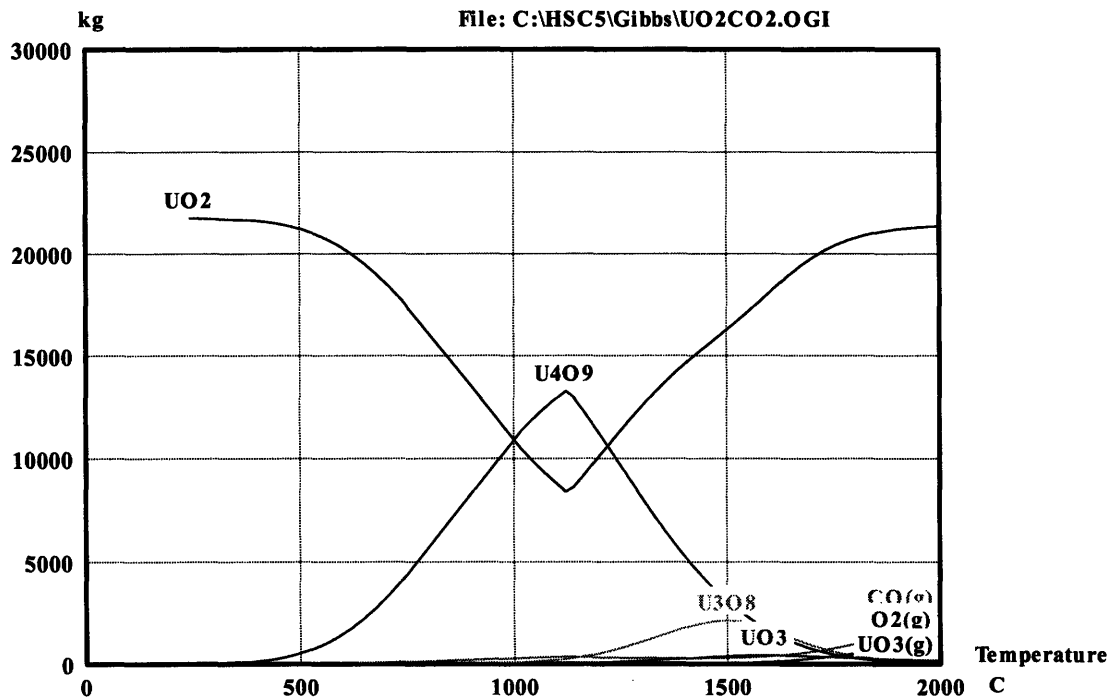


**Figure 4.21: Equilibrium Composition for the  $UO_2$ - $CO_2$  Reaction as a Function of Temperature**

Reassuringly, experience with British Advanced Gas Reactors (AGRs) which also use  $CO_2$  coolant with  $UO_2$  fuel indicates that the formation of  $U_4O_9$  in such a situation can be inhibited by the presence of carbon monoxide (CO) in the coolant [Poulter, 1963]. This is supported by LeChatlier's principle, as examination of the key reaction of interest in Table 4.18 shows that addition of CO would shift the  $UO_2$ - $CO_2$  reaction towards increased formation of the products, and hence stabilization of the  $UO_2$  would occur. Further, the BeO

\* Note that Figure 4.21 shows a large scale version of the equilibrium compositions of the  $UO_2$ - $CO_2$  reaction, omitting  $CO_2$  which occurs in such large quantities as to obscure resolution of the other reactants.

diluent in the inner and middle fuel zones, which Table 4.18 shows as fairly chemically stable with CO<sub>2</sub>, is shown to help inhibit the formation of U<sub>4</sub>O<sub>9</sub> when Figure 4.22 is compared to Figure 4.21. As well, the fact that some gross assumptions have gone into this analysis (outlined in Section 4.3.1) to give a first order assessment of chemical compatibility should be recalled. Most importantly, the present analysis only gives an indication of how thermodynamically favorable a reaction is and says nothing about the rate at which it may occur. Further, it does not account for geometry and the presence of inhibiting passive layers.

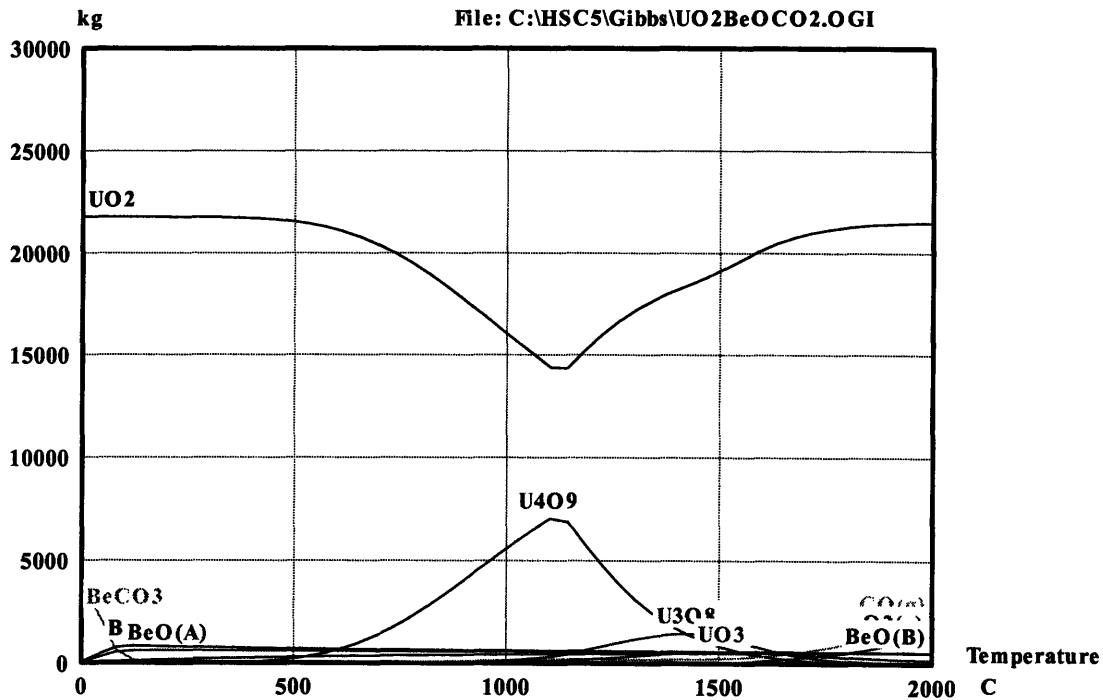


Figure 4.22: Equilibrium Compositions for the UO<sub>2</sub>-BeO-CO<sub>2</sub> System as a Function of Temperature

Somewhat troubling are the larger negative values of  $\Delta G$  found for the axial reflector (Ti) and the shielding and control assemblies (B<sub>4</sub>C), indicating chemical reactivity. While the negative  $\Delta G$  values for Ti suggests chemical reactivity, it should be remembered from Section 4.3.1 that its initial reaction with S-CO<sub>2</sub> forms a thin, passive oxidation layer which inhibits further reaction [O'Driscoll, 1958]. Furthermore, the reaction product, CO, will help suppress the CO<sub>2</sub> + UO<sub>2</sub> reaction, which is beneficial. With respect to the shielding and control assembly material, Table 4.18 suggests that B<sub>4</sub>C is highly chemically reactive with CO<sub>2</sub>. Evaluation of the formation of a passivation layer (B<sub>2</sub>O<sub>3</sub>) will need to be made.

Unfortunately, many of the other materials which exhibit strong neutron absorption capabilities at higher energies, e.g. W and  $\text{Ca}_3\text{N}_2$ , are also chemically reactive with  $\text{CO}_2$ . In order to prevent chemical interaction between  $\text{B}_4\text{C}$  and  $\text{CO}_2$ , the shielding material may need to be put inside of an inert matrix. Should this need arise, helium gas buildup due to the  $\text{B}^{10}(\text{n},\alpha)$  reaction may be harder to accommodate. This would have the downside of increasing the effective volume of the shielding, as the current core design is at the limit of B-10 content (99 %). Hence, further shielding material studies may be in order. As well, this has implications for the use of  $\text{B}_4\text{C}$  control rods in this core design.

#### 4.8 Neutron and Gamma Heating

MCNP was used to calculate both the neutron and gamma heating in the fuel, axial and radial shield, and axial reflector in order to provide data for the ongoing thermal hydraulic analyses of this project. Both a semi-infinite assembly and whole core model were used in order to ensure that the results obtained via the two means were somewhat consistent. Since MCNP calculates only prompt gamma heating, the heat due to gamma energy is multiplied by a 1.53 correction factor in order to account for delayed gamma heating [Xu, 2004].

**Table 4.19: Photon and Gamma Heating for the Semi-Infinite Assembly and Whole Core Models**

	Semi-infinite assembly		Whole Core model	
Total Power	6.3492 MW		2400MW	
	Heating (MW)	Heating (%)	Heating (MW -fueled region only)	Heating (% -fueled region only)
Total Photon heating in the fuel	0.548	8.6	N/A	N/A
Total Photon (prompt and delayed) and neutron heating in the axial reflector	0.0203	0.32	7.77	0.32
Total Photon (prompt and delayed) and neutron heating in the axial shield	0.0079	0.12	3.01	0.12

Table 4.19 compares the results between the semi-infinite assembly and the whole core model. The results between the two models show excellent agreement, as the fractional heating due to photon and neutron heating is identical. Further, the photon heating in the fuel is close to that of other comparable fast reactor designs (~10%).

#### **4.9 Summary and Conclusions**

A robust design for a GFR using TID fuel has been presented and subjected to a comprehensive steady state neutronic and thermal hydraulic analysis. At the heart of this design are several key design choices: (1) the use of TID fuel, (2) the selection of S-CO<sub>2</sub> as a radial reflector, (3) the use of Ti as an axial reflector, and (4) the use of BeO as a fuel diluent. Using a single batch refueling strategy, this core design demonstrates the ability to achieve reasonably long burnups, while maintaining a relatively flat radial power profile and negative values of CVR throughout cycle life without the aid of control rods. This capability was shown not only for a single cycle, but was also demonstrated for a second and third cycles, incorporating a strategy of recycling its own used fuel. While the use of a non-solid radial reflector initially gives concern with respect to RPV fluence, an appropriate limit for RPV fluence was defined and the postulated core vessel fluence was found to be within this limit. These calculations represent a conservative estimate as the actual means for containing the core and internals will not be an RPV, but a much larger, weld-free PCIV. Finally, the chemical compatibility of the core materials with the S-CO<sub>2</sub> coolant was assessed. This is an important factor to consider in the design of this reactor, as the fuel assemblies must be vented in order to mitigate the large stress on the cladding wall due to the large system pressure at which the PCS must operate for maximum efficiency.

## 5 Comparison of Different Fuel Types and Diluent Strategies

### 5.1 Introduction

In previous analytic studies, pin type fuel and Tube-in-Duct (TID) fuel were compared. For a given fuel geometry, i.e. diameter and pitch/diameter ratio (P/D), TID fuel offered the advantages of higher fuel volume fraction, lower pressure drop and lower fuel temperatures. It should be remembered that these analytic studies were rough, “back of the envelope” type studies, and focused only on thermal hydraulic parameters. Hence, a more rigorous and integrated approach is necessary to determine if the TID fuel type is truly superior to the traditional pin-type fuel for application in the S-CO<sub>2</sub> cooled GFR. To this end, a comprehensive neutronic and thermal-hydraulic study has been undertaken to determine the following:

1. Is there an inherent advantage of TID fuel over traditional pin-type fuel?
2. Is there a “better” fuel type out there?

As well, the use of a diluent is a key part of the core design that has been developed. While a study has already been taken which answers the question of how much diluent to use in order to optimize among various neutronic parameters, the thermal hydraulic effect of the diluent as well as the question of how to use the diluent, i.e. homogeneously blended in the fuel or as heterogeneous pellets, have not been addressed. Hence, a third question to be explored in this study:

3. What are the advantages of a heterogeneous v. homogeneous BeO strategy?

The fuel types and diluent strategies chosen for comparison are listed in Table 5.1 and a unit cell illustration of each of the three fuel types studied is shown in Figure 5.1.

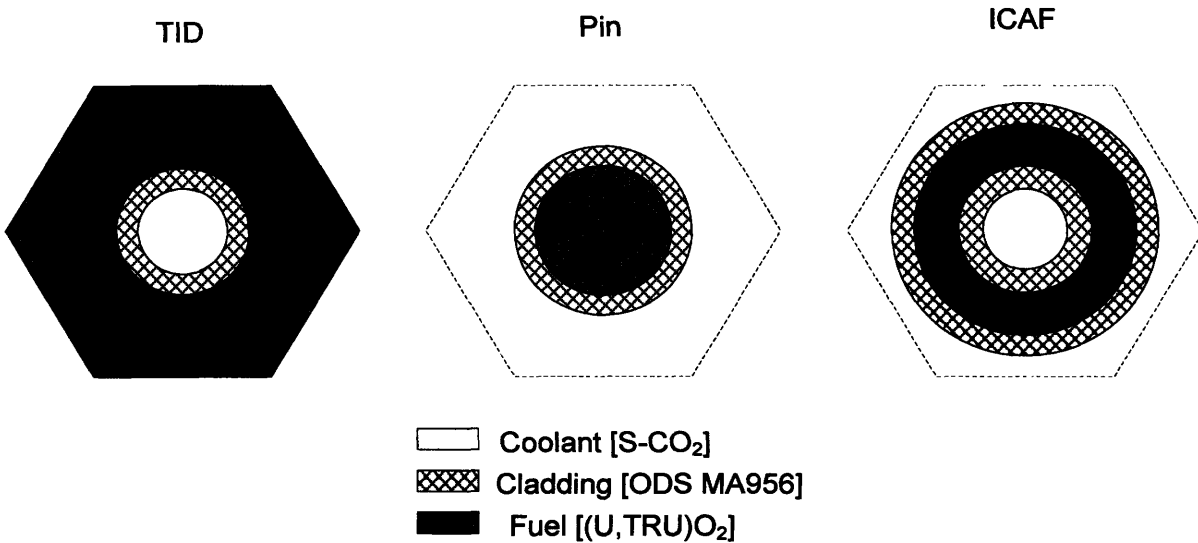


**Figure 5.1: Unit Cell Representation of the Three Different Fuel Types Studied**

The Internally Cooled Annular Fuel (ICAF) listed in Table 5.1 is an annular pellet which has both traditional external, as well as innovative internal, cladding and cooling, developed at MIT as means for extracting more power from existing LWRs [Hejzlar et. al, 2001 and Hejzlar et. al, 2004]. It is being explored for GFR application due to its promise in LWRs, with the hopes that these benefits will translate directly. Specifically, ICAF can provide increased power densities at comparable fuel and cladding temperatures, when compared to pin-type fuel, due mainly to (1) having 2 surfaces for transferring the heat created in the fuel and (2) a reduction in thickness of the heat conduction path (when compared to a traditional fuel pin of the same diameter). The main drawbacks of such a fuel are the lack of comparable irradiation experience and the inherently lower fuel volume fraction. Taking the possible combinations of each column in Table 5.1 yields 7 possible cases that can be examined. These cases will be compared using both neutronic and thermal-hydraulic assessments.

**Table 5.1: Fuel Types and Diluent Strategies Chosen for Comparison**

Fuel Type	Diluent Strategy
<ul style="list-style-type: none"> <li>▪ Pin</li> <li>▪ TID</li> <li>▪ Internally Cooled Annular Fuel (ICAF)</li> </ul>	<ul style="list-style-type: none"> <li>▪ Integrated (homogeneous)</li> <li>▪ Separate (heterogeneous)</li> <li>▪ Slug in the middle (applicable to pin type fuel only)</li> </ul>

## 5.2 Neutronic Study

In order to assess the various neutronic benefits of each of the possible approaches displayed in Table 5.1, a semi-infinite assembly (normal leakage axially, mirror boundary conditions radially) model was constructed. This semi-infinite assembly model was then subject to neutronic and depletion analyses using MCNP and ORIGEN, as coupled in MCODE v2.2.

**Table 5.2: Neutronically Assessed Cases of Fuel Types and Diluent Strategies**

	Case Short Name	Case Description	Critical Enrichment (% TRU)	BOL $\Delta\rho_{VOID}$ ( $\times 10^{-3}$ )	Reactivity Limited Burnup (MWd/kg)	Reactivity Limited Lifetime (EFPY)	$\nu_{BeO_F}$	$\nu_{BeO_A}$	$\nu_{f_A}$
Homogeneous BeO	TID Base	TRU and BeO integrated in TID	17.87	2.64	111.11	11.51	0.38	0.2267	0.370
	Pin Base	TRU and BeO integrated in pins	19.85	4.02	73.16	6.22	0.38	0.1698	0.277
	3	Annular TRU pins with BeO slug in the middle	20.45	3.83	63.68	3.84	0.38	0.1587	0.259
	ICAF1	Internally cooled annular fuel with 38% BeO	23.49	4.30	41.74	2.52	0.38	0.1318	0.215
Heterogeneous BeO	2	TRU pins w/BeO pins in matrix	15.45	5.43	189.38	22.35	0	0.0624	0.384
	1a	TRU pins w/BeO pins on periphery	16.35	5.18	152.46	14.84	0	0.0756	0.342
	2c	TRU pins w/BeO pins in matrix	17.633	3.61	111.87	11.12	0	0.1231	0.324
	2b	TRU pins w/BeO pins in matrix	19.24	3.20	61.07	5.22	0	0.1686	0.278

The neutronic metrics used to assess if a fuel type or BeO strategy is superior are:

- Minimization of Coolant Void Reactivity (CVR)
- Maximization of Reactivity Limited Burnup



- Minimization of Critical Enrichment

While it is unlikely that a single approach will satisfy the maximization or minimization of all of these criteria, an optimization among all of the criteria where there is a trade-off that satisfies the general desired trends is likely achievable.

Table 5.2 shows the eight cases that were assessed neutronically, with their associated results and pertinent parameters. At this point, it is important to define three of the quantities that appear in this table and which will become an important part of the discussion of the neutronic results. The volume fraction of BeO within a given unit cell fuel element is given as  $v_{BeO_F}$ . The volume fraction of BeO with respect to the cross-sectional assembly volume is  $v_{BeO_A}$ . The assumption here is that the assembly is tall enough such that the neutronic effects of what is beyond the fuel region (i.e. the Ti axial reflector and B<sub>4</sub>C axial shield) will not appreciably affect these results. Further, the dimensions and composition of material beyond the fueled region are identical for all cases, so that on a comparative basis, this assumption holds well. Similarly, the volume fraction of fuel with respect to the cross-sectional assembly volume is  $vf_A$ , and the volume fraction of fuel within a given unit cell fuel element is  $vf_F$ .

In order to understand if the heterogeneous or homogeneous diluent would have an effect on neutronics, it is necessary to know the general magnitude of the neutron mean free path. For an undiluted semi-infinite assembly, the neutron mean free path in the fuel is ~4 cm. For case 2c, the neutron mean free path was calculated as 2.4 cm. Two important conclusions can be derived from these results. First, the neutron mean free path size relative to the unit cell dimensions (2-4 cm v. 1-2 cm) is large enough that heterogeneity within the unit cell will not appreciably affect the neutronic performance of a given case. This is why the case with the BeO slug in the middle of an annular fuel pellet (3) is included in the group of homogeneous BeO strategy results throughout this study. The consistent neutronic behavior of this approach as a homogeneous diluent strategy justifies this categorization. Conversely, the neutron mean free path size is small enough relative to the assembly size that unit-cell to unit-cell heterogeneity will have an effect on neutronic performance. This second conclusion provides an important framework with which to analyze the results from this study.

### 5.2.1 Minimization of Coolant Void Reactivity (CVR)

The first metric used in order to assess neutronic performance is the minimization of coolant void reactivity. This metric is used because CVR is a large component of the overall safety performance and its minimization will greatly contribute to the enhanced safety of a given fuel-diluent strategy. In order to assess the impact of the different strategies on this parameter, it is necessary to understand the drivers behind CVR.

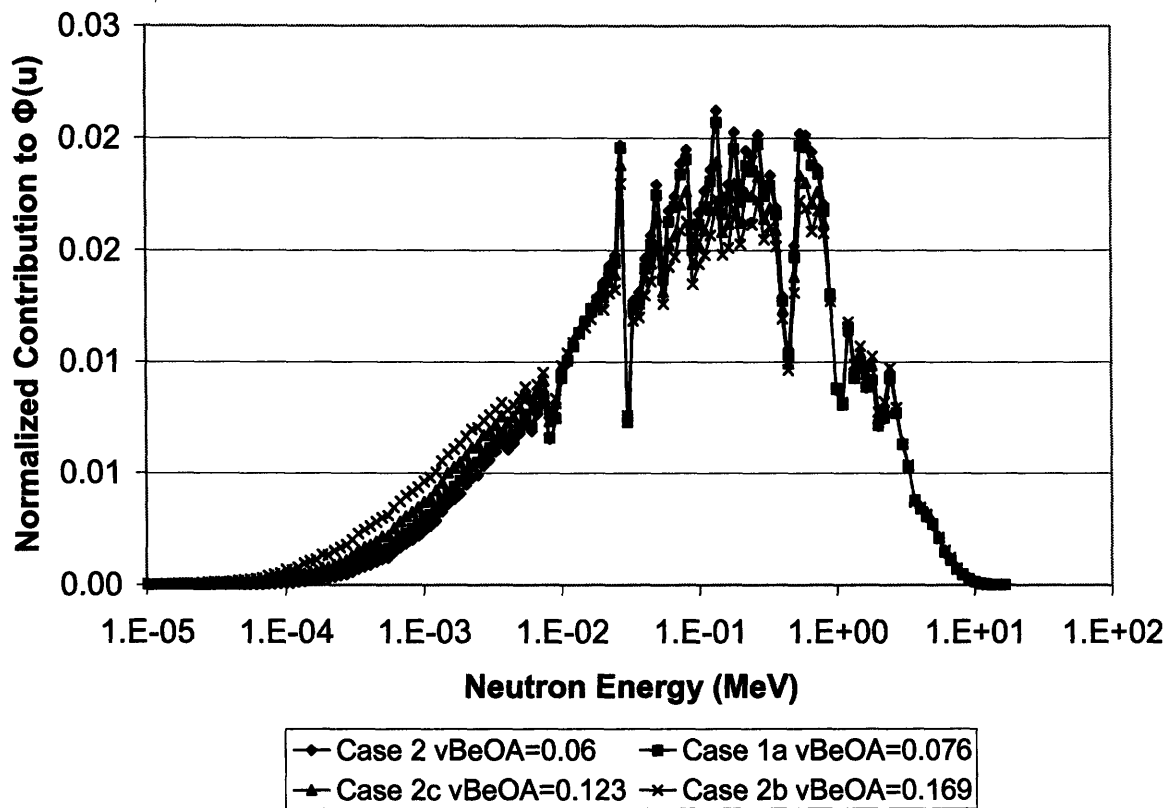


Figure 5.2: Comparison of Neutron Spectra of Heterogeneous Cases

Figure 5.2 shows that for the heterogeneous cases, as  $vBeO_A$  increases, the spectrum softens. This is consistent with results that were seen for the study performed to determine the optimum diluent concentration to be used. Similarly, the spectra for the homogeneous cases are plotted in Figure 5.3. Despite the fact that the  $vBeO_A$  is changing, the spectrum does not shift at all. Noting that each of these cases has the same volume fraction of diluent in the given fuel form,  $vBeO_F$  (38% of the cylindrical/annular/hexnut pellet), it can be concluded that the neutrons interact or see the BeO as if it were uniformly distributed and the

effect of the fuel form and coolant strategy has no impact. This is a direct consequence of the size of the neutron mean free path relative to the size of the unit cell. Understanding how the diluent affects the neutron spectrum differently for both the homogeneous and heterogeneous cases will help understand the behavior of CVR, and more importantly, the drivers behind this key safety parameter.

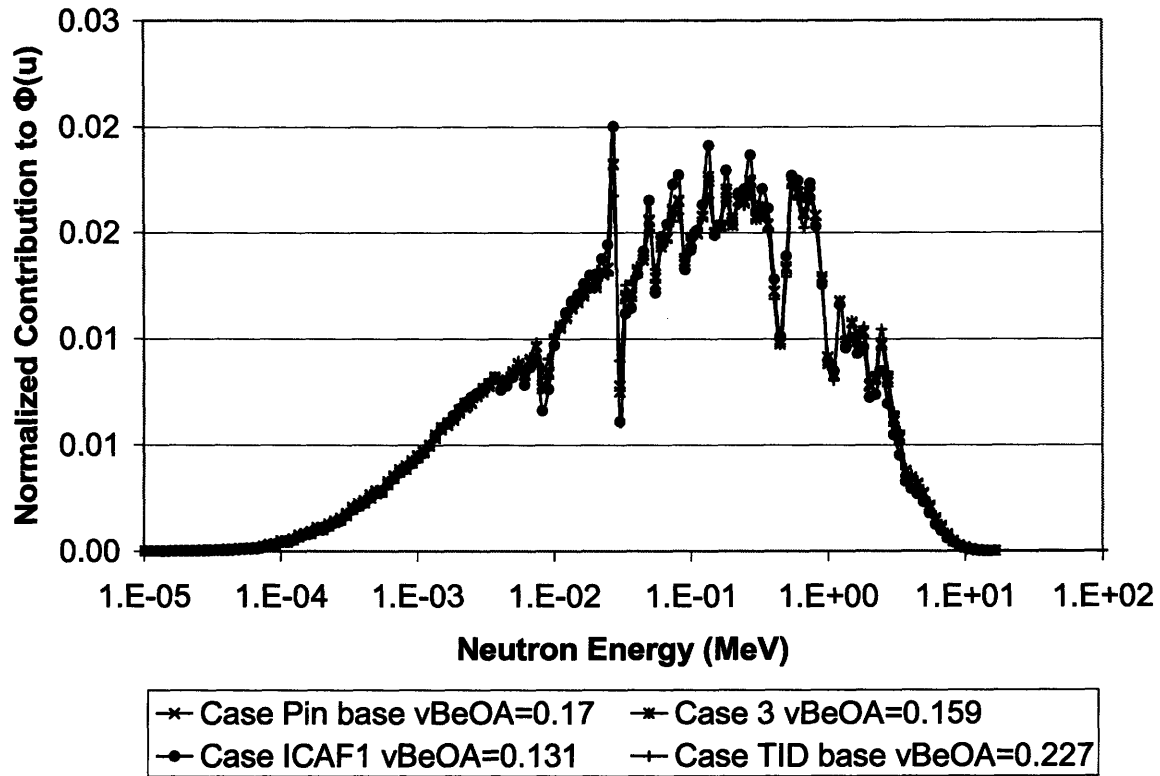


Figure 5.3: Comparison of Neutron Spectra of Homogeneous Cases

From Figure 5.4, it is shown that  $vBeO_A$  is very well correlated with BOL CVR for the heterogeneous case. This is due to the increase in spectral softening with the increase in  $vBeO_A$  effect, shown in Figure 5.2. However, where the spectrum does not soften for the case of homogeneous fuel, BOL CVR also goes down with increasing  $vBeO_A$ . Clearly,  $vBeO_A$  alone is not the driver in this relationship, as the neutron spectrum is roughly the same for all of the homogeneous cases. As well, the increase in  $vf_A$  for an accompanying decrease in CVR shown in Figure 5.5, does not appear to make sense as it implies that as more fuel, i.e. Pu-239, is available, CVR goes down. So how does BOL CVR decrease as  $vBeO_A$  increases if there is no spectral softening effect?

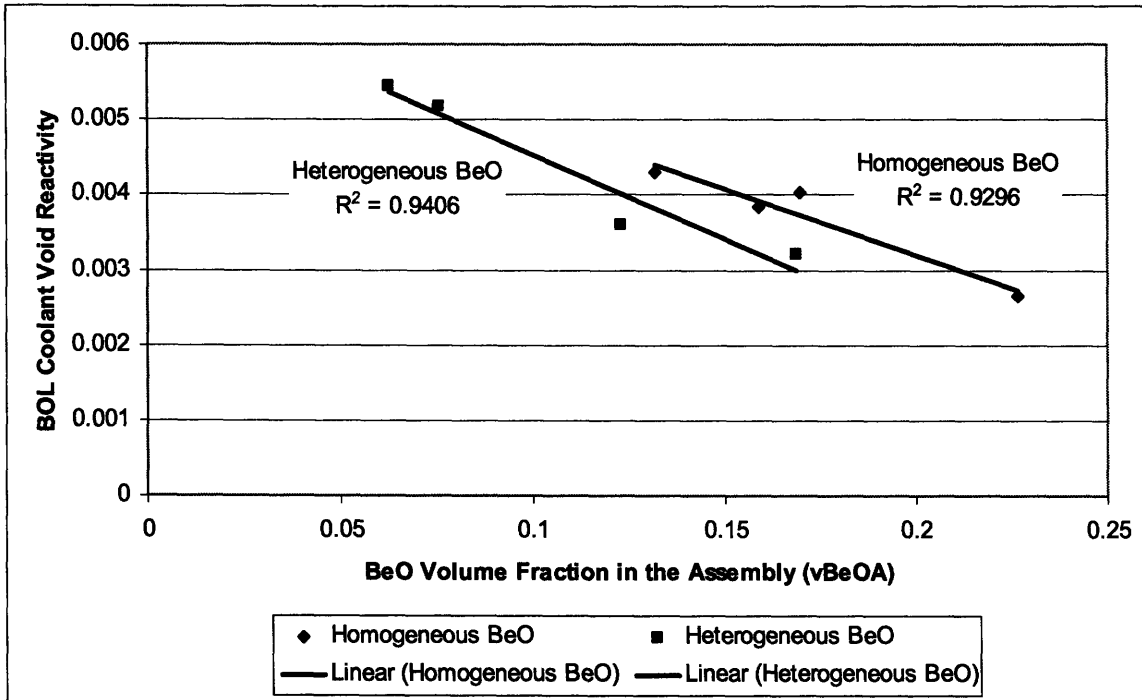


Figure 5.4: Comparison of BOL Coolant Void Reactivity (CVR) Behavior among Diluent Approaches for Varying BeO Volume Fraction in the Assembly

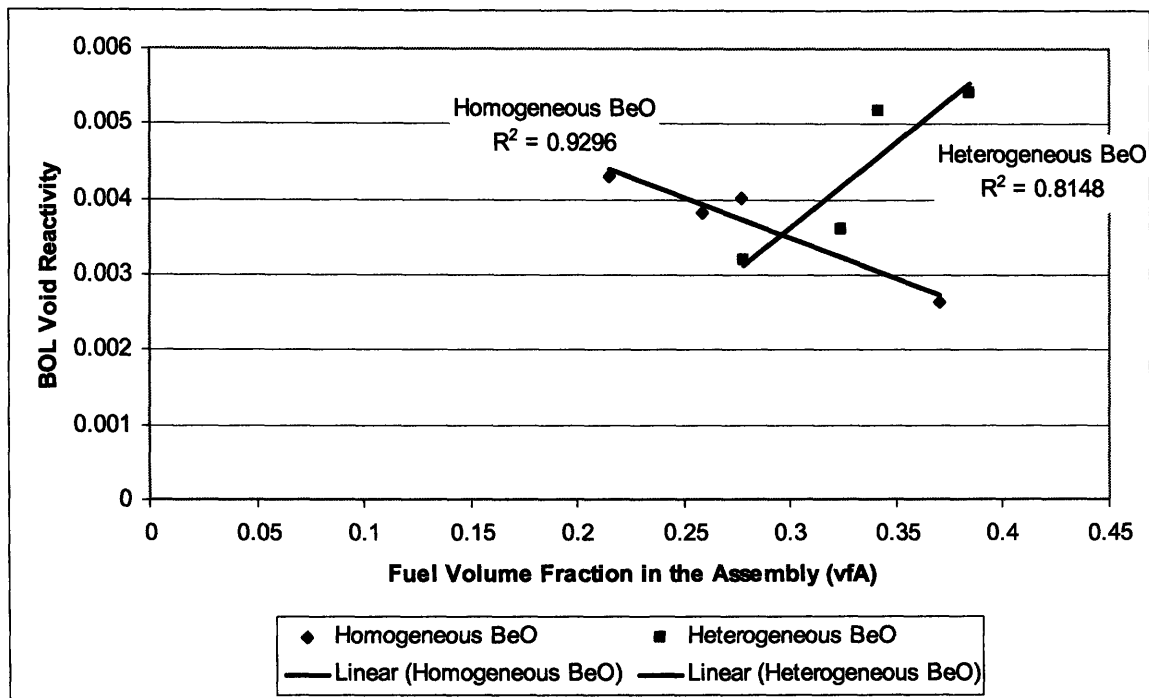
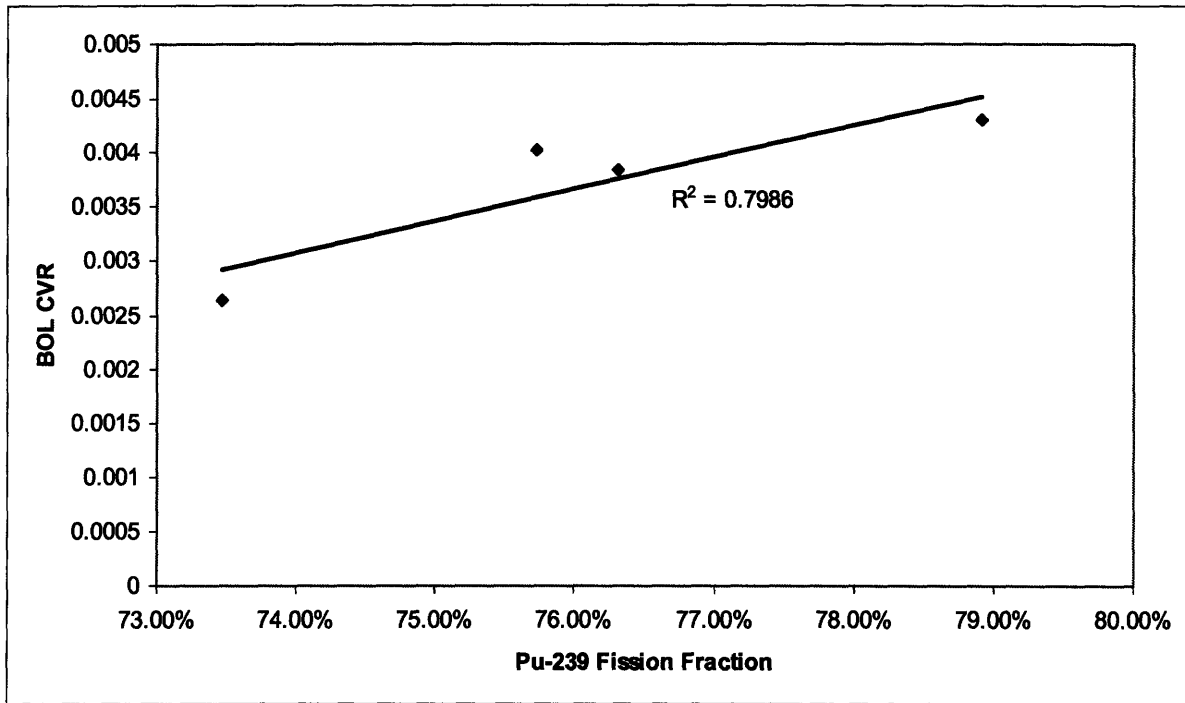


Figure 5.5: Comparison of BOL Coolant Void Reactivity (CVR) Behavior among Diluent Approaches for Varying Fuel Volume Fraction in the Assembly



**Figure 5.6: Relationship between BOL CVR and Pu-239 Fission Fraction for the Homogeneous Diluent Cases**

The answer is that the BOL Pu-239 fission fraction is what drives the BOL CVR. That is, for a given neutron energy spectrum, as is the case with the homogeneous fuels, as the fraction of fissions that come from Pu-239 increases, so does the contribution to the total reactivity from Pu-239. This relationship between BOL CVR and Pu-239 fission fraction is shown in Figure 5.6. This total contribution to reactivity stays roughly the same during voiding. Hence the CVR is proportional to Pu-239 fission fraction in this case.

A good estimate of fission fraction can be calculated by:

$$\text{Fission Fraction of isotope } i = \frac{\Sigma_{f,i}}{\sum_{i=1}^n \Sigma_{f,i}} \quad \{5.1\}$$

where:

$n$  = total number of isotopes that contribute to fission

$\Sigma_{f,i}$  = Macroscopic fission cross section of isotope  $i$

=  $N_i \sigma_{f,i}$

where:

$N_i$  = number density of isotope  $i$

$\sigma_{f,i}$  = microscopic fission cross section of isotope i

Since the energy spectrum is roughly the same for the 4 homogeneous cases, it can be expected that  $\sigma_{f,i}$  will be the same among all homogeneous BeO cases. Therefore, the driver behind fission fraction, and hence BOL CVR, is the relative mixture of the atom densities of the isotopes. Knowing that U-238 plus Pu-239 account for roughly 85% of the fissions in the core in all cases and that all other isotopes contribute a roughly constant fraction of fissions, Eq. {5.1} can be rewritten as:

$$\text{Fission Fraction of Pu-239} = \frac{\Sigma_{f49}}{\Sigma_{f49} + \Sigma_{f28} + \text{constant}} = \frac{\sigma_{f49}N_{49}}{\sigma_{f28}N_{28} + \sigma_{f49}N_{49} + \text{constant}}$$

$$\text{BOL } \Delta\rho_{\text{VOID}} \propto \text{Fission Fraction of Pu-239} = \frac{1}{\frac{\sigma_{f28}N_{28}}{\sigma_{f49}N_{49}} + 1 + \frac{\text{constant}}{\sigma_{f49}N_{49}}}$$

where:

$$\frac{\sigma_{f28}}{\sigma_{f49}} \text{ and } \frac{\text{constant}}{\sigma_{f49}N_{49}} \text{ can be approximated as constant values}$$

Hence, for the homogeneous diluent case:

$$\text{BOL } \Delta\rho_{\text{VOID}} \propto \frac{N_{49}}{N_{28}} \quad \{5.2\}$$

As shown in Figure 5.7,  $\frac{N_{49}}{N_{28}}$  varies nearly linearly with critical enrichment over the range of current interest. This relationship holds regardless of the BeO volume fraction, which would affect the numerator and denominator of this quantity equally. From this, it can be concluded that it is desirable to minimize TRU enrichment in order to minimize BOL CVR for the homogeneous BeO case. This makes intuitive sense, as minimizing enrichment means minimizing Pu inventory, which is the primary driver for BOL CVR.

In summary, the primary drivers of BOL CVR are:

- For the heterogeneous case:  $v\text{BeO}_A$
- For the homogeneous case: Critical Enrichment (for a given unit cell BeO volume fraction).

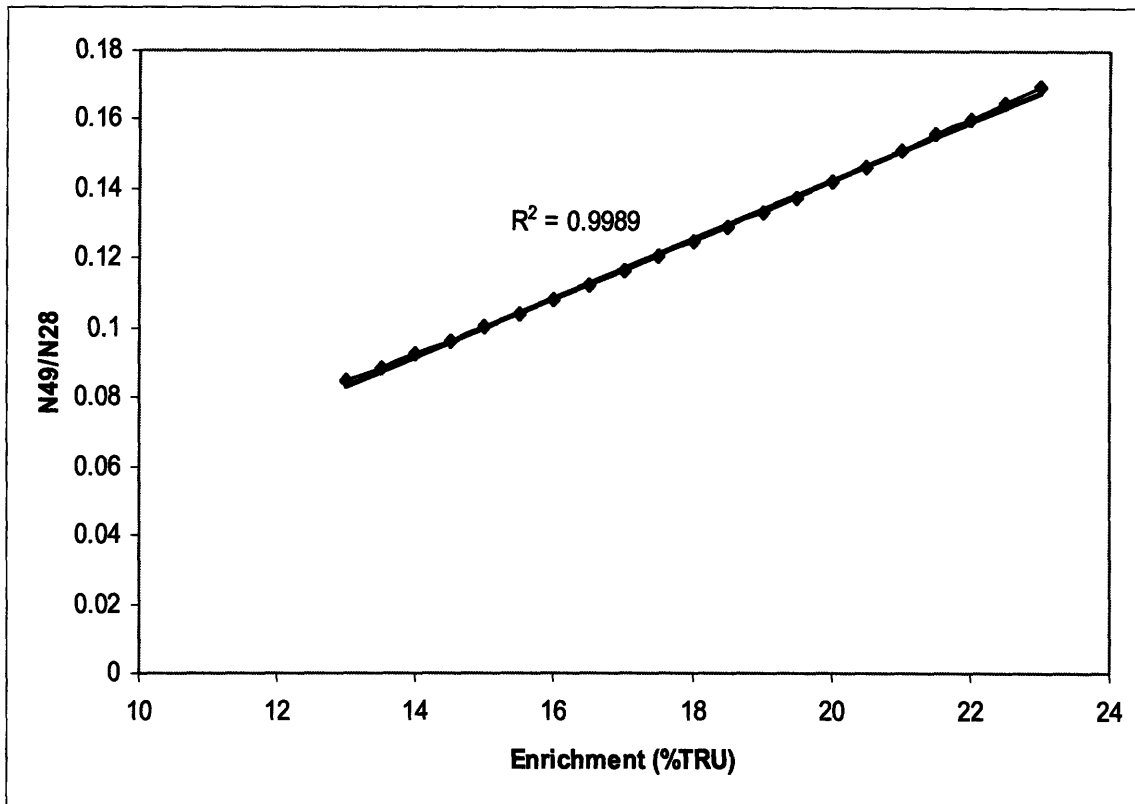


**Figure 5.7: Relationship between  $N_{49}/N_{28}$  and TRU Enrichment**

It is important to remember that for the homogeneous cases, the volume fraction of fuel with the given fuel form is constant (@~38%). Thus the comparisons made among homogeneous fuel options assume a constant fuel volume fraction within the unit cell. This is why the neutron spectrum does not shift among the four homogeneous cases. As shown in earlier studies, if the volume fraction within the unit cell is changed, the neutron spectrum will change accordingly, i.e. the spectrum will soften as the volume fraction of BeO increases, and consequently, BOL CVR will decrease.

It should be noted that there may exist a relationship between the coolant volume fraction and the BOL CVR. While current evidence does not support a major, dominant effect as currently exists for  $v\text{BeO}_A$  for the heterogeneous case and critical enrichment for the homogeneous case, previous analyses have shown this to be a contributor to CVR. Due to

the many competing factors that currently have an effect on CVR, the direct effect of coolant volume fraction is not presently discernable, but likely exists at some smaller level.

### 5.2.2 Maximization of Reactivity Limited Burnup and Minimization of Critical Enrichment

Maximizing the reactivity limited burnup of a given fuel cycle strategy is desirable for political and economic reasons, with economic reasons providing the larger driver. From a political standpoint, under some currently proposed strategies for allowing non-nuclear states to employ this energy technology, member states would provide “battery”-type cores that could be installed and run with little involvement in the nuclear fuel cycle by the consumer nations. Providing a core with a long reactivity limited burnup, hence operating cycle length, would help toward the goal of minimizing the involvement of the consumer nation in the nuclear fuel cycle. While this political motivation is certainly a factor, it is less important than the economic drivers, which will be discussed next.

To understand why maximizing reactivity limited burnup is desirable from an economic standpoint, it is first necessary to understand two of the key components of the cost of operating a nuclear power plant: Operations and Maintenance (O&M) costs and fuel cycle costs. With respect to O&M costs, maximizing reactivity limited lifetime reduces the need to shut down the plant in order to refuel. The avoided replacement power, manpower, and maintenance costs are the key savings associated with a longer cycle length. The longer the cycle, the greater the savings. Hence, this provides motivation for maximizing reactivity limited burnup.

The other key cost component, fuel cycle costs, can be estimated by:

$$fcc = \left( \frac{C}{24\eta B_d} \right) * \left( \frac{XT}{1 - e^{-XT}} \right) \quad \{5.3\}$$

where:

- fcc = fuel cycle cost (mills/kWh<sub>e</sub>)
- C = Cost of fuel at the beginning of irradiation (\$/kg fuel)
- η = thermodynamic efficiency
- B<sub>d</sub> = Fuel discharge burnup (MWd/kg)
- X = discount rate (yr<sup>-1</sup>)
- T = In-core residence time



where:

$$T = \frac{B_d}{0.36525 * P_s * L} \quad \{5.4\}$$

where:

$P_s$  = specific power (kW/kg<sub>HM</sub>)

$L$  = plant capacity factor

For the following given parameters, fcc v. BU is plotted for different values of C in Figure 5.8:

$\eta=0.45$   
 $X=0.1$   
 $P_s=20$  kW/kg HM  
 $L=0.9$

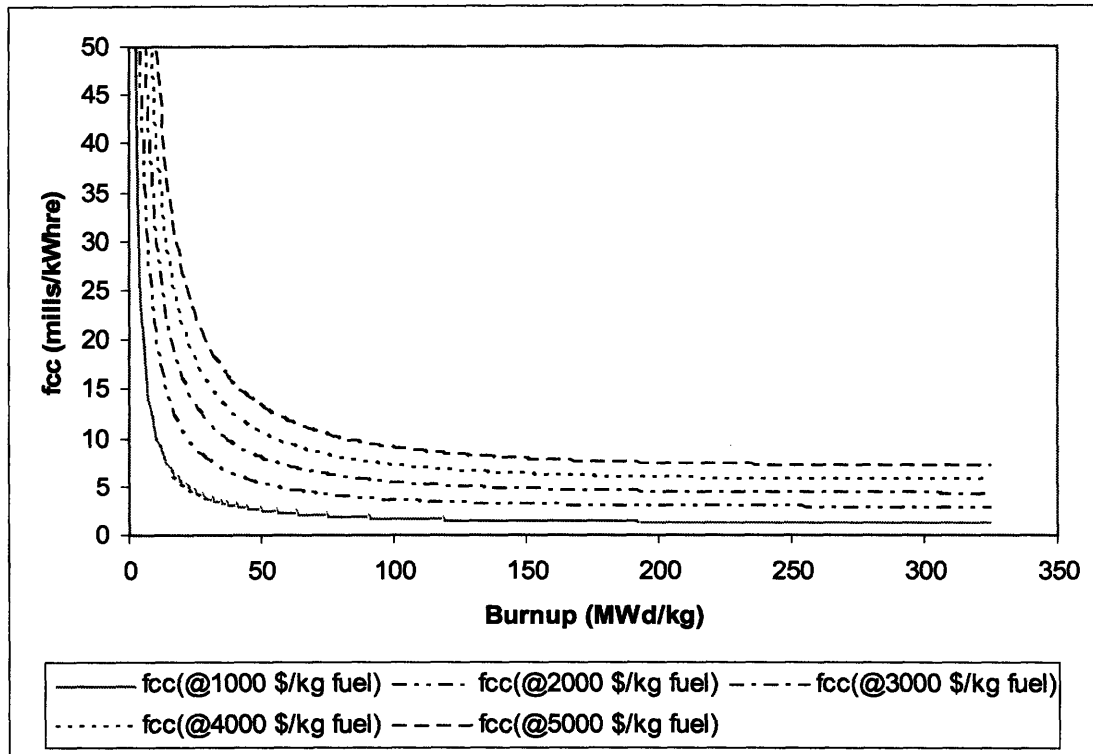


Figure 5.8: Fuel Cycle Cost as a Function of Burnup for Different Unit Fuel Costs

Figure 5.8 shows us that for a given unit cost of fuel, the fuel cycle cost decreases as burnup increases, to the point of saturation. This point of saturation occurs at higher burnups as unit fuel cost increases. Thus, two important conclusions can be drawn from this plot:

- There is an economic incentive to maximize reactivity limited burnup. As burnup increases above the saturation point, fcc stays relatively constant while O&M savings, discussed earlier, will continue to increase.

- For a higher unit fuel cost, there is more of an incentive to go to higher burnups, in order to take advantage of the saturation effect of fcc. Since the largest driver of unit fuel costs is typically either the enrichment cost (for first-time use fuel) or the reprocessing and fabrication costs (for reprocessed fuel), this means that with a higher enrichment or with the use of reprocessed fuel, the larger the economic incentive to go to higher burnups.

Fortunately, from the semi-infinite assembly studies that have been performed, a relatively good correlation between the critical enrichment and the reactivity limited burnup has been developed for both BeO strategies (homogeneous and heterogeneous). From Figure 5.9, it can be seen that in order to maximize reactivity limited lifetime, enrichment should be minimized. Maximizing burnup by minimizing enrichment seems counterintuitive until it is remembered that critical enrichment and  $\nu\text{BeO}_A$  are directly related for the heterogeneous

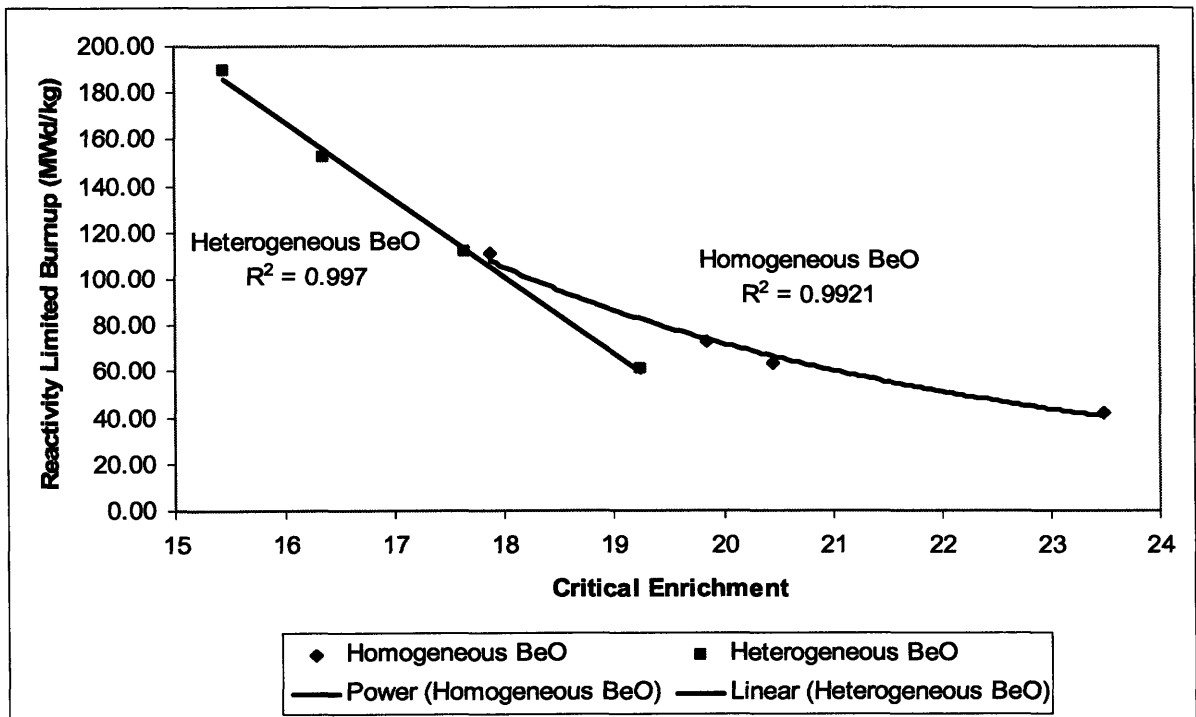


Figure 5.9: Reactivity Limited Burnup as a Function of Critical Enrichment

BeO case, as shown in Table 5.2. For the homogeneous case, critical enrichment is inversely related to  $\nu f_A$ , as there is no relative spectral softening effect for these cases. Hence, the reduction in critical enrichment necessary to achieve higher burnups in Figure 5.9 is really a consequence of the reduction of the  $\nu\text{BeO}_A$  for the heterogeneous case and increase of the  $\nu f_A$  for the homogeneous case.

As shown earlier, a reduction in  $v\text{BeO}_A$  also means a larger BOL CVR. Hence this highlights one of the fundamental trade-offs that becomes apparent as a result of this study: reactivity limited lifetime v. CVR reduction. Increasing the BeO concentration in a given fuel strategy will improve CVR, but will increase critical enrichment and reduce the reactivity limited lifetime, and hence economic attractiveness of a given strategy. Thus, the fundamental question becomes, what is a negative CVR worth? Or, more importantly, where is the best balance between improving CVR and maximizing reactivity limited lifetime while still minimizing critical enrichment?

### 5.2.3 Optimization among all of the variables

In order to optimize among minimizing CVR, maximizing reactivity limited lifetime, and minimizing critical enrichment, a comparison is needed among these three parameters as a function of the key variable that has a significant impact on all of them: volume fraction BeO in the assembly ( $v\text{BeO}_A$ ). Figure 5.10-Figure 5.12 compares the three parameters that are desirable to optimize, all as a function of the  $v\text{BeO}_A$ . Starting with Figure 5.10, showing

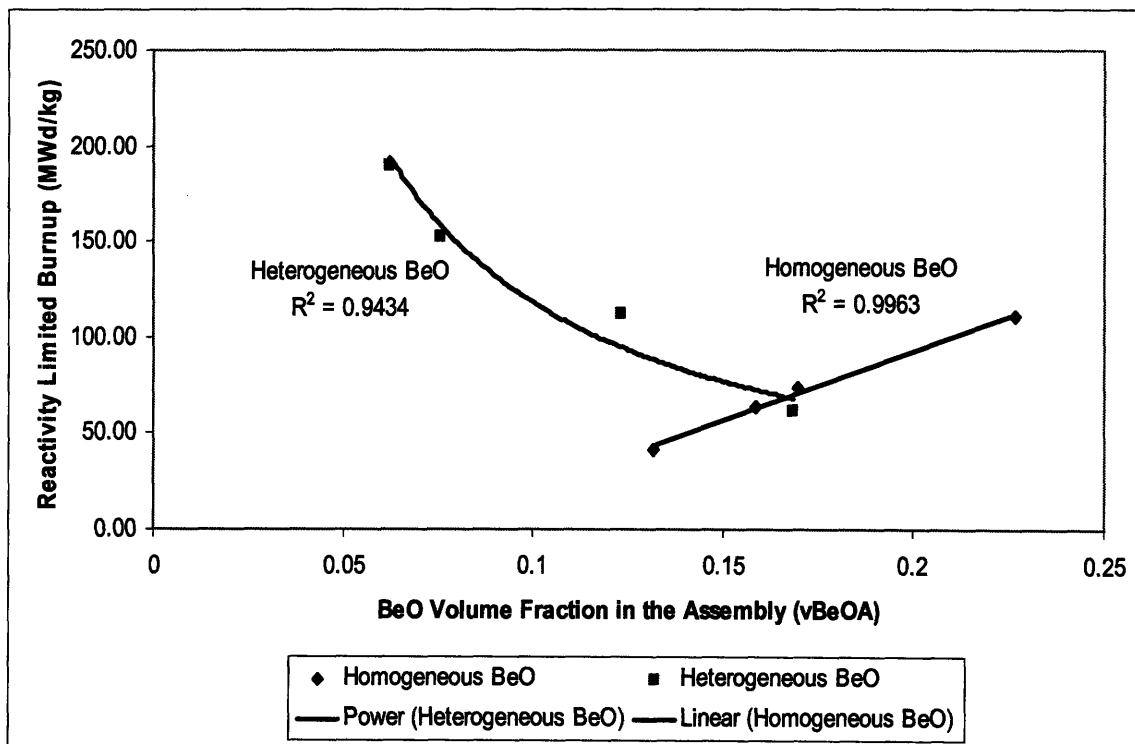


Figure 5.10: Reactivity Limited Burnup as a Function of BeO Volume Fraction

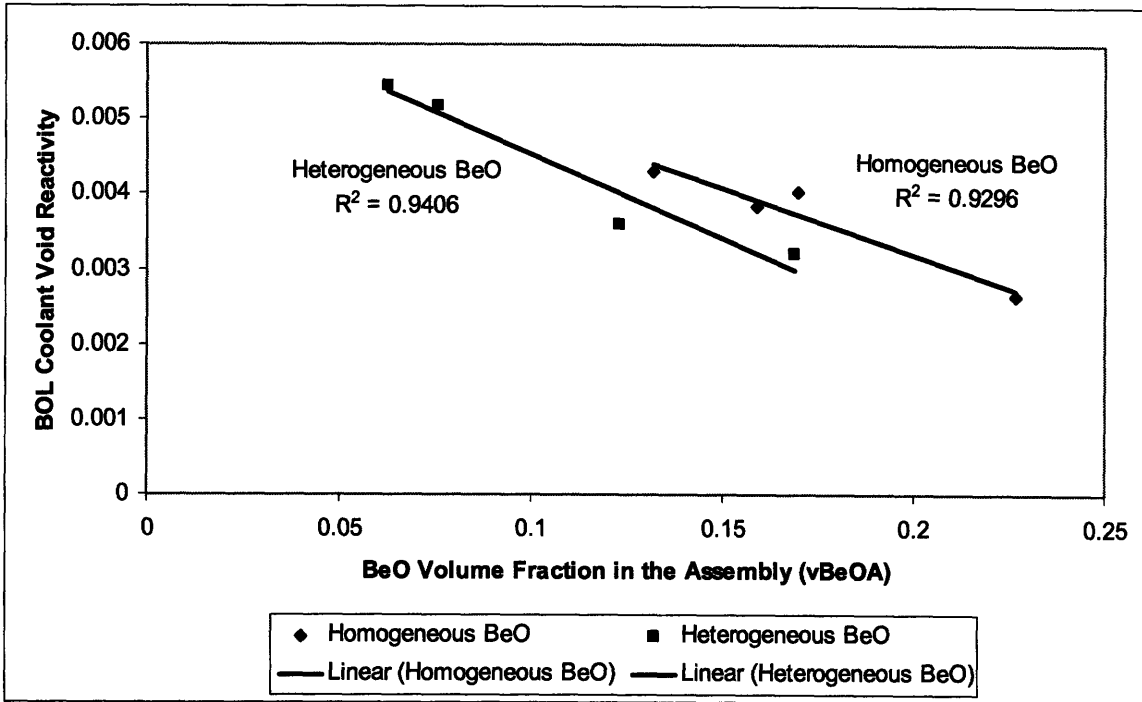


Figure 5.11: BOL Coolant Void Reactivity (CVR) as a Function of BeO Volume Fraction

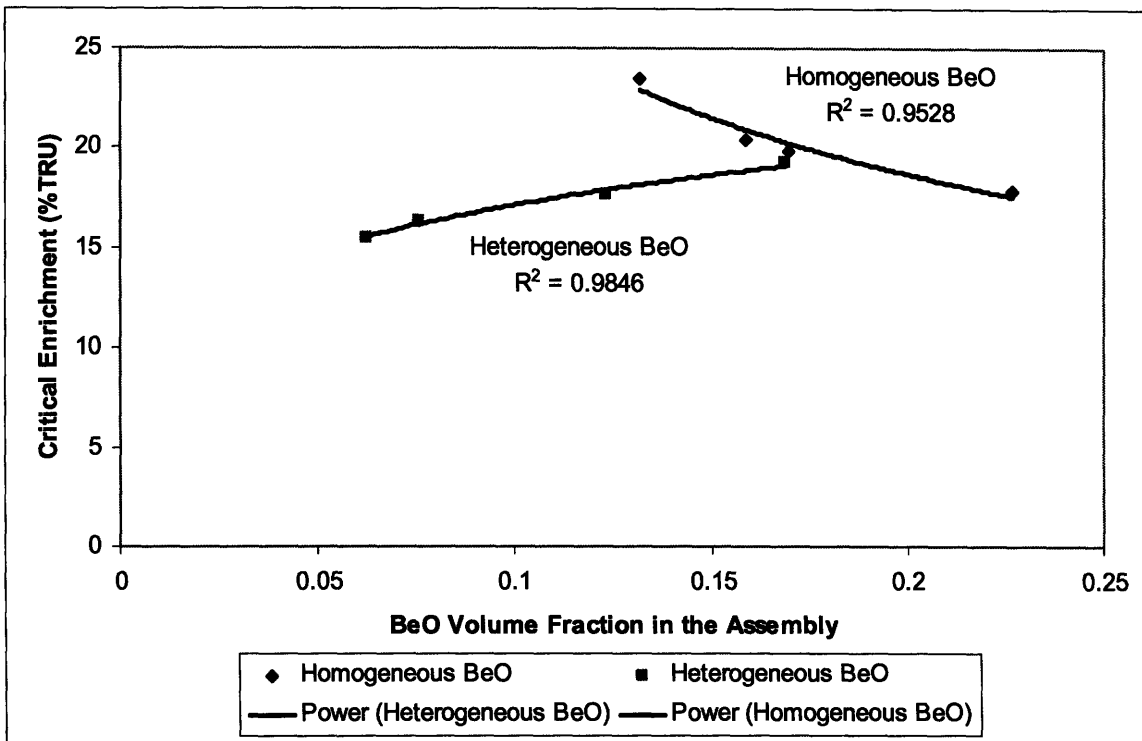


Figure 5.12: Critical Enrichment as a Function of BeO Volume Fraction

the relationship between reactivity limited burnup and  $v\text{BeO}_A$ , it is shown that in order to maximize reactivity limited burnup, either  $v\text{BeO}_A$  needs to be minimized for the heterogeneous case or  $v\text{BeO}_A$  needs to be maximized for the homogeneous case. While it may seem counterintuitive that increasing  $v\text{BeO}_A$  will increase reactivity limited burnup, it should be remembered that the increase in  $v\text{BeO}_A$  for the homogeneous case is accompanied by an increase in fuel volume fraction ( $v_{fA}$ ). Hence, the highest  $v\text{BeO}_A$  option is the fuel type that offers the largest volume fraction for both fuel and BeO: TID.

Minimizing  $v\text{BeO}_A$  in order to maximize reactivity limited burnup for the heterogeneous case will not reduce the CVR, as shown in Figure 5.11. However, maximizing  $v\text{BeO}_A$  in order to maximize reactivity limited burnup for the homogeneous case allows us to maintain a high enough  $v\text{BeO}_A$  such that it will have the desirable effect of reducing CVR. Further, as shown by comparing all three figures, while a lower critical enrichment and longer reactivity limited lifetime can be obtained using a heterogeneous BeO strategy, the optimum heterogeneous case does not allow for as favorable a CVR reduction as with the homogeneous case. Hence, it is clear that the most desirable optimized case is that for the homogeneous BeO case where  $v\text{BeO}_A$  and  $v_{fA}$  are maximized. This occurs for the TID fuel type, as shown in Table 5.2.

#### 5.2.4 Neutronic Study Conclusions

In this neutronic study, the relative neutronic merits of three different fuel types using three different BeO strategies have been compared, in an effort to discern if any of these approaches offers a clear, neutronic advantage. Based on the estimated length of the neutron mean free path for this type of reactor (2-3 cm), heterogeneity below the unit cell level has no effect on neutronic performance, while heterogeneity among unit cells will affect neutronic performance. Hence, the heterogeneous and homogeneous fuel strategies should behave differently neutronically.

The three key parameters of neutronic performance that were optimized were minimization of Coolant Void Reactivity (CVR), maximization of reactivity limited burnup, and minimization of critical enrichment. These parameters and their maximization/minimization were chosen in an effort to achieve the most cost-effective and

safe design possible for this reactor, in support of the Generation IV International Forum (GIF) goals of economics and safety. It was shown that homogeneous BeO in TID fuel provided the best balance among these sometimes competing parameters, as it:

- Maximizes  $\nu_{\text{BeO}_A}$  which minimizes CVR
- Maximizes  $\nu_{f_A}$ , which maximizes reactivity limited burnup while minimizing critical enrichment

### **5.3 Thermal-Hydraulic Study**

Again, using the possible combinations provided in Table 5.1, a comprehensive thermal hydraulic study of the seven proposed fuel strategies was undertaken. Strategies using either TID or pin-type fuel were evaluated using FLOWSPLIT, an in-house FORTRAN thermal-hydraulics code developed at MIT [Hejzlar, 1994]. Strategies using Internally Cooled Annular Fuel (ICAF) were evaluated using a similar internally-generated FORTRAN thermal-hydraulics code called ANNULCO2, tailored specifically for this unique fuel design and adopted for S-CO<sub>2</sub> coolant based on the original code for water cooled reactors, TAFIX [Kazimi, 2001]. Both codes required modifications to account for the following effects: (1) the effect of wirewrap on pressure drop (2) the effect of the BeO diluent on the fuel thermal conductivity and (3) the effect of annular fuel pellet geometry on fuel temperatures (for FLOWSPLIT in the case of the BeO slug in the middle of the pin-type fuel). While some modifications (2) were achieved subsequent to the delivery of the original code and prior to previous modifications [Pope, 2006], the other two (1 and 3) were implemented as a part of the present work.

As well, in order to look at a wide range of fuel geometries, both a FLOWSPLIT-MATLAB interface and ANNULCO2-MATLAB interface were developed. These interfaces automated the generation of the applicable input deck for a given geometry, executed the appropriate program, processed the output data in a usable form, and then repeated the process until all desired geometries were evaluated. In the case of the ANNULCO2-MATLAB interface, an extra iterative process was added which processed the output data from an input deck from a given geometry, evaluated it against the criteria necessary to match the thermal hydraulic conditions in the inner and outer coolant channels, and then modified the size of the inner coolant channel in the subsequent input deck in order to match

the coolant temperatures of the inner and outer channels. For each geometry, this iterative process was repeated until (1) the coolant temperatures of the inner and outer channels were within 5 degrees and (2) the coolant temperature of the outer channel was greater than the inner channel, if any mismatch existed. While it is desirable to have them exactly matched, a tolerance of 5°C was determined to give an acceptable approximation of results without incurring excessive computation time to converge on an exact solution. The second condition was imposed since the outer channel would have the benefit of mixing while the inner channel would not. Hence, the outer channel would have a slight heat transfer advantage over the inner channel and could tolerate a slightly higher temperature.

In solving for pressure drop, it was assumed that wire-wrap would be used for consistency between the pin and ICAF type fuel cases. This is because the TID fuel has a very clear and distinct advantage in this area, and in order to make a more fair comparison among all options, wire-wrap was chosen, as it will give a lower pressure drop than grid spacers. In order to represent the effect of wire-wrap on pressure drop, the Cheng-Todreas correlation was chosen to account for the change in friction factor that accompanies wire wrap [Cheng and Todreas, 1986]. However, it should be remembered that Cheng-Todreas was developed from bare-rod experimental data. Hence, the effect of cladding surface roughness is not accounted for in this correlation.

Since both the effect of surface roughness and wire wrap on the friction factor need to be accounted for, and there is currently no correlation that accounts for both, the following method was used. First the bare rod pressure drop (and other appropriate T/H parameters) was calculated using the default FLOWSPLIT friction factor correlation, which accounts for the surface roughness of the cladding. Next, the bare rod pressure drop was found using the Cheng-Todreas friction factor correlation for bare rods, which does not account for the surface roughness of the cladding. Then, the wire-wrap pressure drop was found for several wire-wrap scenarios, each with a different H/D ratio, using the Cheng-Todreas friction factor correlation for wire wrap, which also does not account for surface roughness. The Cheng-Todreas bare rod pressure drops were then subtracted from these wire-wrapped pressure drops using the Cheng-Todreas wire wrap correlation in order to get a  $\Delta P$  due to the wire-wrap alone. This  $\Delta P$  was then added to the pressure drop calculated for bare rods using the

default FLOWSPLIT correlation for the friction factor which accounted for surface roughness. In this way, what should be a good estimate for the friction (and hence total) pressure drop due to both surface roughness and wire-wrap was obtained. This process can be represented by the following equations:

$$PD_{TOT} = (PD_{HDZZ} - PD_{CTBR}) + PD_{DEFAULT} \quad \{5.5\}$$

where:

$PD_{TOT}$  = Pressure Drop accounting for both the effects of clad surface roughness and wire wrap with a  $H/D=ZZ$ , where  $ZZ$  is a value between 8 and 50, the  $H/D$  range for which the Cheng-Todreas wire wrap correlation is valid.

$PD_{HDZZ}$  = Pressure Drop due to wire wrap with a  $H/D=ZZ$  using the Cheng-Todreas wire-wrap correlation to calculate the friction factor

$PD_{CTBR}$  = Pressure Drop with no wire wrap but using the Cheng-Todreas correlation for bare rods to calculate the friction factor

$PD_{DEFAULT}$  = Pressure Drop with no wire wrap but using the default friction factor correlation which accounts for the effects of surface roughness to calculate friction factor

While this procedure works well for pin type fuel, it is a little more complicated for ICAF, where the flow and pressure drop must be balanced between the inner and outer coolant channels. For ICAF, the effect of wire wrap on pressure drop is quantified by:

$$PD_{TOT} = (PD_{HDZZ,DEFAULT} - PD_{CTBR,DEFAULT}) + PD_{DEFAULT,DEFAULT} \quad \{5.6\}$$

where, generically,  $PD_{A,B}$  represents the Pressure Drop due to correlation A (defined for Eq. 5.5) for the outer channel and correlation B for the inner channel. Balancing the flow, pressure drop, and coolant temperatures between the inner and outer channels is achieved by varying the size of the inner coolant channel, as discussed earlier. Hence for each of the PD values in the right hand side of Eq. 5.6, a different geometry is represented, as the different pressure drops created by each situation yield a different size of the inner channel. Consequently, each of these pressure drops represents a slightly different geometry and their comparison to achieve a result is only an estimate. Still, given the limitations of the



available tools and short of performing experiments to come up with a pressure drop correlation for wire-wrap that accounts for surface roughness for ICAF, this is the best currently available method for obtaining pressure drop due to wire wrap in ICAF and provides reasonable results.

Similar to the thermal hydraulic analysis in the chapter concerning the TID core design, all thermal hydraulic results were calculated assuming (1) a chopped cosine shape for the axial power profile with a peak of 1.3 and (2) a 1.2 radial peaking factor to represent the hot pin and (3) the clad and gap thickness correlation developed by [Garkisch and Petrovic, 2004]. As well, all cases with BeO used a BeO volume fraction of 38%. This value was chosen as it is close to an upper limit on the amount of BeO one would want to add to fuel before becoming neutronically prohibitive, i.e. too high of an enrichment in order to sustain criticality/conversion, as shown in previous studies in the present work. Based on earlier analyses at MIT, it was assumed that this concentration of BeO would enhance the fuel thermal conductivity by a factor of 1.5 [Pope, 2006]. Finally, the H/D value chosen for the wire-wrap was 29, mid-way between the correlation's limiting values of 8 and 50.

Four thermal hydraulic constraints were used in assessing the available options:

5. Cladding Temperature:  $< 800^{\circ}\text{C}$
6. Fuel Temperature:  $< 1800^{\circ}\text{C}$
7. Pressure Drop:  $< 500 \text{ kPa}$
8. Fuel volume fraction in the assembly ( $vf_A$ ):  $> 0$

The rationale for the temperatures and pressure in constraints 1-3 are contained in [Pope, 2006] and are repeated in Chapter 4, "Tube-in-Duct (TID) Fuel Assembly Core Design" for completeness.

The 4<sup>th</sup> constraint is an issue with both the TID and ICAF fuel types. For the TID fuel, there are certain geometries which are not possible for the given clad and gap thickness correlation (discussed in Chapter 4). As well, any clad and gap thickness would physically preclude a limited range of fuel geometries. For ICAF fuel, there are certain geometries for which balancing thermal hydraulic parameters between the inner and outer channels is impossible given fuel outer diameter, pitch, cladding, and gap thicknesses. Using these four criteria, a range of geometries, i.e. fuel pin outer diameter and P/D for ICAF and pin fuel and

coolant channel diameter and P/D for TID fuel, was assessed. All of the constraints and parameters used in this thermal hydraulic study are listed in Table 5.3

**Table 5.3: Constraints and Parameters Used for the Thermal Hydraulic Study**

Parameter	Value
<b>Steady State Thermal Hydraulic Constraints</b>	
Peak Clad Temperature	800°C
Peak Fuel Temperature	1800°C
Core Pressure Drop	500 kPa
Fuel volume fraction in the assembly ( $vf_A$ )	>0
<b>Core Macro-Geometric Parameters</b>	
Core Volume	28.09 m <sup>3</sup>
Core Power	2400MW <sub>th</sub>
Core Diameter (Flat-to-Flat distance of hexagonal core)	4.6 m
Core Height	1.53 m
Core Flow	1.1708x10 <sup>4</sup> kg/s
Core Inlet Temperature	485.5°C
Core Inlet Pressure	19.95 kPa
H/D Ratio for wire wrap	29
Radial Peaking Factor	1.2
Axial Power Shape	Chopped cosine with a peak of 1.3
Diluent (BeO) Loading	>10%

### 5.3.1 Pin-Type Fuel Thermal Hydraulic Results

Figure 5.13-Figure 5.15 shows the results for the three pin-type fuel cases studied, where the x and y axes describe the geometry of the fuel and the z-axis (grayscale gradation) shows the volume fraction of fuel in the assembly,  $vf_A$ . Table 5.4 provides a key to the lines which define the acceptable thermal hydraulic envelope in each case.

**Table 5.4: Key for Graphical Representation of Thermal Hydraulic Limits**

Symbol	Limit
-- (dashed line)	Pressure Drop
. (dotted line)	Clad Temperature
- (solid line)	Fuel Temperature
.- (dots and dashes)	$vf_A$

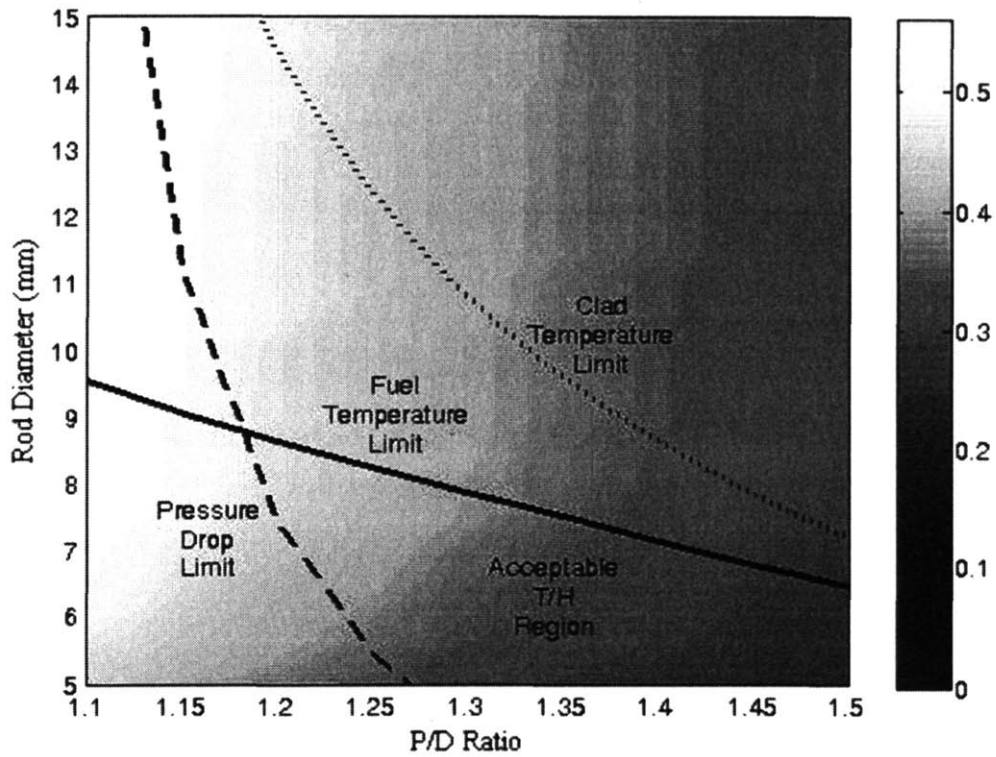


Figure 5.13: Acceptable T/H Envelope for Pin-type Fuel with No BeO

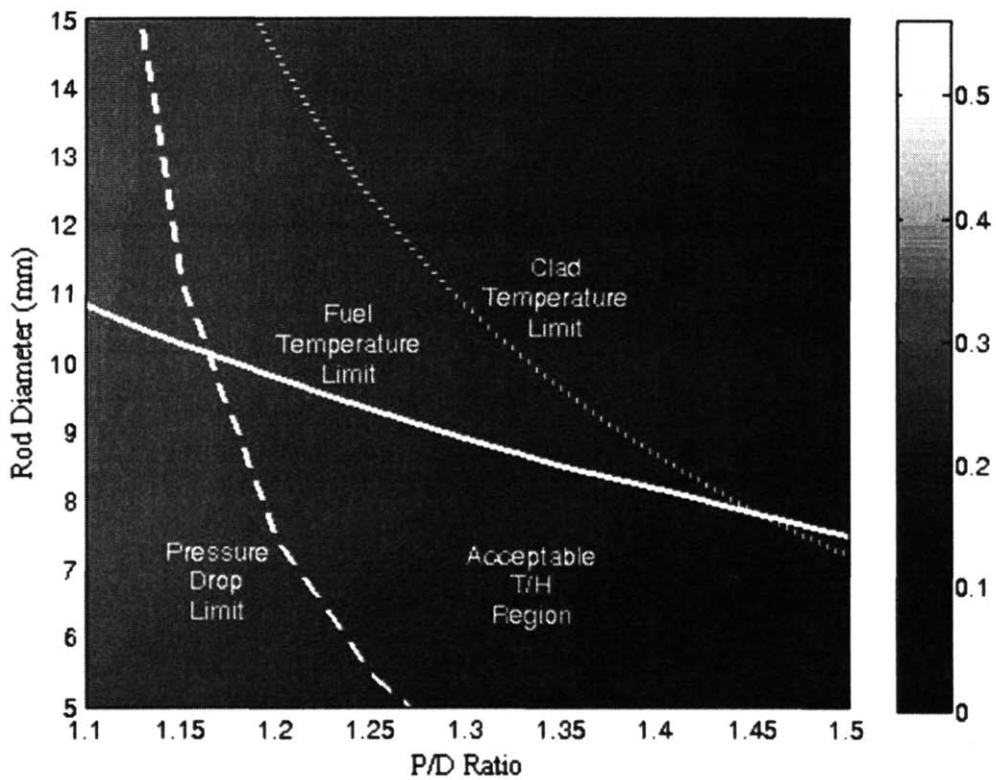
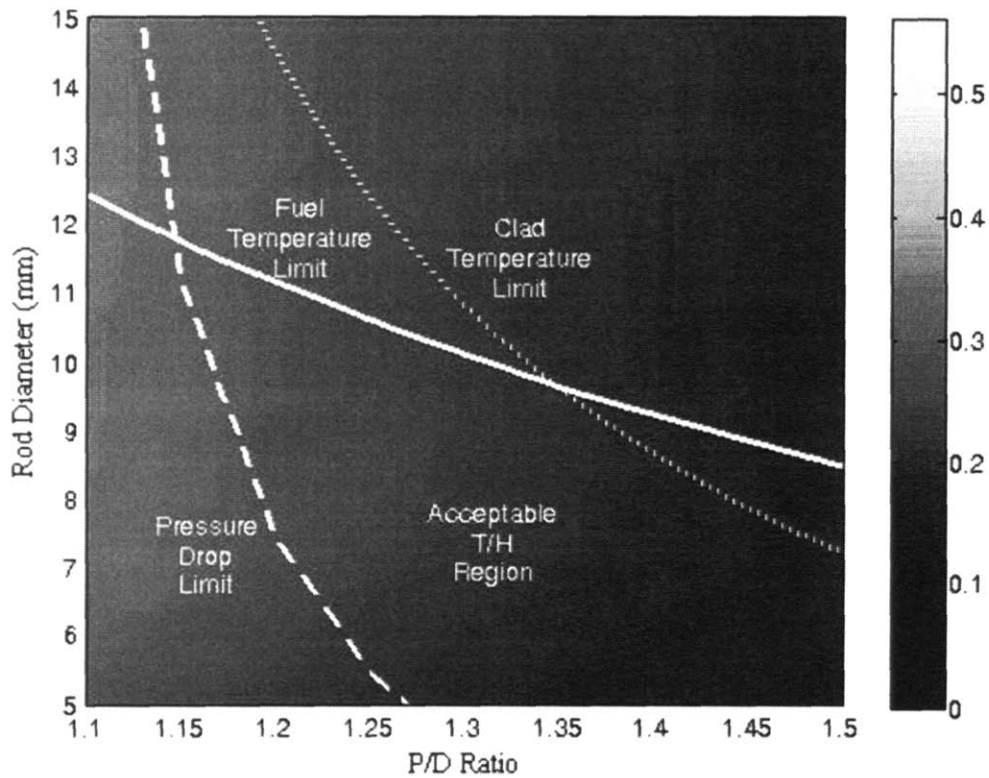


Figure 5.14: Acceptable T/H Envelope for Pin-type Fuel with BeO



**Figure 5.15: Acceptable T/H Envelope for Pin-type Fuel with a BeO Slug**

Comparing Figure 5.13 and Figure 5.14, it is shown that the addition of BeO expands the acceptable thermal hydraulic envelope by lowering the fuel temperature for a given geometry. As well, it reduces the available fuel volume fraction, as expected. Including Figure 5.15 in this analysis shows that using a BeO slug in the middle of an annular fuel pellet further expands the acceptable thermal hydraulic envelope by lowering the fuel temperature for a given geometry. This is expected, as annular fuel produces lower fuel temperatures than cylindrical fuel pellets [Todreas and Kazimi, 1990]. Note that the clad temperature and pressure drop limits do not change among these 3 cases, only the fuel temperature limit. Given that the lowest fuel temperatures are possible with the BeO slug strategy, this strategy provides the best thermal hydraulic capability among the pin-type options group. While Figure 5.14 and Figure 5.15 show a lower  $vf_A$  than the case without BeO (Figure 5.13), the no BeO case would need to have BeO added in separate pins in order to deliver comparable neutronic, i.e. CVR, performance, yielding comparable  $vf_A$  values to that of the other strategies.

### 5.3.2 TID Thermal Hydraulic Results

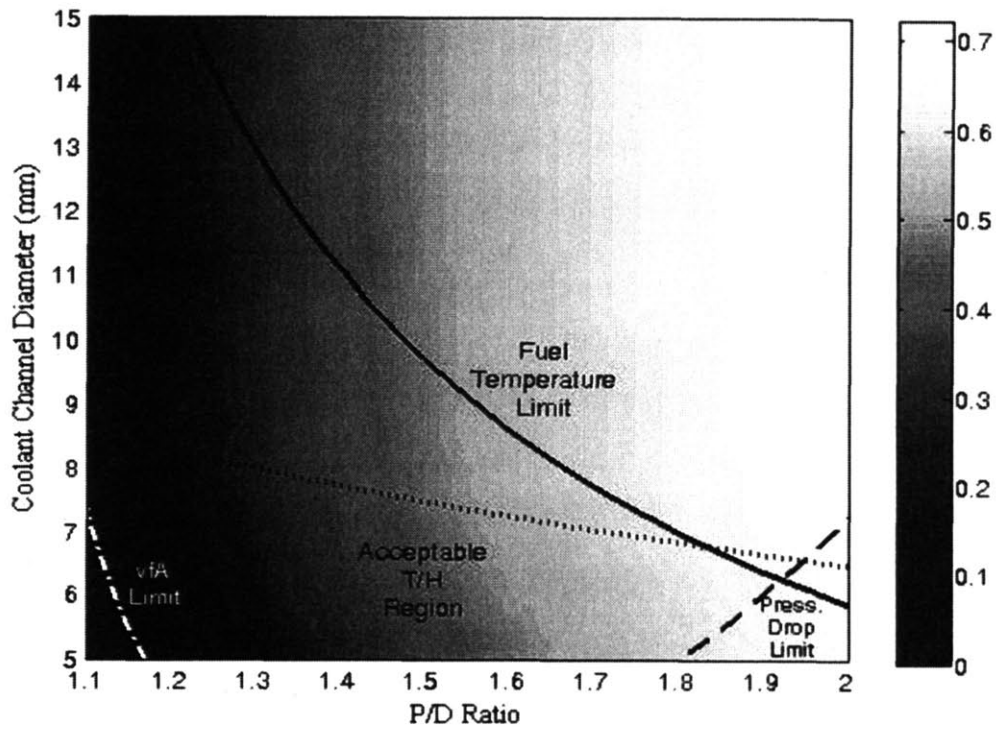


Figure 5.16: Acceptable T/H Envelope for TID Fuel with No BeO

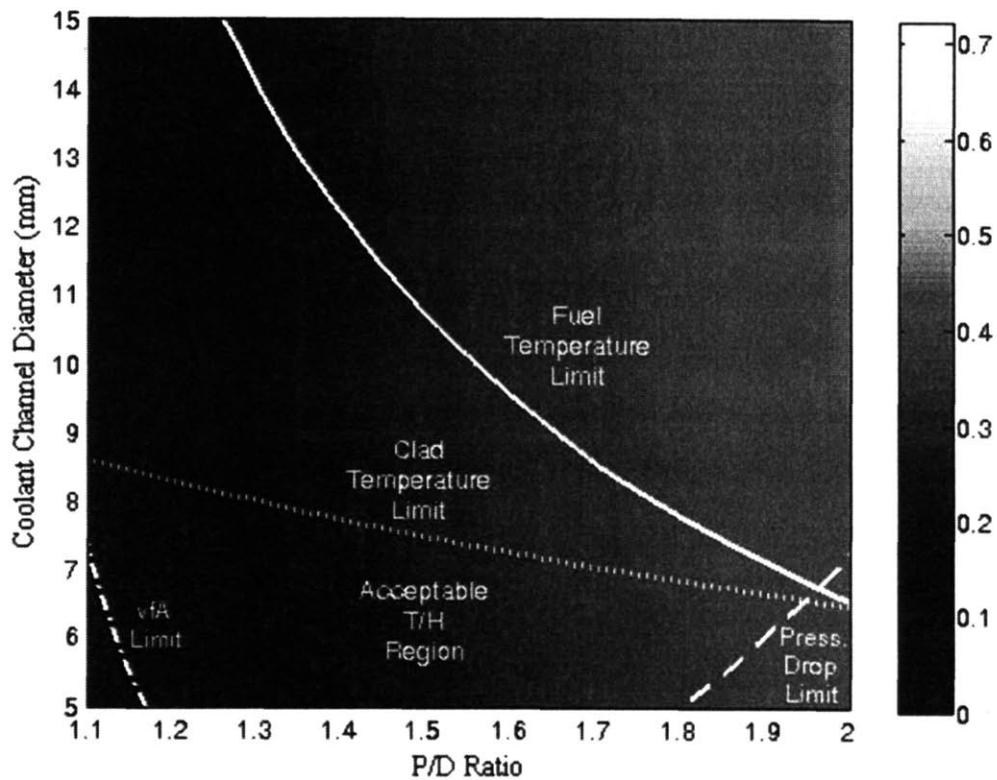
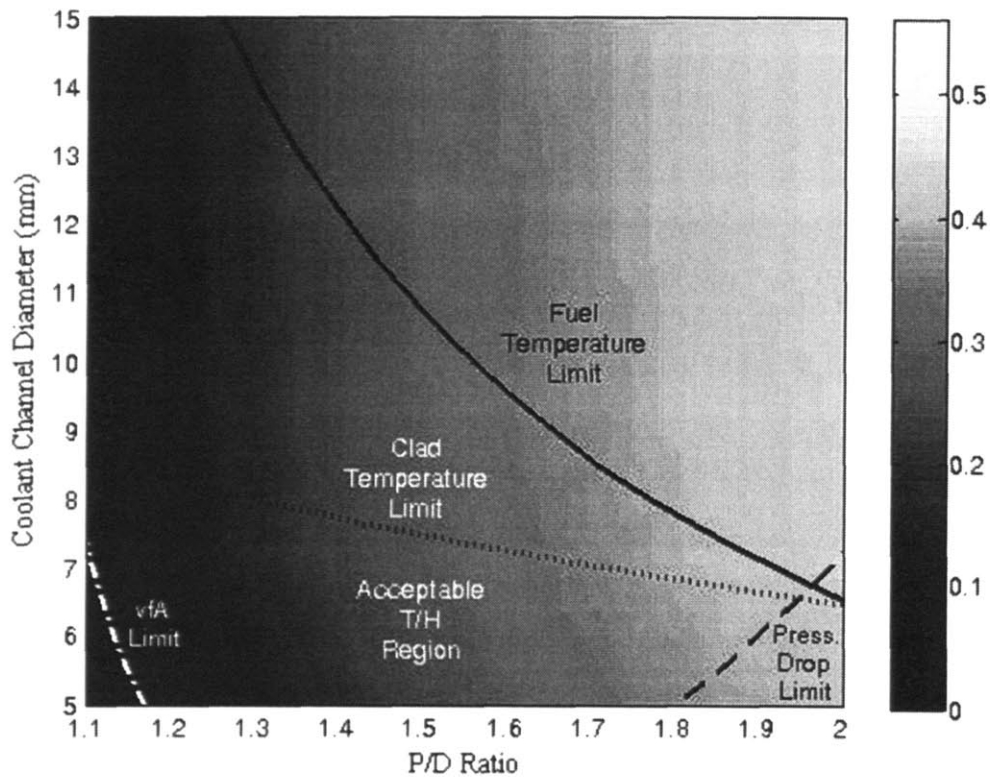


Figure 5.17: Acceptable T/H Envelope for TID Fuel with BeO



**Figure 5.18: Acceptable T/H Envelope for TID Fuel with BeO with Revised Scale**

Figure 5.16 and Figure 5.17 compare the TID fuel with and without BeO diluent. Addition of BeO does not appreciably expand the available thermal hydraulic envelope, as the envelope is limited mainly by clad temperature and pressure drop. It does lower the fuel temperature for a given geometry, but not by much ( $\sim 50^{\circ}\text{C}$ ).

There is, however, a significant fuel temperature reduction between the TID and pin cases, as evidenced by a comparison between Figure 5.14 and Figure 5.17. Further, the TID case yields a significantly lower pressure drop than the pin case, even though it is given favorable pressure drop conditions through the use of wire-wrap. However, the TID case is slightly more limiting with respect to clad temperature than the pin case. Note that the z-axis, i.e. color gradation, for the TID cases is on a different scale than that of the pin-type fuel. This was done so that an even comparison between TID cases could be made. Adjusting this scale to match that of the pin-type fuel in Figure 5.18, it is apparent that the TID fuel can achieve a higher  $v_{fA}$  within the acceptable T/H region than its pin-type counterpart shown in Figure 5.14.

### 5.3.3 ICAF Thermal Hydraulic Results

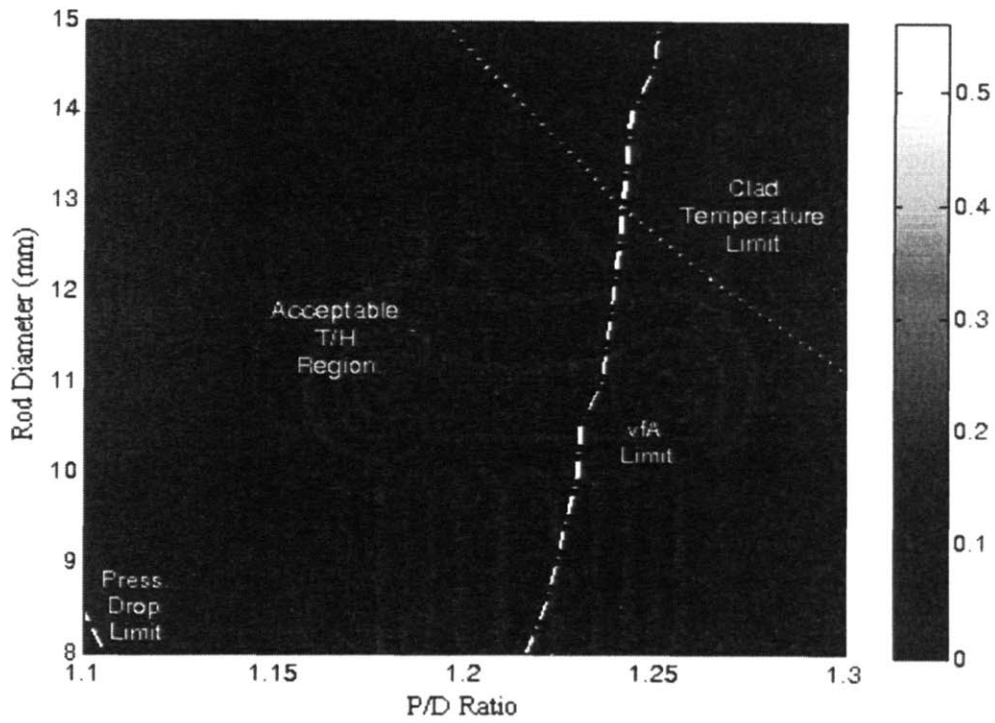


Figure 5.19: Acceptable T/H Envelope for ICAF with No BeO

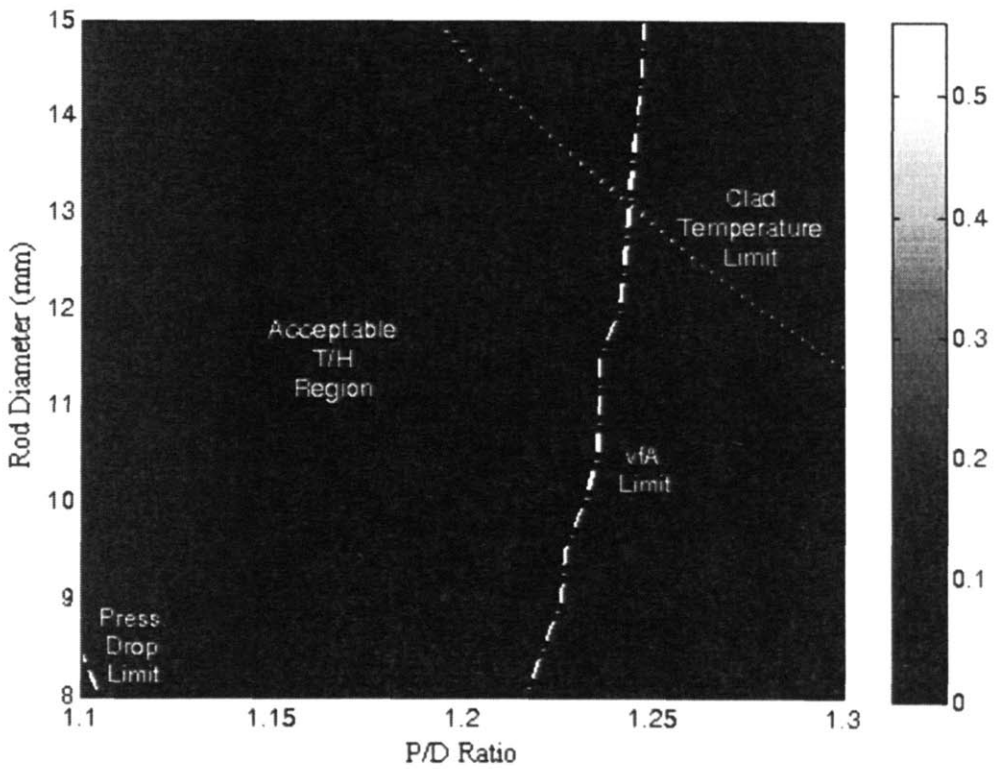


Figure 5.20: Acceptable T/H Envelope for ICAF with BeO

Comparing the ICAF both with and without BeO diluent, the same conclusions about addition of BeO with respect to fuel temperature can be drawn as with the case of TID fuel, i.e. marginal improvement. While this effect is not illustrated in Figure 5.19 or Figure 5.20, it is apparent that the acceptable thermal hydraulic region between the two cases does not change appreciably. Since there is an extra degree of freedom with the size of the internal channel of the ICAF, the fuel volume fractions, pressure drops, and cladding temperatures between the two cases do not change appreciably.

Comparing the ICAF fuel to the other fuel types, it can be seen that for a given geometry, not only is the fuel temperature lower, but also that the clad temperature is lower. This is due to the extra heat transfer area available in the central cooling channel. As well, compared to pin type fuel, pressure drops are lower, yet are not as good as TID fuel. However, the  $vf_A$  values for ICAF are significantly less than those for pin-type fuel, which are already less than those for TID fuel. This shortcoming will play an important part in the comparative assessment of the fuel types

#### 5.3.4 Comparative Thermal Hydraulic Results

Table 5.5 summarizes the comparative results presented in the previous 3 sections, in a qualitative sense.

**Table 5.5: Qualitative Ranking, Best to Worst, of Fuel Types**

Pressure Drop	Fuel Temperature	Clad Temperature	$vf_A$
1. TID	1. ICAF	1. ICAF	1. TID
2. ICAF	2. TID	2. Pin	2. Pin
3. Pin	3. Pin	3. TID	3. ICAF

Now that the general comparison among the four constraints has been made, it should be decided (1) which constraints are more dominant, if any, and (2) the quantitative degree of difference among the options for each constraint, i.e. is the improvement in fuel temperature 5°C or 500°C? From the neutronic results, it was found that the homogenized BeO strategies that maximized  $v_{BeO_A}$  and  $vf_A$  provided the most optimal neutronic performance among all of the options. Further, from the thermal hydraulic results, the integrated BeO cases provide the best thermal hydraulic performance. Hence, in order to do a more quantitative comparison among the fuel types, the geometries for each fuel type that maximize  $vf_A$  and



incorporate BeO into the fuel are compared in Table 5.6. Note that for the pin case, the BeO slug is chosen, as it (1) provides the lowest fuel temperatures among all of the pin-type diluent options with all other thermal hydraulic factors being roughly equal and (2) behaves neutronically like the homogeneous BeO cases.

From these results, it can be seen that TID provides an appreciably larger  $vf_A$  than the other two fuel options. While the TID option listed in Table 5.6 is near the maximum cladding temperature and pressure drop limits, the size of the acceptable T/H region for TID fuel allows for moving to a region of lower pressure drop, lower cladding temperature, and lower fuel temperature while still maintaining a superior  $vf_A$  over the other fuel types. Such an example is demonstrated in the first case of Table 5.7. Further, as one moves away from the pressure drop limiting region, the extra pressure drop margin can be traded off for a reduction in cladding temperature via cladding surface roughening, dimpling, ribbing, or other heat transfer augmentation methods.

Comparing the pin and ICAF results from Table 5.6 (second and third cases) with the TID results for geometries with comparable  $vf_A$ 's (shown in the second and third case of Table 5.7), the TID fuel shows comparable or better performance. For the comparison of the TID and pin fuel at the same  $vf_A$  (the second lines of Table 5.6 and Table 5.7), the TID fuel exhibits a much lower maximum fuel temperature and pressure drop, while giving a slightly higher maximum cladding temperature. This highlights the inherent advantages of TID fuel with respect to these thermal hydraulic parameters.

**Table 5.6: Quantitative Comparison Among Fuel Types where  $vf_A$  is Maximized**

Case	D (mm)	P/D	Max. Fuel Temp. (°C)	Max. Clad Temp. (°C)	Pressure Drop (kPa)	$vf_A$
TID fuel with integrated BeO	6.5	1.95	1723	800	500	0.4156
Pin fuel with BeO slug	11.5	1.15	1766	733	488	0.3218
ICAF with integrated BeO	15	1.1	1177	750	267	0.2070

**Table 5.7: Thermal Hydraulic Results for other TID cases**

Case	D (mm)	P/D	Max. Fuel Temp. (°C)	Max. Clad Temp. (°C)	Pressure Drop (kPa)	$vf_A$
TID fuel with integrated BeO: $vf_A$ superior to that of other fuel types	6	1.8	1438	776	403	0.3740
TID fuel with integrated BeO: $vf_A$ comparable to that of pin in Table 5.6	6.5	1.65	1371	782	265	0.3344
TID fuel with integrated BeO: $vf_A$ comparable to that of ICAF in Table 5.6	5	1.45	1006	739	214	0.2163
Pin fuel with integrated BeO: $vf_A$ comparable to that of ICAF in Table 5.6	6.5	1.35	1437	741	251	0.2096

For the comparison of the TID and ICAF fuel at the same  $vf_A$  (the third lines of Table 5.6 and Table 5.7), the TID fuel exhibits slightly better thermal hydraulic performance in all areas. While the lower pressure drop for the TID fuel can be explained by the absence of wire-wrap, the slightly lower, i.e. comparable, fuel and cladding temperatures can be explained by the nearly identical ratios of heat transfer area to volumetric heat generation for both cases. Hence, while the ICAF has two surfaces for conducting heat per unit cell as opposed to the TID which has only one, the amount of heat being generated for the geometry of the ICAF case is proportionately larger, such that the advantage conferred by this advantage in heat transfer area is effectively negated.

In comparing the ICAF and pin fuel at the same  $vf_A$  (the third line of Table 5.6 and the fourth line of Table 5.7), comparable cladding temperatures and pressure drops are obtained, with the ICAF fuel retaining an advantage with respect to fuel temperatures. With the pin type fuel, lower fuel temperatures (comparable to those achievable by the ICAF) are achievable, but come at the expense of pressure drop. For example, in order to lower fuel temperatures for the same  $vf_A$ , smaller diameter pins need to be used, which lowers the P/D and raises pressure drop. Hence, the fundamental trade-off between these two parameters for

pin-type fuel. Given that pin-type fuel can achieve ~50% greater  $vf_A$  than ICAF while still respecting the established thermal hydraulic limits, it has been selected as the second choice among the three options presented in this chapter. This is based on the flexibility that a larger  $vf_A$  provides with respect to neutronic design as well as the increased lifetime it confers upon a reactor core, a key parameter for a fast breeder-burner reactor. Coupled with this is the established manufacturing and performance track record that exists for pin-type fuel. While the feasibility of design and fabrication for ICAF has been proven [Kazimi, 2006], it lacks the 50+ years of irradiation experience that the pin-type fuel has. As well, TID fuel has never been tested.

#### **5.4 Conclusions**

Performing an integrated neutronic and thermal-hydraulic comparison among fuel types and diluent strategies shows that TID fuel with integrated BeO diluent provides the best all around performance. This stems mainly from the large fraction of the volume inherent in such a strategy that can be used for both diluent and fuel. Neutronically, this larger volume allows for a larger fuel loading, which can help to maximize reactivity limited lifetime while minimizing critical enrichment. As well, this larger volume can accommodate more BeO diluent, which helps to minimize CVR. From a thermal hydraulic standpoint, this larger volume allows greater design flexibility in trade-offs among competing parameters while still achieving superior neutronic performance. For the same reasons, the traditional pin is selected as the preferred second choice, as it capable of achieving nearly 50% greater  $vf_A$  than ICAF, while still respecting established thermal hydraulic limits. While ICAF can confer a unique advantage with respect to fuel temperatures, the design freedom afforded by the higher  $vf_A$  of the pin and TID fuel allows adjusting their geometry to achieve comparable performance in this area. For the pin fuel, this comes at the expense of pressure drop. For the TID fuel, it does not come at any cost.

The conclusions of this study provide the definitive basis for the selection of the TID fuel type for use in this S-CO<sub>2</sub> cooled GFR. While the merits of the pin-type and ICAF fuels should be kept in mind, the superiority of TID fuel for GFR applications makes it the fuel type of choice for all future work in the present project.

## **6 PIN TYPE CORE DESIGN**

### **6.1 Introduction**

While the previous chapter conclusively showed both the neutronic and thermal hydraulic performance advantages of using Tube-in-Duct (TID) fuel, motivation still exists for development of a pin-type core design. First, while conferring many benefits, TID fuel is still an unproven concept, as none of these types of fuel assemblies have yet been built. Conversely, pin-type fuel enjoys more than 50 years of worldwide manufacturing and operating experience. As well, it was also the configuration of choice, both vented and unvented, for the GCFR designs of the 1970's, which included some test pin irradiations [Capana and Lindgren, 1974]. Hence, exploration of a core using pin-type fuel is worthy in the event that insurmountable obstacles arise during the development of TID fuel which precludes their implementation in this or other reactor types. Second, lessons learned from the development of a pin-type core can give insights into both the design process and the physics and thermal hydraulics behavior of this core. While some key lessons can be gleaned from the analysis in the previous chapter, there are some insights that are just not available using the approximate and scaled-down methods there.

### **6.2 Integrated Neutronic-Thermal Hydraulic Core Design Process**

Through performing the work associated with designing the TID GFR core and integrating and accounting for the various neutronic and thermal hydraulic constraints, a process has emerged which provides a somewhat standardized and organized way in which integrated steady state core design can be approached. While the process is standardized, it is not rigid and inflexible, as it allows for incorporation of new ideas and constraints. This

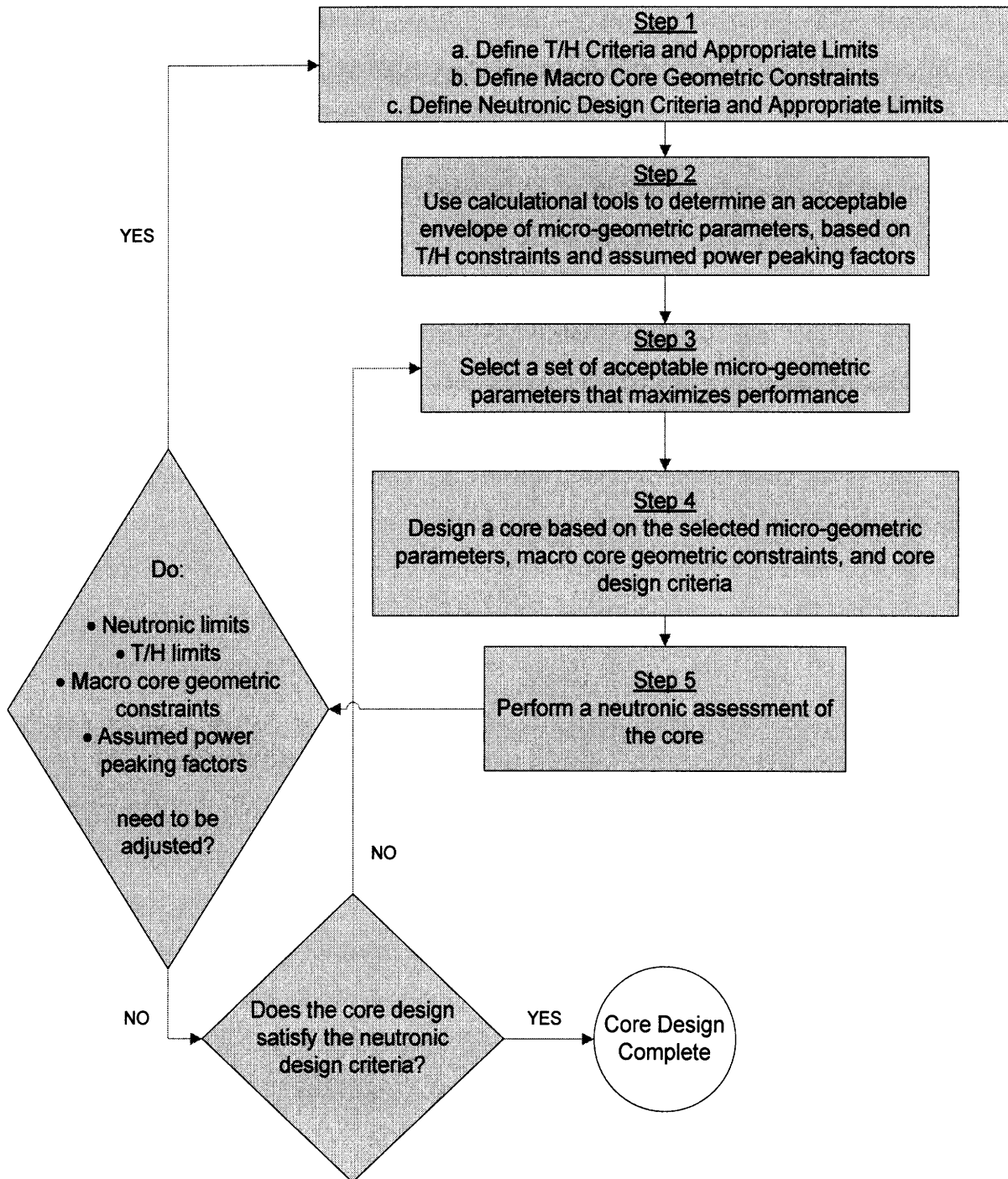


**Figure 6.1: Flowchart of the Integrated Neutronic/Thermal Hydraulic Core Design Process**

process was used in the design of the pin-type and ICAF cores, described in this chapter and the next. Figure 6.1 gives a flowchart of this process. Note that this process is described and

used here for the steady state case. Incorporation of transient analyses could be accommodated and this process would provide a good template.

First, the neutronic and thermal hydraulic (T/H) criteria to be examined must be established, with appropriate limits defined. The fundamental constraints from a steady state operations standpoint are based on observing T/H limits. If these limits are not observed, then degradation of core materials and performance occurs and the possibility of core restructuring and fuel melt increases. Hence it is important to define a comprehensive set of thermal hydraulic constraints around which a core design can be based. Coupled with this is defining a set of appropriate macro-core geometric constraints, i.e. core diameter, core flow, etc. The values for these parameters are typically set by factors external to the core design process, e.g. the size of the core is typically determined by economic drivers, the magnitude of flow through the core is typically driven by ex-core parameters, such as the needs for the PCS, etc. Once all of these criteria and limits have been defined, calculational tools, (FLOWSPLIT and ANNULCO2, in this case) are used to determine an envelope of acceptable micro-geometric parameters, i.e. fuel pin pitch and diameter, based on the previously defined T/H constraints. Implicit in this step is an assumption of the power peaking factors that can be achieved from the core design. Next, a set of micro-geometric parameters, i.e. fuel pin pitch and diameter, are chosen from inside this envelope which maximizes the desired performance of the core design. In this work, the region of this envelope which provided the maximum fuel volume fraction was chosen, in order to maximize reactivity limited burnup. For other applications, the parameter which maximizes desired performance may be something else, i.e. fuel temperature. Once all necessary geometric parameters (both macro and micro) have been established, a core is designed. This step includes selection of an appropriate simulation tool (MCNP and MCODE, in this case), modeling of the core, selection of fuel enrichment (and diluent, in this case) zoning, and any other of a number of considerations. Next, the core is subject to a thorough and rigorous neutronic assessment, using the chosen tools. A T/H assessment is not necessary at this point, as this screening has already been performed in the development of an acceptable T/H envelope from which the micro-core geometric parameters are chosen. Once the core has been assessed neutronically, a consideration of whether all of the neutronic and T/H limits used are exhaustive and appropriate should be made. Oftentimes in the design process,

previously unthought-of of considerations arise that need to be accounted for. As well, new information may become available which requires adjustment of one of the limits or power peaking assumptions, e.g. a power peaking factor of 1.1 was assumed in the T/H calculations in Step 2, but a peaking factor of 1.3 is the minimum achievable that is found in Steps 4 and 5. Hence, the first iterative loop in Figure 6.1. As well, it may be found that the desired performance is not achievable given a previously defined macro-geometric parameter, e.g. the core is too small to achieve a desired burnup. Should all previously defined parameters and limits be found exhaustive and appropriate, then the suitability of the core in meeting the neutronic criteria should be made. If not, then a different iterative process is undertaken in which the previously defined criteria, limits, and macro-geometric constraints are kept constant, and a new set of micro-geometric parameters, i.e. fuel pin pitch and diameter, is used in the design process. If so, then the design process is complete.

### **6.3 Thermal-Hydraulic Analysis and Results**

In order to begin the process of designing the pin-type core, the standardized process discussed in the previous was used. As a first step, the steady state thermal hydraulic constraints\* and core macro-geometric parameters were selected and defined. In order to ensure a fair basis for comparison with the TID fuel assembly core design, these constraints and parameters were kept the same. As well, there were several other factors that needed to be defined in order to carry out the initial thermal hydraulic analysis, specifically an assumed radial peaking factor, an axial power shape, an assumed diluent loading, and a height to diameter ratio (H/D) for the wire-wrap. The assumed radial peaking factor and axial power shape were necessary in order to estimate the peak power in the hottest and hence, most temperature limiting, spot in the core. These values were the same as those used in the TID core analysis in Chapter 4 and in the comparative analysis in Chapter 5 (see Table 5.3). A specific value for diluent loading was not necessary, just an estimation that it would or would not be above the threshold value of 10% which is used in this work as the tripwire for applying a 50% enhancement to the thermal conductivity of the fuel as a result of diluent use.

---

\* See Section 4.4.5 of this work or [Pope et. al, 2006] for the rationale behind these values.

Wire-wrap instead of grid spacers is used for two reasons. First, as discussed in the previous chapter, TID fuel has a very clear and distinct advantage with respect to pressure drop, and in order to make a more fair comparison, wire-wrap was chosen as it will give a lower pressure drop than grid spacers. Second, it is desired to minimize the coolant volume fraction ( $v_c$ ) and to maximize the fuel volume fraction ( $v_f$ ) of the pin-type core design, as the former has been shown to minimize the amount of positive coolant void reactivity (CVR) inserted upon a Loss of Coolant Accident (LOCA), while the latter has been shown to maximize reactivity limited burnup and hence, economic performance of the core. In order to effectively minimize  $v_c$ , it is necessary to use a tight triangular pitch lattice along with wire wrap in order to hold the fuel rods together. With the use of wire wrap comes the need to define an appropriate H/D, which has a significant effect on the value of core pressure drop. A value of 29 was used in this and other analyses in this work, as it represents the mid-point of the H/D range for which the Cheng-Todreas wire-wrap correlation was developed (8-50) [Cheng and Todreas, 1986] All of these parameters and constraints are defined in Table 5.3.

Given these core macro-geometric parameters, a lattice of hexagonal unit cells, each with a fuel pin at its center, was simulated in order to calculate the thermal hydraulic parameters of interest. These calculations were performed using the FLOWSPLIT-MATLAB interface described in the previous chapter, so that many combinations of core micro-geometric parameters, i.e. fuel pin pitch and diameter, could be efficiently analyzed. The details of the FLOWSPLIT-MATLAB interface as well as the algorithms for calculating key core micro-geometric parameters are contained in Appendix A.

The results of these calculations are the same as those presented in the previous chapter for the thermal hydraulic calculations for the pin-type core with integrated BeO and are shown again in Figure 6.2. As discussed earlier, it is desirable from a CVR standpoint to minimize the  $v_c$ . Since there is a one-to-one correspondence between the P/D and  $v_c$ , core micro-geometric parameters which minimize P/D are the target for this design. Within the acceptable thermal hydraulic envelope drawn in Figure 6.2, this occurs at a Rod Diameter of 10 mm and a P/D ratio of 1.1812, corresponding to a  $v_c$  of 35% (for an infinite triangular lattice; hence, for a finite triangular matrix with core internals,  $v_c$  will be slightly higher).



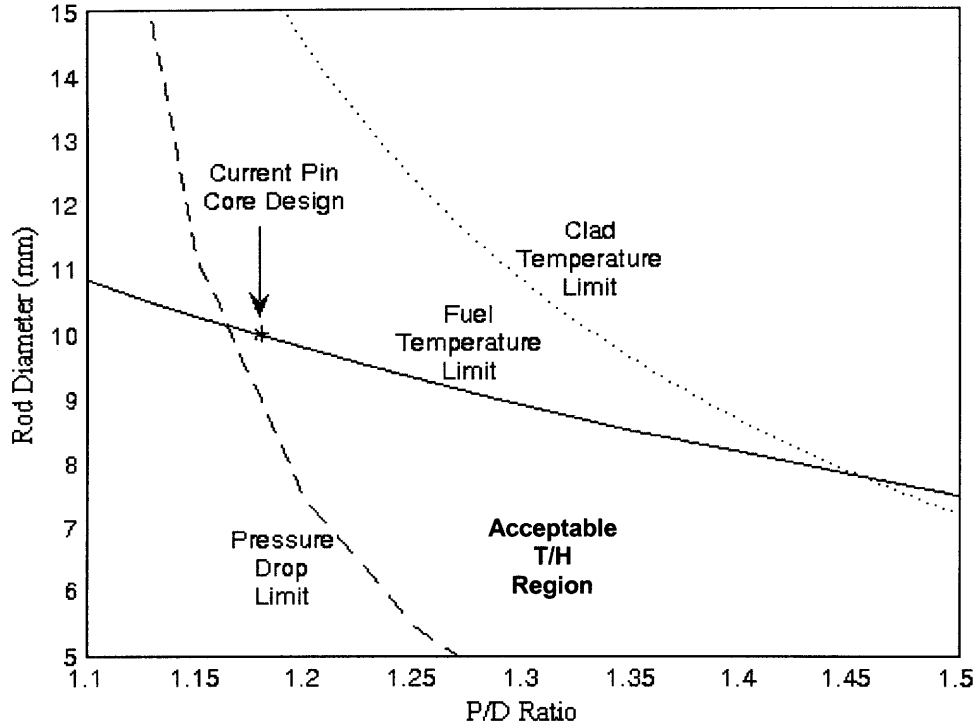


Figure 6.2: Acceptable T/H Envelope for the Pin Core

The values of the key thermal hydraulic constraints for the pin type core at the chosen geometry are compared with those for the TID core design in Table 6.1. It should be remembered that these values can change, depending upon the spot chosen within the applicable acceptable thermal hydraulic envelope for each fuel type. Further, the spot chosen for each of these fuel types was that which maximized some other performance factor: for TID fuel, the spot that maximized fuel volume fraction ( $v_f$ ) and hence, reactivity limited burnup; for pin-type fuel, the spot that minimized  $v_c$  and maximized  $v_f$ . In choosing the spots within the acceptable thermal-hydraulic envelopes which maximized the performance of each of the respective fuel types, a fair comparison between the thermal hydraulic performance of the TID and pin-type core can be made. It is interesting to note that given these constraints, these two core designs compare relatively equally, owing to the fact that the optimum performance point within each of the respective acceptable thermal hydraulic envelopes is near the intersection of the fuel temperature and pressure drop limits. Table 6.1 shows that the pin-type core has a slight advantage with respect to peak cladding temperature. As discussed in the previous chapter, this advantage is easily made up with the TID fuel by

implementation of a heat transfer augmentation method such as cladding surface roughening or dimpling. While a concomitant increase in pressure drop would result, the pressure drop could be kept in check by moving to a region of lower pressure drop within the acceptable thermal hydraulic envelope. While this would place the TID core in a sub-optimal performance condition, as it would move away from the point at which maximum  $v_f$  occurs, the resulting  $v_f$  would still be large enough that the TID core would enjoy a considerable performance advantage in this area. As a result, the steady state T/H performance of the TID and pin-type cores presented in this work can be viewed as comparable.

**Table 6.1: Comparison of Thermal Hydraulic Parameters for TID and Pin Core Designs where Performance is Optimized**

Fuel Type	Peak Cladding Temperature	Peak Fuel Temperature	Pressure Drop
Pin	735.6°C	1800°C	435 kPa
TID	810 °C	1770 °C	420 kPa

#### 6.4 Neutronic Analysis and Results

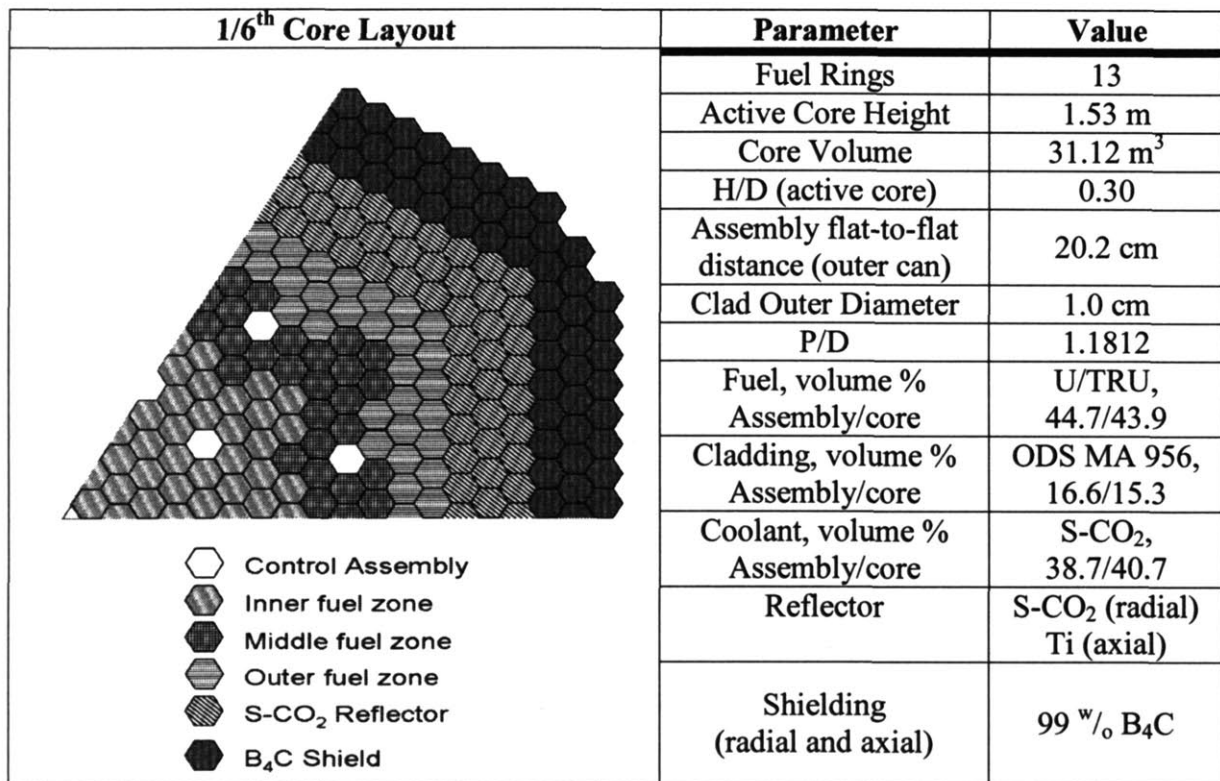


**Figure 6.3: Pin-Type Core Layout and Key Parameters**

Based on the previously defined core-macro geometric constraints and the results of the thermal hydraulic analysis, a pin-type core of layout and parameters described in Figure 6.3 was designed. The same steady state neutronic criteria that were used to evaluate the TID core will be used here for the pin-type core. Further, the results of this analysis will be evaluated against not only the goals of the GFR core design, but also against the performance of the TID core.

#### 6.4.1 Achievable Burnup

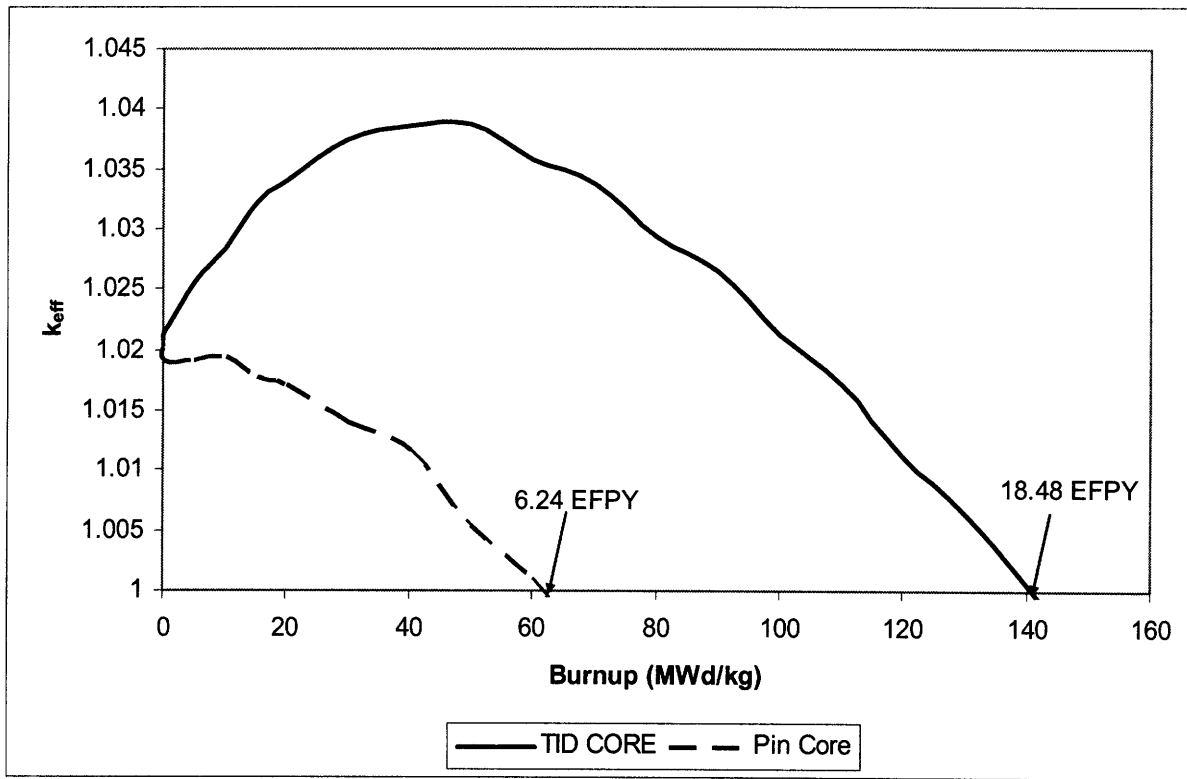


**Figure 6.4: Comparison of Reactivity Limited Burnups of the TID and Pin-type Cores**

Figure 6.4 shows the reactivity limited burnup of the pin type core that was developed. Most notable is the different behavior and the significantly shorter reactivity limited burnup and lifetime of the pin-type core as compared to the TID core (61.6 MWd/kg v. 140 MWd/kg and 6.24 EFPY v. 18.48 EFPY). This is due to the much lower fuel volume fraction ( $v_f$ ) inherent in the pin-type core which does not allow a sufficient conversion ratio (CR) during burnup to achieve a sustainable core without the use of external blankets. This is a drawback, as it does not support the goal of achieving a CR  $\sim 1$  in this work (in support of

the Gen-IV goal of sustainability). Another result of the lower  $v_f$  inherent in the pin-type fuel is the much higher enrichment necessary for criticality. Using the same enrichment and diluent zoning scheme as with the TID core, but applied to the geometry of the pin-type core yielded a core eigenvalue of 0.96091 (stdev = 0.00026), as compared to 1.02075 for the TID core (at beginning of life). In order to get a core eigenvalue comparable to that of the TID core, the enrichment of the pin core had to be raised from a uniform 16.6 % to a uniform 19.85 % (with an appropriate adjustment of diluent zoning to address radial power shaping). Consequently, not only is there a drawback with using pin-type fuel due to the much lower reactivity limited burnup and lifetime achievable, but there is also a significant penalty due to the increased enrichment.

#### 6.4.2 Radial Power Peaking

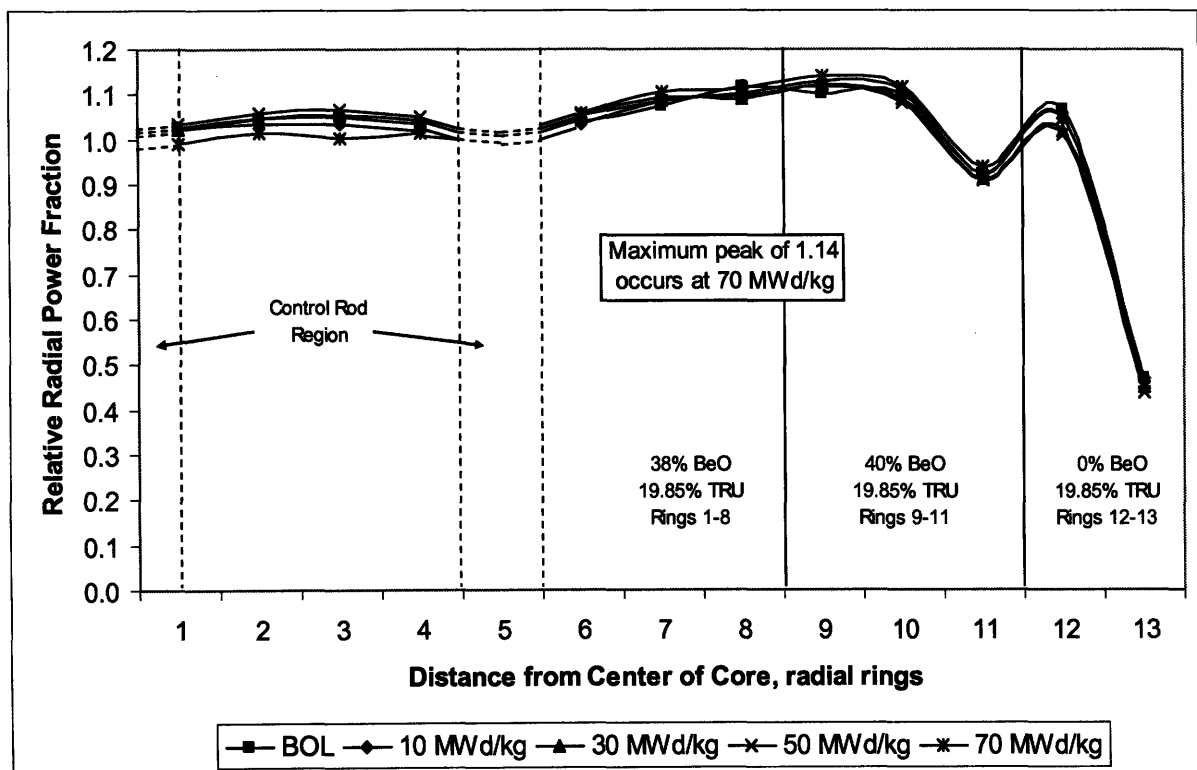


Figure 6.5: Unrodded Radial Power Shape as a Function of Burnup for the Pin Type Core

Once the reactivity limited burnup of the pin-type core was assessed, its ability to hold a relatively flat radial power shape was examined. Displayed in Figure 6.5, the pin type core is shown to hold its unrodded radial power shape very well over its brief life, with the

peak of 1.12, which is maintained throughout much of core life, varying only slightly. The maximum peak for the pin-type core is somewhat lower than that achievable for the TID core (1.34). This is due to two effects. First, the burnup of the pin core is significantly shorter than the TID core, which does not allow comparable spatially disparate fuel burnup throughout the core, as is the case with the TID core. Second, the lower fuel volume fraction of the pin-type core means that there is physically less fuel to burn up in a spatially uneven manner; hence, it is easier to keep the radial power profile flatter over core life. Consequently, the pin core gains an edge over the TID core with respect to neutronic performance in this area; however, this advantage is small and is not likely to overcome the large shortcoming of its shorter lifetime.

### 6.4.3 Passive Reactivity Control

**Table 6.2: Coolant Void Reactivity at BOL and EOL for the Pin Core Design**

Time in Life	keff, nominal	keff, voided	CVR $\Delta\rho$	STDEV ( $\sigma$ )	Effective Delayed Neutron Fraction ( $\beta_{eff}$ )	STDEV ( $\sigma$ )	CVR $\phi$	STDEV ( $\sigma$ ) $\phi$
<b>UNRODDED</b>								
BOL	1.02007	1.01761	-2.37E-03	2.28E-04	0.0038	1.9E-04	<b>-63</b>	<b>7</b>
EOL	1.0010	0.99957	-1.43E-03	1.84E-04	0.0039	1.8E-04	<b>-37</b>	<b>5</b>
<b>RODDED</b>								
BOL	0.99948	0.99509	-4.41E-03	1.98E-04	0.0041	2.1E-04	<b>-108</b>	<b>7</b>
EOL	1.0010	0.99957	-1.43E-03	1.84E-04	0.0039	1.8E-04	<b>-37</b>	<b>5</b>

The CVR of the pin-type core at key times in core life, BOL and EOL, was evaluated, shown in Table 6.2. While it was hypothesized that the larger coolant volume fraction of the pin-type core (40% v. 25% for the TID) would lead to a much larger coolant void reactivity (CVR), the results shown in Table 6.2 indicate that the increased streaming effect during voiding in a pin type core dominates and leads to a lower unrodded CVR at BOL than for the comparable TID core ( $-63 \pm 7\phi$  v.  $-39 \pm 5\phi$ ). While the larger diluent concentration in the pin core might also be a suspected cause of this disparity (26.1% BeO v. 21% in the TID core), the comparison of the two spectra of these cores in Figure 6.6 shows that the extra diluent does not provide appreciable spectral softening. This is due to the fact that the increase in diluent concentration is small. Further, the higher enrichment of the pin core (19.85 % v.

16.6 % for the TID core) necessary to achieve the same BOL eigenvalue introduces more Pu per unit mass of fuel, negating the small favorable effect of CVR reduction provided by the slight spectral softening. Hence, the enhanced BOL unrodded CVR is due to the increased leakage of the core (also evidenced by the higher enrichment required for a comparable BOL core eigenvalue).

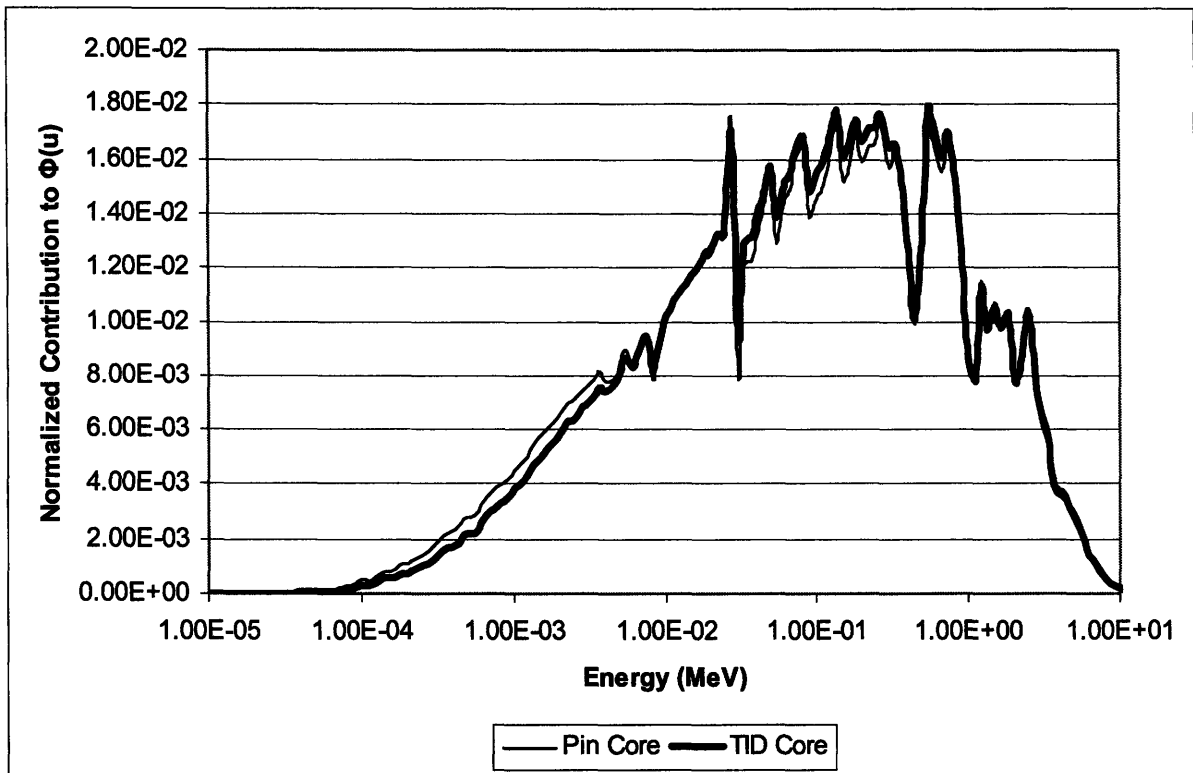


**Figure 6.6: Comparison of BOL Pin-type Core and TID Core Neutron Energy Spectra**

When the BOL rodded and EOL CVRs for the pin-type and TID cores are compared, they are nearly identical ( $-108 \pm 7\%$  at BOL and  $-37 \pm 5\%$  v.  $-35 \pm \%$ , for the Pin and TID cases at EOL), negating any potential advantage that the pin type core may have had in this area. In fact, when comparing the values of rodded CVR for the pin-type core in Table 6.2 with those obtained for the TID core at BOL, the most reactive time in core life, and at EOL ( $-108 \pm 7\%$ ,  $-119 \pm 7\%$ ,  $-35 \pm 5\%$ , respectively), the TID core provides comparable or more favorable CVR values throughout core life.

#### 6.4.4 Active Reactivity Control

Similar to the analyses performed for the TID core in this area, several MCNP runs were performed to determine if the core would be protected against the “stuck rod” criteria. Figure 6.3 shows a schematic of the 1/6<sup>th</sup> pin-type core model and the accompanying control rod positions. Table 6.3 shows the results of these MCNP runs. Clearly there is enough shutdown margin provided by the control rods to satisfy the one stuck rod criterion, no matter which rod gets stuck. Furthermore, the results in Table 6.3 show that the core is protected even if 6 rods get stuck at the most reactive time in core life. It is important to note that depletion in the Boron-10 control assemblies is not simulated with burnup, so the values listed in Table 6.3 are overly optimistic. However, there is enough negative reactivity associated with these control assemblies that these numbers can represent a good first order estimate of meeting the one stuck rod criterion.

**Table 6.3:  $k_{\text{eff}}$  Values for Stuck Rod Scenarios at the Most Reactive Time in Life for the Pin-Type Core**

	$k_{\text{eff}}$	STDEV ( $\sigma$ )
All rods at critical position	0.99945	0.00015
All rods in, center rod stuck at critical position	0.96500	0.00041
All rods in, all rods in 4th ring stuck at critical position	0.97352	0.00042
All rods in, all rods in 8th ring, position 2, stuck at critical position	0.98023	0.00041
All rods in, all rods in 8th ring, position 3, stuck at critical position	0.98006	0.00037

**Table 6.4: Control Rod Worth at the Most Reactive Time in Life for the Pin-Type Core**

	Worth ( $\Delta\rho$ )	Worth (\$)	STDEV ( $\sigma$ ) (\$)
Center Rod	2.72E-03	0.60	0.12
All Rods in 4th Ring (6)	1.11E-02	2.44	0.17
1 rod in 4th ring, assuming equal worth	1.84E-03	0.41	0.03
All Rods in 8th Ring, position 2 (6)	1.29E-02	2.84	0.18
1 rod in 8th ring, position 2, assuming equal worth	2.15E-03	0.47	0.03
All Rods in 8th Ring, position 3 (6)	1.30E-02	2.86	0.18
1 rod in 8th ring, position 3, assuming equal worth	2.16E-03	0.48	0.03
Total Worth all rods	5.81E-02	12.81	0.59
Average Control Rod Worth	3.06E-03	0.67	0.03

Several MCNP runs were performed in an effort to quantify the worth of each of the control rods within the core. Because of the 1/6<sup>th</sup> model symmetry, the worth of each of the

corresponding 6 rods in the whole core, modeled as 1 rod in the 1/6<sup>th</sup> model, was assumed equal. Table 6.4 shows the results of these runs. Of interest is that the worth of all of the control rods (measured individually) is  $\leq$  \$0.60, with the average control rod worth measured from the all-rods-in and all-rods-out core eigenvalues  $\sim$ \$0.67. As well, with the exception of the center rod, all of the values are fairly close, owing to the flat radial power distribution in the core. The relatively low control rod worth and even worth values throughout the core bode well for future safety analyses.

#### 6.4.5 Increase in the Active Height of the Core

In an effort to extend the reactivity limited lifetime of the pin type core, the core height was extended by 1 m, thereby adding more heavy metal inventory. It should be noted that the motivation as well as the analysis for this investigation was purely neutronic in nature. Hence it is likely that the 1m taller core will not meet all of the thermal hydraulic constraints set forth for this core design, specifically the pressure drop criterion. However, this pressure drop criterion is not a hard one and can be relaxed at the expense of PCS efficiency and increased power requirements during decay heat removal. This is because a taller core means increased pressure drop and the shorter pin-type core is already near the limit set for this parameter. However, a taller core with the same power rating translates into a lower linear heat generation rate for the fuel, which would lower the fuel and cladding temperatures. This will be counteracted by the longer axial distance over which heat is added, the balance of which remains to be seen. As well, it should be noted that the comparison between the 1m taller pin core and the TID core is not a “fair” one as the 1m taller core adds  $\sim$ 18.1 m<sup>3</sup> of core volume, a nearly 65% increase. Still, this example is illustrative as it further explores the conditions under which a pin-type core might give performance comparable to a TID core.

Compared with that seen for the Tube-in-Duct (TID) fueled core and the original pin-type core design in Figure 6.7, the reactivity limited burnup for the increased active height pin core was slightly greater than that of the original pin-type core (80 v. 61.6 MWd/kg). The fact that there was a much larger heavy metal loading for the taller pin-type core versus its shorter pin-type cousin (65% - 146767 kg v. 88823) yields a much longer reactivity



limited lifetime (13.39 EFPY v. 6.24 EFPY). Further, the critical enrichment of the 1m taller core is lower (core averaged 18.82 v. 19.85 % TRU), indicating better neutron economy. As well, the sustainably flat radial power profile achieved with the original pin core is obtainable with this 1m taller core, shown in Figure 6.8. Finally, the void reactivity values for the 1m taller core were not as good as for the shorter core, presumably due to the loss of “pancake effect.” These void reactivity values are compared in Table 6.5. Still, the void reactivity remains negative throughout core life for the 1m taller case, but approaches 0 at MOL and EOL, and may even be slightly positive, when uncertainty is accounted for.

**Table 6.5: Void Reactivity Comparison between the Pin-Type Core and the 1m Taller Pin-Type Core**

Time in Life	k <sub>eff</sub> , nominal	k <sub>eff</sub> , voided	CVR Δρ	STDEV (σ)	Effective Delayed Neutron Fraction (β <sub>eff</sub> )	STDEV (σ)	CVR ϕ	STDEV (σ) ϕ
<b>1m taller Pin Core</b>								
<b>UNRODDED</b>								
BOL	1.0203	1.01945	-8.2E-04	2.2E-04	0.0038	2.0E-04	-21	6
MOL	1.02357	1.02341	-1.5E-04	2.1E-04	0.0042	1.9E-04	-4	5
EOL	1.00041	1.00033	-8.0E-05	1.9E-04	0.0043	1.9E-04	-2	4
<b>RODDED</b>								
BOL	0.99969	0.99713	-2.57E-03	2.2E-04	0.0039	2.5E-04	-66	7
MOL	1.00119	0.99974	-1.45E-03	2.1E-04	0.0040	1.9E-04	-37	5
EOL	1.00041	1.00033	-8.0E-05	1.9E-04	0.0043	1.9E-04	-2	4
<b>Original Pin Core</b>								
<b>UNRODDED</b>								
BOL	1.02007	1.01761	-2.37E-03	2.3E-04	0.0038	1.9E-04	-63	7
EOL	1.0010	0.99957	-1.43E-03	1.8E-04	0.0039	1.8E-04	-37	5
<b>RODDED</b>								
BOL	0.99948	0.99509	-4.41E-03	2.0E-04	0.0041	2.1E-04	-108	7
EOL	1.0010	0.99957	-1.43E-03	1.8E-04	0.0039	1.8E-04	-37	5

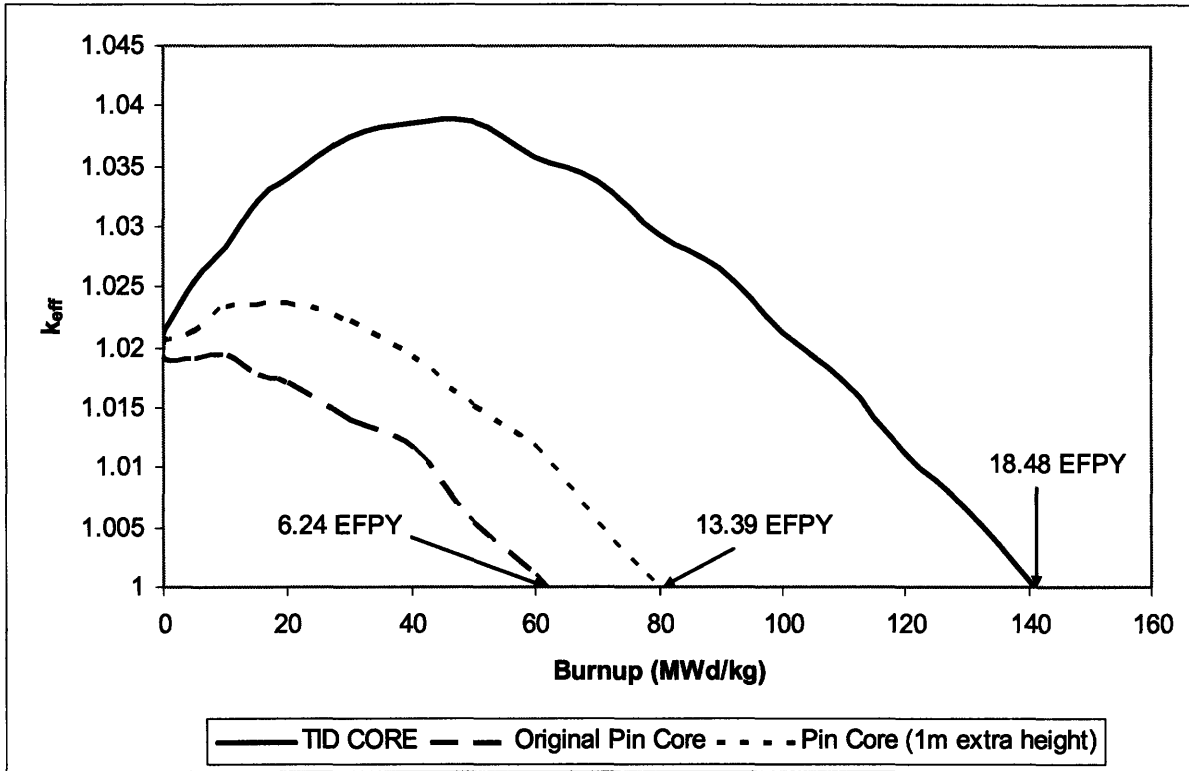


Figure 6.7: Comparison of Reactivity Limited Burnups Among TID and Pin Core Options

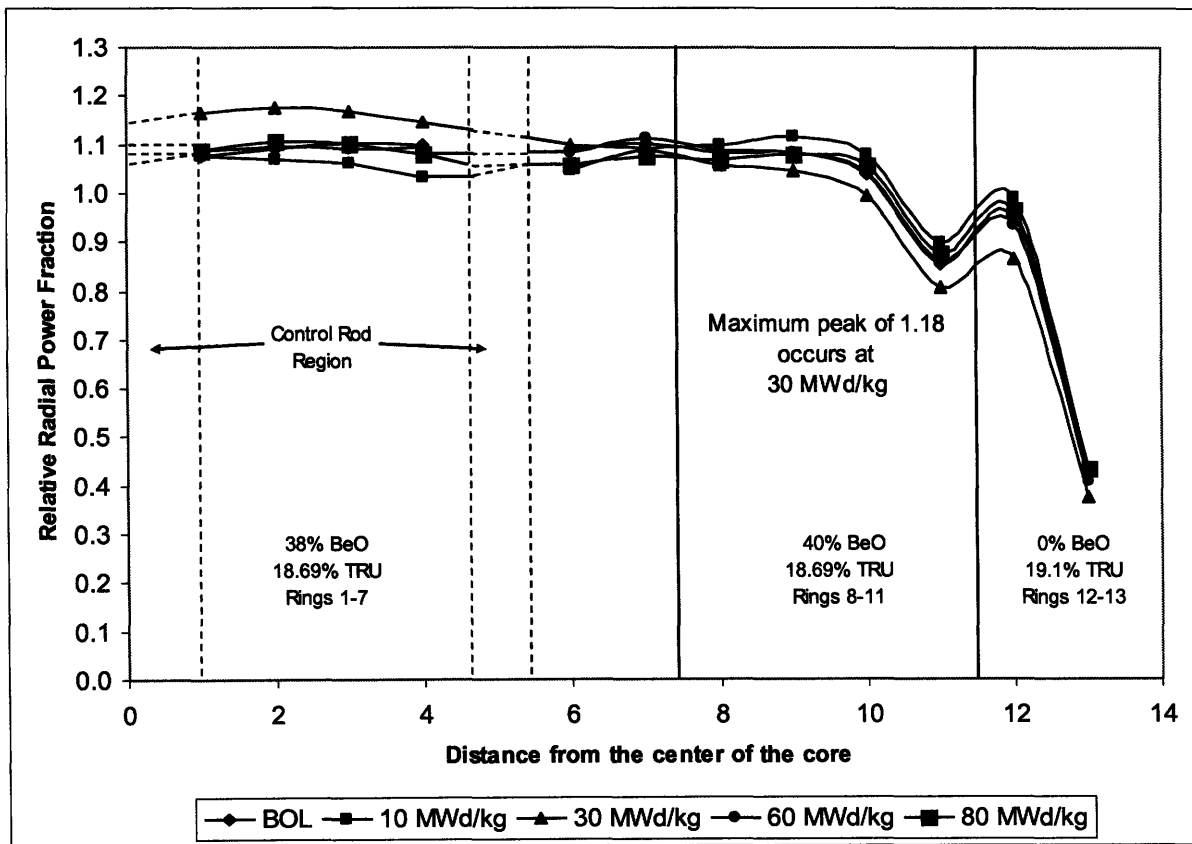


Figure 6.8: Unrodded Radial Power Shape as a Function of Burnup for the Taller Pin Type Core

## 6.5 Summary and Conclusions

**Table 6.6: Comparison of Key Neutronic Performance Criteria Among the TID and Pin-Type Cores**

	TID Core	Pin Core	1 m taller Pin Core
Reactivity Limited Burnup (MWd/kg)	140	61.6	80
Reactivity Limited Lifetime (EFPY)	18.48	6.24	13.39
Specific Power (kW/kg <sub>HM</sub> )	20.7	27.02	16.3524
Heavy Metal Loading (kg <sub>HM</sub> )	115942	88823	146767
Reactivity Swing (pcm)	3726	2017	2312
Diluent (BeO) Zoning (% BeO)	30/33/00	38/40/00	38/40/00
Core Average BeO (volume %)	21	26.1	26.1
Enrichment Zoning (% TRU)	16.6/16.6/16.4	19.85/19.85/19.85	18.69/18.69/19.1
Core Average Enrichment (% TRU)	16.53	19.85	18.83
Coolant Volume Fraction (unit cell)	25	35	35
Maximum Rodded CVR ( $\phi$ )	-36±5 (EOL)	-37±5 (EOL)	-2±4 (EOL)

In the event that the TID fuel concept is not realizable, a pin-type core alternative was designed as a fallback option. Significant shortcomings were observed with pin-type fuel in its much shorter burnup capability, inability to achieve a CR~1, and higher critical enrichment. This is due primarily to the much lower fuel volume fraction ( $v_f$ ) and consequently poor neutron economy. Conversely, the lower  $v_f$  gave very favorable results with respect to CVR, as axial leakage was enhanced. In an effort to improve the short lifetime of the pin-type core, an extra meter of core height was added in order to increase the heavy metal loading and improve the neutron economy by reducing axial leakage. While this was effective in increasing the reactivity limited lifetime and reducing the critical enrichment, it increased the contribution of CVR upon voiding. This demonstrated the fundamental design trade-off between neutron economy and CVR reduction through leakage.

Still, the 1m taller core was able to achieve negative CVR throughout life. It should be noted that the 1m taller core was assessed with respect to neutronic design criteria only, and that it will likely challenge some of the thermal hydraulic design criteria for this core, owing to its increased height. The neutronic performance of the TID core and both pin type cores is summarized in Table 6.6.

In conclusion, the superiority of the TID core has once again been proven, this time on a whole-core scale. Equally as important, both the feasibility and shortcomings of a core design using a more realizable and proven fuel type have been demonstrated.

## 7 Internally Cooled Annular Fuel (ICAF) CORE DESIGN

### 7.1 Introduction

Internally Cooled Annular Fuel (ICAF, illustrated in Figure 7.1) is being explored for GFR application due to its promise in LWRs, with the hopes that these benefits will translate directly. Specifically, ICAF can provide increased power densities at comparable fuel and cladding temperatures, when compared to pin-type fuel, due mainly to (1) having 2 surfaces for transferring the heat created in the fuel and (2) a reduction in thickness of the heat conduction path (when compared to a traditional fuel pin of the same diameter) [Kazimi, 2006]. The main drawbacks of such a fuel are a lack of irradiation and manufacturing experience comparable to pin-type fuel and the inherently lower fuel volume fraction of such an approach. The latter of these disadvantages is crucial in a current generation fast reactor, as higher fuel volume fractions are necessary to ensure a conversion ratio  $\sim 1$  without the use of external blankets.

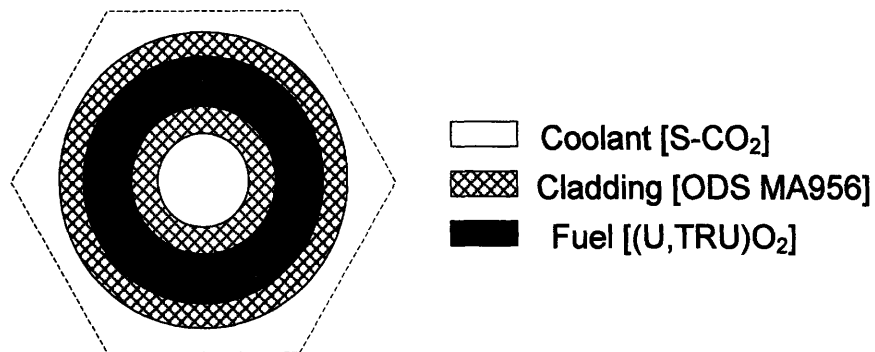


Figure 7.1: Unit Cell Representation of Internally Cooled Annular Fuel (ICAF)

## 7.2 Thermal Hydraulic Analysis and Results

In order to begin the process of designing the ICAF core, the standardized process described in the previous chapter was used (see Section 6.2). The same steady state hydraulic constraints and core-macro design parameters used in the TID and pin-type core designs were used (see Table 5.3 for a listing of these parameters). Again, wire-wrap is used instead of grid spacers for the same two reasons as in the pin-type core case: (1) to put ICAF on a more even comparative basis with respect to TID fuel, which enjoys a distinct advantage with respect to pressure drop (and to be consistent with the analyses done for the pin-type core) and (2) in order to maximize the fuel volume fraction ( $v_f$ ), in an effort to maximize reactivity limited burnup and hence, economic performance of the core.

Given the chosen macro-geometric parameters, a lattice of hexagonal unit cells, each with a ICAF pin at its center, was simulated in order to calculate the thermal hydraulic parameters of interest. These calculations were performed using the FLOWSPLIT-MATLAB interface described in Chapter 5, so that many combinations of core micro-geometric parameters, i.e. fuel pin pitch and diameter, could be efficiently analyzed.

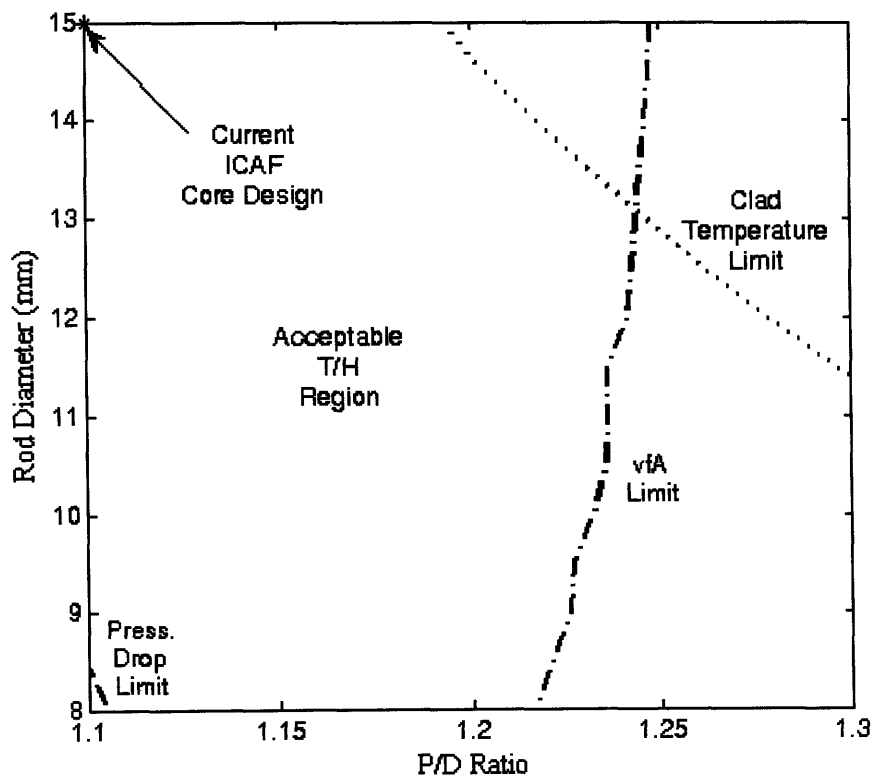


Figure 7.2: Acceptable T/H Envelope for the ICAF Core

The results of these calculations are the same as those presented in Chapter 5 for the thermal hydraulic calculations for the ICAF core with integrated BeO and are shown again in Figure 6.2. As shown in the previous chapter with the pin core design, it is not necessarily desirable to minimize  $v_c$ , hence P/D, in order to minimize CVR. In fact, the leakage effect for pin-type fuel was shown to dominate the contribution to CVR, indicating that one would want to maximize  $v_c$  in order to minimize CVR. This would have the concomitant effect of not only increasing the critical enrichment necessary at BOL, and worsening neutron economy, but also would reduce  $v_f$  and consequently, the BOL heavy metal loading and achievable burnup. Since minimizing P/D for the pin type case still produced acceptable CVR values, and minimizing P/D has the added benefit of reducing leakage, improving neutron economy, and maximizing  $v_f$ , the approach taken here is to minimize P/D and maximize  $v_f$ . This translates into the design point shown in Figure 6.2, which defines the micro-geometric parameters, i.e. fuel pin diameter and pitch, for the ICAF core.

The values of the key thermal hydraulic constraints for the ICAF core at the chosen geometry are compared with those for the TID and pin-type core designs in Table 6.1. It should be remembered that these values can change, depending upon the spot chosen within the applicable acceptable thermal hydraulic envelope for each fuel type. Further, the spot chosen for each of these fuel types was that which maximized fuel volume fraction ( $v_f$ ) and hence, reactivity-limited burnup. In choosing the spots within the acceptable thermal-hydraulic envelopes which maximized the performance of each of the respective fuel types, a fair comparison between the thermal-hydraulic performance of the ICAF, pin-type, and TID cores can be made.

**Table 7.1: Comparison of Thermal-Hydraulic Parameters for TID and Pin Core Designs where Performance is Optimized**

Fuel Type	Peak Cladding Temperature	Peak Fuel Temperature	Pressure Drop
ICAF	750°C	1177°C	267 kPa
Pin	735.6°C	1800°C	435 kPa
TID	810°C	1770°C	420 kPa

Based solely on the T-H results shown in Table 6.1, the ICAF seems to outperform its pin-type and TID contemporaries, as it offers a significantly lower core pressure drop and

peak fuel temperature. However, it should be remembered that the parameters displayed for each of the fuel types in Table 6.1 are for the design point in their respective acceptable thermal hydraulic envelopes which corresponds to the maximum  $v_f$  allowable for that strategy. Recalling the results from Chapter 5, both the TID and pin-type fuel had significantly large enough acceptable thermal-hydraulic envelopes to confer comparable or better performance on the ICAF fuel at comparable or better fuel volume fractions. Hence, when compared on a more even basis, i.e. with respect to  $v_f$ , the ICAF loses any unique advantage it may have had.

### 7.3 Neutronic Analysis and Results

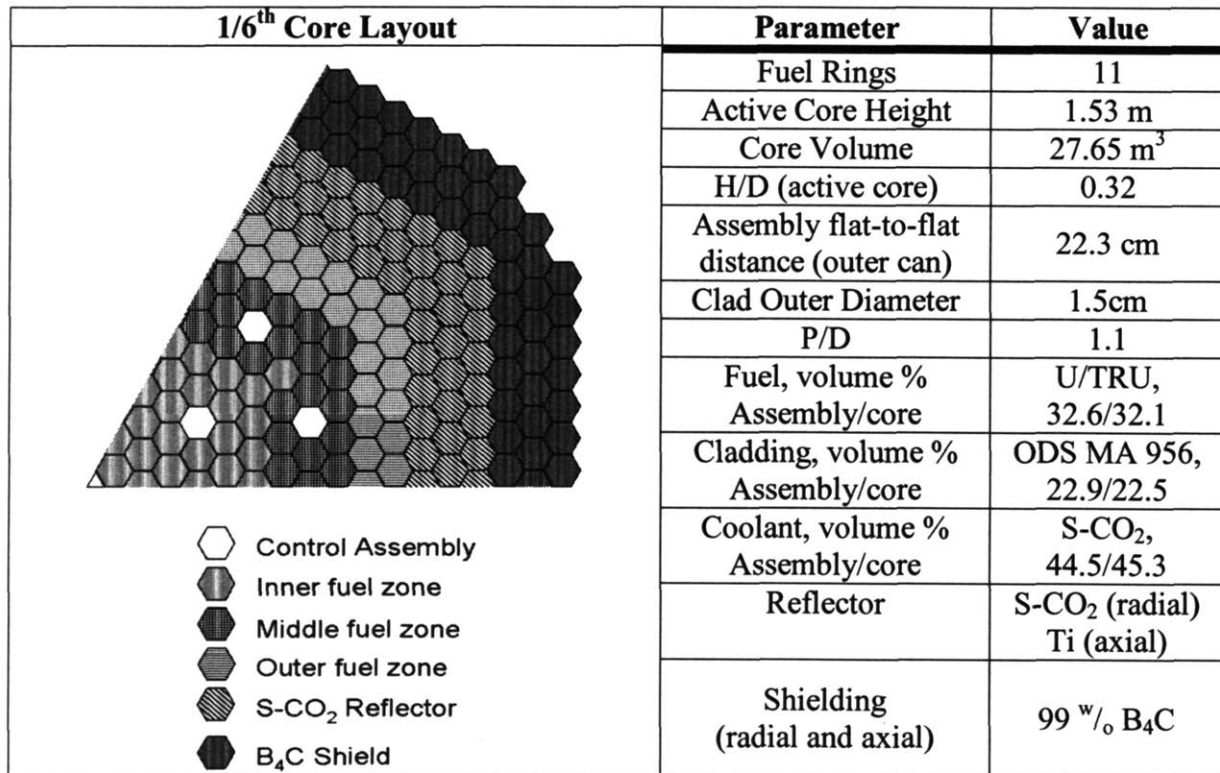


Figure 7.3: Pin-Type Core Layout and Key Parameters

Based on the previously defined core-macro geometric constraints and the results of the thermal hydraulic analysis, an ICAF core of layout and parameters described in Figure 6.3 was designed. The same steady state neutronic criteria that were used to evaluate the TID and pin-type cores were used as for the ICAF core. Further, the results of this analysis are



evaluated against not only the goals of the GFR core design, but also against the performance of the TID and pin-type cores.

### 7.3.1 Achievable Burnup

Figure 6.4 shows the reactivity limited burnup of the ICAF core that was developed, compared with that of the TID and pin-type cores. Most notable is the significantly shorter reactivity-limited burnup and lifetime of the ICAF core as compared to the TID and pin-type cores (26 MWd/kg v. 140 MWd/kg v. 61.6 MWd/kg and 1.71 EFPY v. 18.48 EFPY v. 6.24 EFPY). This is due to the much lower fuel volume fraction ( $v_f$ ) inherent in the ICAF core which does not allow a sufficient conversion ratio during burnup to achieve a sustainable core without the use of external blankets.

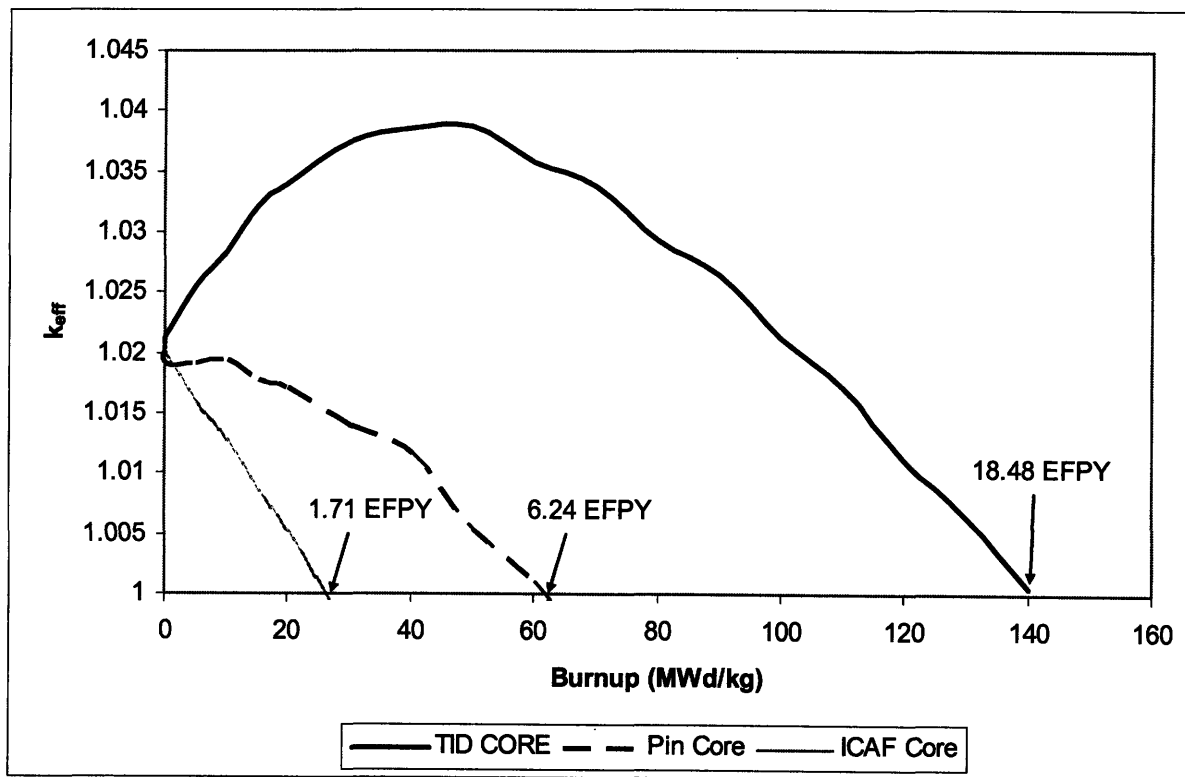


Figure 7.4: Comparison of Reactivity Limited Burnups of the TID and Pin-Type, and ICAF Cores

Another fundamental reason for this difference is the much larger leakage, hence poorer neutron economy, in an ICAF core, demonstrated by the much larger enrichment necessary to achieve the same BOL eigenvalue (16.6 % TRU v. 19.85 % TRU v. 25.1 %).

TRU, for the TID, pin-type, and ICAF cores, respectively). While the increased leakage will be shown to be beneficial from a CVR standpoint, the resulting short reactivity limited lifetime and increased BOC enrichment is too much of a drawback to make such a core economically practical.

Exacerbating an already low  $v_f$  is the use of diluent, which displaces much needed fuel that could be used to extend the lifetime of an ICAF core. While the use of diluent does increase the critical enrichment and shorten the reactivity limited lifetime of the core, its use is necessary in order to effectively shape power. Even without the use of diluent, the large leakage inherent in an ICAF core would still render it at a significant disadvantage with respect to BOC enrichment and reactivity limited burnup when compared with the TID or pin-type cores. As well, the larger diluent concentration used in the ICAF core (27.5% core average, v. 21% for the TID core and 26% for the pin-type core), puts it at a greater disadvantage and is again a consequence of the larger leakage inherent in such a design.

### 7.3.2 Radial Power Peaking

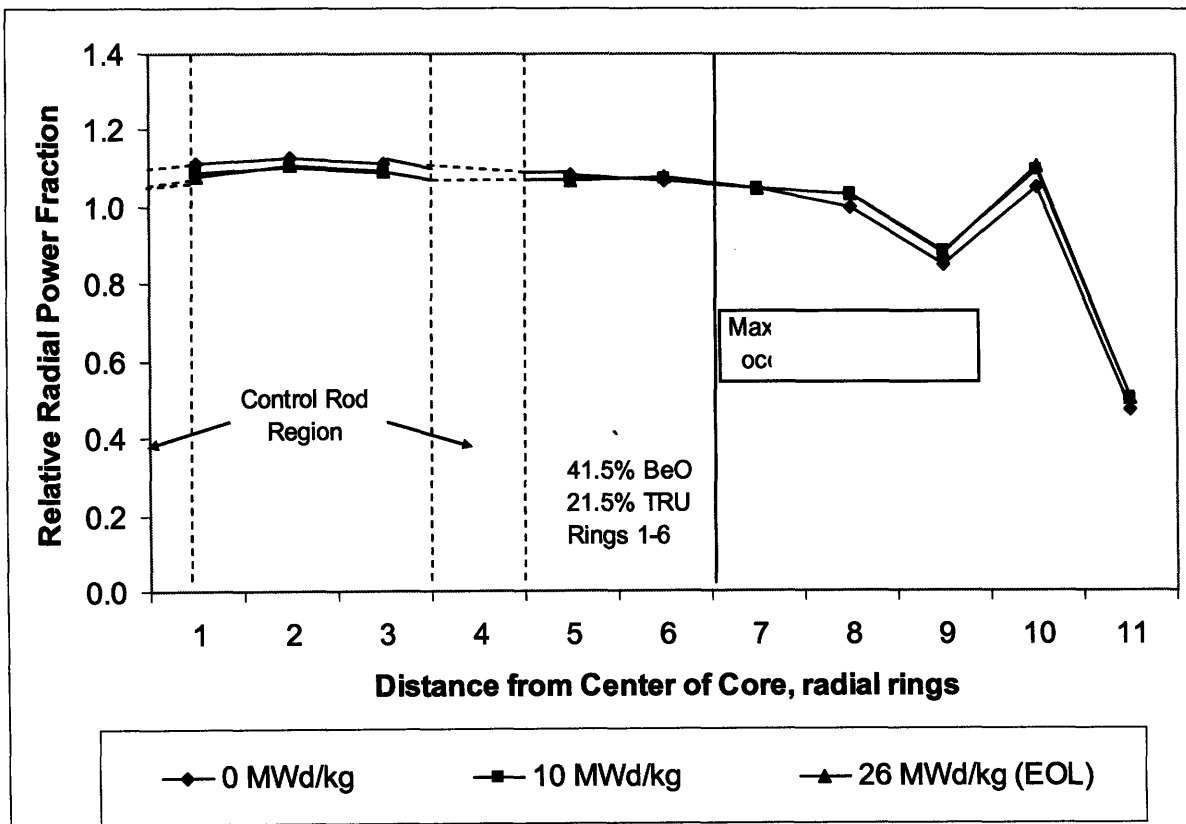


Figure 7.5: Unrodded Radial Power Shape as a Function of Burnup for the ICAF Type Core

Once the reactivity limited burnup of the ICAF core was assessed, its ability to hold a relatively flat radial power shape was examined. Displayed in Figure 6.5, the ICAF core is shown to hold its unrodded radial power shape very well over its brief life, with the peak of 1.13, which is maintained throughout much of core life, varying only slightly. The relatively flat radial power profile achievable for the ICAF core is comparable to that achievable by the pin-type core (1.14) and lower than that achievable for the TID core (1.34). This is for the same two reasons that the pin-type core is able to achieve a relatively flatter radial power shape over its life: (1) significantly shorter burnup and (2) the lower fuel volume fraction of the ICAF core, resulting in physically less fuel to burn up in a spatially uneven manner. Consequently, the ICAF core shares this benefit with the pin-type core when compared with the TID core; however, this advantage is not enough to overcome the large shortcoming of its much shorter lifetime.

### 7.3.3 Passive Reactivity Control

**Table 7.2: Coolant Void Reactivity at BOL and EOL for the Pin Core Design**

Time in Life	keff, nominal	keff, voided	CVR $\Delta\rho$	STDEV ( $\sigma$ )	Effective Delayed Neutron Fraction ( $\beta_{eff}$ )	STDEV ( $\sigma$ )	CVR $\rho$	STDEV ( $\sigma$ ) $\rho$
<b>UNRODDED</b>								
BOL	1.02025	1.01555	-4.54E-03	1.84E-04	0.0036	2.0E-04	<b>-125</b>	<b>9</b>
EOL	1.00088	0.99579	-5.11E-03	1.98E-03	0.0037	1.8E-04	<b>-139</b>	<b>9</b>
<b>RODDED</b>								
BOL	0.99981	0.99345	-6.40E-03	2.06E-04	0.0037	1.9E-04	<b>-173</b>	<b>11</b>
EOL	1.00088	0.99579	-5.11E-03	1.98E-03	0.0037	1.8E-04	<b>-139</b>	<b>9</b>

The CVR of the ICAF core at key times in core life, BOL and EOL, was evaluated, as shown in Table 6.2. Of the cores designed for the three fuel types explored in this work, the ICAF core yields the lowest CVR values throughout core life. Again, this is due to the large leakage inherent in this fuel design, which enhances streaming during voiding. While it does have the largest diluent loading of all of the core design options explored (27.1% v. 26.1% for the pin type core and 21% in the TID core), the slight increase in this factor compared to the pin type core does not account for the larger increase in CVR values (see Table 6.2 for pin core CVR values).

#### 7.3.4 Active Reactivity Control

Given that the control assembly strategy that was used for the TID core, i.e. size and number of assemblies, was nearly identical to that used for the ICAF core and that the reactivity swing of the ICAF core is nearly half that of the TID core (1962 v. 3726 pcm), the active reactivity control requirements for the ICAF core should be sufficient to meet the goals set forth in this area (defined in Chapter 4, Table 4.10). Furthermore, the excessively short reactivity limited lifetime of this type of core eliminates it from competition with the other two fuel types and expenditure of further resources or analysis is not worthwhile.

### **7.4 Summary and Conclusions**

While promising for LWR applications, the inherently smaller  $v_f$  coupled with its large leakage makes ICAF unsuitable for GFR use. The consequence of these two shortcomings is a high BOC enrichment and a prohibitively short core lifetime, both of which make this approach both economically unattractive and inferior to the other two fuel types, pin and TID. While this core is able to maintain a fairly flat radial power profile and has very favorable CVR values over core life, these benefits are not enough to overcome its large shortcomings. Once again, the superiority of the TID core has been confirmed.

## 8 Waste Management

### 8.1 Introduction

An important part of any reactor strategy, the management of Minor Actinides (MA) and Transuranics (TRU) is a central part of the Generation-IV design philosophy. Specifically, Gen-IV reactors should be designed to minimize their waste production in order to reduce the long-term stewardship burden. Minimizing waste production means minimizing not only the physical amount of MA/TRU production, but also minimizing the radiotoxicity of MA and long-lived fission products. Figure 8.1 shows that the key contributors to radiotoxicity for spent PWR fuel in the long term are TRU, Tc-99 and I-129. As well, Sr-90 and Cs-137 play a strong role in the short term, but quickly decay away. It should be noted that the term “radiotoxicity” refers to the amount of water needed to dilute waste in-situ to a permissible concentration, and does not take account of constituent tendencies to migrate back into the biosphere from the site of entombment. Taking into account this tendency for migration, Figure 8.2 shows that the three largest contributors to public radiation exposure due to the stored LWR waste at Yucca Mountain are Tc-99, I-129, and Np-237. In fact, [Kondo and Takizuka, 1994] showed that the radiotoxicity of nuclear waste could be reduced to that of natural uranium ore after about 1000 years if the MA’s, Tc-99, and I-129 were removed. An illustration of this concept is provided in Figure 8.3 [Hejzlar, 2005]. Hence, the mass flows of these constituents will be key parameters of interest.

Coupled closely with waste minimization is the philosophy that Gen-IV fuel cycles should be proliferation resistant and an unattractive target for diversion of weapons-grade materials [GIF, 2002]. This means designing fuel cycles which not only produce less

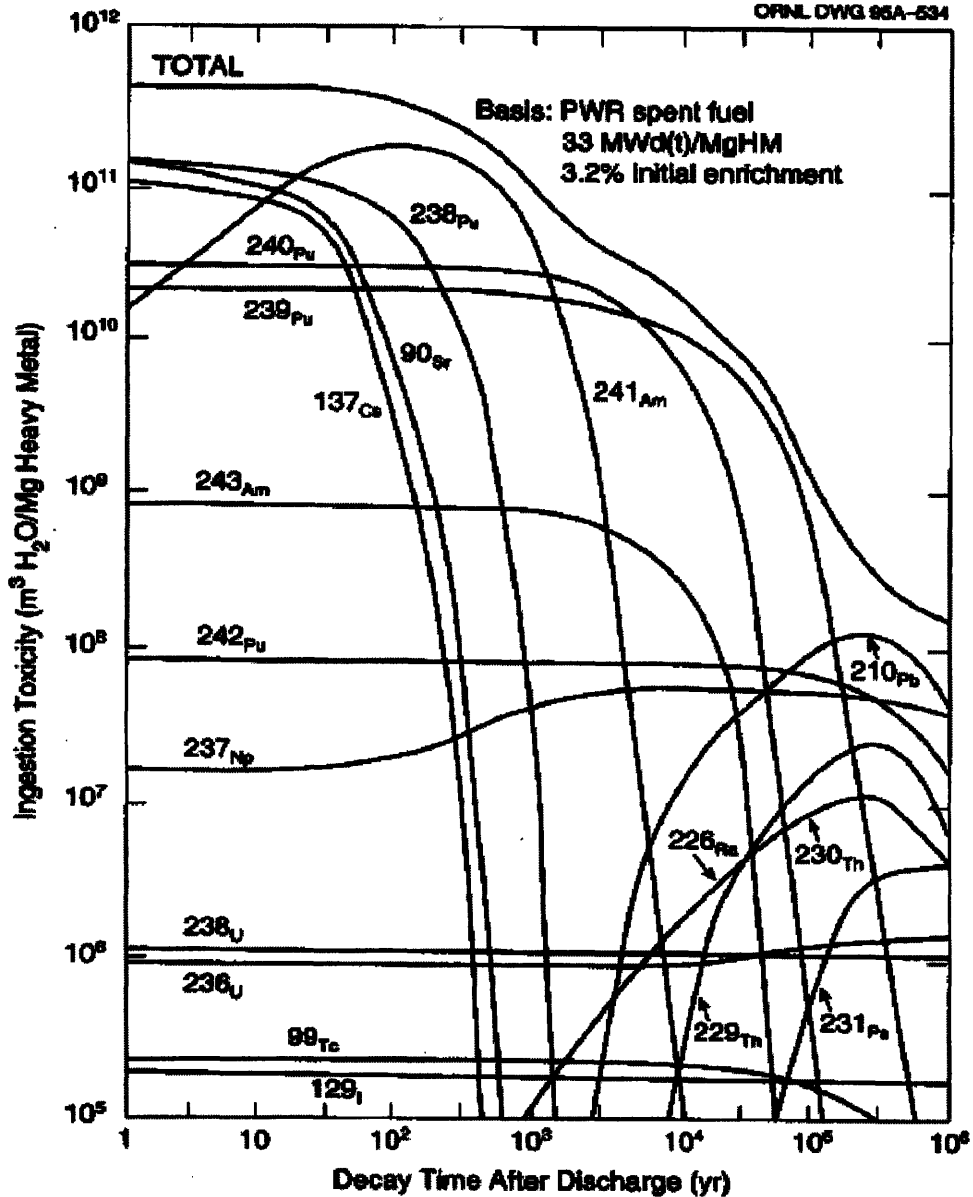


Figure 8.1: Isotopic Contribution of Spent LWR Fuel to Radiotoxicity [ORNL, 1995]

weapons-usable materials, but also make the extraction of these materials more difficult. It is these two philosophical underpinnings which will help to serve as a both a goal for, and a basis for evaluation of, the performance of the core design presented in this work.

In an effort to assess the ability of the subject GFR to manage key long-lived fission products and MA/TRU, the total amount of these constituents, broken down by isotope, will be quantified. These amounts will be assessed on a mass per annum, as well as a mass per

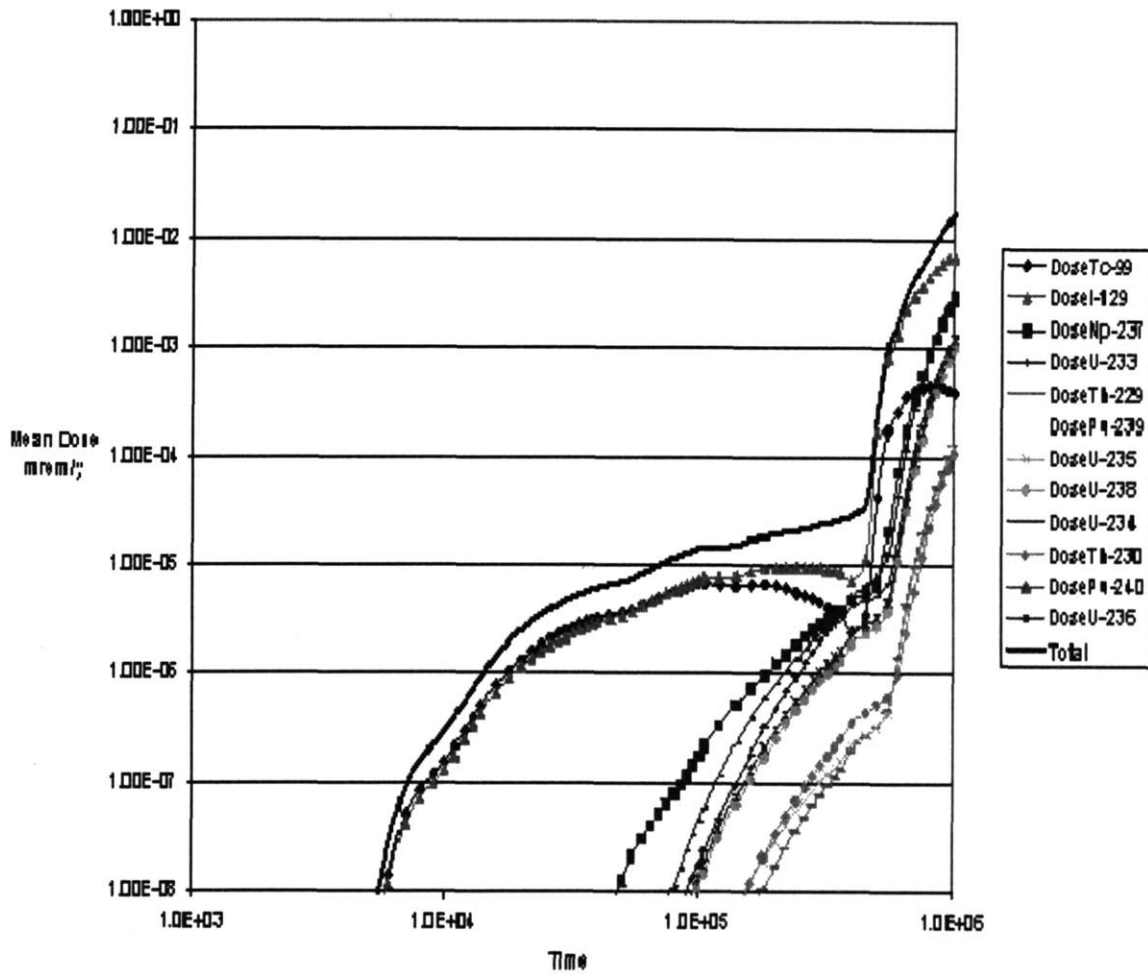


Figure 8.2: Expected Radiation Exposure from Yucca Mountain by Constituent [Forsberg and Driscoll, 2006]

electrical energy produced basis, in order to provide a fair measure of comparison. The TID GFR core will be compared with current once-through LWR practice, as well as a competing closed-cycle Gen-IV design, the Lead-cooled Fast Reactor.\* Table 8.1 lists the relevant characteristics of these three reactors used for the comparison.

\* The LFR used here for comparison is being designed as a flexible conversion ratio type reactor as part of the Nuclear Energy Research Initiative (NERI) Project 06-040: Flexible Conversion Ratio Fast Reactor Systems Evaluation [Todreas and Hejzlar, 2007]. The LFR example used for comparison in this work is the Conversion Ratio (CR) = 1 case.

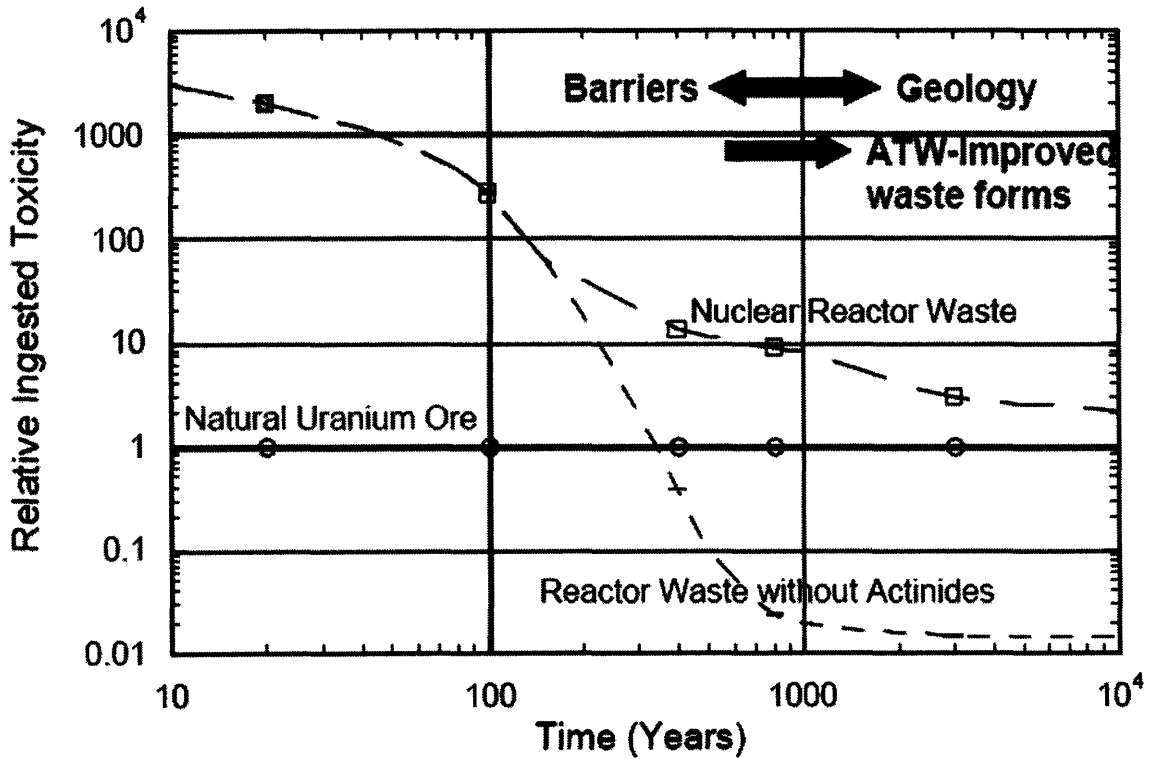


Figure 8.3: The Impact of Removing Actinides from Nuclear Waste on Radiotoxicity [Hejzlar, 2005]

Table 8.1: Comparison of Operating Characteristics of an LWR, GFR, and LFR

	LWR	GFR	LFR
Thermal Rating ( $MW_{th}$ )	3400	2400	2400
Thermal Efficiency	0.33	0.47	0.47
Electrical Rating ( $MW_e$ )	1122	1128	1128
Capacity Factor	0.9	0.9	0.9
Specific Power ( $kW/kg_{HM}$ )	38.7	20.7	42.7
Effective Full Power Days (EFPD) per cycle	N/A (not needed for the calculations performed in this chapter)	6750 EFPD (1 <sup>st</sup> cycle) 6542 EFPD (2 <sup>nd</sup> cycle) 6268 EFPD (3 <sup>rd</sup> cycle)	1800 EFPD



## 8.2 Tc-99 and I-129 Production in the TID Core

While fission product creation is inevitable, it is desired to minimize the amount created from a waste burden perspective. Specifically, Tc-99 and I-129 dominate the long term radiotoxicity of fission products in spent nuclear fuel [Kawashima et al., 1995], as well as the long term radiation dose to the public [Forsberg and Driscoll, 2006]. Consequently, it is desirable to minimize the contribution of these isotopes to minimize the waste burden.

**Table 8.2: Comparison of Long Lived Net Fission Product Production Among a PWR, GFR, and LFR**

Isotope	PWR	GFR TID Core	LFR
	[Tommasi et al, 1995]	Cycle Average	[Shwageraus, 2007]
	(kg/TWh <sub>e</sub> )		
Tc-99	2.94	1.94	2.16
I-129	0.68	0.64	0.70
	(kg/TWh <sub>TH</sub> )		
Tc-99	0.97	0.91	1.01
I-129	0.22	0.30	0.33
	(kg/yr)		
Tc-99	26.02	17.30	19.20
I-129	6.02	5.69	6.25

Table 8.2 compares the production of these 2 isotopes in the TID core against both current PWR practice and a Gen-IV contemporary, the Lead Fast Reactor (LFR). The comparison is made on a mass per unit of electricity produced, a mass per unit of thermal power produced, and a mass per annum basis (assuming a 90% capacity factor for all cases). The TID core enjoys a slight advantage in this area, as it produces less of these radiotoxic isotopes per unit of electricity output and per annum of both Tc-99 and I-129 as compared to the PWR and LFR. The TID core exhibits nearly comparable performance with respect to I-129 production on a kg/TWh<sub>th</sub> basis. With respect to the LWR, the slight performance advantage of the GFR core can be attributed to three factors: (1) the lower thermal rating of the GFR, which translates into a lower number of fissions, and hence fission products, (2) the lower fission yield from the primary fissile isotope in the core (U-235 for the LWR and Pu-239 for the GFR), shown in Table 8.3, and (3) the larger ratio of the spectrum-averaged absorption cross section ( $\overline{\sigma_a}$ ) of Tc-99 and I-129 to that of the respective primary fissile

**Table 8.3: Comparison of Spectrum-Averaged Cross Sections ( $\overline{\sigma}_a$ ) and Fission Yields among a PWR, GFR, and LFR**

	Tc-99	I-129	Pu-239	U-238	U-235
Production					
Fission Yield from U-235 (LWR)	4.16E-05	1.80E-04	-	-	-
Fission Yield from Pu-239 (FR)	6.01E-06	1.80E-04	-	-	-
Consumption					
PWR $\overline{\sigma}_a$ (b) [Croff, 1980]	9.14	3.22	164.8	1	57
$\overline{\sigma}_a$ ratio with U-235	0.16	0.06	-	-	-
GFR $\overline{\sigma}_a$ (b)	0.92	0.60	3.11	0.43	3.40
$\overline{\sigma}_a$ ratio with Pu-239	0.30	0.19	-	-	-
LFR $\overline{\sigma}_a$ (b) [Shwageraus, 2007]	0.48	0.22	2	0.25	2.05
$\overline{\sigma}_a$ ratio with Pu-239	0.24	0.11	-	-	-

isotope (also shown in Table 8.3). With respect to the LFR, the GFR numbers are roughly comparable, with only a slight advantage. Given that the LFR and the GFR have the same thermal rating and roughly the same fission yields for these isotopes, the difference in performance comes from the larger ratio of the spectrum-averaged absorption cross section of Tc-99 and I-129 to that of the primary fissile isotope, Pu-239, shown in Table 8.3. This difference is due to the slightly softer spectrum of the GFR as compared to the LFR, shown in Figure 8.4. This figure shows that the GFR fuel without diluent (~1/3 of the core) has a slightly softer spectrum than the LFR fuel, presumably due to the use of ceramic fuel. Incorporating diluent further softens the spectrum, pushing more neutrons toward the resonance region of Tc-99 and I-129, shown in Figure 8.5. While the actinides in these cores also have strong absorption in the resonance region, the softening of the spectrum in the GFR has a greater impact on the absorption in Tc-99 and I-129, as shown by the larger ratio of

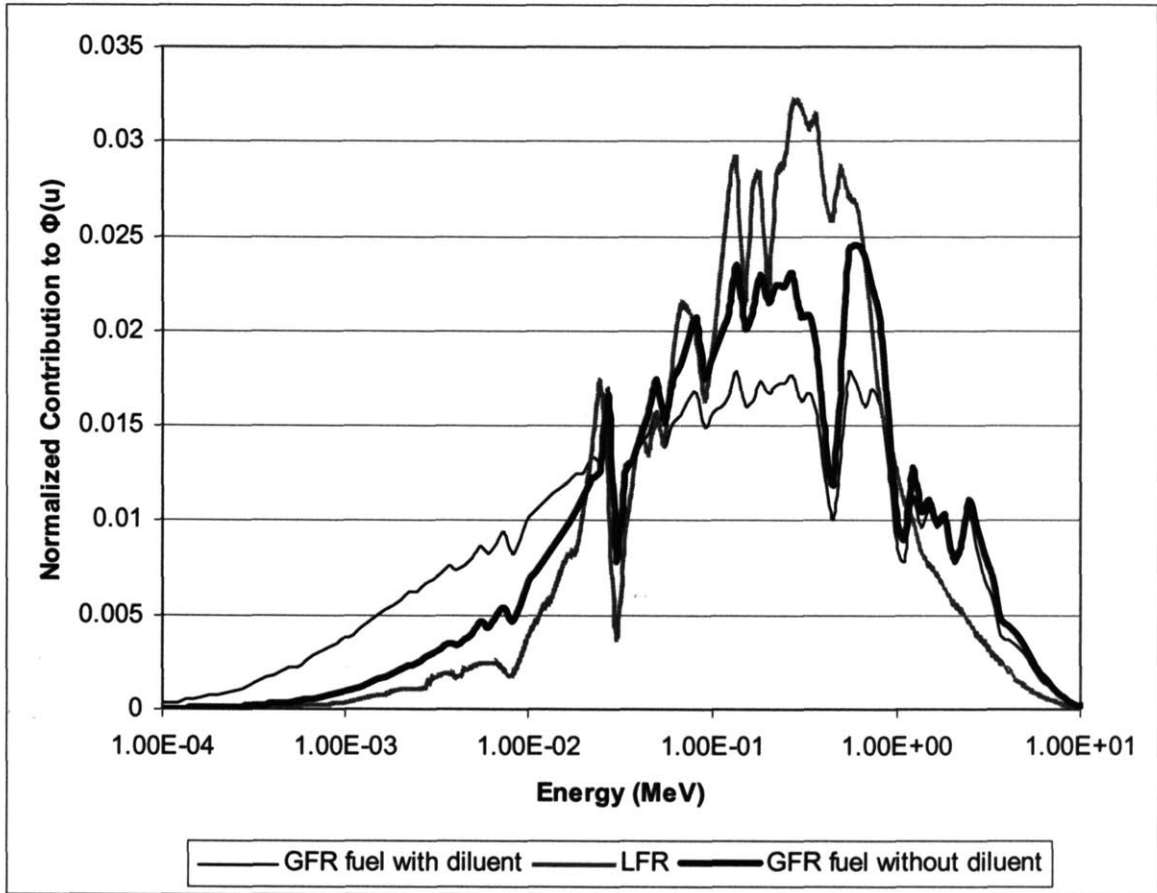


Figure 8.4: Comparison of Neutron Energy Spectra for GFR Fuel with and without diluent with a LFR

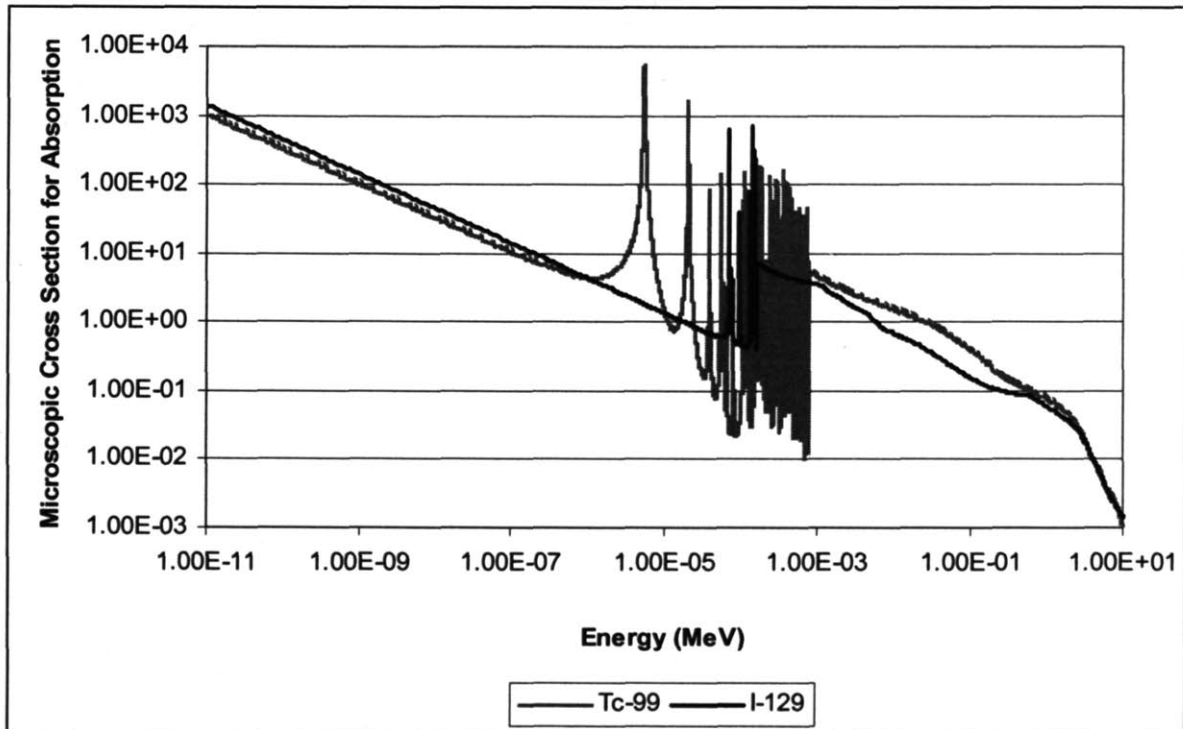


Figure 8.5: Microscopic Cross Section for Absorption (Capture) for Tc-99 and I-129

$\overline{\sigma}_a$  for these isotopes to  $\overline{\sigma}_a$  of Pu-239, shown in Table 8.3. Still, it should be remembered that this advantage is slight and could be within the uncertainty of these numbers.

### **8.3 MA/TRU Management of TID Core**

Table 8.4 gives a detailed accounting of the mass flows of the key MA/TRU isotopes for all 3 cycles of the candidate GFR TID core. The scenario shown assumes no recycle of uranium, in order to stay consistent with the fuel cycle scheme used for the neutronic calculations in Chapter 4; hence, the large amount of net uranium at the end of GFR life. Realistically, the large amount of Uranium used to make up the balance of the fuel matrix would be recycled, significantly lowering the net Uranium usage such that there would be significant uranium consumption instead of the production shown. While there is a small net production of Plutonium, there is a net destruction of MA. The net production of Pu results from (1) a breeding ratio of slightly higher than 1 and (2) the excess Pu that leaves the fuel cycle between “discharge” and “load” between cycles 1 and 2 and cycles 2 and 3. As shown in Table 8.4, the excess Pu that leaves the fuel cycle between cycles 1 and 2 and cycles 2 and 3 is due primarily to (1) the production of higher mass number Pu isotopes with burnup for each cycle and (2) the build-up of Am-242m to near-equilibrium levels at the end of the first cycle. As discussed in Chapter 4, Am-242m is not present in appreciable quantities in LWR spent fuel, but quickly builds up in a fast reactor, due to the harder flux. Since Am-242m has a much larger fission cross section than other actinides, small quantities of Am-242m will add a large amount of reactivity to a reactor, reducing the amount of Pu needed to obtain the same core eigenvalue. Hence, the TRU enrichment for the 2<sup>nd</sup> and 3<sup>rd</sup> cycles (15.9% and 15.8%) is lower than for the first cycle (16.6%), and consequently the amount of the chief fissile isotope in the core, Pu-239, needed for the second and third cycles is less. While Pu-239 remains the dominant fissile isotope in the core throughout cycle burnup, the increase in competition for neutrons (and fission) by Am-242m prevents Pu-239 from returning to beginning of cycle values after building up to a maximum level at the middle of cycle (Pu-239 concentration roughly follows excess reactivity). With more Pu-239 in the core, more Pu-240 is created, and the slight net Pu production throughout GFR life results (due mainly to the Pu-239 and Pu-240, as shown in Table 8.4).

Comparing the results for the candidate TID GFR with those of a PWR [Tommasi et al, 1995] and LFR [Todreas and Hejzlar, 2007], Table 8.5 shows that the candidate GFR performs much better than the PWR with respect to Pu and MA production (not to be confused with inventory, which of course is much larger). In fact, the GFR has a net MA destruction rate, due mainly to its ability to transmute Np-237 and Am-241, as shown in Table 8.4. Recalling Figure 8.2 which showed that Np-237 is one of the key contributors to

**Table 8.4: Detailed Mass Flow of Key MA/TRU Isotopes for All 3 cycles of the Candidate GFR Lifetime**

		Cycle 1			Cycle 2			Cycle 3			
	Isotope ID (ZZAAA)	Load (kg)	Disch. (kg)	After 7y (kg)	Load (kg)	Disch. (kg)	After 7y (kg)	Load (kg)	Disch. (kg)	After 7y (kg)	NET (kg)
U	92234	0	49	78	0	50	75	0	43	65	218
	92236	0	104	109	0	104	108	0	104	109	325
	92235	687	184	187	692	199	201	693	198	200	587
	92238	95917	78871	78871	96624	80322	80322	96736	80362	80362	239554
U TOTAL		96604	79209	79244	97316	80674	80706	97429	80707	80736	240685
Pu	94238	172	531	518	479	465	453	419	409	401	301
	94239	10838	10723	10728	9870	10543	10548	9767	10499	10504	1305
	94240	4989	5958	5975	5491	6174	6197	5739	6322	6345	2299
	94241	172	664	474	428	714	510	472	737	526	438
	94242	1032	899	899	821	765	765	708	694	694	-203
Pu TOTAL		17203	18774	18594	17089	18660	18473	17105	18661	18470	4141
MA	93237	567	259	267	246	153	160	149	119	126	-407
	95241	1233	640	821	756	547	744	688	540	743	-368
	95242M	0	49	47	43	42	41	38	40	39	46
	95243	98	199	199	183	202	202	187	189	189	123
	96242	0	15	0	0	13	0	0	13	0	0
	96243	0	2	1	1	2	1	1	1	1	1
	96244	8	96	73	67	120	92	85	120	91	97
	96245	0	17	17	16	28	28	26	31	31	35
	96246	0	3	3	3	8	8	8	14	14	14
MA TOTAL		1905	1278	1429	1314	1115	1276	1182	1067	1235	-460
TRU (Pu+MA) TOTAL		19108	20053	20023	18403	19775	19749	18287	19728	19705	3681
U+Pu+MA TOTAL		115711	99261	-	115718	100449	-	115716	100435	-	-

**Table 8.5: Comparison of Net Pu and MA Production Among a PWR, GFR, and LFR**

		PWR	GFR	LFR
Pu	kg/TWhr <sub>e</sub>	34.05	7.86	3.32
	kg/yr	241.74	69.91	29.59
MA	kg/TWhr <sub>e</sub>	2.67	-0.87	-12.44
	kg/yr	18.97	-7.77	-110.67
TRU (Pu+MA)	kg/TWhr <sub>e</sub>	36.72	6.98	-9.13
	kg/yr	260.71	62.14	-81.27

personnel dose from a spent fuel repository, i.e. Yucca Mountain, the ability to effectively transmute Np-237 (and Tc-99 and I-129, shown in the previous section) is a big advantage for the GFR, when compared to current LWR practice.

However, when compared to the LFR case, the GFR does not perform as well, as it has a positive TRU (Pu+MA) production rate, while the LFR has a net TRU destruction rate. While the LFR spectrum is slightly harder (as shown in Figure 8.4) which would contribute to greater TRU destruction, the larger reason for the discrepancy in performance between the two is the fuel management philosophy employed in the design of the respective fuel cycles. For the LFR, all of the TRU that remains at the end of a cycle is used in the subsequent cycle. With the GFR, this is not the case. This can be seen by comparing the masses for the GFR and LFR at the end of 7 years of cooling and their respective reloaded masses in the subsequent cycles in Table 8.4 and Table 8.6. Hence, the comparison between the GFR and LFR is not a truly fair one, as different philosophies of actinide management are used for each. It would be possible to use all of the TRU from a previous cycle in the 2<sup>nd</sup> and 3<sup>rd</sup> cycles of the GFR while still maintaining comparable neutronic performance. As demonstrated in previous chapters, this would require an optimization of the diluent zoning strategy in order to get comparable beginning of cycle core eigenvalues, while still maintaining a relatively flat beginning of life radial power shape and acceptable coolant void reactivity values. In this light, the LFR results should not be viewed as a comparison against which the GFR can be measured, but rather a demonstration of what the GFR could be capable of, should such an optimization be performed.

Further, comparison of the numbers in Table 8.4 and Table 8.6 shows that the LFR has less than half of the Pu loading of the GFR. This is due to the fact that the specific power of the LFR core is more than twice that of the GFR (42.7 kW/kg<sub>HM</sub> vs. 20.7 kW/kg<sub>HM</sub>, as

shown in Table 8.1). While this may be advantageous from a fuel cycle cost perspective, the higher specific power of the LFR shortens the reactivity limited lifetime of the LFR, which has an accompanying negative economic consequence.

Therefore, the conclusions that can be drawn from Table 8.5 are: (1) the GFR has a net MA destruction rate, (2) the GFR performs better than the PWR with respect to TRU management, due to its ability to recycle and transmute TRU and (3) given the similarity of the GFR and LFR spectra, the GFR has the potential to achieve near LFR-like TRU performance, should this be desired. On the last point, the GFR's slightly softer spectrum in the diluted regions of the core would lower the number of excess neutrons available for transmutation, but would provide more neutrons in the resonance region for absorption; which effect dominates will determine if it is better or worse suited for TRU destruction than the LFR.

**Table 8.6: Detailed Mass Flow of Key MA/TRU Isotopes for All 3 cycles of the LFR Lifetime  
(Reprinted from [Todreas and Hejzlar, 2007])**

	Cycle-1 TRU			Cycle-2 TRU			Cycle-3 TRU		
	Load, kg	Disch., kg	After 7y, kg	Load, kg	Disch, kg	After 7y, kg	Load, kg	Disch, kg	After 7y, kg
<b>Core Total</b>	56,472	51,878	-	56,531	51,652	-	56,549	51,667	-
Pu	8,131	8,268	8,171	8,171	8,327	8,261	8,261	8,352	8,293
U	47,086	42,657	-	47,335	42,572	-	47,493	42,712	-
MA	1,255	953	1,026	1,026	754	796	796	604	649
Pu+MA	9,386	9,221	9,197	9,197	9,080	9,057	9,057	8,956	8,941

#### **8.4 Proliferation Resistance of TID fuel**

Coupled with the idea of minimizing MA/TRU production is making the fuel proliferation resistant. Unfortunately, the attributes of a fuel that make it proliferation resistant (high radioactivity, difficult to separate constituents) also make it more difficult and consequently, expensive, to handle and reprocess the fuel on the back end of the fuel cycle. Fundamental to making a closed fuel cycle proliferation resistant is the development of a reprocessing technology which does not separate the weapons-attractive isotopes into a separate waste stream during the process. While such a reprocessing technology is integral

to the success of the work presented here, prediction of the results of development of this reprocessing technology is beyond the scope of this work.

Virtually any combination of Pu isotopes can be used to make a nuclear weapon; however, the most common isotope for making a weapon is Pu-239 [USDOE, 1997]. The other isotopes of Pu can create problems with respect to manufacturing a nuclear weapon. First, Pu-238 has a relatively short half-life (~87.7 years) when compared to many of the other Pu isotopes (except Pu-241, which has a half life of 14.4 years), which increases the amount of heat generation in the fuel. If enough Pu-238 is present in a weapon, enough heat is generated such that the weapon is unstable. To this end, international safeguards are not required for plutonium containing greater than 80% Pu-238 [USDOE, 1997]. While the GFR fuel does not meet this extreme standard, the net production of Pu-238 shown in Table 8.4 will enhance the proliferation resistance of the fuel. However, as mentioned earlier, it will also make the reprocessing and refabrication of the fuel more difficult. Second, Pu-240 has a high rate of spontaneous fission [USDOE, 1997]. If significant enough quantities are present in a weapon, the neutrons produced from spontaneous fission could prematurely start the chain reaction of the weapon, reducing weapon effectiveness and yield. Hence, the net Pu-240 production in the TID core enhances the proliferation resistance of the fuel. Finally, Pu-241 has a short half-life (14.4 years) and decays into Am-241, which has highly penetrating gamma rays [USDOE, 1997]. Again, the net Pu-241 production seen in Table 8.4 would bode well from a proliferation standpoint, but not from an ease of reprocessing and fabrication standpoint. It should be remembered that a large part of the reason that there is net Pu-238, Pu-240, and Pu-241 production is because of the intra-cycle fuel management philosophy employed. Employing the fuel cycle philosophy used in the LFR work (where there is no TRU discharged between cycles) would certainly decrease the amount of net Pu-238, Pu-240, and Pu-241 production in the TID fuel at the end of each cycle, and concomitantly reduce the proliferation resistance of the fuel. This would also make the handling, reprocessing, and fabrication of the fuel easier. Reprocessing technologies are currently being developed such as the French Grouped Actinide EXtraction (GANEX) which makes reprocessing more proliferation resistant, as Pu stays chemically combined with the Minor Actinides during the entire process, keeping all of the Actinides in the same waste stream [Carré, 2005]. Given this and other likely technological advances, the burden of Pu-



238, Pu-240, and Pu-241 production in keeping the fuel proliferation resistant is reduced substantially.

Comparing the Pu vectors from LWR spent fuel with that of the average (of all 3 cycles) of the GFR spent fuel and that of the average (of all 3 cycles) of the LFR in Table 8.7 shows that the GFR spent fuel has larger Pu-238, Pu-240, and Pu-241 components than the LWR. Therefore, the GFR can be seen as a more proliferation resistant fuel cycle than the LWR, based on the previous discussion of Pu isotopics. Comparing the GFR with the LFR, the Pu vectors of the spent fuel are roughly equivalent, with the GFR having a slight advantage with respect to proliferation resistance due to a larger Pu-240 component. While these auspicious results bode well from a proliferation standpoint, they are not favorable from an ease of reprocessing and fabrication standpoint. Therefore, the burden will fall on the advancement of reprocessing and fabrication technology to help make this more proliferation resistant fuel cycle strategy viable.

**Table 8.7: Comparison of Pu Component of TRU Vectors for LWR and GFR Spent Fuel**

	LWR Spent Fuel	GFR Spent Fuel (3 Cycle Average)	LFR Spent Fuel (3 Cycle Average)
Pu-238 <sup>w/o</sup>	0.90	2.36	3.89
Pu-239 <sup>w/o</sup>	56.72	53.33	54.83
Pu-240 <sup>w/o</sup>	26.11	30.99	24.97
Pu-241 <sup>w/o</sup>	0.90	3.55	3.21
Pu-242 <sup>w/o</sup>	5.40	3.96	4.64

Note: The balance of the TRU vector is made up by MA, as shown in Table 4.14 for the GFR case

### **8.5 Comparative Analysis of MA/TRU Management of GFR Cores of Different Fuel Types**

Table 8.8 compares the net Pu and MA production among the TID, pin-type and ICAF cores on both a mass per unit of electricity produced and a mass per annum basis (note that only the first cycle of the TID core is used as a fair means of comparison, as the other core strategies were not evaluated for subsequent cycles). While all three have a net MA destruction rate, the pin and ICAF cores have a net TRU (Pu+MA) destruction rate, while only the ICAF core has a net individual Pu and MA destruction rate. The differences in the Pu numbers can be accounted for in that the TID is a breeder-burner with a conversion ratio

(CR) slightly less than 1, whereas the Pin and ICAF cores have CR much less than 1. Hence, the TID core produces more Pu-239 throughout burnup than the other options, and consequently, more higher mass number Pu isotopes. While the in-situ breeding of Pu-239 is slightly disadvantageous from a Pu production standpoint, it is advantageous from a sustainability standpoint.

**Table 8.8: Comparison of Net Pu and MA Production and Initial Core Loading among the TID, Pin-type and ICAF Cores**

		TID	Pin	ICAF
Pu	kg/TW <sub>hr<sub>e</sub></sub>	8.60	5.43	-8.44
	kg/yr	76.51	48.32	-75.14
MA	kg/TW <sub>hr<sub>e</sub></sub>	-3.42	-5.89	-6.80
	kg/yr	-30.49	-52.40	-60.53
TRU (Pu+MA)	kg/TW <sub>hr<sub>e</sub></sub>	5.17	-0.4587	-15.25
	kg/yr	46.02	-4.08	-135.67

Further, the lower TRU enrichment of the TID core places it at a disadvantage (core average 16.53 % TRU v. 19.85 % TRU for the pin core and 25.1 % TRU for the ICAF core). Since UO<sub>2</sub> is used to make up the balance of the fuel matrix, the lower TRU enrichment of the TID core means a greater inventory of U-238, which competes with the other actinides for fast neutrons. Hence, with the higher enrichment of the pin and ICAF cores, there is less U-238 competing for fast neutrons, making more available for TRU and Pu destruction.

While the Pin and ICAF cores have similar MA destruction rates, they have significantly different Pu rates. Not shown in Table 8.8, this is due to the large difference in Pu-239 destruction rates, as the higher mass Pu isotope production is nearly equivalent for these two cases. Since the ICAF and pin cores have nearly identical neutron spectra (also similar to that for the TID core, shown in Figure 8.6), the larger Pu-239 incineration rate in the ICAF core is due to the higher TRU, hence Pu-239, enrichment, which for comparable spectra, leads to a proportionately higher fraction of fissions in Pu-239.

Excluding all other factors, the ICAF and pin core certainly seem to outperform the TID core with respect to TRU management. However, this is due largely to the fact that these cores have a conversion ratio (CR) less than 1. Once the shortcomings of these strategies are remembered (e.g. shorter lifetime, higher BOL enrichment, CR<1), the TRU

management numbers presented in Table 8.8 for the TID core become more acceptable. Further, it should be remembered that the TID core TRU management performance is still better than current LWR practice, as shown earlier in this chapter.

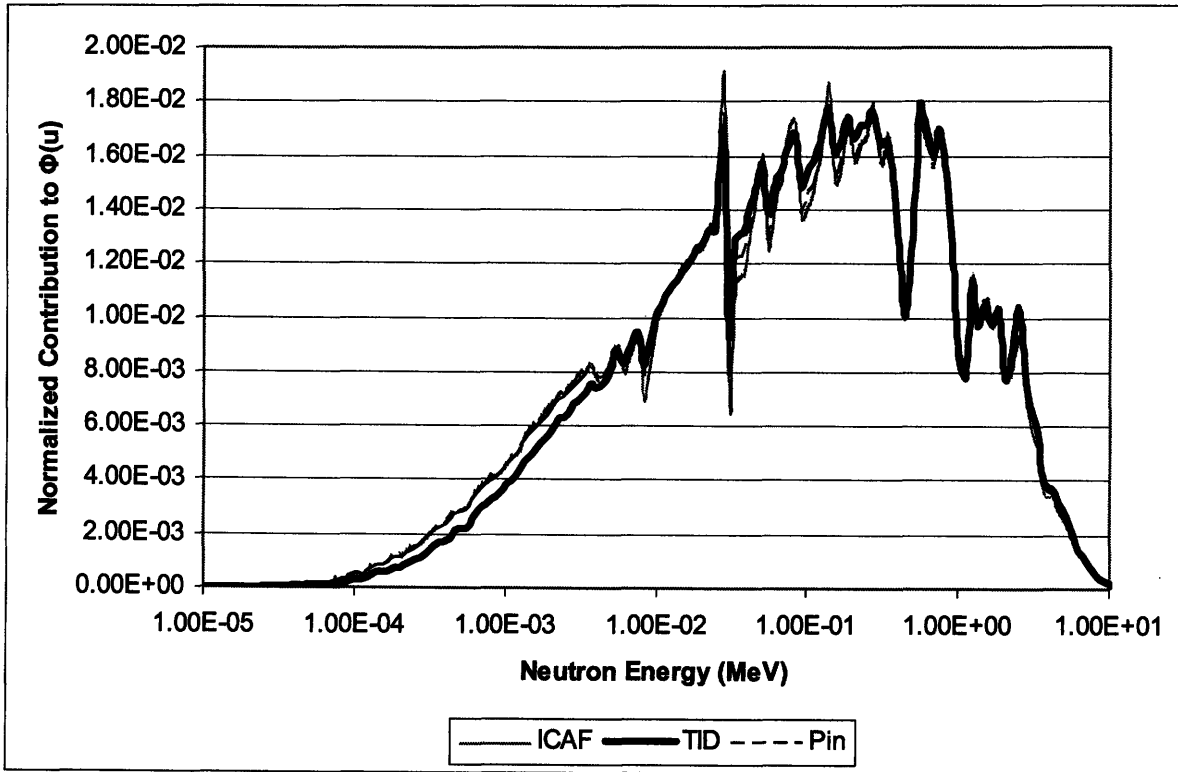


Figure 8.6: Comparison of Neutron Spectra of the TID, Pin and ICAF GFR Cores

## 8.6 Investigation into Suitable Inert Matrix Fuels for Actinide Burning

One approach to effectively minimize not only the production of TRU, but also the radiotoxicity of the spent fuel, is to use an Inert Matrix Fuel (IMF) in a dedicated Actinide Burning Reactor (ABR). The motivation for using an IMF is that it does not contain fertile nuclides for the breeding of TRU; hence, in-situ TRU production is minimized and TRU destruction is maximized. While much research effort has gone into this strategy for waste minimization, other work shows that there may not be a great advantage in using an IMF in an ABR. Specifically, ABRs have been shown to yield no better than comparable time of stockpile TRU depletion with their self-sustaining (i.e. breeder-burner) contemporaries, while posing greater challenges to neutronic safety design and fuel cycle sustainability [Tuček et.

al, 2006 and Hejzlar, 2006]. Still, in order to confirm the ability of a direct cycle S-CO<sub>2</sub> cooled GFR to effectively manage MA/TRU, an exploration of its use as a dedicated MA burner will be undertaken as an alternative to its previously presented breeder-burner function. Additionally, while not a direct goal of this effort, the incidental incineration of Plutonium is also of interest as it will help reduce the availability of proliferation-attractive isotopes.

#### 8.6.1 Neutronic Considerations of Using Inert Matrix Fuels

In order to fulfill the mission of a dedicated MA/TRU burner, the presence of U<sup>238</sup>, which is the progenitor of all of the TRU, should be eliminated from the fuel matrix. While this is attractive from a MA incineration perspective, the removal of Uranium from the fuel matrix may lower the Doppler coefficient to unacceptably low values. While even-numbered Plutonium isotopes have been found to make a negative contribution to the fuel temperature coefficient in inert matrix fuel, specifically Pu-240, this contribution may not be enough [Kloosterman and Konings, 1998]. Further, enhancing the Americium content of fuel in an effort to maximize its incineration will also reduce the Doppler coefficient [Westlen and Wallenius, 2006]. One solution that has been proposed in order to improve the low Doppler reactivity in IMF fuel (specifically the fuel composite PuO<sub>2</sub>-MgO) is to add iron to the matrix to make the fuel composite PuO<sub>2</sub>-MgO-Fe [Krivitski et al., 2001]. Another solution is to add Tc-99 to the fuel, which has capture resonances similar in both size and energy to U-238 [Messaoudi and Tommasi, 2002]. This has the concomitant benefit of burning Tc-99, which has been shown to be a large contributor to the long-term radiotoxicity of spent fuel.

Another effect to consider is that absence of the fertile U-238 may lead to an unacceptably large reactivity swing, which can be ameliorated by mixing the fertile free fuel pins and/or assemblies with those containing conventional ceramic UO<sub>2</sub> fuel [IAEA, 2006]. As well, an absence of U-238 and the resulting increase in the MA concentration will lead to lower values of the effective delayed neutron fraction ( $\beta_{\text{eff}}$ ), which will pose extra challenges from a reactivity control and safety standpoint. These observations serve as a good predictor of what competing effects will need to be considered as the design of a dedicated MA/TRU burning reactor develops.

### 8.6.2 Selection of an Appropriate Inert Matrix Fuel

One of the most important decisions that can be made with respect to designing a dedicated Actinide burner is the selection of an appropriate Inert Fuel Matrix (IFM). Selection of an IFM should consider the following criteria [Shwageraus et. al, 2003, Long et, al., 2003, and IAEA, 2006]:

- Neutron transparency
- Chemical compatibility with the coolant
- Chemical compatibility with the cladding
- Resistance to irradiation damage
- Large heat capacity
- High melting or phase transformation temperature
- Stable crystal structure in the operating temperature range
- Low thermal expansion
- High thermal conductivity
- Good mechanical properties
- Economically reasonable (available)
- Consideration of the end state, i.e. to be reprocessed or sent to a geologic repository
- Ability to be handled and fabricated
- Ability to be reprocessed
- Availability of industrial experience

Just meeting all of these 15 requirements for a given reactor system is an extremely difficult and complex problem, much less finding an optimal solution.

IMF's can be grouped into two general categories: Solid Solution Pellets (SSP) or hybrid fuel types. SSPs are where the fuel and matrix form a homogeneous solid, similar to LWR fuel, and are generally in the form of oxides or metallic fuel. Hybrid Fuel (HF) consists of small spheres of fissile material within a neutronically inert matrix, which typically has thermal and mechanical properties better than that of the fissile spheres. In this way one component of the fuel makes up for the shortcomings of the other. Hybrid fuels typically come in two forms: (1) Ceramic-Ceramic (CERCER), where the fissile spheres are a ceramic dispersed throughout another ceramic matrix and (2) Ceramic-Metallic (CERMET), where the fissile spheres are ceramic and dispersed throughout the metallic matrix.

Typically, melting points of metallic fuels and matrices are much too low for application in this reactor. Further, experimental results show that U-Pu-Zr alloys containing

5% of Np and Am and rare earths interact with the Fe and Ni constituents of stainless steel to form compounds with melting points below 1000K [Sari et al., 1994]. Hence metallic SSPs and all CERMETS can be immediately eliminated. The following is a list of general categories of remaining materials, for use in SSPs or in CERCER type fuel:

1. Oxides
2. Nitrides
3. Carbides

Since the Tube-in-Duct (TID) fuel form implemented in this reactor vents its fission gas (indirectly) to the coolant, the S-CO<sub>2</sub> coolant will come into direct contact with the fuel form during normal operation. Hence, chemical compatibility between the coolant and fuel form is a more limiting constraint than for traditional pin type fuel, where fuel-coolant interaction is conditional upon cladding failure. Thus, the highly chemically reactive nature of Nitride and Carbide fuels with S-CO<sub>2</sub> eliminates them from contention [Thon, 2002].

Another carbide of interest, Silicon Carbide, was examined intensively in the Canadian IMF program because of its high melting temperature, very high thermal conductivity, its known corrosion resistance, and lack of swelling under irradiation [IAEA, 2006]. Further, SiC has displayed chemical compatibility with CO<sub>2</sub> under a wide range of conditions, despite the fact that it is a carbide, due to the formation of a protective layer on the surface of the SiC that inhibits further reaction [Opila and Nguyen, 1998]. However, the thermodynamic incompatibility of a SiC matrix with (austenitic) steel cladding in a fast reactor environment eliminates it as a possibility [Kleykamp, 1999]. Another factor which eliminates SiC is its insolubility in Nitric Acid, making it incompatible with most current reprocessing methods.

Oxide SSPs are attractive from a MA loading standpoint, as the volume fraction of Actinides that can be loaded is much greater with this strategy than with the hybrid option. However, the main limitation of using ceramic oxides in SSPs is the low thermal conductivity inherent in these materials, which is typically even lower than that for UO<sub>2</sub> [Bakker and Konings, 1998 and Ronchi, 2003]. This lower thermal conductivity would present a challenge in the higher temperature environment of this reactor, which already challenges established thermal hydraulic limits, even though the relatively poor thermal

conductivity of UO<sub>2</sub> is augmented by BeO. Still, some SSPs, specifically PuO<sub>2</sub> or MOX, may be necessary in order to provide the necessary reactivity to keep the reactor critical in order to perform its mission of actinide destruction. This gives rise to the question of whether the fuel assembly in the MA burner will be homogeneous or heterogeneous, which can be explored in future work.

Of all the materials under investigation by the international nuclear community for use as a host matrix in IMFs, three remain as promising candidates: MgO, Spinel (MgAl<sub>2</sub>O<sub>4</sub>) and Zirconia (ZrO<sub>2</sub>)-based materials. While initially favored as a leading candidate and pursued in many research programs, irradiation experiments show that Spinel is likely not a suitable matrix candidate, as it shows large swelling, pellet fracturing, and high fission gas release [Neeft et al., 2003 and Meyer, 2006]. While fission gas release into the inner part of the fuel assembly is not a concern given that the fuel assemblies are vented, it does contribute to fuel swelling due to poor diffusion of the fission gases through the Spinel matrix. Additionally, Spinel's susceptibility to radiation damage by fission fragments requires that heterogeneous fuel particle dispersion be reasonably large (50-300 μm) in order to confine this fission fragment damage to the fuel particle, thus lowering the allowed MA loading [Konings et al., 2000]. One advantage of Spinel is that it has great physical and chemical stability, which make it attractive from a long term geologic disposal point of view [IAEA, 2006]. More importantly, Spinel is insoluble in nitric acid, which makes it unusable in the PUREX recycling process [Konings et al., 2000]. This is disadvantageous from a fuel recycling standpoint, but is desirable from a misuse of fissile material standpoint [Hellwig et al., 2006].

Zirconia based materials, specifically Yttria-Stabilized Zirconia (YSZ), are promising host matrix materials due to their high melting point, low neutron capture cross-section, high stability under irradiation damage and compatibility with cladding [IAEA, 2006 and Degueldre et al., 2003]. However, these materials also suffer from relatively low thermal conductivity, lower than that of UO<sub>2</sub> [Degueldre et al., 2003]. Nevertheless, given the other desirable attributes that these materials possess, mixing the YSZ with another inert matrix material with higher thermal conductivity would be a way to take advantage of both materials' benefits [IAEA, 2006]. As far as the processing of the fuel matrix at the end of

irradiation, YSZ is also fairly insoluble in aqueous and acidic solutions, limiting it to once-through use with current reprocessing technologies, but again inhibiting the misuse of fissile material [Hellwig et al, 2006].

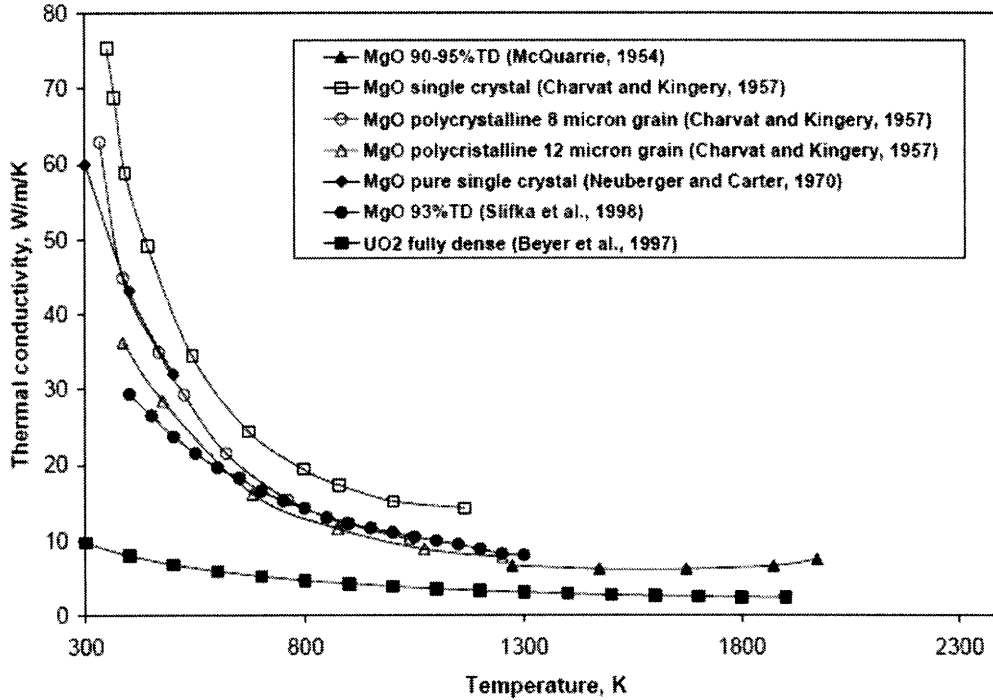


Figure 8.7: Thermal Conductivity of MgO shown in Comparison with that of UO<sub>2</sub> (reprinted from [Medvedev, 2004])

Several references, [Neeft et al., and Chawla and Konings, 2001], suggest that MgO is the best inert matrix material for both Pu burning and transmutation of MA in fast reactors due to its high melting point, good thermal conductivity, and superior performance in a radiation environment. Specifically, several different models of the thermal conductivity of MgO are compared with that of UO<sub>2</sub> in Figure 8.7, showing that MgO as an inert matrix fuel has the potential to yield significantly lower fuel temperatures [Medvedev, 2004]. The melting temperature of MgO is comparable to that of UO<sub>2</sub>: 2832°C for MgO v. 2877°C for UO<sub>2</sub>.

A recent irradiation experiment on inert matrix fuels was conducted in order to compare the irradiation performance among several IMF options, and MgO was shown to be one of the top performers [Neeft et al, 2003]. With the MgO inert matrix, the Pu and MA could be either in the form of simple binary oxides or hosted in a zirconia-based phase, e.g.



YSZ [Chawla and Konings, 2001]. Again, an experiment was recently performed in which a MgO inert matrix hosted binary oxide fuel composed of Pu, Am, and Cm, in order to confirm the transmutation capability of such a strategy [Haeck et al, 2006]. While the experiment was for a subcritical accelerator driven system and the results did not focus on the fuel performance aspects, the transmutation efficacy of this strategy was confirmed [Haeck et al, 2006]. Consequently, synthesis of the results from all of these experiments shows that an IMF using MgO as a host matrix with either binary oxide or zirconia-based fuel would be the best fuel option for transmutation of MA and burning of Pu in a fast reactor.

### 8.6.3 Chemical Compatibility of Inert Matrix Fuel Material and S-CO<sub>2</sub>

While many aspects of IMF use in this reactor have already been explored, the most unique to a S-CO<sub>2</sub> cooled GFR is the chemical compatibility of the S-CO<sub>2</sub> coolant with the matrix itself. Given that the fuel assemblies in this reactor are vented, the fuel matrix will come into direct contact with the coolant, making the chemical compatibility between the fuel and coolant an important criterion. Using the same approach as for assessing the chemical compatibility in the axial reflector study in Chapter 4, the chemical code HSC 5.1

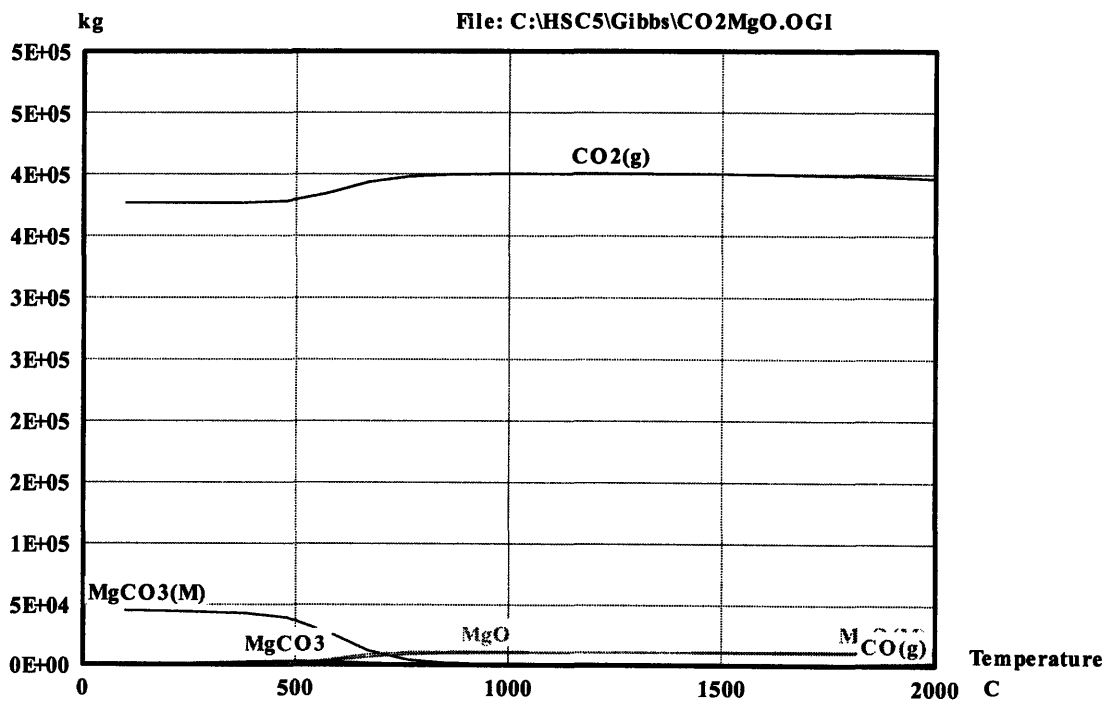


Figure 8.8: Equilibrium Compositions of the S-CO<sub>2</sub>-MgO Reaction

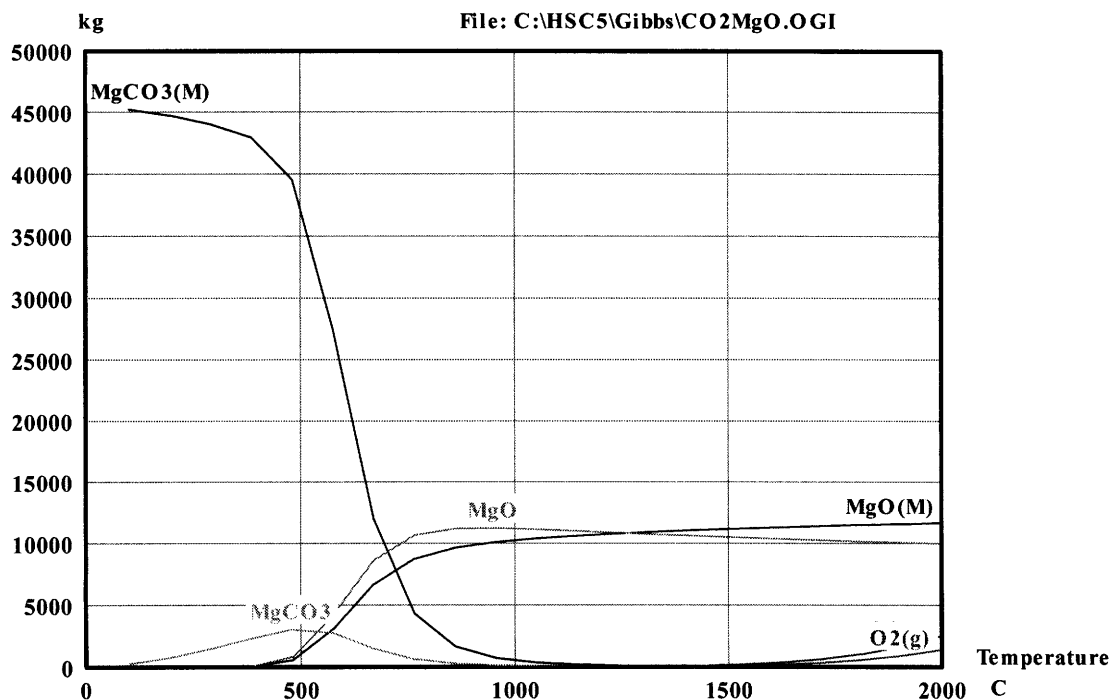


Figure 8.9: Equilibrium Compositions of the S-CO<sub>2</sub>-MgO Reaction, expanded scale

was used to predict both (1) the equilibrium compositions as a result of matrix and coolant interaction and (2) the thermodynamic likelihood of such a reaction occurring, based on Gibbs Free Energy calculations. Figure 8.8 and Figure 8.9 show the results of this analysis for the MgO matrix, with Figure 8.9 showing an expanded view of the information in Figure 8.8, less the CO<sub>2</sub> equilibrium concentrations. These figures show that MgO will form MgCO<sub>3</sub> at low temperatures when interacting with S-CO<sub>2</sub>, leaving almost no MgO. However, at the temperatures at which the fuel will be operating, i.e. >800°C, the MgO is in good equilibrium with the S-CO<sub>2</sub> and the only predicted reaction is the conversion of MgO to monocrystalline MgO (MgO(M)), which has the same material properties as MgO until 1700K (1423°C). However, Table 8.9 shows the Gibbs Free Energy of this system, demonstrating that for temperatures of 500°C and above, this reaction is not thermodynamically favorable and hence, not likely to take place. Further, this simple assessment only evaluates whether or not a reaction will take place and does not take into account reaction rate. Hence, while a reaction may be thermodynamically favorable, the reaction rate may be slow enough that appreciable changes in the composition of the

reactants may not occur. In addition, the effects of the formation of a passive oxide layer that would inhibit further reaction are not captured in this analysis. This effect has been shown to be significant in many materials, specifically the earlier example of S-CO<sub>2</sub> SiC interaction, where the purely thermodynamic present method of prediction of chemical compatibility predicts a reaction, but experimental results show that the formation of a passive inhibiting layer makes the two materials chemically compatible.

**Table 8.9: Gibbs Free Energy of the MgO-SCO<sub>2</sub> system**

<b>Reaction</b>	<b>Temp(°C)</b>	<b>ΔG (kcal)</b>
$2\text{CO}_2(\text{g}) + 3 \text{MgO} = \text{MgCO}_3(\text{M}) + \text{MgCO}_3 + \text{MgO}(\text{M})$	200	-11.6
	500	12.568
	800	35.584
	1200	61.856
	1500	78.459
	1800	93.873

A search of the literature for MgO-CO<sub>2</sub> interaction yielded no direct results. However, several references were found which suggest MgO (often combined with another oxide) acts as a suitable catalyst for CO<sub>2</sub> reforming of methane gas, i.e. hydrogen production from methane gas [Jensen et al., 2005, Philipp and Fujimoto, 1992, and Hu and Ruckenstein, 1997]. Since MgO is a catalyst in this process and does not have very high chemical reactivity with CO<sub>2</sub>, as shown in [Jensen et al., 2005] and [Pacchioni et al., 1994], this suggests that MgO and CO<sub>2</sub> could be chemically compatible. Hence, while our present crude method of predicting chemical compatibility gives a favorable outcome, the only definitive confirmation would be through experimental results.

#### 8.6.4 Quantitative Assessment of Fertile Matrix and Inert Matrix Fuels

To compare the neutronic performance of a fertile matrix fuel with an IMF fuel in this S-CO<sub>2</sub> GFR, three semi-infinite assemblies were subjected to a depletion analysis. The three semi-infinite assemblies were identical, except for the material used for the fuel matrix, the enrichment of the fuel, and the volume fraction of the diluent. Note that the BOL Pu/MA vectors are the same as those used in the first cycle of the TID core, presented in Chapter 4. One of the assemblies (the “Fertile” case) was representative of the inner fuel zone of the TID core (UO<sub>2</sub> matrix with 16.6 % TRU). The other two assemblies were IMF using MgO

as the matrix. Of these two, one had a diluent composition and volume fraction comparable to that of the Fertile case (10.22 % TRU and 30% BeO), while the other had no diluent and an increased TRU enrichment (15 % TRU). The purpose of the former was to compare the performance of an IMF assembly to that of the Fertile case with a comparable BOC eigenvalue, while the purpose of the latter was to compare the performance of an IMF assembly with a much longer reactivity limited lifetime to that of the Fertile case.

The IMF assemblies will be compared with the Fertile assembly on the basis of (1) reactivity swing, (2) reactivity limited lifetime, (3) Coolant Void Reactivity (CVR), (4) effective delayed neutron fraction ( $\beta_{\text{eff}}$ ), (5) Doppler coefficient of reactivity, (6) the ability to effectively reduce the overall TRU inventory and (7) the ability to reduce the MA inventory. While it is certainly recognized that the behavior of a whole core will be different than that of a single assembly, the results presented here will give a good indication of the comparative performance of these three approaches. Coupled with the fact that radial core leakage is neglected in these studies, these results should be used only on a comparative basis, and not as an absolute comparison with data outside of this work.

#### 8.6.4.1 *Reactivity Swing and Reactivity Limited Lifetime*

Figure 8.10 shows the excess reactivity curves for all three semi-infinite assemblies, while Table 8.10 compares their characteristics. The much lower heavy metal loading for the IMF cases, due mainly to the absence of U-238, yields a much higher specific power and much shorter reactivity limited lifetime. Consequently, to get the same lifetime from an IMF single-batch core as for the Fertile case would require a much larger BOC eigenvalue, hence enrichment, and would result in a much larger reactivity swing. This concept is illustrated when comparing the two IMF cases. Removing the BeO and increasing the enrichment dramatically increases the BOC eigenvalue, hence reactivity swing, with only a modest gain in reactivity limited lifetime. Using the relationship between single batch ( $B_1$ ) and n-batch burnup ( $B_n$ ) ( $B_n = \left(\frac{2n}{n+1}\right)B_1$ ), the IMF case without BeO could represent a 4-batch core, with 12 month cycles, assuming a 90% capacity factor [Driscoll et al, 1990]. While this scenario is much more desirable than the other IMF case presented, the shorter reactivity

limited lifetime when compared to the TID case and the accompanying larger reactivity swing highlight the shortcomings of IMF fuel. This larger reactivity swing has not only safety but also economic implications, specifically with respect to the fuel cycle costs

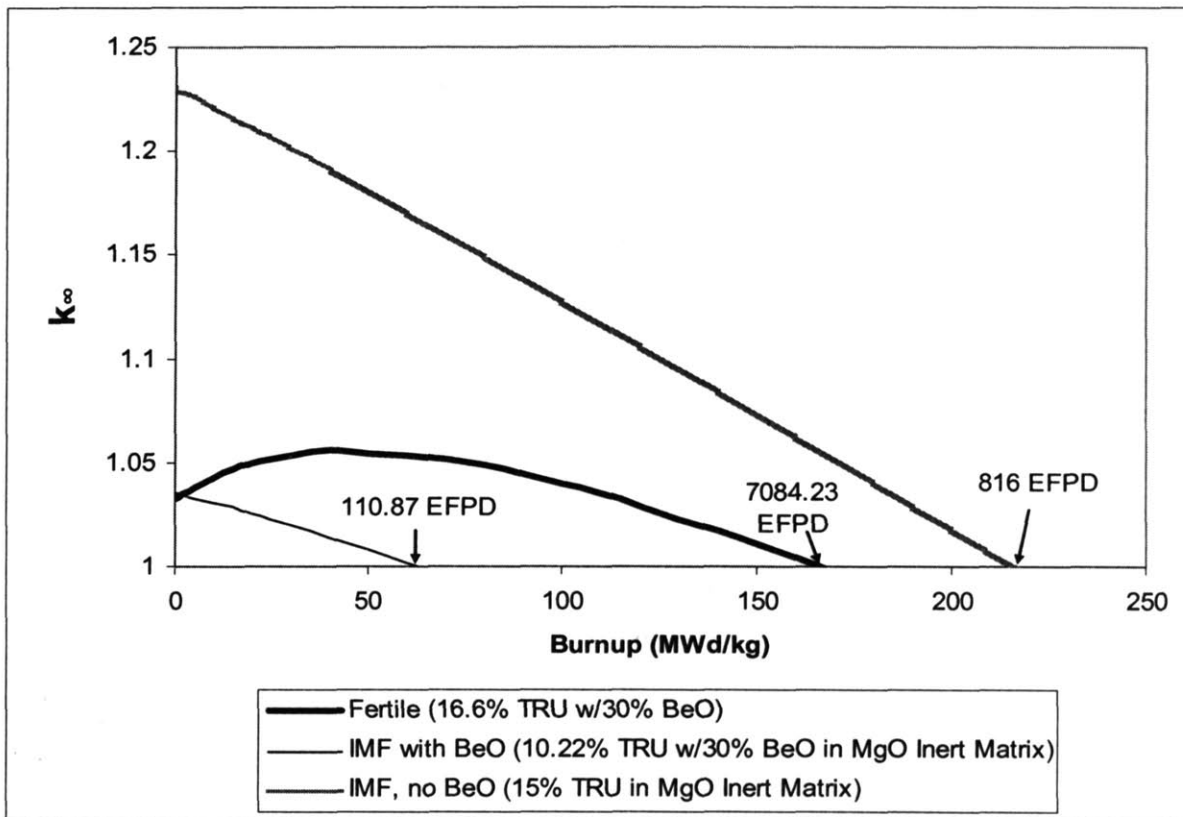


Figure 8.10: Semi-Infinite Assembly Eigenvalue Comparison among the Fertile and IMF Assemblies

Table 8.10: Comparison of Characteristics of the Semi-Infinite Fertile and IMF Assemblies

	IMF with BeO	IMF with no BeO	Fertile
MW <sub>th</sub>	6.349	6.349	6.349
Matrix Material	MgO	MgO	UO <sub>2</sub>
BeO concentration	30%	0%	30%
BOC Enrichment (% TRU)	10.22	15	16.6
Reactivity Limited Burnup (MWd/kg)	62.97	217	165.81
Specific Power (kW/kg <sub>HM</sub> )	567.98	265.94	23.4
Reactivity Limited Lifetime (EFPD)	110.87	815.98	7084.23
Reactivity Swing (pcm)	3372	18778	5299

associated with the enrichment required for such a high BOC eigenvalue. For these reasons alone, the IMF option is not very attractive. The performance of this IMF is not specific to its application in a GFR, but rather is germane to the use of IMFs in general, as discussed earlier.

#### 8.6.4.2 Coolant Void Reactivity (CVR) and Effective Delayed Neutron Fraction ( $\beta_{eff}$ )

**Table 8.11: Comparison of Unrodded CVR and  $\beta_{eff}$  for the IMF and Fertile Assemblies**

Time in Life	$k_{eff}$ , nominal	$k_{eff}$ , voided	CVR $\Delta\rho$	STDEV ( $\sigma$ )	Effective Delayed Neutron Fraction ( $\beta_{eff}$ )	STDEV ( $\sigma$ )	CVR $\phi$	STDEV ( $\sigma$ ) $\phi$
<b>IMF w/BeO</b>								
BOL	1.03486	1.03668	1.7E-03	2.33E-04	0.0026	2.2E-04	<b>64</b>	<b>10</b>
EOL	1.00177	1.00455	2.76E-03	2.27E-04	0.0025	2.3E-04	<b>112</b>	<b>14</b>
<b>IMF w/out BeO</b>								
BOL	1.23035	1.23074	2.58E-04	2.55E-04	0.0024	1.7E-04	<b>11</b>	<b>11</b>
EOL	0.99984	1.00027	4.3E-04	1.98E-04	0.0030	2.1E-04	<b>14</b>	<b>7</b>
<b>Fertile</b>								
BOL	1.0335	1.03669	2.98E-03	2.0E-04	0.0044	1.8E-04	<b>67</b>	<b>5</b>
MOL	1.05513	1.05857	3.08E-03	1.98E-04	0.0042	1.7E-04	<b>74</b>	<b>6</b>
EOL	1.00438	1.00794	3.52E-03	1.63E-04	0.0041	1.6E-04	<b>85</b>	<b>5</b>

Table 8.11 shows the unrodded CVR and  $\beta_{eff}$  for the Fertile and IMF Assemblies. First, as expected, the  $\beta_{eff}$  is much lower for the IMF case as compared to the Fertile case, due to the lack of U-238. This is significant, as the  $\beta_{eff}$  for IMF is half to two-thirds that of the Fertile case, making reactor control extremely difficult. While the BOL (unrodded) CVRs are comparable for the IMF w/BeO and the Fertile cases, the CVR for the IMF w/BeO fuel increases much more rapidly than for the Fertile case, as the EOL IMF CVR at 111 EFPD is much greater than the EOL Fertile CVR at >7000 EFPD. Again, this is due to the lack of U-238 in the fuel matrix, which helps to mitigate the effect of the increasing CVR throughout core life. However, the IMF w/out BeO case has much lower CVRs throughout cycle life than either the Fertile or IMF w/BeO case.

### 8.6.4.3 Doppler Coefficient of Reactivity

Table 8.12 compares the unrodded Doppler reactivity coefficient for the Fertile and IMF cases. A separate relationship was derived for the Doppler coefficient for both the IMF and Fertile cases, using the methodology outlined in Chapter 9 for the Fertile case.

**Table 8.12: Comparison of Unrodded Doppler Reactivity Coefficient for the IMF and Fertile Assemblies**

Time in Life	$k_{\text{eff}}(T_{\text{HOT}})$	$k_{\text{eff}}(T_{\text{COLD}})$	Doppler (pcm/°C)	STDEV ( $\sigma$ ) (pcm/°C)	Doppler ( $\phi$ /K)	STDEV ( $\sigma$ ) ( $\phi$ /K)
<b>IMF w/BeO</b>						
BOL	1.03486	1.03304	<b>0.1865</b>	0.03	<b>0.070</b>	0.013
EOL	1.00177	1.00014	<b>0.1782</b>	0.03	<b>0.072</b>	0.015
<b>IMF w/out BeO</b>						
BOL	1.23035	1.2408	<b>-0.7497</b>	0.02	<b>-0.310</b>	0.024
EOL	0.99984	1.00941	<b>-1.0386</b>	0.03	<b>-0.337</b>	0.025
<b>FERTILE</b>						
BOL	1.0335	1.05553	<b>-2.2359</b>	0.02	<b>-0.503</b>	0.021
MOL	1.05513	1.0728	<b>-1.659</b>	0.02	<b>-0.397</b>	0.017
EOL	1.00438	1.01587	<b>-1.2468</b>	0.02	<b>-0.303</b>	0.012

$$T_{\text{HOT}} = 900 \text{ K}$$

$$T_{\text{COLD}} = 293.6 \text{ K}$$

As expected, the Doppler coefficient of reactivity of the IMF fuel was more positive than that found for the Fertile fuel. Again, the large difference is due to the lack of U-238 in the IMF fuel. While the Doppler for the IMF w/BeO assembly is slightly positive, the Doppler for the IMF w/out BeO case is negative. The improved Doppler performance of the IMF w/out BeO case is due to (1) the harder neutron spectrum of this case (shown later) and (2) the increased Pu-240 content, which helps ameliorate Doppler, as discussed earlier. The increased production of Pu-240 for the IMF w/out BeO case explains why the Doppler gets more negative with burnup for this case. The Fertile assembly has a much more negative Doppler than either case, which bodes well from a safety standpoint. For the Fertile case, the Doppler at MOL and EOL get less negative with burnup, in part due to the depletion of U-238.

Aside from removing the diluent, another possible solution to improve the Doppler seen for the IMF cases is to add Tc-99 to the fuel matrix. Tc-99 neutronically mimics the

resonance absorption behavior of U-238 and has been shown effective in designing IMF cores with negative Doppler coefficients of reactivity [Messouadi and Tommasi, 2002] [Romano et. al, 2004].

#### 8.6.4.4 Actinide (MA/TRU) Burning Capability

**Table 8.13: Comparison of Actinide Destruction Capability for the IMF and Fertile Assemblies**

		IMF w/BeO		IMF w/out BeO		Fertile	
MWth		6.349		6.349		6.349	
Thermal Efficiency		0.47		0.47		0.47	
EFPD		110.87		815.98		7084.23	
Isotope ID (ZZAAA)		NET (kg)	NET (kg/TW <sub>hr<sub>e</sub></sub> )	NET (kg)	NET (kg/TW <sub>hr<sub>e</sub></sub> )	NET (kg)	NET (kg/TW <sub>hr<sub>e</sub></sub> )
U	92234	0.000	0.038	0.007	0.111	0.124	0.244
	92236	0.000	0.013	0.001	0.024	0.267	0.525
	92235	0.000	0.013	0.002	0.029	-1.288	-2.539
	92238	0.000	0.000	0.000	0.000	-46.823	-92.287
U Total		0.001	0.063	0.010	0.164	-47.721	-94.056
Pu	94238	0.055	6.889	0.444	7.596	0.925	1.824
	94239	-1.005	-126.615	-6.785	-116.108	-0.293	-0.577
	94240	0.081	10.201	0.674	11.526	3.529	6.956
	94241	0.252	31.786	1.017	17.399	1.477	2.911
	94242	-0.047	-5.906	-0.029	-0.491	-0.299	-0.590
Pu Total		-0.664	-83.646	-4.680	-80.077	5.339	10.523
MA	93237	-0.054	-6.826	-0.343	-5.876	-0.857	-1.688
	95241	-0.120	-15.074	-0.685	-11.718	-1.561	-3.076
	95242	0.001	0.101	0.001	0.010	0.000	0.000
	95242M	0.019	2.368	0.064	1.100	0.112	0.220
	95243	0.055	6.939	0.142	2.435	0.285	0.561
	96242	0.061	7.732	0.119	2.036	0.041	0.081
	96243	0.002	0.239	0.017	0.286	0.005	0.010
	96244	0.019	2.431	0.099	1.697	0.257	0.507
	96245	0.002	0.239	0.016	0.272	0.055	0.108
	96246	0.000	0.000	0.001	0.017	0.010	0.019
MA Total		-0.015	-1.851	-0.569	-9.740	-1.653	-3.258
Pu+MA Total		-0.679	-85.497	-5.249	-89.817	3.686	7.265
U+Pu+MA Total		-0.678	-85.434	-5.239	-89.653	-44.035	-86.791

Table 8.13 shows a comparison of the net actinide production rate for the IMF and Fertile assemblies, broken down by isotope. As expected, the IMF cases are much more successful at Pu destruction than the Fertile option, owing to the absence of Pu-239 production due to lack of U-238. When the Pu results are combined with those for MA, the



IMF options have a large net TRU destruction capability, especially when evaluated on a mass per energy generated basis. However, if Pu-239 were neglected, the Fertile option produces less Pu and overall TRU than the IMF options.

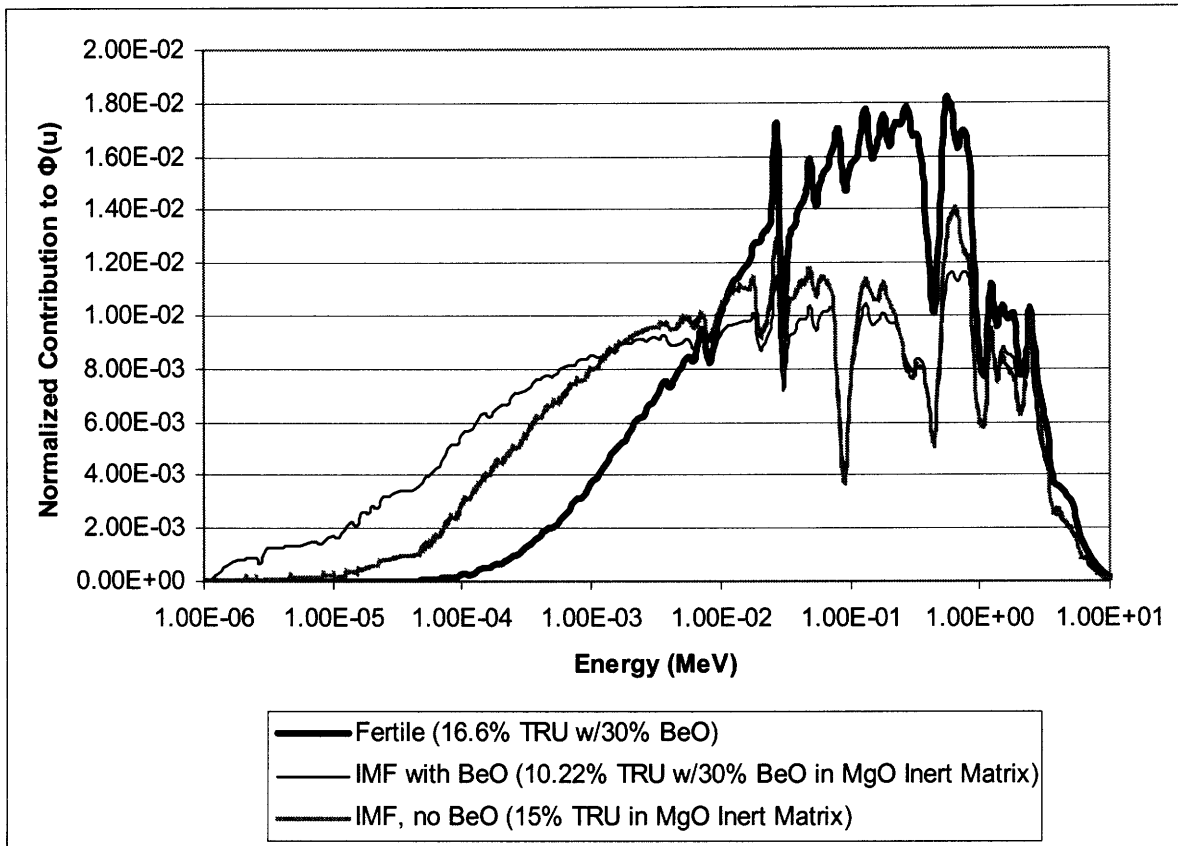


**Figure 8.11: Comparison of Neutron Energy Spectra for the Fertile and IMF Assemblies**

A comparison between the neutron energy spectra of the Fertile and IMF assemblies in Figure 8.11 shows that the IMF cases have a much softer neutron spectrum than the Fertile case. This softer spectrum is attributed to the moderating effect of the MgO matrix and is the likely cause of the larger Pu production (excluding Pu-239). The softer MgO case spectra push more neutrons into the resonance region, where the fission and capture cross sections are comparable for the Pu isotopes. At higher energies, the fission cross sections stay constant, while the capture cross sections typically decrease, leading to increased fission, i.e. destruction. Hence, with the softer IMF spectra, capture competes more readily with fission, and more higher-mass number Pu isotopes are produced. Coupled with this is the fact that at higher energies, the reproduction factor,  $\eta$ , is higher, leaving more high energy excess

neutrons for transmutation. Consequently, the softer IMF spectrum has less excess neutrons for transmutation, contributing to a larger inventory of higher mass number Pu isotopes.

Looking next at the MA destruction capability, the IMF w/out BeO case outperforms both the IMF w/BeO and Fertile cases, due to its larger Np-237 and Am-241 destruction (as compared to the Fertile case) and its lower Am-242m, Am-243, Cm-242, and Cm-244 production (as compared to the IMF w/BeO case). This is due to (1) the absence of U-238, which readily competes for neutrons that would otherwise be used for TRU destruction (when compared to the Fertile case) and (2) the slightly harder spectrum (when compared to the IMF w/BeO case) which promotes the destruction of Np-237 and Am-241 without enhancing the production of the higher mass number actinides (Am-242m, Am-243, Cm-242, and Cm-244).

While the Fertile option does not provide a net TRU destruction capability, it does provide a better MA destruction capability than the IMF w/BeO option, as well as a slight net destruction of Pu-239. Moreover, it provides a lower TRU production rate than in current LWR practice, as shown earlier in this chapter. While the whole-core Fertile results showed an overall slight Pu-239 production, these results are consistent in that they show that the Fertile option provides a net Pu-239 around zero, i.e. Conversion Ratio  $\sim 1$ . Again, the better MA destruction capability of the Fertile case is due to the difference in neutron energy spectra, as explained earlier, and the much longer burnup of the Fertile case. Consequently, the Fertile option is more advantageous with respect to MA incineration, while the IMF w/BeO case is more advantageous with respect to overall TRU destruction. Furthermore, the IMF w/out BeO case has the best net MA and TRU destruction rate of all three cases.

#### 8.6.4.5 *Summary*

Table 8.14 gives a concise summary of the performance comparison of the IMF and Fertile assemblies. The three assemblies were rated in the 7 categories chosen for comparison as either favorable (desirable to have in a reactor), acceptable (could be tolerated in a reactor with some compensatory design measures), or unfavorable (undesirable to have in a reactor). As is clear from Table 8.14, the Fertile case presented throughout this work outperforms the IMF cases studied here, owing mainly to the problems with the large

reactivity swing and short reactivity limited lifetime inherent in an IMF approach. While some IMF cores have been developed which present desirable neutronic performance across most categories, the problems and design challenges of these strategies have been showcased here in the IMF assembly, highlighting the generic problems with such an approach, as also reported elsewhere [Messaoudi and Tommasi, 2002] [Romano et. al, 2004].

**Table 8.14: Summary of Performance Comparison between the Fertile and IMF Assemblies**

	IMF w/BeO	IMF W/out BeO	Fertile
Reactivity Swing	Favorable	Unfavorable	Favorable
Reactivity Limited Lifetime (EFPD)	Unfavorable (Too short - would need to significantly raise BOC Enrichment to achieve same batch-loaded performance as Fertile case. This would have the concomitant effect of increasing reactivity swing.)	Unfavorable	Favorable
CVR	Unfavorable (Much more positive at EOL, with a much quicker growth with burnup than the Fertile case)	Favorable (lowest CVR values among the three options)	Favorable (whole core results show it to be negative throughout core life)
$\beta_{eff}$	Unfavorable ( $<0.0030$ )	Unfavorable ( $\leq 0.0030$ )	Acceptable
Doppler	Unacceptable (Much more positive than the Fertile case and likely positive in the whole core case)	Acceptable	Favorable (whole core results show it to be negative throughout core life)
TRU destruction	Favorable (larger net destruction rate than Fertile) & Unfavorable (larger Pu production than Fertile case, excepting Pu-239)	Favorable (largest net destruction rate among the options) & Unfavorable (larger Pu production than Fertile case, excepting Pu-239)	Acceptable (shown to be better than current LWR practice in previous sections)
MA destruction	Acceptable (net MA destruction rate)	Favorable (largest net destruction rate among the options)	Acceptable (net MA destruction rate)

## **8.7 Summary and Conclusions**

The ability to manage several key long lived fission products (Tc-99 and I-129) and TRU for the TID GFR core were assessed and evaluated against current LWR practice and a competing Gen-IV design, the LFR. The TID GFR core was found to have an advantage in all of these areas with respect to the LWR case, due to the (1) substantially harder neutron spectrum, which leads to a greater in-situ burning capability and (2) the ability to recycle the fuel. While the numbers presented in this work show that the LFR is comparable in Tc-99 and I-129 production/destruction and superior in the ability to incinerate TRU, the difference in inter-cycle actinide management between the TID GFR core and the LFR account for the difference in TRU management performance. The TID GFR still has a net MA destruction rate, and given the similarity of the GFR and LFR spectra, the GFR has the potential to achieve near LFR-like TRU performance, should the same inter-cycle actinide management strategy be used.

As well, the proliferation resistance of the TID GFR core was compared against that of the current LWR practice and the LFR, with the GFR having a great advantage over the LWR and a slight advantage over the LFR in this area. While these auspicious results bode well from a proliferation standpoint, they are not favorable from an ease of reprocessing and fabrication standpoint.

Within the GFR option space, the MA/TRU management of the three core designs of different fuel types was compared. The ICAF and pin core outperform the TID core, stemming mainly from their  $CR < 1$  and their higher TRU enrichment, which means (1) less U-238 competing for fast neutrons, making more available for TRU and Pu destruction and (2) more Pu-239, which for comparable spectra, leads to a proportionately higher fraction of fissions in Pu-239. However, it should be remembered that the pin and ICAF cores have other shortcomings (shorter lifetime, higher BOL enrichment) which are not adequately compensated by this more favorable aspect of performance. Further, the TRU management performance of the TID core is still better than current LWR practice and has the potential to rival that of the LFR.

Finally, the use of the GFR as a dedicated actinide burner, instead of the previously assumed breeder-burner role, was explored. A literature review and comprehensive analysis was conducted to determine that MgO was likely the best IMF to be used in an actinide burner concept for this GFR. This selection was based on the high melting point, good thermal conductivity, and superior irradiation performance in a fast neutron environment of MgO, coupled with its initially assessed chemical compatibility with the S-CO<sub>2</sub> coolant. A quantitative comparison of two GFR IMF semi-infinite assemblies (with and without BeO diluent) was made with a TID GFR core assembly (“Fertile” case), with all evaluated using established neutronic criteria in seven different areas. The performance of the IMF (in both cases) was inferior to that of the Fertile case. While some performance shortcomings were corrected through the removal of the diluent in the fuel, the larger reactivity swing and much shorter reactivity limited lifetime proved the idea of using this GFR as a dedicated actinide burner with fertile-free fuel is not feasible. Moreover, fuel cycle simulations have shown that CR=0 strategies are not needed to manage TRU [Hejzlar, 2006].

## 9 Preliminary Neutronic Safety Assessment

### 9.1 Introduction

Motivated by goals for Generation-IV reactors to excel in safety, designs for the next generation of nuclear reactors should be even safer than today's advanced reactors. Since many current reactors utilize designs with enhanced passive safety features, a standard has been set which makes cores which require active means of safe shutdown less desirable. As well, other Gen-IV designs, i.e. the Liquid Metal Reactor (LMR), have been shown to be passively neutronically safe against limiting accident scenarios, without violating established core thermal limits [Wade and Chang, 1988]. Not only is passive safety desirable from a public acceptance viewpoint, it also has the concurrent potential benefit of reducing capital costs, enhancing the chances of success of a new nuclear technology.

Given that reactors are required to have 2 independent means of reactivity shutdown in order to be licensed and built in the United States, designing a reactor core which will shut itself down upon occurrence of a limiting transient, with the concurrent failure of the active reactivity insertion mechanisms and no violation of core thermal limits, is to design around a very low likelihood event. Hence, while such a design will give added assurance of safety against the most onerous of circumstances, it focuses the design effort on events which are likely to never happen. Table 9.1 shows the likely limiting transients along with the defenses installed to prevent core damage. This table demonstrates that in order for passive core shutdown to be necessary, several reliable systems need to fail. As well, it does not include inherent reactivity feedback mechanisms, such as Doppler, bowing, and leakage. These mechanisms are not accounted for here in order to prevent taking credit for these mechanisms twice (as credit will be taken for them when discussing passive core shutdown), but they are

certainly present, beyond any imposed standard of passive safety. Still, in order to meet the standard set by other contemporary fast reactor designs, an investigation into the feasibility of designing a S-CO<sub>2</sub> cooled GFR core which will passively shut itself down, without violating thermal limits upon the failure of all of the active reactivity mechanisms, will be undertaken.

**Table 9.1: Limiting Transients and Installed Defenses**

Core Damage Mechanism	Transient/Accident Scenario Responsible	Active Defenses	Passive Defense
Excessive Clad Temperature	Loss of Coolant Accident (LOCA)	<ul style="list-style-type: none"> <li>▪ SCRAM (2 independent means)</li> <li>▪ Isolate broken loop</li> <li>▪ Active SCS blowers</li> </ul>	With Containment pressure >7 atm, heat removal via natural convection to the SCS is possible
	Loss of Flow Accident (LOFA)		
	Loss of Heat Sink (LOHS)		
	Transient Overpower (TOP)	<ul style="list-style-type: none"> <li>▪ SCRAM (2 independent means)</li> </ul>	

Additionally, since the Shutdown Cooling System/Emergency Cooling System (SCS/ECS) uses water on the heat removal side in order to remove decay heat from the core, there is a chance of water ingress into the core, should there be a leak in the SCS/ECS heat exchanger and a sufficient pressure differential. As well, there is a water-cooled precooler in the directly connected PCS, providing another means for possible water ingress (note that this scenario is highly unlikely during power operations, as S-CO<sub>2</sub> system pressure is much greater than H<sub>2</sub>O pressure). Further, it may prove of interest to refuel with the reactor cavity flooded with water for heat removal and reactivity control purposes (refueling would only take place every 15-20 years for the batch-loaded TID core presented in Chapter 4). Flooding as a post-accident safety measure of last resort would also be a worthwhile option. Finally, it is desirable to store the spent fuel in water, to provide for an efficient means of decay heat removal. Thus, it is desirable to have the reactor and individual fuel assemblies be sub-critical when water is introduced into the geometry where the S-CO<sub>2</sub> coolant normally is. Hence, an investigation into a water ingress scenario will be undertaken.

## 9.2 Quasi-Static Method

A method has already been developed by Wade and Chang to assess the passive safety capability of a LMR, referred to as the Quasi-Static Method (QSM) [Wade and Chang, 1988] [Wade and Hill, 1997]. While this methodology acts as an excellent generic starting point for undertaking an initial assessment of neutronic passive safety of an advanced reactor, there are several key differences between an LMR and a direct cycle Gas-cooled Fast Reactor (GFR) which may limit the adoption of this methodology. These differences will be examined and a new way for assessing the passive safety capability of a GFR with a S-CO<sub>2</sub> direct cycle Brayton Power Conversion System will be proposed, based on the work originally done in [Wade and Chang, 1988].

The starting point for the QSM is a basic reactivity balance which takes into account all of the ways that core reactivity can be influenced between an initial steady state condition and a final steady state condition [Wade and Chang, 1988]:

$$0 = \Delta\rho = (P - 1)A + \left(\frac{P}{F} - 1\right)B + \delta T_{in} C + \Delta\rho_{ext}^* \quad \{9.1\}$$

where:

$\rho$  = reactivity

$P$  = normalized power (expressed relative to 100% power)

$F$  = normalized flow (expressed relative to 100% flow)

$\delta T_{in}$  = change from normal coolant inlet temperature

$\Delta\rho_{ext}$  = externally imposed reactivity, e.g. in the case of an LMR, addition of reactivity due to a sodium void passing through the core

$A$  = power coefficient of reactivity,  $\phi$ /fractional power change =  $\left(\frac{\partial\rho}{\partial P}\right)$

$B$  = power/flow coefficient of reactivity,  $\phi$ /fractional power/flow

---

\* Throughout this chapter, two difference operators,  $\Delta$  and  $\delta$ , are used.  $\Delta$  is used to represent a difference in a parameter between two geographic locations, e.g.  $\Delta T$  is the difference between core inlet and outlet temperature, while  $\delta$  is used to represent a difference in a parameter between two different points in time, e.g.  $\delta T_{in}$  is the difference in core inlet temperature between the initial steady state condition and the final steady state condition. The exception to this is when  $\Delta$  is used with  $\rho$ , it represents a difference in reactivity between two different points in time, e.g.  $\Delta\rho$  is the difference in reactivity between the initial steady state condition and the final steady state condition. While this is slightly confusing, this nomenclature is adopted to remain consistent with that used by [Wade and Chang, 1988] and [Wade and Hill, 1997].



$$\text{change} = \left( \frac{\partial \rho}{\partial (P/F)} \right)$$

$$C = \text{inlet temperature coefficient of reactivity, } \phi/K = \left( \frac{\partial \rho}{\partial K} \right)$$

Central to the applicability of Equation {9.1} is the fundamental assumption that the limiting transients that may occur between the initial and final steady state condition are “slow enough to preclude non-equilibrium stored energy in the fuel pins and delayed neutron nonequilibrium.” [Wade and Chang, 1988] Hence, the reactivity feedbacks become linear and allow Eq. {9.1} to be solved for the new steady-state core condition resulting from the transient. It is important to remember that the basis of this tool is to help predict the new steady state condition of the core resulting from a particular transient, in an effort to quickly and efficiently influence design choices to maximize safety. Implicit in this method is keeping the core power level at a desirable level (shutdown or 0% in most cases) and not violating established core thermal limits at either of the steady state conditions. This method does not predict or explain the time-dependent transient behavior that occurs between steady state conditions. This fundamental concept of how the results from the QSM should be

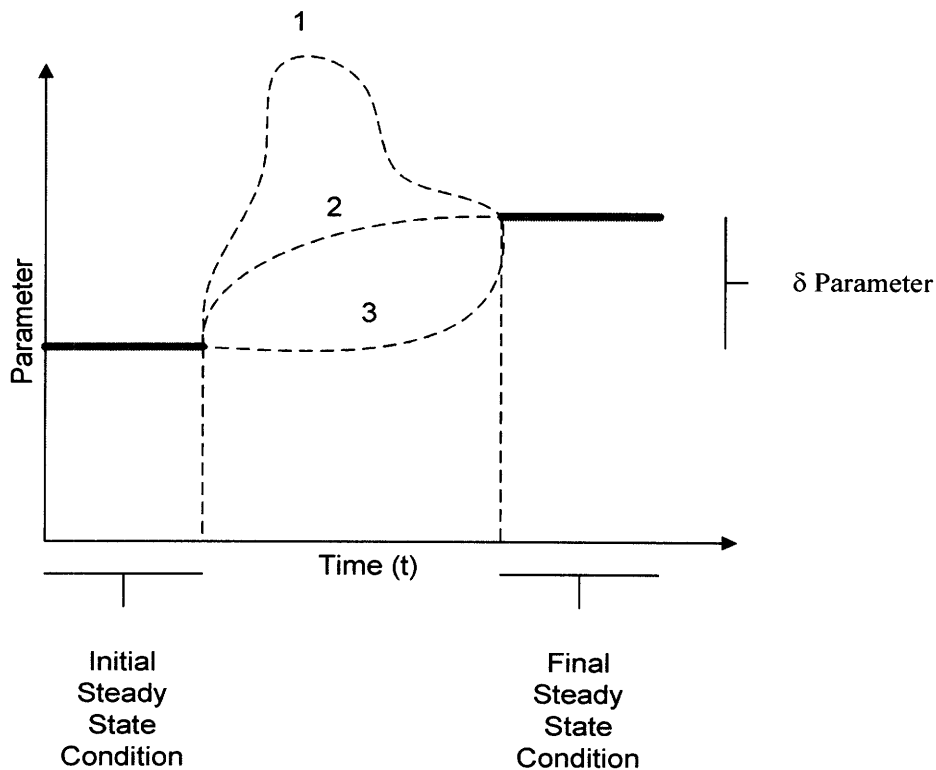


Figure 9.1: Illustration of How the Results of the Quasi-Static Method Should be Viewed

viewed is shown in Figure 9.1, where a parameter can change between an initial and final steady state core condition in a number of ways; however, the QSM is concerned only with the difference in this parameter between the two steady state conditions ( $\delta$  Parameter). In order to explain the time-dependent transient behavior that occurs between steady state conditions, a detailed and comprehensive safety analysis using advanced tools, such as RELAP, must be performed (see [Pope et al, 2006] for an example). Hence, the results presented here and elsewhere using this method should be viewed as helping to guide the initial design process to make choices that will ultimately enhance safety, not a definitive conclusion about a core's ability to be passively safe or to preclude core damage.

[Wade and Chang, 1988] uses the following 3 Anticipated Transients Without SCRAM (ATWS) as the envelope to demonstrate passive core safety, implying that inherent protection from these three limiting transients will ensure core protection from all other ATWS events: Loss of Heat Sink Without SCRAM (LOHSWS), Loss of Flow Without SCRAM (LOFWS), and rod runout Transient Overpower Without SCRAM (TOPWS). However, remembering that this core design has a different coupling to the Power Conversion System (PCS) and Coolant Void Reactivity (CVR) affects this core much differently than the core for which the original QSM was developed, leads to the conclusion that the original QSM is not directly applicable and needs to be modified to account for these differences. Each of the original 3 limiting scenarios, along with others that are necessary due to the differences between the IFR and this core design, will be discussed as a basis for the development of a modified methodology. Throughout these discussions, the simplified plant layouts, shown in Figure 9.2 and Figure 9.3 should be kept in mind.

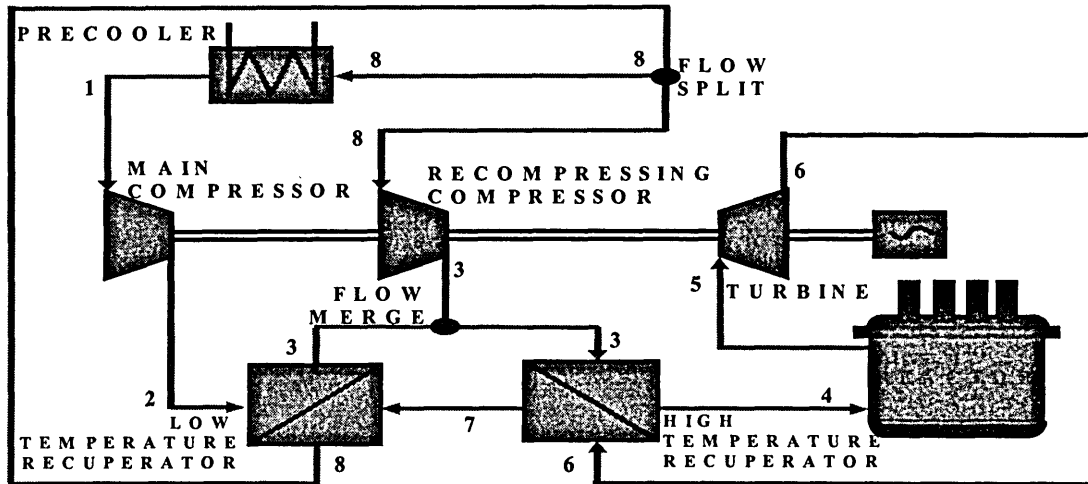


Figure 9.2: Simplified Plant Layout – Line Diagram

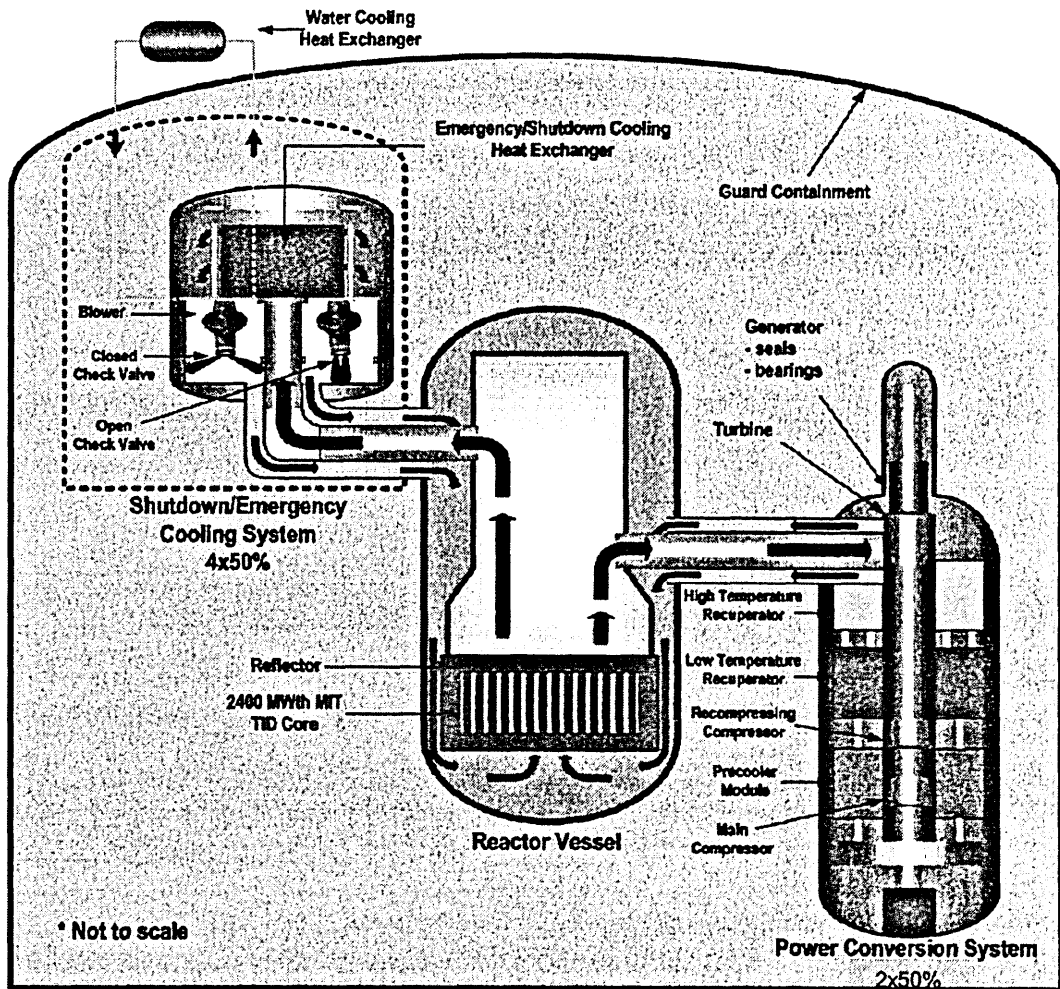


Figure 9.3: Simplified Plant Layout – Cartoon Depiction

### 9.2.1 Loss of Heat Sink Without SCRAM (LOHSWS)

One of the questions for the direct cycle GFR is the mechanisms by which a LOHS can be initiated. Looking at the Brayton cycle Power Conversion System currently in use in Figure 9.2, the simplest would be a loss of (water) flow on the secondary side of the pre cooler. This is the only heat sink loss mechanism which would only affect reactor inlet temperature ( $T_{IN}$ ) and not flow ( $F$ ) through the core. Other LOHS scenarios involve loss of a turbine (and accompanying compressor) which would also affect flow through the reactor core. This assumes that the pressure drop through the stagnant turbines and compressors is great enough to preclude natural circulation. As well, the direct cycle GFR that this analysis is being applied to has 2 loops. Therefore, in order for a complete loss of heat sink to be accomplished, a common cause failure preventing both precoolers from removing heat would need to occur. Such a scenario might be loss of electrical power to the pumps on the heat removal side of the pre cooler.

As a heat sink is lost,  $\delta T_{in} \uparrow$  and flow ( $F$ )  $\leftrightarrow$ . For passive safety, it is desired that  $P \rightarrow 0$ . As well, it is assumed that  $\Delta \rho_{ext} = 0$ . Hence, Eq. {9.1} becomes:

$$0 = \Delta \rho = (0 - 1)A + (0 - 1)B + \delta T_{in} C + 0$$

Since A and B are both negative, positive reactivity is inserted by the reduction in power by the magnitude A+B. Negative reactivity is inserted by the increase in coolant inlet temperature of the magnitude  $\delta T_{in} C$ . Hence, too large of a magnitude of A and B will insert too much positive reactivity following a power reduction.

The asymptotic  $\delta T_{in}$  can be represented by:

$$\delta T_{in} = \frac{A + B}{C}$$

Since:

$$\delta T_{OUT} = \delta T_{IN} - \Delta T_c$$

$$\begin{aligned}\delta T_{OUT} &= \frac{A+B}{C} - \Delta T_c \\ &= \left( \frac{A+B}{C\Delta T_c} - 1 \right) \Delta T_c\end{aligned}$$

$$\delta T_{OUT} = \Delta T_c * \left( \frac{\frac{A/B + 1}{C\Delta T_c} - 1}{B} \right) \quad \{9.2\}$$

These equations for  $\delta T_{in}$  and  $\delta T_{OUT}$  represent the asymptotic temperature limits for this transient, and are consistent with the original QSM developed in [Wade and Chang, 1988].

### 9.2.2 Transient Overpower Without SCRAM (TOPWS)

This scenario involves the involuntary withdrawal of the control rod of the greatest worth, which could represent a continuous rod withdrawal casualty or a rod ejection. In this scenario, no change in  $T_{in}$  is assumed, hence  $\delta T_{in}=0$ . We also assume that  $\Delta\rho_{ext} = \Delta\rho_{TOP}$  (i.e. the reactivity associated with this rod withdrawal) and that the flow stays constant ( $F=1$ ). This makes Eq. {9.1}:

$$0 = \Delta\rho = (P-1)A + (P-1)B + 0 + \Delta\rho_{TOP}$$

However, in the long term, inlet temperature will begin to rise, reducing the power ideally to the nominal heat rejection level. The P/F ratio will return to 1 and  $T_{OUT}$  increases to compensate for the increase in inlet temperature. Consequently, Eq. {9.1} becomes:

$$0 = \Delta\rho = (1-1)A + (1-1)B + \delta T_{IN}C + \Delta\rho_{TOP}$$

Rearranging:

$$\delta T_{in} = \frac{-\Delta\rho_{TOP}}{C} = \delta T_{OUT} \quad \{9.3\}$$

From this balance, we can see that the positive reactivity inserted by the withdrawn rod is ultimately balanced by the increase in  $T_{IN}$ . A possible wrinkle in the application of this to the direct cycle GFR is how the turbine loading may vary with core power. This analysis assumes a constant turbine loading/flow throughout the transient. If the turbine load control is based on reactor power, this may complicate the analysis. However, in keeping with the spirit of passive reactor shutdown, we will assume that the turbine loading/flow is constant until such time as this assumption needs to be re-evaluated. Therefore, the TOPWS analysis developed in [Wade and Chang, 1988] will hold for the direct cycle GFR. Further, another limit placed on this casualty is that  $\Delta\rho_{TOP}$  be less than \$1 to prevent prompt supercriticality. Ideally, it is desirable to keep  $\Delta\rho_{TOP} < \$0.50-0.60$  for reactivity control purposes.

### 9.2.3 Loss of Flow Without SCRAM (LOFWS)

In the LMR scenario, power is lost to the primary pumps and the secondary and tertiary loops continue to remove heat. Hence  $\delta T_{in}=0$  and  $P \rightarrow 0$  for a passive safety response. Again, assuming  $\Delta\rho_{ext}=0$ , Eq. {9.1} becomes:

$$0 = \Delta\rho = (0-1)A + \left(\frac{P}{F}-1\right)B + 0 + 0$$

The increase in P/F will insert negative reactivity which will be opposed by the positive reactivity inserted by a reduction in P. Too large of a magnitude of A relative to the magnitude of B, would insert too much positive reactivity as power goes to zero. One way to combat this would be to use a passive negative reactivity insertion device that actuates upon loss of flow. Such a device would also be useful to provide an insertion of negative reactivity during a loss of coolant accident (LOCA), where a large positive void reactivity associated with such a scenario could have negative consequences. Examples of such devices will be elaborated on in a separate section.

Rearranging, we get:

$$\frac{P}{F} = 1 + \frac{A}{B}$$

Hence:

$$\delta\left(\frac{P}{F}\right) = \frac{A}{B}$$

Since:

$$\delta T_{OUT} = \Delta T_C * \delta\left(\frac{P}{F}\right)$$

$$\delta T_{OUT} = \Delta T_C * \left(\frac{A}{B}\right) \quad \{9.4\}$$

However, examining the system design shown in Figure 9.2 and Figure 9.3, it is hard to envision a scenario where flow is lost without an accompanying degradation in the heat sink. Examples of scenarios where flow is lost and the accompanying effect on the heat sink are listed in Table 9.2: Loss of Flow Scenarios (Without SCRAM) and Accompanying Effect on Heat Sink.

**Table 9.2: Loss of Flow Scenarios (Without SCRAM) and Accompanying Effect on Heat Sink**

Loss of Flow Scenario	Heat Sink(s) Lost	Heat Sink(s) Available
Isolation of a single PCS loop	Loss of pre-cooler in that loop	Pre-coolers in remaining loops
Single compressor failure	Loss of circulation in PCS and subsequent inability of that loop's pre-cooler to remove heat	Pre-coolers in remaining loops
Isolation of both PCS loops	Loss of both pre-coolers and SCS/ECS units	SCS/ECS
Common cause compressor failure	Loss of circulation in both PCS loops and subsequent inability of both loops' pre-coolers to remove heat	SCS/ECS

While the heat removal capability will be degraded upon the loss of flow capability and will be lower than the power produced in the core, reactivity feedbacks may eventually reduce reactor core power commensurate with the ability of the plant to remove that heat. However, the speed and degree with which this is achievable depend upon all of the reactivity feedbacks working in concert and must be evaluated using more detailed and rigorous methods. While the effects of these reactivity feedbacks can not be quantified at this time, we will assume that the reactivity feedback effects are slow enough such that upon a

loss of flow, a mismatch between the heat produced by the core and the ability of the plant to remove this heat will exist. Hence, a loss of flow cannot occur without at least a partial loss of heat sink, and the stand alone LOFWS scenario is not applicable to the direct cycle GFR.

#### 9.2.4 Combined Loss of Flow and Heat Sink without SCRAM (CLOFHSWS)

As discussed earlier, a degradation of heat sink would certainly accompany a loss of flow, making the scenario unique to a direct-cycle GFR. In this transient,  $T_{in} \uparrow$ ,  $F \downarrow$ , and  $\Delta\rho_{ext}=0$ . For the ideal case where  $P \rightarrow 0$ , Eq. {9.1} becomes:

$$0 = \Delta\rho = (0-1)A + \left(\frac{P}{F} - 1\right)B + \delta T_{in} C$$

Positive reactivity is inserted due to the reduction in power and negative reactivity is inserted due to both P/F increasing and  $T_{IN}$  increasing.

Rearranging, we get:

$$\frac{P}{F} = 1 + \frac{A - \delta T_{in} C}{B}$$

Hence:

$$\delta\left(\frac{P}{F}\right) = \frac{A - \delta T_{in} C}{B}$$

Since:

$$\delta T_{OUT} = \Delta T_c * \delta\left(\frac{P}{F}\right)$$

$$\delta T_{OUT} = \Delta T_c * \left(\frac{A - \delta T_{in} C}{B}\right)$$

Noting that:

$$\delta T_{OUT} = \delta T_{IN} - \Delta T_c$$



$$\delta T_{OUT} = \Delta T_C * \left( \frac{A - (\delta T_{OUT} + \Delta T_C) C}{B} \right)$$

Rearranging this equation in terms of the common ratios used in the original QSM:

$$\delta T_{OUT} = \Delta T_C * \left( \frac{\frac{A}{B} - \frac{C \Delta T_C}{B}}{1 + \frac{C \Delta T_C}{B}} \right) \quad \{9.5\}$$

### 9.2.5 Loss of Coolant Without SCRAM (LOCAWS)

One shortcoming of applying the original QSM to a direct-cycle S-CO<sub>2</sub> cooled GFR is that it does not account for the large reactivity changes due to changes in system pressure. This effect is much more significant in the S-CO<sub>2</sub> cooled GFR than for the LMR. While there will be a pressure control system in the plant to maintain the pressure at nominal values during steady state operation and minor transients, scenarios which involve large changes in pressure would not be accounted for in the QSM. This is different than sodium voiding due to boiling, where changes in coolant temperature cause changes in coolant density that are accounted for in the coolant density reactivity coefficient ( $\alpha_{c_0}$ ) which is part of the dimensionless reactivity parameters B and C in Eq. {9.1} (described in a future section). While other sodium voiding scenarios are possible, e.g. cover gas entrainment, the reactivity associated with these events would be accounted for in the  $\Delta\rho_{ext}$  term, similar to how the reactivity associated with GFR voiding will be accounted for. Revisiting the Quasi-Static reactivity balance, Eq. {9.1}, accounting for the insertion of Coolant Void Reactivity ( $\Delta\rho_{VOID}$ ) upon a LOCA:

$$0 = \Delta\rho = (P-1)A + \left(\frac{P}{F} - 1\right)B + \delta T_{in} C + \Delta\rho_{ext} + \Delta\rho_{VOID}$$

Assuming  $\Delta\rho_{ext}=0$  and  $\delta T_{in}=0$ :

$$0 = \Delta\rho = (P-1)A + \left(\frac{P}{F} - 1\right)B + 0 + 0 + \Delta\rho_{VOID}$$

However in the long term, for passive safety,  $P \rightarrow 0$ :

$$0 = \Delta\rho = (0-1)A + \left(\frac{P}{F}-1\right)B + 0 + 0 + \Delta\rho_{VOID}$$

Rearranging:

$$\frac{P}{F} = 1 + \frac{A - \Delta\rho_{VOID}}{B}$$

Hence:

$$\delta\left(\frac{P}{F}\right) = \frac{A - \Delta\rho_{VOID}}{B}$$

Since:

$$\delta T_{OUT} = \Delta T_C * \delta\left(\frac{P}{F}\right)$$

Then:

$$\delta T_{OUT} = \Delta T_C * \left(\frac{A - \Delta\rho_{VOID}}{B}\right)$$

or

$$\delta T_{OUT} = \Delta T_C * \left(\frac{A}{B} - \frac{\Delta\rho_{VOID}}{B}\right) \quad \{9.6\}$$

It should be noted that A and B are negative quantities. Therefore, the greater the positive coolant void reactivity (CVR), the larger the value that the asymptotic outlet temperature will reach ( $\delta T_{OUT}$ ), as shown by Eq. {9.6}. However, in core designs with a negative CVR, the magnitude  $\delta T_{OUT}$  will be increasingly mitigated for more negative values of CVR. Given that the current core design possesses a negative CVR throughout core life, LOCAWS will provide an extra compensatory measure against positive reactivity insertion and may make it a less limiting scenario than other ATWS events.

## 9.2.6 Comparison of ATWS Scenarios

Table 9.3 lists the assumptions made for all of the key parameters examined in this adaptation of the QSM, the Direct Cycle GFR QSM (DCGQSM). The values of N/A in this table (for LOFWS, CLOFHSWS, and LOCAWS) mean that no assumptions are made about the power to flow ratio ( $P/F$ ), as both power and flow go to zero in these scenarios, making it impossible to know from this analysis which gets there faster and the resulting value of  $P/F$ . As shown in the derivation, solving for the  $P/F$  ratio is a key part of determining if this core can achieve passively safe shutdown without violating core thermal limits.

**Table 9.3: Assumptions Made for Key Parameters in the ATWS scenarios from the Initial Steady State Condition to the Final Steady State Condition**

Scenario	P	F	$P/F$	$\delta T_{in}$	$\Delta \rho_{ext}$
LOHSWS	↓ to 0	↔	↓ to 0	↑	=0
TOPWS	↔	↔	↔	=0	= $\Delta \rho_{TOP}$
LOFWS	↓ to 0	↓ to 0	N/A	=0	=0
CLOFHSWS	↓ to 0	↓ to 0	N/A	↑	=0
LOCAWS	↓ to 0	↓ to 0	N/A	=0	= $\Delta \rho_{VOID}$

**Table 9.4: Summary of Reactivity Insertion Mechanisms for Transients in the Direct Cycle GFR Quasi-Static Method (DCGQSM)**

Scenario	Positive Reactivity Insertion Mechanism	Magnitude	Negative Reactivity Insertion Mechanism	Magnitude
LOHSWS	Power ↓	A+B	Inlet Coolant Temperature ↑	$\delta T_{in} C$
TOPWS	Rod W/D	$\Delta \rho_{TOP}$	Inlet Coolant Temperature ↑	$\delta T_{in} C$
LOFWS	Power ↓	A	$P/F$ ↑	$(P/F-1)B$
CLOFHSWS	Power ↓	A	$P/F$ ↑ and Inlet Coolant Temperature ↑	$(P/F-1)B + \delta T_{in} C$
LOCAWS	Power ↓	A	$P/F$ ↑, CVR	$(P/F-1)B + \Delta \rho_{VOID}$

**Table 9.5: Summary of Asymptotic Outlet Temperatures for Bounding ATWS Scenarios**

Casualty	$\delta T_{OUT}$
LOHSWS	$\Delta T_c * \left( \frac{A/B + 1}{\frac{C \Delta T_c}{B}} - 1 \right)$
TOPWS	$\frac{-\Delta \rho_{TOP}}{C}$
LOFWS	$\Delta T_c * \left( \frac{A}{B} \right)$
CLOFHSWS	$\Delta T_c * \left( \frac{\frac{A}{B} - \frac{C \Delta T_c}{B}}{1 + \frac{C \Delta T_c}{B}} \right)$
LOCAWS	$\Delta T_c * \left( \frac{A}{B} - \frac{\Delta \rho_{VOID}}{B} \right)$

Table 9.4 summarizes the reactivity insertion mechanisms hypothesized in the scenarios presented. As well, Table 9.5 summarizes the asymptotic limits for  $\delta T_{OUT}$  for the five casualties of interest, expressed in terms of the key reactivity ratios used in the original QSM. Note that there are no conditions on core inlet temperature, as coolant freezing is not a concern with a direct cycle GFR utilizing  $SCO_2$  as a coolant; therefore, limits on  $\delta T_{IN}$  need not be evaluated.

Upon closer examination of the results in Table 9.4, it can be seen that the reactivity insertion mechanisms among the LOFWS, CLOFHSWS, and the LOCAWS scenarios are similar. Specifically, the positive reactivity that is inserted following these scenarios is equivalent (e.g. magnitude of A) but the compensating negative reactivity insertion mechanisms differ – in the case of CLOFHSWS, by a term of  $\delta T_{in}C$ , and in the case of LOCAWS, by a term of  $\Delta \rho_{VOID}$ . Hence, the LOFWS scenario has less negative reactivity with which it can compensate the insertion of positive reactivity and is the most limiting. It should be noted that this comparison holds only for cores which insert negative reactivity upon voiding. In cores where positive reactivity is inserted upon coolant voiding, the LOCAWS scenario is certainly more limiting than the LOFWS situation (e.g. net reactivity: LOCAWS  $(A + \Delta \rho_{VOID}) - (P/F-1)B$  v. LOFWS  $(A) - (P/F-1)B$ ). However, it has been previously determined that the LOFWS scenario is not credible for the direct-cycle GFR, as a

degradation of heat sink capability is certain to accompany a loss of flow. Hence, the LOFWS is no longer a limiting scenario and it must be determined if the CLOFHSWS or LOCAWS is more limiting. Since both scenarios will experience the same magnitude of positive reactivity insertion, the scenario which inserts less negative reactivity will be more limiting. From Table 9.4, we can see that if  $\Delta\rho_{VOID} > \delta T_{in}C$ , CLOFHSWS will be more limiting and if  $\Delta\rho_{VOID} < \delta T_{in}C$ , LOCAWS will be more limiting. Further developing this relationship:

$$|\Delta\rho_{VOID}| (>, <) |\delta T_{IN}C|$$

Since:

$$\delta T_{IN} = \delta T_{OUT} + \Delta T_c$$

and for the CLOFHSWS:

$$\delta T_{OUT} = \Delta T_c * \left( \frac{\frac{A}{B} - \frac{C\Delta T_c}{B}}{1 + \frac{C\Delta T_c}{B}} \right)$$

$$|\Delta\rho_{VOID}| (>, <) \left| \left[ \Delta T_c * \left( \frac{\frac{A}{B} - \frac{C\Delta T_c}{B}}{1 + \frac{C\Delta T_c}{B}} \right) + \Delta T_c \right] C \right|$$

$$|\Delta\rho_{VOID}| (>, <) \left| \left[ \frac{1 + \frac{A}{B}}{1 + \frac{C\Delta T_c}{B}} \right] C\Delta T_c \right| \quad \{9.7\}$$

This inequality is now in terms of the reactivity coefficients and the CVR in an effort to more simply determine which ATWS scenario, CLOFHSWS or LOCAWS, will be more limiting. With the LOFWS eliminated as a limiting scenario, only the conditions for the LOHSWS, TOPWS, and LOCAWS of CLOFHSWS remain. Comparing the reactivity

insertion mechanisms from Table 9.4 and recognizing that a net negative reactivity is desired for passive core safety:

$$|\text{Negative Reactivity Insertion}| > |\text{Positive Reactivity Insertion}|$$

For the LOHSWS:

$$|C * (\delta T_{in})_{MAX}| \geq |A + B| \quad \{9.8\}$$

For the TOPWS:

$$|C * (\delta T_{in})_{MAX}| \geq |\Delta \rho_{TOP}| \quad \{9.9\}$$

For the CLOFHSWS

$$|B * (\delta (P/F))_{MAX} + C * (\delta T_{in})_{MAX}| \geq |A| \quad \{9.10\}$$

For the LOCAWS:

$$|B * (\delta (P/F))_{MAX} + \Delta \rho_{VOID}| \geq |A| \quad \{9.11\}$$

First, examining the case for the LOHSWS, (Eq. 9.8):

$$|\delta T_{in})_{MAX}| \geq \frac{|A + B|}{|C|}$$

Since:

$$\delta T_{IN} = \delta T_{OUT} + \Delta T_c$$

and

$$\delta T_{OUT})_{MAX} = \gamma \Delta T_{co}^{MAX}$$

Then:

$$\delta T_{IN}|_{MAX} = \gamma \Delta T_{co}^{MAX} + \Delta T_c$$

where:

$\gamma$  = safety margin

$$\Delta T_c = T_{Cout} - T_{Cin} \quad \{9.12\}$$

$$\delta T_{CO}^{MAX} = T_{CFAIL} - T_{C MAXSS} \quad \{9.13\}$$

where:

$\delta T_{CO}^{MAX}$  = Maximum tolerable increase in coolant outlet temperature that will keep cladding temperature below its failure limit

$T_{CFAIL}$  = Temperature at which cladding will fail

$T_{C MAXSS}$  = Maximum Steady State Cladding Temperature

It should be noted that Eq. {9.13} implicitly assumes that the cladding  $\Delta T$  and the coolant  $\Delta T$  will be proportional.

$$|\gamma \delta T_{co}^{MAX} + \Delta T_c| \geq \frac{|A+B|}{|C|}$$

Since  $\gamma$ ,  $\delta T_{co}^{MAX}$ , and  $\Delta T_c$  are all positive numbers, by definition:

$$\left( \frac{\gamma \delta T_{co}^{MAX}}{\Delta T_c} + 1 \right) * \Delta T_c \geq \frac{|A+B|}{|C|}$$

$$\frac{\gamma \delta T_{co}^{MAX}}{\Delta T_c} \geq \left( \frac{|A+B|}{|C| * \Delta T_c} \right) - 1 \quad \{9.14\}$$

Similarly, for the TOPWS (Eq. 9.9):

$$\delta T_{in}|_{MAX} \geq \frac{|\Delta \rho_{TOP}|}{|C|}$$

Since:

$$\delta T_{IN}|_{MAX} = \gamma \delta T_{co}^{MAX} + \Delta T_c$$

$$\left| \gamma \delta T_{co}^{MAX} + \Delta T_c \right| \geq \frac{|\Delta \rho_{TOP}|}{|C|}$$

Since  $\gamma$ ,  $\delta T_{co}^{MAX}$ , and  $\Delta T_c$  are all positive numbers, by definition:

$$\left( \frac{\gamma \delta T_{co}^{MAX}}{\Delta T_c} + 1 \right) * \Delta T_c \geq \frac{|\Delta \rho_{TOP}|}{|C|}$$

$$\frac{\gamma \delta T_{co}^{MAX}}{\Delta T_c} \geq \left( \frac{|\Delta \rho_{TOP}|}{|C| * \Delta T_c} \right) - 1 \quad \{9.15\}$$

For the CLOFHSWS (Eq. 9.10):

$$\left| B * \left( \delta \left( \frac{P}{F} \right) \right)_{MAX} + C * (\delta T_{in})_{MAX} \right| \geq |A|$$

Since:

$$\delta T_{in}|_{MAX} = \gamma \delta T_{co}^{MAX} + \Delta T_c$$

and

$$\delta \left( \frac{P}{F} \right)_{MAX} = \frac{\gamma \delta T_{co}^{MAX}}{\Delta T_c}$$

$$\left| B * \frac{\gamma \delta T_{co}^{MAX}}{\Delta T_c} + C * \left( \frac{\gamma \delta T_{co}^{MAX}}{\Delta T_c} + 1 \right) * \Delta T_c \right| \geq |A| \quad \{9.16\}$$

Finally, for the LOCAWS (Eq. 9.11):

$$\left| B * \left( \delta \left( \frac{P}{F} \right) \right)_{MAX} + \Delta \rho_{VOID} \right| \geq |A|$$

Given:



$$\delta\left(\frac{P}{F}\right)_{MAX} = \frac{\gamma\delta T_{co}^{MAX}}{\Delta T_C}$$

$$\left| B * \left( \frac{\gamma\delta T_{co}^{MAX}}{\Delta T_C} \right) + \Delta\rho_{VOID} \right| \geq |A| \quad \{9.17\}$$

Hence, if the relationships derived in {9.14}, {9.15}, {9.16}, {9.17} are obeyed, the core should be passively safe. As discussed earlier, the CLOFHSWS and LOCAWS scenarios provide similar reactivity feedback mechanisms, save one, and Eq. {9.7} provides guidance on which of these two scenarios is most limiting. Hence, {9.14}, {9.15}, and the more limiting of {9.16} and {9.17} provide the envelope of passive safety for the DCGQSM. These relationships are summarized in Table 9.6.

**Table 9.6: Summary of Limiting Reactivity Relationships that Provide the Passive Safety Envelope for the DCGQSM**

Casualty	Relationship	
LOHSWS	$\frac{\gamma\delta T_{co}^{MAX}}{\Delta T_c} \geq \left( \frac{ A+B }{ C  * \Delta T_c} \right) - 1$	
TOPWS	$\frac{\gamma\delta T_{co}^{MAX}}{\Delta T_c} \geq \left( \frac{ \Delta\rho_{TOP} }{ C  * \Delta T_c} \right) - 1$	
CLOFHSWS v. LOCAWS	If $ \Delta\rho_{VOID}  > \left[ \frac{1 + \frac{A}{B}}{1 + \frac{C\Delta T_c}{B}} \right] C\Delta T_c$ CLOFHSWS is more limiting	$\left  B * \frac{\gamma\delta T_{co}^{MAX}}{\Delta T_c} + C * \left( \frac{\gamma\delta T_{co}^{MAX}}{\Delta T_c} + 1 \right) * \Delta T_c \right  \geq  A $
	If $ \Delta\rho_{VOID}  < \left[ \frac{1 + \frac{A}{B}}{1 + \frac{C\Delta T_c}{B}} \right] C\Delta T_c$ LOCAWS is more limiting	$\left  B * \left( \frac{\gamma\delta T_{co}^{MAX}}{\Delta T_c} \right) + \Delta\rho_{VOID} \right  \geq  A $

### 9.2.7 Results

[Wade and Chang, 1988] provides guidance on how to calculate the values of the reactivity coefficients A, B, and C:

$$A = (\alpha_D) \overline{\Delta T_f} \quad \{9.18\}$$

$$B = \left[ \alpha_D + \alpha_e + \alpha_{CO} + 2 \left( \alpha_{RD} + \frac{2}{3} \alpha_R \right) \right] * \left( \frac{\Delta T_C}{2} \right) \quad \{9.19\}$$

$$C = \alpha_D + \alpha_e + \alpha_{CO} + \alpha_R \quad \{9.20\}$$

where:

$\alpha_D$  = Doppler coefficient of reactivity,  $\phi/K_{\text{fuel}}$

$\alpha_e$  = Fuel axial expansion reactivity coefficient,  $\phi/K$

$\alpha_{CO}$  = Coolant density reactivity coefficient,  $\phi/K$

$\alpha_{RD}$  = Rod driveline reactivity coefficient,  $\phi/K$

$\alpha_R$  = Core radial expansion reactivity coefficient,  $\phi/K$

$\overline{\Delta T_f}$  = core average incremental temperature increase of the fuel above the coolant, K

$\Delta T_C$  = axial coolant temperature rise, K =  $T_{\text{Cout}} - T_{\text{Cin}}$

Further, for this core design, the following values have been adopted:

$\gamma$  = safety margin = 0.95

$T_{\text{CFAIL}}$  = Temperature at which cladding will fail = 1300°C [Special Metals, Inc., 2004]

$T_{\text{CMAXSS}}$  = Maximum Steady State Cladding Temperature = 800°C [Pope et al, 2006]

$T_{\text{Cout}}$  = 650°C

$T_{\text{Cin}}$  = 485.5°C

Then from Eqs. {9.12} and {9.13}:

$$\delta T_{CO}^{MAX} = 500^\circ\text{C}$$

$$\Delta T_c = 164.5^\circ\text{C}$$

Also:

$$\overline{\Delta T_f} = 587.34 \text{ throughout core life}$$

Note that [Wade and Chang, 1988] uses a value of 2/3 for  $\gamma$ . This parameter is used to account for uncertainties in the analysis and is prohibitively conservative at 2/3. Hence, in this analysis, we will use 0.95 to represent a more reasonable value of uncertainty. [Special Metals, Inc., 2004] provides guidance for the selection of the cladding failure temperature, taken as the temperature at which the creep resistance of the MA ODS 956 cladding degrades significantly. The maximum steady state cladding temperature given is described in detail in [Pope et al, 2006], as well as in other sections of this document. It should be noted that

**Table 9.7: Summary of Reactivity Parameters for the GFR TID Core**

Parameter	BOL Value	MOL Value	EOL Value
$\alpha_D$ (1E-03 $\phi$ /K)	-355	-236	-228
$\alpha_e$ (1E-03 $\phi$ /K)	-43	-77	-21
$\alpha_{Co}$ (1E-03 $\phi$ /K)	-1	-1	0
$\alpha_{RD}$ (1E-03 $\phi$ /K)	0	0	0
$\alpha_R$ (1E-03 $\phi$ /K)	-49	-62	-40
A ( $\phi$ )	-238.68	-158.43	-152.99
B ( $\phi$ )	-38.31	-32.59	-24.89
C ( $\phi$ /K)	-0.45	-0.38	-0.29
$\Delta\rho_{TOP}$ ( $\phi$ )	12.8	32.52	0
$\Delta\rho_{VOID}$ ( $\phi$ )	-107.74	-119.12	-35.78
$\beta_{eff}$	0.0045	0.0045	0.0044

while the value of  $T_{Cout}$  is set equal to the core average, i.e. average channel outlet temperature,  $T_{CMAXSS}$  and  $\delta T_{CO}^{MAX}$  are based on the most limiting cladding temperature in the core. Coupled with the fact that it has been assumed that the cladding  $\Delta T$  and the coolant  $\Delta T$  will be proportional, this methodology provides for protection against local hot spot failure.

Table 9.7 gives each of the reactivity parameters for the GFR TID core design for the beginning of life (BOL), middle of life (MOL), and end of life (EOL). The MOL values are taken at the burnup for which the excess reactivity is greatest.

#### 9.2.7.1 Calculation of Doppler Coefficient of Reactivity

The temperature dependence for the Doppler coefficient of reactivity varies greatly among different literature sources and depends strongly on fuel type (i.e. ceramic, metal, etc.) and isotopic composition. Using computational tools, the relationship between  $k_{eff}$  and the fuel temperature was explicitly determined in order to find the Doppler coefficient of reactivity for this core. The first step is to Doppler broaden the cross sections of the fuel. Using NJOY, a cross section manipulation and conversion computer code (see Appendix A for a description), cross sections for the actinides in the fuel were Doppler broadened for a wide range of temperatures. The cross section libraries used were JENDL 3.3, due mainly to them being in the correct form for manipulation via NJOY. Performing high accuracy runs using MCNP, a relationship between core eigenvalue and fuel temperature was derived.

Assuming that the Doppler coefficient of reactivity will be of the form:

$$\alpha_D = \frac{\hat{A}}{T^n} \quad \{9.21\}$$

and recalling that the Doppler Coefficient can be represented by:

$$\alpha_D = \frac{\partial \rho}{\partial T} \quad \{9.22\}$$

Manipulating Eq. {9.22} and substituting the relationship for  $\alpha_D$  assumed in Eq. {9.21}, the values A and n can be found by fitting the following relationship to the data obtained from MCNP:

$$\int_{\rho(T_C)}^{\rho(T_H)} d\rho = \int_{T_C}^{T_H} \alpha_D dT$$

$$\rho(T_{HOT}) - \rho(T_{COLD}) = \int_{T_C}^{T_H} \frac{\hat{A}}{T^n} dT$$

where:

$$\rho(T_{HOT}) = \frac{k_{HOT} - 1}{k_{HOT}} = \text{Reactivity value obtained from MCNP data run at } T_{HOT}$$

$$\rho(T_{COLD}) = \frac{k_{COLD} - 1}{k_{COLD}} = \text{Reactivity value obtained from MCNP data run at } T_{COLD}$$

Hence:

$$\rho(T_{HOT}) - \rho(T_{COLD}) = \hat{A} \left[ \left( \frac{T_{HOT}^{(1-n)}}{1-n} \right) - \left( \frac{T_{COLD}^{(1-n)}}{1-n} \right) \right] \text{ for } n \neq 1 \quad \{9.23a\}$$

$$\rho(T_{HOT}) - \rho(T_{COLD}) = \hat{A} \left[ \ln \left( \frac{T_{HOT}}{T_{COLD}} \right) \right] \text{ for } n=1 \quad \{9.23b\}$$

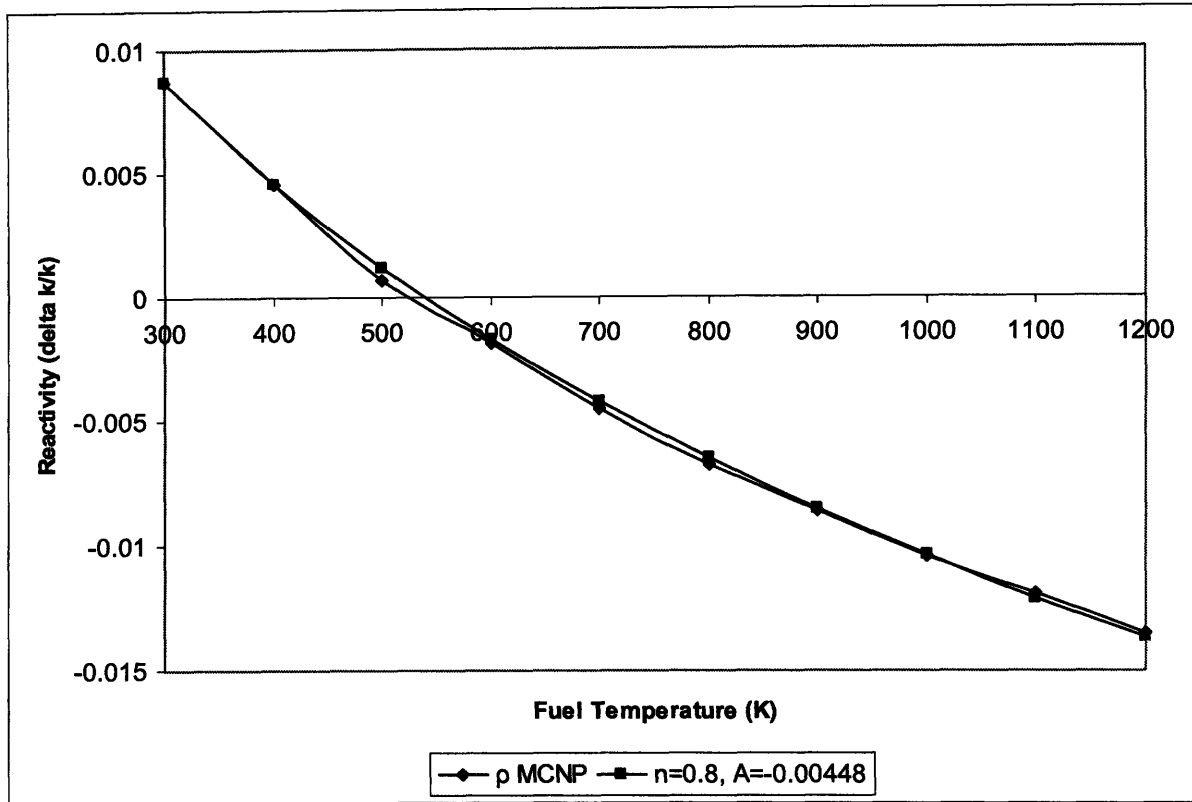


Figure 9.4: Core Reactivity as a Function of Fuel Temperature

Applying the results of the MCNP data runs to Eq. {9.23}, the best fit was obtained for  $n=0.8$  and  $\hat{A} = -0.00448$ , as shown in Figure 9.4.

Hence:

$$\alpha_D = \left( \frac{\rho(T_{HOT}) - \rho(T_{COLD})}{5 * [T_{HOT}^{(0.2)} - T_{COLD}^{(0.2)}]} \right) \frac{1}{T^{0.8}} \approx \frac{-0.00448}{T^{0.8}} \quad \{9.24\}$$

#### 9.2.7.2 Results Using the Original QSM

As a basis for comparison with the revised QSM developed in this chapter, the reactivity parameters calculated for the TID core (shown in Table 9.7) are applied to the original QSM. While this method is initially presented in [Wade and Chang, 1988] and amplified in [Wade and Hill, 1997], [Romano et al, 2003] provides helpful guidance and some more detailed information on the QSM and [Yarsky et al, 2005] provides amplifying guidance on application of the original QSM to GFRs. Combining all of these resources, Table 9.8 lists the limiting ATWS scenarios along with their applicable limits using the

original QSM and Table 9.9 shows the results of the original QSM using the reactivity parameters calculated for the TID core.

**Table 9.8: Limiting ATWS Scenarios and Applicable Limits for the Original QSM**

Casualty	Corresponding Ratio of Reactivity Parameters	Condition	Limit
LOHSWS	$\frac{A}{B}$	$\leq$	$\gamma \frac{\delta T_{CO}^{MAX}}{\Delta T_c}$
LOFWS	$\frac{C\Delta T_c}{B}$	$\geq$	1
TOPWS	$\frac{-\Delta\rho_{TOP}}{ B }$	$\leq$	$\gamma \frac{\delta T_{CO}^{MAX}}{\Delta T_c}$

**Table 9.9: Summary of Passive Safety Evaluation Using the Original QSM**

Limiting Casualty	Relationship to Satisfy Passive Safety	Time in Life	LHS	RHS	Passive Safety Satisfied?
LOFWS	$\frac{A}{B} \leq \gamma \frac{\delta T_{CO}^{MAX}}{\Delta T_c}$	BOL	5.45	2.89	N
		MOL	4.25	2.89	N
		EOL	5.37	2.89	N
LOHSWS	$\frac{C\Delta T_c}{B} \geq 1$	BOL	1.93	1	Y
		MOL	1.90	1	Y
		EOL	1.91	1	Y
TOPWS	$\frac{-\Delta\rho_{TOP}}{ B } \leq \gamma \frac{\delta T_{CO}^{MAX}}{\Delta T_c}$	BOL	0.33	2.89	Y
		MOL	1.00	2.89	Y
		EOL	0	2.89	Y

Using the original QSM, the results in Table 9.9 show that the TID GFR core is will provide passive core protection without violating core thermal limits for two (LOHSWS and TOPWS) of the three limiting scenarios. The limiting scenario which is not protected against is the LOFWS, due to the rather large value of A relative to B. Physically, these results indicate that the  $\frac{A}{B}$  ratio is too large to control the asymptotic temperature rise in a LOFWS. In this case, the value of A (the power coefficient of reactivity,  $\beta$ /fractional power change) is too large. Recalling the definition of A from Eq. {9.18} and that A is a negative number, the large value of A indicates that too much reactivity, hence power, will be inserted into the core upon core cooldown.

While these unfavorable results should be heeded, they should not be acted upon at this time. As discussed earlier, this original QSM falls short in providing an accurate assessment of a direct cycle GFR, as it doesn't accurately account for a more limiting scenario, the LOCAWS. As well, it provides a more conservative estimate of core self-controllability as it de-couples the LOFWS and LOHSWS accidents, which are necessarily coupled in a direct cycle GFR (as discussed earlier). Still, it is useful to look at an assessment of the self-controllability using the original QSM, as a basis for comparison for the revised method developed in this work.

### 9.2.7.3 Results Using the Revised QSM (DCGQSM)

In order to apply the results in Table 9.7 to the DCGQSM, it must first be determined if the CLOFHSWS or the LOCAWS is more limiting throughout core life. Applying the results to the determining relationship, Eq. {9.7}, Table 9.10 shows that the LOCAWS is more limiting at BOL and EOL and that the CLOFHSWS is more limiting at MOL.

**Table 9.10: Evaluation of Whether LOCAWS or CLOFHSWS is More Limiting Throughout Core Life**

	BOL (¢)	Limiting Scenario	MOL (¢)	Limiting Scenario	EOL (¢)	Limiting Scenario
$ \Delta\rho_{void} $	107.74	LOCAWS	119.12	CLOFHSWS	35.78	LOCAWS
$\left[ \left[ \frac{1 + \frac{A}{B}}{1 + \frac{C\Delta T_c}{B}} \right] C\Delta T_c \right]$	162.66		112.02		104.11	

Applying the values summarized in Table 9.7 to the DCGQSM developed in this chapter for the limiting scenarios, Table 9.11 shows that the core is protected against all limiting ATWS events throughout core life except for a LOCAWS at EOL. . This raises two interesting questions: (1) Is the core passively protected against the less limiting of the LOCAWS/CLOFHSWS throughout core life and (2) For what core parameters will the core be passively protected against LOCAWS at EOL? In answering the first question, Table 9.12 shows that the core is passively protected against the less limiting LOCAWS/CLOFHSWS

scenario, supporting the derivation of the DCGQSM, and leaving only the protection against LOCAWS at EOL scenario as a concern.

**Table 9.11: Summary of Passive Safety Evaluation Using DCGQSM**

Limiting Casualty	Time in Life	Relationship to Satisfy Passive Safety	LHS	RHS	Passive Safety Satisfied?
LOHSWS	BOL	$\frac{\gamma\delta T_{co}^{MAX}}{\Delta T_c} \geq \left( \frac{ A+B }{ C  * \Delta T_c} \right) - 1$	2.89	2.34	Y
	MOL		2.89	1.77	Y
	EOL		2.89	2.33	Y
TOPWS	BOL	$\frac{\gamma\delta T_{co}^{MAX}}{\Delta T_c} \geq \left( \frac{ \Delta\rho_{TOP} }{ C  * \Delta T_c} \right) - 1$	2.89	-0.83	Y
	MOL		2.89	-0.47	Y
	EOL		2.89	-1	Y
LOCAWS/ CLOFHSWS	BOL (LOCAWS)	$\left  B * \left( \frac{\gamma\delta T_{co}^{MAX}}{\Delta T_c} \right) + \Delta\rho_{VOID} \right  \geq  A $	218.34	208.67	Y
	MOL (CLOFHSWS)	$\left  B * \frac{\gamma\delta T_{co}^{MAX}}{\Delta T_c} + C * \left( \frac{\gamma\delta T_{co}^{MAX}}{\Delta T_c} + 1 \right) * \Delta T_c \right  \geq  A $	334.29	138.51	Y
	EOL (LOCAWS)	$\left  B * \left( \frac{\gamma\delta T_{co}^{MAX}}{\Delta T_c} \right) + \Delta\rho_{VOID} \right  \geq  A $	107.67	133.68	N

**Table 9.12: Passive Safety Evaluation against the CLOFHSWS/LOCAWS Scenario**

Limiting Casualty	Time in Life	Relationship to Satisfy Passive Safety	LHS	RHS	Passive Safety Satisfied?
LOCAWS/ CLOFHSWS	BOL (CLOFHSWS)	$\left  B * \frac{\gamma\delta T_{co}^{MAX}}{\Delta T_c} + C * \left( \frac{\gamma\delta T_{co}^{MAX}}{\Delta T_c} + 1 \right) * \Delta T_c \right  \geq  A $	397.91	208.67	Y
	MOL (LOCAWS)	$\left  B * \left( \frac{\gamma\delta T_{co}^{MAX}}{\Delta T_c} \right) + \Delta\rho_{VOID} \right  \geq  A $	213.22	138.51	Y
	EOL (CLOFHSWS)	$\left  B * \frac{\gamma\delta T_{co}^{MAX}}{\Delta T_c} + C * \left( \frac{\gamma\delta T_{co}^{MAX}}{\Delta T_c} + 1 \right) * \Delta T_c \right  \geq  A $	256.84	133.68	Y

In order to answer the second question, a closer look at the defining relationship for ensuring passive core shutdown during a LOCAWS, Eq. {9.17}, is necessary:

$$\left| B * \left( \frac{\gamma\delta T_{co}^{MAX}}{\Delta T_c} \right) + \Delta\rho_{VOID} \right| \geq |A|$$

Fundamentally, in order to satisfy this inequality, it is desirable to maximize the left hand side and minimize the right hand side. Table 9.13 shows the value of each parameter



necessary, keeping all other parameter values constant, in order to satisfy the inequality throughout core life. Note that  $\Delta T_C$  is not included in the Table, as it appears in the expression for B (see Eq. {9.19}), and consequently cancels with the  $\Delta T_C$  in the denominator of the  $\left(\frac{\gamma \delta T_{co}^{MAX}}{\Delta T_C}\right)$  term, yielding no effect on inequality {9.17} with a change in value.

Hence, when a change in B is explored in Table 9.13, it is really a change in one of the reactivity parameters that contributes to B that is intended.

**Table 9.13: Values Necessary to Satisfy Passive Safety at EOL for the LOCAWS Scenario**

Parameter	Desired Trend to Satisfy Inequality {9.17}	Value Needed to Satisfy Inequality {9.17}	Current Value	Other Passive Safety Inequalities Satisfied?
$\gamma$	Maximize magnitude	1.3	0.95	Y
$\Delta\rho_{VOID}$	Maximize magnitude	-61.8¢	-35.78¢	Y
$\delta T_{co}^{MAX}$	Maximize magnitude	680	500	Y
A	Minimize magnitude	-107.67	-133.68	Y
B	Maximize magnitude	-33.91	-24.89	Y

First, maximizing the right hand side means maximizing the value of the safety factor,  $\gamma$ . This factor is already set at a fairly high value of 0.95, and Table 9.13 shows that it would have to be set at an impossible value of 1.3 for the inequality to be satisfied ( $\gamma=1$  represents no uncertainty, i.e. perfect information). Hence, there is no room for improvement with respect to this parameter. Next, it is desirable to maximize the magnitude of the negative coolant void reactivity inserted upon voiding. It should be remembered that the TID core design presented in this work represents a design which bounds desirable performance characteristics, i.e. gives the longest reactivity limited burnup without exceeding other neutronic limits, such as manageable reactivity swing. Hence, one possible solution for improving EOL  $\Delta\rho_{VOID}$  and protecting against a LOCAWS at EOL would be to reduce the BOL enrichment, hence core eigenvalue. This would have the concomitant effect of reducing reactivity limited burnup (disadvantage), but would reduce the core inventory of

Pu-239 and consequently reduce the magnitude of  $\Delta\rho_{\text{VOID}}$  throughout core life, specifically at EOL. Looking next at the allowed tolerable increase in cladding temperature before failure,  $\delta T_{\text{co}}^{\text{MAX}}$ , an increase of only 180°C is necessary to ensure passive safety (without violating core thermal limits) against a LOCAWS. This margin is small enough that it may be achievable, with either an alternative cladding material, e.g. SiC, or further research into the maximum allowable temperature of the current cladding, ODS MA956, which may reveal more temperature margin to failure, especially if the duration of the exposure can be limited in time. Improvements in the reactivity coefficient A are shown to yield passive safety improvements with respect to the LOCAWS scenario, while improvements in B can also help to improve passive safety with respect to the LOCAWS scenario, but may do so at the detriment of providing passive safety against the other scenarios. This can be seen by closer examination of Table 9.4, which shows that B acts as both a positive and negative reactivity insertion mechanism, depending upon the scenario. Hence, of the 5 parameters, only an adjustment in A is the one that can be currently further evaluated in having a possibility of achieving passive safety against a LOCAWS at EOL.

Since A is found by:

$$A = (\alpha_D) \overline{\Delta T_f}$$

where:

$\overline{\Delta T_f}$  = core average incremental temperature increase of the fuel  
above the coolant, K

$\alpha_D$  = Doppler coefficient of reactivity,  $\phi/\text{K}$ ,

the magnitude of A can be minimized by either reducing the Doppler coefficient or  $\overline{\Delta T_f}$ . Reducing the Doppler coefficient is not desirable for several reasons. In order to reduce the Doppler coefficient, the amount of diluent in the fuel would need to be reduced to slightly harden the spectrum. This would have the concurrent effect of reducing the amount of negative coolant void reactivity inserted upon voiding, moving the core further away from being passively safe against the LOCAWS. As well, reducing the Doppler coefficient would also reduce the reactivity coefficient B, which would move the core further away from passive safety in the LOCAWS scenario, as maximizing the magnitude of B is the desired trend for satisfying the LOCAWS passive safety inequality.

Hence, the only option to achieve passive safety against the LOCAWS scenario is to reduce the value of  $\overline{\Delta T_f}$ . The value of  $\overline{\Delta T_f}$  needed to satisfy the LOCAWS inequality at EOL is 473°C. Plotting this limit on the TID thermal hydraulic constraints map in Figure 9.5 shows that the acceptable thermal hydraulic region is smaller as a result of imposing this limit, yet geometries which satisfy this new temperature constraint are achievable.

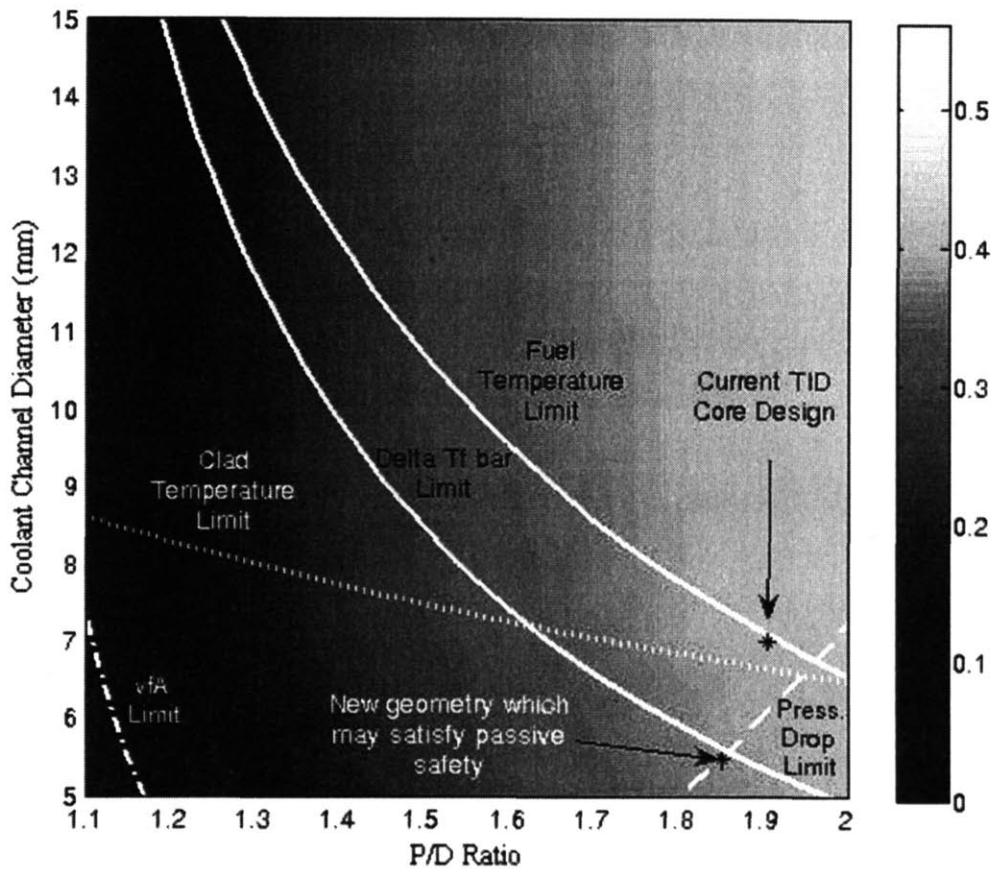


Figure 9.5: Acceptable T/H Envelope for TID Fuel with BeO and  $\overline{\Delta T_f}$  limit

Table 9.14 compares the geometry with the  $\overline{\Delta T_f}$  constraint that maximizes  $vf_A$  (the volume fraction of fuel with respect to the cross-sectional assembly volume) with that of the current TID core design, showing their applicable thermal hydraulic parameters. Maximizing  $vf_A$  has been shown to maximize neutronic and economic performance. While the  $vf_A$  achievable with this new limit imposed is lower than that achievable without the limit, it is still relatively high and is greater than the maximum achievable by other candidate

**Table 9.14: Comparison of geometries which maximize  $\nu f_A$  with and without the  $\overline{\Delta T_f}$  limit**

Case	D	P/D	Max. Fuel Temp. (°C)	Max. Clad Temp. (°C)	Pressure Drop (kPa)	$\nu f_A$
TID fuel with integrated BeO and $\overline{\Delta T_f}$ limit imposed	5.5	1.85	1391	764.8	500	0.3803
TID fuel with integrated BeO and NO $\overline{\Delta T_f}$ limit (current TID design)	7.0	1.905	1770	810	420	0.4199

fuel types explored (e.g. pin and ICAF). As well, while  $\nu f_A$  is lowered as a result of this new constraint, the fuel and cladding temperatures are improved, as the new constraint forces the optimum design into a region of more favorable performance. It should be remembered that lowering  $\overline{\Delta T_f}$  to achieve passive core safety is based on the assumption that by designing a new core with the first set of geometric parameters listed in Table 9.14, i.e. those subject to the  $\overline{\Delta T_f}$  constraint, the other reactivity parameters, i.e. Doppler coefficient, fuel thermal expansion coefficient, etc. will not change appreciably from the values obtained for the second set of geometric parameters listed in Table 9.14, i.e. those used throughout this analysis. One concern that arises with the newly selected geometry to satisfy passive core safety is that the coolant hole size is small, increasing the likelihood that coolant channels could become blocked by in-core debris. Should this become a more restrictive design constraint, geometries which increase the coolant channel size can be chosen which still satisfy all of the other criteria, but will come at the expense of  $\nu f_A$ , as shown in Figure 9.5.

Hence, in order to achieve passive core safety, a reactor core of similar conceptual design yet with different basic geometric parameters than those of the current design, i.e. those shown in the first line of Table 9.14, should be developed. While the current core design does not meet the stringent passive design standard imposed by the DCGQSM and QSM, it is very close and the analysis is useful in showing which parameters should be changed in order to enhance the prospects of passive safe shutdown. Further, the current core demonstrates many of the design parameters necessary to get very close to this stringent

standard and resolving uncertainties in the analysis may show that the current design does indeed satisfy the standard. For this reason, another core design will not be undertaken, as the principles for achieving passive safe shutdown have been adequately demonstrated.

Quantifying the effect of the diluent on the thermal conductivity of the fuel is central to determining whether the  $\overline{\Delta T_f}$  value for the current core design even needs to be improved. The crude approximation used in this and related works, is that the thermal conductivity improves by a factor of 1.5 for volume fractions of 10% BeO and above. Hence, from a thermal conductivity standpoint, there is no benefit from adding more diluent above 10%, using this assumption. This is likely inconsistent with the actual physical effect of increasing diluent concentration above 10%, but provides a rough starting point for an analysis.

### **9.3 Water Ingress**

Since the Shutdown Cooling System/Emergency Cooling System (SCS/ECS) and the precooler in the PCS use water on the heat removal side, there is a chance of water ingress into the core, should there be a leak and sufficient differential pressure condition. Since the primary fissile fuel in the core is Pu-239, the most limiting time in life will either be at the beginning of life (BOL), where the parasitic fission product inventory is at a minimum, or at middle of life (MOL), where the core excess reactivity, hence Pu-239 inventory, is the greatest. The greater fission product inventory at MOL may provide sufficient parasitic absorption of the larger number of thermal neutrons introduced as a result of water ingress, reducing the overall reactivity and making MOL less limiting. The influence of these competing effects will need to be determined in order to figure out which one dominates, and consequently, which time in core life is more limiting with respect to water ingress,

In order to assess the effect of water ingress on the core, the S-CO<sub>2</sub> coolant in the current rodged core model (nominal eigenvalue ~1) was replaced with H<sub>2</sub>O at varying densities, to represent the various temperature and pressure conditions that could be expected in the core during a water ingress incident. Note that in these calculations, all of the S-CO<sub>2</sub> coolant was replaced with the H<sub>2</sub>O at the given density, in an effort to show the effect of water coolant on the core. Figure 9.6 shows that at BOL and MOL, introduction of water at any density will cause the core reactivity to decrease and in particular cause the core to go

subcritical. This effect is due to the large moderating property of water, which significantly reduces the neutron energy, making fission in a fast reactor much less likely. At the same time, not enough water is present to thermalize the spectrum to the point where reactivity increases significantly. This is due to the high volume fraction of fuel/low volume fraction of coolant, resulting from the use of TID fuel. A similar effect was found in [Yarsky et al, 2005] for a “Breed and Burn” GFR core. Other fast reactors not using TID fuel are not likely to behave similarly. Further, since the core eigenvalue is consistently lower for the MOL case, the effect of fission product build-up dominates over increased Pu-239 inventory and the BOL case is found to be more limiting.

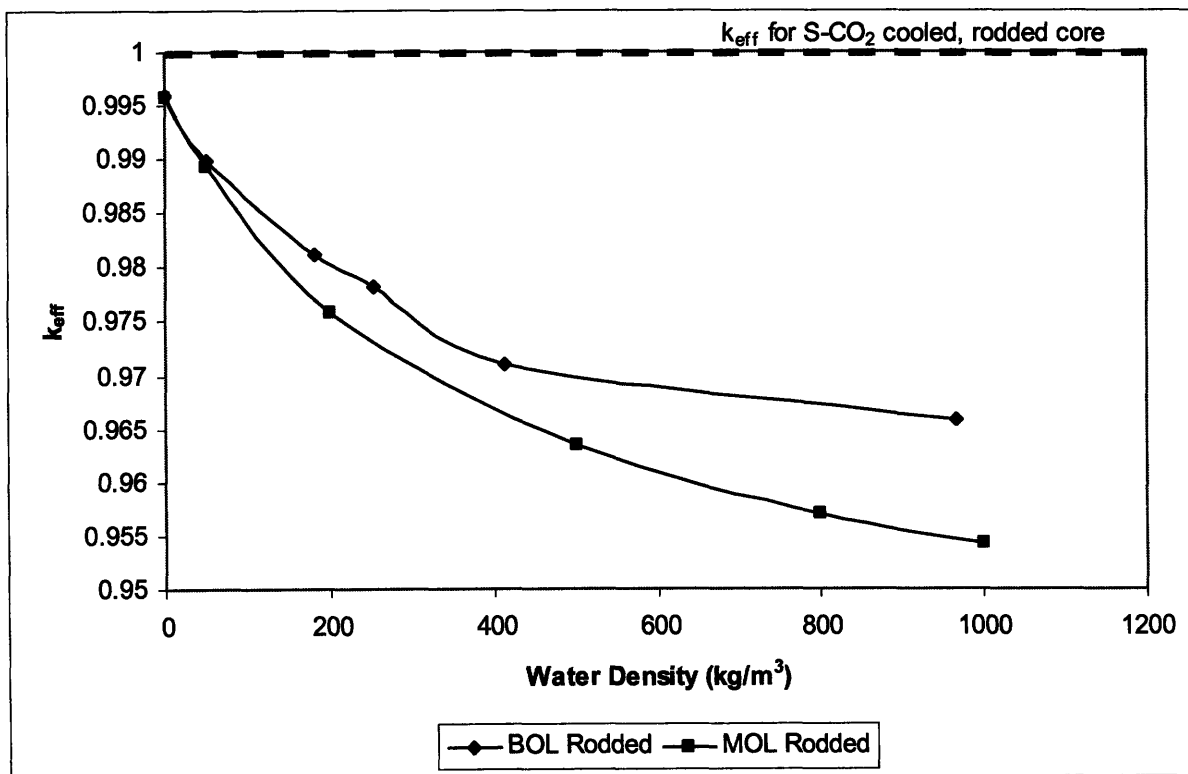


**Figure 9.6: Effect of Water Ingress on Criticality at BOL and MOL for the TID GFR Core**

There are several interesting conclusions that can be drawn from Figure 9.6. First, while water ingress produces favorable results from a safety standpoint, it presents potential problems from an operations standpoint. Should enough water enter the core, the reactor would go subcritical. While this can be compensated for with control rod operation, it adds another dimension to operating the reactor. As well, while the large pressure of the primary coolant (20 MPa) will likely prevent any contaminants from entering the coolant during

operation, the transition from underwater refueling to start-up may leave large amounts of water in the primary system. Not only is this unfavorable from a core reactivity management standpoint, but it also presents problems for the PCS, as H<sub>2</sub>O in the S-CO<sub>2</sub> will not allow the PCS to operate properly. This should be kept in mind as start-up procedures are developed and should be planned for through use of a coolant purification/drying system. Second, the fact that the core can remain subcritical while unrodded with water at densities as little as 200 kg/m<sup>3</sup> (0.2 g/cm<sup>3</sup>) bodes well for safety during both refueling and fuel storage operations. Third, from Figure 9.6, it can be concluded that the fresh fuel will remain subcritical in a spent fuel pool, so long as clusters of assemblies are not surrounded by a thick H<sub>2</sub>O moderator region (which was not analyzed as part of this work). Fourth, since it has been determined that the BOL condition is most limiting from a water ingress standpoint, all of the conclusions and observations made about water ingress and spent fuel handling are applicable to the core throughout core life. This means that in the event of a fuel failure, emergency shutdown, or other need to remove fuel during operation, adequate margins to criticality exist at any time in core life. Finally, given the large effect of water ingress on criticality and the excellent heat removal capabilities of water, support is provided for using a water injection system as a last-resort reactor shutdown and heat removal system.

#### **9.4 Conclusions**

A method for evaluating the passive safe shutdown capability of the TID GFR core was developed from an existing method developed for Liquid Metal Reactors [Wade and Chang, 1988]. The differences between the original method, the Quasi-Static Method (QSM), and the new method, the Direct Cycle GFR QSM (DCGQSM), center around the fact that a loss of flow cannot occur without a degradation of heat sink in a direct cycle system and that Coolant Void Reactivity (CVR) affects this core much differently than the core for which the original QSM was developed. Applying the DCGQSM to the candidate core design shows that passive safe shutdown is achievable against all limiting scenarios at all times in core life except the Loss of Coolant Without SCRAM (LOCAWS) at EOL, due to the large core average incremental temperature increase of the fuel above that of the coolant,  $\overline{\Delta T_f}$ . Solutions for reducing  $\overline{\Delta T_f}$  include altering the geometric specifications of the TID fuel and reducing the large uncertainty currently present in the calculation of this number,

found primarily in the estimation of the effect of the BeO diluent on the fuel thermal conductivity. Since most of the requisite principles for passive core shutdown have been demonstrated and the uncertainty in the calculation of  $\overline{\Delta T_f}$  is fairly large, the candidate core design is deemed sufficiently safe. Hence, a version of this design having the new geometric dimensions is not pursued here and remains a possible area for future work.

Additionally, water ingress scenarios were explored and showed that the large moderating effect of water added enough negative reactivity to ensure adequate margin to criticality throughout core life. The implications with respect to fuel handling and storage were consequently also evaluated as favorable. However, further investigation of configurations in which fuel is dispersed in large volumes of moderator should be investigated.

Finally, since failure to SCRAM is the principal initiation of all dominant accident scenarios, additional measures to increase SCRAM reliability should be investigated.



## 10 Economic Analysis

### 10.1 Introduction

As one of the Gen-IV design cornerstones, economics is an important consideration for any reactor design. While a concept may possess the most desirable performance with respect to a given attribute or set of attributes, it will likely never come to fruition unless it is economically attractive.

A major impediment to the implementation of this GFR (or any other Gen-IV concept) is that LWR technology is proven, reliable, and profitable. This is evidenced specifically in the United States by the recently expanded interest in building new nuclear generating capacity. While the open fuel cycle in use in most LWRs is currently cost-effective, it is wasteful as it uses only a fraction of the energy potential of the fuel and generates hard-to-dispose-of-waste. However, the alternative of closing the LWR fuel cycle is too expensive under current market conditions. Either technological progress will need to drive the cost of spent-fuel reprocessing lower or diminishing resource supply will need to drive Uranium costs higher in order for a LWR-only closed fuel cycle strategy to become more economically attractive. Introducing fast reactors gives a new dimension to fuel recycle, with potentially beneficial economic implications.

The objective of this chapter is to compare the TID GFR concept using (U,TRU)O<sub>2</sub> recycled from legacy LWR spent fuel with that of a once-through LWR using UO<sub>2</sub> in order to determine the cost-competitiveness of the GFR with respect to current practice. While an economic comparison of this GFR with other competing Gen-IV designs might also be useful, the large variety of these designs coupled with the uncertainty associated with their costs prevents this from being a worthwhile effort at present. However, the framework

developed in this chapter for assessing GFR costs could be useful for such a comparison in the future. It should be remembered that the numbers presented in this chapter should only be used on a comparative basis, and are not meant to represent firm values for actual costs in the future.

## 10.2 Nuclear Cost Model

Any nuclear energy cost model is made up of the following 4 components:

$$C_{elec} = C_{cap} + C_{FCC} + C_{O\&M} + C_{D\&D} \quad \{10.1\}$$

where:

- $C_{elec}$  = Busbar cost of electricity, mills/kWh<sub>e</sub>
- $C_{cap}$  = Levelized capital cost of plant, mills/kWh<sub>e</sub>
- $C_{FCC}$  = Levelized fuel cycle cost, mills/kWh<sub>e</sub>
- $C_{O\&M}$  = Levelized Operations and Maintenance (O&M) costs, mills/kWh<sub>e</sub>
- $C_{D\&D}$  = Levelized Decontamination and Disposal (D&D) costs, mills/kWh<sub>e</sub>

In what follows, an accounting of all four factors will be made in order to assess the economic viability of this GFR v. current practice. All of the analyses in this chapter will be made in constant year 2000 dollars. Hence, the effects of inflation will not be accounted for.

### 10.2.1 Capital Cost

Table 10.1 gives capital cost estimates for advanced LWRs (ALWRs) and TRU burning fast reactors (FRs) taken from [NEA, 2002], expressed in year 2000 dollars. It should be noted that the capital cost estimates given for the GFRs are 10%, 25%, and 50% more than the nominal value given for the ALWR. They are also for fast reactors based on sodium technology and not specifically tailored for GFR technology.

**Table 10.1: Capital Cost Estimates [from NEA, 2002]**

	ALWR (\$/kW <sub>e</sub> )	GFR(\$/kW <sub>e</sub> )
Lower Bound	1600	1850
Nominal Value	1700	2100
Upper Bound	1800	2600

A simple first order estimate of levelized capital costs is:

$$C_{cap} = \frac{UC * CRF}{8766 * L} \quad \{10.2\}$$

where:

UC = capital cost of plant in \$/kW<sub>e</sub>

8766 = hours/yr.

L = capacity factor (this represents the average capacity factor over plant operation)

CRF = capital recovery factor for continuous compounding with annual payments, given by:

$$CRF = \left[ \frac{e^{rN} (e^r - 1)}{e^{rN} - 1} \right] \quad \{10.3\}$$

where:

r = interest rate (inflation free, in this case)

N = number of annual payment periods

Assuming an inflation-free interest rate of 10%/yr and that the number of payment periods, N, will equal the life of the plant, i.e. 60 years, CRF = 0.107. Using L=0.9 for both cases and applying the values from Table 10.1 yields the results in Table 10.2.

**Table 10.2: Levelized Capital Cost Estimates of the candidate GFR v. an advanced LWR**

	LWR (mills/kWhr <sub>e</sub> )	GFR(mills/kWhr <sub>e</sub> )	GFR(mills/kWhr <sub>e</sub> )
Capacity Factor	0.9	0.9	0.95
Lower Bound	21.7	25.1	23.7
Nominal Value	23.1	28.5	27.0
Upper Bound	24.2	35.3	33.4

While Table 10.2 shows that the “best-case” (i.e. lower bound) GFR cannot beat the “worst-case” (i.e. upper bound) advanced LWR with respect to capital costs, several things should be considered. First, the longer cycle length inherent in the single-batch GFR fuel cycle is likely to mean an improvement in capacity factor, due to less frequent refueling outages and a lower forced outage rate. A lower forced outage rate is hypothesized to exist for longer cycle length operation due to getting past the infant mortality period of components [Garcia-Delgado and Todreas, 1998]. Assigning an improved capacity factor of 0.95 to the GFR case gives levelized capital cost estimates whose range overlaps with that of

the range for ALWRs. Second, the GFR numbers used are the FR-TRU numbers from [NEA, 2002], which are based on Liquid Metal Reactor (LMR) data. Since LMRs typically have 2 RPVs (a regular and a guard vessel, in the event of a LOCA) and three main loops (primary sodium, intermediate sodium, and secondary Rankine), differences in capital cost likely exist for this GFR that give it an advantage. One such difference is the lower capital cost of the S-CO<sub>2</sub> Brayton Recompression cycle PCS as compared to the Rankine Steam PCS used in LMRs. A comparative cost analysis of a thermal High Temperature Gas Reactor (HTGR) using a direct He Brayton PCS, an indirect steam PCS, and the S-CO<sub>2</sub> Brayton Recompression Cycle PCS used here was made in [Dostal et al, 2004]. This analysis showed that the use of the S-CO<sub>2</sub> Brayton Recompression Cycle PCS saved 8-10% in total capital costs and up to 25% on a \$/KW<sub>e</sub> basis. This alone could provide the reduction in capital cost necessary to make the GFR's capital costs competitive with ALWRs. Further, the highly compact machinery layout and design conceptualized for this plant would mean a smaller containment than ALWRs, adding to the capital cost savings [Gibbs et al, 2006].

While this analysis is relatively simple and first-order, it is suitable for these purposes. [Bunn et al, 2003] gives a more detailed method for calculating capital costs, which accounts for more of the “financial” factors involved in such a process:

$$c_{cap} = \frac{C_{cap} (1 + F_{intc}) (1 + F_{prop}) (1 + F_{cont})}{8766 \eta} (F_{cr} + F_{tax} + F_{ins})$$

where  $C_{cap}$  is the total construction cost, in dollars per kilowatt of installed net electrical capacity (\$/kW<sub>e</sub>),  $F_{intc}$  and  $F_{prop}$  are factors that account for interest during construction and other costs before the plant begins full-scale operation,  $F_{cont}$  is a contingency factor to provide for cost overruns and other unforeseen costs,  $\eta$  is the capacity factor (the total amount of electricity produced in a year divided by the total amount that would be produced from continuous operation at full power), 8766 is the average number of hours in a year, and  $F_{tax}$ , and  $F_{ins}$  are annual charges for property taxes and insurance ( $y^{-1}$ ), which for simplicity are assumed to be proportional to the initial investment. The “fixed charge rate,”  $F_{cr}$  ( $y^{-1}$ ), is the fraction of the initial investment that must be collected each year to repay the initial costs, including interest or return on investment.

Considering these additional financial factors raises the issue that the cost of capital for a GFR will likely be higher than that for an ALWR, given that the GFR is a newer, riskier

technology, and the ALWR has a proven template for success. This will certainly put the GFR at a disadvantage.

### 10.2.2 Front End Fuel Cycle Cost

A simple formula for estimating fuel cycle costs is given by:

$$fcc = \left( \frac{C}{24\eta B_d} \right) * \left( \frac{XT}{1 - e^{-XT}} \right) \quad \{10.4a\}$$

or

$$\frac{fcc}{C} = \left( \frac{1}{24\eta B_d} \right) * \left( \frac{XT}{1 - e^{-XT}} \right) \quad \{10.4b\}$$

where:

$fcc$  = levelized fuel cycle cost (mills/kWh<sub>e</sub>)

$C$  = cost of fuel at the beginning of irradiation (\$/kg fuel)

$\eta$  = thermodynamic efficiency

$B_d$  = fuel discharge burnup (MWd/kg)

$X$  = discount rate (yr<sup>-1</sup>)

$T$  = in-core residence time, given by:

$$T = \frac{B_d}{0.36525 * P_s * L} \quad \{10.5\}$$

where:

$P_s$  = specific power (kW/kg<sub>HM</sub>)

$L$  = plant capacity factor

Comparing the levelized fuel cycle costs of the GFR to a LWR (in this case, Westinghouse 4-loop PWR) in Table 10.3 shows that the break-even levelized fuel cycle cost of a GFR occurs when it is  $\leq \frac{3.05E-3}{1.49E-3}$  or  $\leq 2.05$  times that of LWR fuel on a \$/kg basis at the beginning of irradiation ( $C$ ). The comparison of fuel cycle costs between the two strategies is made this way in order to give an accurate comparison based on calculated core performance, while neglecting the great uncertainty inherent in predicting the value of  $C$ . The uncertainty in  $C$  for LWR fuel is lower and driven primarily by market forces, whereas the uncertainty in  $C$  for the GFR fuel is greater in that it is based on a reprocessing and fabrication technology which has yet to be fully developed. Also note that both cases are

calculated for steady-state refueling (which for the batch-loaded GFR, is the same as a startup core; however, the differences between the LWR start-up core and steady state case are greater.)

**Table 10.3: Levelized Fuel Cycle Cost Estimates of the candidate GFR v. an advanced LWR**

	LWR	GFR
Core Power Rating ( $MW_{th}$ )	3411	2400
Thermodynamic Efficiency	0.33	0.47
Fuel Discharge Burnup [MWd/kg]	50	140
Discount Rate [ $yr^{-1}$ ]	0.1	0.1
Specific Power [ $kW/kg_{HM}$ ]	38.7	20.74
Capacity Factor	0.9	0.9
In core residence time [yr]	3.93	20.53
$f_{cc}/C$	$3.05 \times 10^{-3}$	$1.49 \times 10^{-3}$

Using the plant parameters in Table 10.3, Figure 10.1 and Figure 10.2 show the levelized fuel cycle costs as a function of core average discharge burnup and specific power for different values of C. Figure 10.1 shows that for a given core average discharge burnup

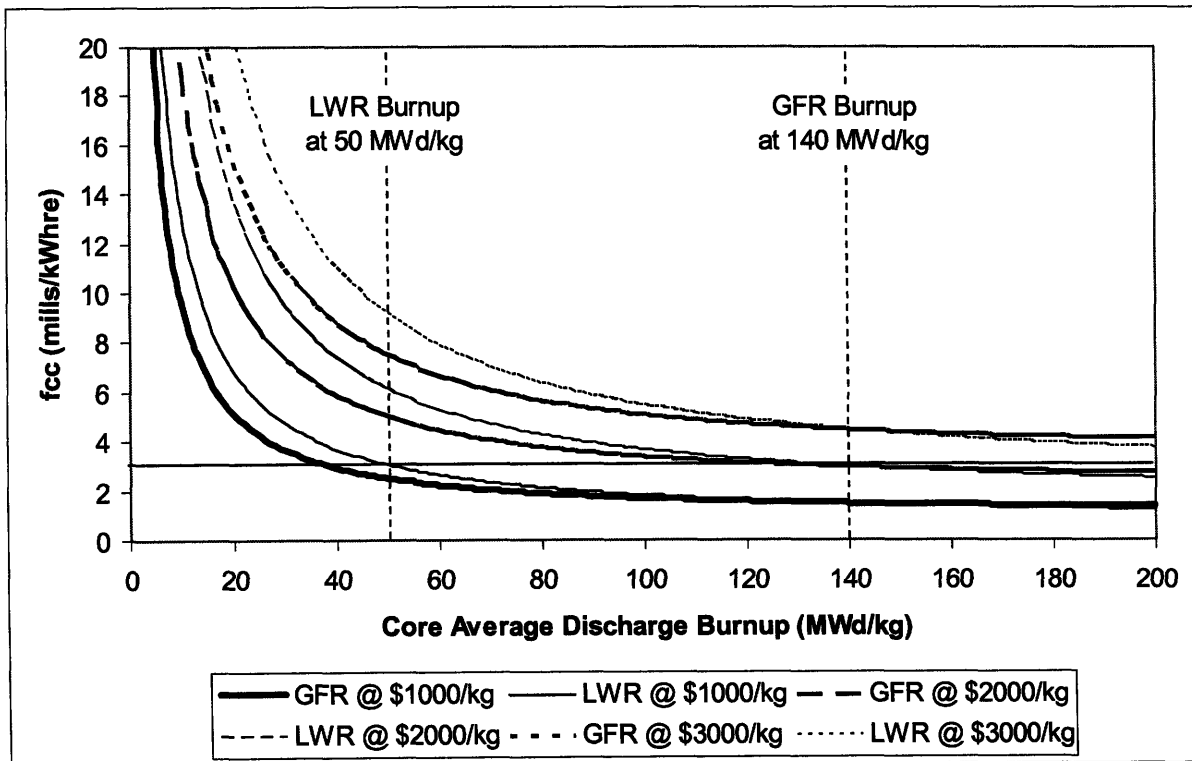


**Figure 10.1: Levelized Fuel Cycle Cost as a Function of Burnup for the GFR v. an LWR**

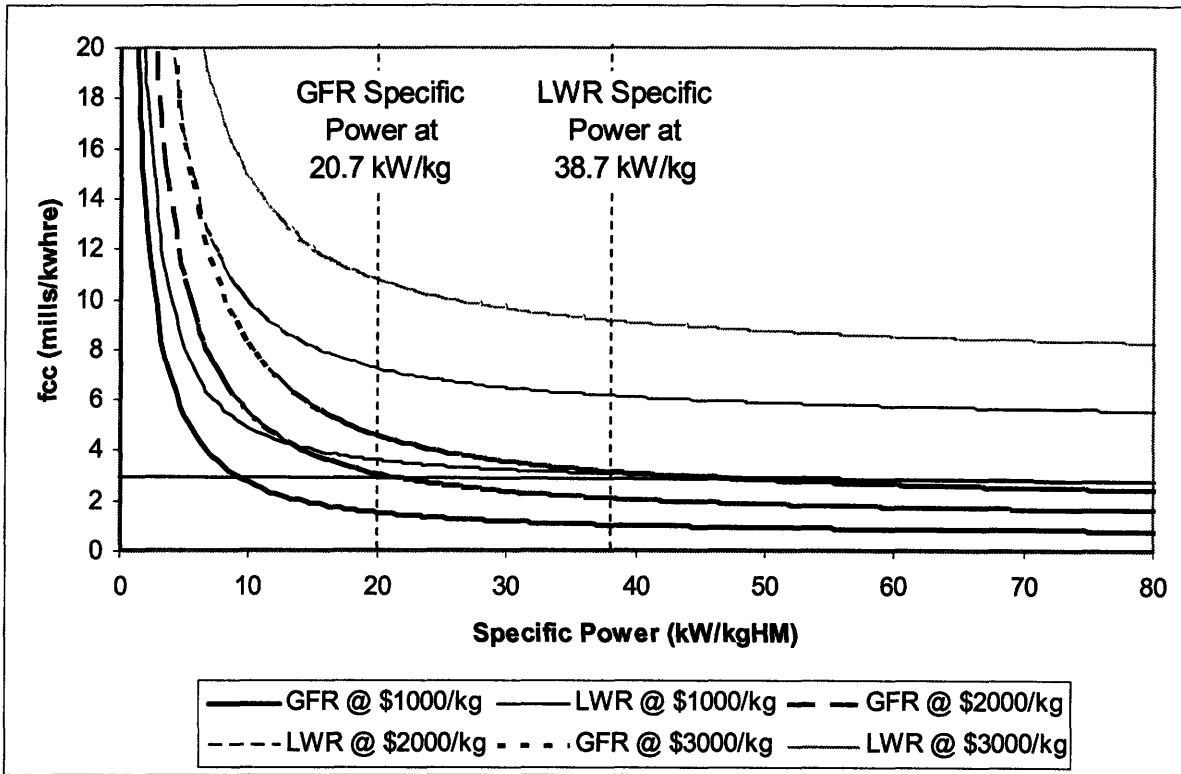


**Figure 10.2: Levelized Fuel Cycle Cost as a Function of Specific Power for the GFR v. an LWR**

and given  $C$ , the GFR will yield a lower levelized fuel cycle cost, due mainly to its lower specific power contributing to a longer in-core residence time. However, given the high costs associated with the reprocessing of the fuel,  $C$  is likely to be higher for the GFR, shifting the advantage to the LWR. Similarly, Figure 10.2 shows that for a given specific power and  $C$ , GFR fuel will provide a lower levelized fuel cycle cost due to its higher achievable burnup. Again, when the higher specific power of the LWR is accounted for, much higher values of  $C$  for the GFR provide the break-even scenario with the LWR. These two figures show that a comparison of levelized fuel cycle costs needs to account for both achievable burnup and specific power in order for an accurate comparison to be made.

While a comparison using specific values for  $C$  has been purposely avoided previously, it is now addressed to show how the uncertainty in this number can affect the fuel cycle cost comparison between an LWR and GFR. In order to calculate  $C$ , the following relation is used:

$$C = \sum_i m_i c_i (1 + X \Delta \tau_i) \quad \{10.6\}$$

where:

$m_i$  = mass flow for the  $i^{\text{th}}$  process step of the front end of the fuel cycle (kg)

$c_i$  = unit cost for the  $i^{\text{th}}$  process step of the front end of the fuel cycle (\$/kg)

$X$  = discount rate ( $\text{yr}^{-1}$ )

$\Delta \tau_i$  = time between  $i^{\text{th}}$  process step of the front end of the fuel cycle and the beginning of irradiation (yr)

It should be noted that Equation {10.6} uses a linear approximation to account for the time value of money for a continuous compounding scenario, with error  $\sim \frac{(X \Delta \tau)^2}{2}$ . This error is  $\sim 2\%$  for the worst case (i.e.  $X=0.1$  and  $\Delta \tau=24$  months for the reprocessing of GFR fuel) and is acceptable for the purposes of this comparison.

In an effort to determine if the factor of 2.05 is achievable with GFR fuel, estimates for the fuel cycle cost in terms of both  $C$  (\$/kg fuel) and mills/kWh<sub>e</sub> are presented in Table 10.4, along with the assumptions used to derive these estimates. Figure 10.3 shows the mass flow and process steps of the front end of the fuel cycle for both the LWR and GFR used to derive the results in Table 10.4. The assumptions regarding unit costs came from

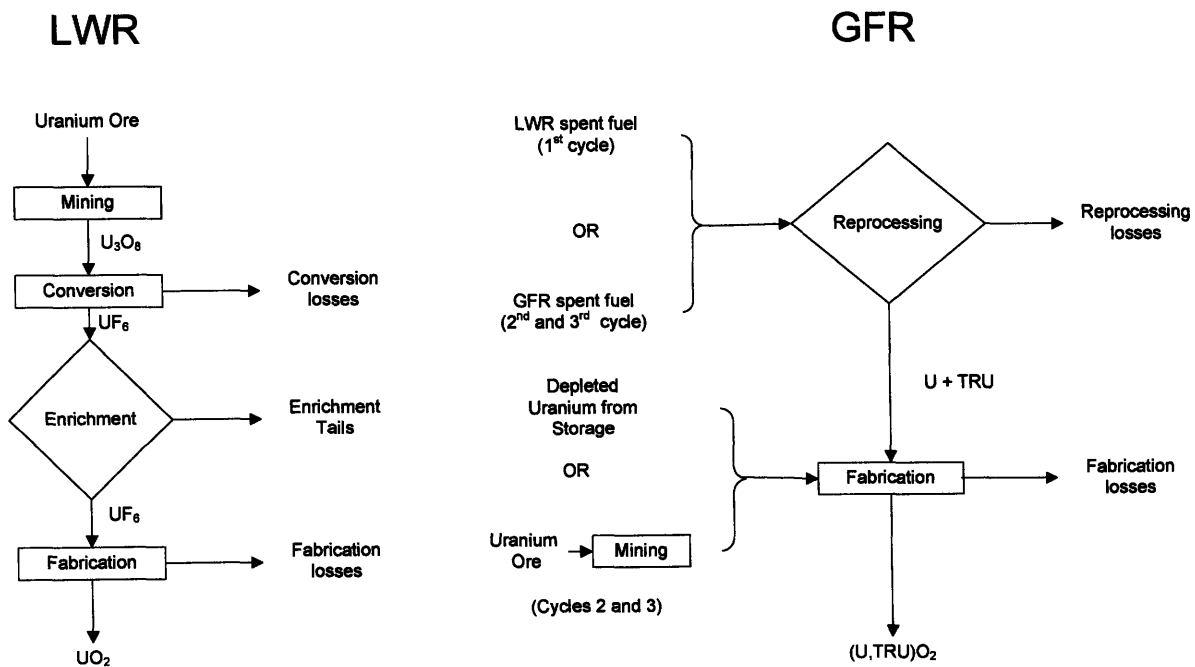


Figure 10.3: LWR and GFR Front End of the Fuel Cycle Flowcharts



[NEA, 2002] and are in terms of year 2000 dollars. It should be noted that while these values are dated, e.g. the current unit cost of mining is approximately twice that of the value listed in Table 10.4, these values are used as they represent a complete set of data which is internally consistent. Hence, as emphasized earlier, the analysis in this chapter is done to give a comparative assessment of GFR and LWR costs, not an absolute assessment of GFR costs in general.

In order to estimate the mass flow for the reprocessing step for GFR fuel for the 1<sup>st</sup> cycle, it was assumed that the LWR spent fuel would have 1 % Pu-239. Multiplying the Pu-239 initial core inventory (10838 kg) for the 1<sup>st</sup> GFR cycle by  $100 \left( \frac{100 \text{ kg spent LWR fuel}}{1 \text{ kg Pu - 239}} \right)$  would give the amount of spent LWR fuel (UO<sub>2</sub>) that would need to need to be reprocessed (1083800 kg UO<sub>2</sub>). In order to account for only the heavy metal content of this UO<sub>2</sub> (upon which the unit reprocessing costs are based), it is assumed that the U-238 and TRU enrichment in the spent fuel is ~80 % U-238 [NEA, 2007] and 1.76 % TRU (based on the LWR spent fuel TRU vector used throughout this work, assuming that LWR spent fuel is 1 % Pu-239). Consequently, there is plenty of Uranium (~867040 kg) in the reprocessed spent fuel to meet the needs of the first cycle (96604 kg).

It should be noted that the cost estimates presented in the GFR-LWR comparison will be for the first cycle of GFR use. While the unit costs for reprocessing of LWR fuel (used for the first GFR cycle, as LWR fuel will be recycled) are lower than those for the GFR fuel (used for the second and third cycle), the mass of heavy metal that needs to be reprocessed for the first cycle is nearly 9 times that of the second and third cycles. Hence, the fuel cycle costs for the first cycle will be larger than the second and third cycles, and this fuel cycle cost represents the most limiting or conservative case. Further, given the long time horizon of the first cycle (~20 years cycle length) and the already great uncertainty associated with the unit reprocessing and fabrication costs at the present time, speculating about what these costs may be for the second and third cycles in 20 or 40 years would not prove useful.

Table 10.4 shows that under best case conditions, the predicted fuel cycle cost (in mills/kWh<sub>e</sub>) for the GFR is significantly greater than that of the LWR, with the ratio of the

**Table 10.4: Supporting Assumptions and Results of Fuel Cycle Costs of the Candidate GFR v. an LWR**

	LWR		GFR		
Assumptions	3411 MW <sub>th</sub>		2400 MW <sub>th</sub>		
	38.7 kW <sub>th</sub> /kg <sub>HM</sub>		20.74 kW <sub>th</sub> /kg <sub>HM</sub>		
	88139 kg <sub>HM</sub>		115712 kg <sub>HM</sub>		
	Mining Δτ = 12 months Conversion Δτ = 6 months Enrichment Δτ = 6 months Fabrication Δτ = 6 months Conversion losses: 0.5% Enrichment of Feed: 0.711 % Enrichment of Product: 4.5 % Enrichment of Tails: 0.3 % Fabrication losses: 1%		Content of spent LWR fuel used for 1 <sup>st</sup> GFR cycle: 1. 1 % Pu-239 2. 80 % U-238 3. 1.76 % TRU (total) Reprocessing Δτ = 24 months Fabrication Δτ = 6 months Mining Δτ = 12 months Reprocessing losses: 1% Fabrication losses: 1%		
	Best Case	Worst Case	Best Case	Worst Case	
	Mining: \$30/kg U Conversion: \$5/kg U Enrichment: \$80/SWU Fabrication: \$250/kg U	= LWR Best Case*2	Reprocessing: LWR (cycle 1): \$700/kg <sub>HM</sub> GFR (cycle 2 & 3): \$1000/kg <sub>HM</sub> Fabrication: \$1400/kg <sub>HM</sub> Mining: \$30/kg U (cycle 2 & 3)	Reprocessing: LWR (cycle 1): \$900/kg <sub>HM</sub> GFR (cycle 2 & 3): \$2500/kg <sub>HM</sub> Fabrication: \$5000/kg <sub>HM</sub> Mining: \$60/kg U (cycle 2 & 3)	
	Cost per kg fuel at start of irradiation, C [\$ /kg fuel]	Best Case	Worst Case	Best Case	Worst Case
		1040	2080	7005	13531
	Fuel Cycle Cost [mills/kWh <sub>r,e</sub> ]	Best Case	Worst Case	Best Case	Worst Case
		3.18	6.35	10.45	17.79

unit fuel costs (in \$/kg<sub>HM</sub>) between the GFR and the LWR (6.74) much greater than the previously calculated break-even value (2.05). While highly speculative, applying the same methodology to the second and third cycles yields fuel cycle costs of ~3.3 mills/kWh<sub>r,e</sub>, showing the disparity between first and subsequent cycle fuel costs discussed earlier. This

highlights one of the initial barriers that the GFR will have to overcome in order to become economically competitive.

It should also be noted that the best case estimates for GFR fuel cycle unit costs represent mature reprocessing and fabrication technologies, both of which have yet to be established. While the LWR reprocessing unit cost used for the first cycle of the GFR is partly based on reported contract prices [NEA, 2002], the technology for which these costs are based is for LWR-LWR recycle, not LWR-GFR recycle. Hence, it is likely that all of these unit costs are actually higher (especially in the near term) and consequently the value for C for the GFR fuel is much higher than the numbers presented here. More generally, the large uncertainty of these unit costs limits the value of the comparison made in Table 10.4, as the comparison is highly sensitive to both reprocessing and fabrication unit costs, with reprocessing unit costs yielding the higher sensitivity.

### 10.2.3 Back End Fuel Cycle Costs

With respect to the back end of the fuel cycle, two main cost drivers prevail: disposal and storage. While a closed fuel cycle does not completely eliminate the need to dispose of fuel, it does significantly reduce the cost of disposal as (1) a smaller volume of waste is created and (2) the radiotoxicity (and thermal loading) of the waste is lower, as shown in Chapter 8. While the US currently charges a 1mill/kWh<sub>e</sub> fee on all nuclear generated electricity as a waste disposal fee, [NEA, 2002] estimates a disposal cost of 0.18 mills/kWh<sub>e</sub> for vitrified waste in a closed fuel cycle. While this is a sizeable reduction (82%), it does not represent a significant savings when compared to the magnitude of the levelized fuel cycle and capital costs discussed earlier.

With respect to storage costs, a closed fuel cycle will likely not incur any of these costs as they typically represent the cost of dry cask storage needed to accommodate the interim storage of the fuel whose volume has exceeded the capacity of the spent fuel pool. In fact, a once-through GFR without recycle with the operating characteristics shown in Table 10.3 generates ~4.6 times less mass of spent fuel than an LWR per annum, as shown in Table 10.5. This is due largely to the much longer in-core residence time of the GFR. When the fact that most of the Plutonium and Minor Actinides are recycled is taken into account, this

savings factor improves to 5. Under the scenario where the depleted uranium is recycled as well, the factor increases to an impressive 12.8. These ratios translate almost directly when the spent fuel generation is assessed on a mass per unit energy generated basis, as the electrical ratings of the two plants are nearly identical (1128 MW<sub>e</sub> for the GFR and 1126 MW<sub>e</sub> for the LWR), assuming an equivalent capacity factor of 90%.

Using a levelized cost of \$100/kg<sub>HM</sub> for dry cask storage obtained from [Bunn et al, 2001], Table 10.5 shows that while a significant reduction in this cost component can be obtained (~92%), the magnitude of the savings is again small. Since storage and disposal costs are based largely on the amount of decay heat generation of the given waste form, a comparison of the decay heat curves of the GFR and LWR fuel needs to be made in order to determine if there is a significant difference between the two which may lead to a cost savings in either case. However, given the small magnitude of the numbers discussed in this section, it is unlikely that such an assessment will yield a large cost savings for either approach.

**Table 10.5: Spent Fuel Volume and Annual Levelized Storage Costs of the Candidate GFR v. an LWR**

	Spent Fuel Volume (kg <sub>HM</sub> /TWh <sub>r<sub>e</sub></sub> )	Spent Fuel Volume (kg <sub>HM</sub> /yr)	Annual Levelized Storage Cost (\$M/yr)	Annual Levelized Storage Cost (mills/kWh <sub>r<sub>e</sub></sub> )
LWR	2525	22425	2.24	0.25
GFR without recycle	543	4834	0.48	0.054
GFR w/ Pu & MA recycle	500	4448	0.44	0.050
GFR w/ U+Pu+MA recycle	196	1747	0.17	0.020

10.2.4 Operations and Maintenance (O&M) Costs and Decontamination and Disposal (D&D) Costs

Consistent with the methodology prescribed in [NEA, 2002], the O&M and D&D costs can be estimated as follows:

$$C_{O\&M} = \frac{UC * f_{O\&M}}{8766 * L} = \left( \frac{C_{cap}}{CRF} \right) * f_{O\&M} \quad \{10.7\}$$

$$C_{D\&D} = \frac{UC * CRF * f_{D\&D}}{8766 * L} = C_{cap} * f_{D\&D} \quad \{10.8\}$$

where:

$f_{O\&M}$  = O&M annual charge for reactor operation as fraction of capital cost

$f_{D\&D}$  = D&D annual charge as fraction of capital cost

Per this approach, D&D costs are accounted for by multiplying the  $C_{cap}$  by a factor of  $f_{D\&D}$ , to reflect an additional annual charge being delivered to a D&D escrow fund, while O&M costs are accounted for by adding  $f_{O\&M}$  directly to the CRF. This can be seen by comparing Equations {10.1}, {10.2}, {10.7} and {10.8}. The base case values assumed for  $f_{O\&M}$  and  $f_{D\&D}$  are 4%/yr and 8%/yr, respectively [NEA, 2002].

**Table 10.6: Levelized O&M and D&D Cost Estimates of the candidate GFR v. an advanced LWR**

	Capacity Factor	$f_{O\&M}$	Lower Bound	Nominal Value	Upper Bound
LWR $C_{O\&M}$ (mills/kWh <sub>e</sub> )	0.9	4%	8.11	8.61	9.12
GFR $C_{O\&M}$ (mills/kWh <sub>e</sub> )	0.9	4%	9.37	10.64	13.18
GFR $C_{O\&M}$ (mills/kWh <sub>e</sub> )	0.95	4%	8.89	10.09	12.49
GFR $C_{O\&M}$ (mills/kWh <sub>e</sub> )	0.9	3%	7.03	7.99	9.89
LWR $C_{D\&D}$ (mills/kWh <sub>e</sub> )	0.9	N/A	1.73	1.84	1.95
GFR $C_{D\&D}$ D&D Costs (mills/kWh <sub>e</sub> )	0.9	N/A	2.01	2.28	2.82
GFR $C_{D\&D}$ (mills/kWh <sub>e</sub> )	0.95	N/A	1.90	2.16	2.67

Table 10.6 compares the levelized O&M and D&D costs for the candidate GFR with that of an advanced LWR. Assuming that there will be no difference in  $f_{O\&M}$  or  $f_{D\&D}$  between the LWR and GFR, Equations {10.7} and {10.8} show that these costs will be driven primarily by the  $C_{cap}$  of the respective reactor types. Hence, this explains why the

GFR shows higher O&M and D&D costs than for the LWR in Table 10.6 for equivalent capacity factors.

It may be feasible to assign a preferentially higher capacity factor to the GFR, based on its single-batch, long-lived “battery” type core operations. Many of the O&M benefits that can be realized by using a one-batch core are similar to those investigated during the (LWR) Extended Cycle Project at MIT from 1995-1998 [Garcia-Delgado and Todreas, 1998]. These O&M benefits will come from avoided refueling outages and lowered forced outage rate, which would combine to provide a preferentially higher capacity factor. Benefits from avoided refueling outages include [Handwerk et al, 1998]:

- Avoided replacement power costs during a refueling outage (RFO)
- Avoided manpower and maintenance costs during a RFO
- Reduction in worker dose during a RFO
  - \$10,000 person-REM from 1997 numbers
  - Improvement of INPO rating, meaning lower insurance costs

A lower forced outage rate would stem from the effect of overcoming infant mortality rates by removing and replacing faulty components early-on in operation. These savings would not only improve the capacity factor, but would also reduce  $f_{O\&M}$  preferentially for the GFR. While these two benefits are seemingly intermingled, the effect of each is examined separately in Table 10.6 for two reasons: (1) in order to show the sensitivity of the results with respect to each individual factor and (2) because it is impossible to predict these beneficial effects with any reasonable certainty. While the GFR’s O&M and D&D costs are higher than those for the LWR under base case conditions (90% capacity factor and  $f_{O\&M}=4\%$ ), assigning a benefit with respect to capacity factor or  $f_{O\&M}$  to the GFR makes it more cost competitive, as expected. As well, these results show that  $C_{O\&M}$  for the GFR is much more sensitive to  $f_{O\&M}$  than to capacity factor.

### **10.3 Economic Factors for Implementing Pin Type or ICAF Cores**

The economic analyses performed thus far have been focused on the GFR core using Tube-In-Duct (TID) fuel. While promising from a conceptual standpoint, TID fuel is unproven, as it has never been manufactured. Further, the manufacturing infrastructure for nuclear fuel has been largely developed around the pin-type fuel concept. Hence, use of TID

fuel would likely result in a cost penalty with respect to fuel fabrication, which could translate into a reasonably significant fuel cycle cost penalty. Obviously, this penalty would not exist with a pin-type core; however, the drawbacks of using pin-type fuel in this GFR have been enumerated throughout this work. Interestingly, Internally Cooled Annular Fuel (ICAF) would not have the same hypothesized fabrication penalty as TID, as studies have been performed investigating not only the feasibility of manufacturing such a fuel form, but the cost of doing so. In fact, the calculated fabrication penalty for ICAF is so small as to be negligible [Lahoda et al, 2007]. Note, however, that these estimates were for U-235, not TRU, enriched LWR fuel.

Reviewing the methodology outlined in this chapter to calculate the cost of electricity (COE), the only cost components that would change for the pin and ICAF cases are the storage and fuel cycle costs, assuming that all three cores would be part of plants with the same lifetime (60 years, in this case). Table 10.7 shows a comparison of the spent fuel volume and the associated annual levelized costs of the three different fuel type GFR cores explored throughout this work. While the Pin and ICAF cores generate 2.5 and 5.9 times the amount of spent fuel on an annual basis, the costs associated with the storage of this fuel are still very small in comparison to the other cost components. In fact, the estimates presented in Table 10.7 are conservative, as they assume no recycle. As shown in Table 10.5, accounting for recycle will lower these costs, making them even more insignificant. Aside from these minor economic implications, the large increase in spent fuel volume generation should be accounted for in an overall comparison of the Pin and ICAF cores with the TID core, as it is a significant liability.

**Table 10.7: Comparison of Spent Fuel Volume and Annual Levelized Storage Costs among the TID, Pin, and ICAF GFR Cores**

	Spent Fuel Volume (kgHM/yr)	Annual Levelized Storage Cost (\$M/yr)	Annual Levelized Storage Cost (mills/kWh <sub>e</sub> )
TID GFR without recycle	4834	0.48	0.054
Pin GFR without recycle	12030	1.2	0.135
ICAF GFR without recycle	28552	2.86	0.321

Looking next at the impact of the different fuel type cores on fuel cycle costs, Table 10.8 shows that the pin and ICAF cores have fuel cycle costs that are 1.6 and 3.6 times higher than the TID core, respectively, under best case circumstances (similar ratios apply to the worst case conditions). These fuel costs were calculated using the same methodology as for the TID fuel cycle costs earlier, accounting for the differences in heavy metal core mass and enrichment. The pin and ICAF fuel costs are higher due to the shorter burnup and higher BOC enrichment; however, this increase is mitigated by their higher specific power and lower core heavy metal loading. These mitigating factors are direct consequences of the inherently lower fuel volume fraction of the pin and ICAF fuel types, as all of the cores have roughly the same volume and identical heights and thermal ratings. Inclusion of the previously mentioned fuel fabrication penalty for TID fuel might make the fuel cycle cost and hence, overall cost of the pin core, more cost competitive with that of the TID core, especially under best-case economic conditions. Further, when the fuel cycle cost of the pin core is compared with the other cost components, an increase of 6 mills/kWhr<sub>e</sub> is not very significant, making the pin core cost competitive with the TID Core at 58 mills/kWhr<sub>e</sub> (pin) v. 52 mills/kWhr<sub>e</sub> (TID). However, as discussed earlier, the best case conditions are not likely to exist, and the advantage that the TID has increases with worsening economic circumstances, as shown in Table 10.8. Consequently, the TID is the most cost effective fuel type for the GFR core.

**Table 10.8: Comparison of Front End Fuel Cycle Cost Factors among the TID, Pin, and ICAF GFR Cores**

		TID	Pin	ICAF
Front End Fuel Cycle Cost (mills/kWhr <sub>e</sub> )	Best Case	10.45	16.29	36.12
	Worst Case	17.79	26.77	57.02
Reactivity Limited Burnup (MWd/kg)		140	61.6	26.9
BOC Enrichment (% TRU)		16.53	19.85	25.1
Specific Power (kW/kg <sub>HM</sub> )		20.74	27.02	43.0
Core Heavy Metal Loading (kg <sub>HM</sub> )		115711	88808	55815



## 10.4 Summary

Using the basic cost model from Equation {10.1} and the information presented throughout this chapter, Figure 10.4 gives a graphical comparison of the cost of electricity among the TID, Pin, and ICAF GFR cores and an advanced LWR. While many scenarios were presented throughout this chapter, the nominal (for  $C_{cap}$ ,  $C_{O\&M}$ ,  $C_{D\&D}$ ) and best case (for  $C_{FCC}$ ) values for each cost component were used in compiling this figure. As well, the uncertainty in all of the cost factors discussed throughout this chapter is shown in the figure with error bars. Combining the larger fuel cycle and capital cost of the TID GFR (represented directly in the capital cost component and indirectly in the O&M and D&D cost component) accounts for the majority of the difference between the LWR and GFR under the best-case scenario, with the LWR COE ~25% less than that of the GFR. Hence, a unique advantage (or combination of advantages) with respect to GFR costs must be found in order to make this strategy cost competitive.

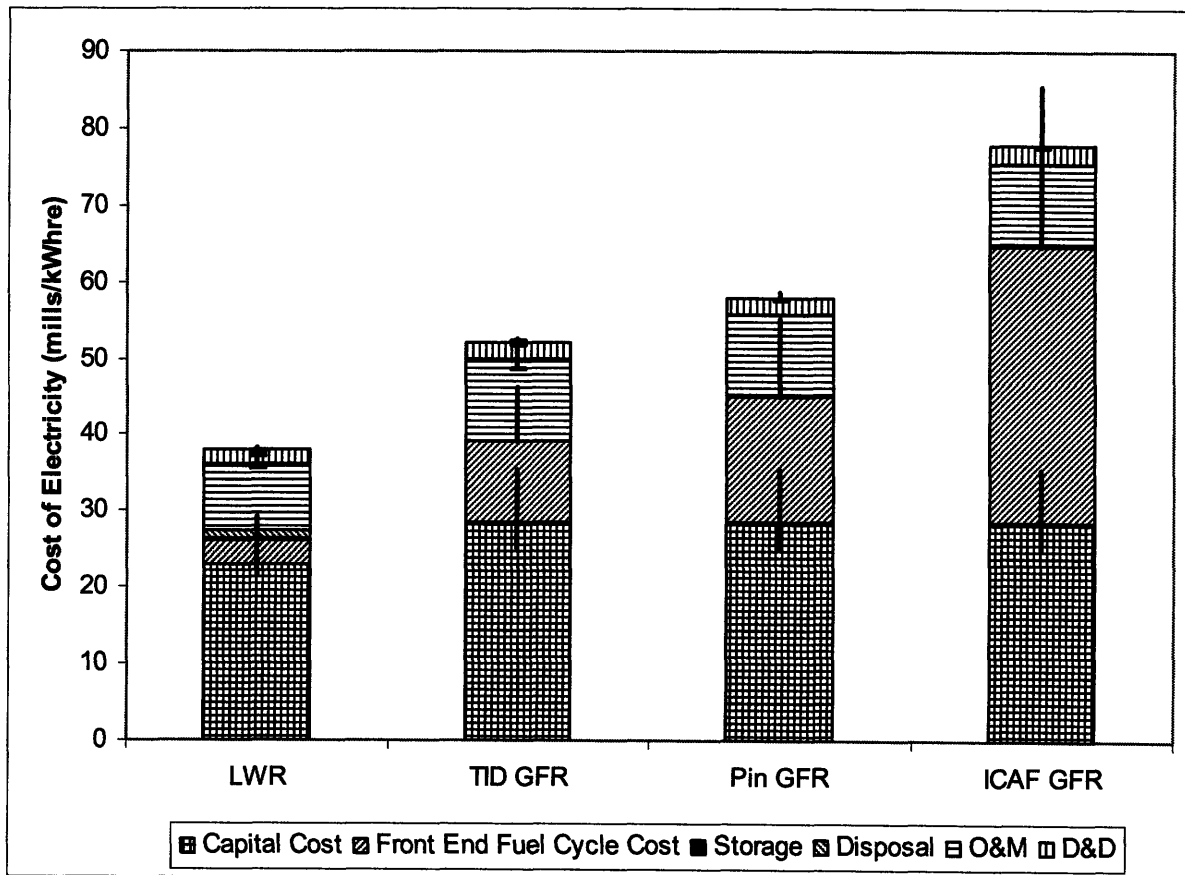


Figure 10.4: Cost of Electricity Comparison between the Candidate GFR and an advanced LWR

Several of these unique benefits are hypothesized to exist. First, the capital cost numbers used in this analysis are based on LMR technology. As discussed earlier, the smaller size of the plant and lower cost of the PCS for the GFR would help to drive down these costs by as much as 25%, making it much more cost competitive with the LWR. Clearly, capital cost reduction must be the priority goal for research in advanced reactor development, e.g. Gen-IV, GNEP, and AFCI. Second, the single-batch strategy of the GFR could lower O&M costs through a higher capacity factor, resulting from avoided refueling shutdowns and a lower forced outage rate. Further, macro-economic factors may also change, making the GFR more cost-competitive. For instance, a unit mining cost of \$523/kg U has been calculated as part of this study as the break-even point between the total COE for a GFR and LWR, assuming all other economic factors stay the same. While this value is much higher than current practice and more than 17 times the value used in this study, it demonstrates that there are economic factors that can change in order to advantage the GFR. Still, any benefit which would uniquely benefit the GFR is highly speculative and extremely hard to quantify at this point.

While serving as a good first order metric, the cost model presented here is admittedly crude. Several important questions need to be answered in order to present a more complete economic analysis of such a strategy. First, the capital and operating costs of a reprocessing facility have not been addressed, as well as the transportation costs associated with implementing such a strategy. In this analysis, these costs have been assumed to have been included in the unit reprocessing and fabrication costs for the GFR presented in Table 10.4. However, the low values used for these unit costs in Table 10.4 are open to question if these other costs are to be accounted for. Second, this analysis has assumed that the LWR spent fuel will be given to the GFR for free, in a reactor park or shared resource type arrangement. Depending upon the existing conditions or agreement, there may be either a cost or credit associated with the use of this fuel in the front end of the GFR fuel cycle. Third, a comparison of the LWR using recycle should be compared against the GFR recycle option, in order to give a fairer basis for comparison between these two technologies.

A final point worth noting is that the high cost of reprocessing LWR spent fuel will put all fast reactors at a disadvantage with respect to their startup fuel cycle costs: the GFR is

by no means unique in this regard [Driscoll and Kim, 2000]. Hence, cost reduction in this area is another high priority initiative which must be addressed in advanced reactor research programs, e.g. Gen-IV, GNEP, and AFCI.

# 11 SUMMARY, CONCLUSIONS, and RECOMMENDED FUTURE WORK

## 11.1 Introduction

Motivated by the goals of the Generation-IV International Forum (GIF), a long-lived Gas-cooled Fast Reactor (GFR) core has been designed. Specifically, a GFR cooled by supercritical carbon dioxide (S-CO<sub>2</sub>), fueled with LWR spent fuel transuranics, and directly coupled to a Brayton cycle has been investigated as part of a Nuclear Energy Research Initiative grant. Table 11.1 lists the key plant parameters of this GFR.

Table 11.1: Key GFR Plant Parameters

Parameter	Value
Core Thermal Output	2400 MW <sub>th</sub>
Power Conversion System (PCS)	Brayton Recompression Cycle [Dostal et al., 2004]
Number of PCS loops	2
Plant Electrical Output	1200 MW <sub>e</sub>
PCS Thermal/Net Efficiency	51/47
Primary to Secondary Plant Coupling	Direct
Primary Coolant/PCS Working Fluid	S-CO <sub>2</sub>
Core Inlet Temperature	485.5°C
Core Outlet Temperature	650°C
Peak Coolant Pressure	20 MPa
Plant Lifetime	60 years
Number of refueling cycles	3
Number of refueling batches	1
Decay Heat Removal (DHR) Capability	(3-4)x(50-100)% Shutdown Cooling Systems (SCSs) – exact configuration TBD [Pope et al., 2006]
DHR System Working Fluid	CO <sub>2</sub> (reactor side) H <sub>2</sub> O (ultimate heat sink side)

The original GFR chosen by the GIF was a 600MW<sub>th</sub> version using Helium as a coolant, whereas the work presented here is for a 2400 MW<sub>th</sub> core using S-CO<sub>2</sub> as a coolant. The decision to develop a much larger scale reactor in this work was based on both the modularity of the Brayton S-CO<sub>2</sub> PCS and the effect of economies of scale. The choice of S-CO<sub>2</sub> as a coolant is based on its comparatively advantageous thermophysical properties. These properties allow for comparable performance to Helium at lower temperatures at the reactor outlet/turbine inlet, i.e. 650°C v. 850°C, which alleviates problems associated with core materials performance at elevated temperature, allowing for a much lower containment pressure for the promotion of natural circulation. These features have spurred the development of the S-CO<sub>2</sub> Brayton Cycle, which shows great promise as a Power Conversion System with predicted thermal efficiencies between 45-50% [Hejzlar et al., 2005] [Dostal et al., 2006]. The downside to using S-CO<sub>2</sub> is that it must be kept at a high pressure in order to ensure efficient operation, i.e. 20 MPa v. 8 MPa for helium, which requires a more robust pressure boundary. However, as shown in [Hejzlar et al., 2006], high pressure and medium temperature (20 MPa and ~650°C) are less challenging than the medium pressure and high temperature (8 MPa and ~850°C) typical of helium, due to the much lower allowable stresses at higher temperatures. The pressure of 20 MPa, while high, is lower than that of modern supercritical steam PCS, which operates at 28-32 MPa.

In accordance with the goals of the GIF for next generation reactors, the core design presented here optimizes performance with respect to sustainability, safety, proliferation, and economics. With respect to sustainability, this GFR uses legacy LWR spent fuel in a fuel cycle with a conversion ratio ~1. Coupled with this approach is the transmutation of the fission products (Tc-99 and I-129) and minor actinides (MA's - neptunium, americium, and curium) that contribute the greatest burden to the waste repository, while minimizing the overall waste production. As a first step toward achieving overall passive safety, this GFR has been specially designed to achieve a negative coolant void reactivity throughout core life. More globally, the core is mostly neutronically passively safe, such that upon an Anticipated Transient Without SCRAM (ATWS), the reactor will shut itself down without violating established core limits. The only transient that it was found not fully protected against was a LOCAWS at EOL; however, design solutions have been offered to correct this deficiency. Proliferation is addressed (1) by burning Plutonium and TRU from legacy LWR waste, (2)

by keeping the weapons-attractive isotopes of Plutonium intermingled with other TRU, (3) by having no opportunity in the fuel cycle where the Plutonium is physically separate from the other TRU, (4) by preventing the buildup of ex-core Plutonium stockpiles, and (5) by putting the Plutonium in a safe, inaccessible place for long periods of time, i.e. in a single batch-loaded “battery” core. The use of Tube-in-Duct (TID) fuel supports the proliferation objective well, as it allows for a large enough heavy metal loading for a sustainable core lifetime without the need for external blankets (which would otherwise be a source of weapons-grade Pu-239). Finally, the capital, O&M, and fuel cycle costs of the GFR are reasonable.

While much of this work centers around the use of TID fuel, traditional pin-type fuel was also examined in case the TID fuel was found unsuitable for use in the future. As well, Internally Cooled Annular Fuel (ICAF) is explored for GFR application due to its promise in LWRs, with the hopes that these benefits will translate directly. ICAF is an annular pellet which has both traditional external, as well as innovative internal, cladding and cooling, developed at MIT as means for extracting more power from existing LWRs. [Hejzlar et. al, 2001][Hejzlar et. al, 2004]. Based on well-reasoned steady state neutronic and thermal hydraulic criteria, a comparative assessment of these three fuel types, both at the unit cell and core design level, is made. An evaluation of the ability to manage current and legacy actinide inventories and to be economically competitive is also performed. As well, a preliminary evaluation of neutronic self-controllability is performed on the TID core, based on a revision of an established methodology which is tailored to fit the unique needs of the TID core design.

## ***11.2 The Use of Diluent in a GFR***

Among the numerous challenges associated with designing a fast reactor is devising a core with acceptable power peaking and coolant void reactivity (CVR). The approach taken in this work is to blend a material, i.e. a “diluent,” into the fuel. The diluent has the effect of both reducing the fuel concentration (minor effect) and softening the neutron energy spectrum (major effect). The effect of diluent in softening the spectrum is shown in Figure 11.1 for varying concentrations of BeO diluent.

By varying the concentration of the diluent, it is possible to vary these two effects and hence, effectively shape power. Traditional means of power shaping in fast reactors, e.g. enrichment zoning and frequent fuel shuffling, were not able to provide fully satisfactory results in the present instance. The ability to achieve a relatively constant radial power profile results from the moderating properties of the diluent. The moderation of the diluent is sufficient to lower enough of the neutron population's energy below the fast fission threshold of many of the transuranic nuclides without lowering it so much as to completely prohibit fast fission. Since the diluent does not get used up like a more traditional burnable poison, it maintains its potency throughout core life. Not only can the diluent achieve a relatively flat power profile, but it can maintain it over long periods of burnup without the need for control rods for power shaping, as shown in Figure 11.2 for the first cycle of the TID core design presented in this work. In essence, diluent is the fast reactor analog to burnable poisons in a thermal reactor.

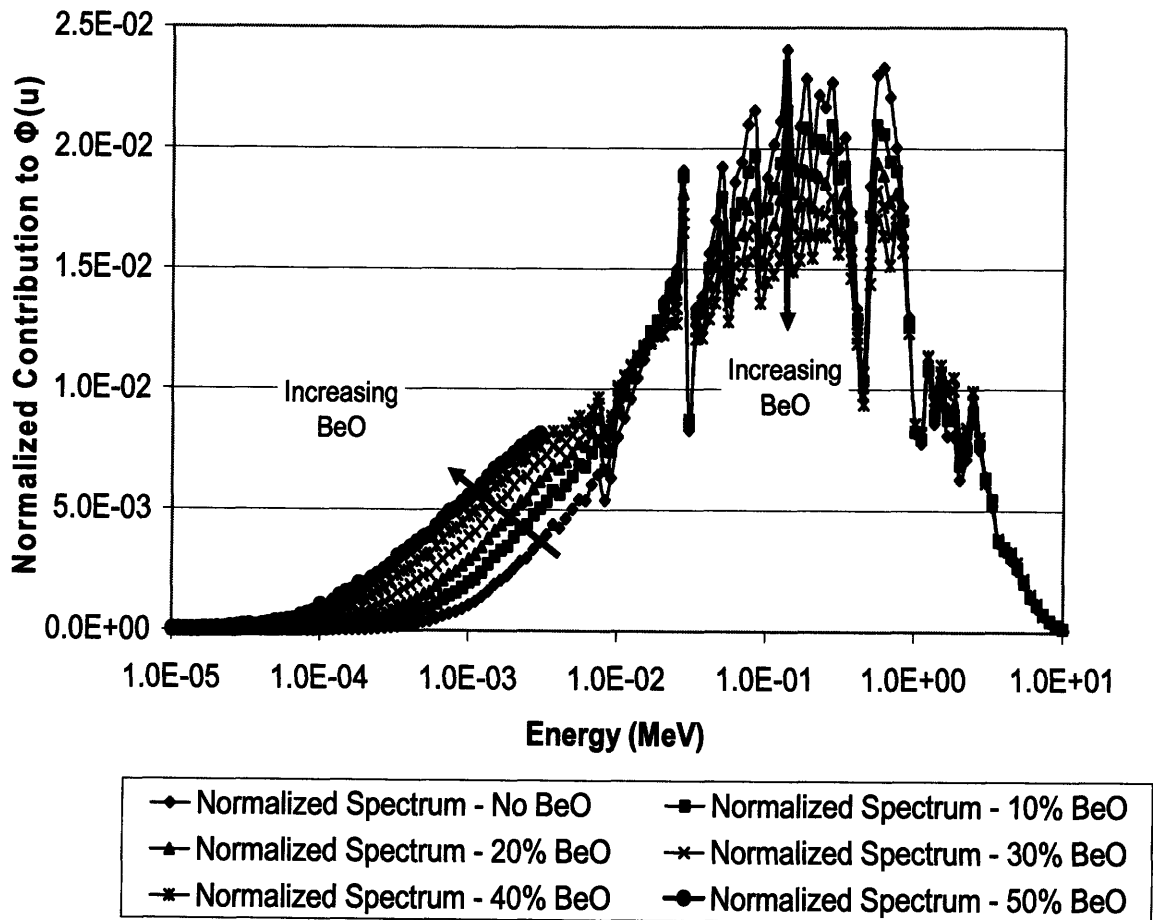


Figure 11.1: Effect of Diluent Concentration on the Neutron Energy Spectrum

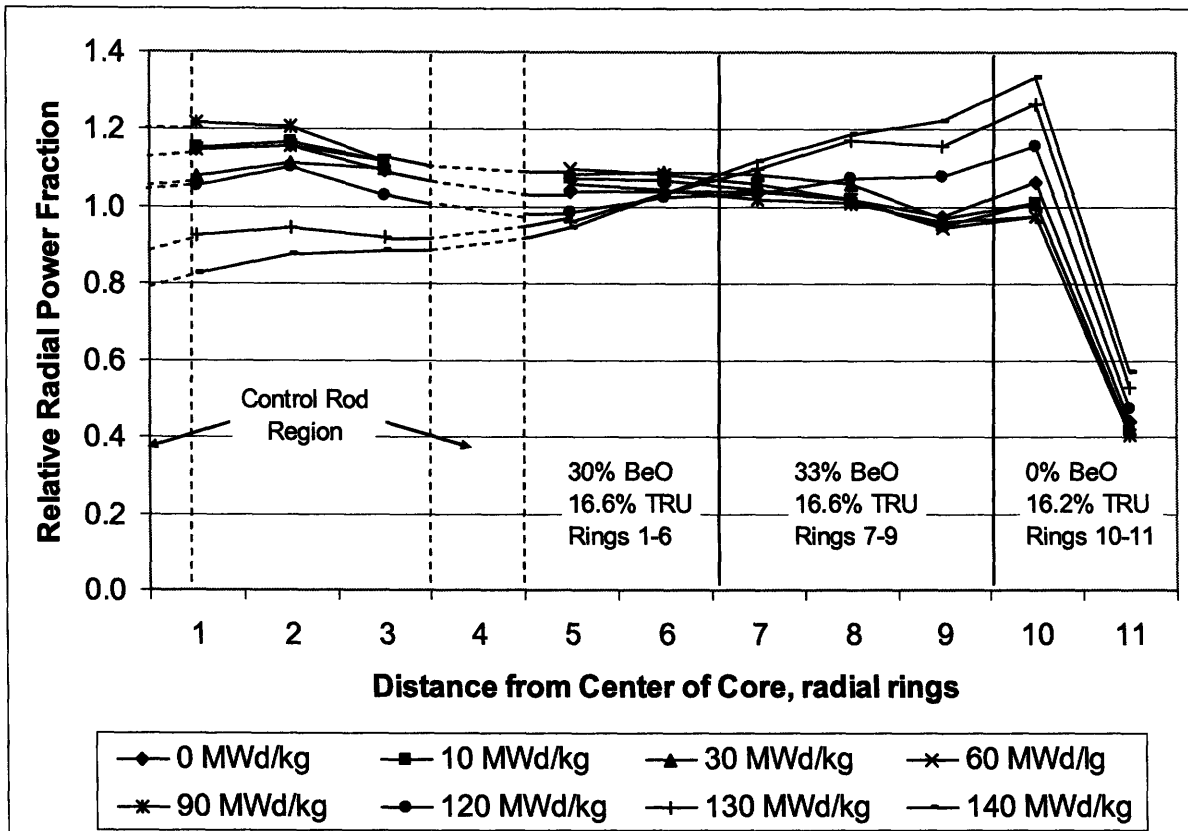


Figure 11.2: Unrodded Radial Power Shape as a Function of Burnup for the TID Core for the 1<sup>st</sup> Cycle

A key trade-off that exists with the use of diluent is the displacement of fuel, which when taken alone would have the effect of limiting the reactivity-limited lifetime of a given core. With respect to radial power shaping, the high fuel volume fraction ( $v_f$ ) provided by the TID fuel permits the use of diluent while still allowing enough of a heavy metal loading to enable not only criticality, but also sufficient conversion ratio during burnup to achieve a sustainable core without the need for external blankets. This provides a proliferation benefit as it causes the weapons-attractive isotopes (e.g. Pu-239) to be intimately mixed with other radioactive transuranics and fission products, making extraction difficult.

Using diluent for axial power shaping was also explored, but was found impractical, as achieving the ideal inlet-peaked axial power profile was not only difficult due to the large leakage at the core periphery, but also not worthwhile, as a thermal hydraulic analysis showed only a marginal benefit ( $<10^\circ\text{C}$ ) with respect to peak cladding temperatures when compared to the default chopped cosine axial shape (with a peak of 1.3).



A concomitant effect of the softening of the neutron spectrum by diluent is to help reduce the effects of coolant void reactivity (CVR). Ignoring the effects of leakage, it can be shown that:

$$\Delta\rho_{VOID} \propto \left( \frac{\sigma_{\gamma,i}^f}{\sigma_{f,i}^f} - \frac{\sigma_{\gamma,v}^f}{\sigma_{f,v}^f} \right) \quad \{11.1\}$$

where:

$\Delta\rho_{VOID}$  = coolant void reactivity

$\sigma_f^f$  = microscopic fission cross section of the fuel

$\sigma_f^\gamma$  = microscopic capture cross section of the fuel

the subscript "v" denotes the voided case

the subscript "i" denotes the initial unvoided case

Hence, the reactivity inserted by voiding of the coolant is proportional to the ratio of the capture to fission microscopic cross section of the unvoided case less that of the voided case. Reactivity in this core is driven primarily by Pu-239, which accounts for ~65-70% of fissions throughout core life. Looking at this ratio for Pu-239 as a function of energy in Figure 11.3 shows that for the undiluted case, as the spectrum hardens due to voiding, the

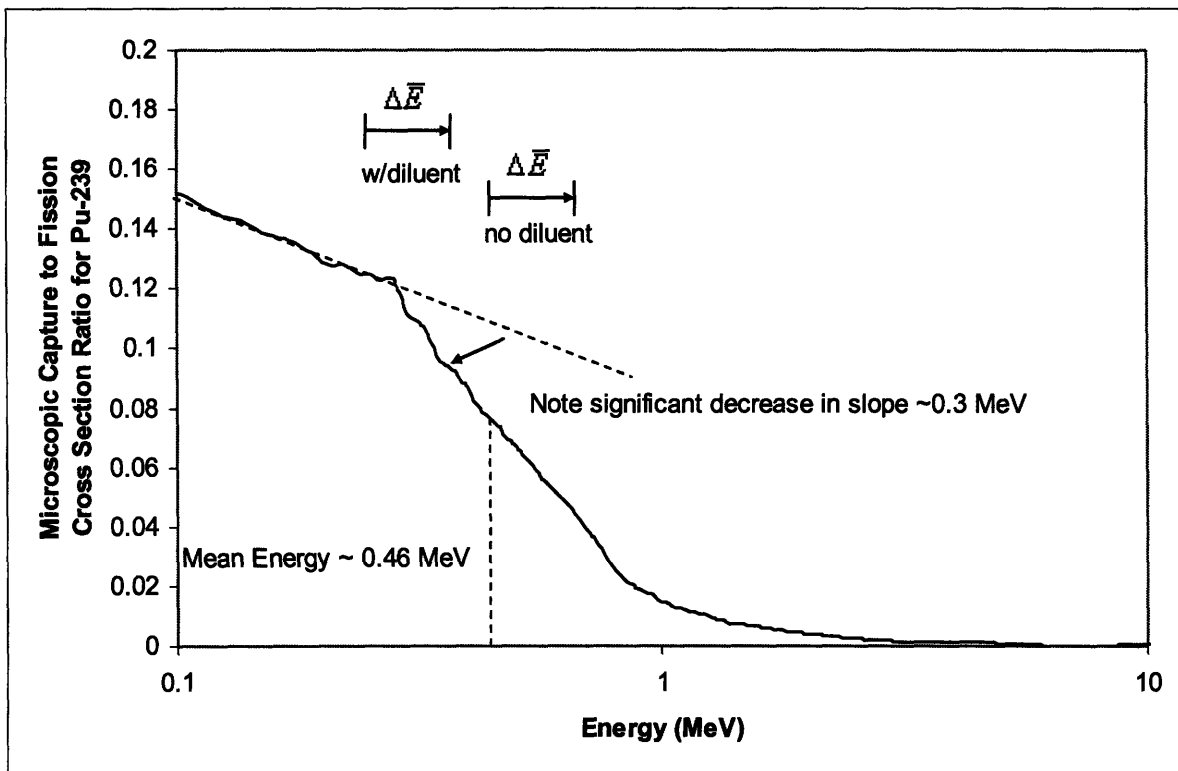


Figure 11.3: Illustration of the Effect of Spectral Softening on Coolant Void Reactivity

voided ratio is smaller than the initial, unvoided ratio and positive reactivity is inserted. However, when diluent is added to the fuel, the initial neutron energy in the unvoided core is lower than that of the undiluted case, shifting the neutron energy increase that occurs upon voiding to begin at lower energies. Since the mean neutron energy in the system is at approximately 0.46 MeV and is near a discontinuity in the slope of the capture to fission cross section ratio (at about 0.3 MeV), lowering the energy through the use of diluent reduces the difference between the ratio for the voided and unvoided cases. It is in this way that softening the neutron energy spectrum through the use of diluent reduces CVR.

Spectral softening also has the concurrent benefits of enhancing the negative Doppler reactivity coefficient and enhancing the worth of traditional reactivity control mechanisms, i.e. B<sub>4</sub>C control rods. However, there exists a trade-off with respect to spectral softening in a fast reactor, as making Doppler reactivity too negative can have the negative consequence of inserting too much positive reactivity upon core cooldown following an Anticipated Transient Without SCRAM (ATWS).

Several candidate diluents were explored: BeO, SiC, and TiC. Of the options, BeO has been selected as the diluent of choice for this work, owing largely to its greater effect on CVR reduction. Several unique issues were identified with using BeO as a diluent, among them: (1) anisotropic growth with accumulation of fast neutron fluence, which can result in microcracking and ultimately pulverization [Hickman et. al, 1964, Keilholtz et. al, 1964] (2) the toxicity of Beryllium [*Nuclear News*, 2006], and (3) the potential for excess Helium (alpha) production due to the neutronic uniqueness of Be-9, affecting irradiation growth in the fuel. Still, these drawbacks are not insurmountable, as BeO has been used in fast reactors, most notably the Southwest Experimental Fast Oxide Reactor (SEFOR). [McVean et al, 1966]. In addition, significant work has been done recently on its use in advanced LWR fuels for enhancing the thermal conductivity [Sarma et al, 2005]. Further study is needed to determine if these issues are truly impediments to using BeO as a diluent. Regardless, the efficacy of a moderating diluent in a fast reactor has been generally demonstrated, and other excellent candidate materials exist, e.g. SiC, should BeO prove unsuitable for use in future analyses.

Given the proven potency of diluent, a study was undertaken to determine the optimum diluent concentration for maximizing CVR reduction, as well as to explore some of the trade-offs that result from the use of diluent. This study used a semi-infinite assembly (normal leakage axially, reflected boundary conditions radially, and no control rods anywhere), where the BeO concentration was varied in an effort to determine the relationship between BeO volume fraction and the parameters of interest. The key findings are:

1. There is a saturation effect at about 30% BeO with respect to BOL CVR as BeO is added. This is due to the spectral softening effect which creates a tradeoff between lowering the contribution of positive coolant void reactivity from Pu-239 and increasing the fission fraction of Pu-239, which contributes to an overall greater positive void reactivity.
2. Reactivity limited burnup and reactivity swing decrease nearly linearly with increasing BeO volume fraction.
3. EOL void reactivity varies roughly linearly with BeO concentration. This is due to the spectral softening effect of BeO, which increases with increasing diluent concentration. The competing effect of increased Pu-239 fission fraction is not seen as with the BOL case, as the spectral softening breeds enough Pu-241 to keep the Pu-239 fission fraction constant with respect to BeO concentration.
4. The increase in EOL void reactivity with respect to BOL void reactivity decreases with increasing BeO concentration.

Several fundamental trade-offs have become apparent as a result of using a moderating diluent in fast reactor fuel. These trade-offs are shown in Figure 11.4 and highlight that the use of diluent adds another dimension to this core design.

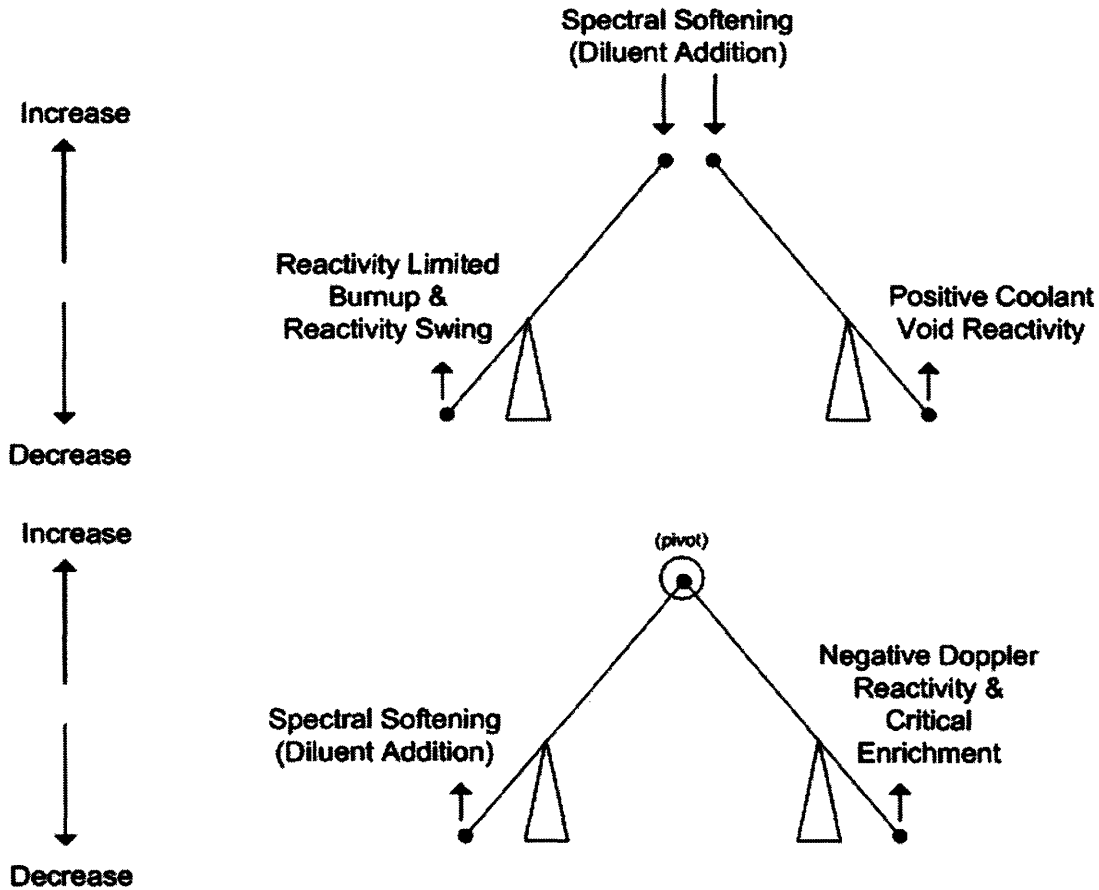


Figure 11.4: Illustration of Fundamental Trade-offs in Neutronic Performance from the Use of Diluent

### 11.3 TID Core Design

The robust design and evaluation of a GFR core using TID fuel is the central focus of this work. Table 11.2 lists the key parameters of the final core design. At the heart of this design are several key choices: (1) the use of BeO as a fuel diluent, (2) the use of TID fuel, (3) the selection of S-CO<sub>2</sub> as a radial reflector, and (4) the use of Ti as an axial reflector. BeO diluent has been used for its favorable effect on power shaping and its concomitant effect on CVR reduction, enumerated in Chapter 3 and the preceding section. TID fuel has been chosen for its high fuel volume fraction, which allows large enough of a heavy metal loading to allow for sustainable burnup, without the need for external blankets. This is especially important with the use of diluent, which displaces some of the necessary heavy metal loading needed for sustainability. As well, the accompanying lower coolant volume fraction allows the moderation by the coolant to play a much smaller role, and its loss results

in a smaller increase in neutron energy upon voiding. Hence, the addition of a positive CVR contribution is smaller. Thermal-hydraulically, for a given fuel volume fraction, TID fuel assemblies provide not only lower fuel temperatures [Hankel, 1960], but also significantly lower pressure drops.

**Table 11.2: Key Parameters of the TID Fuel Assembly Core Design**

Parameter	Value
<b>Whole Core Parameters</b>	
Thermal Power	2400 MW <sub>th</sub>
Specific Power	20.7 kW/kg <sub>HM</sub>
Power Density	85.4 kW/l
Number of fuel batches	1
Reactivity Limited Burnup	1 <sup>st</sup> cycle: 140 MWd/kg, 18.48 EFPY 2 <sup>nd</sup> cycle: 133 MWd/kg, 17.66 EFPY 3 <sup>rd</sup> cycle: 130 MWd/kg, 17.16 EFPY
System Pressure	20 MPa
Core Inlet Temperature	485.5°C
Core Outlet Temperature	650°C
Active Core Height	1.54 m
Effective Core Diameter	4.81 m
H/D (active core)	0.32
Reflector	S-CO <sub>2</sub> (radial), Ti (axial)
Shielding (radial and axial)	99 w/o B <sub>4</sub> C
<b>Fuel Assembly Parameters</b>	
Fuel Assembly Description	Tube-in-Duct (TID)
Fuel Enrichment	16.6% TRU (1 <sup>st</sup> cycle)
Assembly inner can flat-to-flat distance	22.32 cm (cold), 22.49 cm (hot)
Assembly outer can thickness	0.2 cm (cold), 0.2015 cm (hot)
Inter-Assembly gap size	0.28 cm (cold), 0.111 (hot)
Cladding thickness	0.07 cm
Coolant hole diameter	0.7 cm
Fuel, volume %	(U-TRU)O <sub>2</sub> , 59
Cladding, volume %	ODS MA956, 14
Coolant, volume %	S-CO <sub>2</sub> , 27

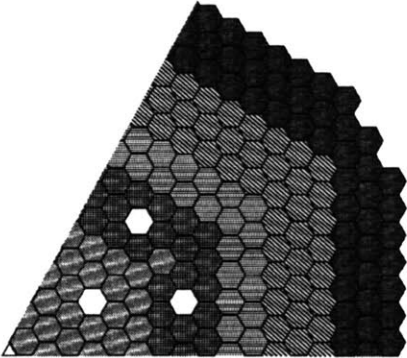
The selection of S-CO<sub>2</sub> as a radial reflector was employed as a strategy for reducing the CVR beyond the use of diluent. This ensures that upon a LOCA and concurrent coolant voiding, the reflector would void or “disappear,” enhancing leakage and reducing CVR. While the use of a lower albedo reflector raises some concerns regarding an increase in the enrichment necessary to sustain criticality (thereby increasing fuel costs), the low radial

leakage of the core mitigates this potentially large negative effect. Specifically, the radial leakage for an axially-reflected, radially-bare permutation of the TID GFR core is only ~6%. Note that this is much less than in older breeder designs using U-238 blankets, where ~1/3 of the neutrons leak out of the enriched fuel zones. The low leakage behavior of this core is due not only to the large size of the core, but also due to the extremely large fuel volume fraction inherent in the use of Tube-in-Duct (TID) fuel assemblies. Further, adjustment of the BeO concentration in the core in order to flatten the radial power (specifically, reduction of BeO in the periphery) has reduced the need for an increase in enrichment due to increased radial reflector transparency. Consequently, the BOL enrichment of the S-CO<sub>2</sub> reflected core is nearly the same as that of its predecessor in the design process, a candidate core with a TiC/Ti radial reflector.

The other potentially significant problem with using S-CO<sub>2</sub> as a radial reflector is the increased fluence on the reactor pressure vessel (RPV). With a more transparent radial reflector, more high energy neutrons will impinge upon the RPV, increasing the damage and limiting the service life of this component. The offsetting effect to the increased transparency of the reflector is that the core has relatively low leakage; therefore, while fast neutrons may have greater ease in getting to the RPV, there are less of them to get there in the first place. Both an appropriate limit and the amount of actual RPV fluence were quantified as part of this core design. Based on a search of the literature for LWRs [General Electric, 2007] [USNRC, 2004], other Gen-IV designs (Supercritical Water Reactor - SCWR) [Buongiorno et. al, 2001], and recent GFR work [Venkatesh, 2004], a conservative core lifetime limit of  $2.5E19$  n/cm<sup>2</sup> (E>1 MeV) has been chosen for reactor pressure vessel fluence. Calculations using MCNP showed that using three rows of B<sub>4</sub>C radial shielding were sufficient to meet this overly conservative limit for a design lifetime of 60 years. Further, another layer of conservatism is added, as the actual means for containing the core and internals will not be an RPV, but a much larger, weld-free PCIV.

The fourth key design choice, using Titanium as an axial reflector, is the result of a comprehensive study which compared the merits of eight candidate materials, chosen for various reasons: Ti, BeO, TiO<sub>2</sub>, PbO, Zr<sub>3</sub>Si<sub>2</sub>, SiO<sub>2</sub>, SiC, and CaO. These candidate materials were evaluated on the basis of: (1) chemical compatibility with the S-CO<sub>2</sub> coolant (due to the

use of vented fuel assemblies) (2) material properties (3) Beginning of Life (BOL) CVR, as assessed via a whole core model, and (4) reactivity limited burnup, reactivity swing, BOL CVR and EOL CVR, using a semi-infinite (mirror boundary conditions radially, normal leakage axially) assembly model. While some of the candidate materials showed performance almost as good as Ti in some of the areas, none of the candidates exhibited performance better than Ti in all of the categories.



-  Control Assembly
-  Inner fuel zone
-  Middle fuel zone
-  Outer fuel zone
-  S-CO<sub>2</sub> Reflector
-  B<sub>4</sub>C Shield

Figure 11.5: 1/6<sup>th</sup> Core Map of the S-CO<sub>2</sub> Reflected Strategy

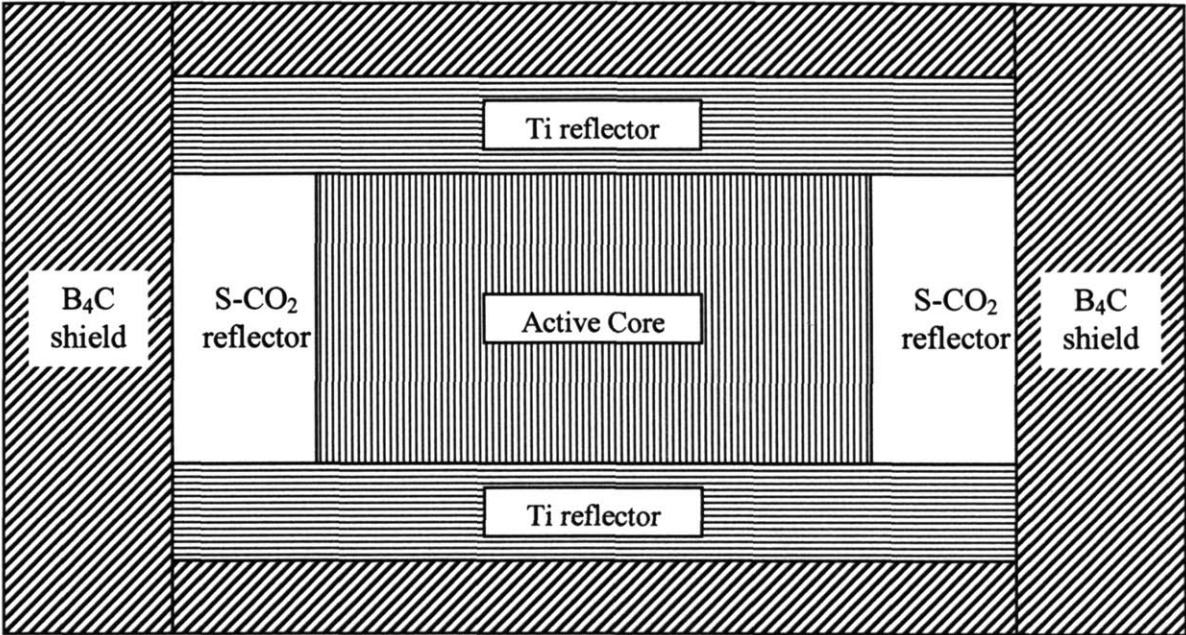


Figure 11.6: Axial Cross Section of the S-CO<sub>2</sub> Reflected Strategy

A radial (i.e. 1/6<sup>th</sup> core representation) and axial cross section of the TID GFR are shown in Figure 11.5 and Figure 11.6. Note that the radial S-CO<sub>2</sub> reflector exists axially only along the fueled region of the core.

**Table 11.3: Neutronic and Thermal Hydraulic Goals for the 1<sup>st</sup> Cycle of the TID Core Design**

Factor	Philosophy	Acceptable Value	Target Value	Current Value (TID, 1 <sup>st</sup> cycle)
<b>Achievable Burnup</b>	Achieve burnups such that the GFR (1) is cost competitive and (2) has fluence (both core and reactor pressure vessel) that is not excessive when compared to other options	100 MWD/kg (ave.)	150 MWD/kg (ave.)	140 MWD/kg (ave.)
<b>Radial Power Peaking</b>	Keep the radial power shape flat enough such that sufficient margin to thermal hydraulic limits is provided	1.3	1.2	1.34 @ 140 MWD/kg (unrodded)
<b>Passive Reactivity Control</b>	Keep coolant void reactivity low enough <u>over core life</u> such that it can be sufficiently offset by the accompanying effect of other passive reactivity mechanisms (i.e. Doppler, flowering, etc). Keep the method for doing this simple.	≤ \$1	≤ \$0	-108±7¢ (BOL) -119±7¢ (MOL) -35±5¢ (EOL)
<b>Peak Cladding Temperature (steady state)</b>	Keep the axial and radial power shapes such that sufficient margin to cladding failure is provided	800 °C	750 °C	810 °C
<b>Peak Fuel Temperature (steady state)</b>	Keep the axial and radial power shapes such that sufficient margin to fuel melting is provided	1800 °C	1700 °C	1770 °C
<b>Core Pressure Drop</b>	Keep the core pressure drop low enough such that (1) the S-CO <sub>2</sub> power conversion system operates at a good efficiency, and (2) natural and forced circulation are not significantly inhibited during decay heat removal	500 kPa	300 kPa	420 kPa
<b>Active Reactivity Control (Reactivity Swing/Control Rod Worth)</b>	Keep the reactivity swing low enough such that control rod worth does not become excessive (i.e. significantly beyond current experience, within rod ejection and stuck rod limits)	Within stuck rod, ejected rod, and current experience envelope	Within stuck rod, ejected rod, and current experience envelope	Within stuck rod, ejected rod, and current experience envelope



Using the criteria set forth in Table 11.3, the performance of the TID GFR core during the first operating cycle is assessed. The performance of the core presented in Table 11.3 represents the limit of maximum achievable burnup, while still maintaining a negative CVR throughout cycle life and acceptable control rod worth. Reducing the BOL enrichment would certainly reduce the BOL eigenvalue, the cycle reactivity limited burnup, the reactivity swing and CVR throughout core life. This limiting case is presented here to demonstrate the capabilities of such a core design.

**Table 11.4: Neutronic Performance Parameter Comparison Among All Three Cycles of the TID Core**

	1 <sup>st</sup> Cycle	2 <sup>nd</sup> Cycle	3 <sup>rd</sup> Cycle
Reactivity Limited Burnup	140	133	130
Effective Full Power Lifetime (EFPY)	18.48	17.66	17.16
Reactivity Swing ( $\Delta\rho$ )	0.03726	0.03091	0.03106
$\beta_{eff}$ unrodded at time of peak excess reactivity	0.0045	0.0038	0.0040
Reactivity Swing	\$8.21	\$8.19	\$7.81
Unrodded Maximum Radial Peaking Factor	1.34 @ EOL	1.28 @ 60 MWd/kg	1.28 @ 60 MWd/kg
BOL CVR (unrodded)	-\$0.39 +/- 5¢	-\$0.42 +/- 5¢	-\$0.35 +/- 5¢
MOL CVR (unrodded)	-\$0.05 +/- 5¢	-\$0.08 +/- 5¢	-\$0.12 +/- 5¢
EOL CVR (unrodded)	-\$0.35 +/- 5¢	-\$0.32 +/- 5¢	-\$0.36 +/- 5¢

Using a single batch refueling strategy, this core design demonstrates the ability to achieve reasonably long burnups, while maintaining a relatively flat radial power profile and negative values of CVR throughout cycle life without the aid of control rods, fuel shuffling, or a scattered batch reload strategy. This capability was shown not only for a single cycle, but was also demonstrated for a second and third cycle, incorporating a strategy of recycling its own used fuel. The neutronic performance parameters of these three cycles are compared in Table 11.4. The thermal hydraulic parameters are not compared in this table, as they are not expected to change appreciably from cycle to cycle, since neither geometry nor power

peaking factors are different. While not representative of normal rodded core operations, the unrodded CVR values are presented in Table 11.4, with the understanding that they can only get more negative when the effect of control rods are accounted for. The important point with respect to the CVR values in Table 11.4 is that they stay negative throughout all three cycles for the unrodded case. It is important to note that this is rare, if not unique, for a fast reactor.

Finally, the chemical compatibility of the core materials with the S-CO<sub>2</sub> coolant was evaluated. This is an important factor to consider in the design of this reactor, as the fuel assemblies must be vented in order to mitigate the large stress on the cladding wall due to the large system pressure at which the PCS must operate for maximum efficiency. While a detailed corrosion model and experiments would be necessary to determine the exact extent of the chemical compatibility of a candidate material with the S-CO<sub>2</sub> coolant at the elevated temperatures and pressures found in this core, a framework for a good first order metric of this factor has been established using a chemistry code called HSC 5.1 [Roine, 2002]. This metric is simply based on calculating if a given chemical reaction is thermodynamically favorable based on its Gibbs Free Energy ( $\Delta G$ ). Four key core materials were assessed: UO<sub>2</sub> (assuming the (U,TRU)O<sub>2</sub> would behave similarly), Ti, BeO, and B<sub>4</sub>C. UO<sub>2</sub> reacts with S-CO<sub>2</sub> to form some U<sub>4</sub>O<sub>9</sub>, which has a lower melting point and thermal conductivity than UO<sub>2</sub>. Reassuringly, experience with British Advanced Gas Reactors (AGRs), which also use CO<sub>2</sub> coolant with UO<sub>2</sub> fuel, indicates that the formation of U<sub>4</sub>O<sub>9</sub> in such a situation occurs quite slowly and can be inhibited by the presence of carbon monoxide (CO), a radiolysis product in the coolant [Poulter, 1963]. Further, the BeO diluent in the inner and middle fuel zones, which is fairly chemically stable with CO<sub>2</sub>, is shown to help inhibit the formation of U<sub>4</sub>O<sub>9</sub>. While the analysis for Ti suggests chemical reactivity with S-CO<sub>2</sub> (i.e. negative  $\Delta G$  values), [O'Driscoll, 1958] shows that its initial reaction with S-CO<sub>2</sub> forms a thin, passive oxidation layer which inhibits further reaction. Furthermore, the reaction product, CO, will help suppress the CO<sub>2</sub> + UO<sub>2</sub> reaction, which is beneficial. The analysis suggests that B<sub>4</sub>C is highly chemically reactive with CO<sub>2</sub>, forming B<sub>2</sub>O<sub>3</sub>. An evaluation of the formation of a passivation layer (B<sub>2</sub>O<sub>3</sub>) will need to be made in order to confirm the feasibility of using B<sub>4</sub>C in a vented shielding assembly; otherwise, a coated particle or CERMET configuration will have to be considered. It should be remembered that the present analysis only gives an

indication of how thermodynamically favorable a reaction is and says nothing about the rate at which it may occur. Further, it does not account for geometry and the presence of inhibiting passive layers.

#### **11.4 Comparison of Different Fuel Types and Diluent Strategies**

A comprehensive neutronic and thermal-hydraulic study was undertaken to determine if the TID fuel type is truly the best fuel type for application in the S-CO<sub>2</sub> cooled GFR. As well, the study sought to answer the question of how to best use the diluent, i.e. homogeneously blended in the fuel or as heterogeneous pellets. Three fuel types (TID, pin and ICAF) were explored in combination with three diluent strategies (integrated/homogeneous, separate/heterogeneous, and slug in the middle (applicable to pin fuel only)), yielding seven possible combinations for examination.

In order to assess the various neutronic benefits of each of the possible approaches, a semi-infinite assembly (normal leakage axially, mirror boundary conditions radially) model was constructed. The three key parameters of neutronic performance that were optimized were minimization of CVR, maximization of reactivity limited burnup, and minimization of critical enrichment. These parameters and their maximization/minimization were chosen in an effort to achieve the most cost-effective and safe design possible for this reactor, in support of the Generation IV International Forum (GIF) goals of economics and safety. It was shown that homogeneous BeO in TID fuel provided the best balance among these sometimes competing parameters, as it (1) maximizes  $v_{\text{BeO}}$  (BeO volume fraction) which minimizes CVR and (2) maximizes  $v_f$  (fuel volume fraction) which maximizes reactivity limited burnup while minimizing critical enrichment.

The seven different fuel diluent combinations were then evaluated thermal hydraulically, using four constraints: (1) Cladding Temperature: <800°C, (2) Fuel Temperature: < 1800°C, (3) Pressure Drop: < 500 kPa, and (4) Fuel volume fraction in the assembly ( $v_{fA}$ ): > 0. From these calculations, an acceptable thermal hydraulic envelope was established for each fuel-diluent combination which bounded the range of fuel geometries, i.e. pin pitch and diameter, that met the established T/H criteria. The envelope generated for

the homogeneous diluent BeO case is shown in Figure 11.7. Note that the z-axis (grayscale gradation) shows the volume fraction of fuel in the assembly,  $vf_A$ .

The results showed that the integrated BeO cases provide the best thermal hydraulic performance, regardless of fuel type. As well, it was found that the acceptable T/H envelope for TID fuel with integrated BeO provides an appreciably larger  $vf_A$  than the other two fuel options, while still respecting the established T/H limits. While the TID option that maximizes  $vf_A$  is near the maximum cladding temperature and pressure drop limits, the size of the acceptable T/H region for TID fuel allows for moving to a region of lower pressure drop, lower cladding temperature, and lower fuel temperature, while still maintaining a superior  $vf_A$  over the other fuel types. Further, as one moves away from the pressure drop limiting region, the extra pressure drop margin can be traded off for a reduction in cladding temperature via cladding surface roughening, dimpling, ribbing, or other heat transfer augmentation methods.

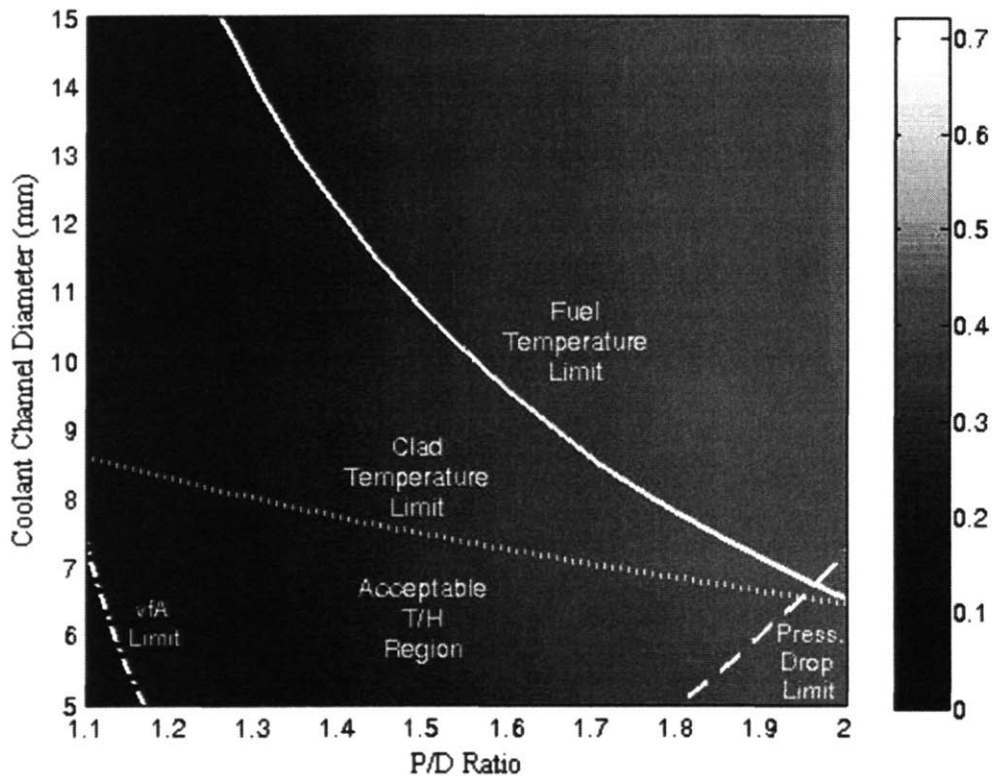


Figure 11.7: Acceptable T/H Envelope for TID Fuel with BeO

Performing an integrated neutronic and thermal-hydraulic comparison among fuel types and diluent strategies shows that TID fuel with integrated BeO diluent provides the best

all-around performance. This stems mainly from the large fraction of the volume inherent in such a strategy, that can be used for both diluent and fuel. Neutronically, this larger volume allows for a larger fuel loading, which can help to maximize reactivity limited lifetime while minimizing critical enrichment. As well, this larger volume can accommodate more BeO diluent, which helps to minimize CVR. From a thermal hydraulic standpoint, this larger volume allows greater design flexibility in trade-offs among competing parameters while still achieving superior neutronic performance. For the same reasons, the traditional pin is selected as the preferred second choice, as it capable of achieving nearly 50% greater  $v_{fA}$  than ICAF while still respecting established thermal-hydraulic limits. While ICAF can confer a unique advantage with respect to fuel temperatures, the design freedom afforded by the higher  $v_{fA}$  of the pin and TID fuel allows adjustment of their geometry to achieve comparable performance in this area. For the pin fuel, this comes at the expense of pressure drop. For the TID fuel, it does not come at any cost.

### ***11.5 Comparison Among TID, Pin Type, and ICAF Core Designs***

Exploration of a core using pin-type fuel is worthwhile in the event that insurmountable obstacles arise during the development of TID fuel which precludes their implementation in this or other reactor types, as pin-type fuel enjoys more than 50 years of worldwide manufacturing and operating experience. As well, it was also the configuration of choice, both vented and unvented, for the GCFR designs of the 1970's, which included some test pin irradiations [Capana and Lindgren, 1974]. In the present work, Internally Cooled Annular Fuel (ICAF) was explored for GFR application due to its promise in LWRs, with the hopes that these benefits will translate directly.

Table 11.5 lists the key parameters for the core designs using these three fuel type options for comparison, while Figure 11.8 shows the excess reactivity behavior of the three fuel type core design options. Shortcomings were observed with pin-type and ICAF fuel due to their much shorter burnup capability and higher critical enrichment. This is a caused primarily by the much lower fuel volume fraction ( $v_f$ ) and consequent poorer neutron economy. Conversely, the lower  $v_f$  gave very favorable results with respect to CVR, as axial leakage was enhanced. Additionally, the maximum radial power peak for the pin-type and

**Table 11.5: Comparison of Key Parameters Among the TID and Pin-Type Cores**

	TID	ICAF	Pin
	<b>Core Geometry</b>		
Unit Cell P/D	1.9	1.1	1.1812
Diameter (cm) <sup>*</sup>	0.7	1.5	1.0
FTF <sup>†</sup> , assembly (cm)	23.00265	22.59044	20.45702
TT <sup>‡</sup> assembly (cm)	26.56117	26.08519	23.62173
Side, assembly (cm)	13.28059	13.0426	11.81086
# of rings of fuel unit cells, assembly	9	7	9
# of rings of assemblies, core	11	11	13
FTF core (m)	4.65	4.56	4.84
Core height (m)	1.54	1.53	1.53
Core vol. (m <sup>3</sup> )	28.89	27.65	31.12
Height/Diameter	0.315	0.32	0.301
Fuel volume fraction, core	0.590	0.321	0.439
Cladding volume fraction, core	0.137	0.225	0.153
Coolant volume fraction, core	0.273	0.453	0.407
	<b>Neutronic Performance</b>		
Enrichment (TRU <sup>w/o</sup> )	16.6	25.1	19.85
Diluent Zoning	30/33/00	41.5/41/00	38/40/00
Achievable Burnup (MWd/kg) <sup>§</sup>	140	26	61.6
Reactivity Limited Lifetime (EFPY) <sup>§</sup>	18.48	1.71	6.24
Specific Power (kW/kg <sub>HM</sub> )	20.7	43	27.02
Core Heavy Metal Loading (kg <sub>HM</sub> )	115942	55814	88823
Reactivity Swing (pcm)	3726	1962	2017
Unrodded Maximum Radial Peaking Factor	1.34 @ EOL	1.13 @ BOL	1.14 @EOL
BOL CVR (rodded)	-\$1.08 +/- 7¢	-\$1.73 +/- 11¢	-\$1.08 +/- 7¢
MOL CVR (rodded)	-\$1.19 +/- 7¢	N/A	N/A
EOL CVR	-\$0.36 +/- 5¢	-\$1.39 +/- 9¢	-\$0.37 +/- 5¢
Peak CVR	-\$0.36 +/- 5¢	-\$1.39 +/- 9¢	-\$0.37 +/- 5¢
	<b>Thermal Hydraulic Performance</b>		
Peak Cladding Temperature (°C)	810	750	735.6
Peak Fuel Temperature (°C)	1770	1177	1800
Core Pressure Drop (kPa)	420	267	435

<sup>\*</sup> inner diameter of the cladding for the coolant hole for TID, outer diameter of the cladding for pin and ICAF.

<sup>†</sup> FTF = Flat-to-Flat

<sup>‡</sup> TT = Tip-to-tip

<sup>§</sup> For approximately the same BOL core eigenvalue

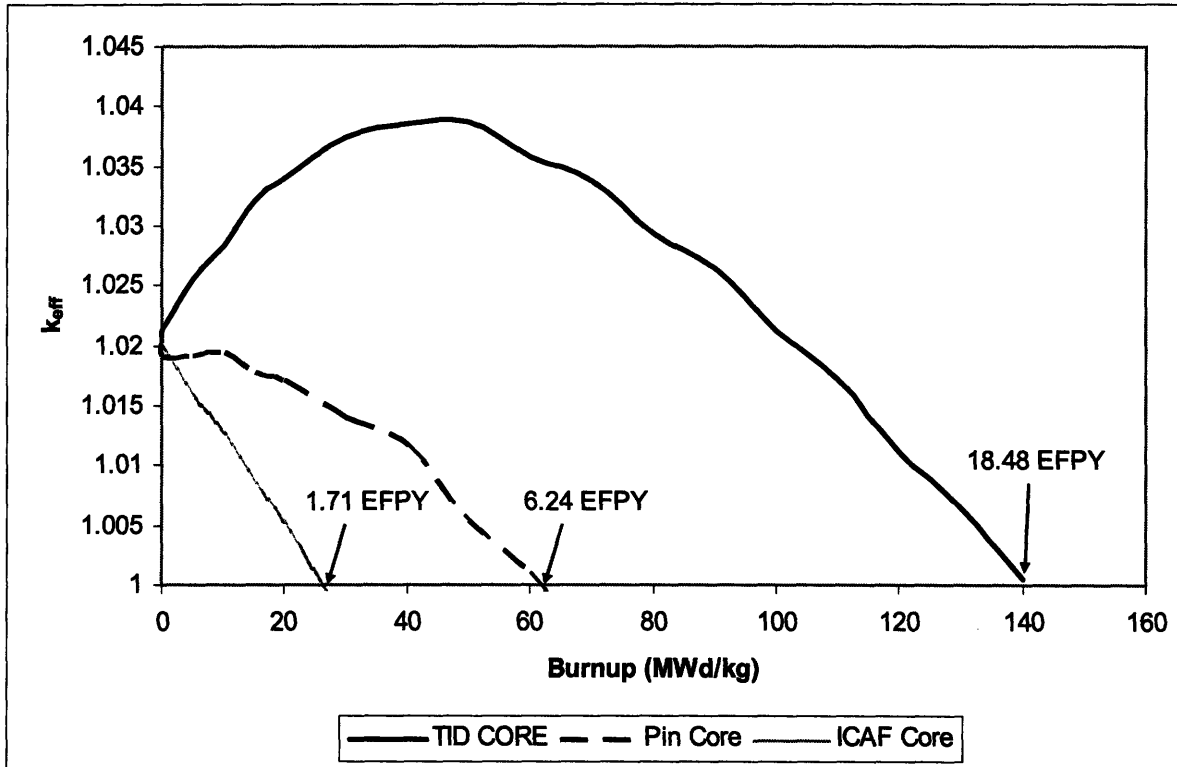


**Figure 11.8: Comparison of Reactivity Limited Burnups of the TID and Pin-Type, and ICAF Cores**

ICAF cores is somewhat lower than that achievable for the TID core, due to (1) the shorter burnup of these cores, preventing large spatial differences in fuel burnup and (2) the lower fuel volume fraction of these cores, meaning that there is physically less fuel to burn up in a spatially uneven manner. While the pin and ICAF cores have advantages in the radial power shaping and CVR categories, these advantages are not large enough to make up for shortcomings in other areas. Further, the performance of the TID core in this area is more than satisfactory. The thermal-hydraulic results, analysis, and comparison are the same as those made in the previous section, as that study provided the basis for the neutronic core design.

In an effort to improve the short lifetime of the pin-type core, an extra meter of core height was added in order to increase the heavy metal loading and improve the neutron economy by reducing axial leakage. While this was effective in increasing the reactivity limited lifetime and reducing the critical enrichment, it increased the positive contribution to CVR upon voiding. This demonstrated the fundamental design trade-off between neutron

economy and CVR reduction through leakage. Still, the 1m taller core was able to achieve negative CVR throughout life, approaching 0 at EOL. It should be noted that the 1m taller core was assessed with respect to neutronic design criteria only, and that it will likely challenge some of the thermal hydraulic design criteria for this core, owing to its increased height. Specifically, it will challenge the pressure drop criterion. However, this pressure drop criterion is not a hard one and can be relaxed at the expense of PCS efficiency and increased power requirements during decay heat removal. This relaxation of the pressure drop criterion and accompanying trade-off can also be applied to the original pin-type core, where a tighter lattice core could be developed to improve the fuel volume fraction, the root cause of the pin core's largest shortcomings. Nevertheless, no improvement would be able to achieve a CR=1 using oxide fuel without the use of external blankets for pin fuel or ICAF, even without the use of diluent in the fuel.

## **11.6 Waste Management**

The ability to manage several key long lived fission products (Tc-99 and I-129) and TRU for the TID GFR core were assessed and evaluated against current LWR practice and a competing Gen-IV design, the Lead Fast Reactor (LFR). The TID GFR core was found to have an advantage in all of these areas with respect to the LWR case, due to the (1) substantially harder neutron spectrum, which leads to a greater in-situ burning capability and (2) the ability to recycle the fuel. While the numbers presented in this work show that the LFR is comparable in Tc-99 and I-129 production/destruction and superior in the ability to incinerate TRU, the difference in inter-cycle actinide management between the TID GFR core and the LFR account for the difference in TRU management performance. The TID GFR still has a net MA destruction rate and given the similarity of the GFR and LFR spectra, the GFR has the potential to achieve near LFR-like TRU performance, should the same inter-cycle actinide management strategy be used.

As well, the proliferation resistance of the TID GFR core was compared against that of current once-through LWR practice and the LFR, with the GFR found to have a great advantage over the LWR, and a slight advantage over the LFR, in this area, due to the larger Pu-238 (increased heat generation), Pu-240 (increased spontaneous fission), and Pu-241



(highly penetrating gamma) components of the Pu vector of the spent fuel. While these auspicious results bode well from a proliferation standpoint, they are not favorable from an ease of reprocessing and fabrication standpoint.

Within the GFR option space, the MA/TRU management of the three core designs of different fuel types was compared. The ICAF and pin core outperform the TID core, stemming mainly from their higher TRU enrichment, which means (1) less U-238 competing for fast neutrons, making more available for TRU and Pu destruction and (2) more Pu-239, which for comparable spectra, leads to a proportionately higher fraction of fissions in Pu-239 and greater TRU destruction. The pin and ICAF cores have a conversion ratio (CR) less than 1 whereas the TID core has a CR~1. While this gives the pin and ICAF cores an inherent advantage with respect to MA/TRU management, it does not let them meet the goal of sustainability set forth by Gen-IV reactors. It should be remembered that the TID core TRU management performance is still better than current LWR practice and has the potential to rival that of the LFR.

Finally, the use of the GFR as a dedicated actinide burner, instead of the previously assumed breeder-burner role, was explored. A literature review and comprehensive analysis was conducted to determine that MgO was the best Inert Matrix Fuel (IMF) to be used in an actinide burner concept for this GFR. This selection was based on the high melting point, good thermal conductivity, and superior irradiation performance in a fast neutron environment of MgO, coupled with its initially assessed chemical compatibility with the S-CO<sub>2</sub> coolant. A quantitative comparison of two GFR IMF semi-infinite assemblies (with and without BeO diluent) was made with a TID GFR core assembly ("Fertile" case), with all evaluated using established neutronic criteria in seven different areas. The performance of the IMF (in both cases) was inferior to that of the Fertile case. While some performance shortcomings were corrected through the removal of the diluent in the fuel, the larger reactivity swing and much shorter reactivity-limited lifetime proved the idea of using this GFR as a dedicated actinide burner with fertile-free fuel is not feasible. Moreover, fuel cycle simulations have shown that CR=0 strategies are not needed to manage TRU [Hejzlar, 2006].

## **11.7 Preliminary Neutronic Safety Assessment**

A method for evaluating the passive safe shutdown capability (without SCRAM) of the TID GFR reactor core was developed from an existing method developed for IFR-type Liquid Metal Reactors [Wade and Chang, 1988]. The differences between the original method, the Quasi-Static Method (QSM), and the new method, the Direct Cycle GFR QSM (DCGQSM), center around the fact that a loss of flow cannot occur without a degradation of heat sink in a direct cycle system and that Coolant Void Reactivity (CVR) affects this core much differently than the core for which the original QSM was developed. Applying the DCGQSM to the candidate core design shows that passive safe shutdown is achievable against all limiting scenarios at all times in core life except the Loss of Coolant Without SCRAM (LOCAWS) at EOL, due to the large core average incremental temperature increase of the fuel above that of the coolant,  $\overline{\Delta T_f}$ . Solutions for reducing  $\overline{\Delta T_f}$  include altering the geometric specifications of the TID fuel and reducing the large uncertainty currently present in the calculation of this number, found primarily in the estimation of the effect of the BeO diluent on the fuel thermal conductivity. Since most of the requisite principles for passive core shutdown have been demonstrated and the uncertainty in the calculation of  $\overline{\Delta T_f}$  is fairly large, the candidate core design is deemed sufficiently safe. Hence, a permutation of this design at the new geometric dimensions is not pursued here and remains a fertile area for future work. Of course, increasing SCRAM reliability would be of great benefit here and in many other severe accident scenarios.

Additionally, water ingress scenarios were explored and showed that the large moderating effect of water added enough negative reactivity to ensure adequate margin to criticality throughout core life. The implications with respect to fuel handling (e.g. refueling) and storage were consequently also evaluated as favorable.

## **11.8 Economic Analysis**

Using a basic cost model, the cost of electricity was compared among the TID, Pin, and ICAF GFR cores and an advanced LWR. A summary of this comparison using best case economic conditions is shown in Table 11.6. Combining the larger fuel cycle and capital

cost of the TID GFR (represented directly in the capital cost component and indirectly in the Operations and Maintenance (O&M) and Decontamination and Disposal (D&D) cost component) accounts for the majority of the difference between the LWR and GFR under the best-case scenario, with the LWR COE ~25% less than that of the GFR. The high cost of reprocessing LWR spent fuel puts this and all fast reactors at a disadvantage with respect to their startup fuel cycle costs. The larger capital cost stems from the larger overnight construction cost predicted for GFRs. However, several unique benefits are hypothesized to exist for the direct cycle GFR which could lower these larger capital costs: (1) the smaller size of the plant and lower cost of the PCS for the GFR could help to drive down these costs by as much as 25% and (2) the single-batch strategy of the GFR could lower O&M costs through a higher capacity factor, resulting from avoided refueling shutdowns and a lower forced outage rate.

**Table 11.6: Comparison of the Cost of Electricity among an LWR and the TID, Pin, and ICAF GFR Cores**  
(all costs are in mills/kWh<sub>e</sub>)

	LWR	TID	Pin	ICAF
Capital Cost	23.06	28.48	28.48	28.48
Front-end Fuel Cycle Cost	3.18	10.45	16.29	36.12
Operations and Maintenance (O&M)	8.62	10.65	10.65	10.65
Storage	0.25	0.02	0.05	0.12
Disposal	1.00	0.18	0.18	0.18
Decontamination and Disposal (D&D)	1.84	2.28	2.28	2.28
<b>TOTAL</b>	<b>37.95</b>	<b>52.06</b>	<b>57.92</b>	<b>77.83</b>

Comparing options among the different fuel type GFR cores, Table 11.6 shows that the pin and ICAF cores have higher fuel cycle costs, due to the shorter burnup and higher BOC enrichment; however, this increase is mitigated by their higher specific power and lower core heavy metal loading. These mitigating factors are direct consequences of the inherently lower fuel volume fraction of the pin and ICAF fuel types, as all of the cores have roughly the same volume and height and identical thermal ratings. When the increase in fuel cycle cost of the pin core relative to the TID core is compared with the other cost components, an increase of 6 mills/kWh<sub>e</sub> is not very significant, making the pin core cost competitive with the TID Core. While the TID is the most cost effective fuel type for the GFR core, relaxation of the core pressure drop limit (as discussed previously) would allow a

larger fuel volume fraction in the pin core, which could cure the root cause of its performance ills.

## **11.9 Conclusions**

A reactor core for use in a direct cycle supercritical carbon dioxide (S-CO<sub>2</sub>) Gas-cooled Fast Reactor (GFR) has been designed which satisfies established neutronic and thermal hydraulic steady state design criteria, while concurrently supporting the Gen-IV criteria of sustainability, safety, proliferation, and economics. Use of TID fuel has been central to accomplishing this objective, as it provides a high fuel volume fraction and lower fuel temperatures and pressure drop when compared to its traditional pin-type contemporaries. Further, this large fuel volume fraction allows for a large enough heavy metal loading for a sustainable core lifetime without the need for external blankets, enhancing the proliferation resistance of such an approach. While pin-type fuel has been shown to be inferior to TID fuel for application in this reactor under present conditions, relaxation of the core pressure-drop limit could widen the pin core design space enough to allow for a design comparable in performance to be achieved. Nevertheless, no improvement would be able to achieve a CR=1 using oxide fuel without the use of external blankets for pin fuel, even without the use of diluent in the fuel.

Three significant contributions have been made as a result of this work. First, this work explores and successfully implements a moderating diluent in the fuel in an effort to not only shape power at the beginning of core life, but also to help maintain a relatively flat power shape throughout core life. This is a significant contribution as it allows optimal use of fast reactor core resources. Second, the core designs in this work successfully maintain  $CVR \leq 0$  throughout core life through the symbiotic combination of diluent use in the fuel and the innovative use of an S-CO<sub>2</sub> reflector. By keeping CVR negative throughout core life, the severity of one of the most serious accidents for this type of reactor, the Loss of Coolant Accident (LOCA), is greatly reduced. This is a significant contribution as there are very few, if any, fast reactors that have been conceptualized with a negative CVR throughout life. Third, this work comprehensively compares the thermal hydraulic and neutronic performance of TID fuel with that of the traditional pin-type fuel, as well as with the innovative Internally-

Cooled Annular Fuel (ICAF). This is a contribution because it not only evaluates these options in an integrated sense, but it also provides detailed supporting analyses to show the fundamental reasons for their performance behavior.

### **11.10 Recommended Future Work**

While many possible areas of future work could follow from this research, the most pressing is the need to perform a comprehensive transient and accident analysis on the TID GFR core design. A relatively simple, first-order assessment of this core's ability to achieve passively safe shutdown without SCRAM and without violating established core thermal limits has been developed and presented. However, this tool was developed as a steady state neutronic design aid and does not provide any insight into the core's neutronic or thermal-hydraulic transient behavior under accident conditions. Hence, a detailed safety analysis, using advanced tools such as RELAP, is needed to not only validate the method developed in this work (DCGQSM), but also to assess the performance of the core under accident conditions. Not only should the less severe ATWS events be examined, but investigation into the more advanced accident scenarios and effects, such as post accident fuel relocation, should be made. In the same vein, a TID GFR with the revised geometry suggested at the end of Chapter 9 should be investigated to determine if protection can be provided against a LOCAWS at EOL. Further, an investigation into the safety performance of the pin core should be undertaken so that any unique differences in this approach can be understood.

Another important area for future work is a further investigation into the suitability of using BeO in a fast reactor and in a closed fuel cycle. While showing much promise from a neutronic design standpoint, BeO has some potential shortcomings which need to be addressed and resolved before it can fulfill its intended purpose as a fuel diluent in this design. Consequently, a similar core design effort using another diluent, e.g. SiC, should be undertaken, in order to confirm comparable performance.

An important part of the GFR being able to maintain a negative CVR throughout core life, the S-CO<sub>2</sub> radial reflector raises questions about two important technical details. First, the prospect of core flow bypass exists with the use of such a radial reflector strategy. Second, the "empty" S-CO<sub>2</sub> space in the radial region of the active core presents a challenge

with respect to the structural design and integrity of the core. While hypothesized solutions have been presented to these problems, the feasibility of their use and their ability to be integrated into the overall core design must be established.

While the method used for assessing chemical compatibility in this work provided a decent first order metric, a more suitable and accurate assessment should be made to account for the configuration of the reactants and the kinetics of the proposed reactions. While a search of the literature answered this question for some of the core materials of interest, a more detailed study needs to be performed, either in the way of simulation or laboratory experiment (preferably involving in-core irradiation). This is especially true for the compatibility of B<sub>4</sub>C and S-CO<sub>2</sub>, which is an unresolved issue.

An important feature of all three GFR core designs is the fission gas venting system, necessary to alleviate the large differential pressure across the cladding. A comprehensive design effort should be undertaken to not only establish the feasibility of such a concept with TID fuel, but to also optimize its performance. More generally, the design and fabrication of TID fuel needs to be explored, especially with respect to how this fuel can be recycled.

In the analysis of waste management performance, the GFR showed a net MA destruction rate, but a net positive TRU production rate. While this compared favorably with current LWR practice, it did not match the performance of one of its Gen-IV contemporaries, the LFR. Fundamentally, this was due to the different approach in inter-cycle actinide management philosophy that the LFR took, where all of the TRU from a previous cycle was used in the subsequent cycle. While it is hypothesized that the same waste management performance is achievable by the GFR upon adoption of this philosophy, this hypothesis should be validated by reperforming the 2<sup>nd</sup> and 3<sup>rd</sup> cycle designs of the GFR TID core.

Integral to the success of a closed fuel cycle, a review of available reprocessing technologies and needed R&D in order to establish the viability of the fuel cycle concept used in this work is needed. Such a review should include a detailed cost analysis and a more detailed design of the fuel cycle concept, including processes, infrastructure, and logistics. Specifically, the feasibility of a reactor park or shared resource type concept needs to be

established – a desirable goal for fast reactors in general. Unique to this GFR, the presence of large amounts of BeO in the fuel needs to be considered.

With respect to the economic assessment of the GFR, many questions have been left unanswered and warrant further investigation, as economics will be the key factor which will determine if one of these plants will ever actually be built. First, a better estimate of the capital costs of such a strategy need to be quantified, as this currently stands as the greatest cost impediment to the development of the GFR. While this work used current and relevant sources, no independent assessment of this economic aspect was made. [Stahle et al , 2005] and [Dostal (b) et al, 2006] provide examples of recent independent work in this area. Second, the capital and operating costs of a reprocessing facility have not been addressed, as well as the transportation costs associated with implementing such a strategy. Third, a better estimate of the costs associated with the reprocessing and fabrication of the GFR fuel, based on established technologies, is needed. Finally, a comparison of the LWR using recycle should be compared against the GFR recycle option, in order to give a fairer basis for comparison between these two technologies.

Finally, all of the neutronic depletion analyses in this work were performed for an unrodded core. The integration of a comprehensive control rod strategy should be implemented, accounting for B-10 depletion throughout core life.

# **A Computational Tools**

## **A.1 Introduction**

In this Appendix, a brief, functional overview of the computational tools used in this work will be given. These descriptions are kept purposely brief, as a well documented list of references is provided for the interested reader. These tools are well tested and some are widely accepted as the standard tool for performing their respective types of calculations.

## **A.2 Neutronic Analysis Tools**

### **A.2.1 MCODE**

MCODE (MCNP-ORIGEN DEpletion Program) is the primary tool used in this work for burnup calculations. MCODE is a linkage code developed at MIT which couples MCNP and ORIGEN in order to do depletion analysis for nuclear fission reactor systems [Xu et al, 2002]. It is similar in concept to other available linkage codes, such as MONTEBURNS or MOCUP.

Initially, a depletion problem is defined in the form of a standard MCNP input deck, with the inputs for MCODE (depletion points, power, file locations, etc.) input as a fourth paragraph in the MCNP input deck (MCODE v2 and later). Upon execution, MCODE processes and modifies the MCNP input deck to include special tallies that calculate fluxes and one-group cross-sections for the materials within the input deck subject to depletion, e.g. fissile materials. After the MCNP input deck is executed, the tallies are then processed by MCODE to generate 1-group cross sections to be used as input for ORIGEN, which uses this information to perform the burnup of specified nuclides, as well as to generate the appropriate concentration and distribution of fission products. The new material



concentrations output by ORIGEN are then processed by MCODE to update the original MCNP input deck for the next depletion step. This process repeats itself until all of the depletion steps have been completed.

Since its inception, several versions of MCODE have been developed. The results in this work come primarily from v2 and later, although some earlier results come from v1. Information about the benchmarking of MCODE and the strengths and weaknesses of each of the versions can be found in [Yarsky et al, 2005], [Xu, 2003], [Xu et al, 2006], and [Xu, 2007]

### A.2.2 MCNP

While MCNP is used as part of MCODE, it was also used as a stand-alone tool in order to calculate many neutronic parameters of interest, including power shapes, reactivity coefficients, and control rod worths. MCNP (Monte Carlo N-Particle) is a general purpose particle transport code developed at Los Alamos National Laboratory (LANL) [Briesmeister, 2000]. MCNP is a stochastic code which uses Monte Carlo methods to solve for the parameters of interest by following individual particles (in this case, neutrons) as they transport through the desired media. The results come as a result of the aggregate or average behavior of these particles. Hence, every solution obtained by MCNP has an accompanying uncertainty. This differs from more traditional deterministic methods, where equations of particle transport are directly solved. In theory, MCNP can provide an exact representation of particle transport, provided that the nuclear input data, i.e. cross sections, are correct and that a sufficient number of particle histories are calculated. [Xu, 2003] shows excellent agreement between MCODE (using MCNP) and deterministic methods (using the CASMO-SIMULATE suite) in providing solutions to neutronics problems.

MCNP was chosen for this work because of its ability to model the very heterogeneous and unique design of this GFR core and its constituent parts, i.e. TID fuel assembly, ICAF, etc. This capability is not found in many deterministic codes. The drawback to using MCNP (and stochastic methods, in general) is the considerable amount of computing time necessary to achieve results with the same accuracy as those achieved with deterministic codes. In order to support the MCNP and MCODE work performed in this

work, a 30-node parallel computing facility (Beowulf cluster) resident at MIT was used [Carstens, 2004]. The version of MCNP used in this work, both as part of MCODE and in its stand-alone capacity, is v4c3. The cross section libraries that were used were either ENDF/B-VI or JENDL-3.3, depending upon the particular calculation performed.

### A.2.3 ORIGEN

In addition to being used as part of MCODE, ORIGEN (Oak Ridge Isotope GENERation) is used in this work to calculate isotopic compositions in post-irradiation decay scenarios. ORIGEN is a computer code system for calculating the buildup and decay of, as well as the processing of, radioactive materials [Croff, 1980]. The code solves the equations for combined radioactive decay and fission production using the neutron flux (for calculations during irradiation, as is the case with MCODE), the half lives of the respective isotopes, and single group cross sections. For decay calculations where one-group cross sections were not available from MCNP, the in-situ ORIGEN libraries for the Fast Flux Test Facility (FFTF) were used. The version of ORIGEN used in this work, both as part of MCODE and in its stand-alone capacity, is v2.2.

### A.2.4 NJOY

NJOY is a computer code that is used to convert nuclear cross section data in the ENDF format into libraries useful for computational applications [LANL, 1994]. While NJOY has many capabilities, the application that it was used for in this work was to Doppler broaden the cross section tables for the actinides in the fuel. This was needed due to the use of older cross-section libraries, which only provided cross section data for certain temperatures. The Doppler broadened cross sections obtained from NJOY were then used to help determine the Doppler coefficient of reactivity of the fuel. With the recent advent of better and more complete libraries, e. g. JEF 3.1, the need for this capability becomes obsolete. Still, the majority of this work was performed prior to the availability of such libraries, and for the sake of consistency, the older libraries with the NJOY capability are used.

### **A.3 Thermal Hydraulic Analysis Tools**

#### **A.3.1 FLOWSPLIT**

FLOWSPLIT is a FORTRAN thermal-hydraulics code developed at MIT which can calculate fuel temperature profiles, cladding temperatures, and pressure drops, for multiple parallel channels given a set of user-defined inputs, e.g. power level, fluid flow rate, channel geometry, etc. [Hejzlar, 1994]. The utility of FLOWSPLIT lies in its simplicity, accuracy, and adaptability to unique geometries. A more detailed explanation of the methodology used in FLOWSPLIT can be found in [Pope, 2006]. In addition to the modifications to the original code made in [Pope, 2006], the present work expanded the capabilities of the code by adding user options to calculate (1) pressure drop due to wire-wrap and (2) the effect of annular fuel pellet geometry (i.e. traditional annular fuel pellet with external cooling only) on fuel temperatures. As well, a FLOWSPLIT-MATLAB interface was developed which allowed a wide range of fuel geometries to be explored thermal hydraulically in an efficient manner. This interface is described in detail in Appendix B.

#### **A.3.2 ANNULCO2**

ANNULCO2 is a modified version of TAFIX, designed to perform thermal hydraulic calculations on Internally Cooled Annular Fuel (ICAF) [Kazimi, 2001]. The main modification made to TAFIX was to make the code work with properties of S-CO<sub>2</sub>, rather than H<sub>2</sub>O for which it was originally designed. This was done prior to its implementation in this work. TAFIX is very similar to FLOWSPLIT, so the output of ANNULCO2 is nearly identical to that of FLOWSPLIT. The key difference between ANNULCO2 and FLOWSPLIT is that ANNULCO2 needs to iteratively solve in order to match thermal hydraulic parameters, i.e. temperature and flow, at the inlet and the outlet of the internal and external channels of the annular fuel. Hence, the computational time using ANNULCO2 is greater than when FLOWSPLIT is used. Similar to the work performed on FLOWSPLIT, ANNULCO2 was modified to account for the effects of wire-wrap and was coupled with a MATLAB interface to allow the automated exploration of a large number of geometries.

## **A.4 Chemical Compatibility Code**

### **A.4.1 HSC Chemistry® 5.1**

HSC (H – enthalpy, S – entropy, C – heat capacity) Chemistry® 5.1 is a powerful computational tool for chemical reactions and equilibria calculations [Roine 2002]. It uses an extensive database of material properties of more than 1700 chemical compounds to perform these calculations. HSC is used in this work as a first-order metric for predicting the chemical compatibility of the core materials with the S-CO<sub>2</sub> coolant, an important consideration given that the fuel is vented (indirectly) to the coolant. Limitations of this code include the inability to model the reactant geometry of a given chemical reaction, and the inability to provide reaction rate data.

## **B MATLAB Interfaces**

### ***B.1 Introduction***

The MATLAB scripts for the 2 interfaces used in the thermal hydraulics part of this work are presented in detail in this appendix. These scripts are based heavily on the work in [Blair, 2003] and [Malen, 2004], which first developed the idea of interfacing MATLAB with a FORTRAN executable in an effort to look at a wide range of similar thermal hydraulic problems with slightly differing geometries. The information in this Appendix is presented in detail to allow complete understanding in the event of interest in, or continuation of these studies.

The function of the MATLAB scripts is to automatically calculate the geometrically dependent variables for a given set of fuel dimensions (i.e. fuel pin diameter and pitch), compile both the geometrically dependent and independent variables into an input deck in a format acceptable for the FORTRAN executable (FLOWSPLIT and ANNULCO2, in this case) and then execute the executable. For the case of the FLOWSPLIT-MATLAB interface, once the FORTRAN program is executed, MATLAB reads specially created output files (created by a simple modification to the source code) and stores the data to be used later in finding thermal-hydraulically acceptable (or optimal) geometries. For the case of the ANNULCO2-MATLAB interface, once the FORTRAN program is executed, MATLAB reads specially created output files, compares the output with the thermal-hydraulic limits of interest, and adjusts the geometric dimensions of the inner coolant channel of the Internally Cooled Annular Fuel (ICAF). These dimensions are adjusted such that the ANNULCO2-MATLAB interface will continue to iterate until: (1) the coolant exit temperatures of the inner and outer channels are within 5 degrees and (2) the coolant

temperature of the outer channel is greater than that of the inner channel, if any mismatch exists. While it is desirable to have the exit temperature of the inner and outer channel exactly matched, a tolerance of 5°C was determined to give an acceptable approximation of results without incurring excessive computation time to converge on an exact solution. The second condition was imposed since the outer channel would have the benefit of mixing, while the inner channel would not. Hence, the outer channel would have a slight heat transfer advantage over the inner channel and could tolerate a slightly higher temperature. Once the two thermal-hydraulic criteria are satisfied, relevant data parameters are recorded to be used later in finding thermal-hydraulically acceptable or optimal geometries.

## B.2 FLOWSPLIT-MATLAB Interface

Of the two interfaces developed, the FLOWSPLIT-MATLAB interface is less complex, as it does not require any feedback or iteration. The program which is the base is *flowsplt\_gen.m*. This program communicates with other programs in order to achieve the goals described in Section B.1. The purpose of each program is listed in Table B.1. Figure B.1 shows a flowchart which outlines the sequence of execution of each program. Combining Figure B.1 and Table B.1 with the programs that were used (documented later in this Appendix) and some knowledge of MATLAB and FLOWSPLIT, should give complete transparency to anyone regarding the FLOWSPLIT-MATLAB interface.

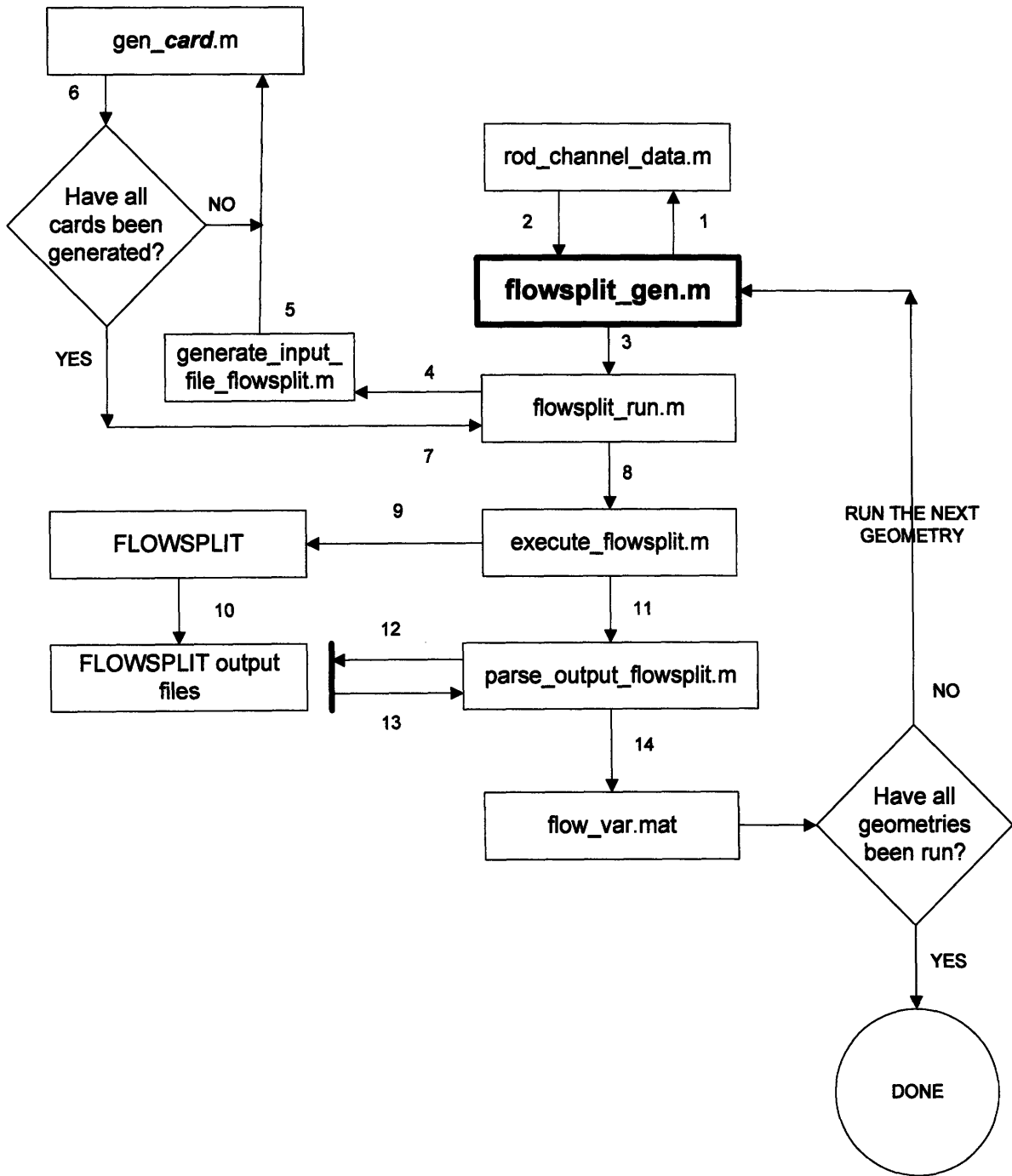
**Table B.1: Description of MATLAB Scripts for the FLOWSPLIT-MATLAB Interface**

Program	Description
flowsplit_gen.m	<ul style="list-style-type: none"> <li>• Main program in the FLOWSPLIT-MATLAB Interface</li> <li>• Collects geometrically independent and dependent FLOWSPLIT input variables from program <i>rod_channel_data.m</i></li> <li>• Saves all geometrically dependent and independent variables needed for a FLOWSPLIT input deck to var_file_name (<i>flow_var.mat</i>)</li> <li>• Executes <i>flowsplit_run.m</i> to begin/continue the feedback loop               <ul style="list-style-type: none"> <li>• Loads FLOWSPLIT output of interest (after it has been formatted by <i>parse_output_flowsplit.m</i>) as file <i>flowsplit_output_data</i></li> </ul> </li> <li>• Collects output of interest for each geometry and saves cumulative data to var file name (<i>flow_var.mat</i>)</li> </ul>

**Table B.1(cont): Description of MATLAB Scripts for the FLOWSPLIT-MATLAB Interface**

Program	Description
Rod_channel_data.m	<ul style="list-style-type: none"> <li>• Calculates the geometrically dependent variables, given fuel rod pitch and fuel rod diameter. Core power, core diameter, core height, wire-wrap option, diluent volume fraction, and fuel type are also needed as inputs, but stay constant over all geometries examined for a given run.</li> </ul>
flowsplit_run.m	<ul style="list-style-type: none"> <li>• Creates a correctly formatted FLOWSPLIT input deck by loading all of the input variables from var_file_name (<i>flow_var.mat</i>) using program <i>generate_input_file_flowsplit.m</i>. <i>generate_input_file_flowsplit.m</i> uses <i>gen_card.m</i> to generate a correctly formatted input for the each card in the input deck (where <i>card</i> is a variable in this case representing the name of the card of interest, i.e. flow1, flow2, flow3, etc.)</li> <li>• Writes the correctly formatted FLOWSPLIT input deck to the file input_file_name (<i>flow_test_input_file</i>)</li> <li>• Executes <i>execute_flowsplit.m</i> so that the feedback loop can continue</li> </ul>
execute_flowsplit.m	<ul style="list-style-type: none"> <li>• Executes the modified version of FLOWSPLIT (<i>flowsplit.exe</i>) using a C program (<i>call_flowsplit.c</i>) and a .dll file (<i>flowsplit.dll</i>)</li> <li>• Executes <i>parse_output_flowsplit.m</i> so that the feedback loop can continue</li> </ul>
parse_output_flowsplit.m	<ul style="list-style-type: none"> <li>• Loads output files of interest and extracts the values of interest, formatting them for use in <i>flowsplit_gen.m</i></li> <li>• Saves these values of interest in file <i>flowsplit_output_data</i></li> </ul>
FLOWSPLIT	Executable modified to give specially formatted output files for use in the FLOWSPLIT-MATLAB interface
flow_var.mat (variable var_file_name)	Working file that is the ultimate repository of the FLOWSPLIT-MATLAB output (i.e. pressure drop for a given geometry, maximum fuel temperature for that geometry, etc.)
flow_test_input_file (input_file_name) (not pictured in Figure B.1)	Working file used to compile the input variables for the FLOWSPLIT input deck
flowsplit_output_data (not pictured in Figure B.1)	Working file used to transfer data of interest among MATLAB programs, specifically output data of interest

Figure B.1: Roadmap for FLOWSPLIT-MATLAB Interface





### B.3 Thermal-Hydraulic Calculations Algorithms

To calculate some of the geometrically dependent parameters of interest, specifically those used in *rod\_channel\_data.m*, an algorithm was developed. In order to make a fair comparison among different fuel dimensions and fuel types, the size (i.e. height and diameter) and power of the active core were kept constant. Based on these constraints, an algorithm was derived to determine some of the pertinent geometrically dependent variables used in both the FLOWSPLIT-MATLAB and ANNULCO2-MATLAB interfaces.

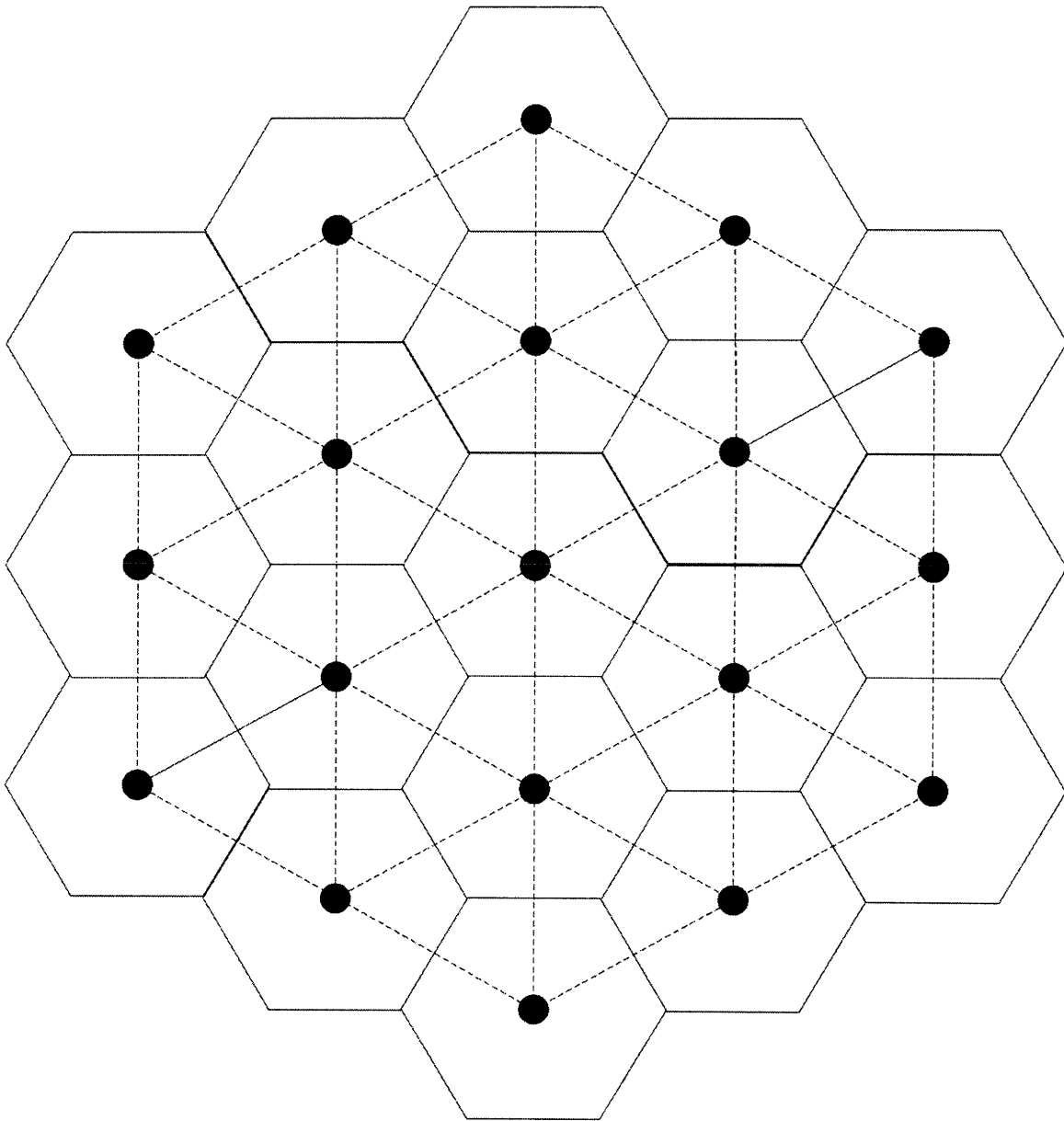


Figure B.2: Pictorial Representation of a Hexagonal Infinite Lattice

To calculate the number of channels in a hexagonal core, Figure B.2 can be used as a visual aid to show the geometry of an infinite lattice of hexagonal unit cells. For a TID core, the fuel can be represented by the white hexagons and the coolant channels can be represented by the solid black circles, both comprising a TID unit cell. For a pin core, the fuel pins can be represented by the black circles and the hexagons can represent the boundaries of their respective unit cells, with the triangular coolant subchannels represented by the triangles with a dotted-line border.

The number of coolant subchannels in a hexagonal core made from  $n$  rings of unit cells for a pin and TID core is:

$$\# \text{ subchannels}_{PIN} = 6n_{PIN}^2 \quad \{\text{B.1a}\}$$

$$\# \text{ subchannels}_{TID} = 3n_{TID}^2 + 3n_{TID} + 1 \quad \{\text{B.1b}\}$$

For a pin core:

$$FTF_{n,PIN} = n_{PIN} * (TT_{UC} + S_{UC}) \quad \{\text{B.2a}\}$$

where:

$FTF_{n,PIN}$  = flat-to-flat of the outermost hexagon formed by  $n$  rings of rods

= Core Diameter,  $D_{CORE}$

$TT_{UC}$  = tip-to-tip of the unit cell

$S_{UC}$  = side of unit cell

Therefore:

$$n_{PIN} = \frac{FTF_{n,PIN}}{TT_{UC} + S_{UC}} = \frac{D_{CORE}}{TT_{UC} + S_{UC}} \quad \{\text{B.3a}\}$$

Similarly, for a TID core:

$$FTF_{n,TID} = (n_{TID} + 1) * (TT_{UC}) + n_{TID} * S_{UC} \quad \{\text{B.2b}\}$$

where:

$FTF_{n,TID}$  = flat-to-flat of the outermost hexagon formed by  $n$  rings of TID unit cells

= Core Diameter,  $D_{CORE}$

$TT_{UC}$  = tip-to-tip of the unit cell

$S_{UC}$  = side of unit cell

Therefore:

$$n_{TID} = \frac{FTF_{n,TID} - TT_{UC}}{TT_{UC} + S_{UC}} = \frac{D_{CORE} - TT_{UC}}{TT_{UC} + S_{UC}} \quad \{\text{B.3b}\}$$

For a unit cell:

$$S_{UC} = \left(\frac{\sqrt{3}}{3}\right) * FTF_{UC} \quad \{\text{B.4}\}$$

$$TT_{UC} = \left(\frac{2\sqrt{3}}{3}\right) * FTF_{UC}$$

$FTF_{UC}$  = flat-to-flat of the unit cell  
 = pitch of TID unit cell = pitch of subchannel (for a pin core) {\text{B.5}}

For a given core flat-to-flat distance, i.e. core diameter, the number of coolant subchannels can be found by substituting {\text{B.2}}, {\text{B.3}}, {\text{B.4}}, and {\text{B.5}} into {\text{B.1}}:

$$\# \text{ subchannels}_{PIN} = 6 * \left(\frac{D_{CORE}}{\sqrt{3} * pitch}\right)^2 \quad \{\text{B.6a}\}$$

$$\# \text{ subchannels}_{TID} = 3 * \left(\frac{D_{CORE} - \frac{2\sqrt{3}}{3} * pitch}{\sqrt{3} * pitch}\right)^2 + 3 * \left(\frac{D_{CORE} - \frac{2\sqrt{3}}{3} * pitch}{\sqrt{3} * pitch}\right) + 1 \quad \{\text{B.6b}\}$$

In order to account for the slight difference in core size between the infinite hexagonal lattice case and the more heterogeneous whole core case (i.e. with inter-assembly gaps and control assemblies), a factor of 1.05 is introduced to effectively shrink the core diameter. Hence, the actual formula used in the FLOWSPLIT-MATLAB script is:

$$\# \text{ subchannels}_{PIN} = 6 * \left(\frac{D_{CORE}}{1.05 * \sqrt{3} * pitch}\right)^2 \quad \{\text{B.7a}\}$$

$$\#subchannels_{TID} = 3 * \left( \frac{\left[ \frac{D_{CORE}}{1.05} \right] - \frac{2\sqrt{3}}{3} * pitch}{\sqrt{3} * pitch} \right)^2 + 3 * \left( \frac{\left[ \frac{D_{CORE}}{1.05} \right] - \frac{2\sqrt{3}}{3} * pitch}{\sqrt{3} * pitch} \right) + 1 \quad \{B.7b\}$$

Another key parameter that needs calculation is the heat flux per subchannel. For a hexagonal lattice, this parameter is calculated as follows:

For the pin core:

$$\frac{q''}{pin} = \frac{Q}{\pi DH * (\# pins)} \quad \{B.8a\}$$

where:

$$\# pins = \# subchannels * \left( \frac{1 pin}{2 subchannels} \right)$$

where the conversion factor of 2 subchannels per pin applies to an infinite hexagonal matrix

For the TID core:

$$\frac{q''}{UC_{TID}} = \frac{Q}{\pi DH * (\# UC_{TID})} \quad \{B.8b\}$$

where:

$$\# UC_{TID} = \# subchannels$$

where the conversion factor of 1 subchannel per TID unit cell applies to an infinite hexagonal matrix

Hence, for the pin core:

$$\frac{q''}{channel} = \frac{2 * Q}{\pi DH * \# subchannels} \quad \{B.9a\}$$

For the TID core:

$$\frac{q''}{channel} = \frac{Q}{\pi DH * \# subchannels} \quad \{B.9b\}$$

where {B.9a} and {B.9b} are the appropriate forms for the FLOWSPLIT input. Note that for the ICAF core calculations in the ANNULCO2-MATLAB interface, the

methodology described here for calculating the number of subchannels for the pin type fuel was used. ANNULCO2 uses Linear Heat Generation Rate per pin ( $q'/\text{pin}$ ) as an input instead of heat flux per subchannel ( $q''/\text{channel}$ ), as FLOWSPLIT does. Therefore the algorithm to determine these values was different

### B.3.1 FLOWSPLIT-MATLAB Interface MATLAB Files

#### B.3.1.1 *flowsplit\_gen.m*

```
function flowsplit_gen;
clear;
warning off;
%GIVE MATLAB ACCESS TO NECESSARY DIRECTORIES IN THE COMPUTER%
addpath('c:\matlab_sr11\work\GFR\FLOWSPLIT');
%CHANGE DIRECTORIES TO WHERE ALL OF THE FILES FOR THIS PROGRAM ARE
cd('c:\matlab_sr11\work\GFR\FLOWSPLIT');
%NAME THE TEXT FILE THAT THE FLOWSPLIT INPUT DECK IS WRITTEN TO%
input_file_name = strcat('flow_test_input_file');
%NAME THE MATLAB FILE THAT HOLDS THE FLOWSPLIT INPUT VARIABLES IN MATLAB SPACE%
var_file_name = strcat('flow_var.mat');

loopindex = 0;%INITIALIZE LOOP INDEX

min_diam = 5;%DEFINE LOWER BOUND OF ROD DIAMETER RANGE (mm)
max_diam = 15;%DEFINE UPPER BOUND OF ROD DIAMETER RANGE (mm)
diam_steps =21;%DEFINE NUMBER OF STEPS IN DIAMETER RANGE

%DEFINE DIAMETER RANGE AS AN ARRAY OF diam_steps EQUALLY SPACED STEPS BETWEEN min_diam AND max_diam
diam_range = linspace(min_diam,max_diam,diam_steps);

%Define the type of fuel that we are using
%If flow5.ish = 1, TID unit cell
%If flow5.ish = 2, cylindrical pin
%If flow5.ish = 3, annular pin, without internal cooling
flow5.ish=1;

%Define variable wire_wrap_flag.
%If wire1.flag=1, wire wrap is on.
%If wire1.flag=0, no wire wrap.
wire1.flag=0;
%the below if statement is a check to make sure that wire wrap is not accidentally applied to TID fuel
if flow5.ish==1;
```

```

    wire1.flag=0;
end

%Define the height to diameter ratio of the wire wrap
wire3.hdratio=29;

%Define a Radial Peaking Factor
%includes both assembly-to-assembly and intra-assembly
flow11.peakfctr=1.2;

%Define the BeO volume fraction of the fuel pellet
beo_frac=0.38;

core_vol = 28.09; % m^3
core_power = 2400; % MW
core_diam = 4.6; % flat to flat of hexagonal core
core_height = core_vol/((sqrt(3)/2)*core_diam^2); % m
flow12.node_height=core_height/20;
flow1.elc = 0.0766*20+2.1;

%BEGIN A for LOOP THAT CYCLES BETWEEN THIS LINE, AND THE FINAL end STATEMENT diam_steps TIMES
%EACH TIME IT, CYCLES k INCREASES IN VALUE BY 1
for k = 1:diam_steps;
    %min_liq_fraction = 12.985;%DEFINE THE LOWER BOUND OF H/HM RATIO
    %max_liq_fraction = 12.985;%DEFINE THE UPPER BOUND OF H/HM RATIO
    min_pdratio = 1.1;
    max_pdratio = 1.9;
    pitch_steps = 15;%DEFINE THE NUMBER OF PITCHES TO BE EVALUATED FOR EACH ROD DIAMETER
    %DEFINE THE ARRAY OF PITCHES FOR THE DIAMETER CORRESPONDING TO THE kTH DIAMETER IN diam_range
    %(diam_range(k))
    %pdratio_range = hm_to_pd(fraction_range, sq_or_tri);
    pdratio_range = linspace(min_pdratio, max_pdratio, pitch_steps);
    pitch_range = pdratio_range.*diam_range(k);
    %BEGIN A for LOOP THAT CYCLES BETWEEN THIS LINE AND THE SECOND TO LAST end STATEMENT pitch_steps TIMES
    %EACH TIME IT CYCLES, l INCREASES IN VALUE BY 1
    for l = 1:pitch_steps;
        %CREATE THE GEOMETRICALLY DEPENDENT VARIABLES NECESSARY FOR THE FLOWSPLIT INPUT DECK

```

```

    [flow2.np flow3.d1 flow6.a1 flow7.ph1 flow11.qppm vc wire2.p_d flow21.rv vf flow20.diameter] =
rod_channel_data(pitch_range(1), diam_range(k), core_power, core_diam, core_height, wire1.flag,
beo_frac, flow5.ish);
    loopindex = loopindex+1
    count1 = 0;
    clear count;
    max_count1 = 15;
    z = 1;
    conv_data(1)=0;
    conv_err=1;
    output(loopindex,2:3) = [pitch_range(1) diam_range(k)];
    count1 = count1 + 1;
    output_que =
char('flow1','flow2','flow3','flow4','flow5','flow6','flow7','flow8','flow9','flow10','flow11','flow12','fl
ow13','wire1','wire2','wire3','flow14','flow15','flow16','flow17','flow18','flow19','flow20','flow21','flow
22','flow23','flow24','flow25','flow26');
    out_que = cellstr(output_que);
    save(var_file_name);
    count = 0;
    max_count = 2;
    save count count max_count;
    flowsplit_run(input_file_name, var_file_name);
    load flowsplit_output_data
    load count;
    output(loopindex,1) = pressure_drop;
    output(loopindex,2) = max_fuel_temp;
    output(loopindex,3) = max_clad_temp;
    output(loopindex,4) = vc;
    output(loopindex,5) = vf;
    output(loopindex,6) = del_TF_bar;
    if count1 == max_count1 | count == max_count
        output(loopindex,1) = NaN;
        output(loopindex,2) = NaN;
        output(loopindex,3) = NaN;
        output(loopindex,4) = NaN;
        output(loopindex,5) = NaN;
        output(loopindex,6) = NaN;
    else
    end

```



```

    end
end
m=1;
for i=1:diam_steps
    for j=1:pitch_steps
        pressure_drop(i,j)=output(m,1);
        max_fuel_temp(i,j)=output(m,2);
        max_clad_temp(i,j)=output(m,3);
        vc(i,j)=output(m,4);
        vf(i,j)=output(m,5);
        del_TF_bar(i,j)=output(m,6);
        m=m+1;
    end
end
%SAVES ALL OF THE VARIABLES IN THE WORKSPACE TO THE OUTPUT FILE
save(var_file_name);

```

### *B.3.1.2 rod\_channel\_data.m*

```

function [np,d1,a1,ph1,qppm,vc,p_d,rv,vf,rea] = rod_channel_data(pitch, diameter, core_power, core_diam,
core_height,wireflag,beo_frac,ish);

%THIS subroutine generates the variable geometry inputs for FLOWSPLIT

p_d = pitch/diameter;

%change units of clad outer diameter and pitch from mm to m
diameter_mm=diameter/1000;
pitch_mm=pitch/1000;

if ish==1; %calculate TID parameters
    np = 3*(round(((core_diam/1.05)*1000-
((2*sqrt(3)/3)*pitch))/(pitch*(sqrt(3)))))^2+3*(round(((core_diam/1.05)*1000-
((2*sqrt(3)/3)*pitch))/(pitch*(sqrt(3)))))+1;
    qppm = core_power*1000000/(np*pi*core_height*(diameter_mm));
    vc = (pi/2)/((sqrt(3)*(p_d^2)));
elseif ish>=2; %calculate pin-type core parameters

```

```

        np = 6*(round(((core_diam/1.05)*1000)/(pitch*(sqrt(3))))^2;
        qppm = 2*core_power*1000000/(np*pi*core_height*(diameter_mm));
        vc = (sqrt(3)*(p_d^2)-(pi/2))/((sqrt(3)*(p_d^2)));
end

ds = (pitch-diameter)/1000; %units = m

%the 4 below quantities are in units of m or m^2

if ish==1;%calculate TID parameters
    a1_nowire=(pi/4)*(diameter_mm)^2;
    ph1_nowire=pi*diameter_mm;
    d1_nowire=diameter_mm;
    rea=sqrt(sqrt(3)/(2*pi))*pitch_mm; %in FLOWSPLIT, REA=equivalent radius of fuel annulus of TID unit cell
for TID fuel
elseif ish>=2;
    a1_nowire = (((sqrt(3)/4)*(pitch^2))-((pi/8)*diameter^2))/(1000*1000);
    ph1_nowire = 0.5*pi*diameter/1000;
    d1_nowire = (((2*sqrt(3)*(pitch^2))-pi*diameter^2)/(pi*diameter))/1000;
    rea=diameter_mm; %in FLOWSPLIT, REA=cladding outer diameter of pin type fuel
end

%calculate parameters without wire wrap
if wireflag==0;
    a1=a1_nowire;
    ph1=ph1_nowire;
    d1=d1_nowire;
%calculate parameters for rods with wire wrap
elseif wireflag==1;
    a1 = a1_nowire-(pi/8)*(ds^2);
    ph1 = ph1_nowire;
    d1 = (4*a1)/(ph1_nowire+((pi/2)*ds));
end

%calculate fuel pellet dimensions

if diameter_mm < 7.747E-03;
    cladth = 0.508E-03;

```

```

        deff = 6.35E-05;
else
    cladth = 0.508E-03 + (diameter_mm - 7.747E-03)*0.0362;
    deff = 6.35E-05 + (diameter_mm - 7.747E-03)*0.0108;
end

%for TID fuel
rfi= (diameter_mm+2*cladth+2*deff)/2;

%for pin type fuel
rfo=(diameter_mm-2*cladth-2*deff)/2; %units are mm
rv=sqrt(beo_frac)*rfo; %units are mm

if ish==1;
    vf=(1-beo_frac)*(((sqrt(3)/2)*(pitch_mm^2)-(pi*rfi^2))/((sqrt(3)/2)*(pitch_mm^2)));
elseif ish>=2;
    vf=(1-beo_frac)*((pi*rfo^2)/(((sqrt(3))/2)*pitch_mm^2));
end

```

### B.3.1.3 *flowsplit\_run.m*

```
function a = flowsplit_run(input_file_name,var_file_name);

load(var_file_name);
generate_input_file_flowsplit(input_file_name,var_file_name);
execute_flowsplit(input_file_name,var_file_name);
```

### B.3.1.4 *generate\_input\_file\_flowsplit.m*

```
%generate_input_file.m

function generate_input_file_flowsplit(input_file_name,var_file_name)

load(var_file_name); %get the variables into the space
%the functions will be called
fid = fopen(input_file_name,'w');
for i = 1:length(out_que) %one cycle required per entry in the output que
    %every entry in the output que corresponds to a card in the input file
    switch char(out_que(i))
        case 'flow1'
            gen_flow1(fid,flow1);
        case 'flow2'
            gen_flow2(fid,flow2);
        case 'flow3'
            gen_flow3(fid,flow3);
        case 'flow4'
            gen_flow4(fid);
        case 'flow5'
            gen_flow5(fid,flow5);
        case 'flow6'
            gen_flow6(fid,flow6);
        case 'flow7'
            gen_flow7(fid,flow7);
        case 'flow8'
            gen_flow8(fid);
        case 'flow9'
            gen_flow9(fid);
        case 'flow10'
            gen_flow10(fid);
        case 'flow11'
            gen_flow11(fid,flow11);
        case 'flow12'
            gen_flow12(fid,flow12);
        case 'flow13'
            gen_flow13(fid);
        case 'wire1'
            gen_wire1(fid,wire1);
        case 'wire2'
            gen_wire2(fid,wire2);
        case 'wire3'
            gen_wire3(fid,wire3);
        case 'flow14'
```

```

        gen_flow14(fid);
    case 'flow15'
        gen_flow15(fid);
    case 'flow16'
        gen_flow16(fid);
    case 'flow17'
        gen_flow17(fid);
    case 'flow18'
        gen_flow18(fid);
    case 'flow19'
        gen_flow19(fid);
    case 'flow20'
        gen_flow20(fid,flow20);
    case 'flow21'
        gen_flow21(fid,flow21);
    case 'flow22'
        gen_flow22(fid);
    case 'flow23'
        gen_flow23(fid);
    case 'flow24'
        gen_flow24(fid);
    case 'flow25'
        gen_flow25(fid);
    case 'flow26'
        gen_flow26(fid);
    end
end

st = fclose(fid);

```

### B.3.1.5 *gen\_flow1.m*

```

function flow1(fid,flow1)

entry = strcat(' === 2400MWth PIN CORE S-CO2 coolant ===');
count = fprintf(fid,'%s \n',entry);
entry = strcat('          EPS          ELT          COSFI');
count = fprintf(fid,'%s \n',entry);

elt = sprintf('%12.5d',flow1.elt);

entry = strcat(' 0.10000E-02 ',elt,' 0.10000E+01');
count = fprintf(fid,'%s \n',entry);

```

### B.3.1.6 *gen\_flow2.m*

```

function flow2(fid,flow2)

entry = strcat('          N1          NZ          ICOOL          NP(I),I=1,N1(av,hot)');
count = fprintf(fid,'%s \n',entry);

```

```

np1dum = flow2.np - 372;
np2dum = 372;

np1 = sprintf('%7i',np1dum);
np2 = sprintf('%7i',np2dum);

entry = strcat('      2      30      1 ',np1,np2,'      0');

count = fprintf(fid,'%s \n',entry);

```

### *B.3.1.7 gen\_flow3.m*

```

function flow3(fid,flow3)

entry = strcat(' D1(I),I=1,N1 - HYDRAULIC DIAMETERS (m) ');
count = fprintf(fid,'%s \n',entry);

d1 = sprintf('%12.5d',flow3.d1);

entry = strcat(d1,d1);

count = fprintf(fid,'%s \n',entry);

```

### *B.3.1.8 gen\_flow4.m*

```

function flow4(fid,flow4)

entry = strcat(' ICS(I),I=1,N1 - CHANNEL STATUS: 0=smooth');
count = fprintf(fid,'%s \n',entry);

entry = strcat('      0      0      0');
count = fprintf(fid,'%s \n',entry);

```

### *B.3.1.9 gen\_flow5.m*

```

function flow5(fid,flow5)

entry = strcat(' ISH(I),I=1,N1 - CHANNEL SHAPE: 1=round');
count = fprintf(fid,'%s \n',entry);

ishdum=flow5.ish;

ish=sprintf('%5i',ishdum);

entry = strcat(ish,ish,ish);
count = fprintf(fid,'%s \n',entry);

```

### *B.3.1.10 gen\_flow6.m*

```

unction flow6(fid,flow6)

```

```
entry = strcat(' A1(I),I=1,N1 - FLOW AREAS (m^2) ');
count = fprintf(fid,'%s \n',entry);
```

```
a1 = sprintf('%12.5d',flow6.a1);
```

```
entry = strcat(a1,a1);
count = fprintf(fid,'%s \n',entry);
```

### *B.3.1.11 gen\_flow7.m*

```
function flow7(fid,flow7)
```

```
entry = strcat(' PH1(I),I=1,N1 - HEATED PERIMETER (m) ');
count = fprintf(fid,'%s \n',entry);
```

```
ph1 = sprintf('%12.5d',flow7.ph1);
```

```
entry = strcat(ph1,ph1);
count = fprintf(fid,'%s \n',entry);
```

### *B.3.1.12 gen\_flow8.m*

```
function flow8(fid,flow8)
```

```
entry = strcat(' EKI(I),I=1,N1 - INLET FORM LOSSES ');
count = fprintf(fid,'%s \n',entry);
```

```
entry = strcat(' 0.10000E+00 0.10000E+00 1.00000E+01 ');
count = fprintf(fid,'%s \n',entry);
```

### *B.3.1.13 gen\_flow9.m*

```
function flow9(fid,flow9)
```

```
entry = strcat(' EKO(I),I=1,N1 - OUTLET FORM LOSSES ');
count = fprintf(fid,'%s \n',entry);
```

```
entry = strcat(' 0.10000E+01 0.10000E+01 0.10000E+01 ');
count = fprintf(fid,'%s \n',entry);
```

### *B.3.1.14 gen\_flow10.m*

```
function flow10(fid,flow10)
```

```
entry = strcat(' DEL(I),I=1,N1 - SURFACE ROUGHNESS ');
count = fprintf(fid,'%s \n',entry);
```

```
entry = strcat(' 0.10000E-04 0.10000E-04 0.00000E-04 ');
count = fprintf(fid,'%s \n',entry);
```

### B.3.1.15 gen\_flow11.m

```
function flow11(fid,flow11)

entry = strcat(' QPPM(I),I=1,N1 - AVERAGE HEAT FLUX (W/m^2) ');
count = fprintf(fid,'%s \n',entry);

qppm1 = sprintf('%12.5d',flow11.qppm);

qppm_peak = flow11.peakfctr*flow11.qppm;
qppm2 = sprintf('%12.5d',qppm_peak);

entry = strcat(qppm1,qppm2);
count = fprintf(fid,'%s \n',entry);
```

### B.3.1.16 gen\_flow12.m

```
function flow12(fid,flow12)

bot_node = 0.22;
top_node = 0.2;

entry = strcat(' DZ(J),J=1,NZ - NODE LENGTH (m) ');
count = fprintf(fid,'%s \n',entry);

dz_bot=sprintf('%8.4f',bot_node);
dz=sprintf('%8.4f',flow12.node_height);
dz_top=sprintf('%8.4f',top_node);

entry = strcat(dz_bot,dz_bot,dz_bot,dz_bot,dz_bot,dz,dz,dz,dz,dz);
count = fprintf(fid,'%s \n',entry);

entry = strcat(dz,dz,dz,dz,dz,dz,dz,dz,dz,dz,dz);
count = fprintf(fid,'%s \n',entry);

entry = strcat(dz,dz,dz,dz,dz,dz_top,dz_top,dz_top,dz_top,dz_top);
count = fprintf(fid,'%s \n',entry);
```

### B.3.1.17 gen\_flow13.m

```
function flow13(fid,flow13)

entry = strcat(' XSI(J),J=1,NZ-AXIAL DISTRIBUTION OF HEAT FLUX loc/av');
count = fprintf(fid,'%s \n',entry);

entry = strcat(' 0.000 0.000 0.000 0.000 0.000 0.517 0.659 0.791
0.911 1.017');
count = fprintf(fid,'%s \n',entry);

entry = strcat(' 1.108 1.183 1.240 1.278 1.298 1.298 1.278 1.240
1.183 1.108');
count = fprintf(fid,'%s \n',entry);
```



```

entry = strcat(' 1.017 0.911 0.791 0.659 0.517 0.000 0.000 0.000
0.000 0.000');
count = fprintf(fid,'%s \n',entry);

```

### *B.3.1.18 gen\_flow14.m*

```

function flow14(fid,flow14)

entry = strcat(' NGRID IGRID ');
count = fprintf(fid,'%s \n',entry);

entry = strcat(' 0 0');
count = fprintf(fid,'%s \n',entry);

```

### *B.3.1.19 gen\_flow15.m*

```

function flow15(fid,flow15)

entry = strcat(' XGRID(J) ');
count = fprintf(fid,'%s \n',entry);

entry = strcat(' 1.100 1.595 2.090 2.483');
count = fprintf(fid,'%s \n',entry);

```

### *B.3.1.20 gen\_flow16.m*

```

function flow16(fid,flow16)

entry = strcat(' XSIGR(J) ');
count = fprintf(fid,'%s \n',entry);

entry = strcat(' 4.540 0.530 0.530 0.180');
count = fprintf(fid,'%s \n',entry);

```

### *B.3.1.21 gen\_flow17.m*

```

function flow17(fid,flow17)

entry = strcat(' TIN (K) PIN(Pa) EMT (kg/s) ');
count = fprintf(fid,'%s \n',entry);

entry = strcat(' 0.75865E+03 0.19950E+08 0.11708E+05');
count = fprintf(fid,'%s \n',entry);

```

### *B.3.1.22 gen\_flow18.m*

```

function flow18(fid,flow18)

entry = strcat(' CLADTH(I), I=1,N1 - CLADDING THICKNESS (m) ');

```

```

count = fprintf(fid, '%s \n', entry);

entry = strcat(' 0.70000E-03 0.70000E-03 0.00000E-03');
count = fprintf(fid, '%s \n', entry);

```

### *B.3.1.23 gen\_flow19.m*

```

function flow19(fid, flow19)

entry = strcat(' KCLAD-cladding thermal conductivity (W/m-K)');
count = fprintf(fid, '%s \n', entry);

entry = strcat(' 0.23000D+02');
count = fprintf(fid, '%s \n', entry);

```

### *B.3.1.24 gen\_flow20.m*

```

function flow20(fid, flow20)

entry = strcat(' REA(I), I=1, N1-RADIUS OF EQUIVALENT ANNULUS OF FUEL (m)');
count = fprintf(fid, '%s \n', entry);

real = sprintf('%12.5d', flow20.diameter);

entry = strcat(real, real);
count = fprintf(fid, '%s \n', entry);

```

### *B.3.1.25 gen\_flow21.m*

```

function flow21(fid, flow21)

entry = strcat(' RV - INNER RADIUS OF ANNULAR FUEL PELLET (m)');
count = fprintf(fid, '%s \n', entry);

rv = sprintf('%12.5e', flow21.rv);

entry = strcat(rv);
count = fprintf(fid, '%s \n', entry);

```

### *B.3.1.26 gen\_flow22.m*

```

function flow22(fid, flow22)

entry = strcat(' KGAP - FUEL-CLAD INTERFACE CONDUCTANCE (W/M^2 K)');
count = fprintf(fid, '%s \n', entry);

entry = strcat(' 0.05700D+05');
count = fprintf(fid, '%s \n', entry);

```

### B.3.1.27 *gen\_flow23.m*

```
function flow23(fid,flow23)

entry = strcat(' HEAT TRANSFER FLAG 0=GNIELINSKI 1=DITTUS-BOELTER');
count = fprintf(fid,'%s \n',entry);

entry = strcat(' 0');
count = fprintf(fid,'%s \n',entry);
```

### B.3.1.28 *gen\_flow24.m*

```
function flow24(fid,flow24)

entry = strcat(' AUGMENT(I) HEAT TRNSFR AUGMENTATION FLAG 0=NO 1=YES');
count = fprintf(fid,'%s \n',entry);

entry = strcat(' 0 0');
count = fprintf(fid,'%s \n',entry);
```

### B.3.1.29 *gen\_flow25.m*

```
function flow25(fid,flow25)

entry = strcat(' NUSSMULT(J), HEAT TRANSFER MULT. IN AUGMENTED CHANNELS');
count = fprintf(fid,'%s \n',entry);

entry = strcat(' 1.0 1.0 1.0 1.0 1.0 1.0 1.0 1.0 1.0 1.0');
count = fprintf(fid,'%s \n',entry);

entry = strcat(' 1.0 1.0 1.0 1.0 1.0 1.0 1.0 1.0 1.0 1.0');
count = fprintf(fid,'%s \n',entry);

entry = strcat(' 1.0 1.0 1.0 1.0 1.0 1.0 1.0 1.0 1.0 1.0');
count = fprintf(fid,'%s \n',entry);
```

### B.3.1.30 *gen\_flow26.m*

```
function flow26(fid,flow26)

entry = strcat(' FMULT(J), FRICTION FACTOR MULTIPLIER IN AUGMENTED CHAN');
count = fprintf(fid,'%s \n',entry);

entry = strcat(' 1.0 1.0 1.0 1.0 1.0 1.0 1.0 1.0 1.0 1.0');
count = fprintf(fid,'%s \n',entry);

entry = strcat(' 1.0 1.0 1.0 1.0 1.0 1.0 1.0 1.0 1.0 1.0');
count = fprintf(fid,'%s \n',entry);

entry = strcat(' 1.0 1.0 1.0 1.0 1.0 1.0 1.0 1.0 1.0 1.0');
count = fprintf(fid,'%s \n',entry);
```

### *B.3.1.31 gen\_wire1.m*

```
function wire1(fid,wire1)

entry = strcat(' WIREFLAG, 0=no wire, 1=wire wrap');
count = fprintf(fid,'%s \n',entry);

wf = sprintf('%7i',wire1.flag);

entry = strcat(wf,wf);

count = fprintf(fid,'%s \n',entry);
```

### *B.3.1.32 gen\_wire2.m*

```
function wire2(fid,wire2)

entry = strcat(' PDRATIO(I)');
count = fprintf(fid,'%s \n',entry);

pdratio=sprintf('%7.3f',wire2.p_d);
entry = strcat(pdratio,pdratio);
count = fprintf(fid,'%s \n',entry);
```

### *B.3.1.33 gen\_wire3.m*

```
function wire3(fid,wire3)

entry = strcat(' HDRATIO(I)');
count = fprintf(fid,'%s \n',entry);

hdratio1=sprintf('%7.3f',wire3.hdratio);

entry = strcat(hdratio1,hdratio1);
count = fprintf(fid,'%s \n',entry);
```

### *B.3.1.34 execute\_flowsplit.m*

```
function execute_flowsplit(inputfile,var_file)

outdirectory = pwd;

current_dir = pwd;
%send the input file to be processed
copyfile(inputfile,'c:\matlab_SR11\bin\FLOWSPLIT\flowsplit.dat');
%transfer control to the directory where the FLOWSPLIT executable is
cd('c:\matlab_SR11\bin\FLOWSPLIT');
addpath('c:\matlab_SR11\bin\FLOWSPLIT');
%execute the system call
call_flowsplit;
%copy the useful files
```

```

copyfile('out2',strcat(outdirectory,'\','out2'));
%delete the files that are no longer useful
delete('out2');
cd(current_dir)
parse_output_flowsplit(var_file);

```

### ***B.3.1.35 parse\_output\_flowsplit.m***

```

function parse_output_flowsplit(var_file_name);

load(var_file_name);

%LOAD THE SPECIALLY FORMATTED OUTPUT FILE
load out2;

max_clad_temp = out2(4);
pressure_drop = out2(8);
max_fuel_temp = out2(10);
del_TF_bar = out2(12);

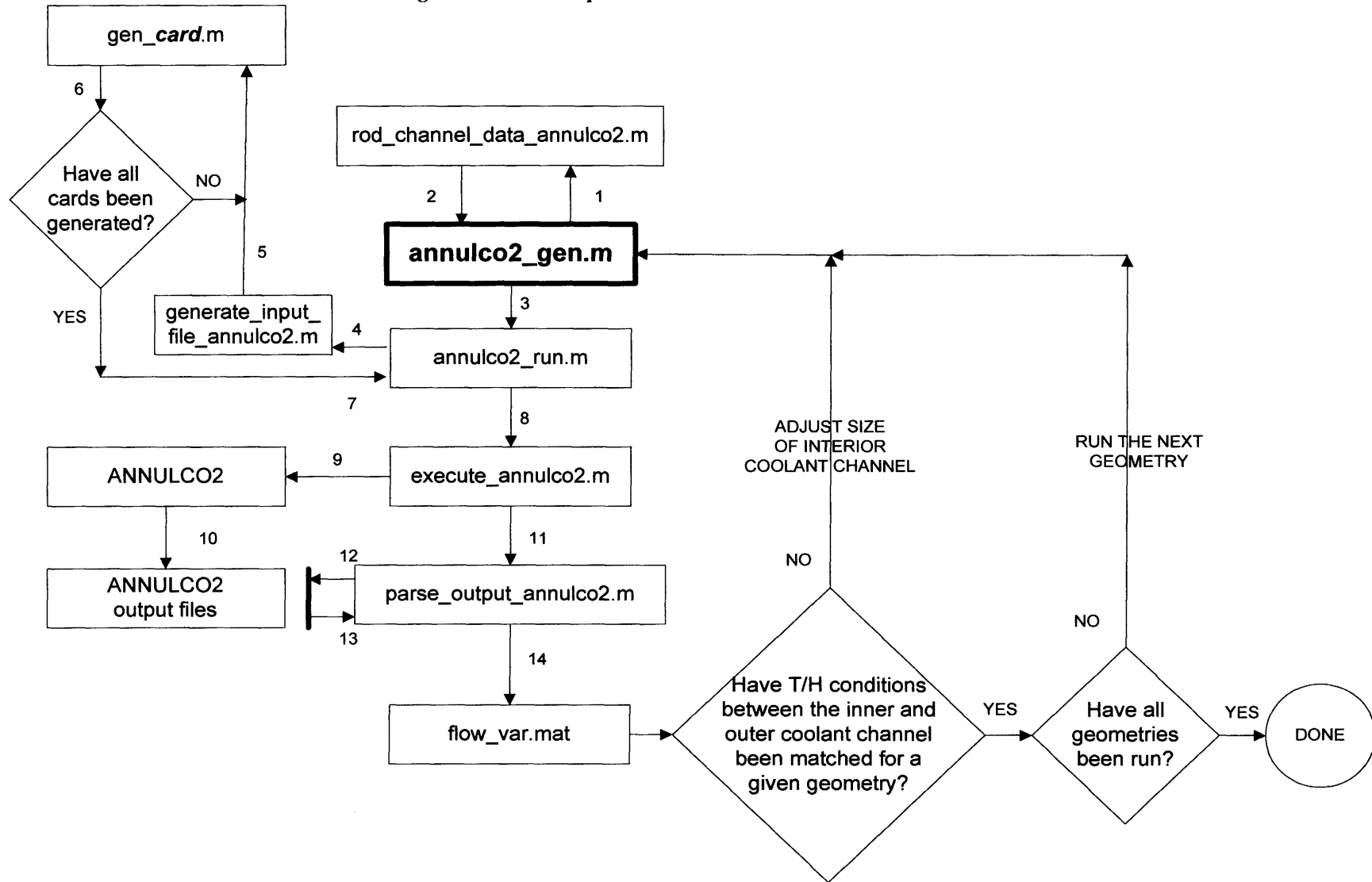
clear out2;
save flowsplit_output_data; %save data to a file so it can be re-loaded

```

## **B.4 ANNULCO2-MATLAB Interface**

The ANNULCO2-MATLAB interface is very similar to the FLOWSPLIT-MATLAB interface, with the exception of a feedback loop added to adjust the dimensions of the interior cooling channel in order to match the thermal hydraulic conditions of the inner and outer coolant channels (discussed in Section B.1). Consequently, the only two programs that are significantly different from those used in the FLOWSPLIT-MATLAB interface, *annulco2\_gen.m* and *rod\_channel\_data\_annulco2.m*, will be presented in this section. All other program descriptions can be translated from the FLOWSPLIT-MATLAB interface to the ANNULCO2-MATLAB interface by simply changing the name from *flowsplit\_filename.m* to *annulco2\_filename.m*. The base program, *annulco2\_gen.m*, is very similar to *flowsplit\_gen.m*, with the exception of the aforementioned feedback loop. This program communicates with other programs in order to achieve the goals described in Section B.1. Figure B.3 shows a flowchart which outlines the sequence of execution each subprogram. Combining Figure B.3 and Table B.1 (modified appropriately for use with ANNULCO2) with the programs presented in Section B.3.1 (modified appropriately for use with ANNULCO2) and Section B.4.1 and some knowledge of MATLAB and ANNULCO2 should give complete transparency to anyone regarding the ANNULCO2-MATLAB interface.

Figure B.3: Roadmap for FLOWSPLIT-ANNULCO2 Interface



## B.4.1 ANNULCO2-MATLAB Interface MATLAB Files

### B.4.1.1 *annulco2\_gen.m*

```
function annulco2_gen;
clear;
warning off;
%GIVE MATLAB ACCESS TO NECESSARY DIRECTORIES IN THE COMPUTER%
addpath('c:\matlab_sr11\work\GFR\ANNULCO2');
%CHANGE DIRECTORIES TO WHERE ALL OF THE FILES FOR THIS PROGRAM ARE
cd('c:\matlab_sr11\work\GFR\ANNULCO2');
%NAME THE TEXT FILE THAT THE ANNULCO2 INPUT DECK IS WRITTEN TO%
input_file_name = strcat('flow_test_input_file');
%NAME THE MATLAB FILE THAT HOLDS THE ANNULCO2 INPUT/OUTPUT VARIABLES IN
MATLAB SPACE%
var_file_name = strcat('flow_var.mat');

loopindex = 0;%INITIALIZE LOOP INDEX

min_diam = 15;%DEFINE LOWER BOUND OF ROD DIAMETER RANGE (mm)
max_diam = 15;%DEFINE UPPER BOUND OF ROD DIAMETER RANGE (mm)
diam_steps = 1;%DEFINE NUMBER OF STEPS IN DIAMETER RANGE

%DEFINE DIAMETER RANGE AS AN ARRAY OF diam_steps EQUALLY SPACED STEPS
BETWEEN min_diam AND max_diam
diam_range = linspace(min_diam,max_diam,diam_steps);

%Define variable wire_wrap_flag.
%If wire1.flag=1, wire wrap is on.
%If wire1.flag=0, no wire wrap.
wire1.flag=1;

%Define the height to diameter ratio of the wire wrap
wire3.hdratio=29;

%Define a Radial Peaking Factor
%includes both assembly-to-assembly and intra-assembly
annul25.radpeakfctr=1.2;

%Define the BeO volume fraction of the fuel pellet
beo_frac=0.38;

%Define the Fuel Burnup for the fuel conductivity calculation
annul22.bur = 0.0;

%Define the fission gas release percent for VIPAC fuel
annul22.fgr=11.0;

%Define error or convergence tolerance
tolerance=5;

core_vol = 28.09; % m^3
```

```

core_power = 2400; % MW
core_diam = 4.6; % flat to flat of hexagonal core
core_height = core_vol/((sqrt(3)/2)*core_diam^2); % m
tot_core_flow = 0.11708E+05; %kg/sec
annul13.node_height=core_height/20;
annul1.elc = 0.0766*20+2.1;

%BEGIN A for LOOP THAT CYCLES BETWEEN THIS LINE, AND THE FINAL end
STATEMENT diam_steps TIMES
%EACH TIME IT, CYCLES k INCREASES IN VALUE BY 1
for k = 1:diam_steps;
    %min_liq_fraction = 12.985;%DEFINE THE LOWER BOUND OF H/HM RATIO
    %max_liq_fraction = 12.985;%DEFINE THE UPPER BOUND OF H/HM RATIO
    min_pdratio = 1.1;
    max_pdratio = 1.1;
    pitch_steps = 1;%DEFINE THE NUMBER OF PITCHES TO BE EVALUATED FOR EACH
ROD DIAMETER
    %DEFINE THE ARRAY OF PITCHES FOR THE DIAMETER CORRESPONDING TO THE KTH
DIAMETER IN diam_range (diam_range(k))
    pdratio_range = linspace(min_pdratio, max_pdratio, pitch_steps);
    pitch_range = pdratio_range.*diam_range(k);
    %BEGIN A for LOOP THAT CYCLES BETWEEN THIS LINE AND THE SECOND TO LAST
end STATEMENT pitch_steps TIMES
    %EACH TIME IT CYCLES, l INCREASES IN VALUE BY 1
    for l = 1:pitch_steps;
        %Define the radius of the inner coolant channel
        rv_fac=0.5; %initialize the rv factor: rv_fac=rv/rco;
        error=100; %initialize error
        loopindex = loopindex+1
        count1 = 0;
        while (abs(error)>tolerance | error>0); %checks if T/H are met. If
not, iterate inner channel
            %dimension until T/H conditions are met. If so, store output
            %data
            rv = (diam_range(k)/1000)*(rv_fac/2);
            [annul3.dlo annul3.dli annul6.a1o annul6.a1i annul7.ph1o
annul7.ph1i annul25.avgqp vc wire2.p_d annul20.emt cladth deff vf] =
rod_channel_data_annulco2(pitch_range(l), diam_range(k), core_power,
core_diam, core_height,wire1.flag, beo_frac, rv, tot_core_flow, rv_fac);
            annul21.dco = diam_range(k)/1000;
            annul21.dci = annul21.dco-2*cladth;
            annul21.dfo = annul21.dci - 2*deff;
            annul22.dcii = 2*rv;
            annul22.dcoi = annul22.dcii+2*cladth;
            annul21.dfi = annul22.dcoi+2*deff;
            annul21.wu = 1.0000-beo_frac;
            clear count;
            max_count1 = 15;
            z = 1;
            conv_data(1)=0;
            conv_err=1;
            output(loopindex,2:3) = [pitch_range(l) diam_range(k)];
            count1 = count1 + 1;
            output_que =
char('annul1','annul2','annul3','annul4','annul5','annul6','annul7','annul
8','annul9','annul10','annul11','annul12','annul13','annul14','wire1','wir

```



```

e2', 'wire3', 'annul15', 'annul16', 'annul17', 'annul18', 'annul19', 'annul20', 'a
nnul21', 'annul22', 'annul23', 'annul24', 'annul25', 'annul26');
    out_que = cellstr(output_que);
    save(var_file_name);
    count = 0;
    max_count = 2;
    save count count max_count;
    annulco2_run(input_file_name, var_file_name);
    load annulco2_output_data
    load count;
    error=max_coolant_temp_inner-max_coolant_temp_outer
    if (abs(error)<=tolerance & error<=0); %if error is less than
tolerance
        output(loopindex,1)=max_coolant_temp_inner;
        output(loopindex,2)=max_coolant_temp_outer;
        output(loopindex,3)=max_fuel_temp;
        output(loopindex,4)=max_clad_temp_inner;
        output(loopindex,5)=max_clad_temp_outer;
        output(loopindex,6)=max_clad_temp;
        output(loopindex,7)=pressure_drop;
        output(loopindex,8)=rv;
        output(loopindex,9)=error;
        output(loopindex,10)=rv_fac;
        output(loopindex,11)=count1;
        output(loopindex,12)=vc;
        output(loopindex,13)=vf;
    else %if difference in temperatures between inner and outer
channels is not within tolerance, adjust the rv factor appropriately
        if (abs(error)>tolerance)
            if error>0;
                rv_fac=rv_fac+((abs(error))/500);
            else
                rv_fac=rv_fac-((abs(error))/500);
            end
        else
            if error>0;
                rv_fac=rv_fac+0.01;
            else
                rv_fac=rv_fac-0.01;
            end
        end
    end
    end
    if count1 == max_count1 | count == max_count
        output(loopindex,1) = NaN;
        output(loopindex,2) = NaN;
        output(loopindex,3) = NaN;
        output(loopindex,4) = NaN;
        output(loopindex,5) = NaN;
        output(loopindex,6) = NaN;
        output(loopindex,7) = NaN;
        output(loopindex,8) = NaN;
        output(loopindex,9) = NaN;
        output(loopindex,10) = NaN;
        output(loopindex,11) = NaN;
        output(loopindex,12) = NaN;
        output(loopindex,13) = NaN;
    else

```

```

        end
    end
end
end
m=1;
for i=1:diam_steps
    for j=1:pitch_steps
        pressure_drop(i,j)=output(m,7);
        max_fuel_temp(i,j)=output(m,3);
        max_clad_temp(i,j)=output(m,6);
        rv_fac(i,j)=output(m,10);
        vc(i,j)=output(m,12);
        vf(i,j)=output(m,13);
        m=m+1;
    end
end
end
%SAVES ALL OF THE VARIABLES IN THE WORKSPACE TO THE OUTPUT FILE
save(var_file_name);

```

#### *B.4.1.2 rod\_channel\_data\_annulco2.m*

```

function [dlo,dli,a1o,a1i,ph1o,ph1i,avgqp,vc,p_d,pin_flow,cladth,deff,vf]
= rod_channel_data_annulco2(pitch, diameter, core_power, core_diam,
core_height,wireflag,beo_frac,rv,tot_core_flow,rv_fac);

```

%THIS subroutine generates the variable geometry inputs for ANNULCO2

```

p_d = pitch/diameter;
np = 6*(round(((core_diam/1.05)*1000)/(pitch*(sqrt(3)))))^2; %number of
subchannels for an infinite triangular lattice
avgqp = 2*core_power*1000000/(np*core_height);
pin_flow = 2*(tot_core_flow/np); %assumes infinite triangular lattice
ds = (pitch-diameter)/1000; %units = m

%the 6 below quantities are in units of m or m^2
a1o_nowire = (((sqrt(3)/2)*(pitch^2))-((pi/4)*diameter^2))/(1000*1000);
%area of outer flow channel
ph1o_nowire = pi*diameter/1000; %heated perimeter of outer flow channel
d1o_nowire = (((2*sqrt(3)*(pitch^2))-(pi*diameter^2))/(pi*diameter))/1000;
%hydraulic diameter of outer flow channel

a1i = pi*rv^2;
ph1i = pi*rv*2;
d1i = 2*rv;

%calculate parameters for rods without wire wrap
if wireflag==0;
    a1o=a1o_nowire;
    ph1o=ph1o_nowire;
    d1o=d1o_nowire;
%calculate parameters for rods with wire wrap
elseif wireflag==1;
    a1o = a1o_nowire-(pi/8)*(ds^2);
    ph1o = ph1o_nowire;

```

```

    dlo = (4*a1o)/(ph1o_nowire+((pi/2)*ds));
end

%calculate fuel pellet dimensions
%change units of clad outer diameter from m to mm
diameter_mm=diameter/1000;
pitch_mm=pitch/1000;

if diameter_mm < 7.747E-03;
    cladth = 0.508E-03; %clad thickness
    deff = 6.35E-05; %gap thickness
else
    cladth = 0.508E-03 + (diameter_mm - 7.747E-03)*0.0362; %clad
thickness
    deff = 6.35E-05 + (diameter_mm - 7.747E-03)*0.0108; %gap
thickness
end

rfi = (rv_fac*diameter_mm+2*cladth+2*deff)/2;
rfo = (diameter_mm-2*cladth - 2*deff)/2;

vc = (1-beo_frac)*(sqrt(3)*(p_d^2) -
(pi/2)+((pi/2)*(rv_fac^2)))/(sqrt(3)*(p_d^2));
vf = (1-beo_frac)*(pi*((rfo^2)-(rfi^2)))/(((sqrt(3))/2)*(pitch_mm^2));

```

## C Example Input Decks

This appendix provides the MCNP/MCODE input deck used for the main focus of this work, the TID GFR core design. This input deck has been modified through numerous permutations in order to calculate and examine the parameters of interest discussed throughout this work. Consequently, it serves as the foundation for much of the neutronic work done in this research.

```
GFR SCO2 reflector, hex core, 3 zone BeO, AVE=569.375, unrodded, 11 ring
c the following are the input data to create this mcnp input deck
c TRU enrichment = 16.6%/16.6%/16.4%
c BeO volume fraction 30%/33%/00%
c SCO2 reflector
c 94.66% smeared dens. (9.35g/cc) (97% theo. Dens. & 97.588% smeared from
c calcs
c ODS Cladding
c
c Spent fuel vectors represent spent fuel from LWR fuel at ~30 MWd/kg
c after about a 30 year cooling period (i.e. nuclear fuel burned in the
c 1970s
c Pu vectors w/o
c      Pu238      Pu239      Pu240      Pu241      Pu242
c      0.0100     0.6300     0.2900     0.0100     0.0600
c MA vectors w/o
c      Np237      Am241      Am242      Am243      Cm244
c      0.3000     0.6450     0.000     0.0510     0.0040
c TRU vector
c Pu w/o  MA w/o
c 0.9     0.1
c
c      shielding blocks of boron carbide at 2.38 g/cc
c
c      cell numbering convention
c
c      first digit: type of cell:
c      1=fuel, 2=cladding,3=coolant,4=absorber,5=reflector,6=parfait,
c      7=control
c      second digit: 1=meat, 2=cladding, 3=coolant
```

```

c  third digit = identifier
c
c  mt density                geometry
111 1 8.9881E-02
    2    u=2 imp:n=1 vol=807722.6249 $ inner fuel
121 20 -7.2 1 -2 u=2 imp:n=1 $ inner cladding
131 30 4.978E-03 -1    u=2 imp:n=1    $ inner coolant
112 2 8.9881E-02
    3    u=92 imp:n=1 vol=74188.13597 $ inner fuel
113 3 9.1909E-02
    2    u=3 imp:n=1 vol=807722.6249 $ middle fuel
122 20 -7.2 1 -2 u=3 imp:n=1 $ middle cladding
132 30 4.978E-03 -1    u=3 imp:n=1    $ middle coolant
114 4 9.1909E-02
    3    u=93 imp:n=1 vol=74188.13597 $ middle fuel
115 5 6.9601E-02
    2    u=5 imp:n=1 vol=807722.6249 $ outer fuel
123 20 -7.2 1 -2 u=5 imp:n=1 $ outer cladding
133 30 4.978E-03 -1    u=5 imp:n=1    $ outer coolant
116 6 6.9601E-02
    3    u=95 imp:n=1 vol=74188.13597 $ outer fuel
c 117 7 1E-24
c    -3 u=94 imp:n=1 vol=1 $ dummy fuel cell
901 30 4.978E-03 -1    u=96 imp:n=1    $ corner cell for venting
902 30 4.978E-03 1    u=96 imp:n=1    $ corner cell for venting
511 50 5.7116E-02 2    u=4 imp:n=1    $ Ti radial reflector
521 20 -7.2 1 -2 u=4 imp:n=1 $ Radial Ti reflector cladding
531 30 4.978E-03 -1    u=4 imp:n=1    $ radial reflector coolant hole
512 50 5.7116E-02 2    u=8 imp:n=1    $ Axial Ti reflector
522 20 -7.2 1 -2 u=8 imp:n=1 $ Axial Ti reflector Cladding
532 30 4.978E-03 -1    u=8 imp:n=1    $ Axial Ti reflector Coolant
411 40 1.3755E-01 2    u=10 imp:n=1 $ Axial B4C shielding
421 20 -7.2 1 -2 u=10 imp:n=1 $ Axial B4C shield Cladding
431 30 4.978E-03 -1    u=10 imp:n=1 $ Axial B4C shield Coolant
412 40 1.3755E-01 2    u=7 imp:n=2 $ Radial B4C shielding
422 20 -7.2 1 -2 u=7 imp:n=2 $ Radial B4C shield Cladding
432 30 4.978E-03 -1    u=7 imp:n=2 $ Radial B4C shield Coolant
711 40 1.3755E-01 -1    u=16 imp:n=1 $ Shutdown rod control material
731 30 4.978E-03 1    u=16 imp:n=1 $ Shutdown rod coolant
712 30 4.978E-03 -1    u=18 imp:n=1 $ Shutdown rod empty assembly,
732 30 4.978E-03 1    u=18 imp:n=1 $ Shutdown rod empty assembly
1101 20 -7.2 -21 22 -23 -24 -25 -26 $ inner fuel
    imp:n=1 u=97 lat=2 fill=-10:10 -10:10 0:0
    0 0 0 0 0 0 0 0 0 0 96 92 92 92 92 92 92 92 92 92 96
    0 0 0 0 0 0 0 0 0 0 92 96 2 2 2 2 2 2 2 2 2 96 92
    0 0 0 0 0 0 0 0 0 92 2 2 2 2 2 2 2 2 2 2 2 92
    0 0 0 0 0 0 0 92 2 2 2 2 2 2 2 2 2 2 2 2 2 92
    0 0 0 0 0 0 92 2 2 2 2 2 2 2 2 2 2 2 2 2 2 92
    0 0 0 0 92 2 2 2 2 2 2 2 2 2 2 2 2 2 2 2 2 92
    0 0 92 2 2 2 2 2 2 2 2 2 2 2 2 2 2 2 2 2 2 92
    0 92 2 2 2 2 2 2 2 2 2 2 2 2 2 2 2 2 2 2 2 92
    96 96 2 2 2 2 2 2 2 2 2 2 2 2 2 2 2 2 2 2 2 96 96
    92 2 2 2 2 2 2 2 2 2 2 2 2 2 2 2 2 2 2 2 2 92 0
    92 2 2 2 2 2 2 2 2 2 2 2 2 2 2 2 2 2 2 2 2 92 0 0
    92 2 2 2 2 2 2 2 2 2 2 2 2 2 2 2 2 2 2 2 2 92 0 0 0

```

```

92 2 2 2 2 2 2 2 2 2 2 2 2 2 2 2 92 0 0 0 0
92 2 2 2 2 2 2 2 2 2 2 2 2 2 2 2 92 0 0 0 0
92 2 2 2 2 2 2 2 2 2 2 2 2 2 2 2 92 0 0 0 0
92 2 2 2 2 2 2 2 2 2 2 2 2 2 2 2 92 0 0 0 0
92 2 2 2 2 2 2 2 2 2 2 2 2 2 2 2 92 0 0 0 0
92 96 2 2 2 2 2 2 2 2 2 2 96 92 0 0 0 0 0 0 0 0
96 92 92 92 92 92 92 92 92 92 96 0 0 0 0 0 0 0 0 0 0
5001 20 -7.2 -27 -28 -29 30 -31 -32 $ part inside wall
      imp:n=1 u=87 lat=2 fill=-1:1 -1:1 0:0
      87 87 87
      87 97 87
      87 87 87
6001 30 4.978E-03 -47 -48 -49 50 -51 -52 $inner fuel block including
c bypass space
      imp:n=1 u=77 lat=2 fill=-1:1 -1:1 0:0
      77 77 77
      77 87 77
      77 77 77
1102 20 -7.2 -21 22 -23 -24 -25 -26 $ middle fuel
      imp:n=1 u=98 lat=2 fill=-10:10 -10:10 0:0
      0 0 0 0 0 0 0 0 0 0 96 93 93 93 93 93 93 93 93 93 96
      0 0 0 0 0 0 0 0 0 0 93 96 3 3 3 3 3 3 3 3 3 96 93
      0 0 0 0 0 0 0 0 93 3 3 3 3 3 3 3 3 3 3 3 93
      0 0 0 0 0 0 93 3 3 3 3 3 3 3 3 3 3 3 3 3 93
      0 0 0 0 0 93 3 3 3 3 3 3 3 3 3 3 3 3 3 3 93
      0 0 0 93 3 3 3 3 3 3 3 3 3 3 3 3 3 3 3 3 93
      0 0 93 3 3 3 3 3 3 3 3 3 3 3 3 3 3 3 3 3 93
      0 93 3 3 3 3 3 3 3 3 3 3 3 3 3 3 3 3 3 3 93
      96 96 3 3 3 3 3 3 3 3 3 3 3 3 3 3 3 3 3 3 96 96
      93 3 3 3 3 3 3 3 3 3 3 3 3 3 3 3 3 3 3 3 93 0
      93 3 3 3 3 3 3 3 3 3 3 3 3 3 3 3 3 3 3 3 93 0 0
      93 3 3 3 3 3 3 3 3 3 3 3 3 3 3 3 3 3 3 3 93 0 0 0
      93 3 3 3 3 3 3 3 3 3 3 3 3 3 3 3 3 3 3 3 93 0 0 0 0
      93 3 3 3 3 3 3 3 3 3 3 3 3 3 3 3 3 3 3 3 93 0 0 0 0
      93 3 3 3 3 3 3 3 3 3 3 3 3 3 3 93 0 0 0 0 0 0 0 0
      93 96 3 3 3 3 3 3 3 3 3 96 93 0 0 0 0 0 0 0 0 0 0
      96 93 93 93 93 93 93 93 93 93 96 0 0 0 0 0 0 0 0 0 0 0
5002 20 -7.2 -27 -28 -29 30 -31 -32 $ part inside wall
      imp:n=1 u=78 lat=2 fill=-1:1 -1:1 0:0
      78 78 78
      78 98 78
      78 78 78
6002 30 4.978E-03 -47 -48 -49 50 -51 -52 $inner fuel block
c w/bypass space
      imp:n=1 u=88 lat=2 fill=-1:1 -1:1 0:0
      88 88 88
      88 78 88
      88 88 88
1103 20 -7.2 -21 22 -23 -24 -25 -26 $ outer fuel
      imp:n=1 u=79 lat=2 fill=-10:10 -10:10 0:0
      0 0 0 0 0 0 0 0 0 0 96 95 95 95 95 95 95 95 95 95 96
      0 0 0 0 0 0 0 0 0 0 95 96 5 5 5 5 5 5 5 5 96 95
      0 0 0 0 0 0 0 0 95 5 5 5 5 5 5 5 5 5 5 5 95

```

```

0 0 0 0 0 0 0 95 5 5 5 5 5 5 5 5 5 5 5 5 95
0 0 0 0 0 0 95 5 5 5 5 5 5 5 5 5 5 5 5 5 95
0 0 0 0 0 95 5 5 5 5 5 5 5 5 5 5 5 5 5 5 95
0 0 0 0 95 5 5 5 5 5 5 5 5 5 5 5 5 5 5 5 95
0 0 95 5 5 5 5 5 5 5 5 5 5 5 5 5 5 5 5 5 95
0 95 5 5 5 5 5 5 5 5 5 5 5 5 5 5 5 5 5 5 95
96 96 5 5 5 5 5 5 5 5 5 5 5 5 5 5 5 5 5 5 96 96
95 5 5 5 5 5 5 5 5 5 5 5 5 5 5 5 5 5 5 5 95 0
95 5 5 5 5 5 5 5 5 5 5 5 5 5 5 5 5 5 5 5 95 0 0
95 5 5 5 5 5 5 5 5 5 5 5 5 5 5 5 5 5 5 95 0 0 0
95 5 5 5 5 5 5 5 5 5 5 5 5 5 5 5 5 95 0 0 0 0 0
95 5 5 5 5 5 5 5 5 5 5 5 5 5 5 5 95 0 0 0 0 0 0
95 5 5 5 5 5 5 5 5 5 5 5 5 5 5 95 0 0 0 0 0 0
95 5 5 5 5 5 5 5 5 5 5 5 5 5 95 0 0 0 0 0 0 0
95 96 5 5 5 5 5 5 5 5 96 95 0 0 0 0 0 0 0 0 0 0
96 95 95 95 95 95 95 95 95 95 96 0 0 0 0 0 0 0 0 0 0
5003 20 -7.2 -27 -28 -29 30 -31 -32 $ part inside wall
      imp:n=1 u=89 lat=2 fill=-1:1 -1:1 0:0
      89 89 89
      89 79 89
      89 89 89
6003 30 4.978E-03 -47 -48 -49 50 -51 -52 $outer fuel block including
c bypass space
      imp:n=1 u=99 lat=2 fill=-1:1 -1:1 0:0
      99 99 99
      99 89 99
      99 99 99
1106 30 4.978E-03 -21 22 -23 -24 -25 -26 $ control assembly w/outrods
      imp:n=1 u=19 lat=2 fill=-10:10 -10:10 0:0
      0 0 0 0 0 0 0 0 0 0 19 19 19 19 19 19 19 19 19 19
      0 0 0 0 0 0 0 0 0 19 18 18 18 18 18 18 18 18 18 19
      0 0 0 0 0 0 0 19 18 18 18 18 18 18 18 18 18 18 18 19
      0 0 0 0 0 19 18 18 18 18 18 18 18 18 18 18 18 18 18 19
      0 0 0 0 19 18 18 18 18 18 18 18 18 18 18 18 18 18 18 19
      0 0 19 18 18 18 18 18 18 18 18 18 18 18 18 18 18 18 19
      0 19 18 18 18 18 18 18 18 18 18 18 18 18 18 18 18 18 19
      19 18 18 18 18 18 18 18 18 18 18 18 18 18 18 18 18 18 19
      19 18 18 18 18 18 18 18 18 18 18 18 18 18 18 18 19 0 0
      19 18 18 18 18 18 18 18 18 18 18 18 18 18 18 19 0 0 0
      19 18 18 18 18 18 18 18 18 18 18 18 18 18 19 0 0 0 0
      19 18 18 18 18 18 18 18 18 18 18 18 18 19 0 0 0 0 0
      19 18 18 18 18 18 18 18 18 18 18 18 18 19 0 0 0 0 0
      19 18 18 18 18 18 18 18 18 18 18 18 19 0 0 0 0 0 0
      19 18 18 18 18 18 18 18 18 18 18 19 0 0 0 0 0 0 0
      19 19 19 19 19 19 19 19 19 19 0 0 0 0 0 0 0 0 0 0
506 20 -7.2 -27 -28 -29 30 -31 -32 $ part inside wall
      imp:n=1 lat=2 u=39 fill=-1:1 -1:1 0:0
      39 39 39
      39 19 39
      39 39 39

```









```

    imp:n=1 fill=0:21 -11:11 0:0 $score
0 0 0 0 0 0 0 0 0 0 0 0 0 0 0 0 0 0 0 0 24 24 24
0 0 0 0 0 0 0 0 0 0 0 0 0 0 0 0 0 0 0 0 24 24 24
0 0 0 0 0 0 0 0 0 0 0 0 0 0 0 0 0 0 0 0 24 24 24
0 0 0 0 0 0 0 0 0 0 0 0 0 0 0 0 0 74 74 24 24 24 24
0 0 0 0 0 0 0 0 0 0 0 0 0 0 0 24 24 74 74 74 24 24 24
0 0 0 0 0 0 0 0 0 0 0 0 0 24 24 24 74 74 74 24 24 24 24
0 0 0 0 0 0 0 0 0 0 99 99 24 24 24 74 74 74 24 24 24 24
0 0 0 0 0 0 0 88 88 99 99 24 24 24 74 74 74 24 24 24 24
0 0 0 0 0 77 88 88 88 99 99 24 24 24 74 74 74 24 24 24 24
0 0 0 0 77 77 77 88 70 88 99 99 24 24 24 74 74 74 24 24 24 24
0 0 77 77 77 77 77 88 88 88 99 99 24 24 24 74 74 74 24 24 24 24
70 77 77 77 70 77 77 77 88 88 99 99 24 24 24 74 74 74 24 24 24 24
0 77 77 77 77 77 88 88 88 99 99 24 24 24 74 74 74 24 24 24 24
0 0 77 77 77 88 70 88 99 99 24 24 24 74 74 74 24 24 24 24 24
0 0 0 77 88 88 88 99 99 24 24 24 74 74 74 24 24 24 24 24 24
0 0 0 0 88 88 99 99 24 24 24 74 74 74 24 24 24 24 24 24 24
0 0 0 0 0 99 99 24 24 24 74 74 74 24 24 24 24 24 24 24 24
0 0 0 0 0 0 24 24 24 74 74 74 24 24 24 24 24 24 24 24 24
0 0 0 0 0 0 0 24 74 74 74 24 24 24 24 24 24 24 24 24 24
0 0 0 0 0 0 0 0 74 74 24 24 24 24 24 24 24 24 24 24 24
0 0 0 0 0 0 0 0 0 24 24 24 24 24 24 24 24 24 24 24 24
0 0 0 0 0 0 0 0 0 0 24 24 24 24 24 24 24 24 24 24 24 24
0 0 0 0 0 0 0 0 0 0 24 24 24 24 24 24 24 24 24 24 24 24
21127 0          +61 +62 -501 403 -407 fill=24 imp:n=1 $ core
11131 30  4.978E-03    -33 -34 -35  36  -37 -38  u=22 lat=2
    imp:n=1 fill=0:21 -11:11 0:0
0 0 0 0 0 0 0 0 0 0 0 0 0 0 0 0 0 0 0 0 22 22 22 22
0 0 0 0 0 0 0 0 0 0 0 0 0 0 0 0 0 0 0 0 22 22 22 22
0 0 0 0 0 0 0 0 0 0 0 0 0 0 0 0 0 0 0 0 22 22 22 22
0 0 0 0 0 0 0 0 0 0 0 0 0 0 0 0 0 74 74 22 22 22 22
0 0 0 0 0 0 0 0 0 0 0 0 0 0 0 74 74 74 74 22 22 22 22
0 0 0 0 0 0 0 0 0 0 0 0 0 74 74 74 74 74 74 22 22 22 22
0 0 0 0 0 0 0 0 0 73 73 74 74 74 74 74 74 74 22 22 22 22
0 0 0 0 0 0 0 0 0 73 73 73 73 74 74 74 74 74 74 22 22 22 22
0 0 0 0 0 0 0 73 73 73 73 73 73 74 74 74 74 74 74 22 22 22 22
0 0 73 73 73 73 73 73 73 73 73 73 74 74 74 74 74 74 22 22 22 22
74 73 73 73 74 73 73 73 73 73 73 73 74 74 74 74 74 74 22 22 22 22
0 73 73 73 73 73 73 73 73 73 73 74 74 74 74 74 74 22 22 22 22
0 0 73 73 73 73 74 73 73 73 74 74 74 74 74 74 22 22 22 22 22
0 0 0 73 73 73 73 73 73 74 74 74 74 74 74 22 22 22 22 22 22
0 0 0 0 73 73 73 73 74 74 74 74 74 74 22 22 22 22 22 22 22
0 0 0 0 0 74 74 74 74 74 74 74 22 22 22 22 22 22 22 22 22
0 0 0 0 0 0 0 74 74 74 74 22 22 22 22 22 22 22 22 22 22
0 0 0 0 0 0 0 0 0 22 22 22 22 22 22 22 22 22 22 22 22
0 0 0 0 0 0 0 0 0 22 22 22 22 22 22 22 22 22 22 22 22
0 0 0 0 0 0 0 0 0 22 22 22 22 22 22 22 22 22 22 22 22
11132 0          +61 +62 -501 411 -402 fill=22 imp:n=1 $ lower shield
11140 30  4.978E-03    -33 -34 -35  36  -37 -38  u=20 lat=2
    imp:n=1 fill=0:21 -11:11 0:0
0 0 0 0 0 0 0 0 0 0 0 0 0 0 0 0 0 0 0 0 20 20 20 20
0 0 0 0 0 0 0 0 0 0 0 0 0 0 0 0 0 0 0 0 20 20 20 20
0 0 0 0 0 0 0 0 0 0 0 0 0 0 0 0 0 0 0 0 20 20 20 20
0 0 0 0 0 0 0 0 0 0 0 0 0 0 0 0 51 51 20 20 20 20

```

```

0 0 0 0 0 0 0 0 0 0 0 0 0 0 51 51 51 51 20 20 20 20
0 0 0 0 0 0 0 0 0 0 0 0 0 0 51 51 51 51 51 51 20 20 20 20
0 0 0 0 0 0 0 0 0 0 0 50 50 51 51 51 51 51 51 20 20 20 20
0 0 0 0 0 0 0 0 50 50 50 50 51 51 51 51 51 51 20 20 20 20
0 0 0 0 0 0 50 50 50 50 51 50 50 50 51 51 51 51 51 20 20 20 20
0 0 50 50 50 50 50 50 50 50 50 50 51 51 51 51 51 51 20 20 20 20
51 50 50 50 51 50 50 50 50 50 50 50 51 51 51 51 51 51 20 20 20 20
0 50 50 50 50 50 50 50 50 50 50 51 51 51 51 51 51 20 20 20 20
0 0 50 50 50 50 51 50 50 50 51 51 51 51 51 51 20 20 20 20 20
0 0 0 50 50 50 50 50 50 51 51 51 51 51 51 20 20 20 20 20 20
0 0 0 0 50 50 50 50 51 51 51 51 51 51 20 20 20 20 20 20 20
0 0 0 0 0 50 50 51 51 51 51 51 51 20 20 20 20 20 20 20 20
0 0 0 0 0 0 51 51 51 51 51 51 20 20 20 20 20 20 20 20 20
0 0 0 0 0 0 0 51 51 20 20 20 20 20 20 20 20 20 20 20 20
0 0 0 0 0 0 0 0 0 20 20 20 20 20 20 20 20 20 20 20 20
0 0 0 0 0 0 0 0 0 20 20 20 20 20 20 20 20 20 20 20 20
0 0 0 0 0 0 0 0 0 20 20 20 20 20 20 20 20 20 20 20 20
11141 0 +61 +62 -501 402 -403 fill=20 imp:n=1 $ bot ref
11150 30 4.978E-03 -33 -34 -35 36 -37 -38 u=21 lat=2
imp:n=1 fill=0:21 -11:11 0:0
0 0 0 0 0 0 0 0 0 0 0 0 0 0 0 0 0 0 21 21 21 21
0 0 0 0 0 0 0 0 0 0 0 0 0 0 0 0 0 0 21 21 21 21
0 0 0 0 0 0 0 0 0 0 0 0 0 0 0 0 0 0 21 21 21 21
0 0 0 0 0 0 0 0 0 0 0 0 0 0 0 0 51 51 21 21 21 21
0 0 0 0 0 0 0 0 0 0 0 0 0 0 0 51 51 51 51 21 21 21 21
0 0 0 0 0 0 0 0 0 0 0 0 0 51 51 51 51 51 51 21 21 21 21
0 0 0 0 0 0 0 0 0 50 50 51 51 51 51 51 51 21 21 21 21
0 0 0 0 0 0 0 0 50 50 50 50 51 51 51 51 51 51 21 21 21 21
0 0 0 0 0 0 50 50 50 50 50 50 51 51 51 51 51 51 21 21 21 21
0 0 50 50 50 50 50 50 50 50 50 50 51 51 51 51 51 51 21 21 21 21
71 50 50 50 71 50 50 50 50 50 50 50 51 51 51 51 51 51 21 21 21 21
0 50 50 50 50 50 50 50 50 50 50 51 51 51 51 51 51 21 21 21 21
0 0 50 50 50 50 71 50 50 50 51 51 51 51 51 51 21 21 21 21 21
0 0 0 50 50 50 50 50 51 51 51 51 51 51 21 21 21 21 21 21
0 0 0 0 0 50 50 51 51 51 51 51 51 21 21 21 21 21 21 21
0 0 0 0 0 0 51 51 51 51 51 51 21 21 21 21 21 21 21 21
0 0 0 0 0 0 0 51 51 21 21 21 21 21 21 21 21 21 21 21
0 0 0 0 0 0 0 0 0 21 21 21 21 21 21 21 21 21 21 21
0 0 0 0 0 0 0 0 0 21 21 21 21 21 21 21 21 21 21 21
0 0 0 0 0 0 0 0 0 21 21 21 21 21 21 21 21 21 21 21
11151 0 +61 +62 -501 407 -408 fill=21 imp:n=1 $ up ref
11133 30 4.978E-03 -33 -34 -35 36 -37 -38 u=23 lat=2
imp:n=1 fill=0:21 -11:11 0:0
0 0 0 0 0 0 0 0 0 0 0 0 0 0 0 0 0 0 23 23 23 23
0 0 0 0 0 0 0 0 0 0 0 0 0 0 0 0 0 0 23 23 23 23
0 0 0 0 0 0 0 0 0 0 0 0 0 0 0 0 0 0 23 23 23 23
0 0 0 0 0 0 0 0 0 0 0 0 0 0 0 0 74 74 23 23 23 23
0 0 0 0 0 0 0 0 0 0 0 0 0 0 0 74 74 74 74 23 23 23 23
0 0 0 0 0 0 0 0 0 0 0 0 0 73 73 74 74 74 74 23 23 23 23
0 0 0 0 0 0 0 0 73 73 73 73 74 74 74 74 74 74 23 23 23 23
0 0 0 0 0 0 73 73 73 73 73 73 74 74 74 74 74 74 23 23 23 23

```

```

0 0 0 0 73 73 73 73 71 73 73 73 74 74 74 74 74 74 23 23 23 23
0 0 73 73 73 73 73 73 73 73 73 73 74 74 74 74 74 74 23 23 23 23
71 73 73 73 71 73 73 73 73 73 73 73 74 74 74 74 74 74 23 23 23 23
0 73 73 73 73 73 73 73 73 73 73 74 74 74 74 74 74 23 23 23 23
0 0 73 73 73 73 71 73 73 73 74 74 74 74 74 74 23 23 23 23 23
0 0 0 73 73 73 73 73 74 74 74 74 74 74 23 23 23 23 23 23 23
0 0 0 0 73 73 73 73 74 74 74 74 74 74 23 23 23 23 23 23 23
0 0 0 0 0 73 73 74 74 74 74 74 74 23 23 23 23 23 23 23 23
0 0 0 0 0 0 74 74 74 74 74 74 23 23 23 23 23 23 23 23 23
0 0 0 0 0 0 0 74 74 74 74 23 23 23 23 23 23 23 23 23 23
0 0 0 0 0 0 0 0 74 74 23 23 23 23 23 23 23 23 23 23 23
0 0 0 0 0 0 0 0 0 23 23 23 23 23 23 23 23 23 23 23 23
0 0 0 0 0 0 0 0 0 23 23 23 23 23 23 23 23 23 23 23 23
0 0 0 0 0 0 0 0 0 23 23 23 23 23 23 23 23 23 23 23 23
11134 0 +61 +62 -501 408 -418 fill=23 imp:n=1 $ upper shield
11135 30 4.978E-03 -33 -34 -35 36 -37 -38 u=25 lat=2
      imp:n=1 fill=0:21 -11:11 0:0
0 0 0 0 0 0 0 0 0 0 0 0 0 0 0 0 0 0 25 25 25 25
0 0 0 0 0 0 0 0 0 0 0 0 0 0 0 0 0 0 25 25 25 25
0 0 0 0 0 0 0 0 0 0 0 0 0 0 0 0 0 0 25 25 25 25
0 0 0 0 0 0 0 0 0 0 0 0 0 0 0 0 0 0 25 25 25 25
0 0 0 0 0 0 0 0 0 0 0 0 0 0 0 0 25 25 25 25 25 25 25
0 0 0 0 0 0 0 0 0 0 0 25 25 25 25 25 25 25 25 25 25 25
0 0 0 0 0 0 0 0 25 25 25 25 25 25 25 25 25 25 25 25 25 25
0 0 0 0 0 0 25 25 25 25 71 25 25 25 25 25 25 25 25 25 25
0 0 25 25 25 25 25 25 25 25 25 25 25 25 25 25 25 25 25 25 25
71 25 25 25 71 25 25 25 25 25 25 25 25 25 25 25 25 25 25 25 25
0 25 25 25 25 25 25 25 25 25 25 25 25 25 25 25 25 25 25 25 25
0 0 25 25 25 25 71 25 25 25 25 25 25 25 25 25 25 25 25 25 25
0 0 0 25 25 25 25 25 25 25 25 25 25 25 25 25 25 25 25 25 25
0 0 0 0 25 25 25 25 25 25 25 25 25 25 25 25 25 25 25 25 25
0 0 0 0 0 25 25 25 25 25 25 25 25 25 25 25 25 25 25 25 25
0 0 0 0 0 0 0 25 25 25 25 25 25 25 25 25 25 25 25 25 25
0 0 0 0 0 0 0 0 25 25 25 25 25 25 25 25 25 25 25 25 25
0 0 0 0 0 0 0 0 0 25 25 25 25 25 25 25 25 25 25 25 25
0 0 0 0 0 0 0 0 0 25 25 25 25 25 25 25 25 25 25 25 25
11136 0 +61 +62 -501 418 -419 fill=25 imp:n=1 $ upper control rod region
51 20 -7.2 -501 61 62 401 -411 imp:n=1 $ lower plate
c 52 3 -7.2 -501 61 62 408 -409 imp:n=1 $ upper plate
403 30 4.978E-03 61 62 -501 419 -410 imp:n=1 $ chimney
404 30 4.978E-03 61 62 -503 400 -401 imp:n=1 $ l.plenum
405 20 -7.2 501 -502 61 62 401 -410 imp:n=1 $ core barrel
406 30 4.978E-03 502 -503 61 62 401 -410 imp:n=1 $ downcomer
407 20 -7.2 503 -504 61 62 400 -410 imp:n=1 $ vessel wall
99999 0 -61:-62: 504:-400:410 imp:n=0 $ outside
c end of cell specification

c surface specification
c
c trn card constants for equations
1 cz 0.35 $coolant chann radius
2 cz 0.42 $clad outer
3 cz 0.01 $small dummy hole for edge assemblies

```

```

c 4      cz      0.35                $clad outer - rad refl assem
21 px                0.6662                $plane 1 unit cell
22 px               -0.6662                $plane 2 unit cell
23 p  0.384873236447188  0.6662  0.0  0.513128393760849 $plane 3 unit cell
24 p -0.384873236447188 -0.6662  0.0  0.513128393760849 $plane 4 unit cell
25 p -0.384873236447188  0.6662  0.0  0.513128393760849 $plane 5 unit cell
26 p  0.384873236447188 -0.6662  0.0  0.513128393760849 $plane 6 unit cell
27 p  11.161325  6.4439939932629  0.0  143.8470225137100 $plane 1 fuel outer
28 p -11.161325 -6.4439939932629  0.0  143.8470225137100 $plane 2 fuel outer
29 py                11.161325                $ plane 3 fuel outer
30 py               -11.161325                $ plane 4 fuel outer
31 p -11.161325  6.4439939932629  0.0  143.8470225137100 $plane 5 fuel outer
32 p  11.161325 -6.4439939932629  0.0  143.8470225137100 $plane 6 fuel outer
33 p  11.161325  6.4439939932629  0.0  148.2289384291290 $plane 1 gas bypass
34 p -11.161325 -6.4439939932629  0.0  148.2289384291290 $plane 2 gas bypass
35 py                11.501325                $ plane 3 gas bypass space
36 py               -11.501325                $ plane 4 gas bypass space
37 p -11.161325  6.4439939932629  0.0  148.2289384291290 $plane 5 gas bypass
38 p  11.161325 -6.4439939932629  0.0  148.2289384291290 $plane 6 gas bypass
*61 p  1.732050807569 -1.0000000  0.0  0.00001 $ symmet for 1/6th core
c *61 p  0.57735026919 -1.0000000  0.0  0.00001 $ symmet for 1/12th core
*62 py                0.00001                $ symmetry
47 p  11.161325  6.4439939932629  0.0  146.4246201110150 $plane 1 duct outer
48 p -11.161325 -6.4439939932629  0.0  146.4246201110150 $plane 2 duct outer
49 py                11.361325                $ plane 3 duct wall outer
50 py               -11.361325                $ plane 4 duct wall outer
51 p -11.161325  6.4439939932629  0.0  146.4246201110150 $plane 5 duct outer
52 p  11.161325 -6.4439939932629  0.0  146.4246201110150 $plane 6 duct outer
400 pz                0                $ bottom boundary
401 pz                10.00                $ lower plate-bottom
411 pz                20.                $ lower shield bottom
402 pz                80.0                $ lower refl-bot
403 pz                120.0                $lower refl-top
407 pz                274.4                $ core-top
408 pz                314.4                $ upper ref-top
418 pz                374.4                $ upper shield top
419 pz                428.8                $ top of w/drawn control rods
410 pz                670.000                $ top boundary
501 cz                407.5                $ barrel in set to fit core
502 cz                413.5                $ barrel out set to 6cm thick
503 cz                443.5                $ vessel in set for 30cm downcome
504 cz                450.5                $ vessel out arbitrarily set
c      end of surface specification

```

```

c      data specification
c
c      problem type
mode  n
c
c      source specification
c
c      9. kcode criticality source card
c      nsrck rkk ikz kct msrk knrm
kcode 25000 1.0 25 75
prtmp 100 100 1
c ptrac file=asc nps=246,247 event=ter
c

```

```

c      10. ksrc  source point for kcode calculation
c      x1      y1      z1... location for initial source point
c ksrc      0.61      0.01      181.      0.61      0.01      202.
c           0.61      0.01      223.      0.61      0.01      244.
c           0.61      0.01      265.
c f15:n     207.      1.      340.      +0.98
c f25:n     179.2673  1.      340.      +0.98
c e15 1. 20.
c e25 1. 20.
c Flux tally at surface of reactor vessel
c f2:n      503
c fc2 flux tally at surface of reactor vessel
c fs2      -7001 -7002 -7003 -7004 -7005 -7006 -7007 -7008 -7009
c sd2      36051.316 3462.556 3462.556 3462.556 3462.556 3462.556 3462.556 3462.556
3462.556
c           3462.556 72713.672
c segment areas calculated by  $((2\pi R)/12)*(H)$ 
c where R = reactor vessel radius = 389 cm
c H= height of segment = 17 cm for middle segments, 177 for bottom, and
c 357 for top
c e2      0.1 1.0 10. T
c
c f4:n 115
c fc4 nu times microcopic fission cross section
c fm4 (1 1 (-6 -7))
c
c f14:n 115
c fc14 microcopic fission cross section
c fm14 (1 1 -6)
c
c f24:n 115
c fc24 fission q value
c fm24 (1 1 -8)
c
c f34:n 115
c fc34 flux in the fuel
c
c      1. fna tally card inner fuel cells
c f4:n (1101<5001<6001<11120[1 0 0]<21127)
c (1101<5001<6001<11120[2 0 0]<21127)
c (1101<5001<6001<11120[3 0 0]<21127)
c (1101<5001<6001<11120[4 0 0]<21127)
c (1101<5001<6001<11120[5 0 0]<21127)
c (1101<5001<6001<11120[6 0 0]<21127)
c (1101<5001<6001<11120[7 0 0]<21127)
c fc4 flux: inner fuel
c fm4 -1.6021917E-19 1 -6 -8
c sd4 40310.79939 40310.79939 40310.79939 40310.79939 40310.79939
c 40310.79939 40310.79939
c
c middle fuel cells
c f24:n (1102<5002<6002<11120[8 0 0]<21127)
c (1102<5002<6002<11120[9 0 0]<21127)
c fc24 flux: middle fuel
c fm24 -1.6021917E-19 3 -6 -8
c sd24 40310.79939 40310.79939
c

```

```

c outer fuel cells
c f34:n (1103<5003<6003<11120[10 0 0]<21127)
c (1103<5003<6003<11120[11 0 0]<21127)
c fc34 flux: outer fuel
c fm34 -1.6021917E-19 5 -6 -8
c sd34 40310.79939 40310.79939
c
c f104:n ( 111 )
c fc104 energy spectrum for inner fuel
c fm104 1.
c e104:n 1.000E-11 6.220E-10 6.874E-10 7.597E-10 8.396E-10 9.279E-10
c 1.026E-09 1.133E-09 1.253E-09 1.384E-09 1.530E-09 1.691E-09
c 1.869E-09 2.065E-09 2.282E-09 2.522E-09 2.788E-09 3.081E-09
c 3.405E-09 3.763E-09 4.159E-09 4.596E-09 5.079E-09 5.614E-09
c 6.204E-09 6.856E-09 7.578E-09 8.374E-09 9.255E-09 1.023E-08
c 1.130E-08 1.249E-08 1.381E-08 1.526E-08 1.686E-08 1.864E-08
c 2.060E-08 2.276E-08 2.516E-08 2.780E-08 3.073E-08 3.396E-08
c 3.753E-08 4.148E-08 4.584E-08 5.066E-08 5.599E-08 6.188E-08
c 6.839E-08 7.558E-08 8.353E-08 9.231E-08 1.020E-07 1.128E-07
c 1.246E-07 1.377E-07 1.522E-07 1.682E-07 1.859E-07 2.054E-07
c 2.271E-07 2.509E-07 2.773E-07 3.065E-07 3.387E-07 3.743E-07
c 4.137E-07 4.572E-07 5.053E-07 5.585E-07 6.172E-07 6.821E-07
c 7.538E-07 8.331E-07 9.207E-07 1.018E-06 1.125E-06 1.243E-06
c 1.374E-06 1.518E-06 1.678E-06 1.854E-06 2.049E-06 2.265E-06
c 2.503E-06 2.766E-06 3.057E-06 3.378E-06 3.734E-06 4.126E-06
c 4.560E-06 5.040E-06 5.570E-06 6.156E-06 6.803E-06 7.519E-06
c 8.310E-06 9.184E-06 1.015E-05 1.122E-05 1.240E-05 1.370E-05
c 1.514E-05 1.673E-05 1.849E-05 2.044E-05 2.259E-05 2.496E-05
c 2.759E-05 3.049E-05 3.370E-05 3.724E-05 4.116E-05 4.549E-05
c 5.027E-05 5.556E-05 6.140E-05 6.786E-05 7.500E-05 8.288E-05
c 9.160E-05 1.012E-04 1.119E-04 1.236E-04 1.367E-04 1.510E-04
c 1.669E-04 1.845E-04 2.039E-04 2.253E-04 2.490E-04 2.752E-04
c 3.041E-04 3.361E-04 3.715E-04 4.105E-04 4.537E-04 5.014E-04
c 5.541E-04 6.124E-04 6.768E-04 7.480E-04 8.267E-04 9.136E-04
c 1.010E-03 1.116E-03 1.233E-03 1.363E-03 1.506E-03 1.665E-03
c 1.840E-03 2.033E-03 2.247E-03 2.484E-03 2.745E-03 3.033E-03
c 3.352E-03 3.705E-03 4.095E-03 4.525E-03 5.001E-03 5.527E-03
c 6.108E-03 6.751E-03 7.461E-03 8.246E-03 9.113E-03 1.007E-02
c 1.113E-02 1.230E-02 1.359E-02 1.502E-02 1.660E-02 1.835E-02
c 2.028E-02 2.241E-02 2.477E-02 2.738E-02 3.026E-02 3.344E-02
c 3.695E-02 4.084E-02 4.514E-02 4.988E-02 5.513E-02 6.093E-02
c 6.733E-02 7.442E-02 8.224E-02 9.089E-02 1.005E-01 1.110E-01
c 1.227E-01 1.356E-01 1.499E-01 1.656E-01 1.830E-01 2.023E-01
c 2.236E-01 2.471E-01 2.731E-01 3.018E-01 3.335E-01 3.686E-01
c 4.074E-01 4.502E-01 4.975E-01 5.499E-01 6.077E-01 6.716E-01
c 7.422E-01 8.203E-01 9.066E-01 1.002E+00 1.107E+00 1.224E+00
c 1.352E+00 1.495E+00 1.652E+00 1.826E+00 2.018E+00 2.230E+00
c 2.464E+00 2.724E+00 3.010E+00 3.326E+00 3.676E+00 4.063E+00
c 4.490E+00 4.963E+00 5.484E+00 6.061E+00 6.699E+00 7.403E+00
c 8.182E+00 9.042E+00 1.000E+01 1.105E+01 1.221E+01 1.350E+01
c 1.492E+01 1.649E+01 1.822E+01 2.000E+01
c sd104 1396111.174
c f114:n ( 112 )
c fc114 energy spectrum for outer fuel
c fm114 1.
c e114:n 1.000E-11 6.220E-10 6.874E-10 7.597E-10 8.396E-10 9.279E-10
c 1.026E-09 1.133E-09 1.253E-09 1.384E-09 1.530E-09 1.691E-09

```



```

c      1.869E-09 2.065E-09 2.282E-09 2.522E-09 2.788E-09 3.081E-09
c      3.405E-09 3.763E-09 4.159E-09 4.596E-09 5.079E-09 5.614E-09
c      6.204E-09 6.856E-09 7.578E-09 8.374E-09 9.255E-09 1.023E-08
c      1.130E-08 1.249E-08 1.381E-08 1.526E-08 1.686E-08 1.864E-08
c      2.060E-08 2.276E-08 2.516E-08 2.780E-08 3.073E-08 3.396E-08
c      3.753E-08 4.148E-08 4.584E-08 5.066E-08 5.599E-08 6.188E-08
c      6.839E-08 7.558E-08 8.353E-08 9.231E-08 1.020E-07 1.128E-07
c      1.246E-07 1.377E-07 1.522E-07 1.682E-07 1.859E-07 2.054E-07
c      2.271E-07 2.509E-07 2.773E-07 3.065E-07 3.387E-07 3.743E-07
c      4.137E-07 4.572E-07 5.053E-07 5.585E-07 6.172E-07 6.821E-07
c      7.538E-07 8.331E-07 9.207E-07 1.018E-06 1.125E-06 1.243E-06
c      1.374E-06 1.518E-06 1.678E-06 1.854E-06 2.049E-06 2.265E-06
c      2.503E-06 2.766E-06 3.057E-06 3.378E-06 3.734E-06 4.126E-06
c      4.560E-06 5.040E-06 5.570E-06 6.156E-06 6.803E-06 7.519E-06
c      8.310E-06 9.184E-06 1.015E-05 1.122E-05 1.240E-05 1.370E-05
c      1.514E-05 1.673E-05 1.849E-05 2.044E-05 2.259E-05 2.496E-05
c      2.759E-05 3.049E-05 3.370E-05 3.724E-05 4.116E-05 4.549E-05
c      5.027E-05 5.556E-05 6.140E-05 6.786E-05 7.500E-05 8.288E-05
c      9.160E-05 1.012E-04 1.119E-04 1.236E-04 1.367E-04 1.510E-04
c      1.669E-04 1.845E-04 2.039E-04 2.253E-04 2.490E-04 2.752E-04
c      3.041E-04 3.361E-04 3.715E-04 4.105E-04 4.537E-04 5.014E-04
c      5.541E-04 6.124E-04 6.768E-04 7.480E-04 8.267E-04 9.136E-04
c      1.010E-03 1.116E-03 1.233E-03 1.363E-03 1.506E-03 1.665E-03
c      1.840E-03 2.033E-03 2.247E-03 2.484E-03 2.745E-03 3.033E-03
c      3.352E-03 3.705E-03 4.095E-03 4.525E-03 5.001E-03 5.527E-03
c      6.108E-03 6.751E-03 7.461E-03 8.246E-03 9.113E-03 1.007E-02
c      1.113E-02 1.230E-02 1.359E-02 1.502E-02 1.660E-02 1.835E-02
c      2.028E-02 2.241E-02 2.477E-02 2.738E-02 3.026E-02 3.344E-02
c      3.695E-02 4.084E-02 4.514E-02 4.988E-02 5.513E-02 6.093E-02
c      6.733E-02 7.442E-02 8.224E-02 9.089E-02 1.005E-01 1.110E-01
c      1.227E-01 1.356E-01 1.499E-01 1.656E-01 1.830E-01 2.023E-01
c      2.236E-01 2.471E-01 2.731E-01 3.018E-01 3.335E-01 3.686E-01
c      4.074E-01 4.502E-01 4.975E-01 5.499E-01 6.077E-01 6.716E-01
c      7.422E-01 8.203E-01 9.066E-01 1.002E+00 1.107E+00 1.224E+00
c      1.352E+00 1.495E+00 1.652E+00 1.826E+00 2.018E+00 2.230E+00
c      2.464E+00 2.724E+00 3.010E+00 3.326E+00 3.676E+00 4.063E+00
c      4.490E+00 4.963E+00 5.484E+00 6.061E+00 6.699E+00 7.403E+00
c      8.182E+00 9.042E+00 1.000E+01 1.105E+01 1.221E+01 1.350E+01
c      1.492E+01 1.649E+01 1.822E+01 2.000E+01
c sd114 1083857.747
c material specification
c
c 1. mm material card
c zaid1 fraction1 zaid2 fraction2 ....
c fuel meat (U,TRU)O2 16.6 w/o TRU enrichment with 30% BeO in inner
unit cells
m1      8016.54C 5.3061E-02 4009.78C 2.0580E-02 35081.55C 1.0000E-24
36083.50C 1.0000E-24 36084.50C 1.0000E-24 37085.55C 1.0000E-24
37087.55C 1.0000E-24 39089.42C 1.0000E-24 40090.86C 1.0000E-24
40091.86C 1.0000E-24 40092.86C 1.0000E-24 40093.86C 1.0000E-24
40094.86C 1.0000E-24 40096.86C 1.0000E-24 41095.96C 1.0000E-24
42095.50C 1.0000E-24 42096.96C 1.0000E-24 42097.60C 1.0000E-24
42098.50C 1.0000E-24 42100.50C 1.0000E-24 43099.60C 1.0000E-24
44100.96C 1.0000E-24 44101.50C 1.0000E-24 44102.60C 1.0000E-24
44103.50C 1.0000E-24 44104.96C 1.0000E-24 45103.86C 1.0000E-24
46104.96C 1.0000E-24 46105.50C 1.0000E-24 46106.96C 1.0000E-24
46107.96C 1.0000E-24 46108.50C 1.0000E-24 46110.96C 1.0000E-24

```

47109.86C	1.0000E-24	48110.86C	1.0000E-24	48111.86C	1.0000E-24	
48112.86C	1.0000E-24	48113.86C	1.0000E-24	48114.86C	1.0000E-24	
49115.60C	1.0000E-24	50117.96C	1.0000E-24	51121.96C	1.0000E-24	
51123.96C	1.0000E-24	52125.96C	1.0000E-24	52128.96C	1.0000E-24	
52130.96C	1.0000E-24	53127.86C	1.0000E-24	53129.86C	1.0000E-24	
54128.86C	1.0000E-24	54130.86C	1.0000E-24	54131.86C	1.0000E-24	
54132.86C	1.0000E-24	54134.86C	1.0000E-24	54136.86C	1.0000E-24	
55133.86C	1.0000E-24	55134.86C	1.0000E-24	55135.86C	1.0000E-24	
55137.86C	1.0000E-24	56130.96C	1.0000E-24	56132.96C	1.0000E-24	
56135.86C	1.0000E-24	56136.86C	1.0000E-24	56134.86C	1.0000E-24	
56137.86C	1.0000E-24	56138.86C	1.0000E-24	57139.60C	1.0000E-24	
58140.96C	1.0000E-24	58142.96C	1.0000E-24	59141.50C	1.0000E-24	
60142.96C	1.0000E-24	60143.50C	1.0000E-24	60144.96C	1.0000E-24	
60145.50C	1.0000E-24	60146.96C	1.0000E-24	60148.50C	1.0000E-24	
60150.96C	1.0000E-24	61147.50C	1.0000E-24	61148.50C	1.0000E-24	
62147.50C	1.0000E-24	62148.96C	1.0000E-24	62149.49C	1.0000E-24	
62150.49C	1.0000E-24	62151.50C	1.0000E-24	62152.49C	1.0000E-24	
62154.96C	1.0000E-24	63151.60C	1.0000E-24	63152.49C	1.0000E-24	
63153.60C	1.0000E-24	63154.49C	1.0000E-24	63155.50C	1.0000E-24	
64154.86C	1.0000E-24	64155.86C	1.0000E-24	64156.86C	1.0000E-24	
64157.86C	1.0000E-24	64158.86C	1.0000E-24	65159.96C	1.0000E-24	
66160.96C	1.0000E-24	66161.96C	1.0000E-24	66162.96C	1.0000E-24	
90232.86C	1.0000E-24	90233.09C	1.0000E-24	91231.09C	1.0000E-24	
91233.09C	1.0000E-24	92232.09C	1.0000E-24	92233.86C	1.0000E-24	
92234.86C	1.0000E-24	92236.86C	1.0000E-24	92237.86C	1.0000E-24	
92239.42C	1.0000E-24	93235.09C	1.0000E-24	93236.09C	1.0000E-24	
93238.09C	1.0000E-24	94237.86C	1.0000E-24	95242.92C	1.0000E-24	
96242.82C	1.0000E-24	96243.09C	1.0000E-24	96245.09C	1.0000E-24	
92235.16C	9.7627E-05	92238.16C	1.3461E-02	93237.82C	8.0329E-05	
94238.86C	2.4291E-05	94239.16C	1.5239E-03	94240.86C	6.9857E-04	
94241.86C	2.3989E-05	94242.86C	1.4334E-04	95241.82C	1.7192E-04	
95243.09C	1.3482E-05	96244.82C	1.0530E-06			
95242.98C	1.0000E-24	48115.96C	1.0000E-24	61148.91C	1.0000E-24	
c fuel meat (U,TRU)O2 16.6 w/o TRU enrichment with 30% BeO in side						
Cells						
m2	8016.54C	5.3061E-02	4009.78C	2.0580E-02	35081.55C	1.0000E-24
	36083.50C	1.0000E-24	36084.50C	1.0000E-24	37085.55C	1.0000E-24
	37087.55C	1.0000E-24	39089.42C	1.0000E-24	40090.86C	1.0000E-24
	40091.86C	1.0000E-24	40092.86C	1.0000E-24	40093.86C	1.0000E-24
	40094.86C	1.0000E-24	40096.86C	1.0000E-24	41095.96C	1.0000E-24
	42095.50C	1.0000E-24	42096.96C	1.0000E-24	42097.60C	1.0000E-24
	42098.50C	1.0000E-24	42100.50C	1.0000E-24	43099.60C	1.0000E-24
	44100.96C	1.0000E-24	44101.50C	1.0000E-24	44102.60C	1.0000E-24
	44103.50C	1.0000E-24	44104.96C	1.0000E-24	45103.86C	1.0000E-24
	46104.96C	1.0000E-24	46105.50C	1.0000E-24	46106.96C	1.0000E-24
	46107.96C	1.0000E-24	46108.50C	1.0000E-24	46110.96C	1.0000E-24
	47109.86C	1.0000E-24	48110.86C	1.0000E-24	48111.86C	1.0000E-24
	48112.86C	1.0000E-24	48113.86C	1.0000E-24	48114.86C	1.0000E-24
	49115.60C	1.0000E-24	50117.96C	1.0000E-24	51121.96C	1.0000E-24
	51123.96C	1.0000E-24	52125.96C	1.0000E-24	52128.96C	1.0000E-24
	52130.96C	1.0000E-24	53127.86C	1.0000E-24	53129.86C	1.0000E-24
	54128.86C	1.0000E-24	54130.86C	1.0000E-24	54131.86C	1.0000E-24
	54132.86C	1.0000E-24	54134.86C	1.0000E-24	54136.86C	1.0000E-24
	55133.86C	1.0000E-24	55134.86C	1.0000E-24	55135.86C	1.0000E-24
	55137.86C	1.0000E-24	56130.96C	1.0000E-24	56132.96C	1.0000E-24
	56135.86C	1.0000E-24	56136.86C	1.0000E-24	56134.86C	1.0000E-24
	56137.86C	1.0000E-24	56138.86C	1.0000E-24	57139.60C	1.0000E-24

58140.96C	1.0000E-24	58142.96C	1.0000E-24	59141.50C	1.0000E-24	
60142.96C	1.0000E-24	60143.50C	1.0000E-24	60144.96C	1.0000E-24	
60145.50C	1.0000E-24	60146.96C	1.0000E-24	60148.50C	1.0000E-24	
60150.96C	1.0000E-24	61147.50C	1.0000E-24	61148.50C	1.0000E-24	
62147.50C	1.0000E-24	62148.96C	1.0000E-24	62149.49C	1.0000E-24	
62150.49C	1.0000E-24	62151.50C	1.0000E-24	62152.49C	1.0000E-24	
62154.96C	1.0000E-24	63151.60C	1.0000E-24	63152.49C	1.0000E-24	
63153.60C	1.0000E-24	63154.49C	1.0000E-24	63155.50C	1.0000E-24	
64154.86C	1.0000E-24	64155.86C	1.0000E-24	64156.86C	1.0000E-24	
64157.86C	1.0000E-24	64158.86C	1.0000E-24	65159.96C	1.0000E-24	
66160.96C	1.0000E-24	66161.96C	1.0000E-24	66162.96C	1.0000E-24	
90232.86C	1.0000E-24	90233.09C	1.0000E-24	91231.09C	1.0000E-24	
91233.09C	1.0000E-24	92232.09C	1.0000E-24	92233.86C	1.0000E-24	
92234.86C	1.0000E-24	92236.86C	1.0000E-24	92237.86C	1.0000E-24	
92239.42C	1.0000E-24	93235.09C	1.0000E-24	93236.09C	1.0000E-24	
93238.09C	1.0000E-24	94237.86C	1.0000E-24	95242.92C	1.0000E-24	
96242.82C	1.0000E-24	96243.09C	1.0000E-24	96245.09C	1.0000E-24	
92235.16C	9.7627E-05	92238.16C	1.3461E-02	93237.82C	8.0329E-05	
94238.86C	2.4291E-05	94239.16C	1.5239E-03	94240.86C	6.9857E-04	
94241.86C	2.3989E-05	94242.86C	1.4334E-04	95241.82C	1.7192E-04	
95243.09C	1.3482E-05	96244.82C	1.0530E-06			
95242.98C	1.0000E-24	48115.96C	1.0000E-24	61148.91C	1.0000E-24	
c fuel meat (U,TRU)O2 16.6 w/o TRU enrichment with 33% BeO middle zone in inner unit Cells						
m3	8016.54C	5.3727E-02	4009.78C	2.2638E-02	35081.55C	1.0000E-24
	36083.50C	1.0000E-24	36084.50C	1.0000E-24	37085.55C	1.0000E-24
	37087.55C	1.0000E-24	39089.42C	1.0000E-24	40090.86C	1.0000E-24
	40091.86C	1.0000E-24	40092.86C	1.0000E-24	40093.86C	1.0000E-24
	40094.86C	1.0000E-24	40096.86C	1.0000E-24	41095.96C	1.0000E-24
	42095.50C	1.0000E-24	42096.96C	1.0000E-24	42097.60C	1.0000E-24
	42098.50C	1.0000E-24	42100.50C	1.0000E-24	43099.60C	1.0000E-24
	44100.96C	1.0000E-24	44101.50C	1.0000E-24	44102.60C	1.0000E-24
	44103.50C	1.0000E-24	44104.96C	1.0000E-24	45103.86C	1.0000E-24
	46104.96C	1.0000E-24	46105.50C	1.0000E-24	46106.96C	1.0000E-24
	46107.96C	1.0000E-24	46108.50C	1.0000E-24	46110.96C	1.0000E-24
	47109.86C	1.0000E-24	48110.86C	1.0000E-24	48111.86C	1.0000E-24
	48112.86C	1.0000E-24	48113.86C	1.0000E-24	48114.86C	1.0000E-24
	49115.60C	1.0000E-24	50117.96C	1.0000E-24	51121.96C	1.0000E-24
	51123.96C	1.0000E-24	52125.96C	1.0000E-24	52128.96C	1.0000E-24
	52130.96C	1.0000E-24	53127.86C	1.0000E-24	53129.86C	1.0000E-24
	54128.86C	1.0000E-24	54130.86C	1.0000E-24	54131.86C	1.0000E-24
	54132.86C	1.0000E-24	54134.86C	1.0000E-24	54136.86C	1.0000E-24
	55133.86C	1.0000E-24	55134.86C	1.0000E-24	55135.86C	1.0000E-24
	55137.86C	1.0000E-24	56130.96C	1.0000E-24	56132.96C	1.0000E-24
	56135.86C	1.0000E-24	56136.86C	1.0000E-24	56134.86C	1.0000E-24
	56137.86C	1.0000E-24	56138.86C	1.0000E-24	57139.60C	1.0000E-24
	58140.96C	1.0000E-24	58142.96C	1.0000E-24	59141.50C	1.0000E-24
	60142.96C	1.0000E-24	60143.50C	1.0000E-24	60144.96C	1.0000E-24
	60145.50C	1.0000E-24	60146.96C	1.0000E-24	60148.50C	1.0000E-24
	60150.96C	1.0000E-24	61147.50C	1.0000E-24	61148.50C	1.0000E-24
	62147.50C	1.0000E-24	62148.96C	1.0000E-24	62149.49C	1.0000E-24
	62150.49C	1.0000E-24	62151.50C	1.0000E-24	62152.49C	1.0000E-24
	62154.96C	1.0000E-24	63151.60C	1.0000E-24	63152.49C	1.0000E-24
	63153.60C	1.0000E-24	63154.49C	1.0000E-24	63155.50C	1.0000E-24
	64154.86C	1.0000E-24	64155.86C	1.0000E-24	64156.86C	1.0000E-24
	64157.86C	1.0000E-24	64158.86C	1.0000E-24	65159.96C	1.0000E-24
	66160.96C	1.0000E-24	66161.96C	1.0000E-24	66162.96C	1.0000E-24

90232.86C	1.0000E-24	90233.09C	1.0000E-24	91231.09C	1.0000E-24	
91233.09C	1.0000E-24	92232.09C	1.0000E-24	92233.86C	1.0000E-24	
92234.86C	1.0000E-24	92236.86C	1.0000E-24	92237.86C	1.0000E-24	
92239.42C	1.0000E-24	93235.09C	1.0000E-24	93236.09C	1.0000E-24	
93238.09C	1.0000E-24	94237.86C	1.0000E-24	95242.92C	1.0000E-24	
96242.82C	1.0000E-24	96243.09C	1.0000E-24	96245.09C	1.0000E-24	
92235.16C	9.3443E-05	92238.16C	1.2884E-02	93237.82C	7.6887E-05	
94238.86C	2.3250E-05	94239.16C	1.4586E-03	94240.86C	6.6863E-04	
94241.86C	2.2960E-05	94242.86C	1.3719E-04	95241.82C	1.6455E-04	
95243.09C	1.2904E-05	96244.82C	1.0079E-06			
95242.98C	1.0000E-24	48115.96C	1.0000E-24	61148.91C	1.0000E-24	
c fuel meat (U,TRU)O2 16.6 w/o TRU enrichment with 33% BeO middle zone in side cells						
m4	8016.54C	5.3727E-02	4009.78C	2.2638E-02	35081.55C	1.0000E-24
	36083.50C	1.0000E-24	36084.50C	1.0000E-24	37085.55C	1.0000E-24
	37087.55C	1.0000E-24	39089.42C	1.0000E-24	40090.86C	1.0000E-24
	40091.86C	1.0000E-24	40092.86C	1.0000E-24	40093.86C	1.0000E-24
	40094.86C	1.0000E-24	40096.86C	1.0000E-24	41095.96C	1.0000E-24
	42095.50C	1.0000E-24	42096.96C	1.0000E-24	42097.60C	1.0000E-24
	42098.50C	1.0000E-24	42100.50C	1.0000E-24	43099.60C	1.0000E-24
	44100.96C	1.0000E-24	44101.50C	1.0000E-24	44102.60C	1.0000E-24
	44103.50C	1.0000E-24	44104.96C	1.0000E-24	45103.86C	1.0000E-24
	46104.96C	1.0000E-24	46105.50C	1.0000E-24	46106.96C	1.0000E-24
	46107.96C	1.0000E-24	46108.50C	1.0000E-24	46110.96C	1.0000E-24
	47109.86C	1.0000E-24	48110.86C	1.0000E-24	48111.86C	1.0000E-24
	48112.86C	1.0000E-24	48113.86C	1.0000E-24	48114.86C	1.0000E-24
	49115.60C	1.0000E-24	50117.96C	1.0000E-24	51121.96C	1.0000E-24
	51123.96C	1.0000E-24	52125.96C	1.0000E-24	52128.96C	1.0000E-24
	52130.96C	1.0000E-24	53127.86C	1.0000E-24	53129.86C	1.0000E-24
	54128.86C	1.0000E-24	54130.86C	1.0000E-24	54131.86C	1.0000E-24
	54132.86C	1.0000E-24	54134.86C	1.0000E-24	54136.86C	1.0000E-24
	55133.86C	1.0000E-24	55134.86C	1.0000E-24	55135.86C	1.0000E-24
	55137.86C	1.0000E-24	56130.96C	1.0000E-24	56132.96C	1.0000E-24
	56135.86C	1.0000E-24	56136.86C	1.0000E-24	56134.86C	1.0000E-24
	56137.86C	1.0000E-24	56138.86C	1.0000E-24	57139.60C	1.0000E-24
	58140.96C	1.0000E-24	58142.96C	1.0000E-24	59141.50C	1.0000E-24
	60142.96C	1.0000E-24	60143.50C	1.0000E-24	60144.96C	1.0000E-24
	60145.50C	1.0000E-24	60146.96C	1.0000E-24	60148.50C	1.0000E-24
	60150.96C	1.0000E-24	61147.50C	1.0000E-24	61148.50C	1.0000E-24
	62147.50C	1.0000E-24	62148.96C	1.0000E-24	62149.49C	1.0000E-24
	62150.49C	1.0000E-24	62151.50C	1.0000E-24	62152.49C	1.0000E-24
	62154.96C	1.0000E-24	63151.60C	1.0000E-24	63152.49C	1.0000E-24
	63153.60C	1.0000E-24	63154.49C	1.0000E-24	63155.50C	1.0000E-24
	64154.86C	1.0000E-24	64155.86C	1.0000E-24	64156.86C	1.0000E-24
	64157.86C	1.0000E-24	64158.86C	1.0000E-24	65159.96C	1.0000E-24
	66160.96C	1.0000E-24	66161.96C	1.0000E-24	66162.96C	1.0000E-24
	90232.86C	1.0000E-24	90233.09C	1.0000E-24	91231.09C	1.0000E-24
	91233.09C	1.0000E-24	92232.09C	1.0000E-24	92233.86C	1.0000E-24
	92234.86C	1.0000E-24	92236.86C	1.0000E-24	92237.86C	1.0000E-24
	92239.42C	1.0000E-24	93235.09C	1.0000E-24	93236.09C	1.0000E-24
	93238.09C	1.0000E-24	94237.86C	1.0000E-24	95242.92C	1.0000E-24
	96242.82C	1.0000E-24	96243.09C	1.0000E-24	96245.09C	1.0000E-24
	92235.16C	9.3443E-05	92238.16C	1.2884E-02	93237.82C	7.6887E-05
	94238.86C	2.3250E-05	94239.16C	1.4586E-03	94240.86C	6.6863E-04
	94241.86C	2.2960E-05	94242.86C	1.3719E-04	95241.82C	1.6455E-04
	95243.09C	1.2904E-05	96244.82C	1.0079E-06		
	95242.98C	1.0000E-24	48115.96C	1.0000E-24	61148.91C	1.0000E-24

c fuel meat (U,TRU)O2 16.4 w/o TRU enrichment with 00% BeO outer zone  
in inner unit Cells

m5	8016.54C	4.6401E-02	35081.55C	9.9999E-25	36083.50C	9.9999E-25
	36084.50C	9.9999E-25	37085.55C	9.9999E-25	37087.55C	9.9999E-25
	39089.42C	9.9999E-25	40090.86C	9.9999E-25	40091.86C	9.9999E-25
	40092.86C	9.9999E-25	40093.86C	9.9999E-25	40094.86C	9.9999E-25
	40096.86C	9.9999E-25	41095.96C	9.9999E-25	42095.50C	9.9999E-25
	42096.96C	9.9999E-25	42097.60C	9.9999E-25	42098.50C	9.9999E-25
	42100.50C	9.9999E-25	43099.60C	9.9999E-25	44100.96C	9.9999E-25
	44101.50C	9.9999E-25	44102.60C	9.9999E-25	44103.50C	9.9999E-25
	44104.96C	9.9999E-25	45103.86C	9.9999E-25	46104.96C	9.9999E-25
	46105.50C	9.9999E-25	46106.96C	9.9999E-25	46107.96C	9.9999E-25
	46108.50C	9.9999E-25	46110.96C	9.9999E-25	47109.86C	9.9999E-25
	48110.86C	9.9999E-25	48111.86C	9.9999E-25	48112.86C	9.9999E-25
	48113.86C	9.9999E-25	48114.86C	9.9999E-25	49115.60C	9.9999E-25
	50117.96C	9.9999E-25	51121.96C	9.9999E-25	51123.96C	9.9999E-25
	52125.96C	9.9999E-25	52128.96C	9.9999E-25	52130.96C	9.9999E-25
	53127.86C	9.9999E-25	53129.86C	9.9999E-25	54128.86C	9.9999E-25
	54130.86C	9.9999E-25	54131.86C	9.9999E-25	54132.86C	9.9999E-25
	54134.86C	9.9999E-25	54136.86C	9.9999E-25	55133.86C	9.9999E-25
	55134.86C	9.9999E-25	55135.86C	9.9999E-25	55137.86C	9.9999E-25
	56130.96C	9.9999E-25	56132.96C	9.9999E-25	56135.86C	9.9999E-25
	56136.86C	9.9999E-25	56134.86C	9.9999E-25	56137.86C	9.9999E-25
	56138.86C	9.9999E-25	57139.60C	9.9999E-25	58140.96C	9.9999E-25
	58142.96C	9.9999E-25	59141.50C	9.9999E-25	60142.96C	9.9999E-25
	60143.50C	9.9999E-25	60144.96C	9.9999E-25	60145.50C	9.9999E-25
	60146.96C	9.9999E-25	60148.50C	9.9999E-25	60150.96C	9.9999E-25
	61147.50C	9.9999E-25	61148.50C	9.9999E-25	62147.50C	9.9999E-25
	62148.96C	9.9999E-25	62149.49C	9.9999E-25	62150.49C	9.9999E-25
	62151.50C	9.9999E-25	62152.49C	9.9999E-25	62154.96C	9.9999E-25
	63151.60C	9.9999E-25	63152.49C	9.9999E-25	63153.60C	9.9999E-25
	63154.49C	9.9999E-25	63155.50C	9.9999E-25	64154.86C	9.9999E-25
	64155.86C	9.9999E-25	64156.86C	9.9999E-25	64157.86C	9.9999E-25
	64158.86C	9.9999E-25	65159.96C	9.9999E-25	66160.96C	9.9999E-25
	66161.96C	9.9999E-25	66162.96C	9.9999E-25	90232.86C	9.9999E-25
	90233.09C	9.9999E-25	91231.09C	9.9999E-25	91233.09C	9.9999E-25
	92232.09C	9.9999E-25	92233.86C	9.9999E-25	92234.86C	9.9999E-25
	92236.86C	9.9999E-25	92237.86C	9.9999E-25	92239.42C	9.9999E-25
	93235.09C	9.9999E-25	93236.09C	9.9999E-25	93238.09C	9.9999E-25
	94237.86C	9.9999E-25	95242.92C	9.9999E-25	96242.82C	9.9999E-25
	96243.09C	9.9999E-25	96245.09C	9.9999E-25	92235.16C	1.3980E-04
	92238.16C	1.9276E-02	93237.82C	1.1337E-04	94238.86C	3.4283E-05
	94239.16C	2.1508E-03	94240.86C	9.8593E-04	94241.86C	3.3856E-05
	94242.86C	2.0230E-04	95241.82C	2.4264E-04	95243.09C	1.9027E-05
	96244.82C	1.4862E-06				
	95242.98C	1.0000E-24	48115.96C	1.0000E-24	61148.91C	1.0000E-24

c fuel meat (U,TRU)O2 16.2 w/o TRU enrichment with 00% BeO outer zone  
in side cells

m6	8016.54C	4.6401E-02	35081.55C	9.9999E-25	36083.50C	9.9999E-25
	36084.50C	9.9999E-25	37085.55C	9.9999E-25	37087.55C	9.9999E-25
	39089.42C	9.9999E-25	40090.86C	9.9999E-25	40091.86C	9.9999E-25
	40092.86C	9.9999E-25	40093.86C	9.9999E-25	40094.86C	9.9999E-25
	40096.86C	9.9999E-25	41095.96C	9.9999E-25	42095.50C	9.9999E-25
	42096.96C	9.9999E-25	42097.60C	9.9999E-25	42098.50C	9.9999E-25
	42100.50C	9.9999E-25	43099.60C	9.9999E-25	44100.96C	9.9999E-25
	44101.50C	9.9999E-25	44102.60C	9.9999E-25	44103.50C	9.9999E-25
	44104.96C	9.9999E-25	45103.86C	9.9999E-25	46104.96C	9.9999E-25

46105.50C	9.9999E-25	46106.96C	9.9999E-25	46107.96C	9.9999E-25
46108.50C	9.9999E-25	46110.96C	9.9999E-25	47109.86C	9.9999E-25
48110.86C	9.9999E-25	48111.86C	9.9999E-25	48112.86C	9.9999E-25
48113.86C	9.9999E-25	48114.86C	9.9999E-25	49115.60C	9.9999E-25
50117.96C	9.9999E-25	51121.96C	9.9999E-25	51123.96C	9.9999E-25
52125.96C	9.9999E-25	52128.96C	9.9999E-25	52130.96C	9.9999E-25
53127.86C	9.9999E-25	53129.86C	9.9999E-25	54128.86C	9.9999E-25
54130.86C	9.9999E-25	54131.86C	9.9999E-25	54132.86C	9.9999E-25
54134.86C	9.9999E-25	54136.86C	9.9999E-25	55133.86C	9.9999E-25
55134.86C	9.9999E-25	55135.86C	9.9999E-25	55137.86C	9.9999E-25
56130.96C	9.9999E-25	56132.96C	9.9999E-25	56135.86C	9.9999E-25
56136.86C	9.9999E-25	56134.86C	9.9999E-25	56137.86C	9.9999E-25
56138.86C	9.9999E-25	57139.60C	9.9999E-25	58140.96C	9.9999E-25
58142.96C	9.9999E-25	59141.50C	9.9999E-25	60142.96C	9.9999E-25
60143.50C	9.9999E-25	60144.96C	9.9999E-25	60145.50C	9.9999E-25
60146.96C	9.9999E-25	60148.50C	9.9999E-25	60150.96C	9.9999E-25
61147.50C	9.9999E-25	61148.50C	9.9999E-25	62147.50C	9.9999E-25
62148.96C	9.9999E-25	62149.49C	9.9999E-25	62150.49C	9.9999E-25
62151.50C	9.9999E-25	62152.49C	9.9999E-25	62154.96C	9.9999E-25
63151.60C	9.9999E-25	63152.49C	9.9999E-25	63153.60C	9.9999E-25
63154.49C	9.9999E-25	63155.50C	9.9999E-25	64154.86C	9.9999E-25
64155.86C	9.9999E-25	64156.86C	9.9999E-25	64157.86C	9.9999E-25
64158.86C	9.9999E-25	65159.96C	9.9999E-25	66160.96C	9.9999E-25
66161.96C	9.9999E-25	66162.96C	9.9999E-25	90232.86C	9.9999E-25
90233.09C	9.9999E-25	91231.09C	9.9999E-25	91233.09C	9.9999E-25
92232.09C	9.9999E-25	92233.86C	9.9999E-25	92234.86C	9.9999E-25
92236.86C	9.9999E-25	92237.86C	9.9999E-25	92239.42C	9.9999E-25
93235.09C	9.9999E-25	93236.09C	9.9999E-25	93238.09C	9.9999E-25
94237.86C	9.9999E-25	95242.92C	9.9999E-25	96242.82C	9.9999E-25
96243.09C	9.9999E-25	96245.09C	9.9999E-25	92235.16C	1.3980E-04
92238.16C	1.9276E-02	93237.82C	1.1337E-04	94238.86C	3.4283E-05
94239.16C	2.1508E-03	94240.86C	9.8593E-04	94241.86C	3.3856E-05
94242.86C	2.0230E-04	95241.82C	2.4264E-04	95243.09C	1.9027E-05
96244.82C	1.4862E-06				
95242.98C	1.0000E-24	48115.96C	1.0000E-24	61148.91C	1.0000E-24
c ODS steel					
m20	26054.10c		-.042454		
	26056.10c		-.684431		
	26057.10c		-.01595		
	26058.10c		-.002164		
c	26000.50c		-0.745	\$ Fe	
	24050.10c		-.008347		
	24052.10c		-.167402		
	24053.10c		-.019345		
	24054.10c		-.004907		
c	24000.50c		-0.200	\$ Cr	
	13027.10c		-0.045	\$ Al	
	22000.60c		-0.005	\$ Ti	
	06000.78c		-0.0005	\$ C	
	39089.42c		-0.00394	\$ Y	
	08016.78c		-0.00106	\$ O	
c					
m50	22000.60c	1.00		\$ reflector-Ti	
c					
c Titanium Carbide Reflector blocks					
m51	22000.60c	0.5		\$ Ti	
	6000.78c	0.5		\$ C	

```

c
c carbon dioxide coolant
m30      8016.54c    3.31849E-03    $ O2
          6000.78c    1.65925E-03    $ C
c boron carbide shielding
m40      6000.78c    0.20000          $ 99w/o enriched boron carbide
          5010.60c    0.7927
          5011.60c    0.0070

c
m41      1002.78c    .666666666    $ H2
          40000.60c    .333333333    $ Zr

c
c 7. void material void card
c void
c energy and thermal treatment specification
c
c 1. phys energy physics cutoff cards
c      emax  emcnf
phys:n   20   0.0
c
c 3. tmp free-gas thermal temperature card
c      t1n t2n...n=index of time,t1n=temp for cell 1 at time n
#      tmp1
111     8.38563E-08
121     8.38563E-08
131     8.38563E-08
112     8.38563E-08
113     8.38563E-08
122     8.38563E-08
132     8.38563E-08
114     8.38563E-08
115     8.38563E-08
123     8.38563E-08
133     8.38563E-08
116     8.38563E-08
c 117   8.38563E-08
901     8.38563E-08
902     8.38563E-08
511     8.38563E-08
521     8.38563E-08
531     8.38563E-08
512     8.38563E-08
522     8.38563E-08
532     8.38563E-08
411     8.38563E-08
421     8.38563E-08
431     8.38563E-08
412     8.38563E-08
422     8.38563E-08
432     8.38563E-08
711     8.38563E-08
731     8.38563E-08
712     8.38563E-08
732     8.38563E-08
1101    8.38563E-08
5001    8.38563E-08
6001    8.38563E-08

```

```

1102 8.38563E-08
5002 8.38563E-08
6002 8.38563E-08
1103 8.38563E-08
5003 8.38563E-08
6003 8.38563E-08
1106 8.38563E-08
506 8.38563E-08
606 8.38563E-08
1107 8.38563E-08
507 8.38563E-08
607 8.38563E-08
1108 5.71436E-08
508 5.71436E-08
608 5.71436E-08
1109 5.71436E-08
509 5.71436E-08
609 5.71436E-08
1104 8.38563E-08
504 8.38563E-08
604 8.38563E-08
1105 5.71436E-08
505 5.71436E-08
605 5.71436E-08
11120 5.71436E-08
11131 5.71436E-08
c 11135 5.71436E-08
c 11122 5.71436E-08
11132 5.71436E-08
11140 5.71436E-08
11133 5.71436E-08
11134 5.71436E-08
11135 5.71436E-08
11136 5.71436E-08
11141 5.71436E-08
11150 5.71436E-08
11151 5.71436E-08
c 21100 5.71436E-08
21127 5.71436E-08
51 5.71436E-08
403 7.52393E-08
404 3.90479E-08
405 3.90479E-08
406 3.90479E-08
407 3.90479E-08
99999 2.53e-08
c
c 4. thtme thermal times cards
thtme 0
c problem cutoff cards
c
c user data array
c
c periferal cards
c
print -60 -85 -130 -126 -128

```



```

c mcode221 input deck
c
mce /home/handwerk/bin/mcnp.exe
c          mcnp xs summary
mcxs /usr/local/bin/mcode22/mcnpxs.sum.csh
c  opt (0=no source, 1=source every mcnp, 2=source all through)
mcs 2 srctpl
c          executable
orge /usr/local/bin/origen22/origen22
c          org-library-path          decay          gamma
orgl /usr/local/bin/origen22/LIBS DECAY.LIB GXUO2BRM.LIB
c
c m#  vol(cc)          org-xs-lib  temp imp  mcnp-xs-opt  ntal
c          (K)          optional  optional
c          0=original (default)
c          1=new
1      846526.7871    FFTFC.LIB  900  -1.0    0          11
2      39930.42009   FFTFC.LIB  900  -1.0    0          11
3      846526.7871    FFTFC.LIB  900  -1.0    0          11
4      39930.42009   FFTFC.LIB  900  -1.0    0          11
5      846526.7871    FFTFC.LIB  900  -1.0    0          11
6      39930.42009   FFTFC.LIB  900  -1.0    0          11
c optional tally specification
c tal
c
c since vol is for the cell watts here is
c
pow 400000000 $ watts
c
nor 1 $ 1=flux(iterated) 2=flux(once)
c
cor 1 $ predictor-corrector, 0=OFF, 1=ON (1 mcnp) default, 2=ON (2 mcnp)
c
c depletion description
c  opt  days/BU  rel-pow-level  NMD
c  D/E  (absolute) (default 1, negative means decay only) (default 20)
dep  E   0.1      1          40      $1
      5         1          40      $2
      10        1          40      $3
      15        1          40      $4
      20        1          40      $5
      30        1          40      $6
      40        1          40      $7
      50        1          40      $8
      60        1          40      $9
      70        1          40     $10
      80        1          40     $11
      90        1          40     $12
     100        1          40     $13
     110        1          40     $14
     120        1          40     $15
     130        1          40     $16
     140        1          40     $17
     150        1          40     $18
mci -1
sta 0 $ start pint, default 0
end 18 $ end point, default max

```

## References

- ASTM** (American Society for Testing and Materials), “Standard Practice for Characterizing Neutron Exposures in Iron and Low Alloy Steels in Terms of Displacements Per Atom (DPA),” E693-01, ASTM Book of Standards, Vol. 12.02, 2005.
- Bakker, K.** and R. J. M. Konings, “On the Thermal Conductivity of Inert-Matrix Fuels Containing Americium Oxide”, *J. Nucl. Matl.* **254** (1998) 129–134.
- Blair, S.** “Thermal Hydraulic Performance Analysis of a Small Integral PWR Core,” Engineers Thesis, MIT, Department of Nuclear Engineering, September 2003.
- Briesmeister, J. F.** (editor), “MCNP™ — A General Monte Carlo N-Particle Transport Code, Version 4C,” LA-13709M, Los Alamos National Laboratory, April 2000.
- Bunn, M. et. al.**, “Interim Storage of Spent Nuclear Fuel: A Safe, Flexible, and Cost-Effective Near-Term Approach to Spent Fuel Management,” A Joint Report from the Harvard University Project on Managing the Atom and the University of Tokyo Project on Sociotechnics of Nuclear Energy, June 2001.
- Bunn, M. et. al.**, “The Economics of Reprocessing vs. Direct Disposal of Spent Nuclear Fuel,” Project on Managing the Atom, Belfer Center for Science and International Affairs, John F. Kennedy School of Government, Harvard University, Report# DE-FG26-99FT4028, December 2003.
- Buongiorno, J. et al.** “Supercritical Water Reactor (SCWR): Survey of Materials Experience and R&D Needs to Assess Viability,” INEEL/EXT-03-00693 (Rev. 1), September 2003.
- CANES** (Center for Advanced Nuclear Energy Systems), *Symposium on the Supercritical CO<sub>2</sub> Power Cycle for Next Generation Systems*, Massachusetts Institute of Technology, Cambridge, MA, March 6, 2007. (<http://web.mit.edu/canes/symposia/sco2/overview.html>)
- Capana, R.J.**, and J.R. Lindgren, “Irradiation Testing of Design Models for the GCFR Fuel Pressure Equalization (Vent) System,” *Nuclear Engineering and Design*, **26**, p. 201 (1974).
- Carré, F.**, “CEA R&D Plan for Gen. IV Systems: The Rationale for GFR,” presented at the Joint MIT/CEA Workshop, *Development of Gas Cooled Fast Reactors (GFR) and Their Nuclear Fuel Cycle*, January 13, 2005, MIT, Cambridge, MA, USA.
- Carstens, Nate**, “Speedup of MCNP(X) Parallel KCODE Execution Via Communication Algorithm Development and Beowulf Cluster Optimization,” SM thesis, Nuclear Engineering Department, MIT, January 2004.
- Carstens, N.**, P. Hejzlar, and M.J. Driscoll, “Control Systems Strategies and Dynamic Response for Supercritical CO<sub>2</sub> Power Conversion Cycles,” MIT-GFR-038, Sept. (2006).

- Chawla, R.** and R. J. M. Konings, "Categorisation [SIC] and Priorities for Future Research on Inert Matrix Fuels: An Extended Synthesis of the Panel Discussions," *Prog. Nuc. En.* **38** 3-4 (2001) 455-458.
- Cheng, S.K.,** and N. E. Todreas, "Hydrodynamic Models and Correlations for Bare and Wire-wrapped Hexagonal Rod Bundles – Bundle Friction Factors, Subchannel Friction Factors and Mixing Parameters," *Nuclear Engineering and Design*, **92**, pp. 227-251, 1986.
- Croff, A.G.,** "A User's Manual for the ORIGEN2 Computer Code," ORNL/TM-7175, Oak Ridge National Laboratory, July 1980.
- Degueldre, C. et al.,** "Thermal Conductivity of Zirconia Based Inert Matrix Fuel: Use and Abuse of the Formal Models for Testing New Experimental Data," *J. Nucl. Matl.* **319** (2003) 6-14.
- de Hoffmann, F.** and C.L. Rickard, "High Temperature Gas-Cooled Reactors," *Proceedings of the 3<sup>rd</sup> International Conference on the Peaceful Uses of Atomic Energy*, Vol. 5 (1965).
- de Podesta, M.,** *Understanding the Properties of Matter*, Taylor & Francis, Bristol, PA, 1996.
- Delaney, M.J.,** G. E. Apostolakis, and M. J. Driscoll, "Risk-Informed Design Guidance for Future Reactor Systems," *Nuclear Engineering and Design*, **235**, (2005).
- Dostal, V.,** M.J. Driscoll, and P. Hejzlar, "A Supercritical Carbon Dioxide Cycle for Next Generation Nuclear Reactors," MIT-ANP-TR-100, March 2004.
- Dostal, V.,** P. Hejzlar and M.J. Driscoll, "High-Performance Supercritical Carbon Dioxide Cycle for Next-Generation Nuclear Reactors," *Nuclear Technology*, 154, No. 3, June (2006).
- Dostal (b), V.,** P. Hejzlar and M.J. Driscoll, "The Supercritical Carbon Dioxide Power Cycle: Comparison to Other Advanced Power Cycles," *Nuclear Technology*, 154, No. 3, June (2006).
- Driscoll, M. J.,** T. J. Downar, and E. E. Pilat, *The Linear Reactivity Model for Nuclear Fuel Management*, American Nuclear Society, 1990.
- Driscoll, M. J.** and D. Kim, "The Need for Actinide Burner Reactor Fuel Cycle Cost Reduction," *Trans. Am. Nucl. Soc.*, **82**, 208-209 (2000).
- Driscoll, M.J.,** P. Hejzlar, N. E. Todreas, and B. Veto, "Modern Gas-Cooled Fast Reactor Safety Assurance Considerations," MIT-ANP-TR-087, May 2003.
- Forsberg, C.W.** and M. J. Driscoll, "Specialized Disposal Sites for Different Reprocessing Plant Waste," presented at the Materials Research Society Fall Meeting, November 30, 2006, Boston, MA, USA.

**Garcia-Delgado, L.** and N.E. Todreas, “Improvement in Nuclear Plant Capacity Factors Through Longer Cycle Length Operation: Final Report,” MIT-NFC-TR-011, July 1998.

**Garkisch, H.D.** and B. Petrovic, “Proposed correlations for cladding thickness and fuel-cladding gap for UO<sub>2</sub> and U-ZrH fuel in PWRs,” NERI02-189-WEC-04, Westinghouse Electric Company LLC Prepared under Sub-agreement No. SA3748-32244 Prime Grant DE-FG03-02SF22615, NERI Project 02-189: Use of Solid Hydride Fuel for Improved Long-Life LWR Core Designs, December 13, 2004.

**GBRA** (Gas Breeder Reactor Association), “The Gas Cooled Breeder Reactor – Economic Power with Breeding,” *Nucl. Eng. Intl.*, **19**, No. 218, July 1974.

**General Atomic Company**, “Gas-Cooled Fast Breeder Reactor Preliminary Safety Information Document: Amendment 10,” *GA-10298*, September (1980).

**General Electric**, *Lungmen Units 1&2 Preliminary Safety Analysis Report*. Available at: <http://japan.nonukesasiaforum.org/lungmen/> as of January 16, 2007.

**Gezelius, K., M.J. Driscoll, P. Hejzlar**, “Design of Compact Intermediate Heat Exchangers for Gas Cooled Fast Reactors,” MIT-ANP-TR-103, May (2004).

**Gibbs, J.P., P. Hejzlar, and M. J. Driscoll**, “Applicability of Supercritical CO<sub>2</sub> Power Conversion Systems to Gen IV Reactors,” MIT-GFR-037, September 2006.

**Gibbs, J.P., P. Hejzlar, Y. Gong, and M. J. Driscoll**, “Plant Layout for a 1200MWe Direct Brayton Cycle GFR,” *Trans. Am. Nucl. Soc.*, **96**, (2007).

**GIF** (Generation IV International Forum), “A Technology Roadmap for Generation IV Nuclear Energy Systems,” GIF-002-00, issued by the US DOE Nuclear Energy Research Advisory Committee and the Generation IV International Forum, 2002.

**Gratton, C. P.**, “The GCFR Revisited,” *Nuclear Energy*, **42**, No.1, February 2003, 25-34.

**Gratton, C. P.**, “The gas-cooled fast reactor in 1981,” *Nuclear Energy*, **20**, No.4, August 1981, 287-295.

**Haeck, W. et al.**, “Assessment of Americium and Curium Transmutation in Magnesia Based Targets in Differential Spectral Zones of an Experimental Accelerator Driven System,” *J. Nucl. Matl.* **352** (2006) 285-290.

**Handwerk, C. S. et al.**, “Economic Analysis of Extended Operating Cycles in Existing LWRs,” MIT-NFC-TR-007, January 1998.

**Hankel, R.** “Stress and Temperature Distributions,” *Nucleonics*, **18**, No. 11, November (1960).

**Heatric**<sup>TM</sup> webpage. Available at <http://www.heatric.com> accessed January 24, 2007.

**Hejzlar, P.**, “Conceptual Design of a Large, Passive, Pressure-Tube Light Water Reactor,” Sc.D. Thesis, Nuclear Engineering Department, MIT, May 1994.

**Hejzlar, P.**, M. J. Driscoll, and M. S. Kazimi, “High Performance Annular Fuel For Pressurized Water Reactors,” *Transactions of the American Nuclear Society*, Vol. 84, Milwaukee, June 17-21, p. 192, 2001.

**Hejzlar, P.**, D. Feng, Y. Yuan, M. S. Kazimi, H. Feinroth, B. Hao, E. J. Lahoda, and H. Hamilton, „The Design and Manufacturing of Annular Fuel for High Power Density and Improved Safety in PWRs“, *2004 International Meeting on LWR Fuel Performance*, Orlando, Florida, September 19-22, 2004.

**Hejzlar, P.**, “Reactor Physics Design Parameters for GFRs,” class lecture for course 22.39: *Elements of Reactor Design, Operations, and Safety*, Fall 2005, Massachusetts Institute of Technology, Cambridge, MA, Fall 2005.

**Hejzlar, P.**, V. Dostal, and M. J. Driscoll, “Assessment of Gas Cooled Fast Reactor with Indirect Supercritical CO<sub>2</sub> Cycle,” *Proceedings of the International Congress on Advanced Nuclear Power Plants 2005 (ICAPP '05)*, Seoul, Korea, May 15-19, 2005, Paper 5090, (2005).

**Hejzlar, P.**, "Do We Need Fast Actinide Burners for Waste Management?" Presentation at the MIT International Symposium: *Rethinking the Nuclear Fuel Cycle*, Cambridge, MA, October 30-31, 2006.

**Hejzlar, P.**, V. Dostal, and M. J. Driscoll, “A Supercritical CO<sub>2</sub> Cycle- a Promising Power Conversion System for Generation IV Reactors,” *Proceedings of the International Congress on Advanced Nuclear Power Plants 2006 (ICAPP '06)*, Reno, NV, June 4-8, 2006, Paper 6307, (2006).

**Hellwig, Ch. et al.** “Inert Matrix Fuel Behavior in Test Irradiations,” *J. Nucl. Matl.* **352** (2006) 291-299.

**Hickman, B.S.**, and A.W. Pryor, *Journal of Nuclear Materials*, **14**, pp. 96-110 (1964).

**Hu, Y.H.** and E. Ruckenstein, “The Characterization of a highly effective NiO/MgO solid solution catalyst in the CO<sub>2</sub> reforming of CH<sub>4</sub>,” *Catalysis Letters* **43** (1997) 71-77.

**IAEA** (International Atomic Energy Agency), “Reactivity Accidents,” Technical Report Series No. 354, Vienna, Austria, 1993.

**IAEA** (International Atomic Energy Agency), “Viability of Inert Matrix Fuel in Reducing Plutonium Amounts in Reactors,” IAEA-TECDOC-1516, August 2006.

- Jensen, M.B., L.G.M. Pettersson, O. Swang, and U. Olsbye,** “CO<sub>2</sub> Sorption on MgO and CaO Surfaces: A Comparative Quantum Chemical Cluster Study,” *J. Phys. Chem. B* **109** (2005) 16774-16781.
- Kawashima, K. et al.,** “Utilization of Fast Reactor Excess Neutrons for Burning Long Lived Fission Products,” *Prog. Nuc. En.* **29 (Supp.)** (1995) 281-288.
- Kazimi, M.S.,** “High Performance Fuel Design for Next Generation PWRs,” 1<sup>st</sup> Quarterly Progress Report, MIT-NFC-PR-001, MIT Department of Nuclear Engineering, November 2001.
- Kazimi, M.S.,** “High Performance Fuel Design for Next Generation PWRs: Final Report,” MIT-NFC-PR-082, MIT Department of Nuclear Engineering, January 2006.
- Keilholtz, G.W., J. E. Lee, Jr., R.E. Moore, and R.L. Hamner,** “Behavior of BeO Under Neutron Irradiation,” *Journal of Nuclear Materials*, **14**, pp. 87-95 (1964).
- Kemmish, W.B.,** “Gas-Cooled Fast Reactors,” *Nuclear Energy*, **21**, Feb. 1982.
- Kemmish, W.B., M.V. Quick, and I.L. Hirst,** “The Safety of CO<sub>2</sub> Cooled Breeder Reactors Based on Existing Gas Cooled Reactor Technology,” *Progress in Nuclear Energy*, **10**, No. 1, 1982.
- Khan, J.A., S. B. Pakala, T.W. Knight, J.S. Tulenko,** “Enhanced Thermal Conductivity for LWR Fuel,” *Transactions of the American Nuclear Society*, **93**, pp.469-470 (2005).
- Kondo, Y. and T. Takizuka,** “Technology Assessment of Partitioning Process,” JAERI-M-94-067 (1994).
- Kleykamp, H.,** “Selection of materials as diluents for burning of plutonium fuels in nuclear reactors”, *J. Nucl. Mater.* **275** (1999) 1–11.
- Kloosterman, J. L. and R. J.M. Konings** “Investigation of the Fuel Temperature Coefficient of Innovative Fuel Types,” Proceedings on the Workshop on Advanced Reactors with Innovative Fuels, PSI, Villigen, Switzerland, 21-23 October 1998.
- Konings, R. J. M. et al.,** “The EFTTRA-T4 Experiment on Americium Transmutation,” *J. Nucl. Matl.* **282** (2000) 159-170.
- Krivitski, I. Y. et al.,** “Neutronic and safety Aspects of Inert Matrix Fuel Utilization in Fast Reactors for Plutonium and Minor Actinides Transmutation,” *Prog. Nuc. En.* **38** 3-4 (2001) 391-394.
- Lahoda, E., J. Mazzocchi, and J. Beccherle,** “High Power Density Annular Fuel for PWRs: Manufacturing Costs and Economic Benefits,” accepted for publication in *Nuclear Technology*, 2007.

**LANL** (Los Alamos Nuclear Laboratory) "The NJOY Nuclear Data Processing System, Version 91," LA-12740-M, 1994.

**Legault, D.M., P. Hejzlar, and M. J. Driscoll,** "Effect of Pressure Drop in Brayton Cycle Efficiency Calculations," *Trans. Am. Nucl. Soc.*, **95**, (2006).

**Long, Y., Y. Zhang, and M. Kazimi,** "Inert Matrix Materials as Hosts of Actinide Nuclear Fuels," MIT-NFC-TR-055, March 2003.

**Malen, J. A., N. E. Todreas, & A. Romano,** "Thermal Hydraulic Design of Hydride Fueled PWR Cores," MIT-NFC-TR-062, MIT Department of Nuclear Engineering Internal Report and associated computer files, March 2004.

**McVean, R. L., R. W. Goin, A. Weitzburg, and A. Leridon,** "Critical Assembly Mockup of the SEFOR Reactor In ZPR-3," *Transactions of the American Nuclear Society*, **9**, (1966).

**Memmott, M.J., M. J. Driscoll, and P. Hejzlar,** "Synergistic Configuration of a GFR for Hydrogen Production by Steam Electrolysis," *Trans. Am. Nucl. Soc.*, **95**, (2006).

**Messaoudi, N. and J. Tommasi,** "Fast Burner Reactor Devoted to Minor Actinide Incineration," *Nucl. Tech.* **137** (2002) 84-96.

**Medvedev, P.,** "Development of Dual Phase Magnesia-Zirconia Ceramics for Light Water Reactor Inert Matrix Fuel", Ph.D. thesis, Texas A&M Univ., Dec. 2004.

**Meyer, Mitch,** Personal Communication by Phone, Idaho National Laboratory, December 13, 2006.

**NEA/OECD** (Nuclear Energy Agency/Organisation for Economic Co-operation and Development), "Accelerator-driven Systems (ADS) and Fast Reactors (FR) in Advanced Nuclear Fuel Cycles: A Comparative Study," NEA-3109, 2002.

**NEA/OECD** (Nuclear Energy Agency/Organisation for Economic Co-operation and Development), "Post Irradiation Examination for the Spent Fuel Samples: Calvert Cliffs-1," Spent Fuel Isotopic Composition Database, last accessed on March 30, 2007, available at [http://www.nea.fr/sfcompo/Ver.2/Eng/Calvert\\_Cliffs-1/index.html](http://www.nea.fr/sfcompo/Ver.2/Eng/Calvert_Cliffs-1/index.html).

**Neef, E. A. C. et al.,** "The EFTTRA-T3 Irradiation Experiment on Inert Matrix Fuels," *J. Nucl. Matl.* **320** (2003) 106-116.

**Nuclear News,** "Beryllium Contamination; IG: Control Procedures not followed at ORNL," Nov. 2006.

**Okano, Y., P. Hejzlar, N. E. Todreas, and M. J. Driscoll,** "Thermal-Hydraulics and Post-Shutdown Cooling of a CO<sub>2</sub>-Cooled, Gas Turbine Fast Reactor," *Trans. Am. Nucl. Soc.*, **86**, (2002).

**O'Driscoll**, W. G. et al., "Development of Zr Alloys Resistant to Gaseous Oxidation," Proceedings of the Second United Nations International Conference on the Peaceful Uses of Atomic Energy, Vol. 5, Paper P/1450, pp. 75-105, Geneva, September 1-13, 1958.

**O'Neill**, G.E. et. al., "A Technical and Economic Evaluation of Vented Fuel for Sodium-Cooled Fast Ceramic Reactors," GEAP-4770, May 1965.

**Opila**, E. J. and Q. N. Nguyen, "Oxidation of Chemically-Vapor-Deposited Silicon Carbide in Carbon Dioxide," *J. Am. Ceram. Soc.*, **81**, [7], 1998.

**ORNL** (Oak Ridge National Laboratory), ORNL DWG 95A-534. Oak Ridge, Tenn.: Oak Ridge National Laboratory, 1995.

**Pacchioni**, G., J. Ricart, and F. Illas, "Ab Initio Cluster Model Calculations on the Chemisorption of CO<sub>2</sub> and SO<sub>2</sub> Probe Molecules on MgO and CaO (100) Surfaces. A Theoretical Measure of Oxide Basicity," *J. Am. Chem. Soc.* **116** (1994) 10152-10158.

**Philipp**, R. and K. Fujimoto, "FTIR Spectroscopic Study of CO<sub>2</sub> Adsorption/Desorption on MgO/CaO Catalysts," *J. Phys. Chem.* **96** (1992) 9035-9038.

**Planchon**, H.P, J. I. Sackett, G. H. Golden, and R. H. Sevy, "Implications of the EBR-II Inherent Safety Demonstration Test," *Nucl. Eng. Des.*, **101**, (1987).

**Pope**, M.A. P. J. Yarsky, M. J. Driscoll, P. Hejzlar, and P. Saha., "An Advanced Vented Fuel Assembly for GFR Applications," *Trans. Am. Nucl. Soc.*, **92**, (2005).

**Pope**, M. A., M.J. Driscoll, P. Hejzlar, "Thermal Hydraulics of a 2400 MWth Supercritical CO<sub>2</sub>-Direct Cycle GFR," MIT-ANP-TR-112, September 2006.

**Poulter**, D.R. (ed.), *The Design of Gas-Cooled Graphite Moderated Reactors*, Oxford University Press, London, 1963.

**Roine**, A., Outokumpu HSC Chemistry® for Windows: Chemical Reaction and Equilibrium Software with Extensive Thermochemical Database, Version 5.1., User's Guide, 02103-ORC-T, Outokumpu Research Oy, Finland, 2002.

**Romano**, A., P. Hejzlar, N. E. Todreas "Optimization of Actinide Transmutation in Innovative Lead-Cooled Fast Reactors," MIT-NFC-TR-059, October 2003.

**Romano**, A. P. Hejzlar, and N. E. Todreas, "Fertile-Free Fast Lead Cooled Incinerators for Efficient Actinide Burning," *Nucl. Tech.* **147** (2004) 368-387.

**Ronchi**, C. et al., "Thermophysical Properties of Inert Matrix Fuels for Actinide Transmutation," *J. Nucl. Matl.* **320** (2003) 54-65.



**Ronen, Y., M. Aboudy, and D. Regev, "Breeding of  $^{242m}\text{Am}$  in a Fast Reactor," *Nucl. Tech.* **153** (2006) 224-233.**

**Sari, C. et al., "Interaction of U-Pu-Zr alloys containing minor actinides and rare earths with stainless steel," *J. Nucl. Matl.* **208** (1994) 201-210.**

**Sarma, K.H., J. Fourcade, S-G Lee and A.A. Solomon, "New Processing Methods to Produce Silicon Carbide and Beryllium Oxide Inert Matrix and Enhanced Thermal Conductivity Oxide Fuels," *European Materials Research Society Spring Meeting, Strasbourg, France, May 31-June 3* (2005).**

**Shenoy, A., L. Parme, M. LaBar, "The Gas Cooled Fast Breeder Reactor 1960-1980," GLOBAL-2003, New Orleans, LA, November 16-20, 2003.**

**Shwageraus, E., and P. Hejzlar, M. Kazimi, "Optimization of the LWR Nuclear Fuel Cycle for Minimum Waste Production," MIT-NFC-TR-060, October 2003.**

**Shwageraus, E., Ben Gurion University of the Negev, Personal Communication, 2007.**

**Special Metals, Inc., Publication number SMC-008, September (2004).**

**Stahle, P. W., M. J. Driscoll, and P. Hejzlar, "Supercritical CO<sub>2</sub> Power Conversion System Design and Layout for 300 MW<sub>e</sub> Plant," MIT-GFR-025R, September 2005.**

**Todreas, N.E. and M.S. Kazimi, *Nuclear Systems I: Thermal Hydraulic Fundamentals*, Hemisphere Publishing Corporation, New York, NY, 1990.**

**Todreas, N. E. and P. Hejzlar, "Flexible Conversion Ratio Fast Reactor Systems Evaluation: 3<sup>rd</sup> Quarterly Report," MIT-NFC-PR-090, January 2007.**

**Tuček, K., J. Carlsson, and H. Wider, "Lead-Cooled Breeders and Burners – are the latter Even Necessary?," *American Nuclear Society's Topical Meeting on Reactor Physics (PHYSOR 2006)*, Vancouver, BC, Canada, September 10-14, 2006.**

**Tommasi, J., M. Delpech, and J. Grouiller, "Long Lived Waste Transmutation in Reactors," *Nucl. Tech.* **111** (1995) 133-147.**

**Thon, S., "Selection of Materials for a Supercritical CO<sub>2</sub> Cooled GCFR," MIT-GCFR-001, August 2002.**

**UKAEA (United Kingdom Atomic Energy Authority), "The Dounreay Fast Reactor," informational brochure, Jan. 2004. Last accessed on March 22, 2007 at: [http://www.ukaea.org.uk/downloads/dounreay/dounreay\\_fast\\_reactor.pdf](http://www.ukaea.org.uk/downloads/dounreay/dounreay_fast_reactor.pdf).**

**USAEC**, (United States Atomic Energy Commission), "Naval Reactors Physics Handbook, Volume III: The Physics of Intermediate Spectrum Reactors," J. R. Stehn, Ed., Knowles Atomic Power Laboratory, Sept. 1958.

**USDOE** (United States Department of Energy), Report of the Nonproliferation Alternative Systems Assessment Program, Vol. IX: Reactor and Fuel Cycle Description, NE-0001 through 9, June 1980.

**USDOE** (United States Department of Energy), "Nonproliferation and Arms Control Assessment of Weapon-Usable Fissile Material Storage and Excess Plutonium Disposition Alternatives," (Springfield, Va.: National Technical Information Services:1997), pp. 5, 37-39.

**USNRC** (United States Nuclear Regulatory Commission), *Regulatory Guide 1.99*, Rev. 2, May 1988.

**USNRC** (United States Nuclear Regulatory Commission), "Incorporating Aging Effects into Probabilistic Risk Assessment — A Feasibility Study Utilizing Reliability Physics Models," NUREG/CR-5632, August 2001.

**USNRC** (United States Nuclear Regulatory Commission), "Final Safety Evaluation Report Related to Certification of the AP1000 Standard Design", NUREG-1793, September 2004.

**Venkatesh**, M. C., "Radiation Embrittlement of Chromium Martensitic Steels," Internal memo, General Atomics Corporation, March 2004.

**Wade**, D.C., and Y. I. Chang, "The Integral Fast Reactor Concept: Physics of Operation and Safety", *Nucl. Sci. Eng.* **100**, (1988) 507-524.

**Wade**, D.C., and R. N. Hill, "The Design Rationale of the IFR", *Prog. Nucl. Energy* **31**, (1997) 13-42.

**Waltar**, A.E. and A.B. Reynolds, *Fast Breeder Reactors*, Pergamon Press, New York, 1981.

**Weaver**, K.D., J. Carbonnier, T. Mizuno, J. Rouault, T.Y.C. Wei, M.J. Driscoll, "Generation IV Nuclear Reactors: The Gas-Cooled Fast Reactor (GFR)," *Proceedings of the 14th Pacific Basin Nuclear Conference*, Honolulu, Hawaii, March 21-25, 2004.

**Westlen**, D. and J. Wallenius, "Neutronic and Safety Aspects of a Gas-Cooled Subcritical Core for Minor Actinide Transmutation," *Nuc. Tech.*, **154** (2006) 41-51.

**Xu**, Zhiwen et al., "An Improved MCNP-ORIGEN Depletion Program (MCODE) and its Verification for High-Burnup Applications," *International Conference on the New Frontiers of Nuclear Technology: Reactor Physics, Safety and High-Performance Computing (PHYSOR 2002)*, Seoul, Korea, October 7-10, 2002.

**Xu, Zhiwen**, “Design Strategies for Optimizing High Burnup Fuel in Pressurized Water Reactors,” Ph.D. thesis, Nuclear Engineering Department, MIT, January 2003.

**Xu, Z. et al.**, “MCNP Simulation of High Temperature Irradiation Facility (HTIF) in the MIT Research Reactor ,” *Massachusetts Institute of Technology, Center for Advanced Nuclear Energy Systems (CANES) Internal Report*, Revised November 10, 2004.

**Xu, Z.**, P. Hejzlar, and M. S. Kazimi, “MCODE, Version 2.2 – An MCNP-ORIGEN DEpletion Program,” MIT Department of Nuclear Science and Engineering Internal Report, February 2006.

**Xu, Zhiwen**, Studsvik Scandpower, personal communication, 2007.

**Yarsky, P.**, M.J. Driscoll, P. Hejzlar, “Integrated Design of a Breed and Burn Gas-cooled Fast Reactor Core,” MIT-ANP-TR-107, September 2005.